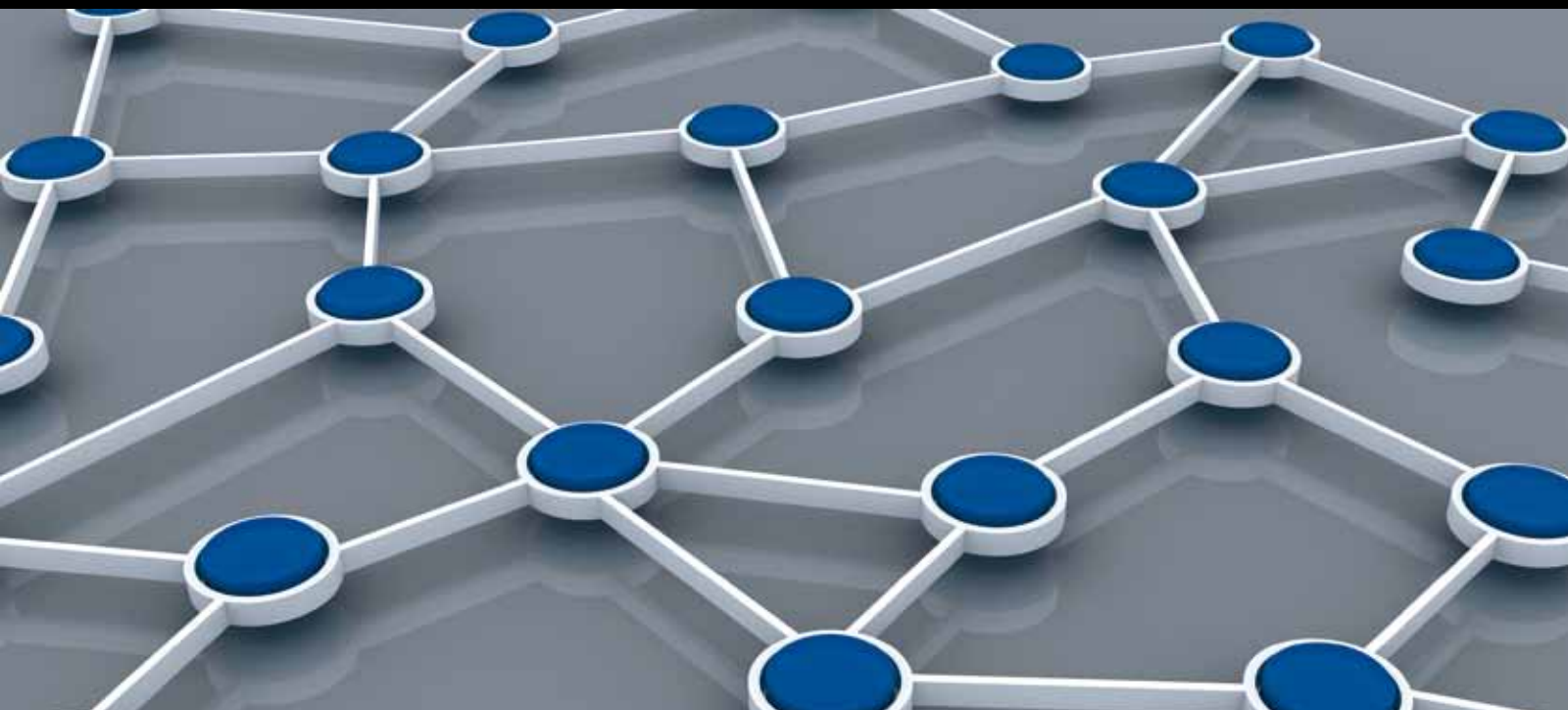


SENSING METHODOLOGIES AND SENSOR NETWORKS FOR HEALTH MONITORING OF CIVIL INFRASTRUCTURES 2013

GUEST EDITORS: HONG-NAN LI, GANGBING SONG, JEONG-TAE KIM, AND TING-HUA YI





**Sensing Methodologies and Sensor Networks for
Health Monitoring of Civil Infrastructures 2013**

International Journal of Distributed Sensor Networks

**Sensing Methodologies and Sensor Networks for
Health Monitoring of Civil Infrastructures 2013**

Guest Editors: Hong-Nan Li, Gangbing Song, Jeong-Tae Kim,
and Ting-Hua Yi



Copyright © 2014 Hindawi Publishing Corporation. All rights reserved.

This is a special issue published in “International Journal of Distributed Sensor Networks.” All articles are open access articles distributed under the Creative Commons Attribution License, which permits unrestricted use, distribution, and reproduction in any medium, provided the original work is properly cited.

Editorial Board

Miguel Acevedo, USA
Sanghyun Ahn, Korea
Mohammad Ali, USA
Jamal N. Al-Karaki, Jordan
Habib M. Ammari, USA
Javier Bajo, Spain
Prabir Barooah, USA
Alessandro Bogliolo, Italy
Richard R. Brooks, USA
James Brusey, UK
Erik Buchmann, Germany
Jian-Nong Cao, Hong Kong
João Paulo Carmo, Portugal
Jesús Carretero, Spain
Luca Catarinucci, Italy
Henry Chan, Hong Kong
Chih-Yung Chang, Taiwan
Periklis Chatzimisios, Greece
Ai Chen, China
Peng Cheng, China
Jinsung Cho, Korea
Kim-Kwang Choo, Australia
Chi-Yin Chow, Hong Kong
W.-Y. Chung, Republic of Korea
Mauro Conti, Italy
Dinesh Datla, USA
Amitava Datta, Australia
Danilo De Donno, Italy
Ilker Demirkol, Spain
Der-Jiunn Deng, Taiwan
Longjun Dong, China
Chyi-Ren Dow, Taiwan
George P. Efthymoglou, Greece
Frank Ehlers, Italy
Melike Erol-Kantarci, Canada
Giancarlo Fortino, Italy
Luca Foschini, Italy
David Galindo, France
Weihua Gao, USA
Deyun Gao, China
Athanasios Gkelias, UK
Iqbal Gondal, Australia
Jayavardhana Gubbi, Australia
Cagri Gungor, Turkey
Song Guo, Japan

Andrei Gurtov, Finland
Qi Han, USA
Zdenek Hanzalek, Czech Republic
Tian He, USA
Junyoung Heo, Korea
Zujun Hou, Singapore
Jiun-Long Huang, Taiwan
Yung-Fa Huang, Taiwan
Xinming Huang, USA
Baoqi Huang, China
Chin-Tser Huang, USA
Wei Huangfu, China
Mohamed Ibnkahla, Canada
Tan Jindong, USA
Ibrahim Kamel, UAE
Li-Wei Kang, Taiwan
Rajgopal Kannan, USA
Sherif Khattab, Egypt
Lisimachos Kondi, Greece
Marwan Krunz, USA
Kun-Chan Lan, Taiwan
Yee W. Law, Australia
Young-Koo Lee, Republic of Korea
JongHyup Lee, Korea
Kyung-Chang Lee, Korea
Yong Lee, USA
Sungyoung Lee, Republic of Korea
Seokcheon Lee, USA
Joo-Ho Lee, Japan
Shijian Li, China
Minglu Li, China
Shuai Li, USA
Zhen Li, China
Shancang Li, UK
Ye Li, China
Jing Liang, China
Weifa Liang, Australia
Yao Liang, USA
Wen-Hwa Liao, Taiwan
Alvin S. Lim, USA
Kai Lin, China
Zhong Liu, China
Ming Liu, China
Donggang Liu, USA
Yonghe Liu, USA

Chuan-Ming Liu, Taiwan
Zhigang Liu, China
Leonardo Lizzi, France
Giuseppe Lo Re, Italy
Seng Loke, Australia
Jonathan Loo, UK
Juan Riquelme, Spain
Pascal Lorenz, France
KingShan Lui, Hong Kong
Jun Luo, Singapore
Álvaro Marco, Spain
Jose Martinez-de Dios, Spain
Nirvana Meratnia, The Netherlands
Shabbir N. Merchant, India
Mihael Mohorcic, Slovenia
José Molina, Spain
Vallipuram Muthukkumarasamy, Australia
Eduardo Freire Nakamura, Brazil
Kameswara Rao Namuduri, USA
George Nikolakopoulos, Sweden
Marimuthu Palaniswami, Australia
Ai-Chun Pang, Taiwan
Seung-Jong J. Park, USA
Soo-Hyun Park, Korea
Miguel A. Patricio, Spain
Wen-Chih Peng, Taiwan
Janez Perš, Slovenia
Dirk Pesch, Ireland
Shashi Phoha, USA
Antonio Puliafito, Italy
Hairong Qi, USA
Nageswara S. V. Rao, USA
Md. Abdur Razzaque, Bangladesh
Pedro Pereira Rodrigues, Portugal
Joel J. P. C. Rodrigues, Portugal
Jorge Sa Silva, Portugal
Mohamed Saad, UAE
Sanat Sarangi, India
Stefano Savazzi, Italy
Marco Scarpa, Italy
Arunabha Sen, USA
Xiao-Jing Shen, China
Weihua Sheng, USA
Louis Shue, Singapore
Antonino Staiano, Italy



Tan-Hsu Tan, Taiwan
Guozhen Tan, China
Shaojie Tang, USA
Bulent Tavli, Turkey
Anthony Tzes, Greece
Agustinus B. Waluyo, Australia
Yu Wang, USA
Ran Wolff, Israel
Jianshe Wu, China
Wen-Jong Wu, Taiwan

Chase Qishi Wu, USA
Bin Xiao, Hong Kong
Qin Xin, Faroe Islands
Jianliang Xu, Hong Kong
Yuan Xue, USA
Ting Yang, China
Hong-Hsu Yen, Taiwan
Li-Hsing Yen, Taiwan
Seong-eun Yoo, Korea
Ning Yu, China

Changyuan Yu, Singapore
Tianle Zhang, China
Yanmin Zhu, China
T. L. Zhu, USA
Yi-hua Zhu, China
Qingxin Zhu, China
Li Zhuo, China
Shihong Zou, China

Contents

Sensing Methodologies and Sensor Networks for Health Monitoring of Civil Infrastructures 2013, Hong-Nan Li, Gangbing Song, Jeong-Tae Kim, and Ting-Hua Yi
Volume 2014, Article ID 739807, 2 pages

Corrosion Monitoring and Evaluation of Reinforced Concrete Structures Utilizing the Ultrasonic Guided Wave Technique, Dongsheng Li, Shuaifang Zhang, Wei Yang, and Wenyao Zhang
Volume 2014, Article ID 827130, 9 pages

Application of Sensor Networks to the Measurement of Subway-Induced Ground-Borne Vibration Near the Station, Hong Zhong, Di Qu, Gao Lin, and Hongjun Li
Volume 2014, Article ID 181453, 10 pages

Thermal Load in Large-Scale Bridges: A State-of-the-Art Review, Guang-Dong Zhou and Ting-Hua Yi
Volume 2013, Article ID 217983, 17 pages

Optimal Sensor Placement for Stay Cable Damage Identification of Cable-Stayed Bridge under Uncertainty, Li-Qun Hou, Xue-Feng Zhao, Rui-Cong Han, and Chun-Cheng Liu
Volume 2013, Article ID 361594, 18 pages

Design of System for Monitoring Seepage of Levee Engineering Based on Distributed Optical Fiber Sensing Technology, Huaizhi Su and Yeyuan Kang
Volume 2013, Article ID 358784, 10 pages

Bridge Assessment and Health Monitoring with Distributed Long-Gauge FBG Sensors, Chunfeng Wan, Wan Hong, Jianxun Liu, Zhishen Wu, Zhaodong Xu, and Shu Li
Volume 2013, Article ID 494260, 10 pages

Review of Bolted Connection Monitoring, Tao Wang, Gangbing Song, Shaopeng Liu, Yourong Li, and Han Xiao
Volume 2013, Article ID 871213, 8 pages

Development of a Multitype Wireless Sensor Network for the Large-Scale Structure of the National Stadium in China, Yanbin Shen, Pengcheng Yang, Pengfei Zhang, Yaozhi Luo, Yujia Mei, Huaqiang Cheng, Li Jin, Chenyu Liang, Qiaqin Wang, and Zhouneng Zhong
Volume 2013, Article ID 709724, 16 pages

Long-Term Vibration Monitoring of Cable-Stayed Bridge Using Wireless Sensor Network, Khac-Duy Nguyen, Jeong-Tae Kim, and Young-Hwan Park
Volume 2013, Article ID 804516, 9 pages

Vibration Characteristics of Gravity-Type Caisson Breakwater Structure with Water-Level Variation, So-Young Lee, Thanh-Canh Huynh, Jeong-Tae Kim, Han-Sam Yoon, and Sang-Hun Han
Volume 2013, Article ID 261396, 10 pages

A Combined Optimal Sensor Placement Strategy for the Structural Health Monitoring of Bridge Structures, Can He, Jianchun Xing, Juelong Li, Qiliang Yang, Ronghao Wang, and Xun Zhang
Volume 2013, Article ID 820694, 9 pages

Multiscale Structural Health Monitoring of Cable-Anchorage System Using Piezoelectric PZT Sensors, Khac-Duy Nguyen, Jeong-Tae Kim, and Young-Hwan Park
Volume 2013, Article ID 254785, 9 pages

Near-Field Ultrasonic Phased Array Deflection Focusing Based CFRP Wing Box Structural Health Monitoring, Yajie Sun, Yonghong Zhang, Chengshan Qian, and Zijia Zhang
Volume 2013, Article ID 621297, 6 pages

Active Sensing Based Bolted Structure Health Monitoring Using Piezoceramic Transducers, R. L. Wang, H. Gu, and G. Song
Volume 2013, Article ID 583205, 6 pages

Evaluation of Vibration Characteristics of an Existing Harbor Caisson Structure Using Tugboat Impact Tests and Modal Analysis, Jin-Hak Yi, Woo-Sun Park, So-Young Lee, Thanh-Canh Huynh, Jeong-Tae Kim, and Chun-Kyo Seo
Volume 2013, Article ID 806482, 11 pages

Development and Application of Structural Health Monitoring System Based on Piezoelectric Sensors, Shi Yan, Jianxin Wu, Wei Sun, Haoyan Ma, and Han Yan
Volume 2013, Article ID 270927, 12 pages

Feasibility Study of Stress Measurement in Prestressing Tendons Using Villari Effect and Induced Magnetic Field, Changbin Joh, Jung Woo Lee, and Imjong Kwahk
Volume 2013, Article ID 249829, 8 pages

Microseismic Monitoring and Numerical Simulation of Rock Slope Failure, Zhengzhao Liang, Nuwen Xu, Ke Ma, Shibin Tang, and Chunan Tang
Volume 2013, Article ID 845191, 10 pages

A SA-Based Wireless Seismic Stress Monitoring System for Concrete Structures, S. Hou, Y. Yu, H. B. Zhang, X. Q. Mao, and J. P. Ou
Volume 2013, Article ID 978313, 7 pages

Mechanism of a Hair Cell Bioinspired Sensor with Ultrasensitivity to Weak and Low Frequency Vibration Signals, L. J. Liu and Y. Lei
Volume 2013, Article ID 278151, 10 pages

A Revised Counter-Propagation Network Model Integrating Rough Set for Structural Damage Detection, Shao-Fei Jiang, Chun Fu, Chun-Ming Zhang, and Zhao-Qi Wu
Volume 2013, Article ID 850712, 10 pages

Measurement of Additional Strains in Shaft Lining Using Differential Resistance Sensing Technology, Guangsi Zhao, HuaFu Pei, and Hengchang Liang
Volume 2013, Article ID 153834, 6 pages

Measurement Model for the Maximum Strain in Beam Structures Using Multiplexed Fiber Bragg Grating Sensors, Se Woon Choi, Jihoon Lee, Bo Hwan Oh, and Hyo Seon Park
Volume 2013, Article ID 894780, 9 pages

Study on the Stress Relaxation Behavior of Large Diameter B-GFRP Bars Using FBG Sensing Technology, Li Guo-wei, Pei Hua-Fu, and Hong Cheng-yu
Volume 2013, Article ID 201767, 12 pages

Feasibility Study on Crack Detection of Pipelines Using Piezoceramic Transducers, Guofeng Du, Qingzhao Kong, Timothy Lai, and Gangbing Song
Volume 2013, Article ID 631715, 7 pages

Health Condition Evaluation of Cable-Stayed Bridge Driven by Dissimilarity Measures of Grouped Cable Forces, Dan-Hui Dan, Yi-Ming Zhao, Tong Yang, and Xing-Fei Yan
Volume 2013, Article ID 818967, 12 pages

Real-Time Monitoring System for Workers' Behaviour Analysis on a Large-Dam Construction Site, Peng Lin, Qingbin Li, Qixiang Fan, and Xiangyou Gao
Volume 2013, Article ID 509423, 10 pages

The Node Arrangement Methodology of Wireless Sensor Networks for Long-Span Bridge Health Monitoring, Guang-Dong Zhou and Ting-Hua Yi
Volume 2013, Article ID 865324, 8 pages

The Nonuniform Node Configuration of Wireless Sensor Networks for Long-Span Bridge Health Monitoring, Guang-Dong Zhou and Ting-Hua Yi
Volume 2013, Article ID 797650, 9 pages

An Intelligent Energy Management System for Educational Buildings, Ahmad Al-Daraiseh, Nazaraf Shah, and Eyas El-Qawasmeh
Volume 2013, Article ID 209803, 13 pages

Field Measurement of Wind Effects of Roof Accessory Structures on Gable-Roofed Low-Rise Building, Peng Huang, Ming Gu, Chun-guang Jia, and Da-long Quan
Volume 2013, Article ID 280186, 7 pages

Probabilistic Fatigue Assessment Based on Bayesian Learning for Wind-Excited Long-Span Bridges Installed with WASHMS, Zhi-Wei Chen and Xiao-Ming Wang
Volume 2013, Article ID 871368, 8 pages

Calibration of the Performance of Bidirectional Shaker Table in Centrifuge Model Tests Using Sensor Networks, Hongjun Li, Hong Zhong, Xuedong Zhang, Yanyi Zhang, and Yujing Hou
Volume 2013, Article ID 648916, 9 pages

Editorial

Sensing Methodologies and Sensor Networks for Health Monitoring of Civil Infrastructures 2013

Hong-Nan Li,¹ Gangbing Song,² Jeong-Tae Kim,³ and Ting-Hua Yi¹

¹ *School of Civil Engineering, Dalian University of Technology, Dalian 116023, China*

² *Department of Mechanical Engineering, University of Houston, Texas, TX 77004, USA*

³ *Department of Ocean Engineering, Pukyong National University, Busan 608-737, Republic of Korea*

Correspondence should be addressed to Ting-Hua Yi; yth@dlut.edu.cn

Received 23 January 2014; Accepted 23 January 2014; Published 4 March 2014

Copyright © 2014 Hong-Nan Li et al. This is an open access article distributed under the Creative Commons Attribution License, which permits unrestricted use, distribution, and reproduction in any medium, provided the original work is properly cited.

All load-carrying civil infrastructures, such as long-span bridges, high-rise buildings, or large-scale offshore platforms, continuously accumulate damage during their long-term service life [1]. Any deformation or damage in a structure may affect the structural integrity, durability, and reliability. Structural health monitoring (SHM) systems that report in real time the structural condition in terms of stresses, strains, accelerations, and displacements, and so forth are central to meet the demanding goals of increasing structural safety and reliability, while reducing structure operating and maintenance costs. In general, a typical SHM system includes four major components: sensor subsystem, data acquisition and transmission subsystem, data storage subsystem, and condition evaluation subsystem [2]. Among them, the sensor subsystem is the first and most important one since the performance of whole SHM system is strongly dependent on available sensor measurements. It implies two critical constraints existing in such sensor subsystem applications: the suitable sensors available for the network and the optimal sensor placement (OSP) strategies working to maximize the ability to detect and discriminate relevant data features. It is, therefore, of increasing interest to seek ideal sensing methodologies and design methods of sensor networks. Recently, the advances of bioinspired, nanobased, piezoelectric, fiber optic, wireless and remote sensing technologies bring a new dimension to smart sensors. And, at the same time, with the rapid development in the sensor network design

approach, such as the effective independence (Efi), modal kinetic energy (MKE), and SVD-based methods, the use of large-scale but economical and efficiency sensor networks for the SHM has become possible [3].

Over the last decade, the development in this most rapidly increasing research field has been periodically summarized and reviewed by many colleagues, focusing on one topic or another regarding specific technical aspects. Given the significant amount of work involved globally and the unique elongated feature of the sensing methodologies and sensor networks for the SHM and their applications, with an emphasis on civil engineering, it is important to have a platform that allows active researchers to present their new development in a timely and efficient manner. With this intention in mind, the first special issue “Sensing Methodologies and Sensor Networks for Health Monitoring of Civil Infrastructures,” containing 26 peer-reviewed papers, was published in 2012 in the International Journal of Distributed Sensor Networks and was obviously a great success. Based on the sensational effect of the 2012’s special issue, this topic is elected officially as one of the annual special issues. This simply means that it has become a series of special issues which will be published each year. The guest editors are pleased with this decision since such a series will have a long-term impact and in time gather a civil SHM community around it in much the same way a successful annual conference or a conference session does without a doubt.

A total of 33 papers are presented in the current issue. Comparing with the first special issue, it can be found as the flourishing and diverse research activities in this area. The guest editors deeply believe that this issue will attract the special interest to the scientists and engineers in the field of civil engineering.

Acknowledgments

The guest editors would like to express their sincere appreciation and thanks to all the authors and coauthors for their scientific contribution to this special issue. The guest editors would also like to express their whole-hearted thanks to the reviewers from all the world for their valuable time and dedication to this special issue. This meaningful work was jointly supported by the National Natural Science Foundation of China (Grant nos. 51121005, 51222806, and 51327003), the Specialized Research Fund for the Doctoral Program of Higher Education (Grant no. 20130041110031), and the 2013 Science and Technology Project of Dalian Urban and Rural Construction Committee.

*Hong-Nan Li
Gangbing Song
Jeong-Tae Kim
Ting-Hua Yi*

References

- [1] T.-H. Yi, H.-N. Li, and X.-D. Zhang, "Sensor placement on Canton Tower for health monitoring using asynchronous-climbing monkey algorithm," *Smart Materials and Structures*, vol. 21, no. 12, Article ID 125023, 2012.
- [2] T.-H. Yi, H.-N. Li, and M. Gu, "Recent research and applications of GPS-based monitoring technology for high-rise structures," *Structural Control and Health Monitoring*, vol. 20, no. 5, pp. 649–670, 2013.
- [3] T.-H. Yi, H.-N. Li, and M. Gu, "Optimal sensor placement for structural health monitoring based on multiple optimization strategies," *Structural Design of Tall and Special Buildings*, vol. 20, no. 7, pp. 881–900, 2011.

Research Article

Corrosion Monitoring and Evaluation of Reinforced Concrete Structures Utilizing the Ultrasonic Guided Wave Technique

Dongsheng Li,¹ Shuaifang Zhang,¹ Wei Yang,² and Wenyao Zhang²

¹ School of Civil Engineering, Dalian University of Technology, Dalian 116024, China

² Fujian Academy of Building Research, Fuzhou 350025, China

Correspondence should be addressed to Dongsheng Li; lidongsheng@dlut.edu.cn

Received 10 July 2013; Revised 6 December 2013; Accepted 2 January 2014; Published 20 February 2014

Academic Editor: Gangbing Song

Copyright © 2014 Dongsheng Li et al. This is an open access article distributed under the Creative Commons Attribution License, which permits unrestricted use, distribution, and reproduction in any medium, provided the original work is properly cited.

Corrosion of reinforced concrete structures has become a major problem worldwide, leading to very high repair costs. A dearth of studies has focused on the corrosion damage evolution of reinforced concrete. In this paper, the ultrasonic guided wave (UGW) technique is adopted to monitor the reinforced concrete corrosion damage evolution process. The properties of different guide wave modes were studied by steel rebar dispersion curves of UGWs through numerical calculation. The availability and validity of the UGW testing-reinforced concrete corrosion damage is proved by corrosion experiment. The experiment shows that the first wave peak value could describe the whole process of steel rebar corrosion. As the corrosion damage level increases, the relative variation for the first UGW peak value increases first and then decreases.

1. Introduction

Reinforced concrete has been employed as an economical construction material in civil engineering structures, such as buildings, bridges, and dams. However, environmental factors such as acid rain, chloride, loading fatigue, and carbonization have simultaneous harmful effects on concrete. The results lead to steel corrosion. At present, steel corrosion has become a major problem worldwide, especially for structures exposed to aggressive environments. This problem has reached alarming proportions in the past three decades, leading to very high repair costs, sometimes even above the initial construction cost, or to the final collapse of the structures in extreme situations [1].

The current methods of detecting concrete structural damage of steels include electrochemistry detection, ultrasonic wave testing, acoustic emission technique, and Fiber Bragg Grating sensors [2, 3]. However, these methods have shortcomings. Electrochemical methods are sensitive to the surface state of engineering structures and have been widely utilized for corrosion monitoring [4]. As the double layer

does not result from pure capacitive conditions and the data cannot be actually analyzed according to partial data of electrochemical impedance spectroscopy, the corrosion monitoring methods based on electrochemical impedance techniques still need to be improved [5]. Ultrasonic waves propagate in short distances and are only sensitive to significant defects [6]. Acoustic emission is not sensitive to slight corrosion damage degree because of the low corrosion energy release. Thus, a more precise and efficient method is urgently needed.

A type of ultrasonic wave propagation involves a wave that is guided between two parallel surfaces of the test object. Ultrasonic guided waves (UGWs), as a developed tool, have many advantages compared with traditional detection methods. It can propagate in long distances because of its slight attenuation in steel [7]. This characteristic is especially suitable to detect long range bridges. Guided waves were chosen because of the possibility of analyzing guided wave behavior in certain frequency ranges to distinguish between the loss of bar cross-sectional area and change of interface conditions [8]. High sensitivity is another merit of this

method. UGWs have many different modes at a single frequency, and these modes are sensitive to different defects [9].

The progressions of rebar corrosion in concrete in chloride and oxide environments were monitored by UGWs. The effect of corrosion rates, surface and core-seeking guided wave modes, and effective combination of guided wave modes were introduced [9]. Corrosion has been simulated in various ways, such as by introducing debonding between steel and concrete in the form of polyvinyl chloride pipes or by wrapping a tape on the bar [10, 11]. The sweep frequency technique was adopted to optimize the guided wave exciting frequency. The waveform energy attenuation at different frequencies was presented and discussed in terms of corrosion damage. The testing results were verified because the fundamental longitudinal mode of propagation can correctly express steel corrosion damage. Ervin et al. [12] employed high-frequency UGWs monitoring corrosion of rebar embedded in mortar. Through different guided mode comparisons, the $L(0, 9)$ mode was adopted to monitor uniform and localized corrosion in reinforced mortar undergoing accelerated corrosion. Thus, ample evidence shows that corrosion could be detected by UGW techniques. However, the whole steel corrosion process and damage evolution has not been reported utilizing UGW testing. This study reports that the steel corrosion damage monitoring adopted UGW. The testing results were verified through another corrosion evaluation method.

2. UGW Propagation Theories in Steel Rebar

The geometry profile of a rebar is presented in Figure 1. Three different modes propagate in cylindrical waveguide, longitudinal modes $L(0, m)$, torsion modes $F(n, m)$, and flexural modes $F(n, m)$. In this expression, m and n stand for circumferential order and modulus, respectively. The displacement is symmetrical corresponding to $n = 0$, where $n = 1, 2, 3 \dots$ that refers to asymmetrical displacements. Therefore, $L(0, m)$, $T(0, m)$ are symmetrical modes and $F(n, m)$ are asymmetrical modes.

The longitudinal modes that propagate in steel rebar only have two types of displacement: radial and axial displacements. The boundary condition is $u_\theta = 0$, and u_z, u_r are independent of θ . Considering the boundary condition $\sigma_{rr} = \sigma_{rz} = 0$ ($r = a$), the Pochhammer frequency equation can be achieved by solving the wave equation [13]:

$$\frac{2\alpha}{a} (\beta^2 + k^2) J_1(\alpha a) J_1(\beta a) - (\beta^2 - k^2) J_0(\alpha a) J_1(\beta a) - 4k^2 \alpha \beta J_0(\beta a) = 0, \quad (1)$$

where λ is the length of guided waves, ω is the angular velocity, k is the wave number, J is the Bessel function, coefficients $\alpha^2 = \omega^2/c_L^2$, $\beta^2 = \omega^2/c_T^2 - k^2$, c_L is the velocity of longitudinal guided wave, c_T is the velocity of transverse guided waves, and c_p is the phase velocity. This expression is a transcendental equation with independent variables ω

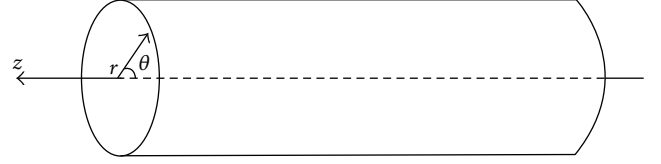


FIGURE 1: Geometry profile of steel rebar.

and k ; thus, the same frequency ω corresponds to multiple wave numbers; namely, more than one solution existing at a single frequency ω . This phenomenon corresponds well with the fact that many modes exist at a single frequency. This condition is the multiple modes property of UGW.

3. Dispersion Curves of UGW Propagation in Steel Rebar

The curves that depict the relationships between frequency and eigenvalue, as well as phase velocity and group velocity, are called dispersion curves. The parameters utilized to characterize the properties of wave guided propagation are phase velocity and group velocity, which have been described above. All waveguides, both symmetrical and asymmetrical, and other irregular shapes have special dispersion curves. Besides, only with the dispersion curves of UGW in steel rebar could an ideal UGW mode be excited by selecting the appropriate excitation frequency.

Take a 20 mm diameter rebar as an example. HRB335 ribbed bars were employed in this study, whose properties are shown in Table 1.

The effect of ribs on a ribbed bar can be ignored when the ratio of the diameter and the length is less than 0.4 [8]. The ratio between the diameter and the length is 0.029; thus, the steel rebar can be seen as a smooth cylinder. Based on Section 2, the transcendental equation can be solved with guided wave propagation theory. The dispersion curve of guided waves propagating in the steel rebar can be obtained by numerical calculation. The relationship between wave velocity and frequency (wave number and frequency) is represented by dispersion equation (1) and dispersion curve. However, as a transcendental equation, wave velocity and frequency (wave number and frequency) analytic solutions are too complicated to be obtained from dispersion equation (1), which could only be solved by the numerical analysis method. The program is divided into several steps as follows:

- (a) The cutoff frequency that corresponds with the corresponding mode is determined. The solution of the dispersion equation is based on the cutoff frequency, and the roots that meet the equation are determined by scanning the frequency range. These roots are cutoff frequencies that correspond with the corresponding mode, and these roots are set as initial points of each modal dispersion curve.
- (b) Each modal begins with the initial point. The next point that meets the dispersion equation with a certain step length is searched (e.g., 5 Hz). The initial

TABLE 1: Properties of HRB335 ribbed bars.

Diameter	Length	Cross-sectional area	Density	Young's module	Poisson ratio
20 mm	700 mm	254.5 mm ²	7858.5 kg/m ³	206 GPa	0.28

TABLE 2: C30 mix proportion of concrete (kg/m³).

PC32.5R cement	Water	Medium grained sand	Rock fragment
434	182.5	524.9	1226.5

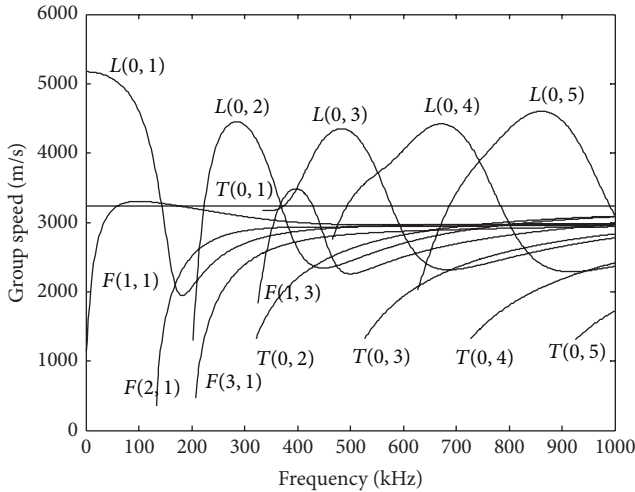


FIGURE 2: Dispersion curves of group velocity.

point is then renewed until all the points in the frequency range are obtained.

- (c) Let the cutoff frequency in (a) be the initial point. A dispersion curve is obtained by connecting all the points searched in the frequency range. This step begins with the next initial point, and the above process is repeated. Finally, all dispersion curves are obtained.

The 20 mm diameter rebar dispersion curve is displayed in Figure 2. Only three modes can be produced, namely, $L(0, 1)$ longitudinal mode, $T(0, 1)$ torsion mode, and $F(1, 1)$ flexural mode. These modes could be acquired in the vicinity of the 40 kHz frequency, where the slopes degree of UGW in these three modes is most mild. 40 kHz is selected as the excitation frequency to excite the longitudinal UGW mode. The guided wave of $L(0, 1)$ mode, which disperses most indistinctly and propagates fastest at this frequency, is chosen to detect the corrosion damage of reinforced concrete.

4. Steel Rebar Corrosion UGW Detection Experiment and Results Analysis

4.1. Reinforced Concrete Corrosion Specimen Preparation. In this experiment, the size of the specimen was 500 mm × 120 mm × 150 mm, in which the thickness of steel rebar's protective layer was 20 mm and the concrete grade was C30.

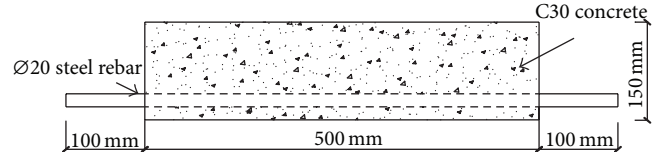


FIGURE 3: Reinforced concrete beam.

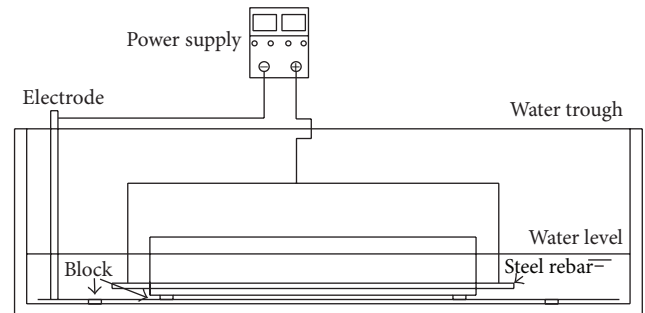


FIGURE 4: Reinforced concrete corrosion experimental devices.

The hot rolled ribbed steel rebar had a diameter of 20 mm. The steel rebar was outstretched by 100 mm outside the concrete to satisfy the need of UGW detection when the specimen was corroded. The weight of the steel rebar was weighed before the concrete specimen was casted. Ordinary Portland cement 32.5R from the China Dalian Jinzhou third cement factory was utilized to prepare concrete. Medium grained sand was selected for the experiment. The rock fragment particle size was 5 mm to 15 mm. The water cement ratio was 0.42, whose detailed mix proportion is shown in Table 2. The laboratory temperature was 25°C, and the relative humidity was 80% when the specimen was casted. The test was conducted after a 28 d of storage in a standard curing room. The detailed size is presented in Figure 3.

The corrosion of reinforced concrete in the natural environment is so slow that the method of electrochemistry is employed to accelerate corrosion to obtain a higher amount of corrosion within a short time. The device utilized in the experiments was a stable DC power supply (Figure 4), which could ensure the stability of the current. The device model was PS-603D with exporting current of 0 A to 3 A (precision of 10 mA) and exporting voltage of 0 V to 60 V (precision of 0.1 V). In the electrochemistry experiment, the steel rebar was selected as the anode, whereas stainless steel was the cathode.

TABLE 3: Parameters of the piezoelectric ceramic.

PZT constant d_{33}	Density kg/m^3	Dielectric loss	Relative permittivity ϵ_{r3}	Curie temperature $^{\circ}\text{C}$	Electromechanical coupling coefficient k_{33}
10^{-12} C/N	7500	0.02	1700	320	0.75

4.2. *Design of Reinforced Concrete Corrosion.* The amount of electrochemical corrosion of the steel reinforcement was calculated in accordance with Faraday's law:

$$m = kIt, \quad (2)$$

where m is the loss of corroded metal (g), k is the coefficient of different metals with different properties, I is the current size (A), and t is the conduction time (s).

Based on Faraday's law, the amount of electrochemical corrosion of steel reinforcement could also be calculated with

$$m = \frac{t \times I \times 55.487}{2 \times 96487}. \quad (3)$$

The amount of electrochemical corrosion of the steel reinforcement is in proportion to the conduction time and current size. In this equation, 55.487 is the molar mass of iron atoms, 2 is the number of electrons lost when an iron atom turns into a ferrous ion, and 96487 is the charge needed as electrolysis consumes one mole of substance.

The corrosion current should be neither too large nor too small. If the current was too large, the reinforcement would corrode faster and the damage of the steel rebar would be concentrated at both ends of the steel rebar; thus, the steel rebar does not corrode uniformly. If the current was too small, the reinforcement would corrode slower and the time of corrosion would last much longer, resulting in the loss of human and financial resources. Approximately 1 mA/mm^2 is the standard value, wherein the corrosion current equal to the parcel area of the steel rebar in reinforced concrete is multiplied by 1 mA/mm^2 and calculated as follows:

$$I = 1 \times 3.14 \times 20 \times 500 = 314 \text{ mA} = 0.314 \text{ A}. \quad (4)$$

Thus, 0.3 A is selected as the corrosion current of electrochemical corrosion of steel rebar. Five specimens were corroded for 0, 5, 10, 15, and 20 d. During the corrosion, a UGW device was employed to detect the specimens every day to record the voltage and current sizes.

4.3. *Experimental Results and Analysis.* A UGW device was utilized to detect guided waves of the steel rebar in reinforced concrete. The specified detection principle is shown in Figure 5.

The oscilloscope was utilized to acquire data. Two signal channels were chosen: one received the output waveform of power amplifier, whereas the other received the waveform obtained by the sensor receiver. In this paper, lead zirconate titanate piezoelectric ceramics (PZT-5) was adopted as the ultrasonic sensor. The performance parameters are shown in Table 3.

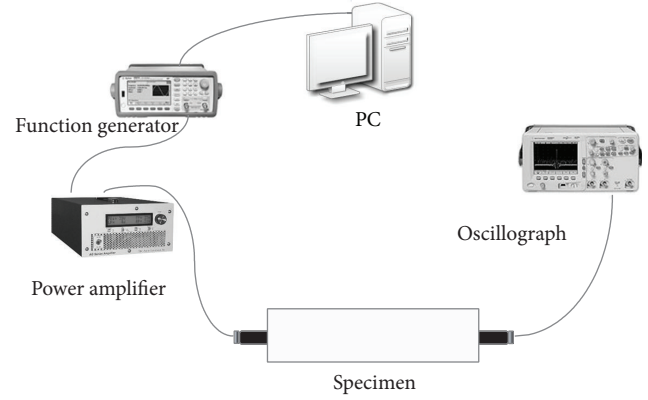


FIGURE 5: Sketch of ultrasonic guided wave detection.

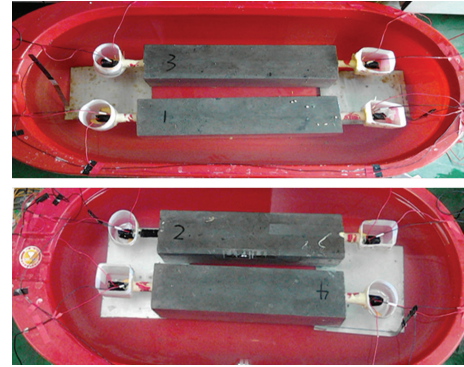


FIGURE 6: The UGW sensors placement for reinforced concrete structures corrosion.

Two piezoelectric ceramics were arranged at both sides, one of which was the exciting sensor while the other was the receiving sensor. The sensor placement is shown in Figure 6.

Five-cycle sinusoidal waves with central frequency of 40 kHz are modulated utilizing the Hanning window employed as UGW excitation signals (Figure 7).

4.3.1. *Appearance of the Specimen.* The appearance of the reinforced concrete beam after corrosion is shown in Figure 8.

No. 5 specimen was kept from corrosion, which greatly contrasted with the other specimens. By comparing Figures 8 and 5, the steel rebar would expand during the corrosion of the reinforcing steel, and then longitudinal through-going cracks would appear along the length of the surface direction of the concrete protective layer that caused damage. As the corrosion time increased, cracks on each specimen's appearance became wider and even the protective layer would

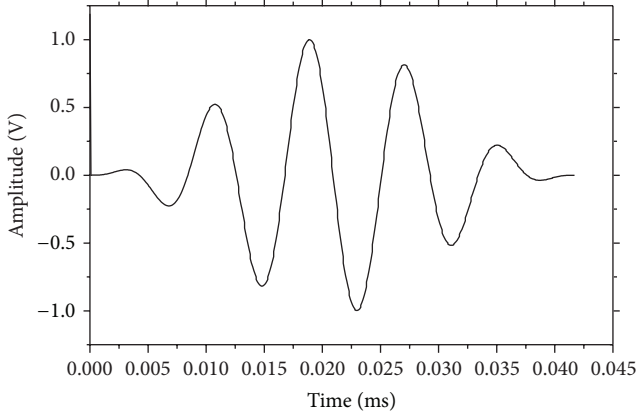


FIGURE 7: Five-cycle sinusoidal waves modulated by Hanning window.

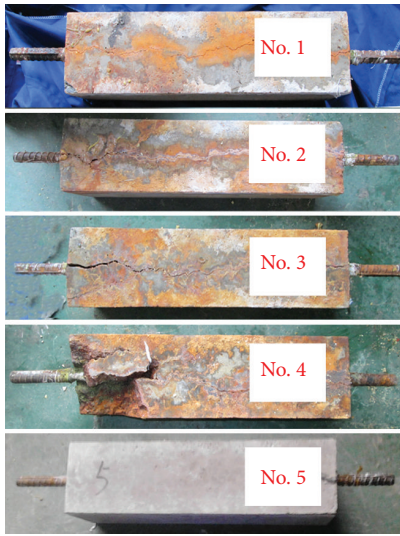


FIGURE 8: The case of the specimen after corrosion.

fall off, as No. 4 specimen shows. The four specimens were corroded for 5, 10, 15, and 20 d.

4.3.2. UGW Monitoring for Steel Rebar Corrosion. During the corrosion, a UGW device was utilized to detect the specimens' corrosion every day. The UGW testing signals of the reinforced concrete before and after corrosion were only listed to save space.

Figures 9, 10, 11, and 12 show that, although the signals of the UGW propagation in reinforced concrete were very complex, the signals of the first wave were very significant and had the typical characteristics of a first-order longitudinal guided wave. With the arrangement of the sensor in this test, only the longitudinal wave guide mode was excited in terms of theory. According to the waveform observed in this test, a series of waveforms after the first wave had other forms of modals apart from the longitudinal modal. This scenario was mainly caused by the manufacturing errors at the end of the steel rebar induced bending mode. The

reflection and refraction of the guided wave at the end of the steel rebar and in the contact interface of the steel rebar and concrete make the modes convert. Both reflection and refraction could occur again when the guided wave arrives at the receiving end, and the superposition of the incident wave makes the guided wave more complex. The steel rebar in the reinforced concrete also defected after corrosion because the defects disorganizing the reflection, refraction, and the mode conversion of the guided wave could occur repeatedly. The modes of the testing signal are much richer after the corrosion test. Thus, the amplitude of the first wave was only needed in this study. As seen in Figures 9–12, the amplitude of the head wave of UGW decreased gradually as time progressed after corrosion, except for the No. 1 specimen. The UGW device was employed to detect the specimens every day to record the amplitude of the first wave. The relationship of this set of specimens from Nos. 1 to 4 between the amplitude of the first wave and the time of corrosion is presented as in Figure 13.

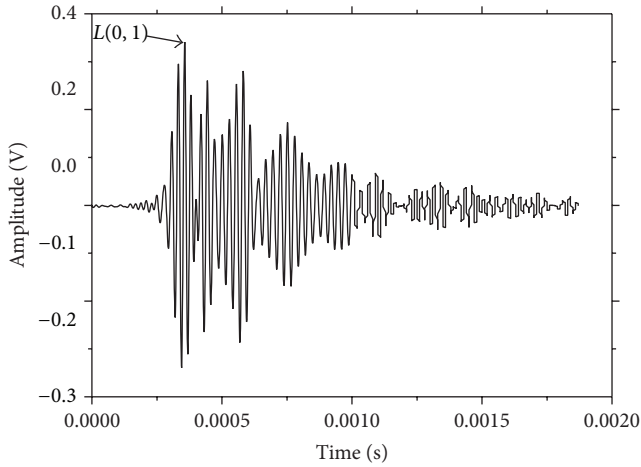
Figure 13 shows that the UGW first wave peak value first increased and then decreased slowly. The peak value of the first wave of reinforced concrete specimens with the same degree of corrosion also decreased over time. This condition is because the corrosion products increased during the steel rebar corrosion process, resulting in an increase in the delamination degree between the steel rebar and concrete. The decrease in the UGW energy in the steel rebar leaked into the concrete; thus, the peak value of the first wave of UGW increases. However, as the reinforced concrete corrosion level increases, the pit on the steel becomes larger. This condition would lead to great reflection in the first wave energy, and the direct transmission wave energy would become low. The first wave peak value then decreased slowly.

A steel rebar was removed from reinforced concrete after the test to examine the accuracy of the UGW test. The steel rebar with different degrees of corrosion is shown in Figure 14. The weight was measured after washing the corrosion on the steel rebar with pure water and hydrochloric acid. By evaluating the degree of corrosion with the mass loss rate method, the calculation formula is presented as in formula (5). The degrees of corrosion of reinforced concrete specimens are shown in Table 4:

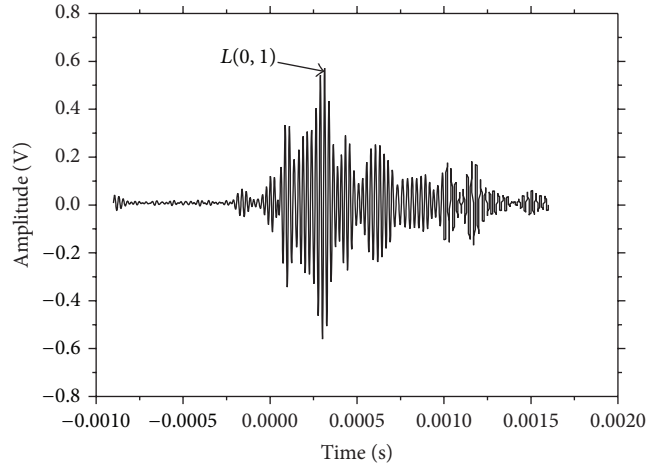
$$c = \frac{m_b - m_a}{m_b} \times 100\%, \quad (5)$$

where c is the mass loss rate, m_b is the mass of the steel rebar before corrosion, and m_a is the mass of steel rebar after corrosion.

We made a graph shown in Figure 15 to quantitatively describe the changing rule of the UGW signal of reinforced concrete. The x -coordinate is the mass loss rate of reinforced concrete and the y -coordinate is the change in the peak value (first wave peak value before corrosion subtracted from the first wave peak value after corrosion) of the UGW first wave. No. 1 specimen is not considered in this figure as its peak value increased. From Figure 15, the relative variation peak value of the UGW first wave increased along with the increase in the degree of corrosion, which shows that utilizing the peak value change of the UGW first wave could roughly judge the damage degree of reinforced concrete.

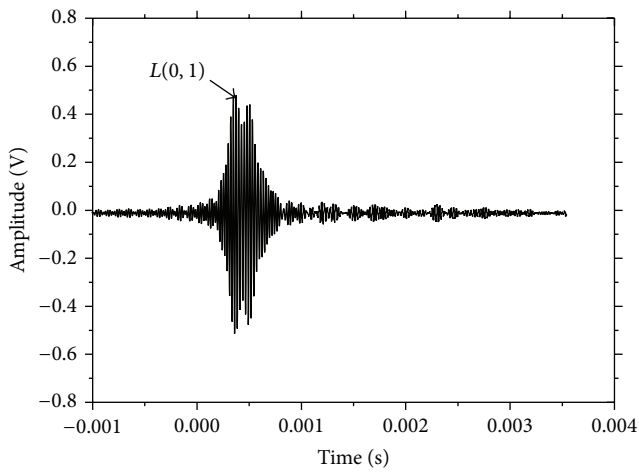


(a) UGW waveform before corrosion

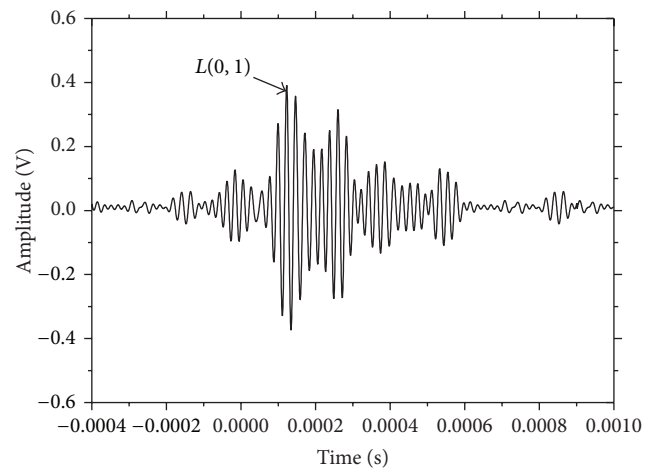


(b) UGW waveform after corrosion

FIGURE 9: UGW waveform for No. 1 corrosion specimen.

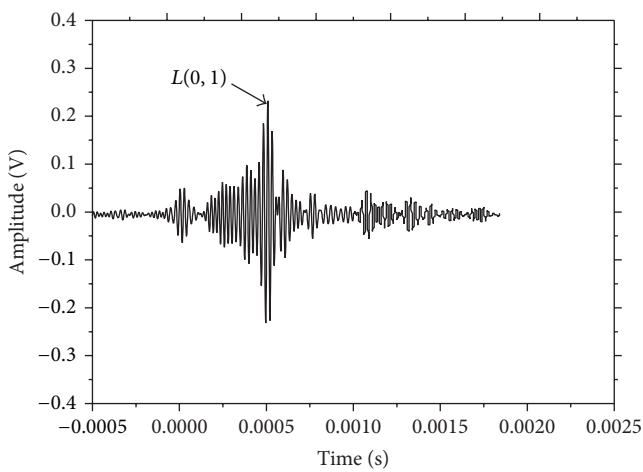


(a) UGW waveform before corrosion

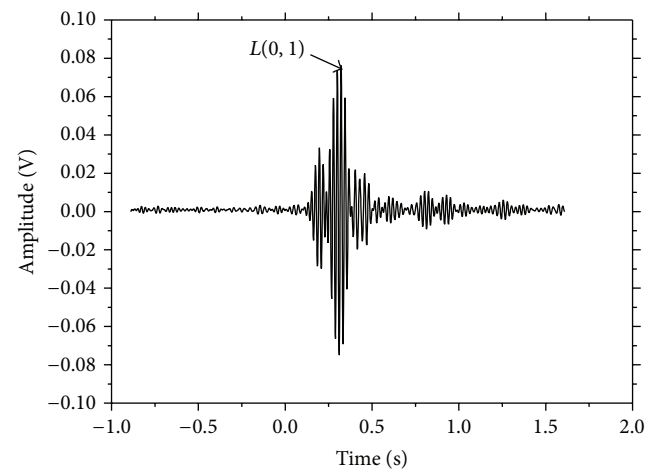


(b) UGW waveform after corrosion

FIGURE 10: UGW waveform for No. 2 corrosion specimen.

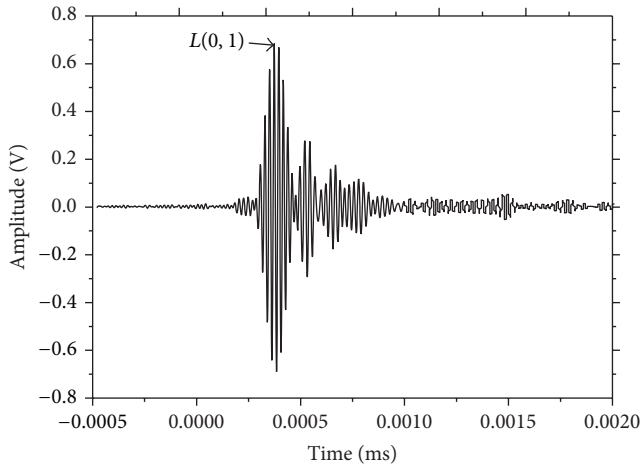


(a) UGW waveform before corrosion

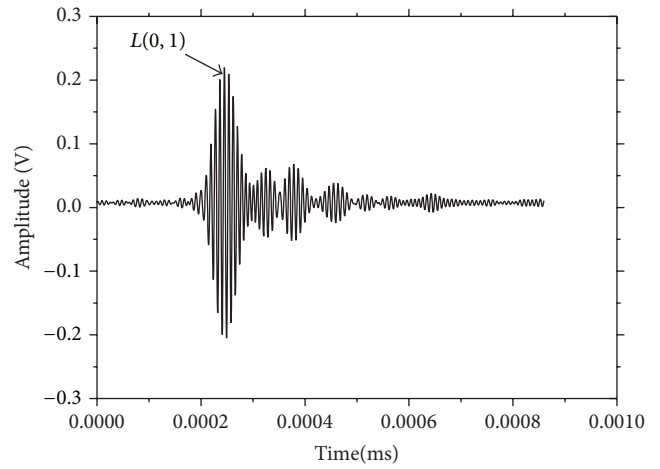


(b) UGW waveform after corrosion

FIGURE 11: UGW waveform for No. 3 corrosion specimen.

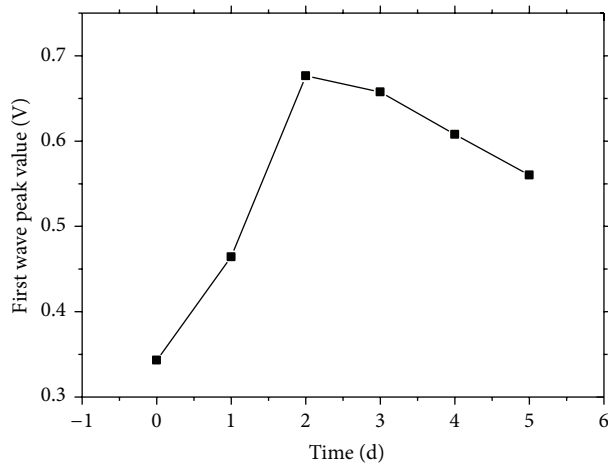


(a) UGW waveform before corrosion

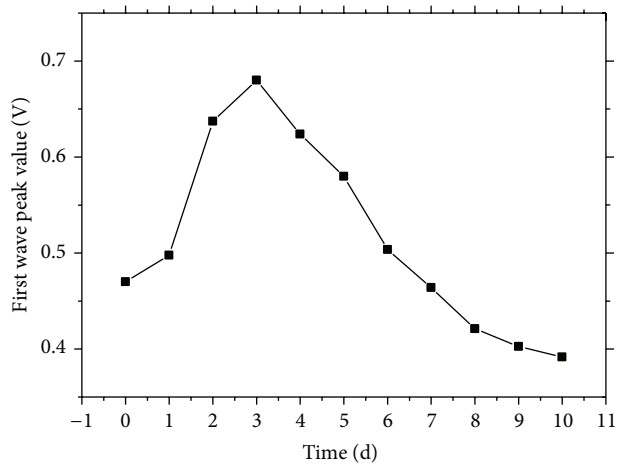


(b) UGW waveform after corrosion

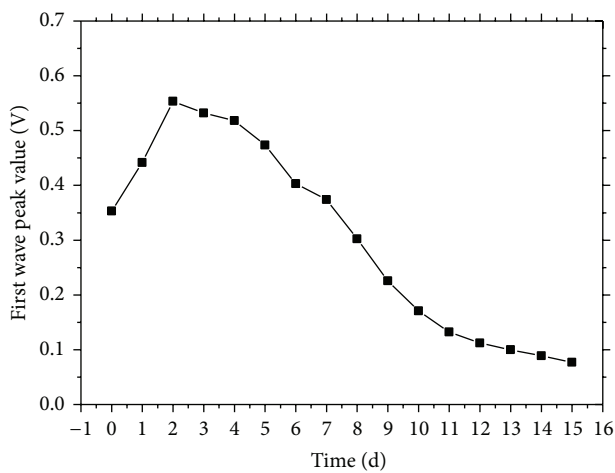
FIGURE 12: UGW waveform for No. 4 corrosion specimen.



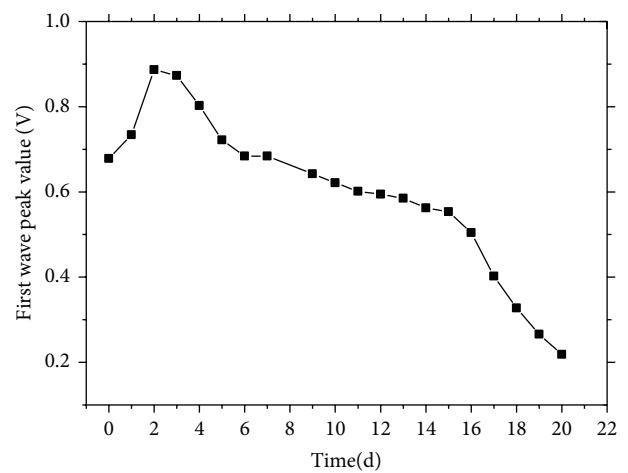
(a) UGW peak variation for No. 1 specimen



(b) UGW peak variation for No. 2 specimen



(c) UGW peak variation for No. 3 specimen



(d) UGW peak variation for No. 4 specimen

FIGURE 13: UGW peak variation during the whole corrosion process.

TABLE 4: Degree of corrosion.

Specimen number	Corrosion time (d)	Mass before corrosion (g)	Mass after corrosion (g)	Mass loss (g)	Mass loss rate (%)
1	5 d	1583	1543	40	2.59
2	10 d	1575	1506	69	4.38
3	15 d	1590	1474	116	7.29
4	20 d	1584	1426	158	9.97
5	0 d	1581			0

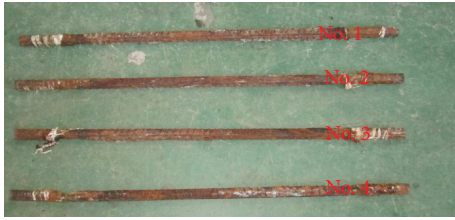


FIGURE 14: Corrosion steel rebar surface.

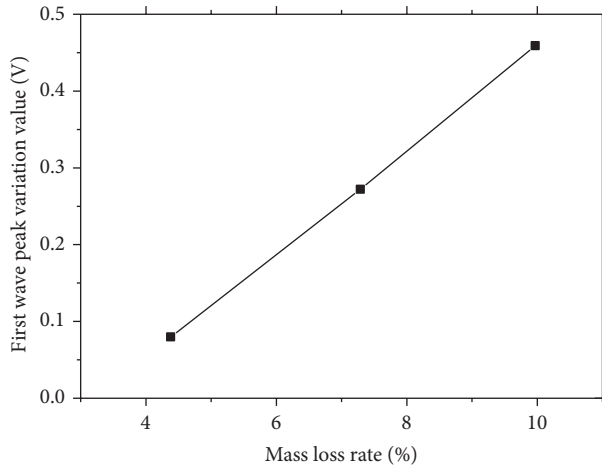


FIGURE 15: Relationship between the ultrasonic guided first wave changes and the corrosion damage level of steel rebar.

5. Conclusion

The selection of UGW excitation signals, analysis of UGW dispersion curves, and test of reinforced concrete corrosion damage are researched in this paper. The principal conclusions are as follows.

- (1) The properties of different guide wave modes are studied by steel rebar dispersion curves of UGW through numerical calculation. Based on the dispersion curves, the use of guided waves of $L(0, 1)$ mode with 40 kHz is proposed in the test for reinforced concrete corrosion damage.
- (2) The availability and validity of the UGW and the test for reinforced concrete corrosion damage is proved by the reinforced concrete corrosion experiment. The experiment shows that the head wave value could describe the whole process of steel rebar corrosion.

- (3) The steel rebar corrosion level could be estimated roughly with the relationship of the ultrasonic guided first wave changes in amplitude and the corrosion damage level of the steel rebar. As the corrosion damage level increases, the relative variation for UGW first wave peak value increases first and then decreases.

Conflict of Interests

The authors declare that there is no conflict of interests regarding the publication of this paper.

Acknowledgments

The authors are grateful for the financial support from National Natural Science Foundation of China (NSFC) under Grant no. 51278083, the Fundamental Research Funds for the Central Universities (Grant no. DUT12LK12), Science and Technology Project of Fujian Province (Grant no. 2012Y01010047), and Science and Technology Support Program of China no. 2011BAK02B04.

References

- [1] X. F. Zhao, P. Gong, G. F. Qiao, J. Lu, X. Lv, and J. Ou, "Brillouin corrosion expansion sensors for steel reinforced concrete structures using a fiber optic coil winding method," *Sensors*, vol. 11, no. 11, pp. 10798–10819, 2011.
- [2] Y. Moslehy, H. Gu, A. Belarbi, Y. L. Mo, and G. Song, "Smart aggregate based damage detection of circular RC columns under cyclic combined loading," *Smart Materials and Structures*, vol. 19, no. 6, Article ID 065021, 2010.
- [3] G. Song, H. Gu, Y. L. Mo, T. T. C. Hsu, and H. Dhonde, "Concrete structural health monitoring using embedded piezoceramic transducers," *Smart Materials and Structures*, vol. 16, no. 4, article 003, pp. 959–968, 2007.
- [4] H. J. de Bruyn, "Current corrosion monitoring trends in the petrochemical industry," *International Journal of Pressure Vessels and Piping*, vol. 66, no. 1–3, pp. 293–303, 1996.
- [5] F. Kuang, J. N. Zhang, C. J. Zou et al., "Electrochemical methods for corrosion monitoring: a survey of recent patents," *Recent Patents on Corrosion Science*, vol. 2, pp. 34–39, 2010.
- [6] D. S. Li, T. Ruan, and J. H. Yuan, "Inspection of reinforced concrete interface delamination using ultrasonic guided wave non-destructive test technique," *Science China Technological Sciences*, vol. 55, pp. 2893–2901, 2012.
- [7] B. Kolesnikov, L. Herbeck, and A. Fink, "CFRP/titanium hybrid material for improving composite bolted joints," *Composite Structures*, vol. 83, no. 4, pp. 368–380, 2008.

- [8] B. L. Ervin, J. T. Bernhard, D. A. Kuchma et al., "Estimation of corrosion damage to steel reinforced mortar using frequency sweeps of guided mechanical waves," in *Smart Materials and Structures*, vol. 6174 of *Proceedings of SPIE*, p. 12, 2006.
- [9] S. Sharma and A. Mukherjee, "Monitoring corrosion in oxide and chloride environments using ultrasonic guided waves," *Journal of Materials in Civil Engineering*, vol. 23, no. 2, pp. 207–211, 2011.
- [10] F. Wu and F.-K. Chang, "Debond detection using embedded piezoelectric elements in reinforced concrete structures—part I: experiment," *Structural Health Monitoring*, vol. 5, no. 1, pp. 5–15, 2006.
- [11] H. Reis, B. L. Ervin, D. A. Kuchma, and J. T. Bernhard, "Estimation of corrosion damage in steel reinforced mortar using guided waves," *Journal of Pressure Vessel Technology, Transactions of the ASME*, vol. 127, no. 3, pp. 255–261, 2005.
- [12] B. L. Ervin, D. A. Kuchma, J. T. Bernhard, and H. Reis, "Monitoring corrosion of rebar embedded in mortar using high-frequency guided ultrasonic waves," *Journal of Engineering Mechanics*, vol. 135, no. 1, pp. 9–19, 2009.
- [13] J. L. Rose, *Ultrasonic Waves in Solid Media*, Cambridge University Press, London, UK, 2004.

Research Article

Application of Sensor Networks to the Measurement of Subway-Induced Ground-Borne Vibration Near the Station

Hong Zhong,¹ Di Qu,^{1,2} Gao Lin,¹ and Hongjun Li³

¹ State Key Laboratory of Coastal and Offshore Engineering, Dalian University of Technology, Dalian 116023, China

² Shanghai Municipal Engineering Design Institute (Group) Co. Ltd, Shanghai 200092, China

³ State Key Laboratory of Simulation and Regulation of Water Cycle in River Basin, China Institute of Water Resources and Hydropower Research, Beijing 100048, China

Correspondence should be addressed to Hong Zhong; hzhong@dlut.edu.cn

Received 24 August 2013; Accepted 2 January 2014; Published 19 February 2014

Academic Editor: Gangbing Song

Copyright © 2014 Hong Zhong et al. This is an open access article distributed under the Creative Commons Attribution License, which permits unrestricted use, distribution, and reproduction in any medium, provided the original work is properly cited.

The subway-induced ground-borne vibration poses great challenge to the environment in the nearby districts. This problem is more prominent for near-station sections of subways since more buildings and human activities are influenced. And the train would be either accelerating or decelerating in this section; the vibration induced would be different from that induced by the train running on long straight subway sections. For the purpose of evaluating human comfort and designing vibration mitigation systems in the buildings, it is necessary to measure the ground-borne vibration induced by the subway. In the presented paper, a measurement system based on the CompactRIO system and LabVIEW platform is constructed. A network of acceleration sensors is placed to collect the vibration signals. This system is used to measure the ground vibration in terms of acceleration and the corresponding Fourier spectra at a near-station section of the Shanghai Metro Line 9. Some observations have been obtained towards the ground-borne vibration induced by a train running underground near the station as well as the vibration decay with the distance from the subway tunnel.

1. Introduction

During the urbanization process, many subways have been constructed to meet the growing needs for fast and massive transportation. Taking the metro system in Shanghai as an example, twelve lines have been built in the past twenty years. In addition, two more lines are under construction and seven more are already on the city's construction plan. It is known that subways are highly demanding on the environment. Among others, ground-borne vibration from underground tunnels is a major environmental concern for nearby areas.

The problem of ground-borne vibration [1] has been studied by using different approaches, including in-situ measurement, laboratory test, and numerical modelling. Among others, Gupta et al. [2] investigated the influence of the vibration induced by the Beijing Metro on a physics laboratory by both vibration measurements and numerical simulation. For the purpose of designing vibration mitigation system in buildings, Sanayei et al. [3] compared the vibration measurements

inside the buildings at foundation level with the open field measurements. Nicolosi et al. [4] considered the interaction between the railway vehicle and the superstructure and developed a unified model to predict the vibration induced by underground railway. Yang et al. [5] considered the variation of soil properties with depth and studied the ground-borne vibration through centrifuge test and numerical modelling. Forrest and Hunt [6] developed a refined track model based on the floating-slab track to assess its effectiveness.

However, most of the studies have focused on the vibration induced by trains running in long straight tunnels. For the ground near a subway station, the train would be in a state of accelerating or decelerating, as compared to the constant high speed on long straight sections. And there are more buildings and human activities in the nearby area; the ground-borne vibration would impose more influence on the vibration-sensitive equipments in the buildings and comfort of human. It is thus imperative to reduce these vibrations inside buildings and on the ground to acceptable levels with

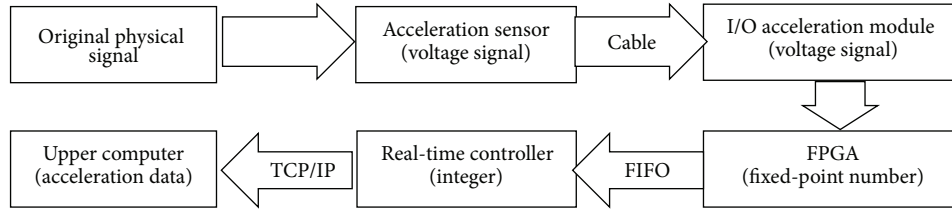


FIGURE 1: Flowchart of data acquisition.

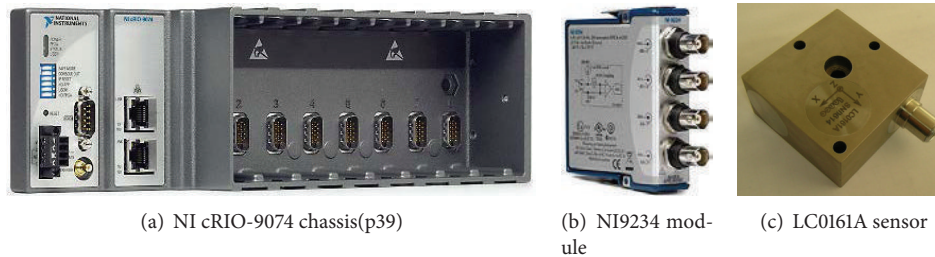


FIGURE 2: The measurement system.

the design of an efficient vibration mitigation system. Incorporation of a vibration mitigation system in a building in the design phase requires prior understanding and characterization of the subway-induced base excitations of the ground to meet serviceability criteria. In-depth investigation into the influence of ground vibration is significant in a practical sense.

In-situ test is the most straightforward approach to obtain the real-time ground-borne vibration. It is known that the automation and control systems for the real-time data via networks including the data acquisition system (DAQ) and the personal computer (PC) can be realized during the complex test processes. Several manufacturers including Wizcon and Wizfactory-Pc Soft International Inc., RSI-Rockwell Automation, LabVIEW-National Instruments, and Windows-Eclipse Software Ltd. provide efficient networks for maximization of data changes and increase in flexibility. Sensor networks are the critical part in in-situ test. Advances in sensing technology have greatly promoted the application of sensor networks [7–9]. To make the best use of the measured results, remarkable progress has been made toward the optimal sensor placement technology [10, 11], the intelligent algorithms in the design of sensor networks [12], its evaluation criteria [13], data processing method [14], uncertainty analysis [15], and so forth. Up to now sensor networks have been applied to measurement of different types of infrastructures [16–19].

In the presented paper, a virtual instrument system is built by integrating computer technology, virtual instrument technology, and digital signal processing technology. The system is used to measure the subway-induced ground motion near a subway station in Shanghai Metro. A network of sensors is distributed to collect the vibration signals due to the running train. Some observations are obtained towards the ground motion in all the three dimensions in terms of acceleration time history, acceleration spectra, and the 1/3 octave band RMS spectra of the vertical acceleration.

2. The Measurement System

The measurement system consists of a personal computer (PC) and a data acquisition system (DAQ). The latter is developed based on the CompactRIO system which is an embedded platform based on real-time operating system. It includes a real-time controller, a reconfigurable field programmable gate array (FPGA), and a hot-pluggable industry module. The personal computer and the data acquisition system are connected through an ethernet cable. All the programming work is finished on the computer. Then the program is downloaded to the real-time controller and FPGA through the LabVIEW real-time module.

In the measurements, a set of sensors are distributed at designated locations to collect the signals, which are then transformed, amplified, and sent to the I/O data acquisition module. The I/O module further transfers the data to the FPGA through the FPGA program, from which the real-time controller reads the data through the RT program and transfers to the upper computer through the internet protocol. By using the data interaction program, the data are received and stored real-time after certain processing. Taking the acceleration signal as an example, the data acquisition process is shown in Figure 1.

The CompactRIO system is comprised of the cRIO-9074 chassis and acceleration acquisition module provided by the National Instruments (NI) company [20] (Figure 2). In the NI cRIO-9074 system, the real-time controller and the reconfigurable FPGA are integrated in the same chassis for the purpose of embedded machine control and monitoring. 128 MB dynamic random access memory for embedded operation and 256 MB nonvolatile memory for storing signals collected are integrated in the chassis. Two 10/100 Mb/s ethernet ports are available for communication and inclusion of I/O modules into the system through distributed slots. NI9234 module is used to collect dynamic signals, that is, acceleration

TABLE 1: Technical characteristics of the cRIO-9074 chassis.

Type	Operating system	FPGA	Number of gates	Number of slots	Operating temperature
CompactRIO	Real-time system	Spartan-3	Two million	8	-22°C~-55°C

TABLE 2: Technical characteristics of NI9234 module.

Operating system	Signal conditioning	Resolution rate	Sampling rate	Bandwidth	Synchronous
Windows	Antialiasing filter, current excitation	24 bits	51.2 ks/s	23.04 KHz	Yes

TABLE 3: Technical characteristics of acceleration sensor.

Sensitivity (mV/g)	Range (g)	Frequency range (Hz)	Resonance frequency (KHz)	Resolution rate	Shock resistance (g)
1000	5	0.1~1000	5	0.00002	300

in the present case. The relevant parameters for the cRIO-9074 chassis and NI9234 module are listed in Tables 1 and 2, respectively.

LC0161A piezoelectric acceleration sensors produced by the LANCE Technologies Inc. are used for collecting acceleration signals in all the three directions. This type of sensors has inherited the advantages of traditional piezoelectric acceleration sensors. In addition to that, a mini IC amplifier is embedded in it, making the measurement process greatly simplified. For the same reason, the measurement precision as well as reliability in adverse environment is also remarkably improved. Listed in Table 3 are the main technical characteristics of the acceleration sensors.

This system is verified through a bridge pier placed on a shaking table. Twelve sensors were distributed on the pier and table to record the acceleration when the table was excited by white noise. The response was compared and accorded well with that obtained by commercial data acquisition system [21].

3. Vibration Measurement Site and Environmental Vibration

The measurement site is located at a crossroad 500 m from the Zhongchun Road Station on the Jiuting Station—Zhongchun Road Station section of Line 9 of the Shanghai Metro. The site is shown by the star symbol in Figure 3(a) and a photo of the site is shown in Figure 3(b). There are three tunnels underground including a pair of straight ones and a curved one (Figure 4(a)); only the ground-borne vibration induced by train running in the bottom tunnel has been investigated. The area surrounded by the blue lines indicates a pavement on the ground. This location is close to the station and the train underground is either accelerating or decelerating. In addition, there are more buildings and human activities in this area. The influence of ground vibration is more important as compared to the case of long straight subway sections, which is associated with less buildings and populations. The site is open in the direction perpendicular to the line. The tunnel is 13.8 meters underground which is not deep; the soil above the tunnel is approximately horizontally layered and detailed information of the soil is available in Figure 4(b).

The background environmental vibration was tested first. During the measurement process, normal road traffic and human activities were present. There were no train transportation or construction activities in the nearby area. The measurement points were placed on a line perpendicular to the tunnel as shown in Figure 4(a) by the red points numbered from 1 to 6. The distances of points 1 to 6 to the center line of the tunnel were 0 m, 5 m, 10 m, 15 m, 20 m, and 30 m, respectively.

Since point 1 was the closest to the main road (perpendicular to the pavement shown in Figure 4(a)), it is supposed to be influenced by the environmental vibration the most. The response at measurement point 1 was taken as an example for the environmental vibration. The vibration in X, Y, and Z directions was recorded and displayed in Figure 5. X refers to the direction perpendicular to the tunnel, Y refers to the direction along the center line of the tunnel, and Z refers to the vertical direction.

It could be seen that the ground-borne vibration induced by normal vehicles and environmental noise was small. The acceleration amplitude in the X direction and Y direction was both less than 0.005 m/s^2 , while the amplitude in the Z direction was about 0.02 m/s^2 . The dominant frequency range of acceleration in the X direction was [0, 10] Hz and [50, 60] Hz. The dominant frequency range of acceleration in Y direction was [0, 10] Hz and [25, 35] Hz. The range for the acceleration in the Z direction was [0, 10] Hz and [50, 60] Hz. For all the three directions, dominant frequencies for background vibration were all below 60 Hz. It could also be seen that no obvious interference source was present.

4. Measurement of Vibration Induced by Underground Train

To measure the ground-borne vibration induced by the running underground train, the sensors have been placed at the same locations as that for measurement of environmental vibration.

4.1. Vibration at Measurement Point 1. Shown in Figure 6 are the time history and corresponding Fourier spectra of the vibration acceleration at the measurement point 1. As can be



FIGURE 3: The subway section and measurement setup.

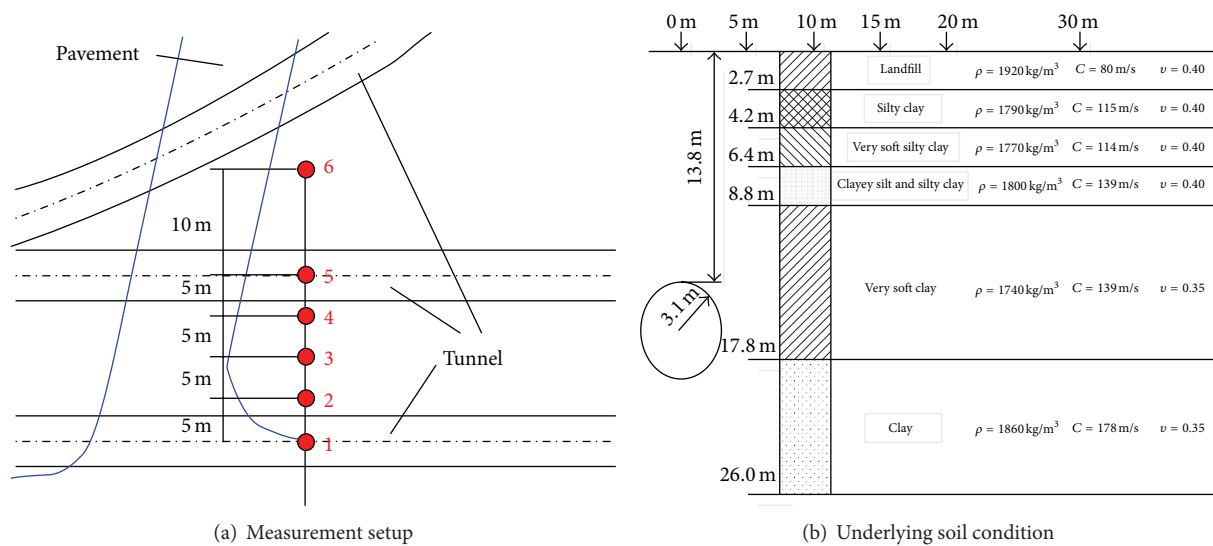


FIGURE 4: Measurement setup and soil condition of the measurement site.

seen from the figure, the vibration induced by the underground train lasted for about 20 seconds. Between the time intervals 8 s to 28 s, twelve peaks of accelerations were observed. The first peak and last peak corresponded to the vibration induced by the front wheels and back wheels of the train. For the remaining ten peaks, five pairs of peaks for wheel set could be clarified, which was consistent with the actual conditions. From the duration of the five pairs of peaks for wheel sets and length of the train, the speed of the train was estimated to be 30 km/h, which accorded with the speed for low-speed operation near the station.

The acceleration amplitude in the X and Y directions was about 0.062 m/s^2 and 0.044 m/s^2 , respectively, which were much more prominent than the corresponding environmental vibration. The amplitude in the Z direction was 0.145 m/s^2 , also much higher than the corresponding environmental vibration. So, for all the three directions, the influence of the environmental vibration could be neglected. The amplitude in Z direction was remarkably higher than that in the X and Y directions, so, in the investigated case, vibration in the Z direction was dominant.

Through fast Fourier transformation (FFT), the Fourier spectra for the acceleration at measurement point 1 were obtained. It could be seen that, for all the three directions, the acceleration corresponding to a frequency range of [30, 60] Hz was dominant, which was consistent with the frequency range for vibration of wheel tracks. It could also be seen that the acceleration spectra in the Z direction were wider than those in the other two directions, and the distribution was more complex. The stronger vertical vibration could be attributed to the shape of wave front caused by underground train. The wave front was a cylinder with the central axis coinciding with the train, so the dominant vibration at the ground would be vertical. As it is known that the human comfort is influenced more by the vertical vibration of the ground, so main attention should be paid to the ground-borne vibration in the Z direction. In the subsequent sections, only the acceleration in the Z direction was discussed.

4.2. Vibration of All Measured Points. The acceleration time history of measure points 1 to 6 is shown in Figure 7, standing

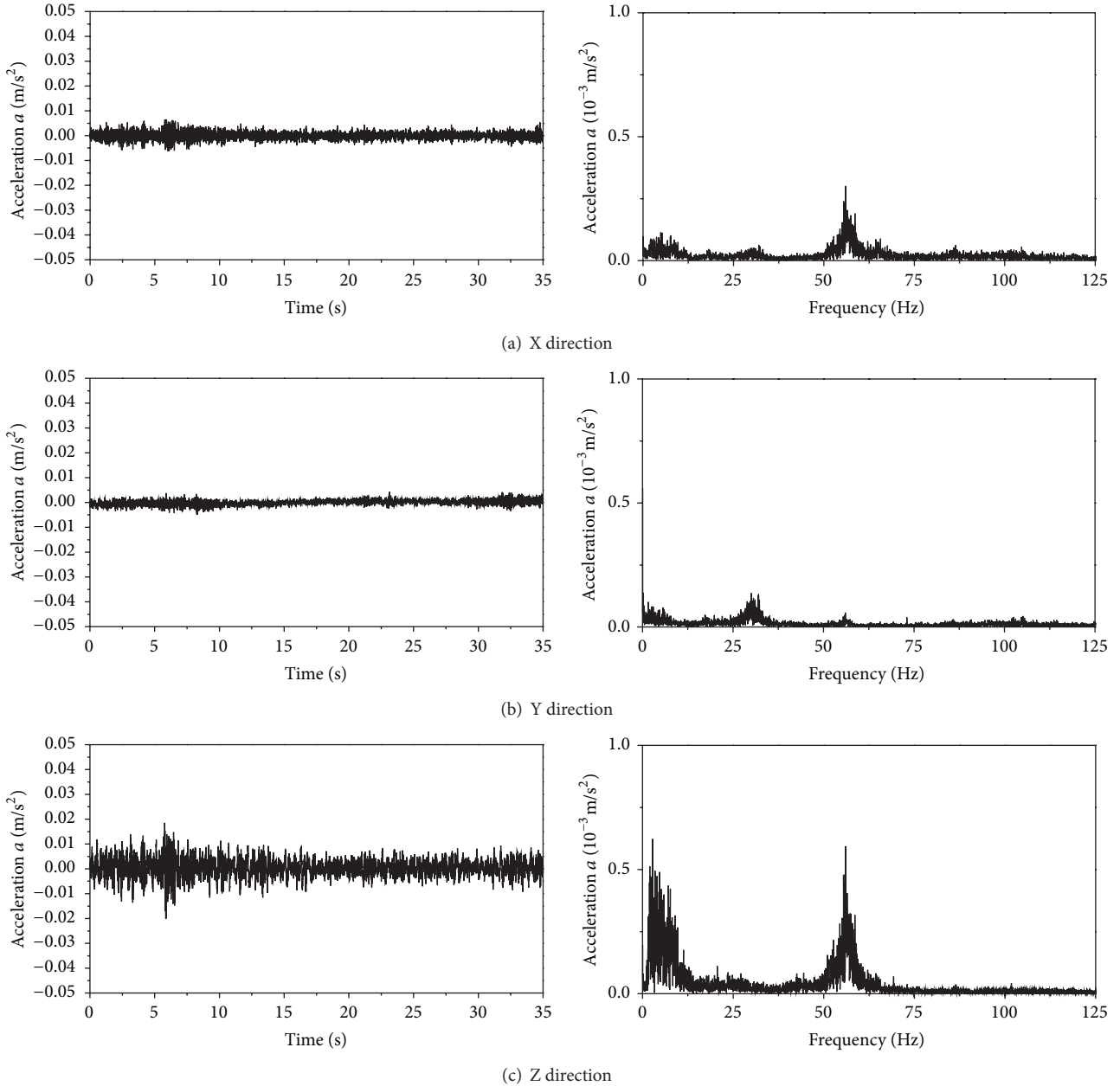


FIGURE 5: Time history and Fourier spectra of the background vibration acceleration.

for the vibration of ground 0 m, 5 m, 10 m, 15 m, 20 m, and 30 m from the center line of the tunnel. The corresponding Fourier spectra are shown in Figure 8.

4.3. Vibration Decay with respect to Distance in terms of Acceleration and Fourier Spectra. From the time history of acceleration in Figure 7, wheel track peaks were observed at time 8 s, 10 s, 14 s, 18 s, 22 s, 26 s, and 28 s. Based on the vibration at these time instants, the amplitude of acceleration for all the measurement points is plotted in Figure 9. The characteristics of the acceleration distribution could be analyzed through the damping effect and filtering effect of the soil, as stated below.

From the Fourier spectra of acceleration in Figure 8 and acceleration amplitude in Figure 9, it could be clearly seen that the acceleration amplitude and the corresponding spectra decreased as the distance from the tunnel increased. When the distance between the measurement points and center line of tunnel reached 30 m, the vibration decayed to a very low level, and the high-frequency components decayed faster than the low-frequency components. This phenomenon was caused due to the damping effect of the soil.

For all the time instants recorded, the vibration of the ground decreased with the distance on the whole. The acceleration amplitude at point 4 (15 m from the tunnel) was obviously higher than that at point 3 (10 m from the tunnel),

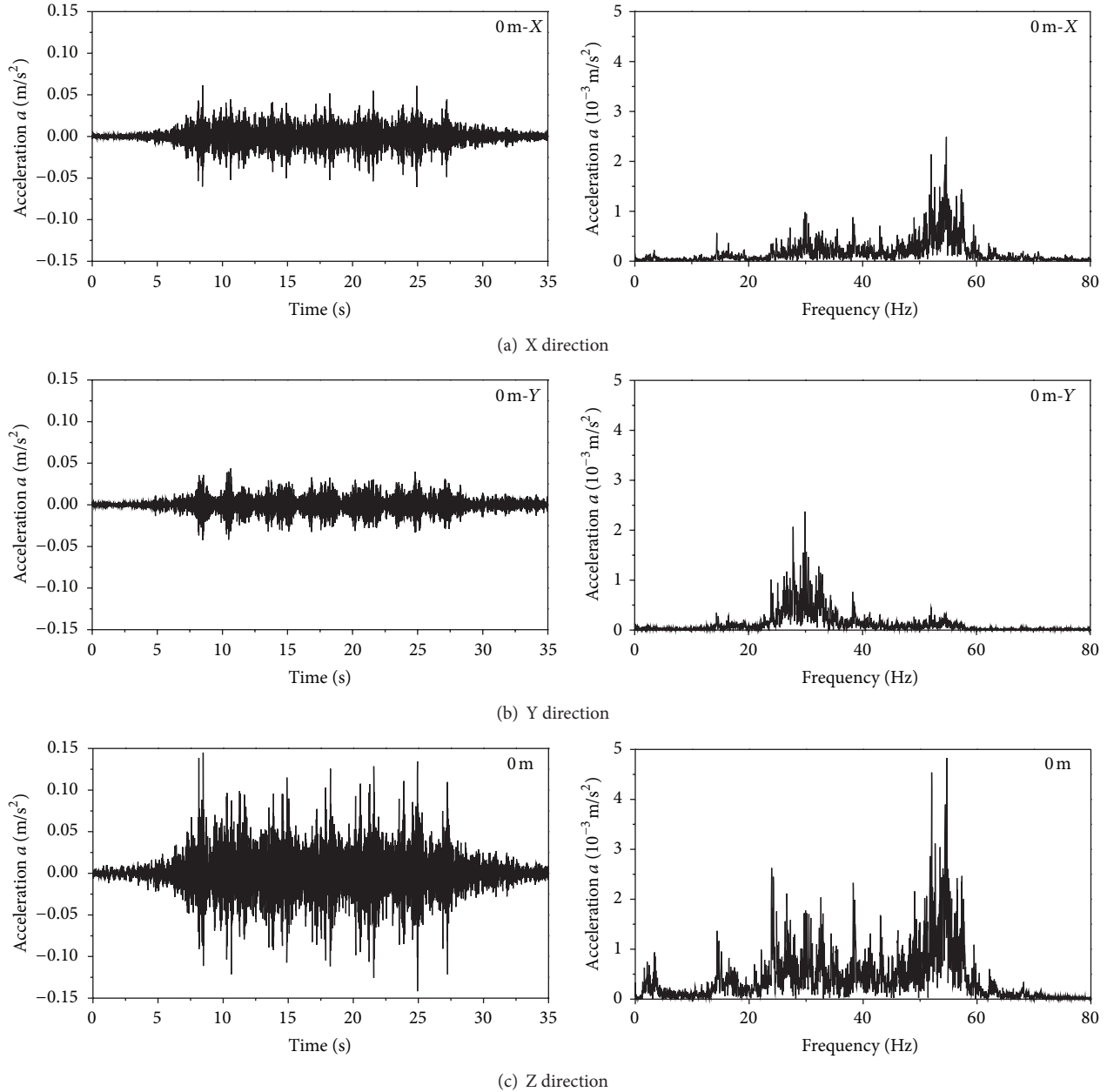


FIGURE 6: Time history and Fourier spectra of the vibration acceleration recorded by measurement point 1.

indicating amplification of vibration at point 4. For a train running underground, the vibration at the ground was transferred through the track, the shield, and the soil. Different soil configurations have different effects on the vibration. It can be reckoned that the soil under point 4 was not strictly horizontal or there were inclusions below this point, which caused the vibration beneath this point to be relatively easier to propagate. However, this easy-to-propagate effect was confined only to a small region and did not change the overall trend of vibration decay with distance.

By examining the corresponding spectra, it is found that the acceleration has been amplified for component within the frequency range 15~35 Hz, while the components for

higher frequency were decreased. This indicated that vibration amplification might appear for ground-borne vibration induced by underground trains, and for the current configuration of soil this happened for low frequency components. It could also be seen that the amplitude for the component with frequency around 20 Hz was extremely low, indicating that present soil has strong filtering effect to vibration with frequency components falling in this range.

4.4. Vibration Decay with respect to Distance in terms of the 1/3 Octave Band RMS Spectra. The 1/3 octave band RMS spectra of all points are shown in Figure 10. The relation between

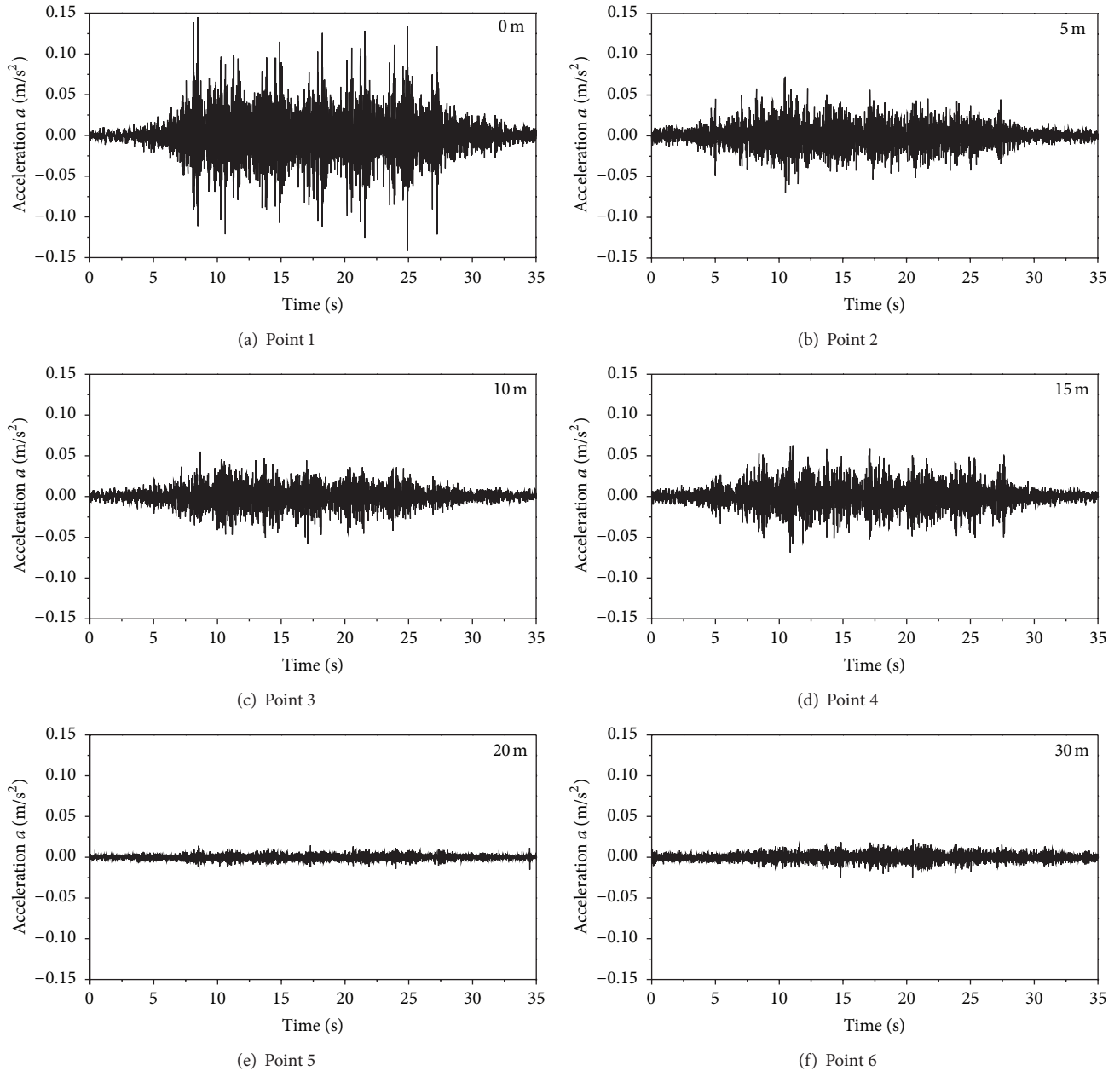


FIGURE 7: Time history of the vibration acceleration.

the spectrum and the distance is shown in Figure 11. On the whole, the spectrum decreased as the distance between the measurement point and tunnel increased. The low-frequency components decayed slower than the high-frequency components. Particularly the curve for the component with a frequency equal to 1 Hz was almost flat, with negligible fluctuation. The vibration of buildings nearby would be influenced by lower frequency components.

However, the spectrum was amplified at the measurement point 4 (15 m from the tunnel) for frequency ranging from 8 Hz to 31 Hz. From 13 m to 18 m, peak spectrum was obtained for these low frequency components. For components with higher frequency, the spectrum decayed with the distance and

no amplification zone was observed. This was consistent with the vibration amplification as stated in the previous section.

For all the measuring points, the vibration was reduced for frequency around 10 Hz, indicating a necking phenomenon. The explanation could be as follows. The vibration for components lower than 10 Hz was caused mainly by the environmental vibration and the influence of distance was small. But for higher frequency components, the vibration was attributed mainly to the underground train and the influence of environmental vibration was secondary. A similar phenomenon has been observed in [22], in which the frequency 10 Hz could be named as the joining frequency according to their definition.

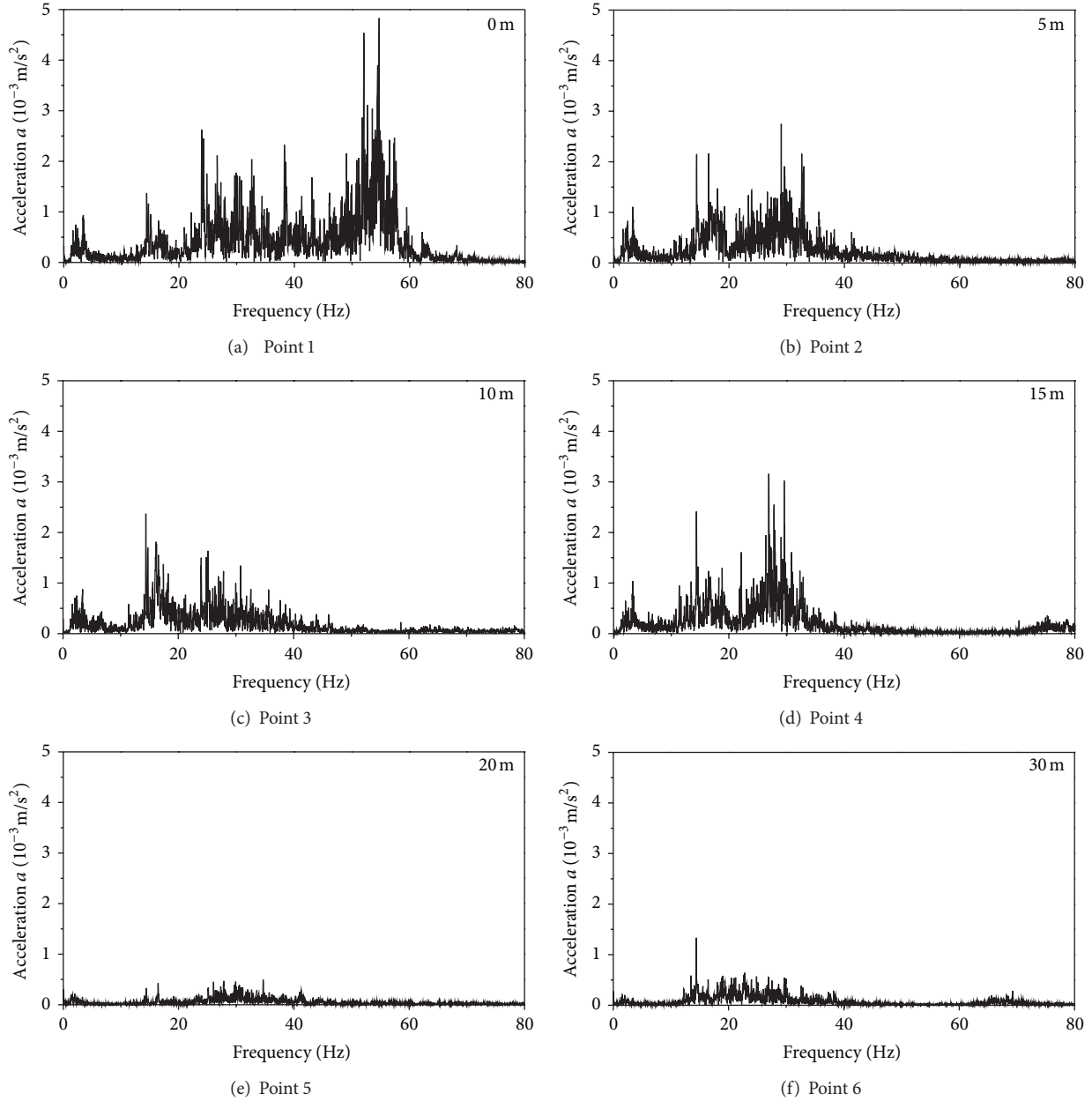


FIGURE 8: Fourier spectra of the vibration acceleration.

5. Conclusion

For measurement of ground-borne vibration induced by trains running underground near the subway station, a system based on the CompactRIO system and LabVIEW platform has been constructed, and a distributed network of sensors has been applied for in-situ measurement. The following conclusions were arrived at.

- (1) Among the three directions, the vibration in the Z (vertical) direction is dominant as compared to that in the horizontal directions.
- (2) The ground-borne vibration decreases as the distance from the tunnel increases and the high-frequency

components decay faster than the low-frequency components, so the buildings on the ground are subjected mainly to the vibration of low-frequency components.

- (3) For the presented site on the Shanghai Metro, there exists a vibration amplification zone which is about 15 m from the center line of the tunnel. The performance of buildings located by this distance from the tunnel should be paid with special attention. The components with a frequency between 8 Hz and 31 Hz are amplified in this zone, while those components beyond this range are not. Buildings with resonant

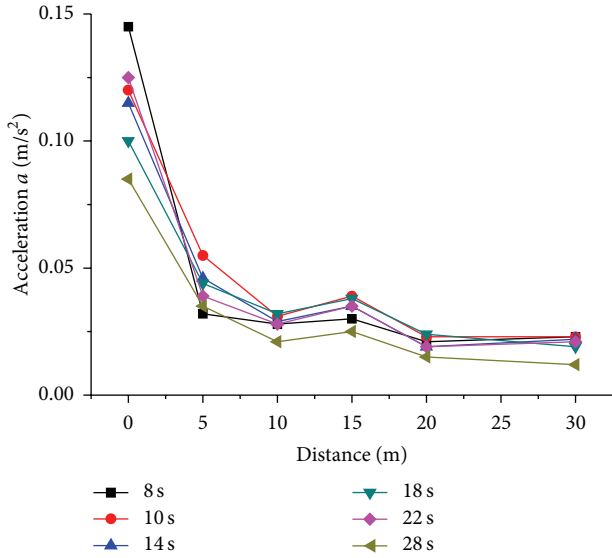


FIGURE 9: Fourier spectra of the vibration acceleration.

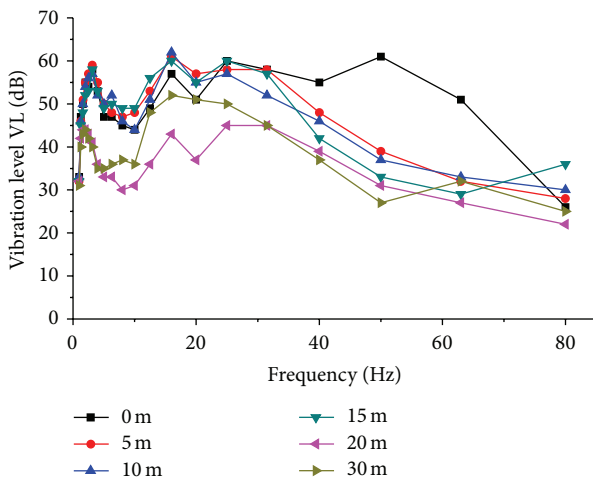


FIGURE 10: The 1/3 octave band RMS spectra with respect to the octave frequency.

frequency between 8 Hz and 31 Hz may be subjected to stronger influence from the running train.

- (4) The environmental vibration for near-station locations is similar to that for long straight subway sections. However, the position of the amplification zone, dominant frequency range, and corresponding 1/3 octave band RMS spectra are different. Considering the significance of near-station section on human's lives, more attention should be placed on this section.
- (5) By taking advantage of the sensing technology, networks of sensors have great potential in measuring and monitoring the vibration of ground and infrastructures induced by trains running underground.

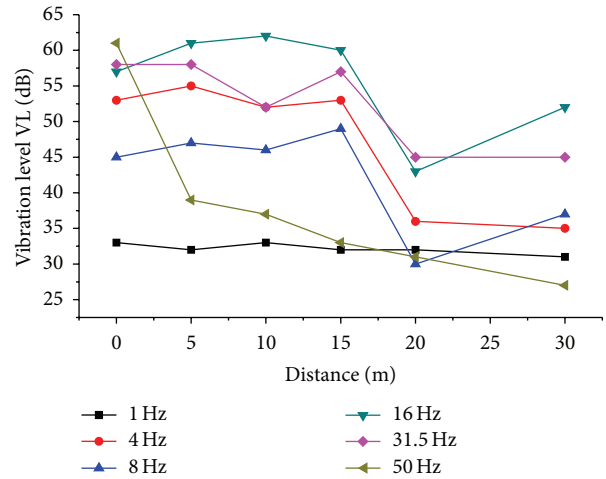


FIGURE 11: The 1/3 octave band RMS spectra with respect to the distance.

Conflict of Interests

The authors declare that there is no conflict of interests regarding the publication of this paper.

Acknowledgments

The research has been supported by the National Science Foundation of China under the Grant no. 51009019 and Sino-German Science Foundation under the Grant no. GZ566.

References

- [1] K. H. Chua, T. Balendra, and K. W. Lo, "Groundborne vibrations due to trains in tunnels," *Earthquake Engineering & Structural Dynamics*, vol. 21, no. 5, pp. 445–460, 1992.
- [2] S. Gupta, W. F. Liu, G. Degrande, G. Lombaert, and W. N. Liu, "Prediction of vibrations induced by underground railway traffic in Beijing," *Journal of Sound and Vibration*, vol. 310, no. 3, pp. 608–630, 2008.
- [3] M. Sanayei, P. Maurya, and J. A. Moore, "Measurement of building foundation and ground-borne vibrations due to surface trains and subways," *Engineering Structures*, vol. 53, pp. 102–111, 2013.
- [4] V. Nicolosi, M. d'Apuzzo, and E. Bogazzi, "A unified approach for the prediction of vibration induced by underground metro," in *Proceedings of the 5th International SIIV Congress—Sustainability of Road Infrastructures*, Rome, Italy, 2012.
- [5] W. Yang, M. F. M. Hussein, and A. M. Marshall, "Centrifuge and numerical modeling of ground-borne vibration from an underground tunnel," *Soil Dynamics and Earthquake Engineering*, vol. 51, pp. 23–34, 2013.
- [6] J. A. Forrest and H. E. M. Hunt, "Ground vibration generated by trains in underground tunnels," *Journal of Sound and Vibration*, vol. 294, no. 4, pp. 706–736, 2006.
- [7] T.-H. Yi, H.-N. Li, and M. Gu, "Recent research and applications of GPS-based monitoring technology for high-rise structures," *Structural Control and Health Monitoring*, vol. 20, no. 5, pp. 649–670, 2013.

- [8] H.-N. Li, D.-S. Li, and G.-B. Song, "Recent applications of fiber optic sensors to health monitoring in civil engineering," *Engineering Structures*, vol. 26, no. 11, pp. 1647–1657, 2004.
- [9] H.-M. Pan, F.-L. Zhou, and S. Liang, "Shaking table test for the structural model of Guangzhou new TV tower," *Engineering Mechanics*, vol. 25, no. 11, pp. 78–85, 2008.
- [10] T.-H. Yi, H.-N. Li, and M. Gu, "Characterization and extraction of global positioning system multipath signals using an improved particle-filtering algorithm," *Measurement Science and Technology*, vol. 22, no. 7, Article ID 075101, 2011.
- [11] T.-H. Yi, H.-N. Li, and M. Gu, "Optimal sensor placement for structural health monitoring based on multiple optimization strategies," *The Structural Design of Tall and Special Buildings*, vol. 20, no. 7, pp. 881–900, 2011.
- [12] D.-D. Ho, K.-D. Nguyen, H.-S. Yoon, and J.-T. Kim, "Multiscale acceleration-dynamic strain-impedance sensor system for structural health monitoring," *International Journal of Distributed Sensor Networks*, vol. 2012, Article ID 709208, 17 pages, 2012.
- [13] I. Ledvich and A. Segall, "Threshold-related throughput—a new criterion for evaluation of sensor network performance," *Ad Hoc Networks*, vol. 5, no. 8, pp. 1329–1348, 2007.
- [14] X. Zhao, M. Li, G. Song, and J. Xu, "Hierarchical ensemble-based data fusion for structural health monitoring," *Smart Materials and Structures*, vol. 19, no. 4, Article ID 045009, 2010.
- [15] M. Collett, T. J. Esward, P. M. Harris, C. E. Matthews, and I. M. Smith, "Simulating distributed measurement networks in which sensors may be faulty, noisy and interdependent: a software tool for sensor network design, data fusion and uncertainty evaluation," *Measurement*, vol. 46, no. 8, pp. 2647–2660, 2013.
- [16] S. M. S. L. Cheekiralla, *Development of a wireless sensor unit for tunnel monitoring [M.S. thesis]*, Civil Engineering Department and Ambient of the MIT-Massachusetts Institute of Technology, Cambridge, Mass, USA, 2004.
- [17] H. Gu, Y. Mosleh, D. Sanders, G. Song, and Y. L. Mo, "Multi-functional smart aggregate-based structural health monitoring of circular reinforced concrete columns subjected to seismic excitations," *Smart Materials and Structures*, vol. 19, no. 6, Article ID 065026, 2010.
- [18] Q. Huang, B. Xu, B. Li, G. Song, and J. Teng, "Monitoring for large cross-section CFSTs of a super high-rise building with piezoceramic actuators and sensors," *Advanced Materials Research*, vol. 163–167, pp. 2553–2559, 2011.
- [19] T.-H. Yi, H.-N. Li, and X.-D. Zhang, "Sensor placement on Canton tower for health monitoring using asynchronous-climbing monkey algorithm," *Smart Materials and Structures*, vol. 21, no. 12, Article ID 125023, 2012.
- [20] National Instruments Corporation, "The measurement and automation catalog," user manual, 1996.
- [21] W. Qu, H. Zhong, and G. Lin, "Set up of multi-channel system for vibration measurement and analysis of bridge along high-speed railway based on LabVIEW," *Instrument Technique and Sensor*, no. 8, pp. 15–18, 2012 (Chinese).
- [22] R. Li, W. Liu, and H. Zhang, "Test analysis of metro induced ground vibrations at interval," *China Railway Science*, vol. 29, no. 1, pp. 120–126, 2008 (Chinese).

Review Article

Thermal Load in Large-Scale Bridges: A State-of-the-Art Review

Guang-Dong Zhou¹ and Ting-Hua Yi^{2,3}

¹ College of Civil and Transportation Engineering, Hohai University, Nanjing 210098, China

² School of Civil Engineering, Dalian University of Technology, Dalian 116024, China

³ State Key Laboratory for Disaster Reduction in Civil Engineering, Tongji University, Shanghai 200092, China

Correspondence should be addressed to Guang-Dong Zhou; dagongzhougd@163.com

Received 2 August 2013; Accepted 31 October 2013

Academic Editor: Gangbing Song

Copyright © 2013 G.-D. Zhou and T.-H. Yi. This is an open access article distributed under the Creative Commons Attribution License, which permits unrestricted use, distribution, and reproduction in any medium, provided the original work is properly cited.

Thermal load is an important factor that must be taken into account during the procedure of bridge design and structural condition evaluation especially for those statically indeterminate bridges and cable-supported bridges. This paper presents an overview of current research and development activities in the field of thermal load in bridge, in which emphasis is placed on the thermal load models established by numerical analysis and field measurement. The theoretical formulations and boundary conditions of heat transfer in bridge are firstly outlined. And then, the states of the art of numerical solutions for temperature distribution in bridge including finite difference method and finite element method are reviewed in detail. Following that, the progress on thermal load in three types of representative bridges that are concrete bridge, steel-concrete composite bridge, and steel bridge based on field measurement data is discussed extensively. Finally, some existing problems and promising research efforts about thermal load in bridge are remarked.

1. Introduction

Different forms of bridges, such as cable-supported bridge, arch bridge, multispan continuous bridge and simple supported bridge, which are key elements of the highway infrastructure, have been built throughout the world to fulfill the requirements of modern society for advanced transportation [1–4]. Recent advances of design methodologies and construction technologies have made it possible to construct bridges with great size. Up to now, the span of bridge exceeds 1900 m, and the depth and the width of the box girder are more than 13 m and 35 m, respectively [5–7]. It is well known that the service life of those bridges almost exceeds 50 years or even 100 years sometimes. During the lifetime, it is inevitable that bridges are subjected to daily, seasonal, and yearly repeated cycles of heating and cooling induced by solar radiation and surrounding air. The up and down temperatures in structural components may cause nonlinear thermal load that influences the performance of bridges significantly.

In practice, the variation of temperatures affects bridges in a complicated manner. From the point of view of global response, uniform temperature changes cause large overall expansion and contraction in bridge components. On one hand, the deformation induces the shift of structural dynamic characteristics, which has significant influence on the results of damage identification using vibration-based methods. Researchers from Los Alamos National Laboratory found that the first three natural frequencies of the Alamosa Canyon Bridge varied about 4.7%, 6.6%, and 5.0% during a 24 h period as the temperature of the bridge deck changed by approximately 22°C [8, 9]. Liu and DeWolf [10] reported that, during a 1-year measurement, the first three frequencies of a curved concrete box bridge decreased by 0.8, 0.7, and 0.3% as temperature increased by one degree Celsius. Xu and Wu [11] analyzed the effects of change in environmental temperature on the frequencies and mode shape curvatures of a cable-stayed bridge considering seasonal temperature difference and sunshine temperature difference by finite element method. The outcome of the study indicates that

changes in dynamic characteristics of the bridge due to damage in girders or cables may be smaller than those due to variations in temperature. On the other hand, the continuous expansion and contraction may damage critical member of bridge, such as expansion joint, bearing, and anchor head. The service life and interval for replacement of expansion joints rely to a great extent on the cumulative displacements. Ni et al. [12] concluded that the movements of the expansion joints are highly correlated with the effective temperature based on the long-term monitoring data of expansion joint displacement and bridge temperature. Xu et al. [13] investigated the displacement responses of the Tsing Ma Bridge in Hong Kong from 1997 to 2005 using the measurement data recorded by structural health monitoring system. It was found that the longitudinal displacement responses of the bridge towers, deck sections, and cables show strong linear relationships with the effective deck temperature, and the vertical displacement of the deck sections and cables at the main span is also correlated with the effective deck temperature. And from the point of view of local response, temperature variations result in considerable thermal stresses if the thermal deformation of bridge components is restricted, which may be comparable to that induced by dead or live load. In concrete bridge, such stresses can initiate tensile failure for the low tensile strength of concrete. Those minute cracks due to tension may subsequently grow into large cracks that allow the reinforcing steel to be exposed to possible corrosion. The effect of corruptions of reinforced concrete on new and existing structures can be aggravated as a result of these thermal cracks in addition to the existing service load cracks [14]. In steel bridge, the fatigue performance of weld joints is degraded dramatically when those stresses superpose the welding residual stresses and the stresses induced by service load. Furthermore, the thermal stresses tend to change the stress distribution in steel and concrete of steel-concrete composite bridge and cause deterioration in material. Therefore, thermal load is an important factor that should be considered during the whole life of bridge. Failure to closely understand temperature effects may result in considerable damages in bridge and false alarms of structural deterioration [15, 16].

According to the different effects, the thermal load can be classified as effective temperature, vertical temperature difference (temperature gradient), and horizontal temperature difference. The effective temperature, which accounts for the expanding and contracting of bridge components in the longitudinal direction, is the weighted mean value of temperature distributed along the cross section. The vertical temperature difference, which results in supplementary internal axial forces and bending moments in vertical plane when the section ends are restrained, refers to the difference of temperatures between the top surface and other levels in the cross section [17]. The horizontal temperature difference, which induces secondary internal axial forces and bending moments in horizontal plane if the deformation is constrained, represents the difference of temperatures between two positions on the same level in the cross section. The effective temperature and vertical temperature difference are included in almost all bridge design specifications. According

to the definition, the effective temperature T_e , vertical temperature difference T_v , and horizontal temperature difference T_h can be expressed as

$$\begin{aligned} T_e &= \frac{1}{A} \iint_A T(x, y) dx dy, \\ T_v &= \frac{H}{I_x} \iint_A T(x, y) y dx dy, \\ T_h &= \frac{W}{I_y} \iint_A T(x, y) x dx dy, \end{aligned} \quad (1)$$

where A represents the area of the cross section; $T(x, y)$ represents the two-dimensional temperature over the cross section, and x and y represent the horizontal and vertical axis of the cross section, respectively; I_x and I_y represent the moments of inertia of the section about the x and y axes, respectively; and H and W represent the depth and width of the cross section, respectively.

Early in the 1960s, Zuk [18] started a study on the thermal behaviour of highway bridges. It was concluded that the thermal load is affected by air temperature, wind, humidity, intensity of solar radiation, and material type after investigation on several bridges. Subsequently, researchers and engineers were aware of the nonlinear temperature distribution developed within a bridge gradually. Study on thermal load in different bridges subjected to the change of environmental factors has been performed all over the world. Those researches can be roughly divided into three categories, which are theoretical method, numerical approach, and field measurement. The theoretical method is aimed to pursue the closed-form solutions of the heat transfer equation and reveal the temperature distribution in bridges, which must employ a series of assumptions. The numerical approach solves the heat transfer equation by finite element method or finite difference method, which can give acceptable results if the input parameters are adjusted properly. The field measurement obtains the temperature distribution by temperature sensors installed on full-scale bridges in real environment, which provides the most meaningful thermal load of bridges. Each one has its advantages and disadvantages. It is difficult to say that one method is better than others.

In this paper, the research progress of thermal load in bridge over the past several decades is reviewed in detail. A brief overview of the theoretical model of heat transfer in bridge is outlined in Section 2. And then, the numerical approach used to solve the theoretical model is provided in Section 3. After that, the field measurement results of concrete bridges, steel-concrete composite bridges, and steel bridges, in addition to temperature sensor and data processing methodology, are investigated in Section 4. Finally, the conclusions and recommendations are given in Section 5. This paper is not intended to list all literatures about thermal load in bridge but to exhibit some representative achievements. Through pertinent assessment, the problems and promising directions about the topic of thermal load in bridge are expected to be extracted for future research.

2. Theoretical Model

Temperature distribution within a bridge is governed by heat conduction inside its body and the convective and radiative heat exchange with the surrounding environment. The heat conduction can be modeled by applying the principle of the Fourier's law, and the heat exchange is formulated by boundary condition.

In 1822, Fourier stated that the rate of heat transfer is proportional to the temperature gradient in a solid and established the well-known Fourier partial differential equation, which is [14, 19, 20]

$$\frac{\partial}{\partial x} \left(k_x \frac{\partial T}{\partial x} \right) + \frac{\partial}{\partial y} \left(k_y \frac{\partial T}{\partial y} \right) + \frac{\partial}{\partial z} \left(k_z \frac{\partial T}{\partial z} \right) + Q = c\rho \frac{\partial T}{\partial t}, \quad (2)$$

where x , y , and z represent Cartesian coordinates, which are the horizontal, vertical, and longitudinal axes of bridge, respectively; k_x , k_y , and k_z represent thermal conductivities corresponding to the x , y , and z Cartesian axes; t represents time; T represents temperature at position (x, y, z) at time t ; Q represents the rate of heat generated per unit volume; c represents coefficient of specific heat of medium; and ρ represents density of medium.

For a bridge exposed to solar radiation, it can be assumed that the material is continuum, isotropic, and homogeneity. Based on the results investigated by McClure et al. from the field measured data obtained by thermocouples [21], the thermal flow along the direction of the longitudinal axis can be normally neglected. After the hydration of cement in concrete bridge and the action of welding in steel bridge, the rate of generating heat Q can be set to zero. Therefore, (2) can be simplified as a two-dimensional model as

$$k \left(\frac{\partial^2 T}{\partial x^2} + \frac{\partial^2 T}{\partial y^2} \right) = c\rho \frac{\partial T}{\partial t}, \quad (3)$$

where k represents thermal conductivity.

If only the vertical temperature gradient is considered, the temperature differential in x direction can be ignored. Equation (3) can be further rewritten as

$$k \frac{\partial^2 T}{\partial y^2} = c\rho \frac{\partial T}{\partial t}. \quad (4)$$

Considering heat exchange, the boundary condition associated with (3) is expressed as follows [20]:

$$k \left(\frac{\partial T}{\partial x} n_x + \frac{\partial T}{\partial y} n_y \right) + q = 0, \quad (5)$$

where n_x and n_y represent the direction cosines of the unit outward vector normal to the boundary surfaces, and q represents the rate of heat exchanged between the boundary and the environment per unit area.

The heat exchange between the boundary of bridge and the environment is very complex, as shown in Figure 1. It is composed of three principal mechanisms: solar radiation, convection, and thermal irradiation. And the solar radiation

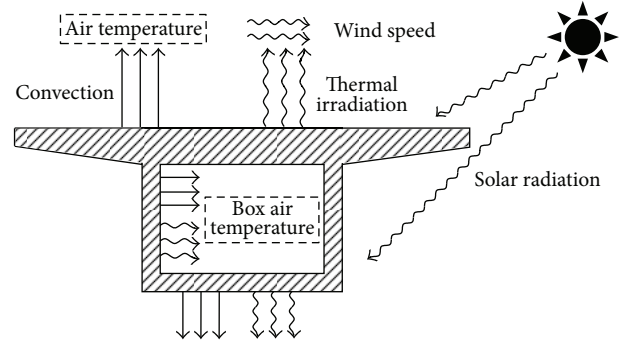


FIGURE 1: Heat exchange between the boundary and the environment.

is generally considered to be the most important one among the three mechanisms. The rate of heat exchange q is the sum of the three actions,

$$q = q_s + q_c + q_r, \quad (6)$$

where q_s represents the solar radiation; q_c represents the convection; and q_r represents the irradiation from the surface to the surrounding air. Each of these parameters varies with the positions considered and the time.

The rate of heat due to solar radiation q_s , that is, shortwave radiation, received by the bridge can be expressed as [22]

$$q_s = \alpha I, \quad (7)$$

where α represents the dimensionless absorptivity of the surface of the bridge; I represents the total solar radiation on a tilted surface, which depends upon the point considered and the incidence angle of sun rays. In shaded areas, I is equal to 0.

The total solar radiation on the inclined surface can be formulated as a function of variables related to the location and orientation of the bridge (latitude, altitude, solar declination, transmission factor, the bridge azimuth, etc.) [23]. Another way obtaining the value of this climatic parameter starts from the beam (direct) radiation, diffuse radiation, and ground-reflected radiation and using sinusoidal functions, which is in good agreement with experimental results [14]. In this way, the total solar radiation on the inclined surface is divided into three components: beam (direct) radiation, diffuse radiation, and ground-reflected radiation [20, 22, 24]. Beam radiation, the major component of solar radiation, is the solar radiation received from the sun not scattered by the atmosphere. It is often referred to as direct solar radiation. Diffuse radiation is the solar radiation received from the sun after its direction is changed by the atmosphere through a process of scattering. This makes things, even indoors, visible without direct sunlight. Ground-reflected radiation is radiation reflected from the ground cover and bodies of water on the surface of the earth. Although beam radiation is the major component causing nonuniform temperature distribution in the bridge, diffuse radiation and ground-reflected radiation are not negligible [25]. So the total solar radiation can be calculated by the equation presented by

Duffie and Beckman [22] and Orgill and Hollands [24], which is

$$I = I_b \frac{\cos \theta}{\cos \theta_z} + I_d \left(\frac{1 + \cos \beta}{2} \right) + (I_b + I_d) \eta \left(\frac{1 - \cos \beta}{2} \right), \quad (8)$$

where I_b and I_d represent the beam solar radiation and the diffuse radiation on a horizontal surface, respectively; θ represents the angle of incidence (the angle between the beam radiation on a surface and the normal to that surface); θ_z represents the zenith angle; β represents the slope, that is, the angle between the plane surface in question and the horizontal surface; η represents the diffuse ground reflection.

The heat lost to or gained from the surrounding air by convection as a result of temperature differences between the bridge surface and the air is given by Newton's law of cooling as [23]

$$q_c = h_c (T_s - T_a), \quad (9)$$

where h_c represents the convection coefficient of heat transfer; T_s represents the temperature of the surface contact with the air; and T_a represents the air temperature. Because of the complexity of heat transfer by convection, the convection coefficient of heat transfer h_c is a function of many variables such as wind speed, surface roughness, and geometric configuration of the exposed structure. The accurate analytical expression that describes those factors is unavailable now.

The heat transfer between the bridge surface and the surrounding atmosphere due to thermal irradiation, that is, long wave radiation, produces a nonlinear boundary condition which can be modeled by Stefan-Boltzmann radiation law as [20, 23, 26]

$$q_r = C_s e [(T_s + T^*) - (T_a + T^*)], \quad (10)$$

where C_s represents the Stefan-Boltzmann constant; e represents the emissivity coefficient relating the radiation of the bridge surface to that of an ideal black body ($0 \leq e \leq 1$); and T^* represents the constant used to convert temperature in degree Celsius to degree Kelvin.

It can be seen from (6) to (10) that parameters q_s , q_c , and q_r , which depend greatly on environmental factors and material properties, cannot be formulated by simple equations. If all these effects are taken into account, (2), (3), and (4) become nonlinear. Although the heat transfer equation was developed for many years and the parameters in the equation were discussed extensively, it is almost impossible to give a closed-form solution of (2), (3), and (4) since the temperature T changes with time, position, and a large number of climate parameters, especially in the analysis of bridges with complicated geometric configuration. Therefore, the numerical approaches such as finite difference method and finite element method are adopted in general.

3. Numerical Analysis

3.1. Finite Difference Method. The partial differential equation (3) is so complex that finding its solutions in closed

form or by purely analytical means (e.g., by Laplace and Fourier transform methods, or in the form of a power series) is either impossible or impracticable, and one has to resort to seeking numerical approximations to the unknown analytical solution very frequently. One idea is to replace the derivatives appearing in the partial differential equation by finite difference equations that approximate them. This concept promotes a significant type of numerical methods for approximating the solutions to partial differential equations, which is named as the finite difference method. The finite difference equations are derived from Taylor's polynomial. The approach allows the treatment of different environmental boundary condition separately at each time step [27].

In the 1970s, Emerson [28] extended the finite difference method to calculate the distribution of temperature in concrete, steel, and composite bridges resulting from solar radiation, ambient air temperature, and wind speed by assuming that the flow of heat through the bridge is linear. Then, this method was improved by Hunt and Cooke [29] and was used to solve the one-dimensional heat transfer equation for a concrete box girder bridge. In this model, the bridge was considered as two layers with different thermal properties, while only the homogeneous bridge decks were considered. This method has also been used by Zichner with the same purpose [30].

Through improving the deficiencies of the existing method, Dilger et al. [26] developed a systemic one-dimensional finite difference program to predict the temperature distribution in the cross section of composite box girder bridges with arbitrary geometry and orientation for a given geographic location and environmental conditions. After a large number of calculations, it was found that the thermal load is the highest under the following conditions: extreme diurnal variation of the ambient temperature, dark surface of the steel box, snow or ice cover on top of the bridge, high solar radiation intensity in areas of no air pollution and elevations high above sea level, winter and spring conditions, no wind, small or no overhanging cantilever, and large steel box. The worst combine of those parameters may result in a maximum temperature difference up to 70°C. Furthermore, they suggested the methods to reduce temperature difference between steel and concrete, which are painting the steel box in a bright color, providing a long cantilevering deck, and sloping the webs of the box.

Potgieter and Gamble [31] developed a one-dimensional finite difference method to simulate transient heat flow in bridges. The method was used to calculate the distribution of temperatures through the depth of a concrete section, based on ambient climatic variables (solar radiation, daily air temperature fluctuations, and wind speed) and material properties (absorptivity, density, specific heat, and conductivity). Reasonable agreement was found between computed temperature distributions and experimental measurements for the Kishwaukee River Bridge at Rockford, Illinois. By using this method, they [32] conducted a comprehensive study of nonlinear thermal gradients of bridges at various locations in the United States in 1989. The interest was in overall response of bridge structures to a relatively large number of different climatic conditions. An extreme temperature difference of

32°C was obtained for a bare concrete deck located in the desert southwest United States.

Almost at the same time, Ho and Liu [33] assumed a one-dimensional finite difference model. Particular emphasis was placed on the statistical aspect of the thermal loading. Calibration of the mathematical model was based on a comparison of the statistics of the measured and calculated thermal loadings and not, as is often the case, by comparing the analytical results with field data observed on any one particular day (or days). In the statistical analysis, instead of simulating thermal loads one by one, which requires lengthy calculations, Evans's method [34] based on the idea of Gaussian integration was used.

Mirambell and Aguado [35] expanded the finite difference method from one dimension to two dimensions in order to determine the time-dependent vertical and transverse temperature differences within the cross section of concrete bridges. The same assumptions about environment condition used by Elbadry and Ghali [23] were adopted in this study. The main objective of this study is investigating the influence of the cross section geometry of concrete box girder bridges on their thermal distribution. The results indicated that the maximum vertical temperature difference and the daily range of effective temperature of the cross section decrease with an increase in the superstructure depth, as shown in Figure 2. In the figure, the depths of sections A-A, B-B, and C-C are 2.2 m, 3.1 m, and 5.0 m, respectively. The outcome of the study also indicated that the ranges of the daily variation of the vertical temperature difference and the effective temperature are higher in the unicellular cross section than those in multicellular cross section. In concrete box girder bridges with variable bending stiffnesses along the longitudinal axis of the bridge, the cross section subjected to the greatest vertical temperature difference and to the greatest temperature difference between the external air and the air enclosed in the cells is the midspan section, while the cross sections of the intermediate supports are subjected to the greatest transverse temperature differences. Comparing the geometrical parameters, it was found that the superstructure depth and the ratio between the deck's upper and bottom slab width are those with the greatest influence on the temperature distributions of concrete box girder bridges. It should be noted that this investigation pointed out the transverse temperature difference caused by the difference of temperature between the external air and the air enclosed within the cells which is significant and should be considered in design when the superstructure depth is large, which was rarely mentioned before. According to the study, the daily evolution of transverse temperature difference at the three cross sections is displayed in Figure 3.

In the following ten years, the researches of temperature distribution in bridge by finite difference method are seldom. Until 2007, Riding et al. [36] proposed a mass concrete temperature prediction model employing the finite difference method to characterize the heat transfer at the top and side surfaces of concrete members. The model includes solar radiation, atmospheric radiation, ground surface radiation, radiation exchange with formwork bracing, and irradiation. The effects of free convection, forced convection, and

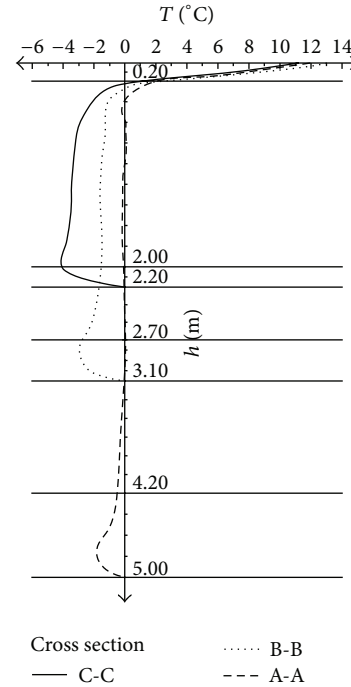


FIGURE 2: Temperature distributions along the depth of cross section [35].

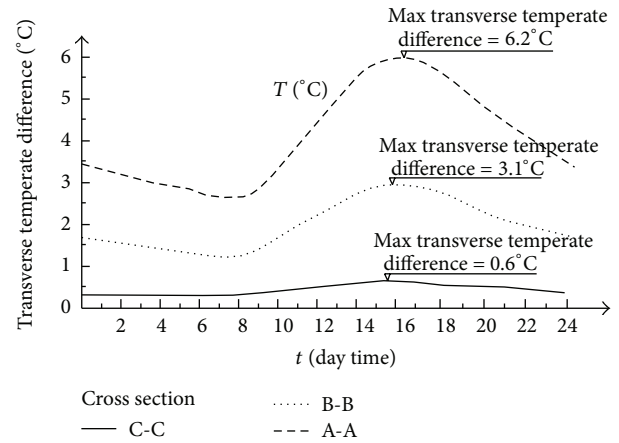


FIGURE 3: Daily evolution of transverse temperature difference at the three cross sections [35].

surface roughness were also characterized in the model. The predicted temperatures were compared with concrete temperature data collected from 12 concrete members of varying geometry, formwork, location, construction methods, and materials. The results showed that the finite difference heat transfer model can accurately estimate the near-surface concrete temperatures, the maximum temperature, and maximum temperature difference of the 12 concrete members.

3.2. Finite Element Method. Apart from the finite difference method, another particular class of numerical techniques for the approximate solution of partial differential equations is

the finite element method, which originated from the need to solve complex elasticity and structural analysis problems in civil and aeronautical engineering. This method was proposed in a seminal work of Richard Courant in 1943 [37] and obtained its real impetus from the contributions of many forerunners, like Argyris, Clough, Zienkiewicz, and Richard Gallagher, in the 1960s and 70s. Now, finite element methods have been developed into one of the most general and powerful class of techniques for the numerical solution of partial differential equations and are widely used in structure design and analysis.

By assuming that the thermal variation in the longitudinal direction of the bridge and the transverse heat flow are insignificant, Priestley [38] conducted a one-dimensional finite element analyse and proposed a most widely accepted thermal gradient model of box girder concrete bridge. The model describes the thermal gradient by fifth-order curve and has been validated for sections with relatively small depths by several theoretical and experimental programs. This model was then adopted by bridge design code in New Zealand.

In 1978, Emanuel and Hulsey [39] provided a finite element model to predict the vertical temperature distribution through the cross section of a composite bridge beam at different hours of day and night from weather data by assuming concrete as homogeneous and isotropic. They showed how the ambient conditions influence the temperature distribution in a composite section. Afterward, Berwanger [40] established an accurate two-dimensional finite element procedure for predicting transient temperatures in composite slab-steel beam highway bridges. A linear temperature rectangular finite element is used. The numerical integration for successive time increments was carried out using the Crank-Nicolson approximation. Statistical analyses indicated a better than 0.99 probability of correlation between the predicted and measured temperatures.

Elbadry and Ghali [23] proposed a two-dimensional finite element method to predict the time-dependent nonlinear temperature distribution over concrete bridge cross sections of arbitrary geometry and orientation. By using the bilinear quadrilateral interior elements to simulate the inner body and linear one-dimensional fictitious elements to represent the boundaries, the finite element formulations were established. A series of transient finite element analyses were performed to study the influences of various parameters including bridge axis orientation, ambient temperature extremes, wind speed, surface cover, and section shape on the temperature distribution of concrete bridges of various cross section types. The outcome of the study indicates that the temperature gradient is in general greater in summer than it is in spring or winter. The temperature gradient increases with increasing the daily range of the ambient temperature. Higher wind speed tends to bring the temperature of the bridge surfaces closer to that of the ambient air. The presence of asphalt overlay on the concrete deck results in an increase in the top surface temperature, and snow reduces each of these variables. Bridges of the same depth but with different cross section shapes have almost the same temperature distribution, and the temperature distribution varies considerably with the section depth being verified.

Based on a finite element program ADINAT, a two-dimensional analysis was performed by Fu et al. [14] to study the thermal behavior of three types of composite bridge structures subjected to solar radiation, namely, a plate-girder, a single-cell box, and a two-cell box girder concrete-steel composite bridge. A series of transient temperature distributions for a few selected temperature cases corresponding to a given geographic location and assumed environmental conditions was computed. The results of this study confirmed that a steady-state thermal condition never exists within a bridge structure. Meaningful conclusions were drawn in this research including the most influential variable on the temperature distribution within a bridge deck which appears to be the slab overhang-to-depth ratio; the effects of heating of air inside an enclosed box should be included in predicting the temperature distribution for box girder bridges; the convection constant, that is, the cooling or heating produced by the wind, substantially affects the temperature distribution when the bridge is being heated by solar radiation; and daily air temperature extremes have a marked influence on the thermal distribution of a composite bridge.

Moorty and Roeder [41] conducted a two-dimensional analysis for a typical bridge with concrete box girder, concrete T-beam, and steel girder with a composite deck using the finite element program ANSYS. The isoparametric quadrilateral thermal shell elements were used to model the deck, concrete T-beams, and box girders. Two-dimensional conducting bar elements were used to model the steel girders. The convection boundary conditions were achieved using convection links. The analysis was conducted for four days in order to eliminate the effect of the assumed initial conditions and suggested that concrete bridges sometimes are designed for smaller temperature ranges than expected values in practice, and steel bridges with composite concrete decks sometimes are designed for larger temperature ranges than expected values at many locations in the United States. Subsequently, Branco and Mendes [42] provided a numerical technique for the resolution of the Fourier heat transfer equation based on the two-dimensional finite element method. The results obtained with this technique had been demonstrated by several cases with experimental measurements. To come up with design thermal linear gradients, a parametric study had been developed for three types of typical deck cross sections: slab deck, T-beam deck, and box girders. The results formed two vertical temperature differences for two solar radiation conditions, and the design temperature differences for other situations can be calculated from the reference ones through the adjustive coefficients estimated by the parametric study. Furthermore, it was found that temperature differences occur among the deck, towers, and cables during the day in cable-stayed bridges due to the different orientation of the structural elements to the sun. In long-span cantilever bridges, the variation of the cross section leads to different design thermal gradients along the span.

Early researches concentrate on concrete bridges and composite bridges; with the wide use of steel in bridges all over the world, the study on thermal load in steel bridges was also implemented. Tong et al. [43] developed a numerical two-dimensional heat transfer model for

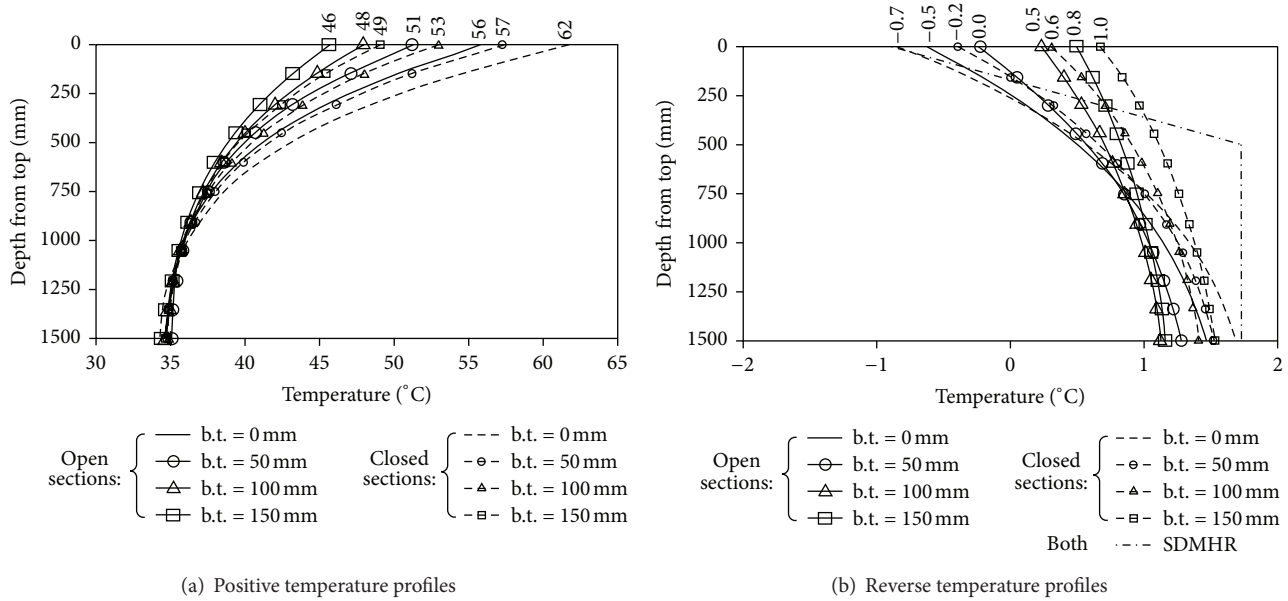


FIGURE 4: Design temperature profiles for various bitumen thicknesses (b.t.) for 50-year return period [44].

the analysis of temperature distribution in steel bridges. By assuming that the longitudinal heat flow in a prismatic deck can be neglected under normal circumstances and there is negligible temperature gradient across the thickness of steel plates because of the high thermal conductivity and small thickness of steel plates, the matrix “equilibrium” equation for steel plate was established, and then the temperature distribution of the bridge had been obtained by carrying-out time marching following the standard finite element procedure. The proposed approach was validated by two scaled steel box models. Sensitivity analysis showed that the top film coefficient and absorptivity have significant effect on temperature distribution. In addition, a least square method was suggested for backfiguring best values for the input parameters, if they are not available. Then, they integrated a statistical model, which was established by the numerical integration technique suggested by Evans [34] and subsequently modified by Ho and Liu [33] into this finite element model and developed a statistical approach to determine site-specific temperature profiles for code documents where the requisite climatic information for a particular geographic location is available [44]. Based on the method, some fifth-order design temperature profiles had been developed for both open and closed steel sections in tropical region, with adjustments for various thicknesses of bituminous surfacing, as shown in Figure 4. The proposed method avoids very lengthy calculations and facilitates the development of site-specific temperature profiles for code documents if the field measurement temperatures are unavailable, and it can also be applied to create zoning maps for temperature loading for large countries like the United States where there are great climatic differences.

In the 21st century, the commercial finite element software has been developed rapidly. The powerful processing capability makes the temperature distribution analysis of bridges with complex geometric configuration competent.

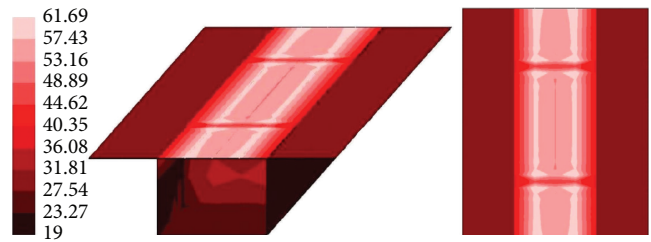


FIGURE 5: Temperature distribution in the steel part of a typical box girder bridge (unit: °C) [45].

Backer et al. [45] established a detailed finite element model of a steel box girder within the Vilvoorde Viaduct, including stiffeners, diaphragms, and wearing courses, by using commercial finite element software in order to reach a fundamental insight into the temperature distribution of the cross section with orthotropic stiffeners, subjected to a variable thermal load. All thermal fluxes within this system were modeled including solar radiation, radiation with the environment, mutual radiation, and convective airflow, which allowed verification of the temperature variations in the steel box during a 24-hour cycle as well as during a longer period. The finite element models developed for this research had validated the possibility to model mutual radiation between the different objects within the model and the surrounding environment. The simulated results were demonstrated by the field measurement data. The temperature distribution in such a steel box girder on a sunny summer day at noon is plotted in Figure 5. The asphalt layer is not displayed in this figure. It is immediately obvious that an important temperature difference can arise between the upper and lower part of the box girder. For this specific example, the temperature difference rises to a value of more than 40°C. Studying the top view of the deck plate of the bridge, as shown in the right

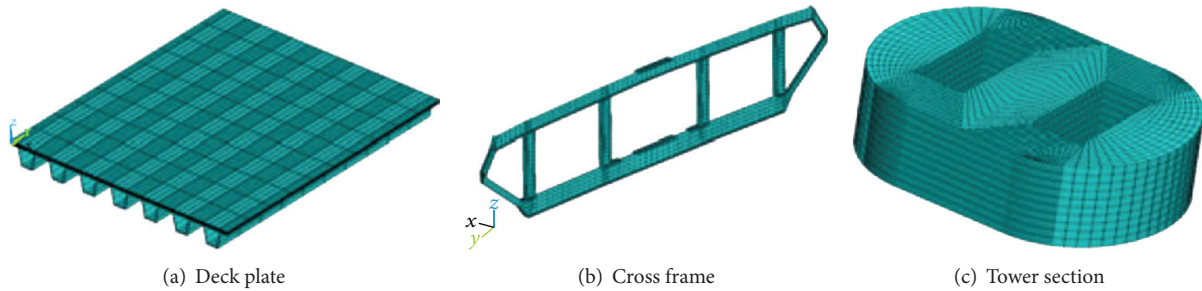


FIGURE 6: Finite element models of bridge components for thermal analysis [46].

side of Figure 5, the influence of the underlying structure and the diaphragms is quite obvious. Kim et al. [25] proposed a method to predict the 3-dimensional temperature distribution of curved steel box girder bridges using a theoretical solar radiation energy equation together with a commercial FEM program. The diverse range of bridges directions, radii, span lengths, and bearing setup directions was taken into consideration. It was strongly suggested that the nonuniform temperature distribution brought about by solar radiation should be considered in the design of curved bridges.

Xia et al. [46], for the first time, investigated the temperature distribution in a long-span suspension bridge—the 2132-m-long Tsing Ma Bridge—through finite element analysis. With appropriate assumptions, the bridge was divided into deck plate, section frame, and bridge tower, as shown in Figure 6. Fine finite element model of each component was constructed to facilitate thermal analysis. With ambient temperature measurements and a solar radiation model, the time-dependent temperature distribution within each of these components was calculated through transient heat transfer analysis. The numerical results were verified by comparing them with field monitoring data on temperature distributions and variation at different times and in different seasons, which provide thermal loads for thermal effect analysis of long-span suspension bridge.

In addition, Lee [47] performed a 2D heat-transfer analysis based on finite element method. The model was firstly validated and then used to determine the seasonal temperature gradients in four standard PCI girder sections at eight cities in the United States. The proposed vertical thermal gradient and transverse thermal gradients with respect to the locations across the top flange, the web, and the bottom flange of prestressed concrete bridge girders were shown in Figures 7 and 8, respectively. On the basis of the numerical model and the extreme environmental conditions, the maximum vertical temperature differentials were found in the summer in an east-west orientation, and the maximum transverse temperature differentials were found in the winter in an east-west orientation. The differences in the maximum vertical and transverse temperature differentials between the exterior and interior girders were negligible during construction, prior to the placement of concrete decks. The results show that, among the four AASHTO-PCI sections, the deeper and wider sections of Type-V and BT-63 girders exhibited the largest vertical and transverse temperature differentials.

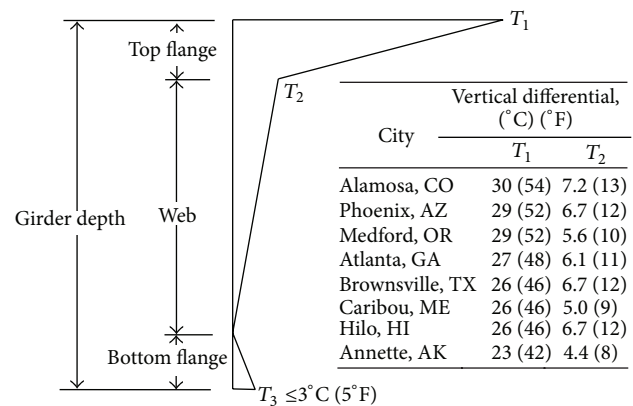


FIGURE 7: Vertical thermal gradient of prestressed concrete bridge girders [47].

Numerical analysis provides a perfect approach to predict the thermal load in bridge with different boundary conditions and makes it possible to perform extensive study on the influence of environment conditions, geometrical configuration, and material property. It is useful for a thorough understanding of the temperature behavior of various types of bridges and gives basic concept for thermal stresses calculation in bridge design. However, numerical approaches are input parameters dependent. The simulated results rely on the values of input parameters. As some input parameters depend greatly on environmental factors and change with time, the predicted values for these parameters may not match perfectly with the practical ones. As a result, the calculated thermal load may deviate from the real case. Moreover, it is impossible to simulate the thermal load for several months or several years. Field measurement, which can provide practical thermal load in bridge for a long time and is immune to input parameters, is a powerful alternative.

4. Field Measurement

The thermal load in bridge is affected by air temperature, wind, humidity, intensity of solar radiation, material type, and so forth, which make it not easy to be modeled by theoretical or numerical approach. Field measurement that monitored the temperature in bridge by temperature sensors installed on it can give the most objective data of temperature

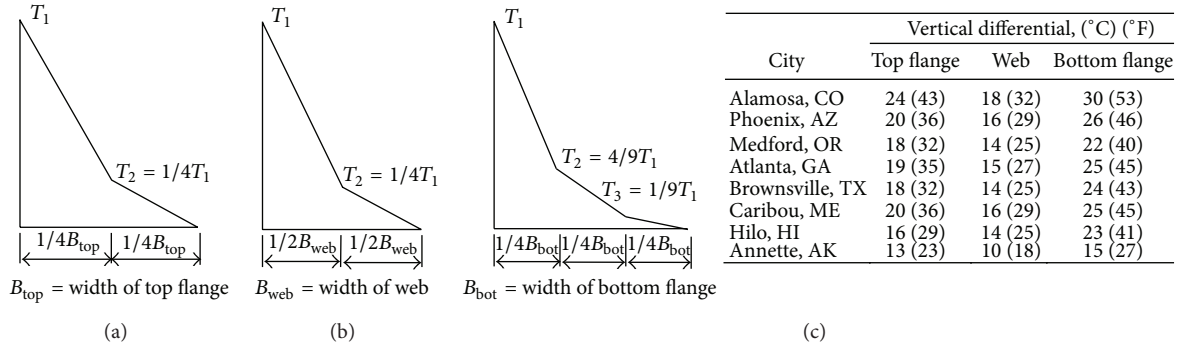


FIGURE 8: Transverse thermal gradients of prestressed concrete bridge girders: (a) top flange, (b) web, and (c) bottom flange [47].

subjected to real climatic change. It also provides the criterion for demonstrating the validation of theoretical or numerical results. With the development of sensor and computer technology, field measurements of thermal loads in bridges have been carried out extensively in various bridges. In particular, recent advances in sensing, data acquisition, computing, communication, and data and information management, have greatly promoted the applications of structural health monitoring (SHM) technology in bridge structures [48, 49]. Successful implementation and operation of SHM systems on bridges have been widely reported in different countries. Almost all SHM systems include temperature monitoring subsystem, for example, a total number of 83 sensors were installed on the Ting Kau Bridge to monitor the temperature of air, concrete, steel, and asphalt, and more than 200 temperature sensors were configured on the Tsing Ma Bridge and the Kap Shui Mun Bridge [50, 51]. The temperatures of bridge components are measured continuously for a long-term period, which provide valuable data for study of temperature distribution in bridge and allow carrying out prediction of the extreme thermal loads with a certain return period.

4.1. Temperature Sensor. The temperature sensor is the key component when implementing field measurement of thermal load in bridge. There are many types of temperature sensors that are capable of measuring temperature such as thermocouple, platinum resistance thermometer, fiber Bragg grating (FBG) temperature sensor, and wireless temperature sensor.

The thermocouple is the most common one. A thermocouple consists of two dissimilar conductors in contact, which produces a voltage when heated. The voltage produced is dependent on the difference of temperature of the junction to other parts of the circuit. Commercial thermocouples are inexpensive and interchangeable and can measure a wide range of temperatures. In contrast to most of other methods of temperature measurement, thermocouples are self-powered and require no external form of excitation. The main limitation with thermocouples is accuracy; system errors of less than one degree Celsius (°C) can be difficult to achieve.

Platinum resistance thermometer is another type of electrical temperature sensor used for field measurement of

thermal load in bridge. It determines the temperature by measuring the electrical resistance of a piece of pure platinum wire. By using the characteristic that the electrical resistance of platinum increases approximately linearly with absolute temperature, the resistance of a wire of platinum is measured by passing a current through it, and the reading is converted to temperature using a calibration equation. With proper design, the resolution of less than 0.1°C can be obtained.

For the outstanding properties of small size, high sensitivity, insensitivity to electric or magnetic interference, localized strain measurement ability, and multiplexing capability, the FBG temperature sensor is widely used for temperature test [52–54]. The FBG is an optical fiber which is formed by exposure to a fringe of UV light. Only the specified Bragg wavelength related to its grating period is reflected for an input light wave from a broadband source. The temperature change causes shift of Bragg wavelength. Then the temperature variation can be tested by recording the change of Bragg wavelength. The resolution of FBG temperature sensor is less than 0.1°C.

The wireless sensor network is a promising technology for structural test. By many attractive features of wireless communication, onboard computation, relatively low cost, and small size, the shift of field temperature measurement away from traditional wired sensor toward the use of wireless sensor has been motivated. In general, the sensing element of wireless temperature sensor does not have much difference with wired temperature sensor, and the biggest difference lies in the fact that the collected temperatures are transmitted to the base station by wireless sensor network. Now, the wireless temperature sensor has been applied in many bridges [55, 56].

Furthermore, temperature sensing component is frequently integrated in those sensors used test other physical parameters, for examples, strain sensor [57], displacement sensor [58], and wireless acceleration sensor [59]. It is worth to say that there are a large number of types of temperature sensors. Only four typical types of sensors are introduced here for the limited space. What is more, the contributions of researchers make the novel temperature sensors emerge every year.

4.2. Data Processing Methodology. For both daily air temperature and daily global solar radiation varying in a random manner, rational conclusions about thermal load in bridge

can only be obtained by statistical approach [33]. So, generally, the processing of field measurement data can be divided into four stages including data preprocessing, trend analysis, statistical analysis, and extreme value analysis (EVA). Those stages are not indispensable, and some procedures may be omitted on specific occasion.

In field measurement, it is inevitable that the test data is disturbed by noise and malfunctions of data acquisition system. So there are some unreasonable data with abnormal magnitude existence in the records. Prior to extract thermal load, those problematic records should be identified. Xu et al. [13] suggested three criteria to identify the abnormal data. The first one is that the difference between the hourly maximum and minimum values is greater than a problem specific limitation. The second one is that the standard deviation of measured hourly records is equal to zero. And the third one is the hourly mean value of temperature that is smaller than a threshold value of minimum temperature. One way to deal with those problematic records is elimination. The problematic data are eliminated directly and left blank in the data series. And another way is repair. The problematic samples are repaired by either interpolation between normal records within the sample or replacement by other samples with similar recordings [6].

Trend analysis is a common data processing method. For the slow change of temperature, the hourly, daily, or monthly average temperatures are calculated firstly. The time histories of those mean values are then plotted in figures. The trend of temperature changing with time can be investigated. The data measured in different locations can also be compared.

Statistical analysis is using the probability density function (PDF) to describe the frequency distributions of different temperatures. The normal distribution, logarithmic normal distribution, and Weibull distribution are usually adopted. For estimating the PDF of random temperatures, two statistical methods, that is, nonlinear regression and hypothesis testing, are used.

EVA is a special field that concentrates on the behaviour of the extreme observations instead of the complete sample population, which allows generalization of return periods of extreme events by extrapolating from the available observations and has been widely used in various engineering fields where extreme values are of importance [60, 61]. The results of EVA can provide reference values of extreme thermal loads for bridges design.

4.3. Concrete Bridge. From 1982 to 1984, Ho et al. [62] carried out field measurements on a prestressed concrete bridge in Hong Kong. A total of 72 thermal sensors had been installed in the multicellular and the solid portion of a prestressed concrete bridge deck of depth 1.4 m. Temperature readings were taken at hourly intervals, and the data were stored on cassette tapes. The measuring system was designed for a temperature range of 0°C–75°C and a system accuracy of $\pm 0.5^\circ\text{C}$. The results were used to verify the proposed one-dimensional finite difference model by statistical manner. In 1984, McClure et al. [21] studied the longitudinal, horizontal, and vertical temperature variations in a posttensioned segmental concrete box girder bridge from the measured data

obtained by thermocouples. Based on a regression analysis, it was concluded that there was no significant longitudinal temperature variation. Furthermore, the results showed that there was little transverse temperature variation. These results confirmed earlier assumptions that the three-dimensional heat-flow problem in a bridge can be reduced essentially to a one-dimensional state comprising of a vertical temperature variation through the section depth of the bridge.

In 1998, large amount of thermocouples was instrumented on the North Halawa Valley Viaduct in Hawaii by Shushkewich and readings were been taken over a five-year period [63]. A simplification to the computation procedure for the analysis of nonlinear thermal gradient was proposed. The processing of the data revealed that the results correlate extremely well with the positive and negative thermal gradients in proposed revision to an AASHTO specification [64]. The reduction of the negative thermal gradient by 40% and the maintaining of the positive thermal gradient in the new edition were validated duly.

Supported by the San Antonio “Y” project, a segmental concrete box girder bridge was instrumented with several thermocouples through the depth, which recorded temperatures every half hour for 2 1/2 years [65]. The maximum recorded positive and negative thermal differentials were investigated by Roberts-Wollman, and it was reported that both the typical positive gradient curve and negative gradient curve can be approximated by a fifth-order parabola with different points of zero temperature difference. When comparing to design recommendations, the conservative values of the AASHTO recommendations were found out for the San Antonio area. A simplified expression was sought to calculate the temperature difference only in terms of the solar radiation and the difference between daily high temperature and 3-day average temperature. The predicted maximum temperature differences were compared with the results calculated by original Potgieter and Gamble method [31], modified Potgieter and Gamble method [31], and field measurement as shown in Table 1. It can be seen that all methods are within 1°C of predicting the maximum temperature difference for the 50 mm asphalt condition. For the no-topping condition, the Potgieter and Gamble method overestimates the magnitude of the difference. And the simplified expression better predicts the magnitudes for the no-topping case.

A renovated continuous three-span curved post-tensioned concrete bridge with a five-cell curved prismatic box girder had been monitored by twelve thermocouples for at least one year [16]. The temperature data were collected at fifteen-minute intervals. The data were evaluated by Fu et al. and showed that there are large changes in the ambient temperature and mean temperature within the bridge during the year; however, there is very little change in the magnitude of the differential temperatures through the bridge during the year. Review of the temperature data for the bridge and the ambient temperature data indicated there is a time lag of approximately 10.6 hours between the peak of ambient temperature and the peaks of the measured bridge interior surface temperatures. Li et al. [6] monitored the Confederation Bridge, which is the world’s longest bridge built over ice-covered water, by 142 thermocouples.

TABLE 1: Maximum temperature difference predictions [65].

Method	2 inches Asphalt topping		No topping	
	Temperature difference (°C)	Date	Temperature difference (°C)	Date
Original Potgieter and Gamble method	18.4	8/14/1994	22.2	10/3/1992
	17.9	5/14/1993	22.2	8/11/1992
Modified Potgieter and Gamble method	18.5	8/14/1994		
	18.1	5/14/1993	19.2	8/11/1992
Simplified expression	17.2	4/10/1993	15.8	3/8/1993
	16.7	5/14/1993	12.8	8/11/1992
Field measurement	17.4	5/14/1993	13.7	8/11/1992

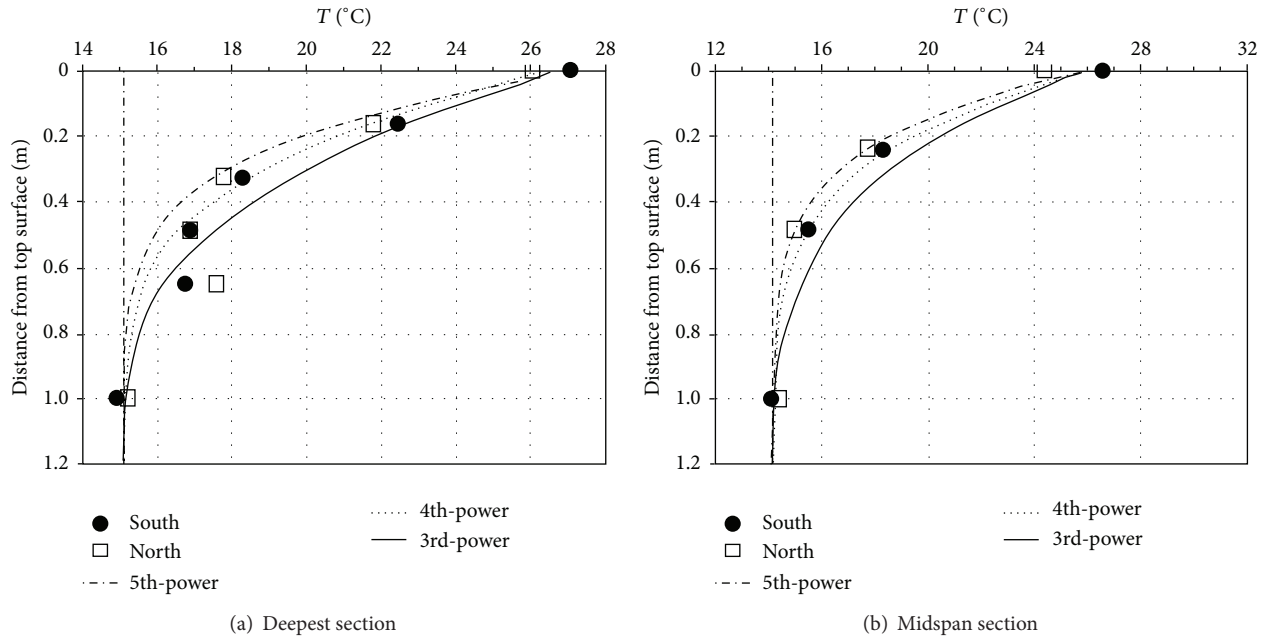


FIGURE 9: Fit of the temperature distribution to $T = T_{top}[(1200 - y)/1200]^n$ [6].

The temperatures that were recorded at hourly intervals from 1998 to 2000 were analyzed. The data were firstly carefully screened to identify the outliers and unrealistic values and spatially reduced to a set of thermal variables including average, differential, and residual temperatures. The measurements of the south and north haunches and at the top of the webs in the deepest section and in the midspan section of the bridge were plotted in Figure 9 together with curves produced by $T = T_{top}[(1200 - y)/1200]^n$, with $n = 3, 4, \text{ and } 5$. y denotes the distance from top surface. It was observed that temperatures in the deepest section fit the cubic curve ($n = 3$) better than the 5th-power curve ($n = 5$) of Priestley, and the 5th-power curve follows the observations of midspan section more closely. EVA showed that all the thermal variables follow a Gumbel distribution, and the Canadian highway bridge design code gives a fairly good estimation for average temperatures but underestimates positive linear differential temperatures by 20% for the Confederation Bridge. Those findings improve our knowledge of extreme thermal behaviour of concrete bridges and are helpful for future development of thermal design criteria in bridge codes.

Kulprapha and Warnitchai [66] equipped several temperature sensors on a continuous prestressed concrete bridge model with an I-shaped cross section. It was found that the temperature distribution is approximately uniform and stable from around midnight until early morning. From early morning until early afternoon, the temperatures at the deck and at other levels close to the deck rise at a much higher rate than those at the lower levels and the soffit. The maximum difference between deck and soffit during the day is about 20°C. From late afternoon to early night, the temperatures at the deck and other levels close to the deck fall at a much higher rate than those at the lower levels and the soffit. The maximum recorded deck and soffit temperatures are 56.3°C and 40.5°C, respectively. In addition, these measurement results confirmed that cross sectional temperature distribution is a function of only the height measured from the soffit. Lee [47] conducted measurements on a five-foot-long prestressed BT-63 girder from April 2009 to March 2010 in Atlanta, with the girder in an east-west orientation such that only the top surface and one side of the girder received direct solar radiation. Both the vertical temperature distribution and the transverse temperature

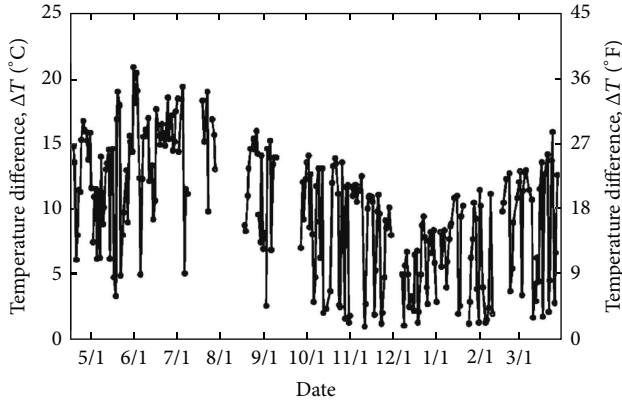


FIGURE 10: Daily vertical temperature difference along the depth of the girder [47].

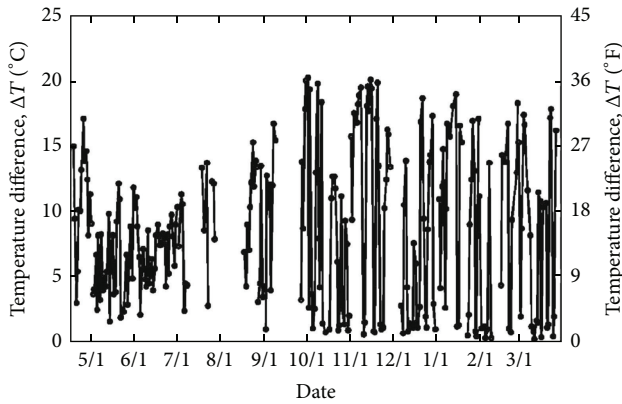


FIGURE 11: Daily transverse temperature difference across the bottom flange [47].

distribution were measured. The daily maximum vertical temperature difference, as shown in Figure 10, was the largest in the summer and decreased from summer to winter. Unlike the vertical temperature difference, the maximum transverse temperature difference, as shown in Figure 11, was the largest in the late fall and winter as a result of higher solar radiation on the vertical surfaces of the girder facing the south.

4.4. Steel-Concrete Composite Bridge. The steel-concrete composite bridge is composed of steel beam and concrete slab. The different heat transfer coefficients of steel and concrete make a nonlinear thermal gradient along the vertical axis of the cross section. As a result, the model of thermal load is different from that in homogeneous material. In composite bridge, the thermal stresses were found to be comparable to the dead load and live load stresses. So the thermal load in steel-concrete composite bridge is particularly important.

In 1957, Naruoka et al. [67] carried out temperature tests on the interior of the Shigita Bridge in Japan, which is a simply supported bridge with a reinforced deck slab-on-steel girders. A typical vertical temperature distribution in the month of July was obtained. The results of the tests showed that the distribution is almost constant in the steel girder and fairly

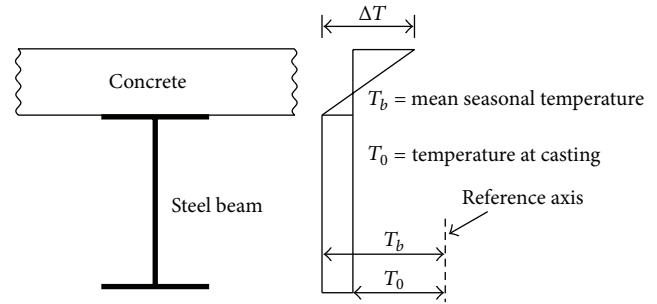


FIGURE 12: Proposed linear-uniform vertical temperature distribution [70].

linear in the concrete deck slab. The maximum differential temperature between the top and bottom of the concrete deck slab is about 22°C . It was also observed that the thermal gradient in the blacktopping is quite steep.

In 1965, Zuk [68] found that the temperature differentials between the top and bottom of the concrete deck slab can be as high as 22°C during the summer and as low as -6°C in the winter from field measurements on six simply supported composite bridges. In another study, he obtained the vertical temperature distribution from field data in a composite bridge over the Hardware River near Charlottesville, North Carolina [18]. The results revealed that the temperature differences between the top and bottom of the concrete deck slab ranged from 11°C to 19°C during the day and -2°C to 4°C during the night. The vertical temperature distribution was almost linear in the concrete deck slab with very small variation through the depth of the steel girder. So for all practical purposes, it can be considered to be uniform and equal to the ambient temperature gradient.

Based on a synthesis of several theoretical studies and experiments on prototype composite concrete slab-on-steel beam bridges conducted by Naruoka et al. [67], Zuk [18, 68], Berwanger [69], Emanuel and Hulsey [39], and so on, a simple but realistic vertical temperature distribution through the section depth is proposed by Kennedy and Soliman [70], as shown in Figure 12. The proposed distribution is linear through the depth of the slab and uniform through the depth of the steel beam. This distribution leads to simple formulas to estimate the thermal stresses in simple and continuous composite bridges.

Au et al. [71] conducted a comprehensive investigation on the thermal behavior of bridges in Hong Kong with special emphasis on composite bridges. The outcome of the study demonstrated that the temperature distribution in bridge depends primarily on the solar radiation, ambient air temperature and wind speed in the vicinity. Apart from data of the meteorological factors, good estimates of the thermal properties of material and the file coefficients are necessary for the prediction of thermal load. A fifth-order equation of the design temperature profile for tropical regions was suggested, which is very similar to the one proposed by Priestley [72] for concrete box girders.

Im and Chang et al. [73] monitored a steel-concrete composite box girder bridge located at the south of Seoul by 30 copper-constant thermocouples over a 6-year period.

The thermal load parameters including effective temperature, vertical temperature difference, and horizontal temperature difference were computed based on measured data. The hourly variation of the horizontal temperature differences revealed that the horizontal temperature differences are no longer negligible since they are of the same order of magnitude as the vertical temperature differences in the winter months. EVA indicated that all the thermal load parameters of hourly maximum and hourly minimum values obey the Gumbel distribution.

4.5. Steel Bridge. Because of the high thermal conductivity, steel adjusts its temperature many times faster than concrete, leading to a more rapid heat exchange between steel bridge and surrounding air. As a result, the thermal loads in steel bridges have much difference with that in concrete bridges.

Ni et al. [12] investigated one-year (the year of 1999) continuous measurement data recorded by a total of 83 temperature sensors, which had been installed at different locations of the Ting Kau Bridge in Hong Kong to measure (1) steel-girder temperature, (2) temperature inside concrete deck, (3) temperature in tower legs, (4) temperature in asphalt pavement, and (5) atmosphere temperature. It was observed that, in general, the temperatures in asphalt are the highest and the temperatures in atmosphere are the lowest. The temperatures measured at different locations, on the same cross section, attain their maxima almost at the same hour. The EVA was employed to estimate the extreme effective temperatures of bridge deck with a certain return period. The predicted maximum and minimum effective temperatures for a return period of 120 years are 36.9°C and -3.6°C , respectively, which agree well with the design values. De Backer et al. [45] implemented an autonomous monitoring system for temperatures in the southern box girder of the Vilvoorde Viaduct during the spring months of 2008. The results illustrated the validity of the claim that a second internal heating takes place, due to mutual radiation and heat conduction, after the solar radiation has reached its peak.

Xu et al. [13] installed a total number of 109 sensors to implement temperature measurement on the Tsing Ma Bridge. The temperatures of bridge cross section, cable, and air were monitored. Subsequently, the temperature monitoring data from 1997 to 2005 were evaluated. After the problematic data were eliminated, monthly statistics of effective deck temperature including mean, minimum, and maximum temperatures were computed. The results indicated that there is a clear and fairly stable cycle of ambient air temperature variation. The ambient air temperature reaches the lowest values normally in January every year, while the highest level is in July or August every year. The comparison of monthly effective deck temperature and ambient air temperature in 1999–2005 revealed that the effective bridge deck temperature has similar variation patterns to those of the ambient air temperature. The minimum effective temperature of bridge deck, main cable, and air is almost the same, while the maximum effective temperature of bridge deck is significantly higher. Cao et al. [74] studied the monitored temperatures including steel deck, stayed cables, and concrete tower of the Zhanjiang Bay Bridge, located in an inner gulf of South

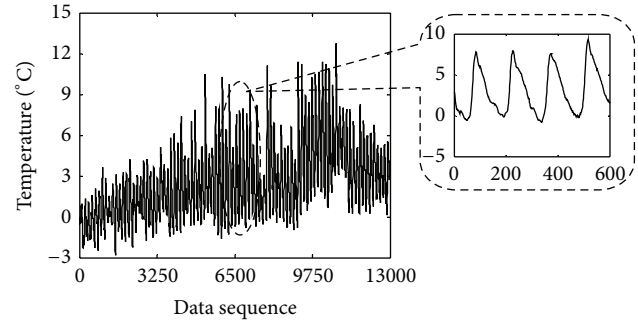


FIGURE 13: Time history of vertical temperature differential [75].

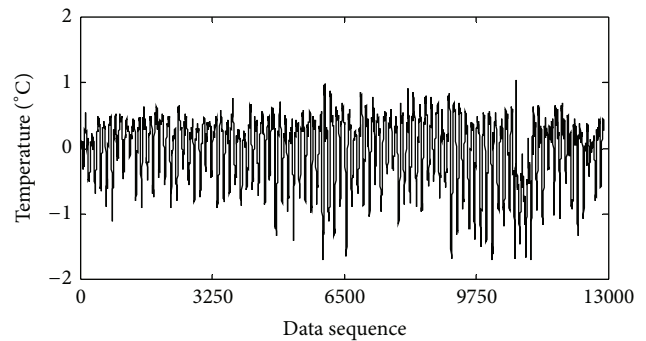


FIGURE 14: Time history of horizontal temperature differential in bottom deck [75].

China, and found that the maximum temperature gradient in the steel girder was more than twice the original design value. The concrete temperature lagged significantly behind ambient air by 5–6 hours, and stayed cable temperatures were between those of ambient air and concrete.

The temperatures of the Runyang Suspension Bridge (RSB), with a span of 1490 m, were monitored since 2005 at a sample frequency of 1 Hz. The flat steel box girder was employed as the main girder in the bridge. Eight temperature sensors were embedded in one section and four cross sections were measured. Ding et al. [75] analyzed the representative data of 90 days that scatter to four seasons in one year uniformly. The results indicated that the temperatures in cross section have close relation with season. The time history of vertical temperature differences, horizontal temperature differential in bottom deck, and horizontal temperature differential in top deck were investigated, as shown in Figures 13, 14, and 15, respectively. It can be seen that the vertical temperature differences are mainly governed by solar radiation intensity, the horizontal temperature gradient in bottom deck is very small and can be neglected, and the horizontal temperature differentials in top deck have no relationship with time and cannot be ignored. Statistical results showed that the combined probability distribution model defined by the weighted sum of one Weibull distribution and one normal distribution can well describe the temperature differences. EVA results indicated that the daily extreme temperature differences in flat steel box girder cross section of the RSB followed the Weibull distribution, which have

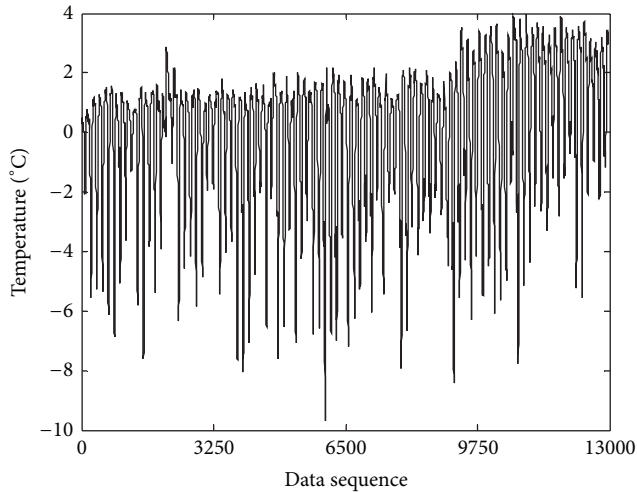


FIGURE 15: Time history of horizontal temperature differential in top deck [75].

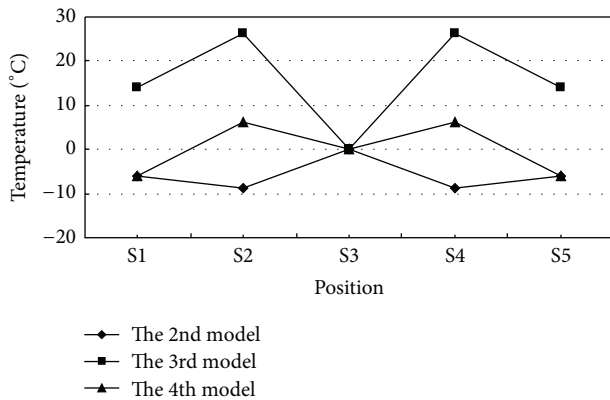


FIGURE 16: The critical temperature difference models in top plate [75].

much difference with the general cases that the Gumbel distribution is obeying. According to correlation analysis, the critical temperature difference models in top plate of the flat steel box girder were proposed for thermal stresses calculation, as shown in Figure 16. The results provide a thorough understanding of thermal field in flat steel box girder bridges and have reference values for structural design and evaluation.

5. Conclusions and Recommendations

The thermal load, which provides foundation for calculating thermal stresses, is one of the key parameters that affect the service ability of bridges. The research of thermal load in bridge by theoretical model, numerical analysis, and field measurement is progressed remarkably, and design guidance about thermal loads is also provided in specifications for general form of bridges. However, it is far from sufficient. At least, the following aspects need to be further attempted.

- (1) The development of SHM technology makes performing automatic and real-time field measurement

of temperature in bridge convenient. Although some bridges are monitored by temperature sensors, the measurement data are left unused, unlike the vibration and stress data that are investigated extensively. The effect of thermal load on the performance of bridges is not fully understood. So carrying out wide field measurements of temperature on different bridges in different regions should be encouraged, and particular emphasis should be placed on extracting thermal load models from field measurement data.

- (2) Nowadays, new concepts are employed in bridge design continuously. A lot of new bridges with complicated geometric configuration are constructed. At the same time, new materials are invented for bridge structures. The heat properties such as emissivity and absorptivity of those new materials are different from general cases. For those bridges, the existing design specifications are useless. In addition, the global climate has much difference with that in several decades years ago because of the development of industry and improvement of technology. So it is important to investigate thermal load in bridge with different schemes comprehensively.
- (3) Due to the complexity of heat transfer and heat exchange, it is difficult to predict the thermal load for all the cases and codify the results to simple rules and guidelines that accommodate climatic, geographic, geometric, and material variations. Definition of critical thermal loads varying from region to region, bridge to bridge, and section to section becomes significant. In addition, the modern transportation system had been extended to the extremely cold area and extremely hot area, but the research of thermal load on bridge in those regions has attracted little attention.
- (4) It is impossible that the temperature distribution in a bridge is described completely by limited data obtained by temperature sensors. So numerical models are powerful supplements. However, up to now, fine numerical models including all key components for simulating temperature distribution in large-scale bridges have not been developed. The intensity of solar radiation, the coupling effect of air temperature and wind speed, and the heat exchange between the surface and surrounding environment are not defined exactly. Moreover, the perfect transition from heat transfer analysis to thermal stresses analysis is not achieved.
- (5) Current specifications provide engineers with a temperature gradient across the depth of the cross section to predict the vertical thermal behavior of bridges based on one-dimensional heat flow. But the specifications do not provide any guidance for transverse temperature gradients that cause additional lateral deformations in the girders especially prior to the placement of the bridge decks during construction.

Investigation results already demonstrated that those transverse temperature differences exist in many bridges and the values are greater than those of vertical temperature differences sometimes.

Acknowledgments

This research work was jointly supported by the Science Fund for Creative Research Groups of the NSFC (Grant no. 51121005), the National Natural Science Foundation of China (Grant nos. 51278104 and 51308186), the Natural Science Foundation of Jiangsu Province of China (Grant no. BK20130850), and the Research Fund of State Key Laboratory for Disaster Reduction in Civil Engineering (Grant no. SLDRCE12-MB-03).

References

- [1] T. Wu and A. Kareem, "Aerodynamics and aeroelasticity of cable-supported bridges: identification of nonlinear features," *Journal of Engineering Mechanics*, vol. 139, no. 12, pp. 1886–1893, 2013.
- [2] F. Magalhães, A. Cunha, and E. Caetano, "Vibration based structural health monitoring of an arch bridge: from automated OMA to damage detection," *Mechanical Systems and Signal Processing*, vol. 28, supplement 1, pp. 212–228, 2012.
- [3] C. Johansson, C. Pacoste, and R. Karoumi, "Closed-form solution for the mode superposition analysis of the vibration in multi-span beam bridges caused by concentrated moving loads," *Computers & Structures*, vol. 119, pp. 85–94, 2013.
- [4] R. S. Jalali, M. Bahari Jokandan, and M. D. Trifunac, "Earthquake response of a three-span, simply supported bridge to near-field pulse and permanent-displacement step," *Soil Dynamics and Earthquake Engineering*, vol. 43, pp. 380–397, 2012.
- [5] T. Miyata, H. Yamada, H. Katsuchi, and M. Kitagawa, "Full-scale measurement of Akashi-Kaikyo Bridge during typhoon," *Journal of Wind Engineering and Industrial Aerodynamics*, vol. 90, no. 12–15, pp. 1517–1527, 2002.
- [6] D. Li, M. A. Maes, and W. H. Dilger, "Thermal design criteria for deep prestressed concrete girders based on data from confederation bridge," *Canadian Journal of Civil Engineering*, vol. 31, no. 5, pp. 813–825, 2004.
- [7] A. Q. Li and C. Q. Miao, *Health Monitoring of Bridge Structures*, China Communications Press, Beijing, China, 2009.
- [8] H. Sohn, M. Dzwonczyk, E. G. Straser, A. S. Kiremidjian, K. Law, and T. Meng, "An experimental study of temperature effect on modal parameters of the Alamosa Canyon Bridge," *Earthquake Engineering and Structural Dynamics*, vol. 28, no. 7–8, pp. 879–897, 1999.
- [9] Y. Xia, B. Chen, S. Weng, Y. Q. Ni, and Y. L. Xu, "Temperature effect on vibration properties of civil structures: a literature review and case studies," *Journal of Civil Structural Health Monitoring*, vol. 2, no. 1, pp. 29–46, 2012.
- [10] C. Liu and J. T. DeWolf, "Effect of temperature on modal variability of a curved concrete bridge under ambient loads," *Journal of Structural Engineering*, vol. 133, no. 12, pp. 1742–1751, 2007.
- [11] Z.-D. Xu and Z. Wu, "Simulation of the effect of temperature variation on damage detection in a long-span cable-stayed bridge," *Structural Health Monitoring*, vol. 6, no. 3, pp. 177–189, 2007.
- [12] Y. Q. Ni, X. G. Hua, K. Y. Wong, and J. M. Ko, "Assessment of bridge expansion joints using long-term displacement and temperature measurement," *Journal of Performance of Constructed Facilities*, vol. 21, no. 2, pp. 143–151, 2007.
- [13] Y. L. Xu, B. Chen, C. L. Ng, K. Y. Wong, and W. Y. Chan, "Monitoring temperature effect on a long suspension bridge," *Structural Control and Health Monitoring*, vol. 17, no. 6, pp. 632–653, 2010.
- [14] H. C. Fu, S. F. Ng, and M. S. Cheung, "Thermal behavior of composite bridges," *Journal of Structural Engineering*, vol. 116, no. 12, pp. 3302–3323, 1990.
- [15] S. Moorthy and C. W. Roeder, "Thermal responses of skewed bridges. Developments in short and medium span bridge engineering," in *Proceedings of the 3rd International Conference on Short and Medium Span Bridges*, 1990.
- [16] Y. Fu and J. T. DeWolf, "Effect of differential temperature on a curved post-tensioned concrete bridge," *Advances in Structural Engineering*, vol. 7, no. 5, pp. 385–397, 2004.
- [17] M. A. Maes, W. H. Dilger, and P. D. Ballyk, "Extreme values of thermal loading parameters in concrete bridges," *Canadian Journal of Civil Engineering*, vol. 19, no. 6, pp. 935–946, 1992.
- [18] W. Zuk, "Thermal behaviour of composite bridges-insulated and uninsulated," *Highway Research Record*, vol. 76, pp. 231–253, 1965.
- [19] A. Saetta, R. Scotta, and R. Vitaliani, "Stress analysis of concrete structures subjected to variable thermal loads," *Journal of Structural Engineering*, vol. 121, no. 3, pp. 446–457, 1995.
- [20] B. H. Oh, S. C. Choi, and S. W. Cha, "Temperature and relative humidity analysis in early-age concrete decks of composite bridges," in *Measuring, Monitoring and Modeling Concrete Properties*, pp. 305–316, Springer, Dordrecht, The Netherlands, 2006.
- [21] R. M. McClure, H. H. West, and P. C. Hoffman, "Observations from tests on a segmental bridge," *Transportation Research Record*, vol. 2, pp. 60–67, 1984.
- [22] J. A. Duffie and W. A. Beckman, *Solar Engineering of Thermal Processes*, John Wiley & Sons, Hoboken, NJ, USA, 2013.
- [23] M. M. Elbadry and A. Ghali, "Temperature variations in concrete bridges," *Journal of Structural Engineering*, vol. 109, no. 10, pp. 2355–2374, 1983.
- [24] J. F. Orgill and K. G. T. Hollands, "Correlation equation for hourly diffuse radiation on a horizontal surface," *Solar Energy*, vol. 19, no. 4, pp. 357–359, 1977.
- [25] S.-H. Kim, K.-I. Cho, J.-H. Won, and J.-H. Kim, "A study on thermal behaviour of curved steel box girder bridges considering solar radiation," *Archives of Civil and Mechanical Engineering*, vol. 9, no. 3, pp. 59–76, 2009.
- [26] W. H. Dilger, A. Ghali, M. Chan, M. S. Cheung, and M. A. Maes, "Temperature stresses in composite box girder bridges," *Journal of Structural Engineering*, vol. 109, no. 6, pp. 1460–1478, 1983.
- [27] F. P. Incropera, A. S. Lavine, and D. P. DeWitt, *Fundamentals of Heat Transfer*, John Wiley & Sons, New York, NY, USA, 2011.
- [28] M. Emerson, "The calculation of the distribution of temperature in bridges," TRRL Report LR 561, Department of the Environment, 1973.
- [29] B. Hunt and N. Cooke, "Thermal calculations for bridge design," *Journal of the Structural Division*, vol. 101, no. 9, pp. 1763–1781, 1975.

- [30] T. Zichner, "Thermal effects on concrete bridges," *Bulletin d'Information*, vol. 154, pp. 291–314, 1982.
- [31] I. C. Potgieter and W. L. Gamble, *Response of Highway Bridges to Nonlinear Temperature Distributions*, University of Illinois, Urbana-Champaign, Ill, USA, 1983.
- [32] I. C. Potgieter and W. L. Gamble, "Nonlinear temperature distributions in bridges at different locations in the United States," *PCI Journal*, vol. 34, no. 4, pp. 80–103, 1989.
- [33] D. Ho and C.-H. Liu, "Extreme thermal loadings in highway bridges," *Journal of Structural Engineering*, vol. 115, no. 7, pp. 1681–1696, 1989.
- [34] D. H. Evans, "An Application of numerical integration techniques to statistical tolerancing," *Technometrics*, vol. 9, no. 3, pp. 441–456, 1967.
- [35] E. Mirambell and A. Aguado, "Temperature and stress distributions in concrete box girder bridges," *Journal of Structural Engineering*, vol. 116, no. 9, pp. 2388–2409, 1990.
- [36] K. A. Riding, J. L. Poole, A. K. Schindler, M. C. G. Juenger, and K. J. Folliard, "Temperature boundary condition models for concrete bridge members," *ACI Materials Journal*, vol. 104, no. 4, pp. 379–387, 2007.
- [37] S. C. Brenner and L. R. Scott, *The Mathematical Theory of Finite Element Methods*, Springer, New York, NY, USA, 2008.
- [38] M. J. N. Priestley, "Design thermal gradients for concrete bridges," *New Zealand Engineering*, vol. 31, no. 9, pp. 213–219, 1976.
- [39] J. H. Emanuel and J. L. Hulsey, "Temperature distributions in composite bridges," *Journal of the Structural Division*, vol. 104, no. 1, pp. 65–78, 1978.
- [40] C. Berwanger, "Transient thermal behavior of composite bridges," *Journal of Structural Engineering*, vol. 109, no. 10, pp. 2325–2339, 1983.
- [41] S. Moorthy and C. W. Roeder, "Temperature-dependent bridge movements," *Journal of Structural Engineering*, vol. 118, no. 4, pp. 1090–1105, 1992.
- [42] F. A. Branco and P. A. Mendes, "Thermal actions for concrete bridge design," *Journal of Structural Engineering*, vol. 119, no. 8, pp. 2313–2231, 1993.
- [43] M. Tong, L. G. Tham, F. T. K. Au, and P. K. K. Lee, "Numerical modelling for temperature distribution in steel bridges," *Computers & Structures*, vol. 79, no. 6, pp. 583–593, 2001.
- [44] M. Tong, L. G. Tham, and F. T. K. Au, "Extreme thermal loading on steel bridges in tropical region," *Journal of Bridge Engineering*, vol. 7, no. 6, pp. 357–366, 2002.
- [45] H. de Backer, A. Outtier, and P. van Bogaert, "Numerical and experimental assessment of thermal stresses in steel box girders," in *Proceedings of the 11th Nordic Steel Construction Conference (NSCC '09)*, pp. 65–72, Swedish Institute of Steel Construction (SBI), 2009.
- [46] Y. Xia, B. Chen, X.-Q. Zhou, and Y.-L. Xu, "Field monitoring and numerical analysis of Tsing Ma Suspension Bridge temperature behavior," *Structural Control and Health Monitoring*, vol. 20, no. 4, pp. 560–575, 2013.
- [47] J. H. Lee, "Investigation of extreme environmental conditions and design thermal gradients during construction for prestressed concrete bridge girders," *Journal of Bridge Engineering*, vol. 17, no. 3, pp. 547–556, 2012.
- [48] Y. Q. Ni, X. W. Ye, and J. M. Ko, "Monitoring-based fatigue reliability assessment of steel bridges: analytical model and application," *Journal of Structural Engineering*, vol. 136, no. 12, pp. 1563–1573, 2010.
- [49] Y. Q. Ni, X. W. Ye, and J. M. Ko, "Modeling of stress spectrum using long-term monitoring data and finite mixture distributions," *Journal of Engineering Mechanics*, vol. 138, no. 2, pp. 175–183, 2012.
- [50] J. M. Ko and Y. Q. Ni, "Technology developments in structural health monitoring of large-scale bridges," *Engineering Structures*, vol. 27, no. 12, pp. 1715–1725, 2005.
- [51] K.-Y. Wong, "Instrumentation and health monitoring of cable-supported bridges," *Structural Control and Health Monitoring*, vol. 11, no. 2, pp. 91–124, 2004.
- [52] L. Ren, H. Li, L. Sun, and D. Li, "FBG sensors for on-line temperature measurements," in *Smart Structures and Materials 2004: Sensors and Smart Structures Technologies for Civil, Mechanical, and Aerospace Systems*, vol. 5391 of *Proceedings of SPIE*, pp. 94–99, March 2004.
- [53] H.-N. Li, G.-D. Zhou, L. Ren, and D.-S. Li, "Strain transfer analysis of embedded fiber Bragg grating sensor under nonaxial stress," *Optical Engineering*, vol. 46, no. 5, Article ID 054402, 2007.
- [54] H.-N. Li, G.-D. Zhou, L. Ren, and D.-S. Li, "Strain transfer coefficient analyses for embedded fiber bragg grating sensors in different host materials," *Journal of Engineering Mechanics*, vol. 135, no. 12, pp. 1343–1353, 2009.
- [55] M. J. Chae, H. S. Yoo, J. Y. Kim, and M. Y. Cho, "Development of a wireless sensor network system for suspension bridge health monitoring," *Automation in Construction*, vol. 21, no. 1, pp. 237–252, 2012.
- [56] S. Jang, H. Jo, S. Cho et al., "Structural health monitoring of a cable-stayed bridge using smart sensor technology: deployment and evaluation," *Smart Structures and Systems*, vol. 6, no. 5-6, pp. 439–459, 2010.
- [57] B.-O. Guan, H.-Y. Tam, X.-M. Tao, and X.-Y. Dong, "Simultaneous strain and temperature measurement using a superstructure fiber Bragg grating," *IEEE Photonics Technology Letters*, vol. 12, no. 6, pp. 675–677, 2000.
- [58] Y. Yu, H. Tam, W. Chung, and M. S. Demokan, "Fiber Bragg grating sensor for simultaneous measurement of displacement and temperature," *Optics Letters*, vol. 25, no. 16, pp. 1141–1143, 2000.
- [59] S. Kim, S. Pakzad, D. Culler et al., "Health monitoring of civil infrastructures using wireless sensor networks," in *Proceedings of the 6th IEEE International Symposium on Information Processing in Sensor Networks (IPSN '07)*, pp. 254–263, April 2007.
- [60] E. Castillo, *Extreme Value Theory in Engineering*, Academic Press, New York, NY, USA, 1988.
- [61] A. S. Hadi, N. Balakrishnan, and J. M. Sarabia, *Extreme Value and Related Models with Applications in Engineering and Science*, John Wiley & Sons, Hoboken, NJ, USA, 2005.
- [62] D. Ho, Y. P. Ma, L. S. Cornish, and L. G. Currie, "Temperature measurements in Castle Peak/Texaco Road flyover," *Hong Kong Engineer*, vol. 12, no. 9, pp. 29–33, 1984.
- [63] K. W. Shushkewich, "Design of segmental bridges for thermal gradient," *PCI Journal*, vol. 43, no. 4, pp. 120–137, 1998.
- [64] AASHTO, *Guide Specifications for Design and Construction of Segmental Concrete Bridges*, American Association of State Highway and Transportation Officials, Washington, DC, USA, 2nd edition, 1999.
- [65] C. L. Roberts-Wollman, J. E. Breen, and J. Cawrse, "Measurements of thermal gradients and their effects on segmental concrete bridge," *Journal of Bridge Engineering*, vol. 7, no. 3, pp. 166–174, 2002.

- [66] N. Kulprapha and P. Warnitchai, "Structural health monitoring of continuous prestressed concrete bridges using ambient thermal responses," *Engineering Structures*, vol. 40, no. 4, pp. 20–38, 2012.
- [67] M. Naruoka, I. Hirai, and T. Yamaguti, "The measurement of the temperature of the interior of the reinforced concrete slab of the shigita bridge and presumption of the thermal stress," in *Proceedings of the Symposium on the Stress Measurements for Bridges and Structures*, Japan Society for the Promotion of Science, Tokyo, Japan, 1956.
- [68] W. Zuk, *Simplified Design Check of Thermal Stresses in Composite Highway Bridges*, Highway Research Record, no. 103, 1965.
- [69] C. Berwanger, *The Modulus of Concrete and the Coefficient of Expansion of Concrete and Reinforced Concrete at below Normal Temperatures*, vol. 25, ACI Special Publication, 1971.
- [70] J. B. Kennedy and M. H. Soliman, "Temperature distribution in composite bridges," *Journal of Structural Engineering*, vol. 113, no. 3, pp. 475–482, 1987.
- [71] F. T. K. Au, S. K. Cheung, and L. G. Tham, "Design thermal loading for composite bridges in tropical region," *Steel & Composite Structures*, vol. 2, no. 6, pp. 441–460, 2002.
- [72] M. J. N. Priestley, "Design of concrete bridges for temperature gradients," *Journal of the American Concrete Institute*, vol. 75, no. 5, pp. 209–217, 1978.
- [73] C. K. Im and S. P. Chang, "Estimating extreme thermal loads in composite bridge using long-term measured data," *International Journal of Steel Structures*, vol. 4, no. 1, pp. 25–31, 2004.
- [74] Y. Cao, J. Yim, Y. Zhao, and M. L. Wang, "Temperature effects on cable stayed bridge using health monitoring system: a case study," *Structural Health Monitoring*, vol. 10, no. 5, pp. 523–537, 2011.
- [75] Y. Ding, G. Zhou, A. Li, and G. Wang, "Thermal field characteristic analysis of steel box girder based on long-term measurement data," *International Journal of Steel Structures*, vol. 12, no. 2, pp. 219–232, 2012.

Research Article

Optimal Sensor Placement for Stay Cable Damage Identification of Cable-Stayed Bridge under Uncertainty

Li-Qun Hou,¹ Xue-Feng Zhao,² and Rui-Cong Han²

¹ School of Civil Engineering and Architecture, Northeast Dianli University, Jilin 132012, China

² School of Civil Engineering, Dalian University of Technology, Dalian 116024, China

Correspondence should be addressed to Li-Qun Hou; hlq_work@sina.com

Received 4 July 2013; Revised 14 October 2013; Accepted 21 October 2013

Academic Editor: Jeong-Tae Kim

Copyright © 2013 Li-Qun Hou et al. This is an open access article distributed under the Creative Commons Attribution License, which permits unrestricted use, distribution, and reproduction in any medium, provided the original work is properly cited.

Large cable-stayed bridges utilize hundreds of stay cables. Thus, placing a sensor on every stay cable of bridges for stay cable damage identification (SCDI) is costly and, in most cases, not necessary. Optimal sensor placement is a significant and critical issue for SCDI. This paper proposes the criteria for sensor quantity and location optimization for SCDI on the basis of the concept of damage identification reliability index (*DIRI*) under uncertainty. Random elimination (RE) algorithm and heuristic random elimination (HRE) algorithm are proposed to solve the sensor quantity optimization calculation problem. Multistage global optimization (MGO) algorithm is also proposed to solve the sensor location optimization calculation problem. A case study is conducted to evaluate and verify the criteria and algorithms. Results indicate that the HRE algorithm can provide better solution with less elapsed time than the RE algorithm in some cases, and the MGO algorithm can meet the multistage criterion for sensor location optimization and give a satisfying optimized solution. Theoretical analysis and case study results confirm that the criteria are reasonable and suitable for optimal sensor placement for SCDI. The proposed algorithms are effective and efficient for practical optimization calculation.

1. Introduction

In recent years, bridge health monitoring system (BHMS) has been developed rapidly and widely used in large bridges, especially in cable-stayed bridges. Sensors, which are required to monitor the structural status and influential environmental parameters, are the most important foundation of BHMS. Since the project budget of BHMS is always limited, how to optimally place the limited sensors in a large bridge in order to obtain the best data for parameter and damage identification is a challenging task. Research activities in the last few years have been focused on the design and optimization of sensor placement. Some latest representative studies are presented as follows. Kim et al. [1–3] presented a design of autonomous smart sensor nodes to monitor tendons and girders in prestressed concrete (PSC) bridges and a design of hybrid acceleration-impedance sensor nodes on Imote2-platform for damage monitoring in steel girder connections. Ho et al. [4] presented a type of solar-powered, multiscale, vibration-impedance sensor node on

Imote2 platform for hybrid structural health monitoring (SHM) in cable-stayed bridge. Yi et al. [5] attempted to explore the sensitive range of the Fiber Bragg Grating (FBG) sensor and proposed an optimal placement for FBG sensor network fitting with the feature of FBG sensor. Rafael et al. [6] investigated the influence of parametric uncertainties on the optimal sensor placement methodologies for the modal analysis of a truss bridge. Costas et al. [7] investigated the effect of spatial correlation of the prediction error on the optimal sensor placement for modal identification or parameter estimation in finite element model updating of Footbridge in Wetteren.

During the past decades, cable-stayed bridges have found wide application in the world. Stay cables, which bear most of the weight of girders, are the key components in cable-stayed bridges. Therefore, identifying stay cable damage on the basis of cable tension is significant for cable-stayed bridge health monitoring. Considering that hundreds of stay cables are used in large cable-stayed bridges, placing a sensor on

every stay cable of bridges is costly and, in most cases, not necessary. Therefore, determining the number and location of sensors for stay cable damage identification (SCDI), namely, the optimal sensor placement (OSP) problem for SCDI, is worth an in-depth study.

Two main problems require further studies in the OSP research area. The first problem is the determination of optimization criterion. Many research activities in previous years have focused on the optimization criterion. Numerous optimization criteria [8, 9], including (1) modal assurance criterion [10], (2) singular value decomposition ratio, (3) measured energy per mode, (4) Fisher information matrix (FIM) [11, 12], (5) mean square error, (6) information entropy, (7) mutual information (MI), (8) representative least squares criterion, (9) visualization of mode shape, (10) modal contribution in output energy [13], and (11) probability-based damage detection criterion, have been proposed. However, most of these criteria, except for probability-based damage detection criterion, were not aimed at damage identification. Therefore, they cannot be used as optimization criteria for SCDI. The probability-based damage detection criterion was developed by Flynn and Todd on the basis of damage detection. This criterion seeks to determine the OSP by minimizing the expected appearance of types I and II error, that is, the global false alarm rate and the global detection rate [8, 14], respectively. An appropriate statistical estimation model of the accuracy of damage detection is needed to optimize sensor placement for damage detection by using this criterion. However, this model is difficult to obtain in large-scale bridge structures. Moreover, the probability-based damage detection criterion was not aimed at SCDI. To solve the first problem, we proposed the criteria for sensor quantity and location optimization for SCDI on the basis of the concept of damage identification reliability index (*DIRI*) under uncertainty. This criterion does not need complex statistical calculation and can be used in practical engineering.

The second problem is the development of optimization algorithms. Many algorithms have been developed for general optimized solution search. Among these algorithms, the most representative and commonly cited algorithm is the effective independence (EI) algorithm [15–17], which maximizes the determinant of FIM corresponding to the target modal partitions. The following typical improved variants of the EI algorithm have also been proposed: (a) EI driving-point residue (EFI-DPR) algorithm [18, 19], (b) energy coefficient-EI (EC-EI) algorithm [20], (c) QR decomposition (QRD) algorithm [21]. In recent years, some stochastic optimization algorithms have been introduced to solve the OSP problem, which is usually a complex, time-consuming, multiobjective, combinatorial optimization problem [8]. Such algorithms include genetic algorithm [22–27], particle swarm optimization [28], simulated annealing algorithm [29], and ant colony optimization algorithm [30]. Although not the best algorithm available [8], the sequential sensor placement algorithm is a relatively systematic and computationally efficient approach for obtaining a satisfying solution. However, given that most of the abovementioned optimization algorithms are specific (e.g., EI, EFI-DPR, EC-EI, and QRD) or common (e.g., stochastic optimization

algorithms), applying them directly to solve the sensor placement optimization calculation problem for SCDI is inefficient. Effective and efficient optimization algorithms should be developed based on certain optimization criteria and problems. In this paper, based on the specific analysis of the sensor placement problem for SCDI and the idea of sequential sensor placement algorithm, we proposed the random elimination (RE) algorithm and the heuristic random elimination (HRE) algorithm to solve the sensor quantity optimization problem. We also proposed the multistage global optimization (MGO) algorithm to solve the sensor location optimization problem.

This study focused on the OSP for the SCDI of cable-stayed bridges under uncertainty. Section 2.1 presents the optimization criteria for sensor quantity and location optimization. Section 2.2 proposes the corresponding optimization algorithms on the basis of the optimization criteria. Section 3 elucidates the case study on an actual cable-stayed bridge to verify the effectiveness of the proposed optimization criteria and algorithms. This section also discusses some problems encountered when using these criteria and algorithms. Finally, Section 4 concludes the paper.

2. Proposed Method

The OSP problem is a kind of combinatorial optimization problem with two key subproblems to be discussed as follows: (1) how to determine the appropriate optimization criterion of sensor placement for SCDI; (2) what kind of algorithm should be applied to solve the complex, time-consuming, multiobjective, combinatorial optimization problem.

2.1. Optimization Criterion

2.1.1. Background and Scope. To solve the first problem, we should focus on the purpose of the sensor placement optimization. This study aimed to accurately and reliably identify the stay cable damage by using a limited number of sensors. Therefore, the optimization criterion should express “accuracy and reliability” by appropriate objective function. Objective functions are constructed based on the SCDI method. Therefore, different types of SCDI methods require different objective functions. The SCDI method based on the change of cable tension (*dCT*), which is measured by accelerometers or other sensors placed on cables, is currently widely used in practical engineering. Thus, we studied only the optimization criterion for this kind of SCDI method.

2.1.2. Theory Foundation for the Reliability Analysis of Stay Cable Damage Identification. The proposed SCDI method can identify only the cable damage that can lead to significant *dCT*. Higher SCDI reliability can be acquired when sensors are placed on cables with larger *dCT* due to cable damage. Accordingly, the rules of *dCT* should be analyzed to study the SCDI reliability.

Stay cables are considered to be the elastic support of the bridge deck. Considering this fact, a simple finite element model (FEM) of continuous slab was studied. The model,

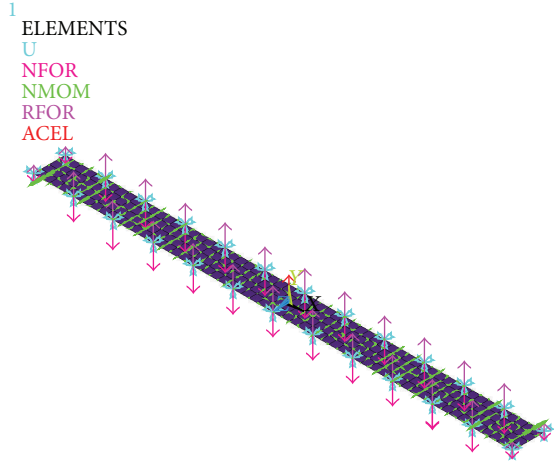


FIGURE 1: FEM of continuous slab.

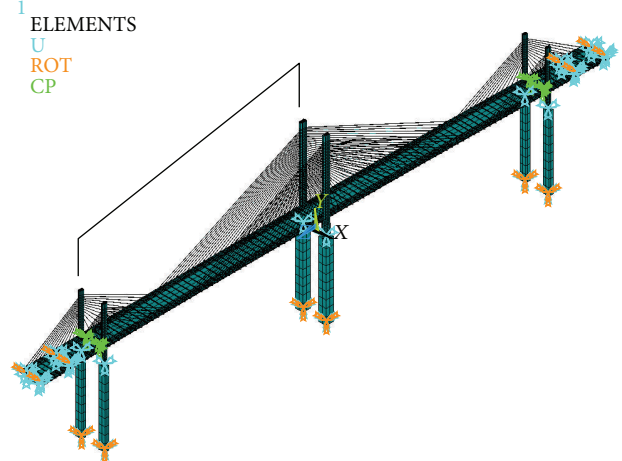
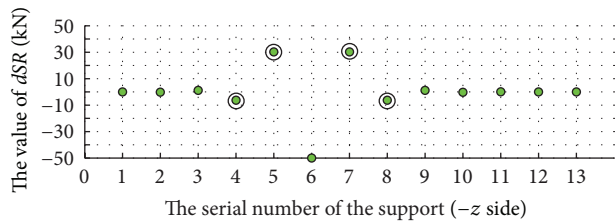
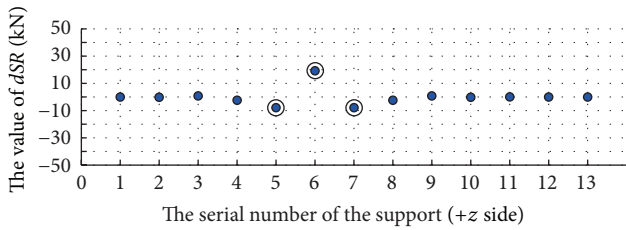


FIGURE 3: FEM of the Binzhou Yellow River Highway Bridge.



(a)

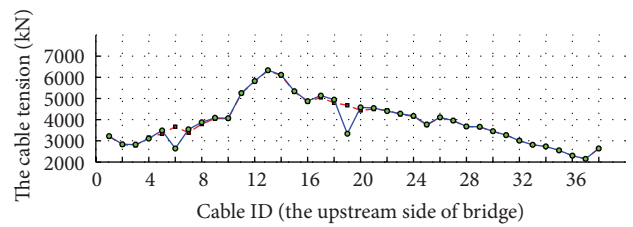


(b)

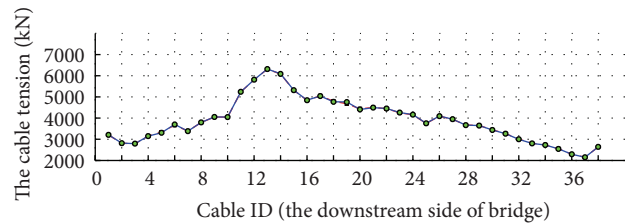
FIGURE 2: Change of the support reaction (dSR) caused by removing number 6 support.

which is shown in Figure 1, has 26 supports that provide the constraints of x , y , z directions. We removed the constraints of the y directions of number 6 support and calculated the value of the change of support reaction (dSR) at every support. The result is shown in Figure 2. The rules of dSR are summarized as follows: (1) removing the constraints of the y directions of one support can lead to the dSR at the nearby support; (2) only the support reaction at the supports marked by black circles in Figure 2 changes significantly; (3) the nearer the support is to number 6 support, the larger the support reaction at the support change.

To obtain more specific rules on dCT , we implemented a complex finite element simulation analysis of the cable damage on a real cable-stayed bridge FEM [31] (see Figure 3). Stay cable damage was simulated by the 30% relaxation of the stay cable. Figures 4 and 5 show the result of dCT due to damage on numbers 6 and 19 stay cables. The rules that are similar to the rules of dCT for simple finite element analysis



(a)



(b)

FIGURE 4: Comparison of the cable tension between undamaged and damaged conditions.

can be summarized from Figure 5 as follows: (1) the damage of one stay cable can lead to the dCT of other stay cables; (2) the dCT of the damaged cable (about 30% of the original cable tension) is the largest among all stay cables; (3) only the cable tension of stay cables marked by the black rectangle in Figure 5 changes significantly; (4) the nearer the stay cable is to the damaged stay cables, the larger the dCT of the stay cables.

We conducted finite element simulation analysis of a simple FEM of continuous slab and a complex FEM of a real cable-stayed bridge. Considering the analysis results and for appropriate simplification, we postulate that only the cable tension of the influenced stay cables can be used for

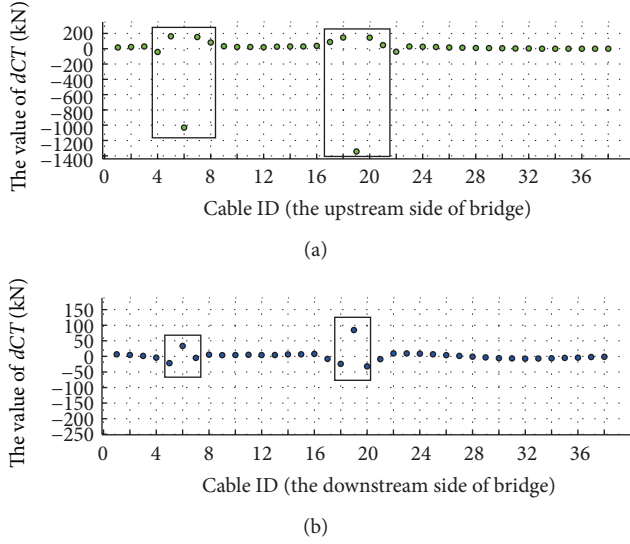


FIGURE 5: Change of cable tension (dCT) due to cable damage.

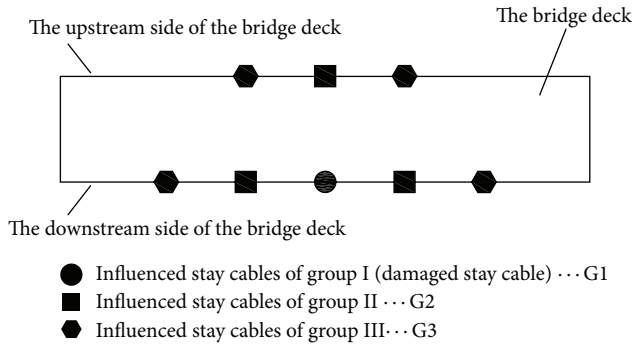


FIGURE 6: Influenced stay cables for a damaged stay cable.

the damage identification of the corresponding damaged stay cable. The influenced stay cables for a damaged stay cable (see Figure 6) can be divided into three groups: (1) the influenced stay cable of group I, which is the damaged stay cable; (2) the influenced stay cables of group II, which are near to the damaged stay cable; (3) the influenced stay cables of Group III, which are farther from the damaged stay cable than the influenced stay cables of group II are.

Given the uncertainty in the measured data and FEM, an SCDI based on the cable tension of only one or few influenced stay cables is unreliable. The best way to identify stay cable damage is to use the cable tension of all influenced stay cables. However, with limited project budget, we cannot place sensors on every influenced stay cable. The reliability of most SCDI is lower than that of the SCDI with enough sensors. Therefore, the reliability of damage identification for damaged stay cables depends on the sensor placement on the corresponding influenced stay cables.

2.1.3. Damage Identification Reliability Index (DIRI). This study aims to determine OSP, with the goal that every stay cable of the bridge has an acceptable, satisfying, and

high reliability. To achieve this goal, we defined the *DIRI* index to quantify the damage identification reliability of stay cables. The calculation method of *DIRI* is associated not only with the sensor placement, as discussed in Section 2.1.2, but also with other factors, including the structure type of the cable-stayed bridge, the specific method of damage identification, the quality of the measured data, and the accuracy of FEM. However, in this paper, we focused only on the relationship between *DIRI* and sensor placement. Before proposing the calculation method of *DIRI*, we provide the following premises: (1) the provided calculation method of *DIRI* is suitable only for cable-stayed bridges with similar rules on dCT ; (2) the provided calculation method of *DIRI* is suitable only for the damage identification methods whose input data are the dCT of the influenced stay cables; (3) assuming that the data uncertainties obtained by sensors on stay cables are of the same level, the effect of uncertainty will not be considered when we calculate *DIRI*; (4) *DIRI* is considered a relative index in this paper.

Based on the aforementioned premises, we considered *DIRI* as a function of sensor placement. However, *DIRI* is difficult to calculate accurately based on a rigorous theoretical system. In this paper, we provided a selectable and reasonable calculation method of *DIRI* on the basis of the rules of dCT discussed in Section 2.1.2 and relevant experience. The rigorous theoretical system for the definition and calculation of *DIRI* needs to be further studied. We considered *DIRI* as the input data for the OSP method, which is the research emphasis of this paper. In practical applications, experts or decision makers of sensor placement can adjust the proposed *DIRI* calculation method according to their personal experience and preferences to obtain different results. These results can provide references and suggestions for the final decision of sensor placement.

The proposed *DIRI* calculation method is described as follows. According to the discussion in Section 2.1.2, the value of *DIRI* for a damaged stay cable depends only on the sensor placement on eight influenced stay cables. These stay cables can be classified into three groups: G1, G2, and G3 (see Figure 6). The G1 group includes one stay cable, the G2 group includes three stay cables, and the G3 group includes four stay cables. One type of sensor placement was denoted as “sensor placement case.” To identify the stay cables, we denoted the number of possible sensor placement cases on eight influenced stay cables as N_c . N_c can be calculated according to the following combination formula:

$$N_c = \sum_{j=1}^8 C_8^j = 2^8 - 1 = 255, \quad (1)$$

where C_n^m is the combination operator symbol. The 255 types of sensor placement can be divided into seven categories (see Table 1 for details). For example, number 4 category includes all possible sensor placement cases, in which sensors were placed on G1 and G2 groups of influenced stay cables. The number of sensor placement cases within number 4 category

is N_{c4} . N_{c4} can be calculated according to the following combination formula:

$$N_{c4} = C_1^1 \cdot \sum_{j=1}^3 C_3^j = 7. \quad (2)$$

To calculate $DIRI$, we defined “reliability contribution score (RCS)” for each stay cable among the influenced stay cables. The RCS of a stay cable quantifies the contribution to $DIRI$ if we place a sensor on this stay cable. Ra , Rb , and Rc are defined to represent the RCS of the stay cables in G1, G2, and G3, respectively. Thus, the $DIRI$ for a damaged stay cable can be calculated by

$$DIRI = \sum Ra_i + \sum Rb_j + \sum Rc_k, \quad (3)$$

where $i = 1$, $j = 1, 2, 3$, and $k = 1, 2, 3, 4$.

The values of Ra_i , Rb_j , and Rc_k in different sensor placement categories are determined based on the discussion in Section 2.1.2 and the following basic considerations: (1) if sensors are placed on all influenced stay cables, then $DIRI = 1$; (2) if no sensors are placed on the influenced stay cables, then $DIRI = 0$; (3) if a sensor is placed on the damaged stay cable, considering the data uncertainty, $DIRI = 0.5$ is reasonable and appropriate because the damaged stay cable has the largest dCT among all cables; (4) if sensors are placed on all of the stay cables of G2, considering the rules on dCT and the data fusion among three sensors, $DIRI = 0.45$ is reasonable and appropriate; (5) if sensors are placed on all of the stay cables of G3, considering the rules on dCT and the data fusion among four sensors, $DIRI = 0.28$ is reasonable and appropriate; (6) if sensors are placed on all of the stay cables of G1 and G2, then $DIRI = 0.8$ is reasonable and appropriate; (7) if sensors are placed on all of the stay cables of G1 and G3, then $DIRI = 0.7$ is reasonable and appropriate; (8) if sensors are placed on all of the stay cables of G2 and G3, then $DIRI = 0.65$ is reasonable and appropriate.

Table 1 shows the values of Ra_i , Rb_j , and Rc_k in different sensor placement categories. If no sensor exists on a stay cable, then the Ra_i , Rb_j , or Rc_k of this stay cable is equal to zero. Table 2 shows the calculation and results of $DIRI$ for some typical sensor placements. Although the calculation method of $DIRI$ was proposed not based on rigorous theoretical system, it is generally reasonable.

2.1.4. Stay Cable Importance Index (SCII). With consideration that the importance of each stay cable in cable-stayed bridges differs, we defined SCII to quantify it. Suppose the value of SCII is an integer; SCII ranges from 0 to 6. Table 3 gives the description of importance for different values of SCII.

The value of SCII can be given by experts or decision makers. We can set the value of SCII of all stay cables as 3 (Normal) at first; and then adjust the value of SCII according to the following aspects.

- (1) Size and location of the stay cable: the importance of the longest stay cable or the shortest stay cable will be higher than other stay cables in general because of their representativeness.

- (2) Probability of stay cable damage occurrence: if historical test data show that potential abnormalities exist in some stay cables, then the probability of damage occurrence on these stay cables will be higher than that of other stay cables. Thus, focus should be given on the former.
- (3) Consequences of stay cable damage: if some damages have been found in a segment of the girder, then the damage of the stay cables which support this segment of girder may lead to more serious consequences than other stay cables do, and we have a reason to believe that the importance of these cables is higher.
- (4) If some stay cables have already been monitored by other means, then the SCII of these stay cables should be set as lower value than other stay cables should be.
- (5) Expert experience and subjective preference of decision makers: if experts or decision makers believe that some stay cables are more important, the SCII of these stay cables will be higher than other stay cables.

On the basis of SCII, experts or decision makers can determine the value of the allowable minimum $DIRI$ and the satisfying $DIRI$ directly. See Sections 3.3.1 and 3.4.1 for details.

2.1.5. Criterion for Sensor Quantity Optimization. The allowable minimum monitoring requirement should be provided to determine the sensor quantity. In this study, the allowable minimum monitoring requirement can be expressed by the allowable minimum $DIRI$, which can be determined directly by experts or decision makers on the basis of the corresponding SCII.

Accordingly, the optimization criterion and the problem description of sensor quantity optimization are given as follows.

Objective. Determine the minimum number of sensor optimally placed on the stay cable and the corresponding sensor placement.

Subject to

$$DIRI_i \geq DIRI_i^{\min}, \quad i = 1, 2, \dots, n, \quad (4)$$

where $DIRI_i^{\min}$ is the allowable minimum $DIRI$ and n is the number of stay cables for sensor placement.

2.1.6. Multistage Criterion for Sensor Location Optimization under the Given Number of Sensors. The core idea of sensor location optimization under the given number of sensors is to increase the $DIRI$ of all stay cables globally under the premise of meeting the requirement of the allowable minimum $DIRI$ of all stay cables and satisfying the $DIRI$ of the stay cables with high SCII. In this study, the satisfying $DIRI$ was determined directly by experts or decision makers on the basis of the corresponding SCII.

On this basis, the multistage criterion and the problem description of sensor location optimization under the given number of sensors are given as follows.

TABLE 1: Value of Ra_i , Rb_j , and Rc_k in different sensor placement categories.

Sensor placement category	Included group	One of all possible sensor placements in the category	Number of sensor placement case	Values of Ra , Rb , Rc
1	G1		$C_1^1 = 1$	$Ra_i = 0.5, Rb_j = 0, Rc_k = 0$
2	G2		$\sum_{j=1}^3 C_3^j = 7$	$Ra_i = 0, Rb_j = 0.15, Rc_k = 0$
3	G3		$\sum_{k=1}^4 C_4^k = 15$	$Ra_i = 0, Rb_j = 0, Rc_k = 0.07$
4	G1 + G2		$C_1^1 \cdot \sum_{j=1}^3 C_3^j = 7$	$Ra_i = 0.5, Rb_j = 0.1, Rc_k = 0$
5	G1 + G3		$C_1^1 \cdot \sum_{k=1}^4 C_4^k = 15$	$Ra_i = 0.5, Rb_j = 0, Rc_k = 0.05$
6	G2 + G3		$\sum_{j=1}^3 C_3^j \cdot \sum_{k=1}^4 C_4^k = 105$	$Ra_i = 0, Rb_j = 0.15, Rc_k = 0.05$
7	G1 + G2 + G3		$C_1^1 \cdot \sum_{j=1}^3 C_3^j \cdot \sum_{k=1}^4 C_4^k = 105$	$Ra_i = 0.5, Rb_j = 0.1, Rc_k = 0.05$

TABLE 2: Calculation and results of $DIRI$ for some typical sensor placements.

Typical sensor placement (some example)	Calculation and result of $DIRI$	Typical sensor placement (some example)	Calculation and result of $DIRI$
	$DIRI = \sum Ra_i + \sum Rb_j + \sum Rc_k$ $= (0.5) + (0) + (0) = 0.5$		$DIRI = \sum Ra_i + \sum Rb_j + \sum Rc_k$ $= (0.5) + (0.1) + (0) = 0.6$
	$DIRI = \sum Ra_i + \sum Rb_j + \sum Rc_k$ $= (0) + (0.15 \times 3) + (0) = 0.45$		$DIRI = \sum Ra_i + \sum Rb_j + \sum Rc_k$ $= (0.5) + (0) + (0.05 \times 2) = 0.6$
	$DIRI = \sum Ra_i + \sum Rb_j + \sum Rc_k$ $= (0) + (0) + (0.07 \times 4) = 0.28$		$DIRI = \sum Ra_i + \sum Rb_j + \sum Rc_k$ $= (0) + (0.1 \times 2) + (0.05 \times 2) = 0.3$
	$DIRI = \sum Ra_i + \sum Rb_j + \sum Rc_k$ $= (0.5) + (0.1 \times 3) + (0.05 \times 4) = 1$		$DIRI = \sum Ra_i + \sum Rb_j + \sum Rc_k$ $= (0.5) + (0.1 \times 1) + (0.05 \times 4) = 0.8$

Stage 1

Objective. Determine the minimum number of sensors and the corresponding sensor placement.

Subject to

$$DIRI_i \geq DIRI_i^{\min}, \quad i = 1, 2, \dots, n. \quad (5)$$

Stage 2

Objective. Under the premise of completing stage 1, determine the minimum additional number of sensors placed on the stay cables where no sensors were placed in stage 1.

Subject to

$$DIRI_j \geq DIRI_j^{\text{sat}}, \quad j \in \text{IS}, \quad (6)$$

TABLE 3: Description of importance for different values of SCII.

Value of SCII	Description of corresponding importance
6	Most important
5	Very important
4	Important
3	Normal
2	Unimportant
1	Very unimportant
0	Most unimportant

where $DIRI_j^{\text{sat}}$ is the satisfying $DIRI$ of stay cables in the priority monitoring group; IS is the index set of the stay cables in the priority monitoring group.

Explanation. Priority monitoring group comprises some stay cables with high SCII, which are determined by experts or decision makers. In this stage, the stay cables in the priority monitoring group will be sorted according to the corresponding SCII. The sensor placement will be subject to Inequation (6) for the stay cable with high SCII preferentially when sensors are not enough for stage 2.

Stage 3

Objective. Under the premise of completing stages 1 and 2, find the optimal placement of the remaining sensors to maximize global $DIRI$ ($GDIRI$), which is defined as follows:

$$GDIRI = \sum_{i=1}^n DIRI_i \cdot w(SCII_i), \quad (7)$$

where $w(SCII_i)$ is the weighting function with the independent variable of SCII.

Subject to. The total number of sensors placed on the stay cables is less than the given number of sensors.

Explanation. $w(SCII_i)$ is defined to adjust the optimization direction. The value of $w(SCII_i)$ meets the following condition:

$$\sum_{i=1}^n w(SCII_i) = 1. \quad (8)$$

The form of $w(SCII_i)$ can be determined by users according to their experience and subjective preference; see Section 3.4.1 for details.

2.2. Optimization Algorithm. As discussed in Section 2.1, sensor quantity and location optimization are a complex, multiobjective, combinatorial optimization problem. An exhaustive search would be extremely time consuming or even impossible. Thus, a systematic and efficient approach is needed to solve such computationally demanding problem [8].

Calculating the exact solution within a limited time is difficult. Therefore, we focused on the approximate approach

for the combinatorial optimization problem. No general approach exists for all types of combinatorial optimization problems. Therefore, we need to develop a specific approach to solve the specific combinatorial optimization problem discussed in this paper.

2.2.1. Algorithm for Sensor Quantity Optimization. The RE algorithm is proposed for sensor quantity optimization. The main idea of the RE algorithm is to set the initial sensor placement and to remove sensors randomly one by one under the condition that the $DIRI$ of any stay cable meets the requirement of Inequation (4). This approach is conducted until no sensor can be removed from the stay cables. The number of sensors left on the stay cables is a feasible solution. However, this solution may not be the best solution. Therefore, we need to repeat the above process (this process is a complete random elimination process which is called a “cycle”) to obtain multiple results and to select the best cycle among all cycles. We cannot ensure that this process will obtain the best solution, but we can obtain the satisfactory solution under the condition that the number of cycles is sufficient.

Figure 7 shows the flowchart of the proposed RE algorithm, which is used to determine the required minimum number of sensors.

The RE algorithm is a random search algorithm in nature and is a common algorithm for sensor quantity optimization with any form of $DIRI^{\text{min}}$ setting. However, for some special form of $DIRI^{\text{min}}$ setting, the RE algorithm may not be the most effective one. By contrast, the heuristic algorithm, which is based on expert knowledge and experience in the OSP aspect, may be more effective than the RE algorithm. Thus, a heuristic algorithm called HRE algorithm is proposed in this paper. The main idea of the HRE algorithm is described as follows. In many cases, the $DIRI^{\text{min}}$ of most stay cables are often the same (see Section 3.3.1). For the same $DIRI$, symmetric staggered placement is the best according to simulation analysis. Therefore, we propose eight types of predefined typical optimal placements for the setting of the same $DIRI^{\text{min}}$ (see the appendix). We first selected one of the eight types of typical optimal placements as the initial sensor placement to meet the requirement of most $DIRI^{\text{min}}$ of the stay cables. On the basis of the initial sensor placement, the RE algorithm was applied to meet the requirement of other higher or lower $DIRI^{\text{min}}$ of the stay cables.

Figure 8 shows the flowchart of the HRE algorithm proposed in this paper to determine the required minimum number of sensors.

2.2.2. MGO Algorithm for Sensor Location under the Given Number of Sensors. The MGO algorithm is proposed for sensor location optimization under a given number of sensors. The main idea of the MGO algorithm is described as follows. We determined the OSP through three stages. In stage 1, the sensor placement with the minimum number of sensors is obtained by using the RE or HRE algorithm to meet the requirement of Inequation (5). In stage 2, if the number of sensors placed on the stay cables in stage 1

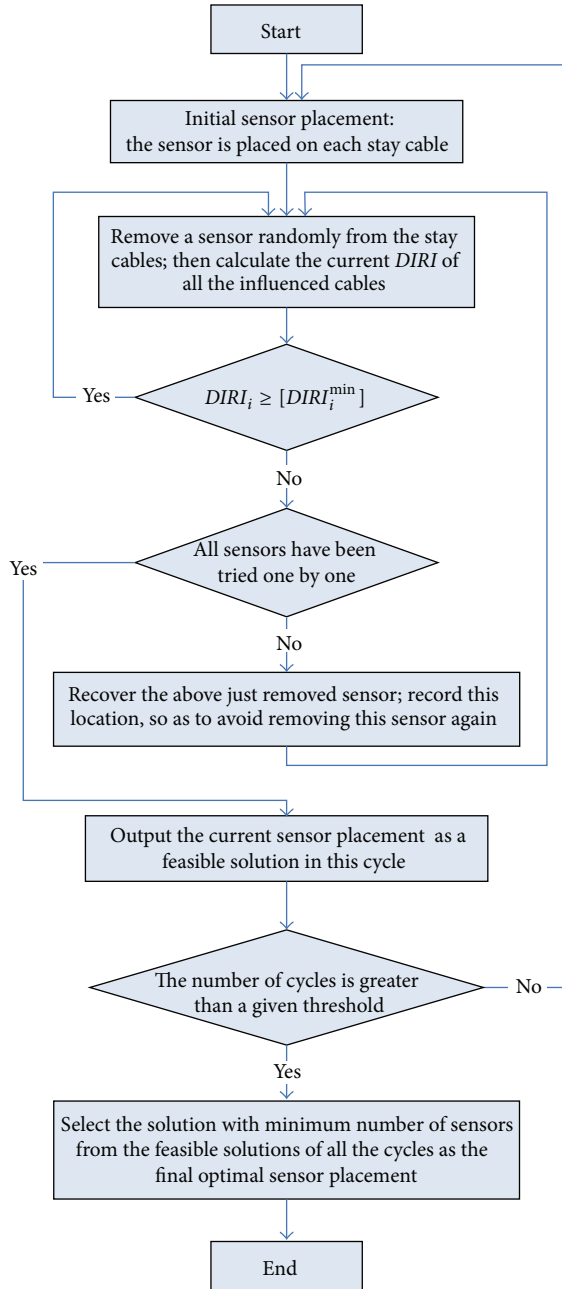


FIGURE 7: Flowchart of the RE algorithm.

is less than the given number of sensors, then additional sensors are placed on stay cables with no sensors to meet the requirement of Inequation (6). By using the RE algorithm, we conduct this step on the stay cables in the priority monitoring group. In stage 3, if the number of sensors placed on the stay cables in stages 1 and 2 is still less than the given number of sensors, then the remaining sensors are placed on stay cables with no sensors placed in stages 1 and 2 to increase globally the $DIRI$ of the stay cables (maximize $GDIRI$). This stage is completed by using the multistep increasing $DIRI$ (MID) algorithm, which is described as follows: the final objective $DIRI$ ($DIRI^{final}$) is increased step by step, and

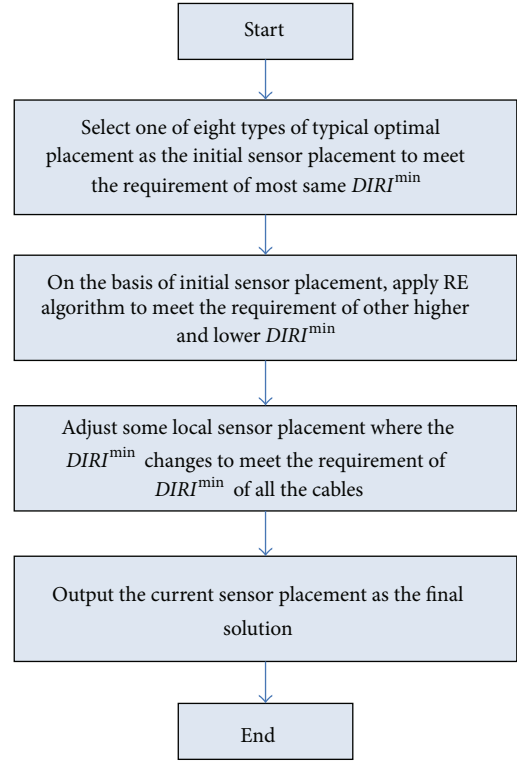


FIGURE 8: Flowchart of the HRE algorithm.

sensors are placed one by one on stay cables with no sensors placed in stages 1 and 2. Each sensor placement should reach the maximum number of stay cables whose $DIRI$ exceeds $DIRI^{final}$. If no stay cable whose $DIRI$ exceeds the $DIRI^{final}$ exists, then the criterion is changed to reach the maximum $GDIRI$ increment of the stay cables, whose $DIRI$ is under the $DIRI^{final}$ line.

Figure 9 shows the flowchart of the MGO algorithm proposed in this paper for determining the OSP under the given number of sensors. The flowchart of the MID algorithm, which is the subalgorithm in the MGO algorithm, is shown in Figure 10.

3. Case Study

3.1. Binzhou Yellow River Highway Bridge (BZ Bridge; Cable-Stayed Bridge). To study and verify the proposed algorithm, a case study for determining the optimal sensor quantity and location on a cable-stayed bridge named BZ Bridge is given in this paper.

The BZ Bridge is a three-tower cable-stayed bridge with a span of $84 + 300 + 300 + 84$ m. It is located between Dudian Town and Zhaodian Town in the Shandong province of China. Figure 11 shows the bird view of the BZ Bridge. The girder of this bridge is prestressed concrete structure. The deck is supported by 200 stay cables which range from 88.940 m to 219.410 m in length, with varying diameters. The design of the stay cables was based on a parallel-wire strands

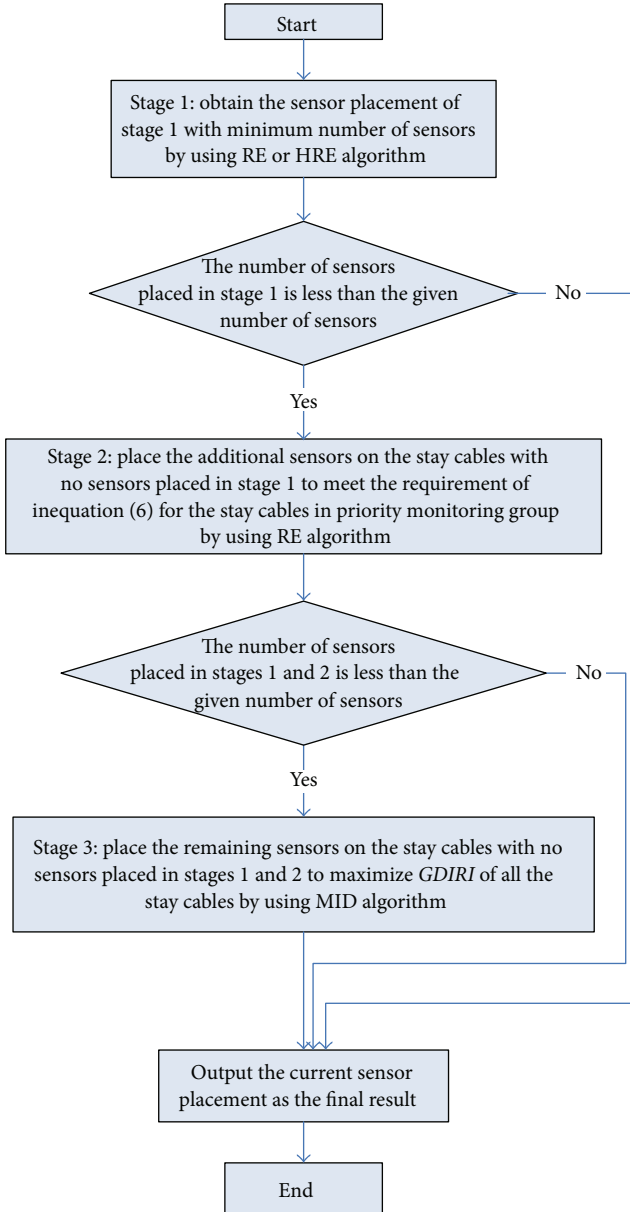


FIGURE 9: Flowchart of the MGO algorithm.

system consisting of 7 mm galvanized low relaxation steel wires with ultimate tensile strength of about 1770 MPa.

The BZ Bridge is divided into four areas by three towers. Considering symmetry and without loss of generality, we focused on the OSP on the stay cables between one edge tower and the middle tower (see Figure 12). To identify the stay cable damage, we applied accelerometer to monitor the cable tension. The total number of these stay cables is 76; thus, the maximum number of sensors (accelerometers) to be placed on the stay cables in this case study is 76.

3.2. Description of Programming. For the case study, the programs for sensor quantity and location optimization were developed based on the proposed algorithm by MATLAB

TABLE 4: Value of $DIRI^{\min}$ corresponding to SCII.

SCII	0	1	2	3	4	5	6
$DIRI^{\min}$	0	0.05	0.1	0.2	0.3	0.4	0.6

R2010b, which is the programming language of technical computing. The related calculation and analysis in the case study were also conducted by MATLAB R2010b.

3.3. Result and Discussion of Sensor Quantity Optimization

3.3.1. Setting of the Main Input Parameters. According to the description in Section 2.1.4, in this case study, we assume that the SCII of the longest and shortest stay cables within a cable plane was set as 5 (very important), the SCII of the stay cables with medium length was set as 2 (unimportant), and the SCII of other common stay cables was set as 3 (normal).

The $DIRI^{\min}$ can be determined according to Table 4. Accordingly, we determined the setting of $DIRI^{\min}$ as shown in Figure 14.

It should be pointed out that the users can also set SCII and $DIRI^{\min}$ as other values on the basis of their own viewpoint.

3.3.2. Result and Discussion of the RE Algorithm. In the RE algorithm, given that sensors are removed randomly each time, the result of each cycle includes some randomness. To determine the optimal solution, we should select the best solution from the results of numerous cycles. Figure 13 shows the result of the minimum sensor quantity of each cycle, which decreased from 44 to 27. The best solution of the minimum sensor quantity in this optimization calculation is 27, which is marked by large, black dots in Figure 13.

Figure 14 shows the sensor quantity optimization result under the condition that the number of cycles in the RE algorithm is set as 500,000. The $DIRI$ of this OSP are all larger than $DIRI^{\min}$. Meanwhile, the $DIRI$ of many stay cables are almost near the $DIRI^{\min}$ line because the sensors were placed at the optimized location as far as possible, with the minimum sensor quantity as far as possible.

As discussed earlier, when the number of cycles is set as a different value, the RE algorithm will give a different result. The more the number of cycles is, the better the result obtained, but the longer time the RE algorithm will spend to obtain the result. Table 5 shows the optimal sensor quantity and the elapsed time corresponding to the different number of cycles. The optimal sensor quantity decreased with the increased number of cycles. However, when the number of cycles is more than 100,000, the optimal sensor quantity does not decrease. Therefore, the number of cycles must not be set to more than 100,000. When the number of cycles is 100,000, the elapsed time is 500 s, which is acceptable for the actual project.

3.3.3. Result and Discussion of HRE Algorithm. In the HRE algorithm, the initial sensor placement is determined first based on expert knowledge and experience. Therefore, the

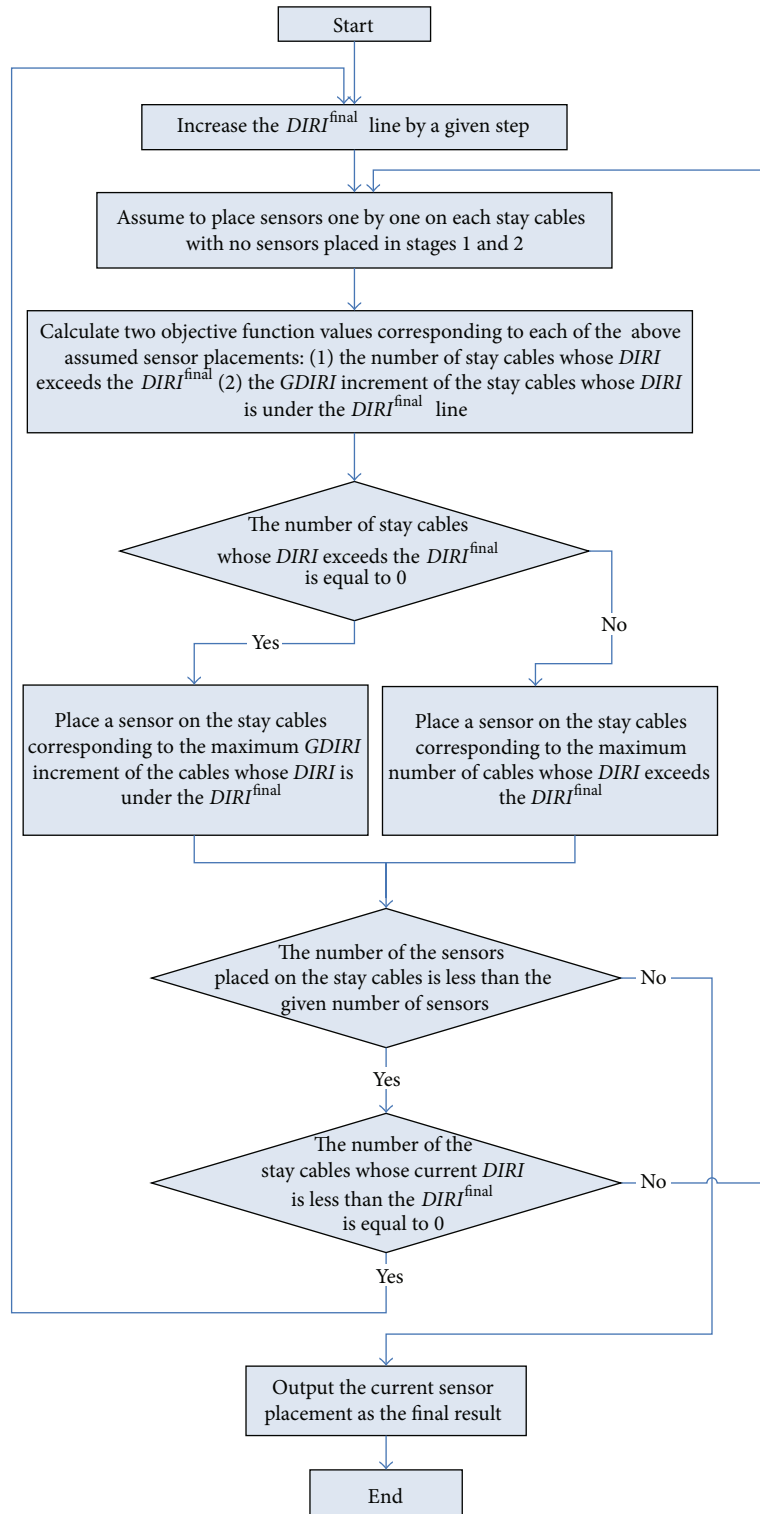


FIGURE 10: Flowchart of the MID algorithm.

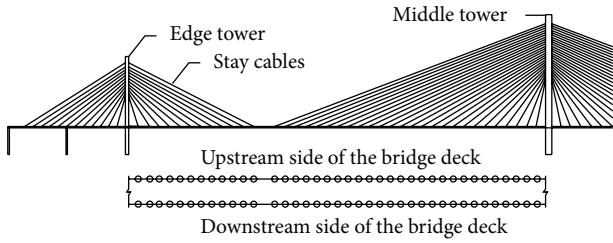
result may be better than that of the RE algorithm under the condition that the $DIRI^{\min}$ of most stay cables are the same.

Figure 15 shows the result from the HRE algorithm. The sensor placement from the HRE algorithm is more

symmetrical than that from the RE algorithm. The minimum number of sensors optimized from the HRE algorithm was 25, which is less than that from the RE algorithm by 2 (see Figure 14). The elapsed time of the HRE algorithm was 70 s,



FIGURE 11: Bird view of the BZ Bridge.



- Location of stay cables which are taken into account in this case study

FIGURE 12: Stay cables considered in this case study.

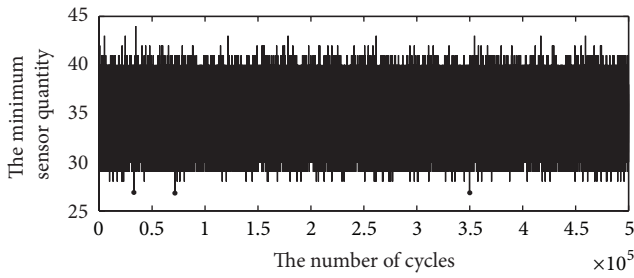


FIGURE 13: Minimum sensor quantity of each cycle.

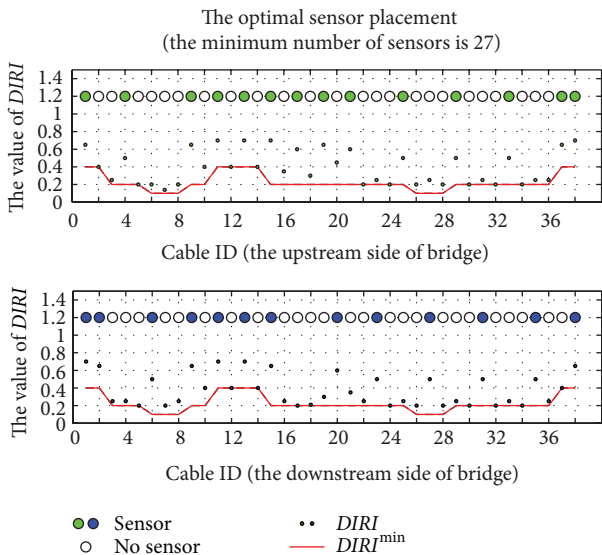


FIGURE 14: RE algorithm result when the number of cycles was set as 500,000.

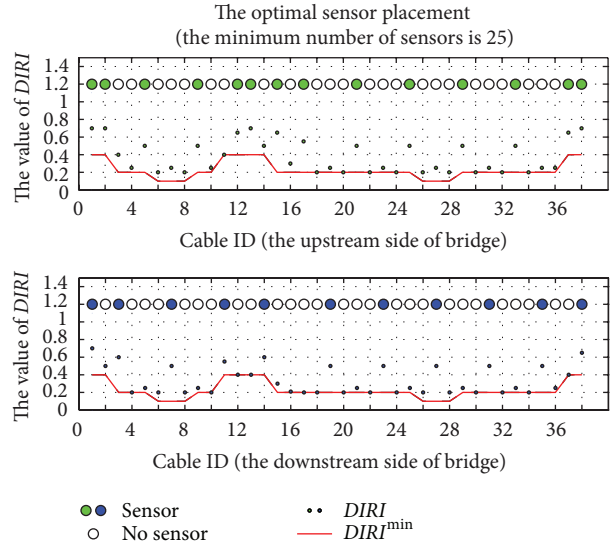


FIGURE 15: Result from the HRE algorithm.

TABLE 5: Optimal sensor quantity and elapsed time corresponding to different number of cycles.

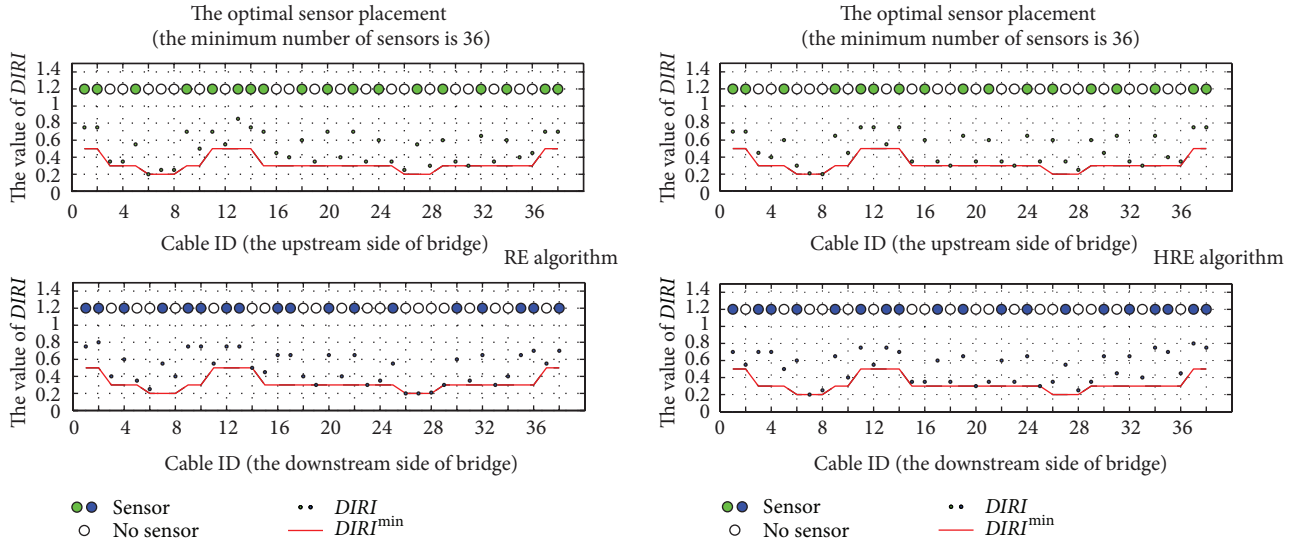
Number of cycles	Corresponding minimum number of sensors	Elapsed time (s)
100	30	0.5
1000	29	5
5000	29	25
10,000	28	50
20,000	28	100
50,000	28	250
100,000	27	500
500,000	27	2500
1,000,000	27	5000

which is significantly less than that of the RE algorithm. Therefore, the HRE algorithm is more effective than the RE algorithm in this $DIRI^{min}$ setting.

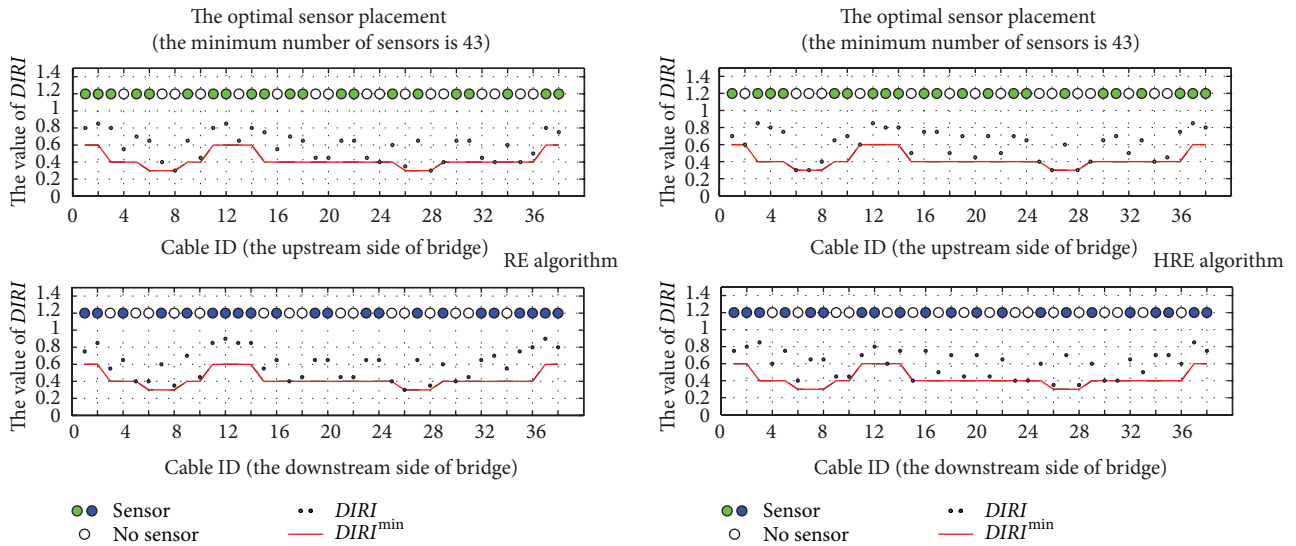
Figure 16 shows the comparison between RE and HRE algorithms, with other forms of $DIRI^{min}$ settings. When the $DIRI^{min}$ of most stay cables are the same and the value of the same $DIRI^{min}$ is near the minimum $DIRI$ of one of the eight predefined typical optimal placements (cases 1, 2, and 4 in Figure 16), the HRE algorithm can give better solution with less elapsed time than the RE algorithm in most cases. However, when the $DIRI^{min}$ do not meet the above requirement (case 3 in Figure 16), we are not sure which algorithm can give a better result. Thus, we need to use both algorithms to calculate the minimum number of sensors and to select the best result between them.

3.4. Result and Discussion of Sensor Location Optimization

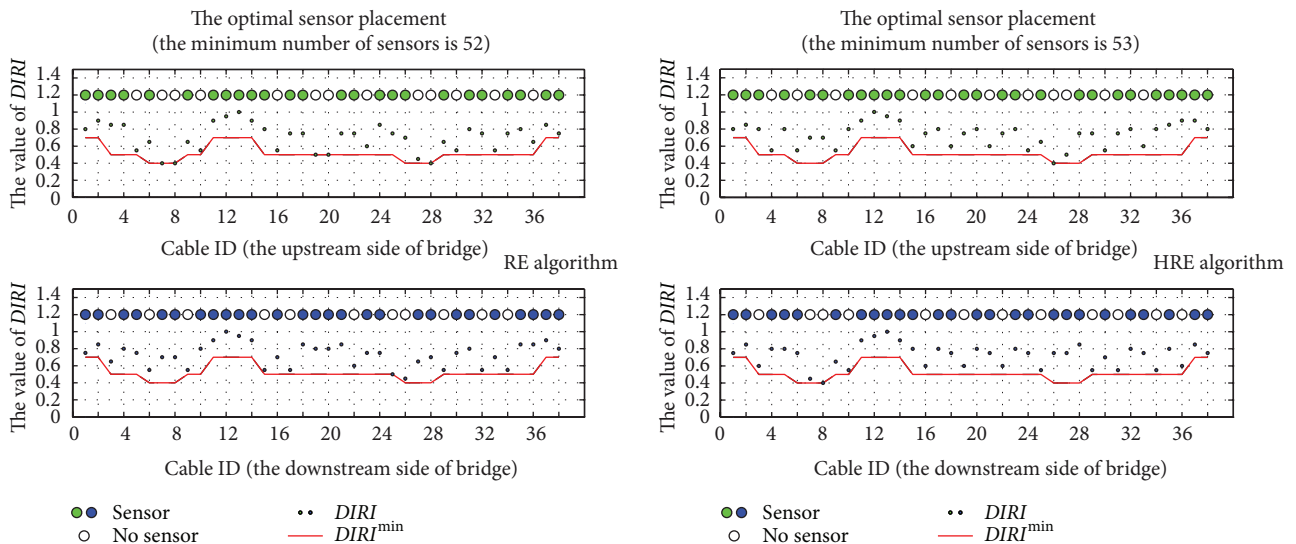
3.4.1. Setting of the Main Input Parameters. The setting of $DIRI^{min}$ is the same as that in Section 3.3.1. Considering that



(a) Case 1



(b) Case 2



(c) Case 3

FIGURE 16: Continued.

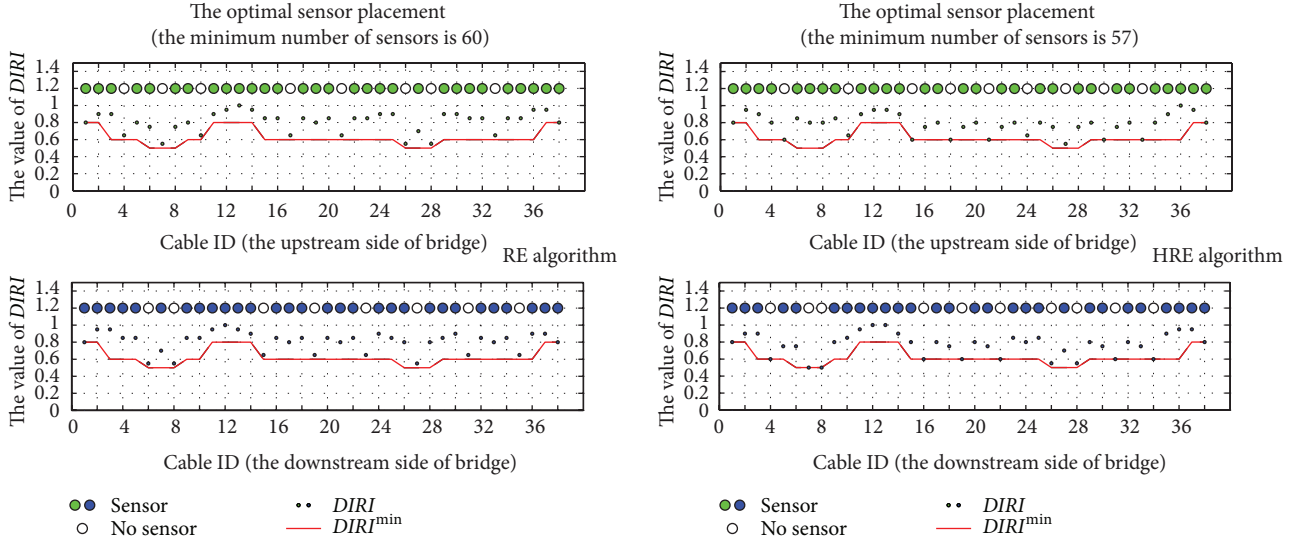


FIGURE 16: Comparison between RE and HRE algorithms.

TABLE 6: Value of $DIRI^{\text{sat}}$ corresponding to SCII.

SCII	4	5	6
$DIRI^{\text{sat}}$	0.6	0.7	0.8

the stay cables with larger $DIRI^{\text{min}}$ (with larger SCII at the same time) are more important than other stay cables, the former should be included in the priority monitoring group, and their $DIRI^{\text{sat}}$ can be determined according to Table 6.

The $DIRI^{\text{sat}}$ of other stay cables will be set the same as the $DIRI^{\text{min}}$. Accordingly, we determined the setting of $DIRI^{\text{min}}$ and $DIRI^{\text{sat}}$ as shown in Figure 17.

To simplify the problem, in this case study, we assume $w(\text{SCII}_i) = 1/76$, it means that in stage 3 of MGO algorithm, we did not consider the difference of SCII and the goal of optimization is to improve the $DIRI$ of all the stay cables evenly. Of course, we also can set $w(\text{SCII}_i)$ as another form, for example,

$$w(\text{SCII}_i) = \frac{\text{SCII}_i}{\sum \text{SCII}_i}, \quad (9)$$

where $w(\text{SCII}_i)$ is a semisubjective parameter, and different form of $w(\text{SCII}_i)$ will result in different result in stage 3 of MGO algorithm.

It should be pointed out that the users can also set $DIRI^{\text{min}}$, $DIRI^{\text{sat}}$, and $w(\text{SCII}_i)$ as other values on the basis of their own viewpoint.

3.4.2. Result and Discussion of the MGO Algorithm. Figure 17 shows the sensor placements after each stage of the MGO algorithm, assuming that the given number of sensor is 35. In stage 1, 25 sensors were placed to meet the requirement of $DIRI^{\text{min}}$. In Stage 2, on the basis of the sensor placement after stage 1, additional six sensors were placed to meet

the requirement of the $DIRI^{\text{sat}}$ of the stay cables in the priority monitoring group. In stage 3, the remaining four sensors were placed through MID algorithm to maximize the increase of $DIRI$ globally (maximize $GDIRI$). The result shown in Figure 17 indicates that the MGO algorithm can meet the multistage criterion for sensor location optimization effectively and can give a satisfying optimized solution.

Figure 18 shows the sensor placement results corresponding to different number of sensors. When the given number is 30, stage 3 is not executed because no sensors remained for sensor placement in stage 3. When the given number is 40 or 50, 9 or 19 sensors remained for sensor placement in stage 3. As shown in Figure 18, with the increase of the given number of sensors, the final $DIRI$ level increased globally. Therefore, the MGO algorithm can be considered in line with the core optimization idea described as follows: increase $DIRI$ of all stay cables globally under the premise of meeting the requirements of $DIRI^{\text{min}}$ and $DIRI^{\text{sat}}$.

4. Conclusion

A study of OSP for the SCDI of cable-stayed bridges under uncertainty is presented in this paper. The following conclusions are obtained from the theoretical analysis and case study.

- (1) The concept of $DIRI$ is presented first. A reasonable and feasible calculation method for $DIRI$ is then given based on FEM analysis and related knowledge in SCDI. The case study shows that the concept and calculation method of $DIRI$ are reasonable and available and can provide the basis and theoretical framework for the determination of the optimization criteria for sensor placement optimization.
- (2) The criterion for sensor quantity optimization based on the concept of $DIRI$ is presented. The core idea

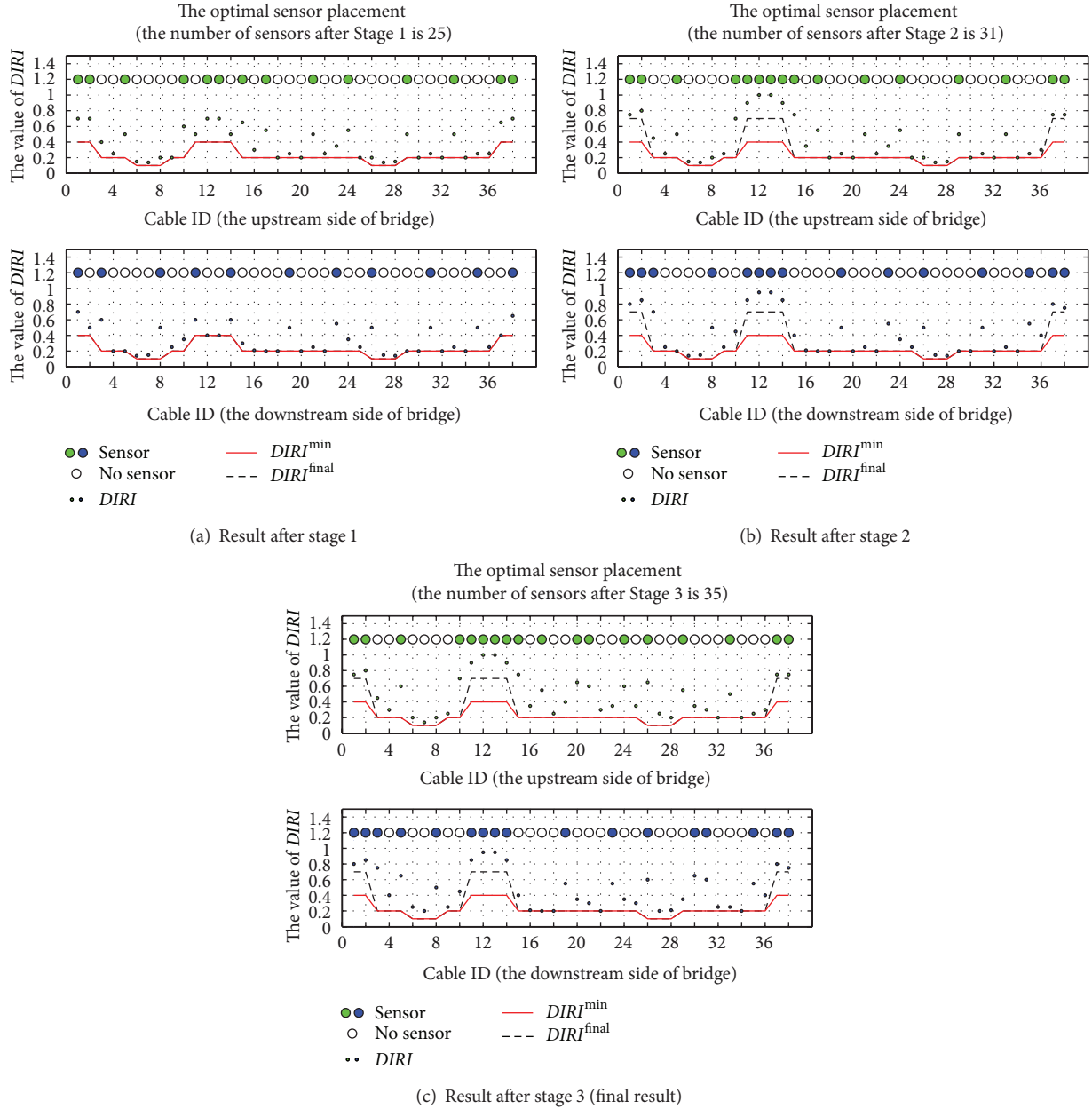


FIGURE 17: Results after each stage of the MGO algorithm.

of the criterion is to meet the minimum requirement of $DIRI$, which is determined directly by experts or decision makers. On the basis of this optimization criterion, the practical sensor quantity optimization problem can be abstracted as a concise, multiobjective, combinatorial optimization problem. Theoretical analysis and case study results show that this criterion is reasonable and suitable for sensor quantity optimization for SCDD.

- (3) A multistage criterion for sensor location optimization under the given number of sensors is presented. Theoretical analysis and case study show that this criterion can represent effectively the core idea of

the sensor location optimization described as follows: increase the $DIRI$ of all stay cables globally under the premise of meeting the requirements of $DIRI^{\min}$ and $DIRI^{\text{sat}}$. The criterion can provide guidance for the following optimization calculation.

- (4) The RE and HRE algorithms are presented for sensor quantity optimization calculation. The RE algorithm is a common algorithm for any form of $DIRI^{\min}$, whereas the HRE algorithm is a special algorithm for a special form of $DIRI^{\min}$. The case study shows that when the $DIRI_i^{\min}$ of most stay cables are the same and the value of the same $DIRI_i^{\min}$ is near the minimum $DIRI$ of one of the eight predefined

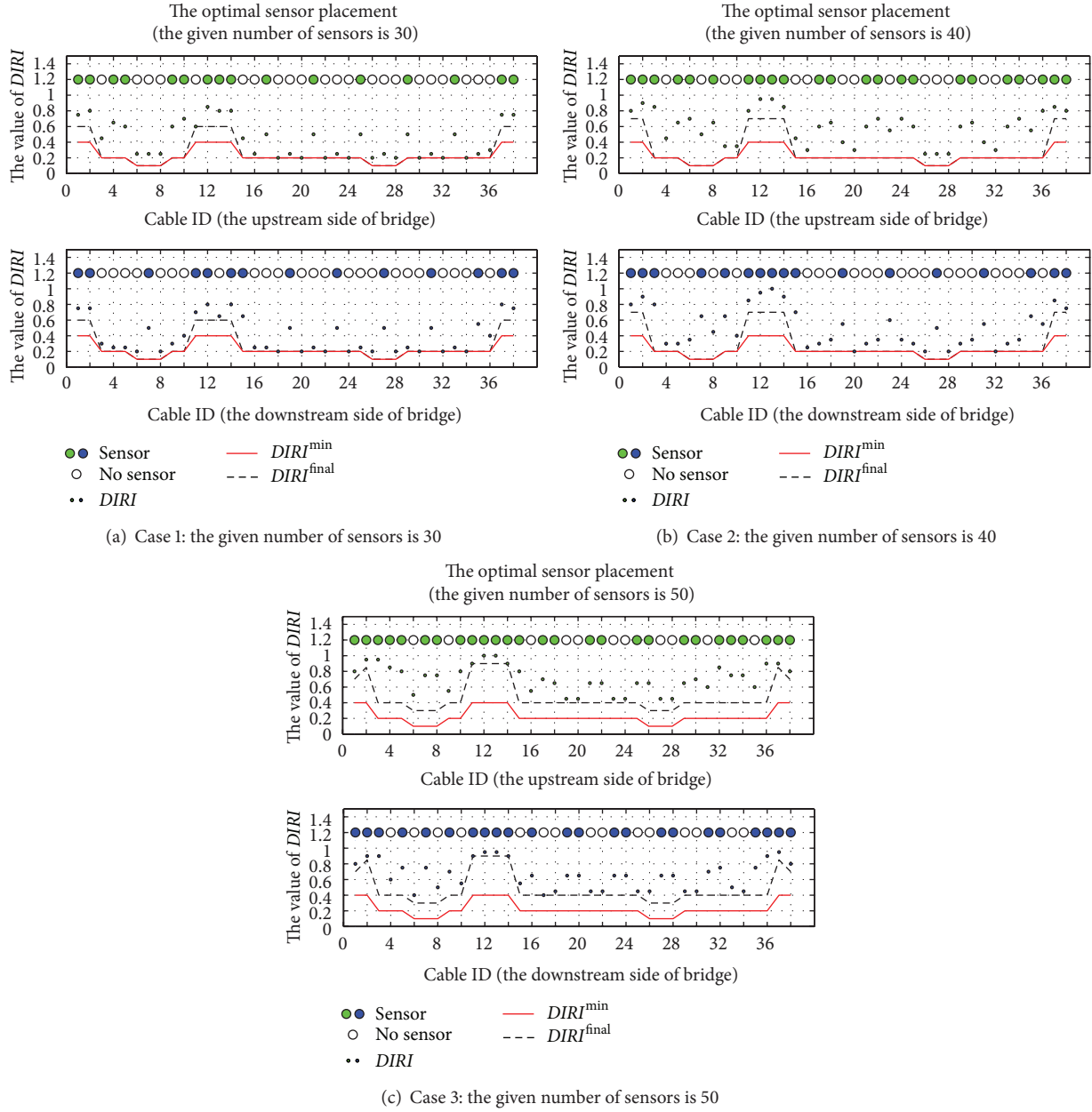


FIGURE 18: Sensor placement results corresponding to different number of sensors.

typical optimal placements, then the HRE algorithm can provide better solution with less elapsed time than the RE algorithm in most cases. However, when the $DIRI^{min}$ does not meet the above requirement, we are not sure which algorithm can give better result. Therefore, we should use both algorithms to calculate the minimum number of sensors and to select the better result between them.

- (5) The MGO algorithm is presented for sensor location optimization calculation. The MGO algorithm includes three stages that correspond to the three stages of the multistage criterion for sensor location optimization. In stages 1 and 2, the MGO algorithm

can give the sensor placement result to meet the requirements of $DIRI^{min}$ and $DIRI^{sat}$ by using the RE or HRE algorithm. In stage 3, a subalgorithm called MID algorithm is presented to place the remaining sensors one by one on the most appropriate location. The case study shows that the MGO algorithm can meet the multistage criterion effectively for sensor location optimization and can give a satisfying optimized solution.

Although some relatively detailed study has been conducted, the following aspects of this paper require further study.

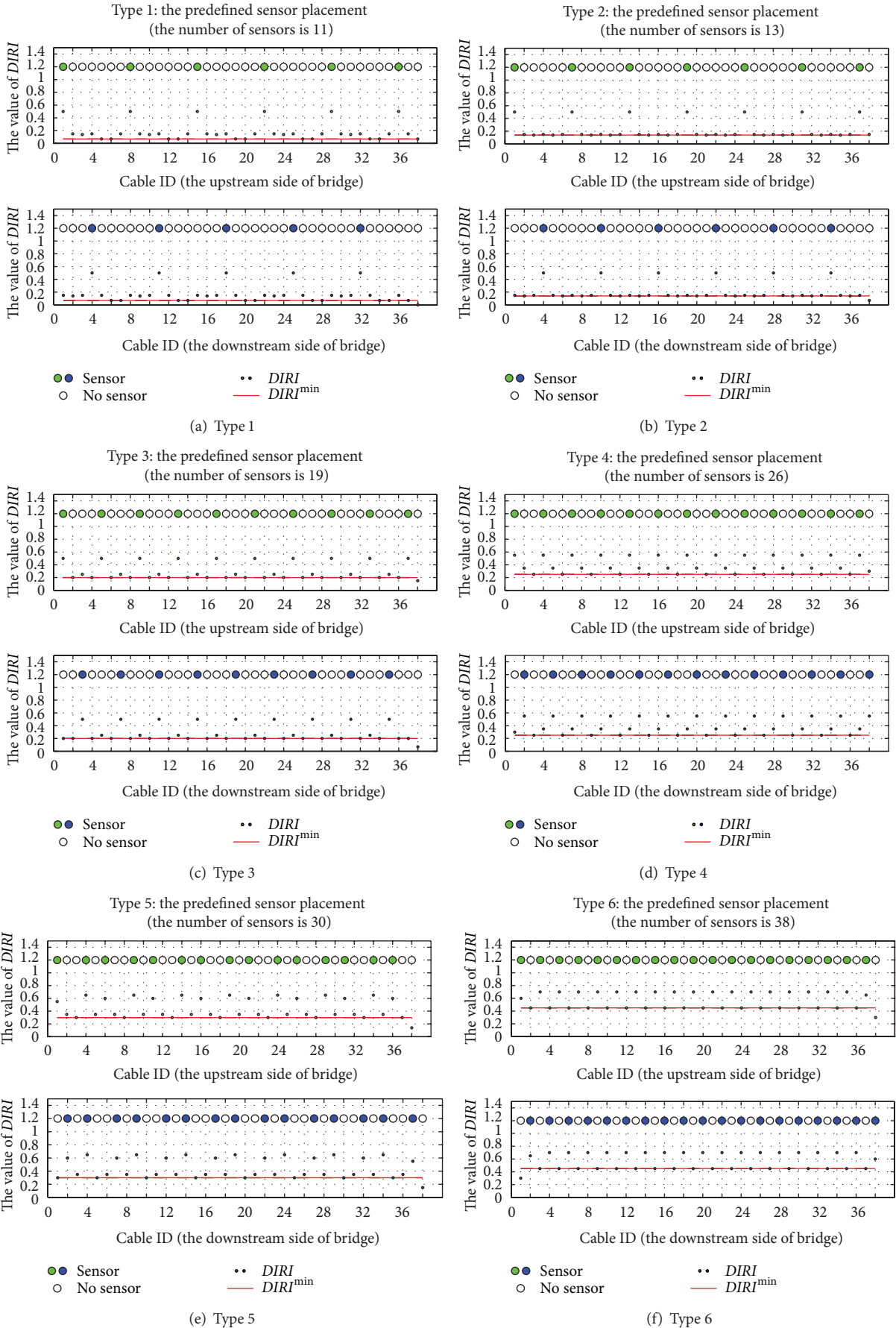


FIGURE 19: Continued.

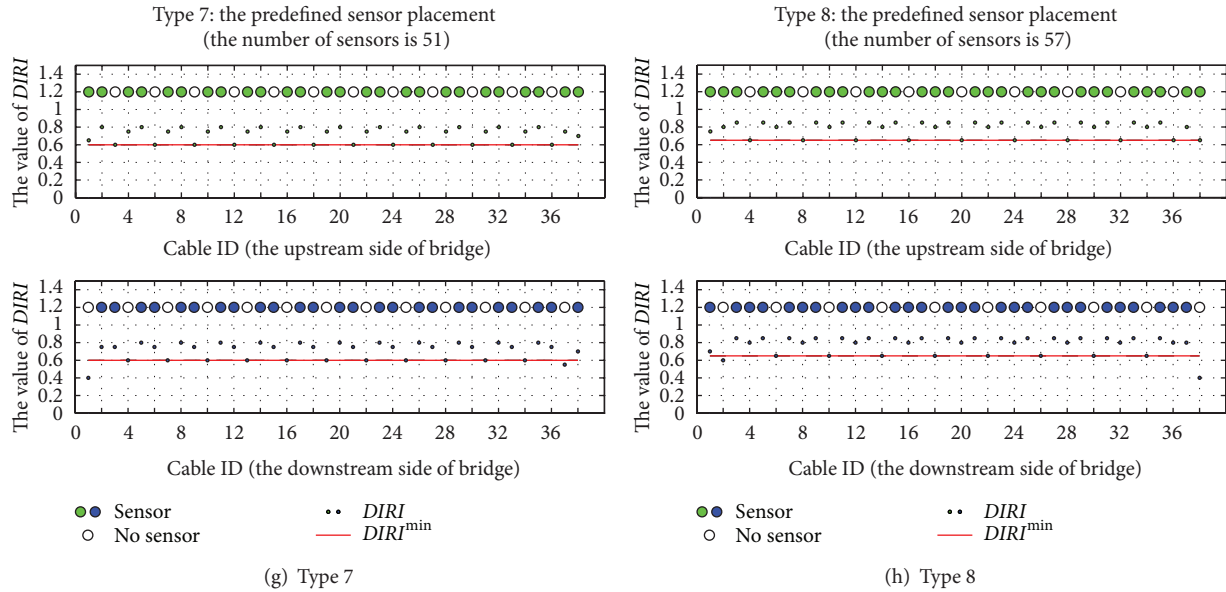


FIGURE 19: Eight types of predefined typical optimal placements for the setting of the same $DIRI$.

- (1) The calculation method of $DIRI$ is based on the finite element analysis about dCT and expert experience in SCDI. A method of calculating $DIRI$ more theoretically needs to be studied in the future.
- (2) The RE, HRE, and MGO algorithms presented in this paper can give satisfying optimized solutions. Although these solutions have already been accepted and are sometimes enough in practical engineering, the more effective and efficient algorithms for sensor quantity and location optimization for SCDI require further research.

Appendix

Eight types of predefined typical optimal placements for the setting of the same $DIRI$ (see Figure 19).

Acknowledgments

This research work was jointly supported by National Natural Science Foundation of China (51308094), Key Projects in the National Science & Technology Pillar Program during the Twelfth Five-Year Plan Period (2011BAK02B02), National Natural Science Foundation of China (51278085), and Doctoral Scientific Research Startup Foundation of Northeast Dianli University (BSJXM-201222). The authors would also like to thank the anonymous reviewers for their valuable suggestions.

References

- [1] J.-H. Park, J.-T. Kim, D.-S. Hong, D. Mascarenas, and J. Peter Lynch, "Autonomous smart sensor nodes for global and local damage detection of prestressed concrete bridges based on accelerations and impedance measurements," *Smart Structures and Systems*, vol. 6, no. 5-6, pp. 711-730, 2010.
- [2] J.-T. Kim, J.-H. Park, D.-S. Hong, H.-M. Cho, W.-B. Na, and J.-H. Yi, "Vibration and impedance monitoring for prestress-loss prediction in PSC girder bridges," *Smart Structures and Systems*, vol. 5, no. 1, pp. 81-94, 2009.
- [3] J.-T. Kim, J.-H. Park, D.-S. Hong, and D.-D. Ho, "Hybrid acceleration-impedance sensor nodes on Imote2-platform for damage monitoring in steel girderconnections," *Smart Structures and Systems*, vol. 7, no. 5, pp. 393-416, 2011.
- [4] D. D. Ho, P. Y. Lee, K. D. Nguyen et al., "Solar-powered multi-scale sensor node on Imote2 platform for hybrid SHM in cable-stayed bridge," *Smart Structures and Systems*, vol. 9, no. 2, pp. 145-164, 2012.
- [5] X. S. Yi, J. Liu, X. Y. Ye et al., "An optimal placement of FBG sensor network based on probability model," *Optik*, vol. 124, pp. 1045-1048, 2013.
- [6] C. T. Rafael, M. Senthil, G. Rafael et al., "Robustness of optimal sensor placement under parametric uncertainty," *Mechanical Systems and Signal Processing*, vol. 41, pp. 268-287, 2013.
- [7] P. Costas and L. Geert, "The effect of prediction error correlation on optimal sensor placement in structural dynamics," *Mechanical Systems and Signal Processing*, vol. 28, pp. 105-127, 2012.
- [8] T. H. Yi and H. N. Li, "Methodology developments in sensor placement for health monitoring of civil infrastructures," *International Journal of Distributed Sensor Networks*, vol. 2012, Article ID 612726, 11 pages, 2012.
- [9] H. F. Lam, J. H. Yang, and Q. Hu, "How to install sensors for structural model updating," *Procedia Engineering*, vol. 14, pp. 450-459, 2011.
- [10] J. Teng and Y.-H. Zhu, "Optimal sensor placement for modal parameters test of large span spatial steel structural," *Engineering Mechanics*, vol. 28, no. 3, pp. 150-156, 2011.
- [11] X.-M. Sun, X. Feng, and J. Zhou, "A method for optimum sensor placement based on damage identifiability," *Journal of Dalian University of Technology*, vol. 50, no. 2, pp. 264-270, 2010.

- [12] X.-M. Sun, X. Feng, and J. Zhou, "Optimum sensor placement for health monitoring of latticed shell structure," *Chinese Journal of Computational Mechanics*, vol. 27, no. 3, pp. 482–488, 2010.
- [13] N. Debnath, A. Dutta, and S. K. Deb, "Placement of sensors in operational modal analysis for truss bridges," *Mechanical Systems and Signal Processing*, 2012.
- [14] E. B. Flynn and M. D. Todd, "A bayesian approach to optimal sensor placement for structural health monitoring with application to active sensing," *Mechanical Systems and Signal Processing*, vol. 24, no. 4, pp. 891–903, 2010.
- [15] D. C. Kammer and M. L. Tinker, "Optimal placement of triaxial accelerometers for modal vibration tests," *Mechanical Systems and Signal Processing*, vol. 18, no. 1, pp. 29–41, 2004.
- [16] D.-S. Li, H.-N. Li, and C.-P. Fritzen, "Load dependent sensor placement method: theory and experimental validation," *Mechanical Systems and Signal Processing*, 2012.
- [17] J. Q. Cheng, W. M. Yan, and Y. J. Chen, "Optimal sensor placement for bridge structure based on improved effective independence," *Journal of Vibration, Measurement & Diagnosis*, vol. 32, no. 5, pp. 812–816, 2012.
- [18] M. Meo and G. Zumpano, "On the optimal sensor placement techniques for a bridge structure," *Engineering Structures*, vol. 27, no. 10, pp. 1488–1497, 2005.
- [19] H. F. Yang, Z. Y. Wu, S. K. Liu, and H. -B. Sun, "Research on optimal sensor placement based on reverberation matrix for structural health monitoring," *International Journal of Distributed Sensor Networks*, vol. 2012, Article ID 454530, 7 pages, 2012.
- [20] Y.-X. Yang, X.-W. Hao, and L. Sun, "Optimal placement of sensors for a bridge structure based on energy coefficient-effective independence method," *Journal of Vibration and Shock*, vol. 29, no. 11, pp. 119–134, 2010.
- [21] S. Carsten and L. Michael, "An approach to optimal pick-up and exciter placement," in *Proceedings of the 14th International Modal Analysis Conference*, pp. 376–382, 1996.
- [22] T.-H. Yi, H.-N. Li, and M. Gu, "Optimal sensor placement for health monitoring of high-rise structure based on genetic algorithm," *Mathematical Problems in Engineering*, vol. 2011, Article ID 395101, 12 pages, 2011.
- [23] T.-H. Yi, H.-N. Li, and M. Gu, "Optimal sensor placement for structural health monitoring based on multiple optimization strategies," *Structural Design of Tall and Special Buildings*, vol. 20, no. 7, pp. 881–900, 2011.
- [24] A. M. Raich and T. R. Liskai, "Multi-objective optimization of sensor and excitation layouts for frequency response function-based structural damage identification," *Computer-Aided Civil and Infrastructure Engineering*, vol. 27, no. 2, pp. 95–117, 2012.
- [25] X.-K. Lin, L.-M. Zhang, Q.-T. Guo, and X.-P. Zhao, "Application of coevolutionary genetic algorithm in optimal sensor placement," *Journal of Vibration and Shock*, vol. 28, no. 3, pp. 190–194, 2009.
- [26] X.-D. Sun and J.-P. Ou, "Optimal sensor placement based on sensitivity of damage parameters," *Journal of Harbin Institute of Technology*, vol. 42, no. 10, pp. 1530–1535, 2010.
- [27] T. Yi, H. Li, and M. Gu, "Multiple optimization strategies based sensor placement method for structural health monitoring," *Journal of Building Structures*, vol. 32, no. 12, pp. 217–223, 2011.
- [28] K. Nikitha, R. T. Babu, and L. D. Rajya, "Sensor deployment using particle swarm optimization," *International Journal of Engineering Science and Technology*, vol. 2, no. 10, pp. 5395–5401, 2010.
- [29] X. K. Gou and M. Y. Cui, "Application of genetic and simulated annealing algorithms in placement optimization of sensor/actuator," *Machinery & Electronics*, vol. 11, pp. 39–41, 2008.
- [30] S. Fidanova, P. Marinov, and E. Alba, "Ant algorithm for optimal sensor deployment," *Studies in Computational Intelligence*, vol. 399, pp. 21–29, 2012.
- [31] L. Q. Hou, *Model Updating, Damage Diagnosis and Prewarning Methods Based on Health Monitoring of Large Cable Stayed Bridges*, Harbin Institute of Technology, Harbin, China, 2009.

Research Article

Design of System for Monitoring Seepage of Levee Engineering Based on Distributed Optical Fiber Sensing Technology

Huaizhi Su^{1,2} and Yeyuan Kang^{2,3}

¹ State Key Laboratory of Hydrology-Water Resources and Hydraulic Engineering, Hohai University, No. 1 Xikang Road, Nanjing 210098, China

² College of Water Conservancy and Hydropower Engineering, Hohai University, No. 1 Xikang Road, Nanjing 210098, China

³ National Engineering Research Center of Water Resources Efficient Utilization and Engineering Safety, Nanjing 210098, China

Correspondence should be addressed to Huaizhi Su; su_huaizhi@hhu.edu.cn

Received 5 June 2013; Revised 28 July 2013; Accepted 3 November 2013

Academic Editor: Gangbing Song

Copyright © 2013 H. Su and Y. Kang. This is an open access article distributed under the Creative Commons Attribution License, which permits unrestricted use, distribution, and reproduction in any medium, provided the original work is properly cited.

Seepage is the major factor and monitoring index of levee safety. Leakage may be undetected by conventional monitoring methods and techniques, but optical fiber distributed temperature sensor (DTS) temperature measuring system can achieve real-time temperature monitoring in internal soil of levees. According to the temperature field obtained by DTS system, monitoring and inversion methods of seepage velocity based on double-line heat source and single-line heat source are introduced, respectively. An experiment is designed and composed of DTS temperature measuring system, the heating system, the water supply system, and the computer-aided analysis system to test and verify the effectiveness and feasibility of the monitoring method. On this basis, the system of monitoring seepage based on distributed optical fibers is put forward and designed. Optical fiber intelligent monitoring system will improve the current situation of safety monitoring of levee engineering on the basis of its unique superiority.

1. Introduction

To protect cities, villages, mines, and factories on both sides of the river from devastating floods, levee engineering is constructed. Although levee construction technology for flood control has a history of several thousand years, levee engineering is not an exact science at present, because there are lots of random or uncertain factors during the project operation. Therefore, strengthening safety monitoring of levees is very important. The characteristics of levee engineering in China can be summarized as long distance; poor conditions in the levee foundation; poor quality of levee body filling; numerous ponds and lowland in the downstream areas; too many hidden dangers left by history; and lots of seepage disasters in flood season [1]. In view of the complex characteristics of levee engineering above, levee safety monitoring develops slowly and is not perfect compared with the dam safety monitoring, which needs further research and improvement [2]. With the social and economic development, the demand for flood control becomes higher

and higher, and new thoughts of flood control and modernization of water conservancy give more arduous missions for management [3]. The digitization and information of engineering will greatly enhance the efficiency of project management, which will make a revolutionary change in management and method of levees. Safety monitoring of levees is not only beneficial to avoid dangers and disasters but also the precondition for prevention and forecast of levee disasters [4]. Seepage has always been an important factor influencing levee stability. In the flood season, there have been frequent seepage disasters of levee. The complexity of the levee seepage mainly reflects on two aspects: firstly, the complexity of levee foundation and body formation; secondly, the limitation of detecting seepages.

The mission of safety monitoring is to know the “health state” of levee projects at all time, whose core is to discover and forecast abnormal state timely, particularly, dangerous situations for the safety of levees. Therefore, safety monitoring system shall have the ability to capture all the project risk information timely and without omission. Distributed optical

fiber sensing technology has the following advantages [5]: (1) easy to form automatic telemetry system with sensing and transmitting information by a single fiber; (2) high sensitivity, antilighting strike, antielectromagnetic interference; (3) low price, delicate, soft, and small influence on mechanical parameters and property of the material; (4) be able to realize distributed and real-time monitoring, reducing the missing rate of traditional detection greatly, and so forth. Distributed optical fiber temperature sensing technology has been successfully applied to oil and gas wells, pipeline leakage detection, dam monitoring, process monitoring, fire detection, power cable monitoring, and so on. Levee engineering seepage and deformation are the main monitoring items. Kappelmeyer [6] started to study the seepage field of dam through the internal temperature field as early as in 1957, which has been considered to be an effective method and has great application foreground to detect seepages, with the further research and perfection. The development of seepage is a slow process, and to have a correct evaluation needs long-term, real-time online monitoring. The temperature field change caused by seepage in levees is a random event in a large range; thus, traditional detection is easy to miss and difficult to locate seepage [7]. Distributed optical fiber sensing technology can meet the characteristics of levee long-distance monitoring and is suitable for the special requirements of seepage detection, which can realize long-term, real-time, online, and whole section monitoring of levee temperature field and strain field.

2. The Method of Seepage Velocity Inversion Based on DTS System

The heated armored fibers can be considered as a line heat source in the infinite medium. By this assumption, boundary conditions of governing equations can be established, and the temperature field influenced by seepage can be solved. On the other hand, the temperature field can be obtained by DTS system. According to actual measured temperature and model calculation, constantly changing the seepage velocity in the numerical model until the theoretical calculating temperature matches the monitoring temperature, the seepage velocity at this time is the actual one.

2.1. Two-Dimensional Coupling Model of Seepage Field and Temperature Field. Under the case of two-dimensional heat conductivity and seepage within porous media, the heat flux includes two parts [8–10]: the result of heat conduction in porous media, $-\lambda(\partial T/\partial x)dy$; the heat carried by seepage, $c_w\gamma_w vTdy$. As shown in Figure 1, the sketch map of microunit heat flux influenced by seepage, the heat flux imported from the left side and underside of the microunit can be written, respectively as

$$\begin{aligned} Q_x &= -\lambda \frac{\partial T}{\partial x} dy + c_w \gamma_w v T dy, \\ Q_y &= -\lambda \frac{\partial T}{\partial y} dx, \end{aligned} \quad (1)$$

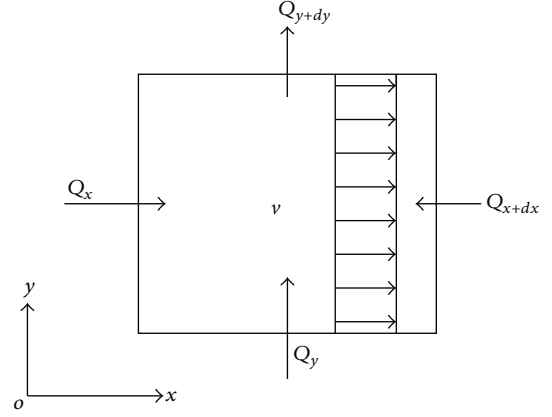


FIGURE 1: The sketch map of microunit heat flux influenced by seepage.

where Q is the heat flux; λ is the heat conductivity coefficient of the porous medium; c_w is the specific heat of seepage water; γ_w is the volume-weight of seepage water; v is the seepage velocity; T is temperature.

Similarly, the heat flux exported from the right side and upside of the microunit can be expressed, respectively as

$$\begin{aligned} Q_{x+dx} &= Q_x + \frac{\partial Q_x}{\partial x} dx \\ &= Q_x + \frac{\partial}{\partial x} \left(-\lambda \frac{\partial T}{\partial x} dy + c_w \gamma_w v T dy \right) dx, \end{aligned} \quad (2)$$

$$Q_{y+dy} = Q_y + \frac{\partial Q_y}{\partial y} dy = Q_y + \frac{\partial}{\partial y} \left(-\lambda \frac{\partial T}{\partial y} dx \right) dy.$$

Therefore, the net heat flowing into the microunit within unit time can be got as

$$\begin{aligned} Q &= Q_{x+dx} + Q_{y+dy} - Q_x - Q_y \\ &= \frac{\partial Q_x}{\partial x} dx + \frac{\partial Q_y}{\partial y} dy \\ &= \frac{\partial}{\partial x} \left(-\lambda \frac{\partial T}{\partial x} dy \right) dx + \frac{\partial}{\partial y} \left(-\lambda \frac{\partial T}{\partial y} dx \right) dy \\ &\quad + c_w \gamma_w \frac{\partial}{\partial x} (v T dy) dx. \end{aligned} \quad (3)$$

The net heat flowing into the microunit should be equal to the increase of thermodynamic energy, namely, the quantity of heat absorbed by porous medium within unit time, $c\gamma(\partial T/\partial t)dx dy$. So the following equation can be obtained as [11, 12]

$$\begin{aligned} c\gamma \frac{\partial T}{\partial t} dx dy &= \frac{\partial}{\partial x} \left(-\lambda \frac{\partial T}{\partial x} dy \right) dx \\ &\quad + \frac{\partial}{\partial y} \left(-\lambda \frac{\partial T}{\partial y} dx \right) dy + c_w \gamma_w \frac{\partial}{\partial x} (v T dy) dx, \end{aligned} \quad (4)$$

where c is the specific heat of porous medium; γ is the volume-weight of porous medium; the other parameters are same as above equations.

Suppose that seepage velocity v is a constant, the above equation can be simplified as

$$\frac{\partial T}{\partial t} = -\frac{\lambda}{c\gamma} \frac{\partial^2 T}{\partial x^2} - \frac{\lambda}{c\gamma} \frac{\partial^2 T}{\partial y^2} + \frac{c_\omega \gamma_\omega v}{c\gamma} \frac{\partial T}{\partial x}. \quad (5)$$

For steady-state heat conduction in plane state, the corresponding differential equation can be given by [10]

$$-\frac{\lambda}{c\gamma} \frac{\partial^2 T}{\partial x^2} - \frac{\lambda}{c\gamma} \frac{\partial^2 T}{\partial y^2} + \frac{c_\omega \gamma_\omega v}{c\gamma} \frac{\partial T}{\partial x} = 0. \quad (6)$$

Let $c_\omega \gamma_\omega v / \lambda = d$, the partial differential equation of steady-state heat conduction affected by steady seepage in plane state can be expressed as

$$\frac{\partial^2 T}{\partial x^2} + \frac{\partial^2 T}{\partial y^2} - d \frac{\partial T}{\partial x} = 0. \quad (7)$$

It can be observed from (7) that the seepage velocity v is the only influencing factor of the temperature field distribution, because c_ω , γ_ω , and λ are constants for the same boundary condition. So the temperature field can be solved by (7).

2.2. The Method of Double-Line Heat Source. By a couple of temperature measurement fibers installed in levees, combining temperature measured by distributed fibers and (7), seepage velocity v can be obtained by inversion. The principle diagram of seepage velocity inversion based on the method of double-line heat source is shown in Figure 2.

2.2.1. Embedded Method of Optical Fibers. Two parallel temperature measurement optical fibers are embedded in the medium, as shown in Figure 2. Number 1 optical fiber is heated, and number 2 optical fiber is not heated, which is used to sense the temperature rise due to heated number 1 optical fiber. Using DTS to record temperatures changes of number 1 optical fiber and number 2 optical fiber, T_1 is the equilibrium temperature of number 1 optical fiber after being heated, and T_2 is the equilibrium temperature of number 2 optical fiber, namely, the temperature of a certain point in the temperature field generating by number 1 optical fiber.

2.2.2. The Model to Solve Temperature Field under the Influence of Seepage Field. Above mentioned T_1 and T_2 are the actual monitoring temperature values by DTS system. If the distribution of theoretic temperature field can be got by (7), seepage velocity v can be achieved with the retrieval method.

In order to solve expediently, the problem can be simplified as the two-dimensional plane model that sets number 1 optical fiber axis side. As shown in Figure 3, OABC is the outer boundary, and its temperature is ambient temperature T_0 ; number 1 optical cable can be simplified as OABC, the internal boundary of model, and its temperature is T_1 .

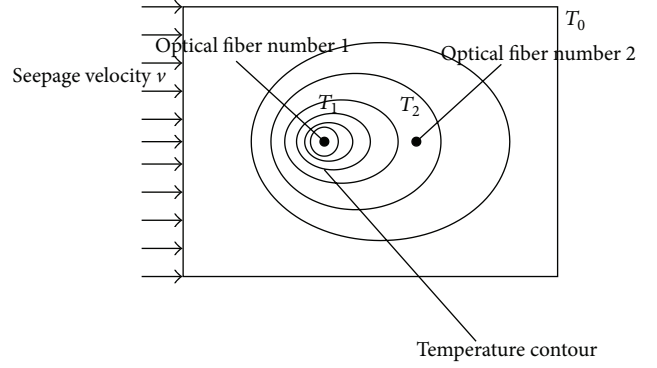


FIGURE 2: The principle diagram of seepage velocity inversion based on the method of double-line heat source.

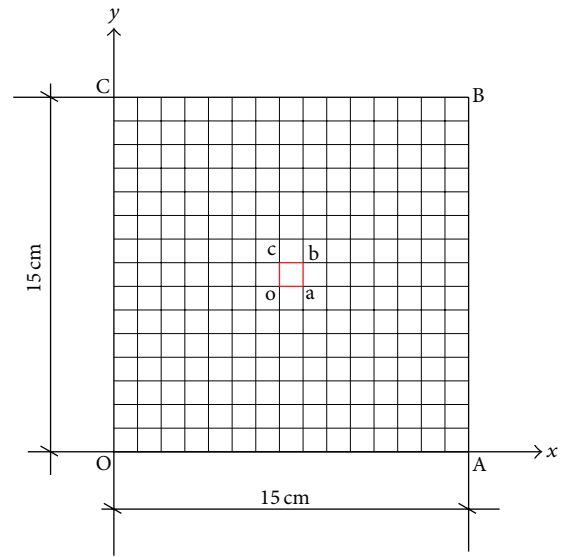


FIGURE 3: The sketch map of seepage velocity inversion model by optical fibers.

To sum up, the model to solve temperature field under the influence of seepage field can be summarized as

$$\begin{aligned} \frac{\partial^2 T}{\partial x^2} + \frac{\partial^2 T}{\partial y^2} - d \frac{\partial T}{\partial x} &= 0, \quad (x, y) \in \Omega \\ T(x, y) &= T_1, \quad (x, y) \in \Gamma_1 \\ T(x, y) &= T_0, \quad (x, y) \in \Gamma_0, \end{aligned} \quad (8)$$

where Ω is the region of the model; Γ_1 is the internal boundary of model, OABC; Γ_0 is the outer boundary of model, OABC.

2.2.3. The Steps of Seepage Velocity Inversion. The flow chart of seepage velocity inversion based on the method of double-line heat source is shown in Figure 4. The specific steps are as follows.

- (1) Ascertain the temperature T_1 of internal boundary Γ_1 (the equilibrium temperature of number 1 optical

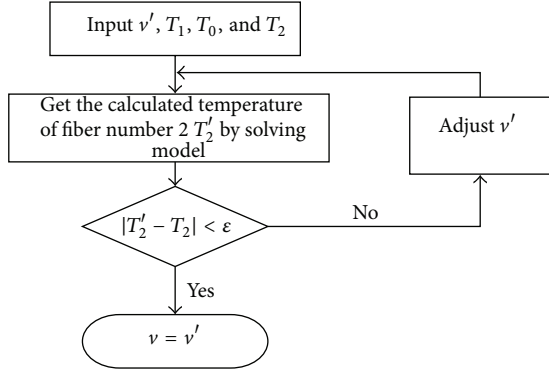


FIGURE 4: The flow chart of seepage velocity inversion based on method of double-line heat source.

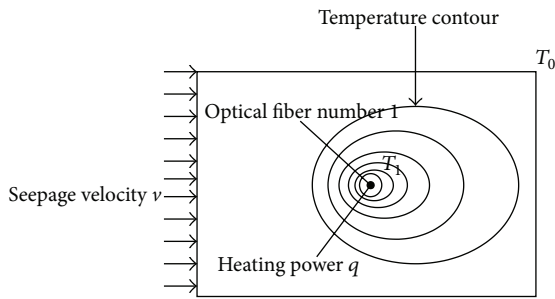


FIGURE 5: The principle diagram of seepage velocity inversion based on single-line heat source method.

fiber after being heated), T_0 of outer boundary Γ_0 (the ambient temperature), and the actual monitoring temperature of number 2 optical fiber T_2 by DTS system.

- (2) Assuming seepage velocity v' , solve the model of (8) so that the temperature field and the calculated temperature T_2' of number 2 optical fiber can be got.
- (3) Compare T_2' and T_2 . If they are equal or differ within a certain range ε (such as $\varepsilon = 0.1$), the inversion ends; namely, the actual seepage velocity v equals to the assumed seepage velocity v' . If the difference between T_2' and T_2 is outside the range, go back to Step 2, assume seepage velocity v' again and continuously cycle until the inversion ends. In the process, the assumption and adjustment of seepage velocity v' should be made according to the difference between T_2' and T_2 .

2.3. The Method of Single-Line Heat Source. The biggest difference between single-line heat source method and double-line heat source method is that the former only requires a heated fiber to make seepage velocity inversion. The steady temperature T_1 , initial temperature T_0 (the ambient temperature), and heating power q of number 1 optical fiber can be measured by DTS system. Making use of these measured data the inversion of seepage velocity v can be made by single-line heat source

method. The principle diagram of seepage velocity inversion is shown by Figure 5 based on single-line heat source method.

2.3.1. The Model to Solve Temperature Field under the Influence of Seepage Field. Taking advantage of above measured T_0 , T_1 , and q , the distribution of temperature field and the calculated temperature T_1' of number 1 optical fiber can be obtained by solving (7) with corresponding boundary conditions. According to measured temperature T_1 and calculated temperature T_1' of number 1 optical fiber, the inversion of seepage velocity v can be made.

The models to solve temperature field of single-line method and double-line method are similar, as shown in Figure 3. The only difference is that the boundary conditions are different, that is to say, the internal boundary of double-line method is the first boundary condition, while the internal boundary of single-line method is the second boundary condition.

The model of single-line method to solve temperature field under the influence of seepage field can be summarized as

$$\begin{aligned} \frac{\partial^2 T}{\partial x^2} + \frac{\partial^2 T}{\partial y^2} - d \frac{\partial T}{\partial x} &= 0, \quad (x, y) \in \Omega \\ -\lambda \frac{\partial T(x, y)}{\partial n} &= q, \quad (x, y) \in \Gamma_1 \\ T(x, y) &= T_0, \quad (x, y) \in \Gamma_0, \end{aligned} \quad (9)$$

where n is the outer normal direction of outer boundary surface.

2.3.2. The Steps of Seepage Velocity Inversion. The flow chart of seepage velocity inversion based on the method of double-line heat source is shown by Figure 6. The specific steps are as follows.

- (1) Obtain the temperature T_1 of internal boundary Γ_1 (the equilibrium temperature of number 1 optical fiber after being heated), temperature T_0 of outer boundary Γ_0 (the ambient temperature) by DTS system, and the heat flux of internal boundary q (heating power).
- (2) Assuming seepage velocity v' , solve the model of (9) so that the temperature field and the calculated temperature T_1' of number 1 optical fiber can be got.
- (3) Compare T_1' and T_1 . If they are equal or differ within a certain range ε (such as $\varepsilon = 0.1$), the inversion ends; namely, the actual seepage velocity v equals to the assumed seepage velocity v' . If the difference between T_1' and T_1 is outside the range, go back to Step 2, assume seepage velocity v' again and continuously cycle until the inversion ends. In the process, the assumption and adjustment of seepage velocity v' should be made according to the difference between T_1' and T_1 .

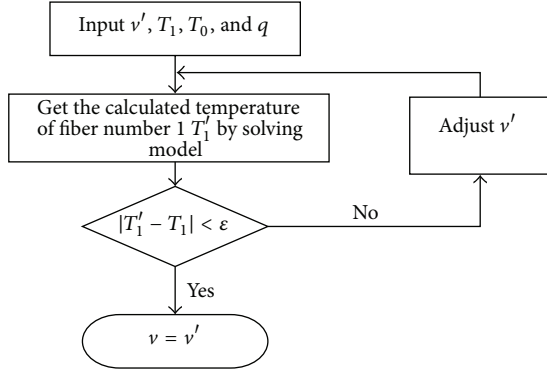


FIGURE 6: The flow chart of seepage velocity inversion based on method of single-line heat source.

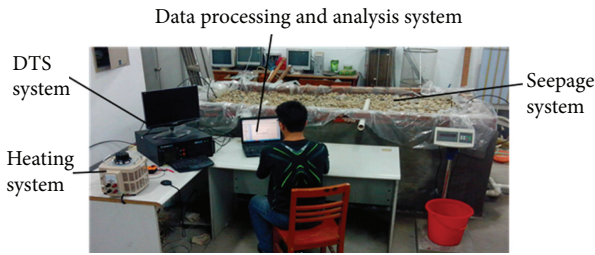


FIGURE 7: The model of seepage monitoring system based on DTS.

3. Model Experiment

3.1. Seepage Monitoring System with Optical Fibers. In order to model seepage by DTS technology, the experiment system is designed, which consists of heating system, seepage system, DTS system, data processing, and analysis system. As shown in Figure 7, the size of model is $2.6 \text{ m} \times 1 \text{ m} \times 1.15 \text{ m}$.

DTS system is the Sentinel DTS-LR with distributed optical fiber temperature measurement hosts produced by United Kingdom Sensornet, which is one of the most advanced distributed optical fiber temperature measurement system on the market. DTS system can get the temperature curves in different places along the whole length of optical fibers, measuring range up to 10 km, spatial resolution 1 m, and temperature resolution up to 0.01°C . When seepage occurs, the temperature curve varies at where seepage occurs, which will be reflected on the software interface.

The ZTT optical cables are used in the experiment. There are two fixed metal wires between restrictive coating and armor layer in the optical cables. The resistance of metal wires is approximately $0.175 \Omega/\text{m}$, and optical cables in the experiment are heated by series heating the two metal wires. There are two optical fibers embedded in the experiment, respectively, recorded as number 1 optical fiber and number 2 optical fiber, and the layout of the two optical fibers is shown in Figure 8 and Figure 9.

3.2. Determination of Modeling Region r . The influence region of heated number 1 optical fiber should be specially considered when modeling region is selected. In order to

TABLE 1: Calculated equilibrium temperature of optical fiber number 1 under three different modeling region r .

λ (W/(m·k))	q (W/m)	T_0 ($^\circ\text{C}$)	T_1 ($^\circ\text{C}$)	Model I T_1' ($^\circ\text{C}$)	Model II T_1' ($^\circ\text{C}$)	Model III T_1' ($^\circ\text{C}$)
0.497	1.933	14.77	16.27	17.50	16.93	16.32
	2.781	14.60	16.94	18.53	17.71	16.84
	3.745	14.60	17.51	19.90	18.79	17.61
	4.651	14.60	18.25	21.18	19.80	18.34
	6.037	14.55	19.29	23.09	21.30	19.40
	7.284	14.30	19.86	24.60	22.44	20.16
	8.769	14.69	21.40	27.09	24.49	21.73

determine the region of influence, the test under saturated without seepage condition is designed, getting the initial temperature and equilibrium temperature of number 1 optical fiber under different heating powers, as shown in Table 1. The inversion of radius r is made by the software module of steady temperature field in the software MARC. Specific methods are as follows.

Models of side length 1 m, 0.4 m, and 0.15 m are established, respectively, named model I, model II, and model III. Each cell is $1 \text{ cm} \times 1 \text{ cm}$ square in the models by automatic mesh generation. Every model has 7 different kinds of working conditions with 7 different kinds of boundary conditions, as shown in Table 1. Figures 10, 11, and 12 are selected from the inversion results of three models under heating power 6.037 W/m condition.

As can be seen from Table 1, Figures 10, 11, and 12, calculated equilibrium temperature of number 1 optical fiber gradually decreases with the diminution of modeling region r . When $2r = 0.15 \text{ m}$, the calculated equilibrium temperature is the nearest to the actual monitoring temperature under different heating powers, so that model III is selected as the modeling region ($2r = 0.15 \text{ m}$).

In order to verify the correctness of modeling region, a test is designed. In the test, heating power $q = 22.9 \text{ w/m}$, seepage velocity $v = 3.34 \times 10^{-3} \text{ m/s}$, number 1 optical fiber, and number 2 optical fiber are installed as Figures 8 and 9. DTS system records the temperature rise of number 2 optical fiber when heating number 1 optical fiber, as shown in Figure 13. As can be seen from Figure 13, the maximum temperature rise of number 2 optical fiber is 0.8°C when $r = 5 \text{ cm}$; that is to say, the range of influence of number 1 optical fiber after being heated is tiny. So modeling region $2r = 15 \text{ cm}$ is not only consistent with numerical inversion results but also with the actual test results.

3.3. The Results of Seepage Velocity Inversion. By experimental validation with different seepage velocity and different heating powers, the results of seepage velocity inversion based on double-line heat source method and single-line heat source method are shown in Table 2. As can be seen from Table 2, the results of two kinds of inversion method basically tally with experimental seepage velocity, and the inversion precision of two kinds of inversion method gets

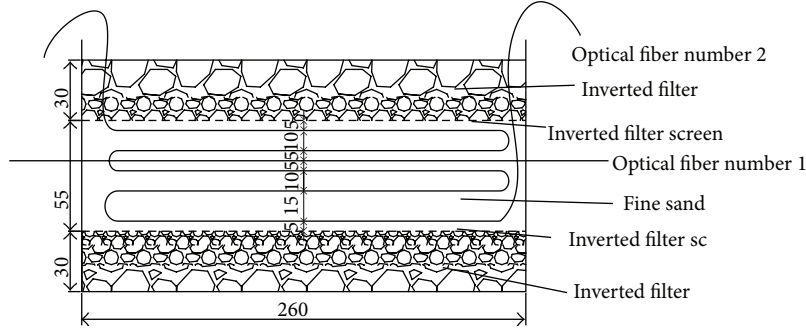


FIGURE 8: The front view of optical fibers layout (cm).

TABLE 2: The results of two inversion methods.

ν (10^{-3} m/s)	q (W/m)	T_0 ($^{\circ}$ C)	T_1 ($^{\circ}$ C)	T_2 ($^{\circ}$ C)	Double-line ν' (10^{-3} m/s)	Single-line ν' (10^{-3} m/s)
0	1.93	14.77	16.27	14.86	0.004	0.012
	3.74	14.6	17.51	14.74	0.003	0.008
	4.65	14.6	18.25	14.78	0.004	0.006
	6.04	14.55	19.29	14.81	0.002	0.008
	7.28	14.3	19.86	14.61	0.003	0.004
	8.77	14.69	21.4	15.12	0.004	0.005
0.057	15.36	17.55	25.56	17.93	0.055	0.054
	8.07	17.22	21.92	17.46	0.054	0.056
	5.36	17.24	20.47	17.37	0.058	0.053
	3.2	17.11	19.22	17.2	0.057	0.055
	11.34	17.02	23.4	17.31	0.057	0.057
	19.53	17.02	27.23	17.42	0.058	0.059
0.097	19.53	17.38	27.5	17.57	0.095	0.094
	8.22	17.66	22.36	17.89	0.096	0.093
	3.2	17.48	19.74	17.57	0.096	0.096
	5.48	17.34	20.94	17.48	0.097	0.099
	11.69	17.49	24.01	17.88	0.097	0.095
	15.57	17.5	25.36	18.02	0.096	0.098
0.113	3.17	16.68	18.75	16.77	0.112	0.111
	5.36	16.79	20.05	16.92	0.112	0.109
	7.98	16.78	21.53	16.97	0.111	0.107
	11.11	16.64	23.27	16.93	0.113	0.112
	15.16	16.28	25.09	16.67	0.113	0.114
	17.63	16	26.4	16.51	0.114	0.116
0.158	3.29	16.87	18.35	16.96	0.152	0.154
	5.48	16.13	19.89	16.25	0.155	0.156
	8.37	16.86	21.26	17.02	0.156	0.155
	11.69	16.53	23.25	16.94	0.158	0.156
	15.36	17.13	24.96	17.52	0.157	0.158
	19.53	17.3	26.92	17.84	0.158	0.157

higher with increasing heating power. The inversion precision of two kinds of inversion method can meet the need of actual engineering, and the inversion precision of double-line heat source method is higher than the one of single-line heat source method, but it needs to embed more optical fibers based on double-line heat source method in actual engineering.

4. Distributed Optical Fiber System for Monitoring Seepage

4.1. Basic Idea. Seepage is the important indicator of levee safety status. Levee seepage occurrence and development are correlated with soil property, soil gradation, flow condition, and the measures of antiseepage and draining. Seepage can

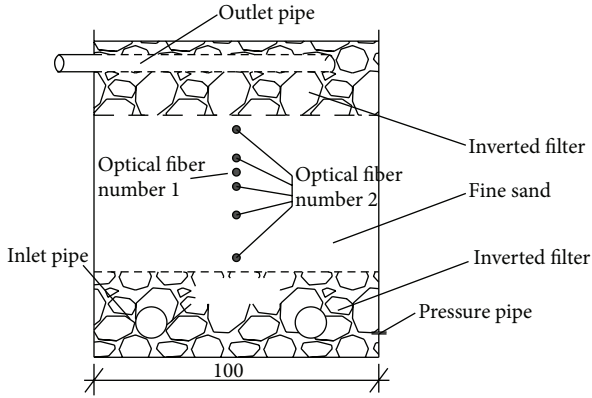


FIGURE 9: The left view of optical fibers layout (cm).

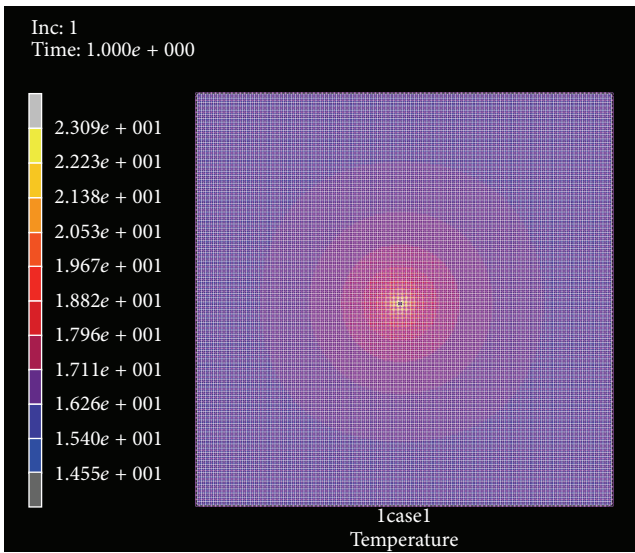


FIGURE 10: Calculated temperature field in the model I when the heating power q is 6.037 w/m (Unit: $^{\circ}\text{C}$).

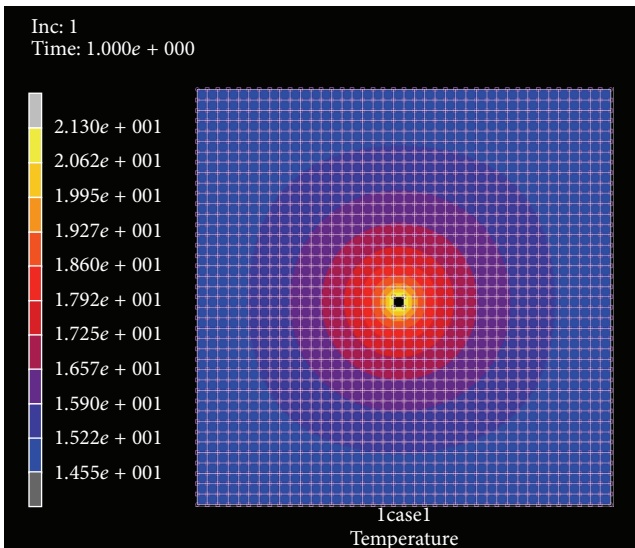


FIGURE 11: Calculated temperature field in the model II when the heating power q is 6.037 w/m (Unit: $^{\circ}\text{C}$).

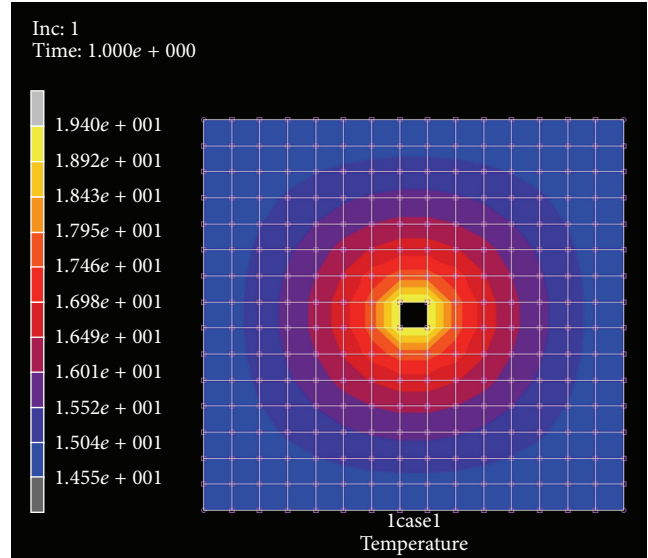


FIGURE 12: Calculated temperature field in the model III when the heating power q is 6.037 w/m (Unit: $^{\circ}\text{C}$).

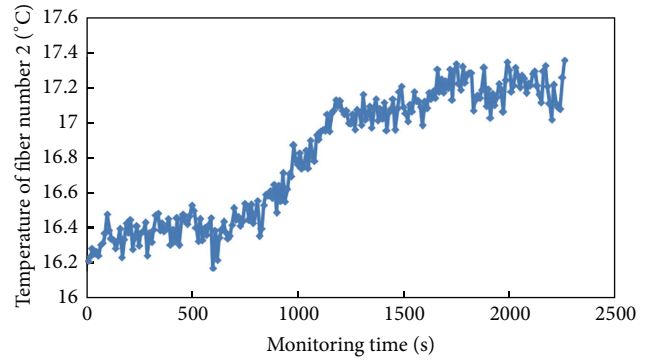


FIGURE 13: Temperature curve of optical fiber number 2 when heating optical fiber number 1 ($q = 22.9$ w/m).

cause dangerous situation, even burst if unable to discover and take the appropriate measures timely. Once seepage occurs, the temperature field in levee soil will redistribute; namely, temperature rise curves of optical fiber will change. According to the inversion methods above, monitoring seepage velocity indirectly can be realized. It needs to pay close attention to changes of temperature field under the influence of seepage velocity, and seepages should be processed to prevent further impact on levee safety. For this point, it is required to build a monitoring system that it can monitor the occurrence of seepage and the seepage state such as seepage flow velocity in real time; and capture position where seepage occurs. Therefore, distributed optical fiber temperature monitoring system can better meet these requirements. Similarly, the distributed optical fiber networks can also real-time monitor stress-strain, settlement, deformation, and crack of levees and buildings across dikes, so as to establish systematic levee intelligent systems for health monitoring, as shown in Figure 14.

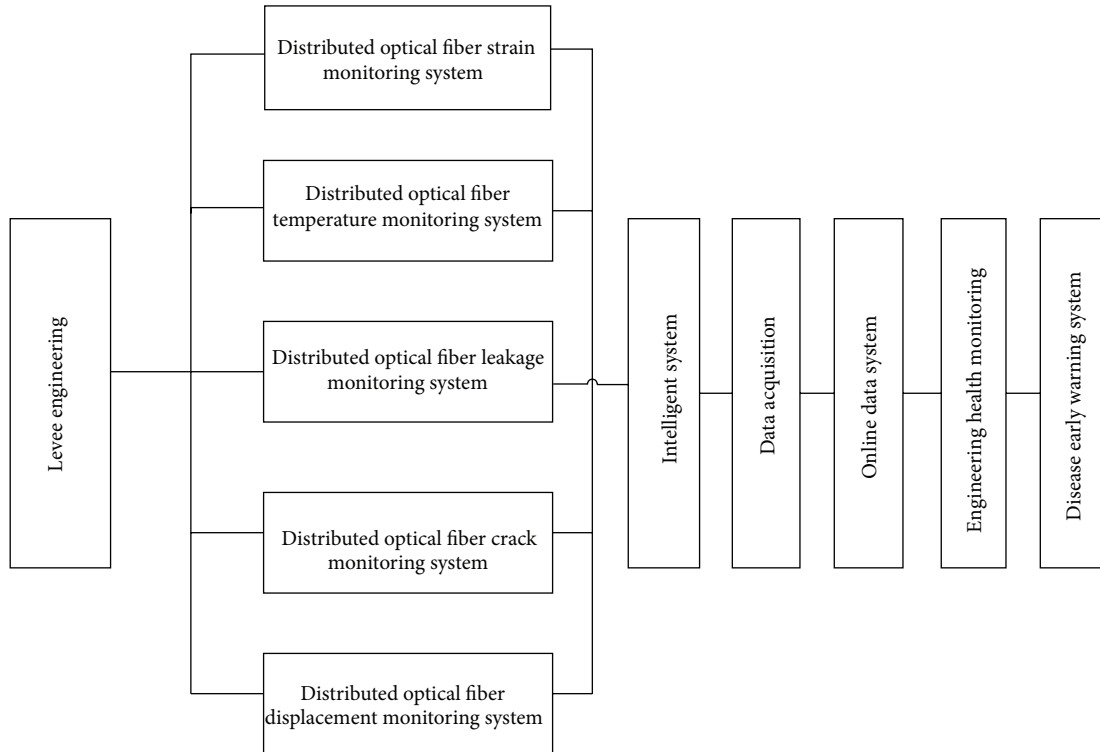


FIGURE 14: Intelligent system for health monitoring of levee engineering.

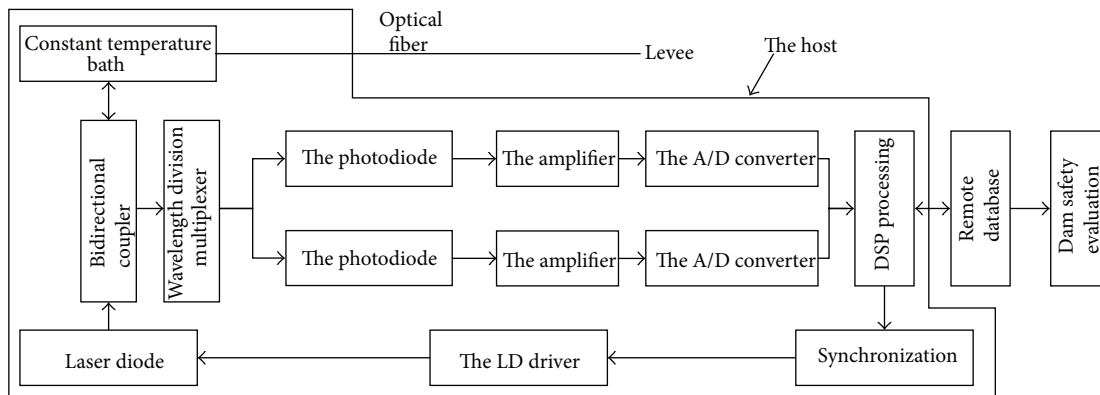


FIGURE 15: Light circuit structure plan for the DTS system.

4.2. *Design of the DTS System.* The DTS system is made up of the host and the DTS network. The light circuit structure plan of the system is shown in Figure 15. In the actual measurement, the two-channel lights intensity comparison method is used. Namely, demodulating Anti-Stokes scattering curves by the optical fiber Stokes scattering curves, Stokes light, and anti-Stokes light are collected, respectively, and then temperature data can be got by demodulating the ratio of two scattering lights intensity. The 3D temperature field distribution of levee can be got by optimal layout of optical fiber network. In the distributed temperature measurement system for levees, effects of optical fibers under loading and bending, drift of light source, splice loss, and environmental interference on temperature measurement precision can be

eliminated with the above methods, and then the levee temperature field can be obtained with higher precision.

4.3. *Establishment of the System.* With continuing advances in construction technology, levee seepage has been controlled to some extent. However, the water load and environmental factors during levee operation period are unforeseen to a great extent, likely to exceed the design standard. A part of levees are in area with frequent earthquakes, and the design standard of levees cannot take all factors into account. Therefore, under unfavorable load, seepages are prone to take place in some weak parts of levees (such as buildings across dykes and concrete antiseepage wall), eventually affecting levees safety when seepages increase.

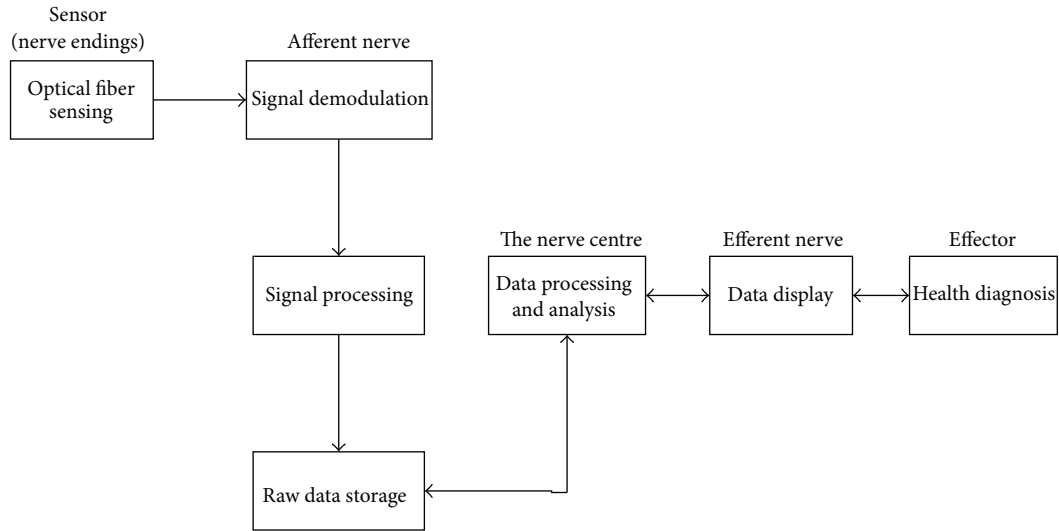


FIGURE 16: Safety monitoring system of levees based on distributed optical fibers.

Levee safety monitoring technology of distributed optical fiber network has the "potential" to acquire comprehensive and continuous levee safety-related information. But due to the economy, as well as distributed optical fiber monitoring mechanism and capabilities, it needs to distribute optical fiber sensor networks reasonably to achieve the optimized arrangement of distributed optical fiber temperature monitoring network. Combining the engineering geologic and hydrological conditions, the possible seepage position of levees can be analyzed under adverse conditions taking advantage of numerical simulation software. In addition, simulation model can also be established using same soil material of engineering in accordance with the principle of proportionality. By applying all possible loads to the model, analysis of levee seepage can be made during operation period. By Finite Element Method (FEM) computation and model experiment comparative analysis, where seepage occurs and seepage may occur can be obtained to optimize the design of sensing optical fiber network layout. In addition to this, it is feasible to increase density of optical fiber network arrangement in weak parts based on past experience for monitoring the joint part seepages. If it is possible to measure the likely seepage location under adverse conditions during operation in the future before construction, distributed optical fiber monitoring system can be arranged during the construction period to acquire the temperature and seepage conditions of internal soil body.

Before levee construction, the distributed optical fiber temperature monitoring system is designed, and the layout of optical fiber network is made in accordance with the design during the construction. Optical fiber temperature monitoring system can analyze the temperature rise of internal soil body for predicting seepage. Once there are temperature rise anomalies in some parts, it is able to analyze and locate the seepage timely. When seepage does not affect the overall performance and safe operation of levee, real-time monitoring and quantitative analysis for the levee seepage can be made based on nominal thermal conductivity method, and

if seepage increases, measures should be taken promptly to control it.

Optical fibers are embedded in some soil layers of levees, and all optical fibers are connected together, constituting a three-dimensional distributed optical fiber sensor networks. A host computer of optical fiber monitoring system can be arranged for each layer or adjacent layers, which is similar to the body's central nervous system. And information is transmitted through optical cables to a central control room, which is similar to the human brain, making analysis and response according to collected information. Due to the optical fiber sensor networks, installment will have an impact on construction progress to some extent, so it only needs to increase density of optical fiber network arrangement in some parts such as the soil under normal water level and high probability of seepage. If the distributed optical fiber sensor network is compared to the human nervous system, increasing density of optical fiber network arrangement where seepage may occur can be compared to human body parts with more nerve endings. Intelligent system of distributed optical fiber for levee seepage prediction and monitoring is built, and its data collection and analysis process are shown in Figure 16.

As can be seen from Section 3, the heating power is bigger, the temperature rise is larger, and the result of experiment is better. However, the practical operability for projects must be taken into account, such as the problem of the total heating power for entire optical cable. On the one hand, if heating power is too big, it will be dangerous and its cost will increase. On the other hand, if heating power is too small, temperature rise of optical cable is not obvious, and the influence of ambient temperature is also big. For large hydraulic structures such as levees, heating power must be controlled in the appropriate range.

5. Conclusions

Through the optimization of optical fiber networks layout, real-time seepage monitoring of levees can be implemented,

and the location and relevant information of seepage can be achieved according to the analysis of anomalous changes in temperature field based on the inversion methods above. The effectiveness and feasibility of the monitoring method is verified by the test designed. Distributed optical fiber sensing system is able to monitor the occurrence and development of seepages, continuously and three-dimensionally, achieving real-time, online and automatic safety monitoring of levee engineering. Optical fiber intelligent monitoring system will improve the current situation of safety monitoring of levee engineering on the basis of its unique superiority. However, the following issues still need further research.

- (1) The compatible issues of laying optical fiber with construction for new levees and how to establish distributed optical fiber monitoring system for the constructed projects are the technical problems need to be solved.
- (2) In view of the long distance of levees and complex geological and environment conditions, how to optimize distributed optical fiber layout in levees has significance to reduce engineering cost and for engineering safety.
- (3) The calculation of seepage flow velocity based on the inversion methods, with more assumption and simplification, is a numerical model with measured temperature data. How to ascertain seepage flow velocity, taking environmental, hydrological, and geological factors into account, is an urgent and practical issue of distributed optical fiber for monitoring seepage.
- (4) There are many buildings across dykes and concrete antiseepage walls in levee engineering, where seepages are prone to take place. Therefore, how to strengthen the seepage monitoring and research of soil-stone joint parts in levees is also a key issue for levee safety monitoring.

Acknowledgments

This research has been partially supported by Jiangsu Natural Science Foundation (SN: BK2012036), Non-profit Industry Financial Program of MWR (SN: 201301061), National Natural Science Foundation of China (SN: 51179066, 51139001), the Program for New Century Excellent Talents in University (SN: NCET-10-0359), and the Specialized Research Fund for the Doctoral Program of Higher Education of China (SN: 20130094110010).

References

- [1] C. X. Mao, X. B. Duan, and P. Y. Mao, *Seepage of Dikes & Scour Defense*, China Waterpower Press, 2003.
- [2] C. S. Gu and Z. R. Wu, *Safety Monitoring of Dams and Dam Foundations: Theories & Methods and Their Application*, Hohai University Press, 2006.
- [3] G. Y. Li, *Dialectics on Water Conservancy*, China Waterpower Press, 2001.
- [4] Y. B. Leng, Y. P. Zhu, and Y. Zhou, "Monitoring technology for embankment dam safety based on distributed optical fiber sensing and its prospect," *Progress in Geophysics*, vol. 22, no. 3, pp. 1001–1005, 2007.
- [5] D. S. Cai, *Applications of the Optical Fiber Sensing Technology in Dam Engineering*, China Waterpower Press, 2002.
- [6] O. Kappelmeyer, "The use of near surface temperature measurements for discovering anomalies due to causes at depths," *Geophysical Prospecting*, vol. 5, no. 3, pp. 239–258, 1957.
- [7] D. R. Wei, H. C. Zhao, and Y. T. Qin, "Development of distributed optical fiber monitoring technology in China," in *Proceedings of the National RCCD Damming Technology Conference*, pp. 354–356, 2004.
- [8] F. Y. Ding and L. M. Pan, "Discussion and modification of experiment of measuring the heat conduction of coefficient of gas based on the hot-wire method," *Physics Experimentation*, vol. 24, no. 12, pp. 39–41, 2004.
- [9] P. Kronenberg, N. Casanova, and D. Inaudi, "Dam monitoring with fiber optics deformation sensors," in *Smart Structure and Material*, vol. 3043 of *Proceedings of SPIE*, pp. 2–11, San Diego, Calif, USA, 1997.
- [10] H.-L. Xiao, H. Bao, C.-Y. Wang, and D.-S. Cai, "Research on theory of seepage monitoring based on distributed optical fiber sensing technology," *Rock and Soil Mechanics*, vol. 29, no. 10, pp. 2794–2798, 2008.
- [11] Z. Xu and G. Xiaobing, "Experimental study on thermal conductivity of soil and its mixture with sand," *Journal of HV&AC*, vol. 34, no. 5, pp. 83–89, 2004.
- [12] A. H. Hartog, "Distributed temperature sensor based on liquid core optical fiber," *Journal of Lightwave Technology*, vol. 1, no. 3, pp. 498–509, 1983.

Research Article

Bridge Assessment and Health Monitoring with Distributed Long-Gauge FBG Sensors

Chunfeng Wan,¹ Wan Hong,¹ Jianxun Liu,¹ Zhishen Wu,^{1,2} Zhaodong Xu,¹ and Shu Li¹

¹ International Institute for Urban Systems Engineering, School of Civil Engineering, Southeast University, Nanjing 210096, China

² Department of Urban and Civil Engineering, Ibaraki University, Nakanarusawa-Cho 4-12-1, Hitachi, Ibaraki 316-8511, Japan

Correspondence should be addressed to Zhishen Wu; zswu@seu.edu.cn

Received 3 July 2013; Accepted 18 November 2013

Academic Editor: Gangbing Song

Copyright © 2013 Chunfeng Wan et al. This is an open access article distributed under the Creative Commons Attribution License, which permits unrestricted use, distribution, and reproduction in any medium, provided the original work is properly cited.

Most sensors for structural testing and health monitoring are “point” sensors which strongly limit the ability to correct damage detection and structural assessment. In this paper, long-gauge FBG sensor which can sense the whole area within the gauge length is introduced. Bridge assessment and health monitoring with the microstrain distribution acquired by the distributed long-gauge FBG sensor are also studied. Experiments were conducted and application to a real prestressed box bridge was also implemented. Static and dynamic testing results show that distributed long-gauge FBG sensing technique can obtain not only the global information such as bridge deflection and natural frequency, but also the local parameters such as strain and modal macrostrain to detect damage of the bridge. It shows that structural assessment and health monitoring based on the proposed technique have great potential in maintenance of civil engineering infrastructures.

1. Introduction

Bridges are the most important facilities for many cities and countries. These infrastructures provide the necessary communication and transportation conditions for the residence. However, progressive deterioration of the civil infrastructure begins once they are built and subjected to normal continuous and occasional excessive loading, or adverse environmental conditions. For the purpose of protecting and maintaining these infrastructures, prompt and intensive monitoring of structural system becomes extremely important. Nowadays, most Structural Health Monitoring (SHM) research has focused either on global damage assessment techniques using structural dynamic responses or on limited local independent damage detection mechanisms. Vibration-based global SHM using typical acceleration measurements still faces some challenges for the reason that structural modal parameters seem too “global” to detect the damage that is an intrinsically local phenomenon in structures. On the other hand, although relatively reliable, local inspections are cost, labor-intensive, and too “local” to obtain the integrated information for the overall structure.

Under this background, the concept of distributed long-gauge FBG sensing techniques, which is dedicated to catching and utilizing the strain distribution throughout the full or some partial areas of structures to detect damage, has been proposed to develop an integrated SHM strategy [1]. As a typical local measurement, strain has been verified to be very sensitive to damage. However, for the health monitoring of large-scale civil structures, strain measurement always serves as an auxiliary role partly due to the fact that it is so “local” that the influence of damage on strain measurement cannot be reflected effectively unless the area where strain sensor is installed happens to cover the damaged region. Therefore, to detect arbitrary and unforeseen damage in a complicated structure, strain sensors have to be installed in a distributed way, which is difficult and even infeasible for conventional foil strain gauges. For such “point” sensing system, how to optimize the limited number of sensors [2–4] to achieve the best performance still needs to be developed. For more comprehensive information, fully distributed sensing, such as Brillouin optical sensing [5–9], actually is desirable, yet its resolution is not enough for bridge assessment and dynamic

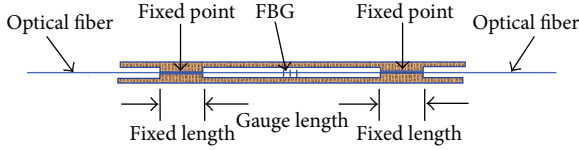
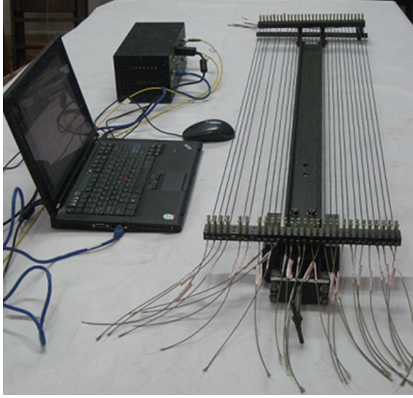
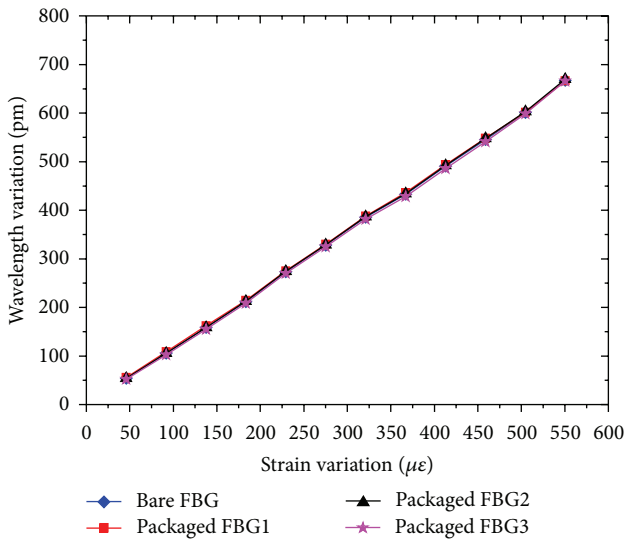


FIGURE 1: Design of the long-gauge FBG sensor.



(a)



(b)

FIGURE 2: Long-gauge FBG sensor and its mechanical property.

analysis. However, distributed long-gauge FBG sensing technique provides a compromise way to balance both sides and therefore becomes an effective method in structural health monitoring. In this paper, the long-gauge FBG sensor will be introduced. Bridge assessment and damage detection stratagem using the microstrain mode will be studied. Experiments are conducted to verify the effectiveness of the long-gauge sensing techniques. Then its application to a real prestressed box bridge is implemented and introduced.

2. Long-Gauge FBG Sensing Techniques

2.1. Long-Gauge FBG Sensors. The long-gauge FBG sensor is designed and fabricated as shown in Figure 1. The gauge

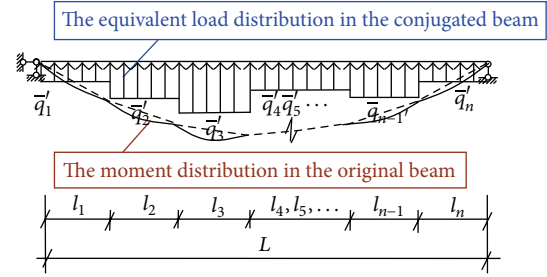


FIGURE 3: Simply-supported beam and its conjugated beam.

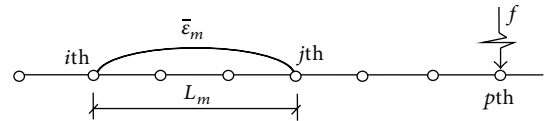


FIGURE 4: Beam structure.

length can be lengthened as desired with a special tube and basalt fibers. The special tube ensures an even strain distribution among the gauge length. The package with basalt fiber reinforced polymer (BFRP) can provide the long-gauge FBG sensor with an exterior protection against harsh environment and improve its durability. The essential processes for the fabrication of long-gauge FBG sensors are the placement of the special tube and treatment of the fixation segments to prevent the possible slippage of optic fibers, inside which bare optic with FBG is fixed at two ends after a certain pretension. When the sensor is installed on the structure, the average strain within the gauge length can be measured.

Experimental results of the sensing property of the sensors are demonstrated in Figure 2, wherein a sensing stability among different long-gauge FBG sensors is shown. From this figure, it is revealed that the package with BFRP has no influence on the sensitivity of FBG sensors.

2.2. Deflection Distribution from Distributed Macrostrain. In structural health monitoring, a useful physical quantity is the strain of the structure. Strain can directly indicate the stress and potential cracks of the structure *in situ*. In dynamic analysis, strain mode analysis was proved to be a very effective method for extracting structural dynamic characteristics and even for structural damage identification. As aforementioned, the macrostrain, that is, the average strain within the gage length can be obtained with the long-gauge FBG sensor. With the sensors being deployed distributedly, the strain distribution of the structure can be obtained, which can provide accurate and all-around strain status for the whole structure for the structural health evaluation.

In most cases, the deformation data are indices for damage accumulation and resistance reduction of engineering structures, such as bridges, tunnels, and pipeline systems until their final failure. The traditional methods for obtaining the structural deformation, such as Geodetic survey, Global Position System (GPS) survey, and direct survey using dial indicators, are characterized as “point” sensing. The main

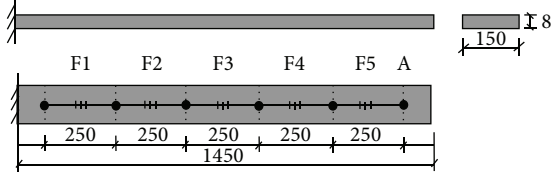


FIGURE 5: A cantilevered beam and sensor deployment.

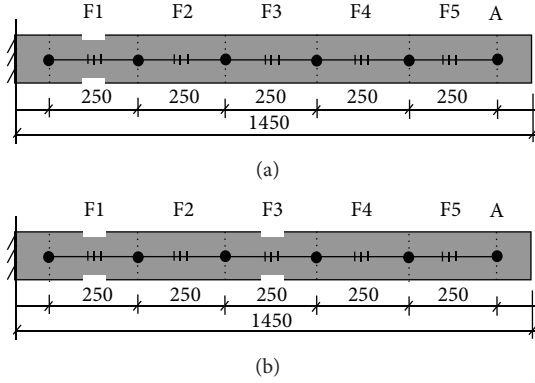


FIGURE 6: Experiment conditions with different damage cases: (a) single damage case and (b) multidamage case.

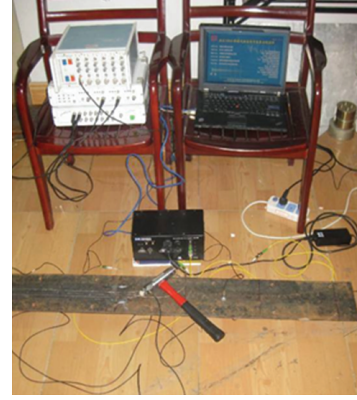
disadvantage of the traditional methods lies in the incomplete deformation data collection, which may result in ignorance of some unforeseen damages. On the contrary, distributed sensing will be very helpful for acquiring continuous structural deformation for damage identification and structural control as well. Shen et al. proposed the conjugated beam method to obtain the deformation distribution from strain distribution [10]. Figure 3 shows the conjugated beam of a joint supported beam. With the averaged strain in a distance l_i is regarded as the equivalent load distribution q_i , and the moment distribution along the whole beam length L of the conjugated beam actually is equal to the displacement distribution, as the solid curve line shows.

In case the gauge length designed to be the same for all long-gauge FBG sensors, with the conjugated beam method, displacement at the boundary point between the p th element and the $(p+1)$ th element v_p and that at the middle point of the $(p+1)$ th element $v_{(p+1)/2}$ can be expressed by (1) and (2) respectively [10]:

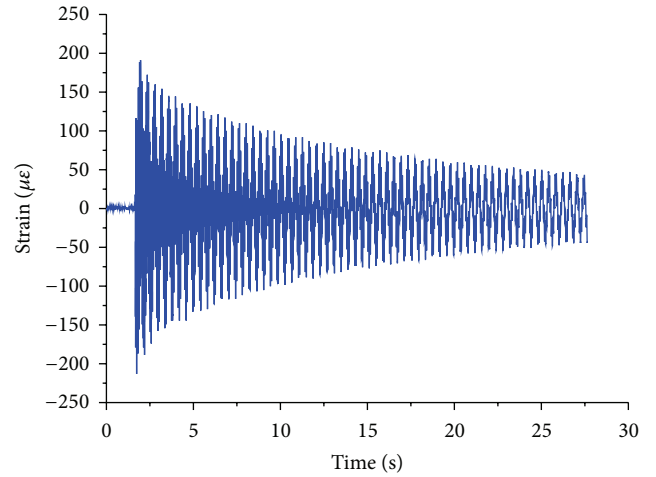
$$v_p = -\frac{L^2}{n^2} \left(\frac{p}{n} \sum_{i=1}^n \bar{\varepsilon}_i \left(n-i + \frac{1}{2} \right) - \sum_{i=1}^p \bar{\varepsilon}_i \left(p-i + \frac{1}{2} \right) \right), \quad (1)$$

$$v_{p+1/2} = -\frac{L^2}{n^2} \left(\frac{p+(1/2)}{n} \sum_{i=1}^n \bar{\varepsilon}_i \left(n-i + \frac{1}{2} \right) - \sum_{i=1}^p \bar{\varepsilon}_i (p-i+1) \right), \quad (2)$$

where $\bar{\varepsilon}_i$ is the averaged strain captured by the i th long-gauge FBG sensor, y_i is the distance from the sensor location to the inertial axis where the i th sensor deployed, n is the total number of sensors, and L is the length of the beam.



(a)



(b)

FIGURE 7: Experiment and strain history at the FBG sensor F3.

2.3. Damage Identification. Macrostrain is the average strain within the gauge length of the long-gauge FBG sensor and therefore is also a local quantity. However, with many sensors deployed throughout the structure as a sensor array, all-around examination of the structure can be fulfilled. Distributed long-gauge FBG sensing techniques were developed by Li and Wu [11] and its effectiveness in structural health monitoring was also proved. In this paper, Modal Macrostrain-Vector (MMSV), a feature vector proposed by Wu and Li [12], will be briefly introduced.

For a beam structure with two local DOFs (one for vertical translation and another for rotation) at each node as Figure 4 shows, on a reasonable assumption that the distance from beam's neutral axis to sensor of each element (denoted as h_m) is same, Macrostrain $\bar{\varepsilon}_m$ within gauge length L_m in frequency domain can be obtained as

$$\bar{\varepsilon}_m(\omega) = \frac{h_m}{L_m} [v_i(\omega) - v_j(\omega)], \quad (3)$$

where v_i and v_j are the rotation degree at the i th and j th node.

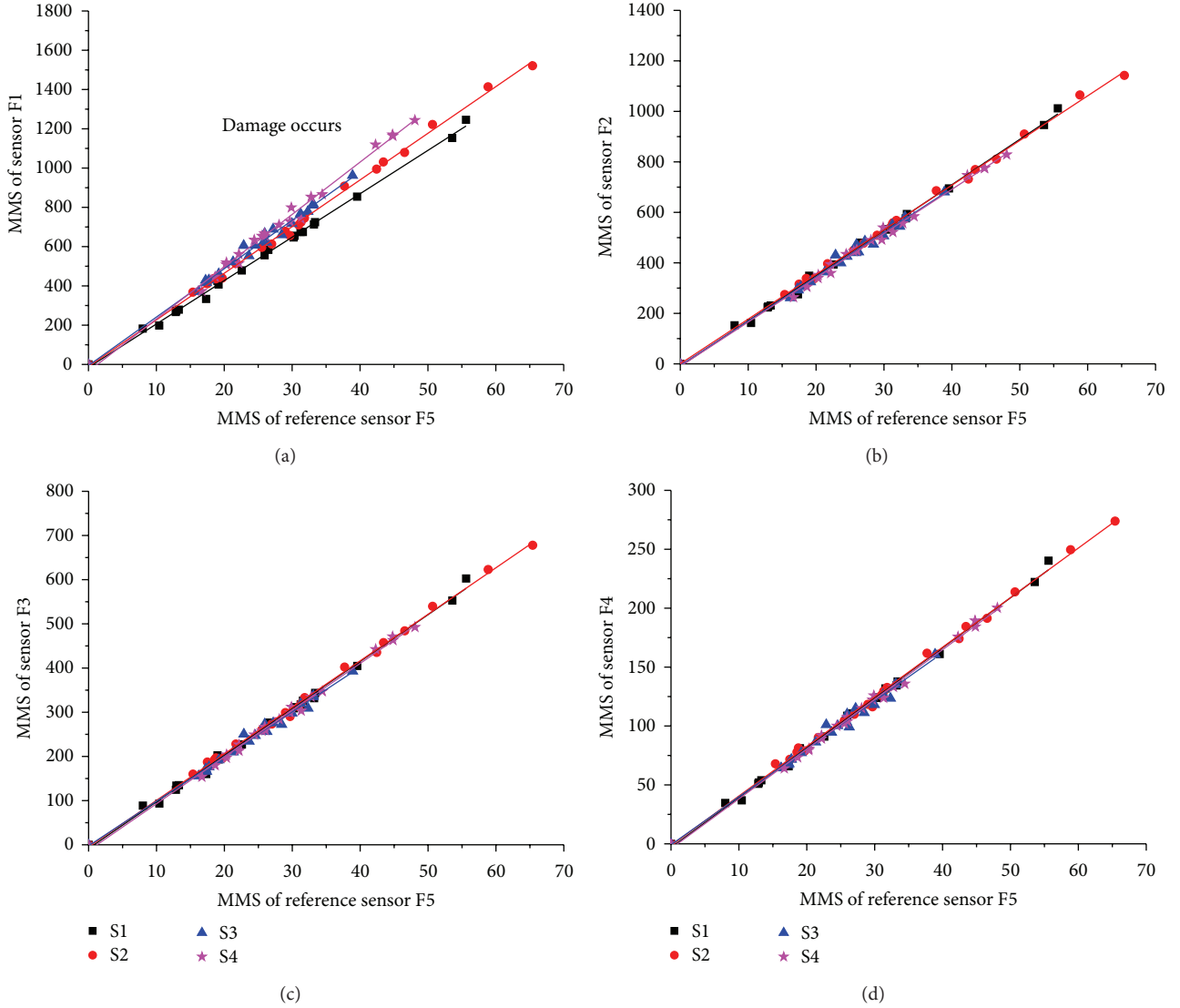


FIGURE 8: MMS of the long-gauge sensors with respected to that of a reference sensor for single damage case.

Therefore, the Macrostrain frequency response function between the measurement from the m th sensor and the excitation at the p th DOF can be achieved by

$$H_{mp}^{\bar{\epsilon}}(\omega) = \frac{\bar{\epsilon}_m(\omega)}{f_p(\omega)}. \quad (4)$$

The value at each peak for the r th mode can be written as

$$\left| {}_r H_{mp}^{\bar{\epsilon}}(\omega = \omega_r) \right| = \frac{\phi_{pr}}{2M_r \xi_r \omega_r^2} \cdot \delta_{mr}, \quad (5)$$

where $\delta_{mr} = (h_m/L_m)(\phi_{ir} - \phi_{jr})$.

For a given mode, $\phi_{pr}/2M_r \xi_r \omega_r^2$ is a constant. Ignoring the amplitude and only emphasizing the relative ratio of all components, the combination of Macrostrain magnitude FRFs from all FBG sensors can construct a vector, that is, MMSV, as

$$\{\delta_{1r}, \delta_{2r}, \dots, \delta_{mr}, \dots\}^T. \quad (6)$$

The detailed theoretical modal analysis based on Macrostrain measurement can be referred to the study of Li and Wu [13].

For convenience, the MMSV can be further normalized by the MMS of a reference sensor as

$$\begin{aligned} & \{\bar{\delta}_{1r}, \bar{\delta}_{2r}, \dots, \bar{\delta}_{(m-1)r}, \bar{\delta}_{mr}\} \\ & = \left\{ \frac{\delta_{1r}}{\delta_{ref}}, \frac{\delta_{2r}}{\delta_{ref}}, \dots, \frac{\delta_{(m-1)r}}{\delta_{ref}}, \frac{\delta_{mr}}{\delta_{ref}} \right\}. \end{aligned} \quad (7)$$

It should be noted that normalized MMS vectors are nondimensional quantities and reflect the structural status. If the structure status at the reference place remains unchanged, then the change of the MMSVs often indicates that damage happened in the structure. Of course, one measurement is not reliable due to noise; however, with multiple measurements, statistics can help provide a sound result.

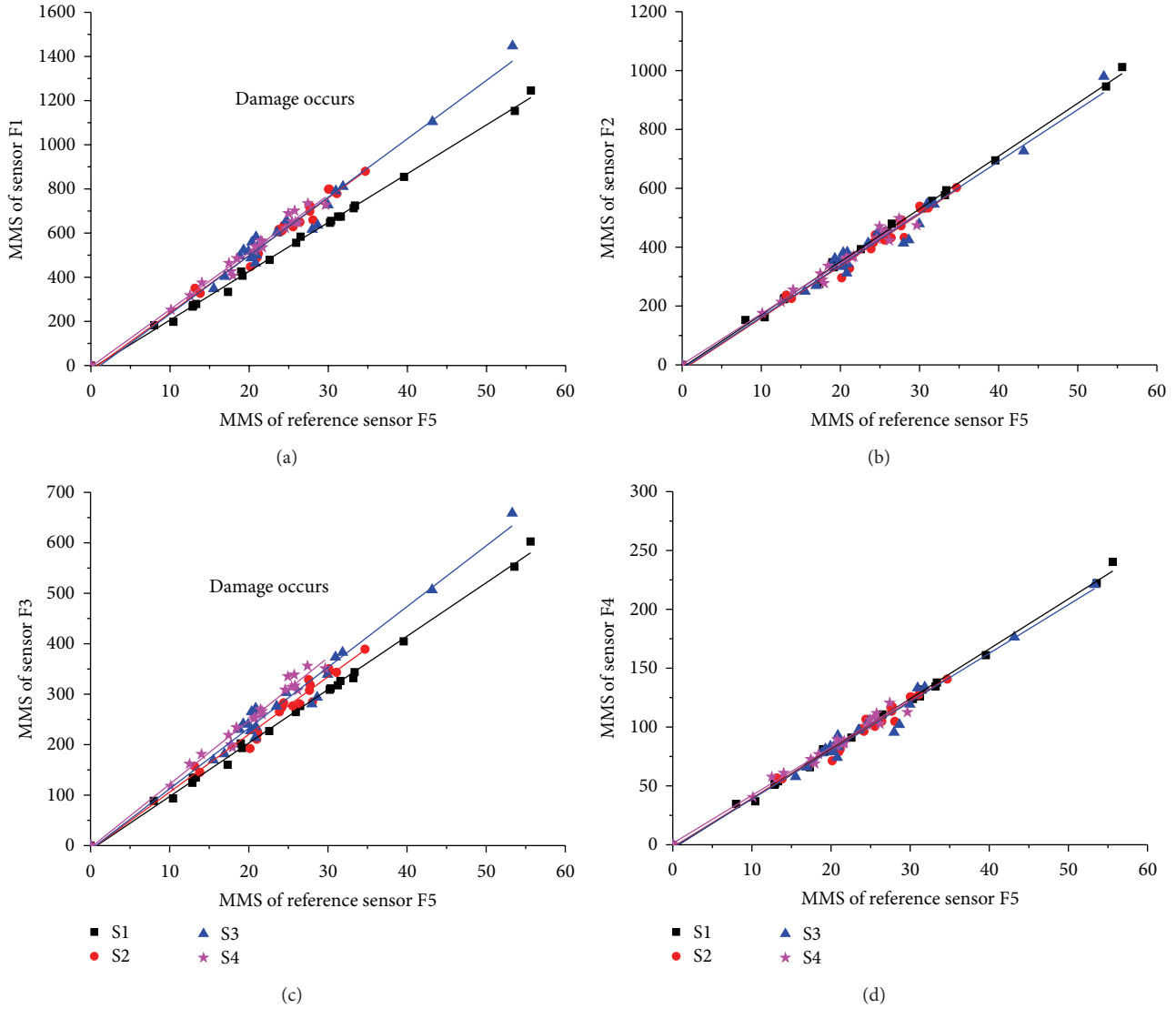


FIGURE 9: MMS of the long-gauge sensors with respect to that of a reference sensor for multidamage case.



FIGURE 10: Hongxing bridge.

3. Experiment Verification

In order to verify the structural health monitoring approach using the distributed long-gauge FBG sensors, related experiments were conducted. A steel cantilever beam is used as

a simple structure. Five long-gauge sensors were deployed on the central line of the upper surface as a sensor array as shown in Figure 5.

The damage of the cantilevered beam was introduced by cutting a part of the beam to reduce the flexural rigidity of the beam, as shown in Figure 6. In this figure, (a) shows a single damage case with a damage located in element 1 and was covered within the gauge length of FBG sensor F1, while (b) shows a multidamage case with two damages which occur in elements 1 and 3 and were covered within the sensors F1 and F3.

An impulsive hammer was used to make an impulsive force to the beam before and after the beam was damaged. FBG interrogator SM-130 was used to collect the optical signal, change to the electrical signal, and save the data. Figure 7 shows the experiment and the strain history in a certain period at the FBG sensor F3 at the moment when the beam was subjected to an impulsive force. It shows

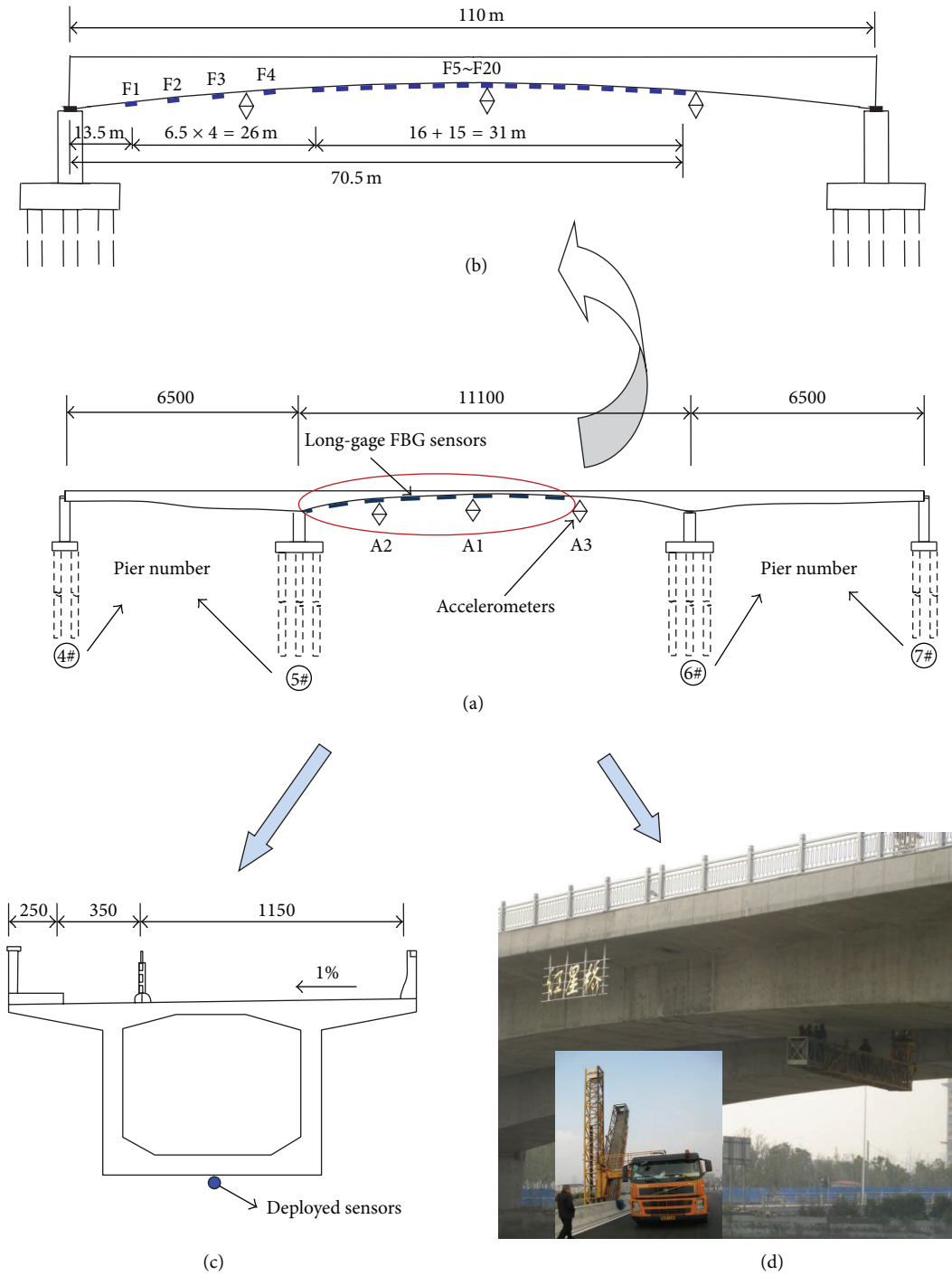


FIGURE 11: Long-gauge FBG sensor deployment.

that the beam vibrated suddenly just after the impulsive force at the beginning and then attenuated gradually. For simplicity, signals after the selected period were omitted and not appeared in the figure.

Also the modal Macrostrain vectors can be obtained, which can be used for damage detection. By deriving the MMSV from time to time, damage can be determined on the judgment whether the fitting curve has remarkable change.

Figure 8 shows some statistics of the MMS of each sensor with respect to that of a reference sensor. Reference sensor is usually selected by choosing the one which is deployed at the place where damage probably will not happen. In this experiment, sensor F5 was selected as the reference sensor. In the experiments, we made 4 tests with different damage scenarios which correspond to different damage extent, with no damage case S1 and increasing damage cases for S2, S3, and



FIGURE 12: On-board load testing.

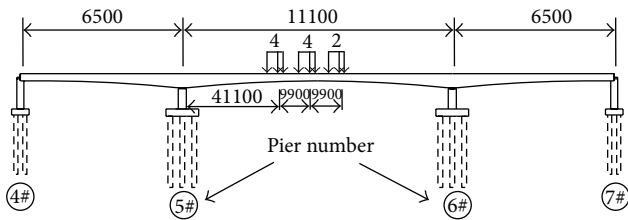


FIGURE 13: Load case 1.

S4. From Figure 8, it can be found that the fitting line of the MMS of sensor F1 to MMS of sensor F5 shifted significantly, while the other fitting lines of MMS of other sensors to that of the reference sensor nearly have no change. This indicates that damage happens at element 1, while there is no damage at elements 2 to 4.

Figure 9 shows the MMS of the long-gauge sensors with respect to that of a reference sensor for multidamage case. It can be found that the fitting lines of the MMS of sensor F1 and F3 to MMS of sensor F5 shifted significantly, while the fitting lines of MMS of sensors F2 and F4 to MMS of reference sensor nearly have no change. This means that damage happens at elements 1 and 3, while no damage happens at elements 2 and 4. It shows that with this approach, damages can be accurately detected also for the multidamage case. At the same time, the damage location can also be determined.

4. Real Bridge Application

In this paper, real bridge assessment and health monitoring were also conducted at the Hongxing Bridge which is a three-span continuous prestressed beam bridge located at Wuxi city of China. The main span of the bridge is 110 m and its side span is 65 m as shown in Figure 10. It is a non-uniform prestressed concrete and consecutive box beam bridge. Before the operation of the bridge but after finishing its construction, load testing was firstly conducted on the bridge.

4.1. Sensors Deployment and Structural Testing Case. Before loading and testing, twenty long-gauge FBG sensors, with a gauge length of 1.0 m, were deployed on the bottom of the bridge as shown in Figure 11. Figure 11(b) shows the detail

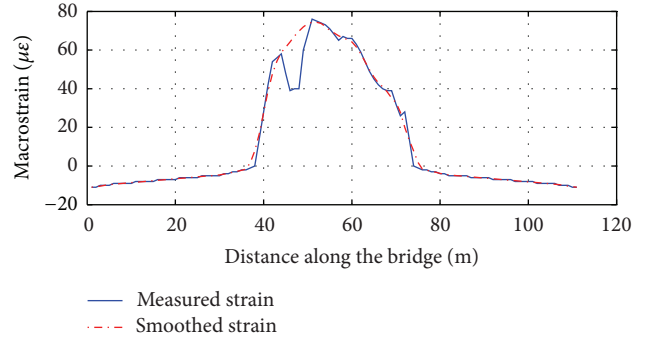


FIGURE 14: Strain distribution along the bridge for load case 1.

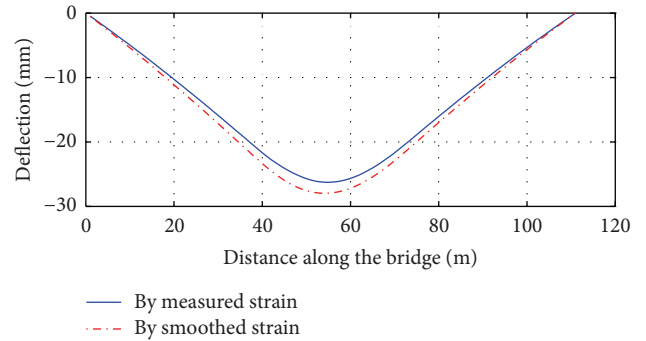


FIGURE 15: Deflection distribution for load case 1.

of the sensor positions. It can be found that sensors were deployed densely around the midspan where damages are easy to happen. While Figure 11(c) shows the sensors were deployed right on the center of the bottom of the box girder. A bridge inspection vehicle was used to carry people to the bottom of the bridge girder and make the sensor deployment just as shown in Figure 11(d). Among the deployed sensors one was kept in slack state and was used for temperature compensation. Other FBG sensors are numbered and labeled as 1 to 19 from the left to the right. Three accelerometers A1, A2 and A3 were installed in the midspan and quarter-span of the bridge as well.

Structural testing includes the static testing and dynamic testing. During the static testing, three load cases were applied. The bridge was loaded with ten 30-ton trucks at the middle of the main-span (load case 1), the quarter-span of the main-span (load case 2), and the middle of the side span (load case 3). Figure 12 shows the on-board load testing scene. Also, vehicle braking testing on the bridge was also conducted in order to study the impact resistance and dynamic coefficient. Dynamic testing was also implemented to study dynamic behavior and damage condition of the structure.

4.2. Static Testing. For load case 1, trucks were stopped at the middle of the main span of the bridge as shown in Figure 13. The corresponding measured strain distribution of the whole bridge (the one third part on the right was estimated via curve fitting) is shown in Figure 14. Maximum strain of the bridge is about $78 \mu\epsilon$, which is also at the middle of the main span.

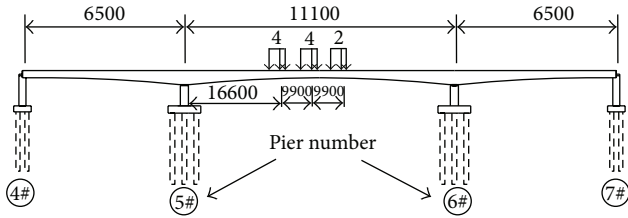


FIGURE 16: Load case 2.

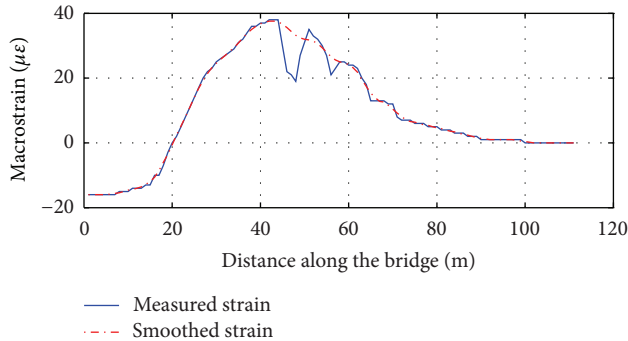


FIGURE 17: Strain distribution along the bridge for load case 2.

A downward peak happens near the midspan which shows the abnormal result. It is probably due to the bad installation of the corresponding sensor, which makes the bad contact interface between the sensor and the structure. If the bad measurement is neglected, then the smoothed Macrostrain distribution can be shown by the dash red line.

Based on the strain distribution and (1) and (2), the deformation distribution can be calculated as shown in Figure 15. It shows that the maximum deflection happens also at the middle of the main span and is approximately 28 mm. However, it should be noted that if the deflection is calculated directly using the measured strain without ruling out bad measurement value, then the maximum deflection value will be about 1.5 mm smaller than that calculated by the smoothed strain distribution

For load case 2, trucks were stopped at the quarter-span of the main span as shown in Figure 16. Figure 17 shows the corresponding strain distribution and Figure 18 shows the deformation distribution calculated based on strain distribution. The maximum strain is $38 \mu\epsilon$ near the midspan and the maximum deflection is about 17 mm (downward) at the midspan. Also it can be found that sensor which is at the place about distance 47 m functions bad. This corresponds to what happens in Figure 14. Red dash line is the smoothed Macrostrain. The maximum deflection calculated by the smoothed Macrostrain distribution is about 0.85 mm larger than that obtained by the direct measured strain.

Figure 19 shows the load case 3 while Figures 20 and 21 demonstrate the corresponding strain distribution and deformation distribution, respectively. The minimum strain is about $-18 \mu\epsilon$ at the quarter-span with the maximum deformation of 6 mm (upward). It is noted that even some peaks for strain distribution happened due to the malfunction

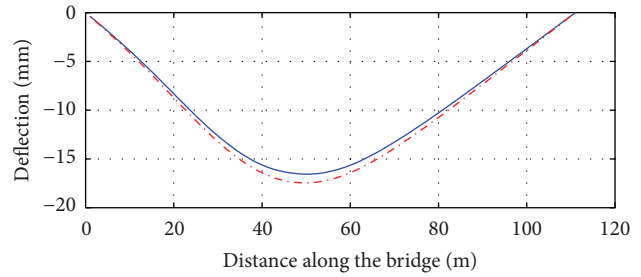


FIGURE 18: Deflection distribution for load case 2.

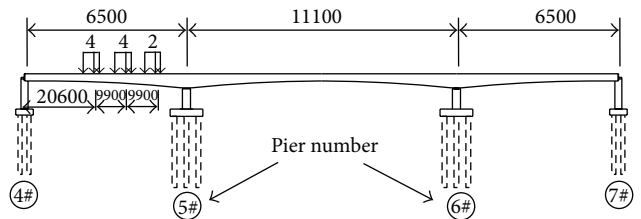


FIGURE 19: Load case 3.

of the sensors, and their deflection curves still remain smooth as shown in Figures 15, 18, and 21. This also shows that deflection (displacement) is a global quantity and is not sensitive to the local change of the structure.

4.3. Braking Testing. In order to study the impact resistance and dynamic characteristics of the bridge, vehicle brake testing was conducted. A 30-ton truck with the speed of 20 km/h suddenly braked at the midspan, and the response of the sensor which was at the midspan shows that the maximum strain is $7.7 \mu\epsilon$ during the whole process. The strain-time curve during the braking testing is shown in Figure 22, while the static strain after the truck completely stopped is $5.9 \mu\epsilon$. The dynamic coefficient can be calculated being about 1.30 due to the impact effect.

4.4. Health Monitoring Using Dynamic Testing. Structural health monitoring of the Hongxing Bridge using distributed long-gage FBG sensor has also been performed via the dynamic testing. Dozens of macrostrain time serial samples with each lasting for about several minutes were collected under ambient vibration. The sampling frequency was adopted to be 500 Hz. The signals were analyzed in frequencydomain and their power spectral densities (PSDs) extracted from 3 randomly selected macrostrain signals and 3 acceleration signals from accelerometers are shown in Figures 23(a) and 23(b), respectively. It is evident that the first order natural frequency from FBG strain response is in accordance with the one from the accelerations, that is, about 2.37 Hz for all cases.

Figure 24 shows the statistical features of the MMS of the target sensor with respect to the reference sensors. Several tests were conducted within the period from June, 2010, to

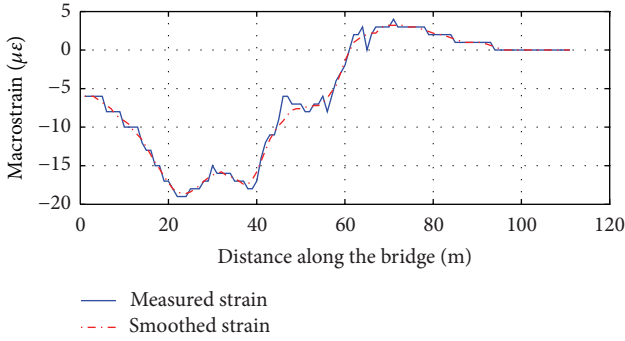


FIGURE 20: Strain distribution along the bridge for load case 3.

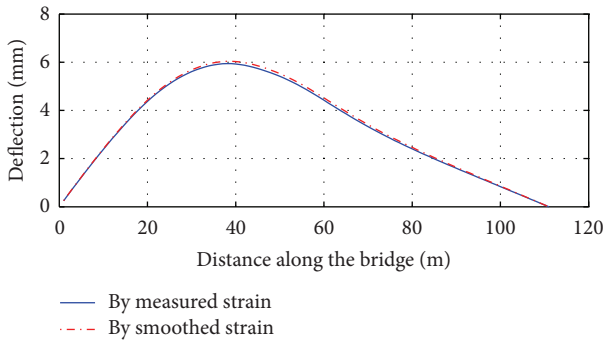


FIGURE 21: Deflection distribution along the bridge for load case 3.

November, 2012. The MMS of other FBG strain response have the analogous results. After testing several times, the ratios of MMS at the target sensor to that of the reference sensor should be stable around at a constant value if no damage occurs within gauge length of the target sensor. In this case, the slope of fitting line from a group of data should keep constant, even though the ratio for every single sample may differ slightly from each other due to noise pollution. However, when damage occurs within the gauge length of the target sensor, the MMS of the structure will change and hence the ratio to the reference MMS will also change. Thus the fitting line will deviate from the one in undamaged case. Figure 24 shows two randomly selected samples of the testing. Results show that fitting line does not have much deviation and therefore indicates the healthy status of the corresponding part of the structure.

5. Conclusions

In this paper, bridge assessment and structural health monitoring with distributed long-gage FBG sensors are introduced. Its application to the laboratory experiments and real bridge is also addressed. It shows the developed long-gage FBG sensors can provide a satisfactory measurement and monitoring for actual large-scale infrastructures. With distributed long-gage FBG sensing technique, the global information of the bridge such as deflection and natural frequency can be obtained effectively. At the same time, the local information, strain distribution, can be also acquired.

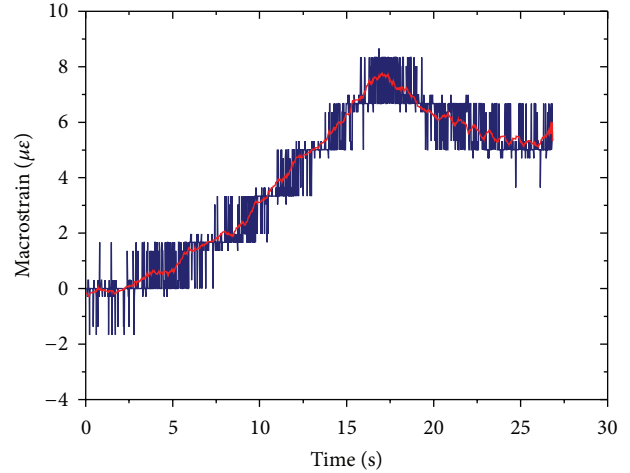


FIGURE 22: Macrostrain time history during brake testing.

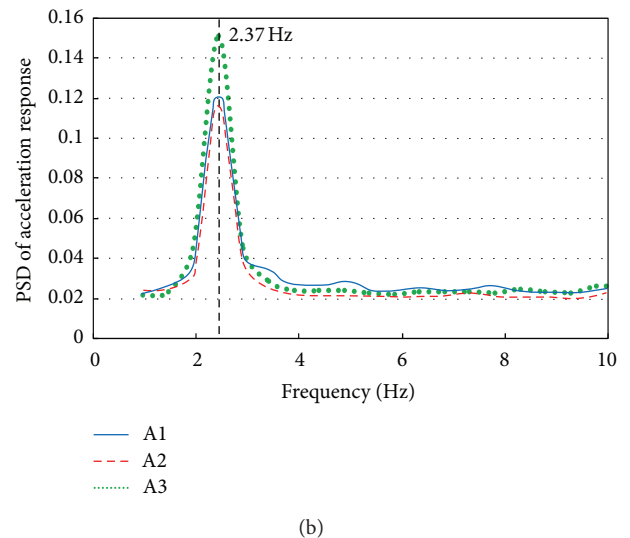
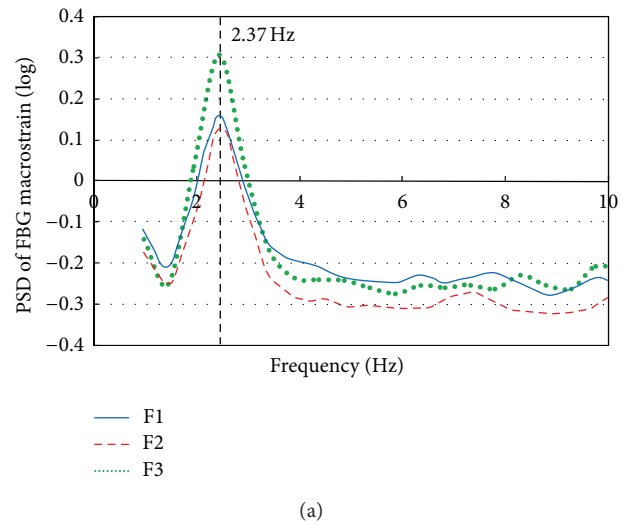


FIGURE 23: Power spectral densities for Macrostrain and acceleration responses.

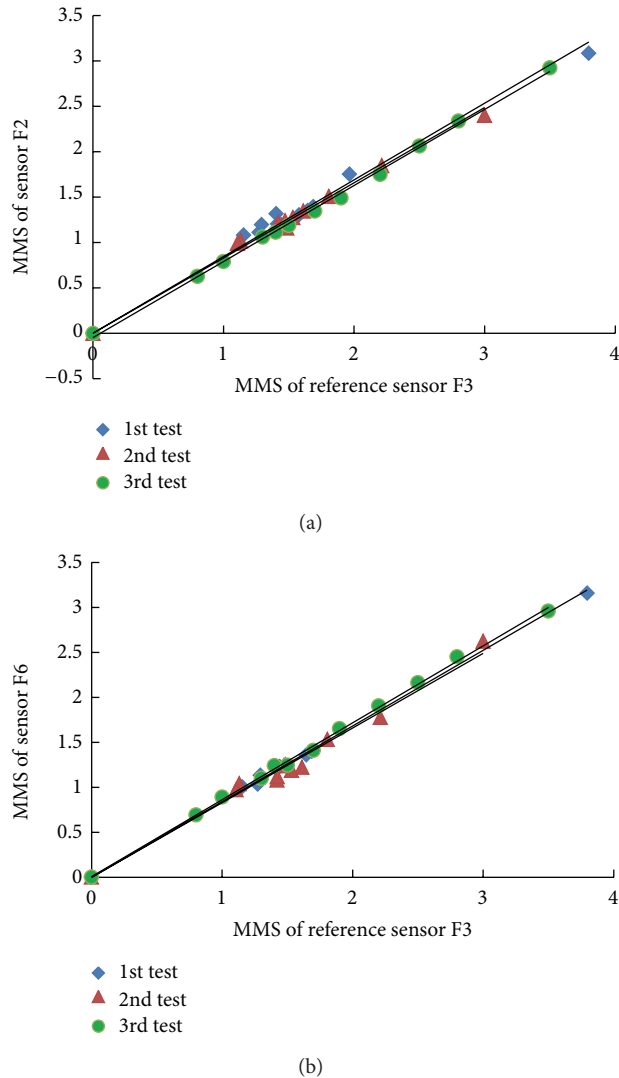


FIGURE 24: MMS of the long-gauge sensors with respect to a reference sensor.

Using the normalized MMS together with the statistics analysis, structural damage identification can be realized, which may be a very useful method for civil engineering structures.

Acknowledgments

This work is supported by the National Key Technology Research and Development Program of the Ministry of Science and Technology of China (Grant no. 2011BAK02B03), the Jiangsu NSF (no. BK2010015), the Project Funded by the Priority Academic Program Development of Jiangsu Higher Education Institutions (PAPD), major project of Department of Communications of Jiangsu Province (2011Y03), and Graduate Research and Innovation Plan Project for the Regular Institution of Higher Learning in Jiangsu Province & Fundamental Research Funds for the Central Universities (no. CXZZ12_1208).

References

- [1] S. Li and Z. Wu, "Development of distributed long-gage fiber optic sensing system for structural health monitoring," *Structural Health Monitoring*, vol. 6, no. 2, pp. 133–143, 2007.
- [2] T.-H. Yi, H.-N. Li, and M. Gu, "A new method for optimal selection of sensor location on a high-rise building using simplified finite element model," *Structural Engineering and Mechanics*, vol. 37, no. 6, pp. 671–684, 2011.
- [3] T.-H. Yi, H.-N. Li, and M. Gu, "Optimal sensor placement for health monitoring of high-rise structure based on genetic algorithm," *Mathematical Problems in Engineering*, vol. 2011, Article ID 395101, 12 pages, 2011.
- [4] T.-H. Yi, H.-N. Li, and M. Gu, "Optimal sensor placement for structural health monitoring based on multiple optimization strategies," *The Structural Design of Tall and Special Buildings*, vol. 20, no. 7, pp. 881–900, 2011.
- [5] X.-F. Zhao, L. Li, Q. Ba, and J.-P. Ou, "Scour monitoring system of subsea pipeline using distributed Brillouin optical sensors based on active thermometry," *Optics and Laser Technology*, vol. 44, no. 7, pp. 2125–2129, 2012.
- [6] X.-F. Zhao, Q. Ba, L. Li, P. Gong, and J.-P. Ou, "A three-index estimator based on active thermometry and anovel monitoring system of scour under submarine pipelines," *Sensors and Actuators A*, vol. 183, pp. 115–122, 2012.
- [7] Z. S. Wu, B. Xu, T. Takahashi, and T. Harada, "Performance of a BOTDR optical fibre sensing technique for crack detection in concrete structures," *Structure and Infrastructure Engineering*, vol. 4, no. 4, pp. 311–323, 2008.
- [8] Z. S. Wu, K. Iwashita, S. Xue, and H. Zhang, "Experimental study on crack monitoring of PC structures with pulse-prepump BOTDA-based distributed fiber optic sensors," *Concrete Research and Technology*, vol. 18, no. 2, pp. 49–57, 2006 (Japanese).
- [9] Z. Wu, B. Xu, K. Hayashi, and A. Machida, "Distributed optic fiber sensing for a full-scale PC girder strengthened with prestressed PBO sheets," *Engineering Structures*, vol. 28, no. 7, pp. 1049–1059, 2006.
- [10] S. Shen, Z. Wu, C. Yang, C. Wan, Y. Tang, and G. Wu, "An improved conjugated beam method for deformation monitoring with a distributed sensitive fiber optic sensor," *Structural Health Monitoring*, vol. 9, no. 4, pp. 361–378, 2010.
- [11] S. Z. Li and Z. S. Wu, "A non-baseline algorithm for damage locating in flexural structures using dynamic distributed macro-strain responses," *Earthquake Engineering & Structural Dynamics*, vol. 36, no. 9, pp. 1109–1125, 2007.
- [12] Z. Wu and S. Li, "Two-level damage detection strategy based on modal parameters from distributed dynamic macro-strain measurements," *Journal of Intelligent Material Systems and Structures*, vol. 18, no. 7, pp. 667–676, 2007.
- [13] S. Li and Z. Wu, "A model-free method for damage locating and quantifying in a beam-like structure based on dynamic distributed strain measurements," *Computer-Aided Civil and Infrastructure Engineering*, vol. 23, no. 5, pp. 404–413, 2008.

Review Article

Review of Bolted Connection Monitoring

Tao Wang,^{1,2} Gangbing Song,^{1,2} Shaopeng Liu,¹ Yourong Li,¹ and Han Xiao¹

¹ College of Mechanical Engineering and Automation, Wuhan University of Science and Technology, Wuhan 430081, China

² Smart Material and Structure Laboratory, Department of Mechanical Engineering, University of Houston, Houston, TX 77204, USA

Correspondence should be addressed to Tao Wang; wangtaw@163.com

Received 5 August 2013; Revised 18 November 2013; Accepted 19 November 2013

Academic Editor: Ting-Hua Yi

Copyright © 2013 Tao Wang et al. This is an open access article distributed under the Creative Commons Attribution License, which permits unrestricted use, distribution, and reproduction in any medium, provided the original work is properly cited.

This paper reviews the research of monitoring technologies for bolted structural connections. The acoustoelastic effect based method, the piezoelectric active sensing method, and the piezoelectric impedance method are the three commonly used to monitor bolted connections. The basic principle and the applications of these three methods are discussed in detail in this paper. In addition, this paper presents a comparison of these methods and discusses their suitability for *in situ* or real-time bolt connection monitoring.

1. Introduction

Bolts are important elements for detachable assembly of components in structures and machines. Bolts provide the required axial or preload forces on the components. A bolt's axial load or preload has to be carefully controlled to ensure the safety and reliability of structures. Insufficient preload or excessive preload is a frequent cause of bolt joint failure [1, 2]. Monitoring the preload of high-tension bolts is critical in maintaining the strength and safety of bolted joints in engineering structures. There are many ways to indirectly measure bolt tension.

Current practice relies on the torque wrench technique. However, with this technique, the torque load dissipates due to the friction between the bolt threads and the nut, which prevents accurate measurements of the axial load. The torque wrench method was reported to show large intrinsic errors in bolt tension measurement by up to 50%. This typically occurs since the torque applied to fastened bolts is consumed mostly by friction—only 10–15% of the torque is converted to the tension in the bolts. Friction consumes about 90% of the torque, with 50% dissipated in the bolt head and 35% in the bolt threads. Additionally, the friction varies so widely from bolt to bolt that errors of 50% are common, even with a perfect torque control. This complication leads to overconservative designs for safety, which in turn increases both weight and cost of bolted connections [3].

An effective way to measure the bolt strain is using a standard resistance strain gauge mounted to the body of the bolt.

This method results in an accurate bolt-strain measurement. Another method, which is used when both sides of the bolt are accessible, involves a caliper to directly measure bolt elongation. However, in many instances, this is impossible since the bolt elongation is so small that it is difficult to measure it accurately. Please note that this method is not suitable for *in situ* monitoring.

An ultrasonic method is considered as a valuable method to measure bolt axial load, which is based on the acoustoelastic effect that the velocity of the ultrasonic wave propagated along the bolt depends on the axial stress.

Interface contact characteristics change with the preload. With the active piezoelectric sensing technique, the variation of the interface contact characteristics can be monitored by the ultrasonic signal generated by the piezoelectric transducer; thus, the bolt connection status can be monitored. This active sensing method has a great potential for *in situ*/real-time monitoring.

Vibration-based damage assessment of bolted structures has also been accomplished using the transmittance function method as described by Caccese et al. [4]. The vibration-based health monitoring strategy has been developed by Razi et al. to detect the loosening of bolts in a pipeline's bolted flange joint, and the empirical mode decomposition is applied to establish an energy-based damage index and several damage scenarios simulated by loosening bolts through adjusting the applied torque were investigated [5]. Zadoks and Yu [6] investigated the self-loosening behavior of bolts under

transverse vibration. Pai and Hess [7] studied the loosening of threaded fasteners due to dynamic shear loads with this traditional dynamic method. Vibration-based damage assessment of bolted structures is a feasible method, and common vibration test equipment can fulfill the purpose [8]. However, for the bolt loosening detection, the subsequent treatment of vibration signal is complex and for the complicated bolted structures, it is difficult to detect the bolt looseness status and loosened bolt position based on this method [9–11].

This paper reviews the measurement technologies for bolt connection status. Three main methods for bolted structure monitoring are discussed in this paper. These three methods are acoustoelastic effect based method, the piezoelectric active sensing method, and the piezoelectric impedance method. This paper presents the basic principle and the applications of these three methods and also discusses their suitability for the *in situ* bolt connection monitoring.

2. Acoustoelastic Effect Based Methods

A bolt's acoustoelastic response changes with its axial stress. The following three properties associated with the acoustoelastic response can be used to compute the axial stress level: (1) the transit time ultrasound along the bolt (portable instruments are commercially available), (2) the transit time ratio between longitudinal and shear waves propagating along the bolt (or mode-converted shear wave at the lateral surface), and (3) the mechanical resonance in the bolt. In this section, three different methods, which are, respectively, based on these three properties, are reviewed.

2.1. Time-of-Flight Method. The time-of-flight (TOF) in the bolt, measured by the sing-around technique with an ultrasonic probe set on the bolt head, is obtained from the time difference between the reflecting waves in the first round trip and the second round trip.

The propagation of ultrasonic waves is sensitive to both residual and applied stresses in materials. The elastic wave propagation depends on the direction and polarization of the waves as well as the direction of the applied stress. Because of these effects, the velocities of ultrasonic waves depend on different stress states in the material.

In the case of plane waves in a homogeneous and isotropic material, the velocities of longitudinal and transverse waves, which propagate in the same direction as the applied stress, can be written in their first-order approximation as [12, 13]

$$V_L = V_{L0} (1 + A_L \sigma), \quad (1a)$$

$$V_T = V_{T0} (1 + A_T \sigma), \quad (1b)$$

where V_{L0} and V_{T0} are the longitudinal and transverse wave velocities in the unstressed state and A_L and A_T are the acoustoelastic constants of the longitudinal and transverse waves, respectively. (Hereafter, subscripts L and T will be omitted if the equations for the longitudinal wave and the transverse wave are identical.) The acoustoelastic coefficients A_L and A_T are negative, which indicates that the wave velocity decreases, while the stress increases. Measurements

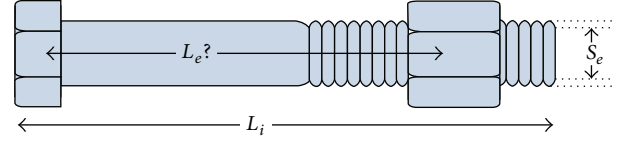


FIGURE 1: Model of an axially loaded bolt.

made to determine the acoustoelastic constant for certain kinds of steel bolts revealed that the acoustoelastic constant is independent of any effects that heat treatment may have on the bolts [14].

For a bolt subjected to an axial load, certain parts of the total length are partially stressed or unstressed. To take this fact into account, assume that the initial bolt length is the sum of the effective length L_e and the unstressed portion L_0 (see Figure 1):

$$L_i = L_0 + L_e. \quad (2)$$

Suppose that L_e is subjected to a uniform uniaxial stress $\sigma = F/S_e$, where F is the axial load and S_e is the effective cross-sectional area. From (1a) and (1b), the pulse-echo time-of-flight related to the ultrasonic wave is given by

$$t = \frac{2L_\sigma}{V} + \frac{2L_0}{V_0}, \quad (3)$$

where $L_\sigma = L_e(1 + E^{-1}\sigma)$ is the stressed length and E is Young's modulus of the bolt material.

Combining (1a), (1b), and (3) results in

$$t = \frac{2L_e(1 + E^{-1}\sigma)}{V_0(1 + A\sigma)} + \frac{2L_0}{V_0}. \quad (4)$$

The first-order development of (4) gives

$$t \cong t_0 \left[\frac{L_e}{L_i} (E^{-1} + A)\sigma + 1 \right], \quad (5)$$

where $t_0 = 2L_i/V_0$ is the pulse-echo time-of-flight corresponding to longitudinal and transverse waves in the unstressed initial length L_i . Equation (5) shows that the time-of-flight under stress is a linear function of the applied stress.

From (5), it can be seen that the bolt axial stress or force can be determined once the time-of-flight of ultrasonic waves under stressed and unstressed states is measured. Once the relationship between F and Δt (the change of time-of-flight due to axial load) is calibrated, the load value can be determined from the precalibration curve based on the measurement of Δt .

Yasui and Kawashima [15] used a broadband normal incidence transducer in the measurement of the bolt load, which excites and receives simultaneously a 10 MHz longitudinal wave and a 5 MHz transverse wave. Hirao et al. [16] used a noncontacting shear-wave electromagnetic acoustic transducer (EMAT) which generates and detects the shear wave propagating in the axial direction of the bolts. Both experiments show a good linear relationship between the load and the TOF or the signal phase.

The variation of ultrasonic velocity in the range of actual stress acting in the bolt is very small, and, as a result, experiments require precise and accurate measurement of the ultrasonic velocity. The phase detection method [17] is adopted for the precise measurement of TOF instead of the conventional pulse-echo technique that is sensitive to noise. 5 MHz ultrasonic transducers are located on the top and bottom of the sample to measure the TOF and the experiment results show that the ultrasonic velocity decreases linearly corresponding to the stress increase.

Since most of the TOF methods use relatively high-frequency (about 5 MHz to 10 MHz) ultrasonic waves, the excitation waveform of the emitter which corresponds to a 230 KHz frequency sine signal truncated by a hamming window was used to measure stress level in the prestressed steel strand [18]. A guided ultrasonic wave for monitoring the stress levels in seven-wire steel strands (15.7 mm in diameter) was proposed and investigative experiment shows the potential and the suitability for evaluating the service stress levels in the prestressed seven-wire steel strands.

Because the time-of-flight in the bolt is only in the range of tens of nanoseconds, the data acquisition process requires a high sampling rate for the data acquisition system (1.0 ns for 1 GS/s in equivalent sampling rate) and thus increases the cost. Most references used oscilloscopes to capture the signals; however, such devices are not suitable for the *in situ* bolt health monitoring.

2.2. Velocity Ratio Method. For fastened bolts in a structure, it is impossible to loosen the bolt to measure the time-of-flight of an ultrasonic wave. The velocity ratio method uses the difference in the acoustoelastic coefficients of longitudinal wave and transverse waves. Using (5), the ratio of the time-of-flight of a transverse wave to that of a longitudinal wave is approximated by the following equation:

$$\frac{t_T}{t_L} \cong \frac{V_{L0}}{V_{T0}} \left[1 - \frac{L_e}{L_i} (A_T - A_L) \frac{F}{S_e} \right]. \quad (6)$$

This method is more practical since the value of axial load is calculated from the ratio of time-of-flight in the stressed state only, without the time-of-flight measurement in the unstressed state [13, 19].

Mode conversion takes place at a solid/liquid interface when two orthogonally polarized components of shear waves convert to longitudinally polarized waves in a solid or when two orthogonally polarized shear and longitudinal components are converted into a longitudinal wave in liquid. In the process of conversion, the mechanical properties and the stress state of the solid medium affect the polarization and speed of waves after refraction. Kim and Hong [3] proposed an ultrasonic technique employing mode-converted ultrasound and applied it to obtain axial stress in high-tension bolts. Simultaneous generation and measurement of both longitudinal and shear waves in bolts are made using mode conversion of longitudinal waves to reduce the experimental error. To measure the TOF of longitudinal and shear waves, multiple mode-converted ultrasonic signals produced in the bolt are captured via an acoustic lens. By

employing mode-converted ultrasonic waves produced by a 10 MHz transducer, it is observed from tensile test results that the TOF ratio of two differently polarized acoustic waves is linearly proportional to the axial stress in bolts as expected from theory.

2.3. Mechanical Resonance Frequency Shift Method. The simple one-dimensional isolated resonator model applies to ultrasonic waves propagating along a bolt. If the assumption is made that complete reflection occurs at the flat and parallel ends of the bolt; then, it can reasonably be assumed that the acoustic resonant frequencies are given by

$$f_n = \frac{nv}{L}, \quad (7)$$

where n is a harmonic integer, v is the velocity of acoustic waves, and $L/2$ is the length of the bolt.

When a stress is applied to the sample, both L and v change, resulting in a change in the resonant frequency. From (7), the fractional change in frequency can be written as

$$\frac{\Delta f_n}{f_n} = \frac{\Delta v}{v} - \frac{\Delta L}{L}. \quad (8)$$

Note that $\Delta L/L = \varepsilon = \sigma/E$, where ε is the strain of the bolt.

The calculation of $\Delta v/v$ as a function of stress is complex. It can be shown that for an isotropic elastic medium, the acoustic wave velocity varies linearly with the stress according to (1a) and (1b). Equation (7) can be written as

$$\frac{\Delta f_n}{f_n} = - \left(A_L + \frac{1}{E} \right) \sigma. \quad (9)$$

This equation shows that the frequency deviation from the resonance is a linear function of the applied stress. The negative sign on the right-hand side indicates that frequency will decrease for a positive (i.e., tensile) stress. Thus, the measurement of Δf_n can be used to determine the stress produced in the sample.

Conradi et al. used the transmission oscillator ultrasonic spectrometer (TOUS) [20] and later Jeyman alternatively used the reflection oscillator ultrasonic spectrometer (ROUS) [21] to measure changes in the resonant frequency of bolts due to stress-induced elongation and change in sound velocity. The experiments used the lead zirconate titanate (PZT) piezoelectric transducer to generate 5 MHz ultrasonic waves to measure the bolt stress. The experimental results confirmed linearity between the frequency shift and the applied stress.

Based on the pseudocontinuous wave technique, Joshi and Pathare [22] used the carrier phase detection technique to track the frequency shift of the mechanical resonance of the bolt. The experiment was carried out with frequency varying from 4891 KHz to 4953 KHz. The frequency changes linearly with the applied stress.

The time-of-flight change in the bolt is only about tens of nanoseconds, and the measurement result is susceptible to the environment interference especially in industrial sites. Additionally, most of the aforementioned methods require high sampling rate of several hundred kilo Hertz or even

mega Hertz. The requirement of the high sampling rate and the associated high cost of the data acquisition systems are among the major obstacles to the practical adoption of *in situ* automated bolt structural health monitoring. In addition, the environmental noise as a main influencing factor for the precise measurement of the time-of-flight also hinders the application of the method in the field.

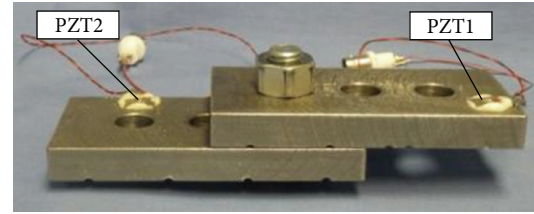
3. Piezoelectric Active Sensing Method

All surfaces, including those machined, are rough to different degrees, and, as a result, the contact between surfaces is restricted to discrete areas at the tips of the surface asperities. In this respect, all bolted joints also develop partial contact at their imperfect interfaces. The applied torque on the bolt may change the interfacial characteristics such as stiffness, damping, and true contact area. Once the interfacial characteristics changes are obtained, the tightness of the bolted connections can be determined.

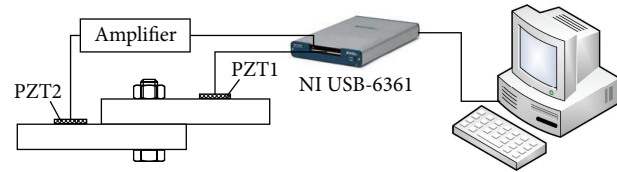
Yang and Chang [23] provide an attenuation-based diagnostic method to identify the location of the loosened bolts, as well as to predict the torque levels of those bolts accordingly. The attenuation-based method is based on the damping phenomena of ultrasonic waves across the bolted joints. Incident waves are split into transmitted and lost waves at the micro contact interface. Considering the fact that waves are power transmission, the energy dissipation phenomena at the imperfect contact interface of bolted joints can be described by examining transmitted wave. Based on the fact that the wave propagation occurs mainly in the true contact area, the amount of transmitted wave energy is proportional to the true contact area. According to the classical Hertz contact theory, within the limit of maximum Hertzian pressure, the true contact area is proportional to the square root of the pressure applied to the contact surface. The torque level in a fastener affects the pressure of a contact surface at the bolted joint. Therefore, the torque level can be determined by measuring the transmitted wave energy.

Based on the above theory, Wang et al. [24] established the experiment apparatus with two PZT patches bonded to different sides of a bolted connection, as shown in Figure 2 [24]. In the active sensing method, one PZT is used to generate a stress wave that will propagate to across connecting surface, and the other PZT is used to detect the stress wave signal. The preloading force determines the connection condition and influences the wave propagation crossing the interface. By monitoring sensor signal, we can indirectly estimate the preloading force on the bolt.

As shown in Figure 2 [24], two steel rectangular/circular plates are connected by a pair of M10 bolt and nut, and the bolted connection is fastened by a torque wrench with different torque levels during the experiments. The computer generates a five-peak Gaussian pulse with a center frequency of 100 KHz every 1 s, and then the signal is converted into analog signals by the NI multifunction DAQ device NI USB-6361 to actuate PZT1. PZT1 produces an ultrasonic wave, which propagates from the top plate to the bottom plate through the bolted interface, and then the transmitted wave



(a) Test specimens



(b) Schematic of bolt connection monitoring system

FIGURE 2: Bolt connection status testing device.

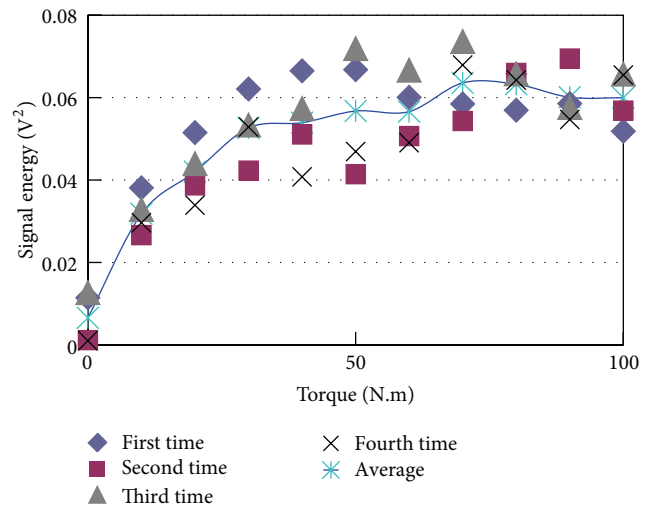


FIGURE 3: Signal energy under different torque levels.

is captured by PZT2. The signal of PZT2 is converted to a digital signal by NI USB-6361 and saved in the computer for further analysis. The received signal energy of PZT2 is then calculated.

The experiment results are shown in Figure 3 [24]. It can be seen that, when the torque is under 40 N·m, with increase of the torque level, the received signal energy of the sensor (PZT2) also increases. However, when the applied torque is beyond 60 N·m, the received energy has little changes and it is in a saturation state. That is, because of exceeding this torque level, there is no more deformation space in the contact interface and the true contact area has basically no change thus; the received energy has little change.

The experimental results demonstrate the feasibility of this method for bolt looseness monitoring. Since this method is easy to implement and nondestructive in nature, it is suitable for *in situ* bolt monitoring for practical use. The piezoelectric active sensing method has a tunable and high-frequency bandwidth. It is especially suitable for monitoring

bolted joints, which involve interfaces. In the active sensing method, the frequency for data acquisition can be much lower than those used in the acoustoelastic effect based methods, thus lowering the hardware cost.

With a piezoelectric wafer as an actuator and a sensor, when the ultrasonic wave generated by the wafer is incident at the interface in the bolted joints, it is transmitted through the asperity junctions and reflected back at the air gaps. When the ultrasonic wavelength is long compared to the scale of the air gaps in the interface, the interface as a whole behaves like a reflector. Marshall et al. use the reflection coefficient of the ultrasonic for measuring the contact pressure relaxation in bolted joints [25].

PZT-induced Lamb wave-based methods are often used for bolt loosening detection. In general, this type of method is also active sensing based. Doyle et al. experimentally investigate the bolted space structures with the acoustoelastic damage detection method and the results show a good linear relationship between the Lamb wave signal delay time in the propagation path and the applied torque [26]. The support vector machine (SVM) was used for damage detection of bolted joints and the feature vectors were created by computing the Fourier amplitude at the excitation frequency using running Fourier transformation [27]. The wavelet transform and pattern recognition techniques, as probabilistic neural networks (PNNs) and support vector machines, are employed for the damage detection for a specimen made of two steel plates jointed by eight steel bolts, in which the damages were introduced by removing several bolts from the joints [28, 29]. The power spectral density (PSD) of the recorded signal was developed to assess the loosening state of joints by Amerini et al. [30]. In [31], the acoustic moment method, the second harmonic method, and the sidebands method were used to analyze the relationship between the tightening/loosening states indices and the torque applied.

For the piezoelectric active sensing method, since lower frequency of the ultrasonic can be used, the cost of test equipment can be dramatically reduced. The signal of active sensing method is relatively easy to analyze and has a better noise immunity; therefore, this method may be more suitable for the industrial application.

4. Piezoelectric Impedance Method

The theoretical development of the application of impedance measurements to structural health monitoring was first proposed by Liang et al. [32] in 1994. In this technique, a piezoceramic patch is surface-bonded to the monitored structure and excited by an alternating voltage sweep signal, typically in the kilohertz range, by an impedance analyzer. The vibrating patch transfers its vibrations to the host structure and simultaneously, the structure influences the electrical circuit comprising the bonded patch and the ac source. A plot of conductance (real part of admittance) as a function of frequency constitutes a unique vibration signature of the structure, reflecting structural characteristics such as inherent stiffness, damping, and mass distribution. In this manner, the same patch acts as an actuator as well as a sensor. By adjusting the

sensing frequency range, the impedance method can cover different sensing areas. For a large structure, the bolted connection status affects only the local dynamic characteristics of the structure. The impedance method is appropriate to study the local dynamics of the bolt joint with appropriate sensing frequency.

Utilizing the electromechanical coupling properties of piezoelectric materials and with the impedance method, Park et al. [33, 34] performed the experiment on a civil pipeline structure connected by bolted joints. The experiment demonstrated the capability of the impedance method to track and monitor the integrity of the typical civil facility. In most impedance methods, a damage index is used to assess the degree of tightness of bolts and it is difficult to quantitatively assess the bolt connection status.

A spectral element method (SEM), based on a wave propagation approach, was used by Ritdumrongkul et al. [35] to model the structure impedance where the piezoelectric ceramic patch is bonded. Through the measurement of the electrical impedance of a PZT actuator-sensor patch bonded on a bolted structure, the change in structural properties due to damage simulated by loosening the bolts is detected. By comparing the simulated result of the proposed model with the experimental results, the loosening of bolts is quantitatively identified as the change in stiffness and damping at the bolted joint. This method solves the problem of the quantitative detection of bolted connection status, but the SEM is a little complicated and not universal.

Combining the impedance method with other ultrasonic methods is another effective bolted structure health monitoring technique. Wait et al. [36] combined the impedance method with the Lamb wave propagation based approach to analyze bolted system's structural integrity. An and Sohn [37] illustrated an integrated impedance and guided wave-based damage detection techniques by utilizing impedance and guided wave signals simultaneously obtained from surface-mounted piezoelectric transducers to the detection of bolt loosening. For the combined impedance method, it can detect the loosened bolt position in bolts group joints.

A precision impedance analyzer has a high cost. Wireless impedance devices based on AD5933 impedance measurement chip have been designed and used for structure health monitoring with reduced cost and size [38–41]. However, the limited scanning and sampling frequency of the impedance chip restricts its wide application [42].

For all above impedance methods, they determine the bolted connection status by impedance signal analysis. An effective monitoring theory is not formed yet because of lack of research for bolted structural dynamic characteristics, especially local high-frequency dynamics. The impedance method is very suitable for local dynamic characteristics study because of its high actuation frequency and tunable sensing area. Using the impedance method to investigate the dynamic characteristics of the bolted join may be the further research interests. Once understanding the effects of the bolt connection status on the local dynamic, the impedance method has a good potential for *in situ* monitoring of bolted connections.

TABLE 1: Comparison of the test method.

	Acoustoelastic effect based methods			Piezo active sensing	Piezo impedance
	Time-of-flight method	Velocity ratio method	Resonance frequency shift		
Nature of signal	Time	Velocity ratio	Frequency	Voltage	Impedance
Requirement on sampling rate	High	High	High	Relatively Low	Depend on the scan frequency and structure
Relative cost of the sensor/probe	High	High	High	Relatively Low	Low
Relative cost of entire system	Relatively high	Relatively high	Relatively high	Relatively cost	High for impedance analyzer; low for AD5933 chip-based circuit
Suitability for real-time monitoring	No	No	No	Yes	Yes

5. Conclusion

Bolts are widely used to assemble components in mechanical and civil structures due to their high reliability, strong load bearing capacity, and easy maintenance. However, bolt connections are often subjected to external dynamic loads, such as impact, vibration, and thermal stresses, and bolt loosening leads to the failure of engineering structures. Therefore, the detection of bolt loosening, as a part of structure health monitoring, attracts much attention, and the development of a nondestructive testing method is needed to evaluate the state of bolt connection. This paper reviews three main methods for the bolted joints monitoring.

For the acoustoelastic effect based method, including time-of-flight method, velocity ratio method and mechanical resonance frequency shift method can determinate the bolt axial stress. It is an ideal way for the bolted structure monitoring, but the stress-induced velocity changes are quite small; thus the time-of-flight variation and frequency shift are very small, requiring a high sampling rate for the data acquisition device and thereby increasing the cost. There are many factors, such as the material-microstructure effects, environmental noise, and the thickness of bonding layer, which can affect the measurement accuracy of the flight time and make *in situ* measurement challenging.

Bolt preload changes the dynamic characteristics of the interface, such as stiffness and damping, and it affects the ultrasonic wave, which is generated by the piezoelectric transducer, passing through the interface. By monitoring and analyzing the received ultrasonic signal, the bolt connection status can be determined. Experimental results show that the piezoelectric sensing method based on interfacial characteristics change is an effective method. With further in-depth research in bolted contact interface properties, contact interface dynamic characteristics, and local dynamics, this method has a great potential for *in situ* bolt health monitoring.

The piezoelectric impedance method has a high sensitivity to the local structure damage and a large-frequency bandwidth. It is specially fitted for monitoring bolted joints which are dominated by local dynamics of high-frequency

characteristics. The impedance method has a good potential for *in situ* monitoring of bolted connections.

The comparison of the methods discussed in this paper is listed in Table 1.

Though fiber optical sensors (FOSs), such as fiber bragg gratings (FBGs), have found many applications in structural health monitoring [43, 44] due to their advantages, including high accuracy, multiplexing capacity, and EMI (electromagnetic immunity), use of FOSs for bolted connection monitoring is rarely reported. The authors think that FOSs, especially FBGs, possess a great potential to monitor bolt looseness in real time, especially for applications involving high electromagnetic interference. The multiplexing capacity of FOSs is another attraction for bolted connection monitoring in case of a large number. With sensor optimization algorithms [45], a limited number of fiber cables can provide *in situ* monitoring of many bolted connections.

Acknowledgments

This research was partially supported by the Open Fund of the Key Laboratory for Metallurgical Equipment and Control of Ministry of Education in Wuhan University of Science and Technology, the Natural Science Foundation of Hubei Province under Grant no. 2011CDA121, and the Natural Science Foundation of China under Grant nos. 51375354 and 51105284.

References

- [1] S. Basava and D. P. Hess, "Bolted joint clamping force variation due to axial vibration," *Journal of Sound and Vibration*, vol. 210, no. 2, pp. 255–265, 1998.
- [2] S. Izumi, T. Yokoyama, A. Iwasaki, and S. Sakai, "Three-dimensional finite element analysis of tightening and loosening mechanism of threaded fastener," *Engineering Failure Analysis*, vol. 12, no. 4, pp. 604–615, 2005.
- [3] N. Kim and M. Hong, "Measurement of axial stress using mode-converted ultrasound," *NDT and E International*, vol. 42, no. 3, pp. 164–169, 2009.

- [4] V. Caccese, R. Mewer, and S. S. Vel, "Detection of bolt load loss in hybrid composite/metal bolted connections," *Engineering Structures*, vol. 26, no. 7, pp. 895–906, 2004.
- [5] P. Razi, R. A. Esmaeel, and F. Taheri, "Improvement of a vibration-based damage detection approach for health monitoring of bolted flange joints in pipelines," *Structural Health Monitoring*, vol. 12, no. 3, pp. 207–224, 2013.
- [6] R. I. Zadoks and X. Yu, "An investigation of the self-loosening behavior of bolts under transverse vibration," *Journal of Sound and Vibration*, vol. 208, no. 2, pp. 189–209, 1997.
- [7] N. G. Pai and D. P. Hess, "Experimental study of loosening of threaded fasteners due to dynamic shear loads," *Journal of Sound and Vibration*, vol. 253, no. 3, pp. 585–602, 2002.
- [8] R. A. Ibrahim and C. L. Pettit, "Uncertainties and dynamic problems of bolted joints and other fasteners," *Journal of Sound and Vibration*, vol. 279, no. 3–5, pp. 857–936, 2005.
- [9] H. Ahmadian and H. Jalali, "Identification of bolted lap joints parameters in assembled structures," *Mechanical Systems and Signal Processing*, vol. 21, no. 2, pp. 1041–1050, 2007.
- [10] Y. Song, C. J. Hartwigsen, D. M. McFarland, A. F. Vakakis, and L. A. Bergman, "Simulation of dynamics of beam structures with bolted joints using adjusted Iwan beam elements," *Journal of Sound and Vibration*, vol. 273, no. 1–2, pp. 249–276, 2004.
- [11] A. Milanese, P. Marzocca, J. M. Nichols, M. Seaver, and S. T. Trickey, "Modeling and detection of joint loosening using output-only broad-band vibration data," *Structural Health Monitoring*, vol. 7, no. 4, pp. 309–328, 2008.
- [12] D. S. Hughes and J. L. Kelly, "Second-order elastic deformation of solids," *Physical Review*, vol. 92, no. 5, pp. 1145–1149, 1953.
- [13] G. C. Johnson, A. C. Holt, and B. Cunningham, "An ultrasonic method for determining axial stress in bolts," *Journal of Testing and Evaluation*, vol. 14, no. 5, pp. 253–259, 1986.
- [14] M. Suda, Y. Hasuo, A. Kanaya, Y. Ogura, T. Takishita, and Y. Suzuki, "Development of ultrasonic axial bolting force inspection system for turbine bolts in thermal power plants," *JSME International Journal I*, vol. 35, no. 2, pp. 216–219, 1992.
- [15] H. Yasui and K. Kawashima, "Acoustoelastic measurement of bolt axial load with velocity ratio method," in *Proceedings of the 15th World Conference on Non-Destructive Testing*, pp. 750–756, Rome, Italy, October 2000.
- [16] M. Hirao, H. Ogi, and H. Yasui, "Contactless measurement of bolt axial stress using a shear-wave electromagnetic acoustic transducer," *NDT and E International*, vol. 34, no. 3, pp. 179–183, 2001.
- [17] K. Y. Jhang, H. H. Quan, J. Ha, and N. Y. Kim, "Estimation of clamping force in high-tension bolts through ultrasonic velocity measurement," *Ultrasonics*, vol. 44, pp. e1339–e1342, 2006.
- [18] S. Chaki and G. Bourse, "Stress level measurement in pre-stressed steel strands using acoustoelastic effect," *Experimental Mechanics*, vol. 49, no. 5, pp. 673–681, 2009.
- [19] S. Chaki, G. Corneloup, I. Lillamand, and H. Walaszek, "Combination of longitudinal and transverse ultrasonic waves for in situ control of the tightening of bolts," *Journal of Pressure Vessel Technology*, vol. 129, no. 3, pp. 383–390, 2007.
- [20] M. S. Conradi, J. G. Miller, and J. S. Heyman, "A transmission oscillator ultrasonic spectrometer," *Review of Scientific Instruments*, vol. 45, no. 3, pp. 358–360, 1974.
- [21] J. S. Heyman, "A CW ultrasonic bolt-strain monitor," *Experimental Mechanics*, vol. 17, no. 5, pp. 183–187, 1977.
- [22] S. G. Joshi and R. G. Pathare, "Ultrasonic instrument for measuring bolt stress," *Ultrasonics*, vol. 22, no. 6, pp. 270–274, 1984.
- [23] J. Yang and F. K. Chang, "Detection of bolt loosening in C—C composite thermal protection panels: II. Experimental verification," *Smart Materials and Structures*, vol. 15, no. 2, pp. 591–599, 2006.
- [24] T. Wang, G. Song, Z. G. Wang, and Y. R. Li, "Proof-of-concept study of monitoring bolt connection status using a piezoelectric based active sensing method," *Smart Materials and Structures*, vol. 22, no. 8, Article ID 087001, 2013.
- [25] M. B. Marshall, R. Lewis, T. Howard, and H. Brunskill, "Ultrasonic measurement of self-loosening in bolted joints," *Proceedings of the Institution of Mechanical Engineers C*, vol. 226, no. 7, pp. 1869–1884, 2012.
- [26] D. Doyle, A. Zagrai, B. Arritt, and H. Çakan, "Damage detection in bolted space structures," *Journal of Intelligent Material Systems and Structures*, vol. 21, no. 3, pp. 251–264, 2010.
- [27] A. Mita and A. Fujimoto, "Active detection of loosened bolts using ultrasonic waves and support vector machines," in *Proceedings of the 5th International Workshop on Structural Health Monitoring (IWSHM '05)*, pp. 1017–1024, September 2005.
- [28] S. H. Park, C. B. Yun, and Y. Roh, "PZT-induced Lamb waves and pattern recognitions for on-line health monitoring of jointed steel plates," in *Smart Structures and Materials 2005: Sensors and Smart Structures Technologies for Civil, Mechanical, and Aerospace Systems*, vol. 5765 of *Proceedings of SPIE*, pp. 364–375, San Diego, Calif, USA, March 2005.
- [29] S. H. Park, C. B. Yun, and Y. Roh, "Active sensing-based real-time nondestructive evaluations for steel bridge members," *KSCSE Journal of Civil Engineering*, vol. 10, no. 1, pp. 33–39, 2006.
- [30] F. Amerini, E. Barbieri, M. Meo, and U. Polimeno, "Detecting loosening/tightening of clamped structures using nonlinear vibration techniques," *Smart Materials and Structures*, vol. 19, no. 8, Article ID 085013, 9 pages, 2010.
- [31] F. Amerini and M. Meo, "Structural health monitoring of bolted joints using linear and nonlinear acoustic/ultrasound methods," *Structural Health Monitoring*, vol. 10, no. 6, pp. 659–672, 2011.
- [32] C. Liang, F. P. Sun, and C. A. Rogers, "Coupled electro-mechanical analysis of adaptive material systems—determination of the actuator power consumption and system energy transfer," *Journal of Intelligent Material Systems and Structures*, vol. 5, no. 1, pp. 12–20, 1994.
- [33] G. Park, H. H. Cudney, and D. J. Inman, "Feasibility of using impedance-based damage assessment for pipeline structures," *Earthquake Engineering and Structural Dynamics*, vol. 30, no. 10, pp. 1463–1474, 2001.
- [34] G. Park, H. Sohn, C. R. Farrar, and D. J. Inman, "Overview of piezoelectric impedance-based health monitoring and path forward," *Shock and Vibration Digest*, vol. 35, no. 6, pp. 451–463, 2003.
- [35] S. Ritdumrongkul, M. Abe, Y. Fujino, and T. Miyashita, "Quantitative health monitoring of bolted joints using a piezoceramic actuator-sensor," *Smart Materials and Structures*, vol. 13, no. 1, pp. 20–29, 2004.
- [36] J. R. Wait, G. Park, and C. R. Farrar, "Integrated structural health assessment using piezoelectric active sensors," *Shock and Vibration*, vol. 12, no. 6, pp. 389–405, 2005.
- [37] Y. K. An and H. Sohn, "Integrated impedance and guided wave based damage detection," *Mechanical Systems and Signal Processing*, vol. 28, pp. 50–62, 2012.
- [38] T. G. Overly, G. Park, C. R. Farrar et al., "Compact hardware development for SHM and sensor diagnostics using admittance measurements," in *Proceedings of the SEM International Modal Analysis Conference*, 2007.

- [39] D. L. Mascarenas, G. Park, K. M. Farinholt, M. D. Todd, and C. R. Farrar, "A low-power wireless sensing device for remote inspection of bolted joints," *Proceedings of the Institution of Mechanical Engineers G*, vol. 223, no. 5, pp. 565–575, 2009.
- [40] D. S. Hong, D. D. Ho, K. D. Nguyen, and J. T. Kim, "Temperature effect on damage monitoring of steel girder connection by wireless acceleration-impedance sensor nodes," in *Proceedings of the 6th International Workshop on Advanced Smart Materials and Smart Structures Technology*, 2011.
- [41] K. D. Nguyen, S. Y. Lee, P. Y. Lee et al., "Wireless SHM for bolted connections via multiple PZT-interfaces and Imote2-platformed impedance sensor node," in *Proceedings of the 6th International Workshop on Advanced Smart Materials and Smart Structures Technology (ANCRiSST '11)*, 2011.
- [42] D. S. Hong, K. D. Nguyen, I. C. Lee, and J. T. Kim, "Temperature-compensated damage monitoring by using wireless acceleration-impedance sensor nodes in steel girder connection," *International Journal of Distributed Sensor Networks*, vol. 2012, 12 pages, 2012.
- [43] H. N. Li, G. D. Zhou, L. Ren, and D. S. Li, "Strain transfer coefficient analyses for embedded fiber bragg grating sensors in different host materials," *Journal of Engineering Mechanics*, vol. 135, no. 12, pp. 1343–1353, 2009.
- [44] L. Ren, H. N. Li, J. Zhou, D. S. Li, and L. Sun, "Health monitoring system for offshore platform with fiber Bragg grating sensors," *Optical Engineering*, vol. 45, no. 8, Article ID 084401, 2006.
- [45] T. H. Yi, H. N. Li, and M. Gu, "A new method for optimal selection of sensor location on a high-rise building using simplified finite element model," *Structural Engineering and Mechanics*, vol. 37, no. 6, pp. 671–684, 2011.

Research Article

Development of a Multitype Wireless Sensor Network for the Large-Scale Structure of the National Stadium in China

Yanbin Shen,¹ Pengcheng Yang,¹ Pengfei Zhang,¹ Yaozhi Luo,¹ Yujia Mei,²
Huaqiang Cheng,¹ Li Jin,¹ Chenyu Liang,³ Qiaqin Wang,⁴ and Zhouneng Zhong⁵

¹ College of Civil Engineering and Architecture, Zhejiang University, Hangzhou 310058, China

² Zhejiang Electric Power Design Institute, Hangzhou 310012, China

³ Beijing Institute of Architectural Design, Beijing 100045, China

⁴ Chongqing Airport Group Co., Ltd., Chongqing 401120, China

⁵ Zhejiang Greentown Architectural Design Co., Ltd., Hangzhou 310007, China

Correspondence should be addressed to Yaozhi Luo; mstcad@163.com

Received 21 June 2013; Accepted 21 October 2013

Academic Editor: Jeong-Tae Kim

Copyright © 2013 Yanbin Shen et al. This is an open access article distributed under the Creative Commons Attribution License, which permits unrestricted use, distribution, and reproduction in any medium, provided the original work is properly cited.

A multitype wireless sensor network (WSN) for structural health monitoring is developed for the National Stadium in China (generally known as “Bird’s Nest”). The stadium is a super large-scale building built for the 2008 Beijing Olympic Games and can house more than 90,000 occupants. The structure is very rigid and weighs more than 40,000 tons in total. Considering the structural features and on-site environment, the system takes multitype sensors as measurement components including stress, displacement, acceleration, wind, and temperature. The monitoring module design consists of four functions: sensing, processing, wireless communication, and energy management. The communication between each sensor node is realized by using an adjustable and artificial-control chain-type network. A total of 290 sensors were installed on the structure, and the data collection work has been carried out for more than one year. This paper mainly focuses on the system development and project application, while the data analysis work is briefly discussed as well. It can be concluded that the customized WSN is robust and durable, which well satisfies the requirement of plenty multitype sensors working in a large-area distribution. The data analysis results reveal that the super large-scale structure is very sensitive to the temperature effect.

1. Introduction

Large-span spatial structures are widely used in large public buildings such as gym, stadium, airport, railway station, and exhibition hall. This type of structures in China has generated a great deal of interest and has entered a new era of fast development. One of the characteristics of large-span spatial structures is being of steel construction and the material is homogeneous throughout. As a result, the structural design mainly focuses on its structural topology [1].

The National Stadium of China, generally known as “Bird’s Nest,” was built for the 2008 Beijing Olympic Games. It is a super large-scale building that has been considered as the symbol of large-span spatial structures in China, as shown in Figure 1. The building on plan view is in the shape of an ellipse with a diameter of 332 meters on north-south direction

and 297 meters on east-west direction. The entire structure is composed of 24 main trusses and each truss consists of 2-layer square-section steel tubes. The average size of the tube section is 1 m in side length and 40 mm in wall thickness; therefore, the entire structure is very rigid which weighs more than 40,000 tons, as shown in Figure 2.

It is such a large-scale public building that can house more than 90,000 occupants, and the safety of the structure is a major concern for owners and structural engineers. Once structural incidents and accidents occur, both the economy and human life loss can be inconceivable. An effective way to avoid such mishap is to develop structural health monitoring (SHM) systems for continually monitoring and assessing the health of the structure. As a matter of fact, health assessment procedures have been developed and applied in civil infrastructures for years especially in the bridge engineering.

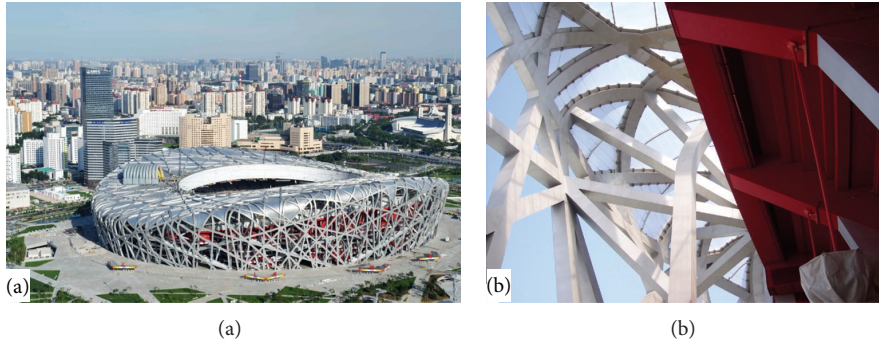


FIGURE 1: Photograph of “Bird’s Nest.” (a) The entire structure of “Bird’s Nest.” (b) Partial view of “Bird’s Nest.”

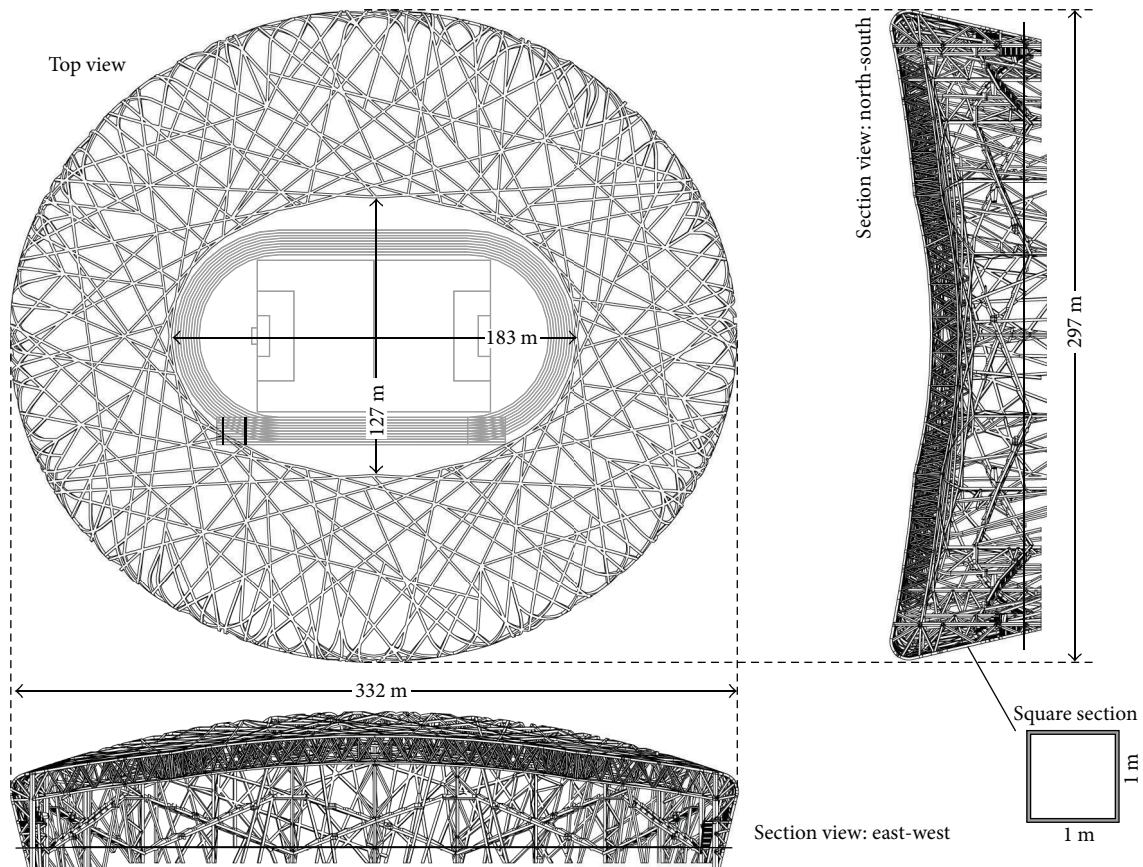


FIGURE 2: Structural view of “Bird’s Nest.”

A lot of research work on sensor technology, optimal sensor placement strategies, damage detection, and health evaluation have been carried out and many engineering applications have been reported [2–10]. By contrast, health assessment work for large-span spatial structures has not started until recent years [11, 12]. One of the main reasons is that traditional SHM systems are not so suitable for this type of structures. In traditional systems, wires and connections are commonly used for data transmission and power supply, which may not be a big problem in application of line-shape structures such as bridges and dams. For large-area-scale structures, however, time and expense will be largely consumed in wires

installation. The cost will increase drastically as the number of sensors increases. Additionally, the complex layout of the wires along with its reliability and aging issues makes such application problematic.

Recent breakthrough in sensor development, wireless communication, and application of high-energy battery has made wireless SHM systems in reality as an efficient and economical solution for the health detection of large-span spatial structures. As early as in 1996, the wireless sensing technology was firstly attempted in a SHM system for civil engineering [13–16]. Since then, a lot of research work was carried out on various types of wireless sensor development.

A remarkable achievement is the design of a wireless sensor node using an 8-bit microchip and taking the accelerometer as the sensor component. It has been verified in the lab and made a foundation for future application in engineering [17]. With the development of the age, the wireless sensor technology becomes more advanced, and the function of SHM system turns more customized [18–20]. In recent years, more and more models of wireless sensors are presented by other researchers for different applications, for example, wireless acceleration sensors, wireless strain sensors, and so on [21–23]. For bridge health assessment, more importance is attached to the development of wireless acceleration sensors [24, 25]. However, for monitoring static building structures, wireless strain sensors are equally or even more important. Among them, the wireless vibrating wire sensor (VWS) is worth mentioning. It has been applied to long-term stress monitoring because of its stable and durable properties [26]. As far as power supply of wireless sensor is concerned, high-energy battery still plays the key role nowadays, and solar energy seems to be another good choice because of its renewable capability [27].

Real-world application of wireless sensor system in civil engineering often falls behind the research work. A relatively early report around the world is the environment and behavior monitoring for a bridge in 1997 [7]. Another typical case in recent years is the monitoring of Golden Gate Bridge. There are totally 64 nodes distributed over the main span and the tower of the bridge [28]. By far, the largest wireless sensor network for the infrastructure monitoring purposes is the network on Jindo Bridge. To be specific, a total of 669 sensing channels with 113 sensor nodes have been deployed [29–32]. In China, a typical case is the health monitoring system developed for Jinmen Bridge, on which 64 wireless acceleration sensors have been installed [10]. Apart from that, a benchmark for tall buildings in recent years is the SHM system designed for Guangzhou Tower, which integrated large amount and various types of sensors and the wireless sensor technology [33, 34]. For large-span spatial structures, the Shenzhen Civilization Center and the Chinese National Aquatic Center (generally known as “Water Cube”) may be the two early cases reported as the application of SHM system. There are some wireless sensors involved in monitoring those two buildings while the fiber sensors are still the main monitoring instruments [11, 35]. Above all, the engineering applications of wireless sensors are still relatively simple, the type of sensors is commonly unitary, the amount of sensors is not very large, and the communication between sensor nodes does not actually require a large-scale complicated network yet.

In the case of a real large-area-scale structure as “Bird’s Nest,” the effective application of a wireless sensor network (WSN) involves such factors as the type of sensors used, the configuration and topology of the monitored structure, and the nature of the instrumentation network. There is no doubt that a customized multitype wireless sensor network for the structure of “Bird’s Nest” is an urgent demand. In recent years, a great deal of research work has been performed on the WSN development. Most of the work focused on the multichannel conflict and time delay problem, which is

the key to the synchronization and efficiency of WSN [36–39]. On the other hand, there is rarely any report for a real-world application of WSN with large amount and type of sensors distributed in a super large-area-scale structure. For that kind of application, more importance should be attached to the stability, durability, and flexibility of WSN.

In this paper, a multitype wireless sensor network is developed aiming for monitoring structural and environmental parameters of the “Bird’s Nest.” The system takes multitype sensors as measurement components including stress, displacement, acceleration, wind, and temperature. The communication between each node is realized by using an adjustable and artificial control chain-type network, and the collected data is transferred via a specified path from the sensor node to the server on site. This paper mainly focuses on the WSN development and engineering application. It is organized as follows. Section 2 presents the research of the hardware design, particularly vibrating wire sensors. Section 3 focuses on the development and application of the network on the “Bird’s Nest.” Section 4 briefly discusses the monitoring data during one year. Finally, a summary of the work is given in Section 5.

2. Hardware Design

Considering the structural features of “Bird’s Nest” and its on-site environment, a multitype wireless sensor network for structural and environmental parameters monitoring is developed. The system takes multitype sensors as measurement components including stress, displacement, acceleration, and wind and temperature sensors, and has in total 290 sensors distributed in the entire building.

2.1. Layout of Wireless Sensor System. The key principles behind the hardware design of wireless sensors for SHM applications are functional modularity, energy efficiency, measurement accuracy, configuration flexibility, and network extensibility. The functional design of the hardware usually consists of four aspects: data acquisition, digital wireless communication, embedded microprocessing, and power management [15–17]. The realization of all four functions is based on several modules, namely, the power management (PM), radio frequency (RF), microcontrol unit (MCU), static RAM (SRAM), and multitype sensing (MTS) modules. Using low-voltage and low-power microchips and integrating proper energy management strategy, the battery-powered wireless sensor units can be operated for extended lifespan. By using various sensors, amplifier circuits and ADCs, different parameters and different levels of measurement range can be switched within several boards. By using an independent RF module, several different wireless network topologies and protocols can be implemented without affecting other circuit units and configurations. Figure 3 illustrates the architecture of the hardware design of the wireless sensor, the RF and MTS modules are actualized in two independent boards, and the other modules are integrated into another single board. The integrated wireless sensor unit using three printed circuit boards (PCB) is shown in Figure 4.

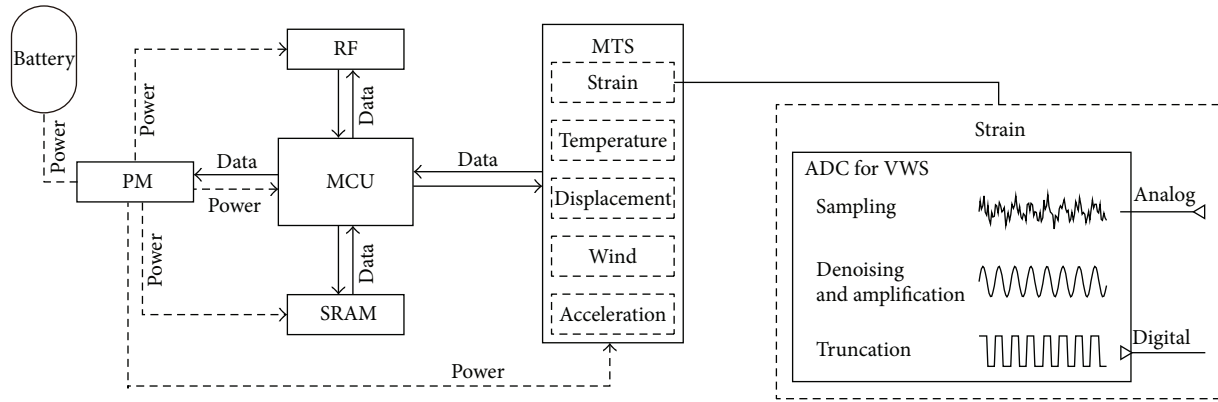


FIGURE 3: Hardware architecture of wireless sensor unit.

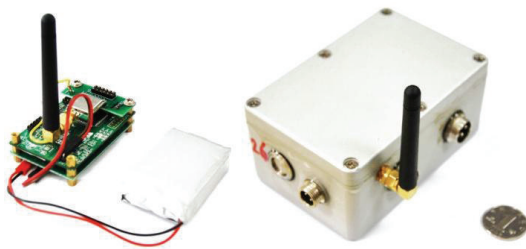


FIGURE 4: Picture of wireless sensor unit.

The function of the MTS module is to measure physical parameters in the network. Various types of sensors with different measurement circuits can be selected for different applications. There are totally four kinds of boards with five parameters sensing can be selected: a digital displacement measurement board, a high-accuracy digital acceleration measurement board, a digital wind speed and direction measurement board, and a vibrating wire sensor board with A/D converter. The temperature sensing module is integrated together with the VWS board. Various MTS modules will be discussed in detail in the following section.

The MCU module has a core of the microchip from Atmel's low-power AVR family. The AVR core combines a rich instruction set with 32 general-purpose working registers. The architecture is code efficient while achieving throughputs up to ten times faster than conventional CISC microcontrollers. By executing instructions in a single clock cycle, such MCU achieves throughputs approaching 1 MIPS per MHz, allowing the system designer to optimize power consumption versus processing speed. Another characteristic of the MCU is that several sleep modes (idle, ADC noise reduction, power-down, power-save, standby, or extended standby) can be used to reduce the total energy consumption.

The function of the PM module is to manage the power supply to other modules. With a low-dropout voltage regulator, TPS7333, the input power in a scope of low voltage like 3.7 V to 9.0 V can be regulated to a suitable output one like 3.5 V for the entire system.

The SRAM module is a temporary data storage that can save the monitoring data up to 4k bytes. It will be automatically cleared every time before sampling. The static

RAM also can be replaced with another memory card for different requirement.

The very last module is the RF module. As mentioned above, the RF module can be separated from the other modules physically and logically. Such feature enables the network topology and protocol to be separated from other modules and to be easily upgraded to other advanced communication techniques in the future without significantly changing other modules. The selection of the RF module depends on the needs and features of engineering application. For "Bird's Nest," the measurement field environment is similar to a 70,000 square meters forest consisting of thousands of steel trees about 1 meter in diameter. It requires that the signal of RF module has the ability of being unaffected by these obstacles and covering a suitable large area. The current RF daughter board with plane dimension 18 mm × 20 mm uses the 2.4 GHz IEEE 802.15.4/ZigBee-ready RF Transceiver CC2420 from Chipcon Semiconductor. The microchip is designed for low-power and low-voltage wireless applications. It includes a digital direct sequence spread spectrum base-band modem providing a spreading gain of 9 dB and an effective data rate of 250 kbps. The transmission distance can easily reach 100 meters long in the field environment, which is required to be longer than the roof width.

2.2. Multitype Sensing Module. The MTS module includes several different types for different kinds of sensors: VWS module for stress and temperature measurement, acceleration module, wind module for wind speed and direction measurement, and displacement module, as shown in Figure 5. Basically all sensors are commercial products with digital signal output that can be obtained directly without ADC. The VWS is an exception, which needs a specified analog circuit for excitation and picking up the signal.

For unified network control, the frequency and time of sampling is usually predetermined according to different types of sensors. It also can be adjusted by users anytime for different requirement. Description for each type of MTS modules will be given one by one below in this section.

2.2.1. Stress and Temperature Measurement. The VWS is used as the measurement component for the MTS module

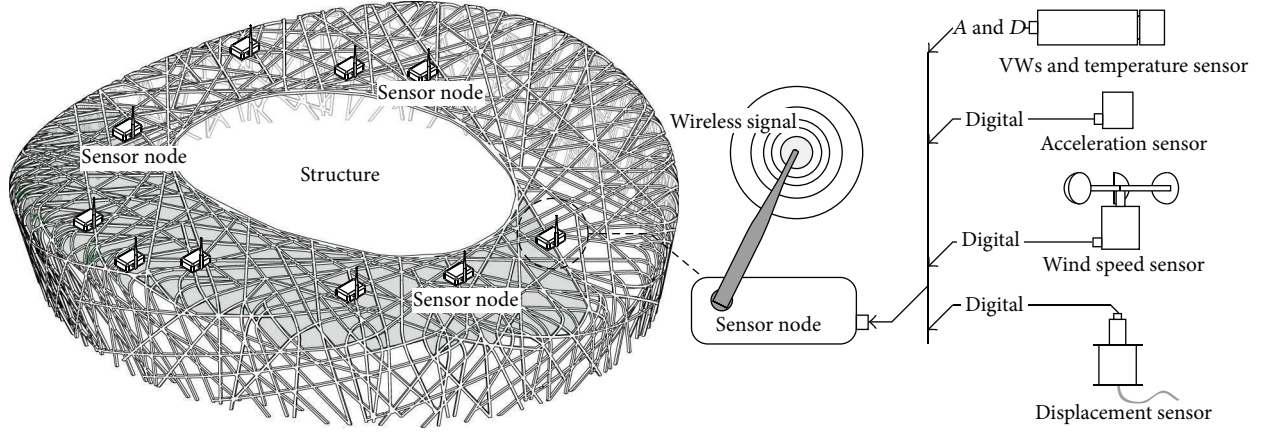


FIGURE 5: Multitype sensors for different measurements.

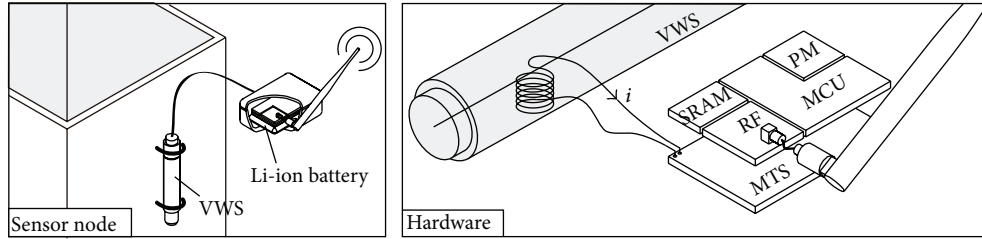


FIGURE 6: VWS node hardware.

development. The function of the module is to measure strain and temperature parameters. There are four channels in the sensor board, and the basic working principle of each channel is identical.

In recent years, the VWS is commonly used for long-term strain measurement because of its stable, durable, and antielectromagnetic properties. It is small, cheap, easily manufactured, and can be packaged in a suitable size. For steel structural health monitoring, the VWS is generally affixed to the surface of the measured component, which would not affect the quality of the structure itself.

As Figure 6 shows, major components of a VWS include a vibrating wire whose frequency changes in response to tension and compression and a plucking and pickup coil which excites the wire and measures its resonance frequencies. A certain kind of fixtures welded on the steel surface can transfer the tension and compression to VWS. A sensor node can take 4 VWSs and be fixed on the measured components.

An analog signal of electric current i generated from VWS to the MTS module contains the information of wire vibration, which can be expressed as

$$\begin{aligned} i(t) &= I(t) + i'(t), \\ I(t) &= I_m \sin(2\pi ft), \end{aligned} \quad (1)$$

where I is the fundamental frequency component of the signal; i' is all other frequency components of the signal; and

f is the fundamental frequency of the signal, the same as of the wire. The strain of VWS can be expressed as

$$\varepsilon = f^2 L^2 \frac{4\rho}{EG}, \quad (2)$$

where L is the wire length; ρ is the mass density of the wire; E is Young's modulus; and G is gravitational acceleration. Once transferred to the MTS module, the signal i will be processed by a precise circuit and filtered down to a sine signal I , as shown in Figure 3. Finally, a square voltage signal U could be obtained with the same frequency as I as follows:

$$U(t) = \begin{cases} \text{HIGH}, & \frac{k}{f} \leq t < \frac{k}{f} + \frac{1}{2f}; \\ \text{LOW}, & \frac{k}{f} + \frac{1}{2f} \leq t < \frac{k}{f} + \frac{1}{f}; \end{cases} \quad (k = 0, 1, 2, \dots). \quad (3)$$

When signal U has been sent into MCU via the digital input capture pin, the value of f can be calculated, and the strain data is obtained accordingly.

For temperature measurement and compensation, a digital temperature chip is integrated in the VWS sensor. The chip DS18B20 produced by DALLAS company is selected, which has tiny size and is easily packaged. The measurement range is from -55°C to 125°C and the precision is 0.0625°C . It is simply digital signal output with 2 bytes and occupies only one pin of the MCU. All features of the chip greatly satisfy

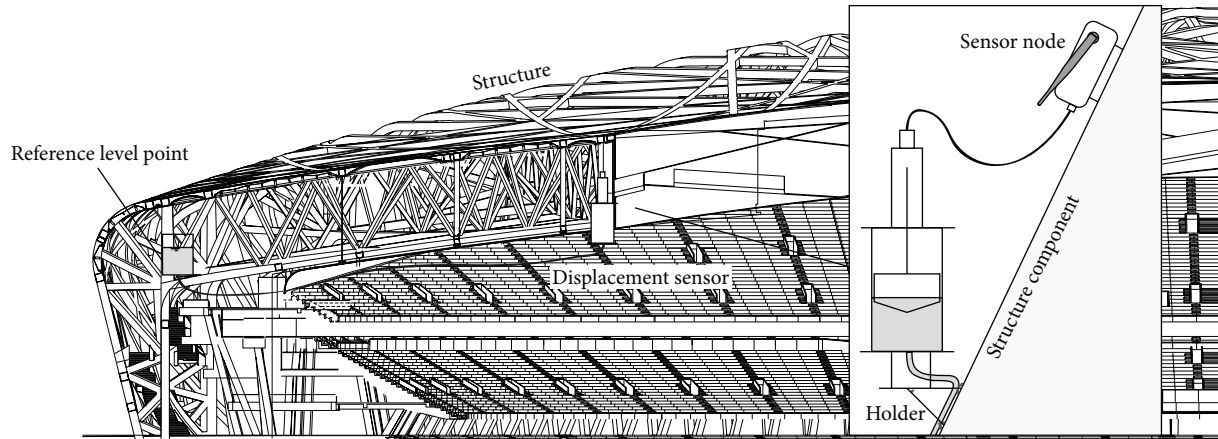


FIGURE 7: Working principle of displacement measurement device.

the requirement of multinodes and distant measurement for “Bird’s Nest.”

2.2.2. Displacement Measurement. The basic working principle of the displacement measurement is that an inductance-sensitive element moves back and forth in an LC oscillator, which causes a change of signal output. To put in details, take a long and slim iron core as the inductance-sensitive element and integrate a solenoid coil in a steel pipe, the magnetic resistance and inductance of coil will be changed when the iron core moves back and forth in the pipe, and the output signal produced by a frequency modulation circuit will be changed accordingly. With proper architecture, material, and manufacture, the frequency of the signal could keep great linear relationship with the displacement value of the iron core in pipe; then the displacement measurement could become available accordingly.

The measurement part of the displacement sensor is a commercial product. Via an integrated ADC module, the output is also converted to a simply digital signal with 2 bytes.

For “Bird’s Nest,” the vertical displacement at cornice location is probably the maximum and main concern. The direct measurement to the vertical displacement is not available because there are no adjacent static points taken as the reference. Thus, a device for vertical displacement measurement of the cornice is designed based on liquid communicating principle. The vertical displacement value could be obtained by measuring the change of liquid level in a special tube-shape container. As shown in Figure 7, the vertical displacement value is relative to a reference static point. The container is put in the measuring point and filled with appropriate amount of liquid. A box full of liquid is put in a reference static point like the top of the column, which is connected with a slim pipe to the container. When a displacement occurs in the measuring point, the liquid will flow in the pipe to keep the new balance of the liquid level. The height change of the liquid level in the container is equal to the vertical displacement. A displacement sensor is installed in the device, and the sensitive element iron core is fixed on the buoy which moves along with the liquid level in the container.

2.2.3. Wind Speed Measurement. The wind velocity and direction sensor is also commonly commercial. The wind velocity could be obtained by calculating the cycles of the wind cup in unit time, and the wind direction could be learned by the vane on the sensor. The digital output signal can be read directly by the MTS module, which consists of 2 bytes 16 bits for velocity and 2 bytes 16 bits for direction.

2.2.4. Acceleration Measurement. A three-axes digital output linear accelerometer (LIS3LV02DQ) is selected for measurement. It includes a sensing element and an IC interface that can take the information from the sensing element and provide the measured acceleration signals to the external world through an I²C/SPI serial interface. The LIS3LV02DQ has a user selectable full scale of $\pm 2g$, $\pm 6g$ and it is capable of measuring acceleration over a bandwidth of 640 Hz for all axes. The device bandwidth may be selected according to the application requirements. For the application on “Bird’s Nest,” the scale of $\pm 2g$ and the bandwidth of 50 Hz are selected, which can satisfy the requirement greatly.

2.3. Sampling Principle. To implement the artificial control chain-type network, a series of custom protocols are developed. The communication packet is set to a length of 64 bytes, including ID of the sensor node, the piconet number, the command type, as shown in Figure 8. The length of data array is defined with 52 bytes considering the requirements of all kinds of MTS modules.

For energy saving, each sensor node is in sleep mode at usual time and wakes up itself for one second at a specified cycle. So if a wakeup command is kept sending to a node, it will be woken up from the sleep mode entirely.

Considering the optimization of a command, the frequency and time for each sampling operation are normally predetermined to different types of sensors. For the application of “Bird’s Nest,” the time and frequency of VWS are 30 seconds and 0.1 Hz, respectively. Similarly, time and frequency are 10 seconds and 50 Hz for acceleration sensor, 10 seconds and 10 Hz for wind speed sensor, and 5 seconds and 1 Hz for displacement sensor.

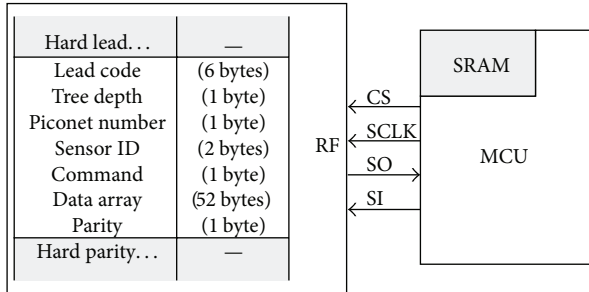


FIGURE 8: Protocol and format of signal in sensor nodes.

3. Wireless Sensor Network

For an appropriate WSN development, such factors as the structural feature and shape, the sensor nodes distribution, the objective of measurement, and the performance of the sensor nodes used should be considered for effectiveness.

The shape of “Bird’s Nest” on plan view is literally an elliptical ring with the outer diameter of 332 meters on north-south direction and 297 meters on east-west, and the inner diameter is 183 meters and 127 meters, respectively, as shown in Figure 2. There are a total of 98 sensor nodes including 290 different types of sensors distributed in the entire structure mostly on several typical main trusses. The transmission distance of the RF module used is designed to reach about 150 meters, which means that each node can satisfy the requirement of covering the circle area from column to cornice. So a chain-type network topology is most suitable for this engineering application. Considering the requirement for synchronism is not of emphasis while the robustness is, the working mechanism of the network is most basically designed as adjustable and artificial control. In conclusion, the communication between each node is realized by using an adjustable chain-type network, and the collected data is transferred via several relay nodes from the sensor node to the server on site.

3.1. Distribution of Multitype Sensors. The entire steel structure of “Bird’s Nest” is composed of 24 main trusses with large amounts of subtrusses connected to each other. Each main truss consists of two-layer square-section steel tubes, which can be divided into four types in detail: upper-layer tubes, lower-layer tubes, middle tubes, and column tubes. Considering the quantitative limitation of sensor nodes, several typical main trusses are selected for sensor placement. According to the structural mechanical behavior, the stress sensors are fixed mainly at the location of columns, corners, 1/4 span points, and 1/2 span points for all four types of tubes, as shown in Figure 9. The average size of the tube section is 1 m side length and 40 mm wall thickness. There are 2 or 4 VWSs fixed on the surface in each section, specifically 2 on upper-layer tubes and 4 on other tubes, which helps to learn the axial force and bending moment. Since the VWS sensor node is designed with 4 channels, one node for each section will satisfy the measuring requirement. The total amounts of sensors are 268 and the wireless nodes count 76 accordingly.

In total, there are 14 acceleration sensors distributed in the steel structure to test the response to the excitation of environment such as earthquake and audience noise. Altogether 4 wind velocity and direction sensors are placed at 4 cardinal points in four directions. And also there are 4 displacement sensor nodes fixed at the location of the cornice where the value of vertical displacement is probably the maximum.

The layout of all sensor nodes distribution is shown in Figure 10 and Table 1. Some pictures of installation in field are shown in Figure 11.

3.2. Artificial-Control Network Design. The network design usually follows a basic principle that all sensor nodes scattered in the sensor field collect data and route data back to the sink node [40]. For “Bird’s Nest,” the chief distinguishing features of the WSN are artificial-control and chain-type. As shown in Figure 12, the wireless sensor system consists of a sink node, several relay nodes, and a large amount of sensor nodes. The network topology is like a chain with each relay node acting as a chain unit connected one by one with each other. The entire chain-type network is separated into several star-type piconets by each relay node. In each piconet, the relay node acts as a parent node in charge of all sensor nodes as children. The piconet could be reorganized via dynamic address assignment. If some connections of sensor nodes to a relay node are weak while other connections are strong, a new route could be redefined by reassigning new addresses to the nodes, which means the relationship of the child node and the parent node will actually be changed. Therefore, the communication of the entire network will keep robust. The sink node is the root of the entire chain-type network and constitutes a base station with a field server together.

For optimizing the operation of each sampling, there are two ways selected for command sending from node to node, namely, broadcast and unicast, as shown in Figure 12. When a command is sent out in the broadcast way, all nodes in the signal area could receive it and decide whether to execute it or not. While the unicast way is chosen, there should be a destination address, and the command will be executed only by the specified node. In general, the broadcast way is only chosen to make the relay nodes wake up sensor nodes and command them to start sampling. When all other commands such as calling back the data or resigning the address are sent, the unicast way will be selected.

The node address is marked as two numbers like *.* since the chain-type network is a two-layer one. The first number indicates the relay node of the piconet and the second number represents the sensor nodes. For example, the ID address for the 27th sensor node in the third relay node’s piconet will be marked as 3.27. And the ID address for each relay node will be like *.0, as shown in Figure 12.

The communication could be realized via a specified route by assigning the addresses one by one. Considering that each node only communicates with specified nodes, the network efficiency can be improved greatly if the ID addresses of relative nodes are saved in each node. For example, the relay node will save the ID addresses of its previous relay node and the next one, and the sensor node will save the ID address

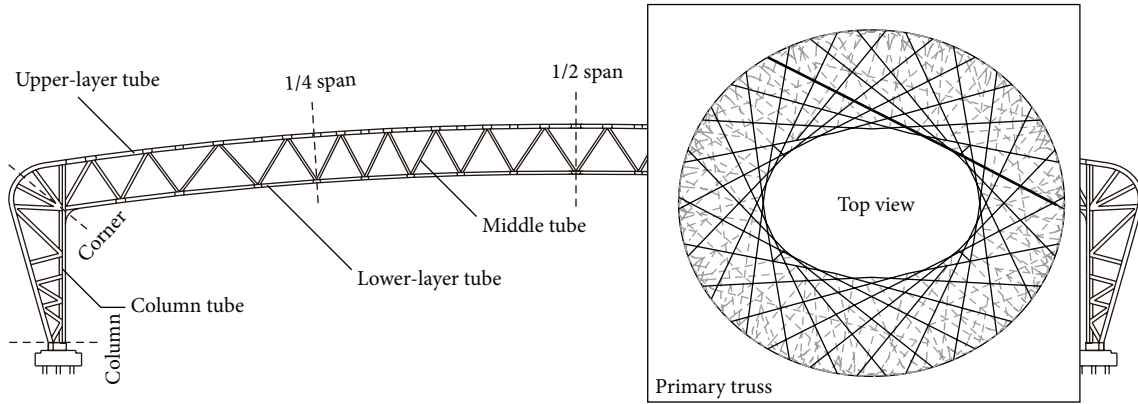


FIGURE 9: Structural components of a single main truss.

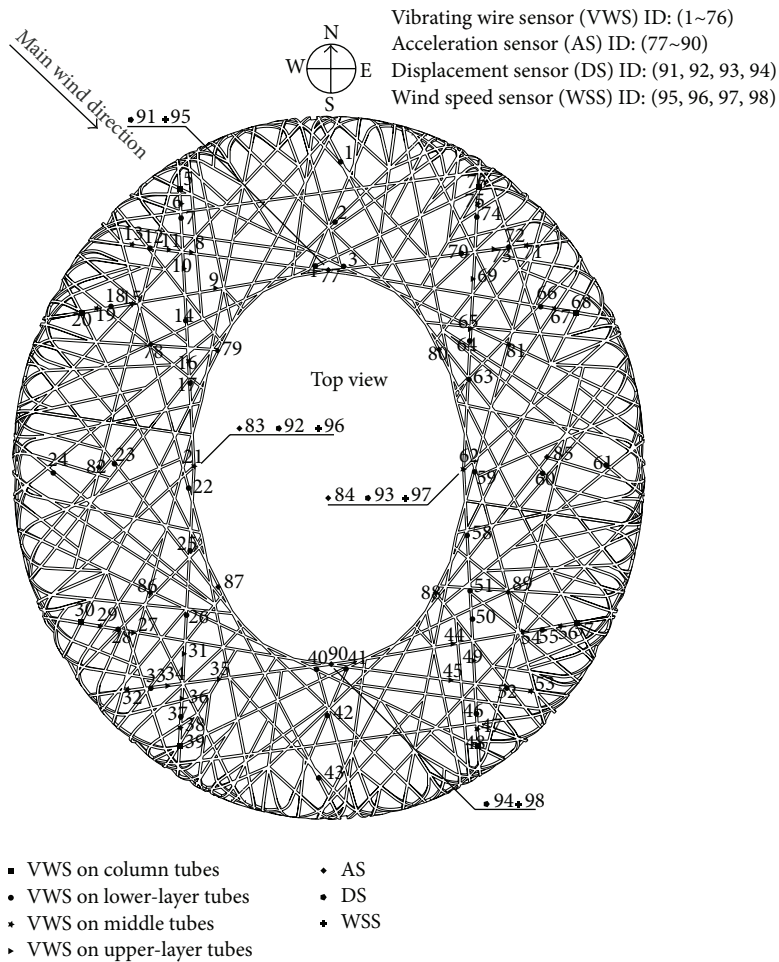


FIGURE 10: Layout of all sensor nodes distribution.

of its parent node, namely, the relay node of the same piconet.

Apparently relay nodes play an important role in the chain-type network. The network paralysis may happen due to the failure of one relay node especially the one at the head. For the sake of a robust network, two approaches have been

adopted. One is the backup of relay nodes, and the other is the switch of routing on reverse direction.

Backup of Relay Nodes. In order to improve reliability of the network, double relay nodes strategy is applied to service. One of the double relay nodes serves as the regular one,

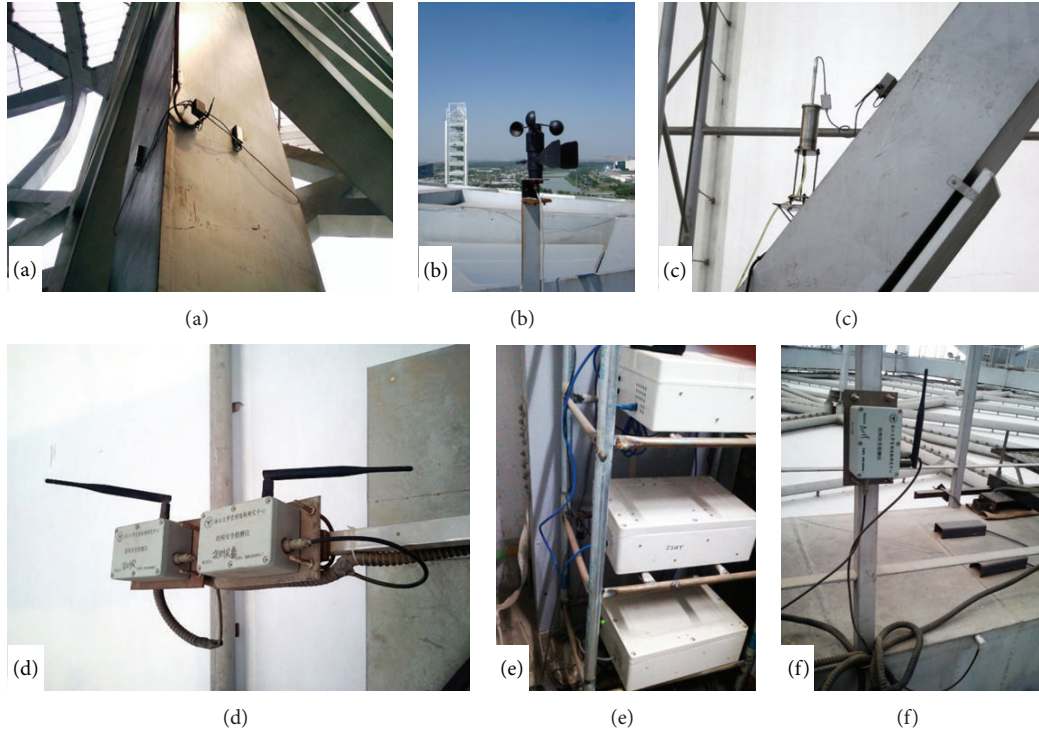


FIGURE 11: Pictures of sensor nodes installation: (a) VWS, (b) wind, (c) displacement, (d) relay nodes, (e) base station, and (f) acceleration.

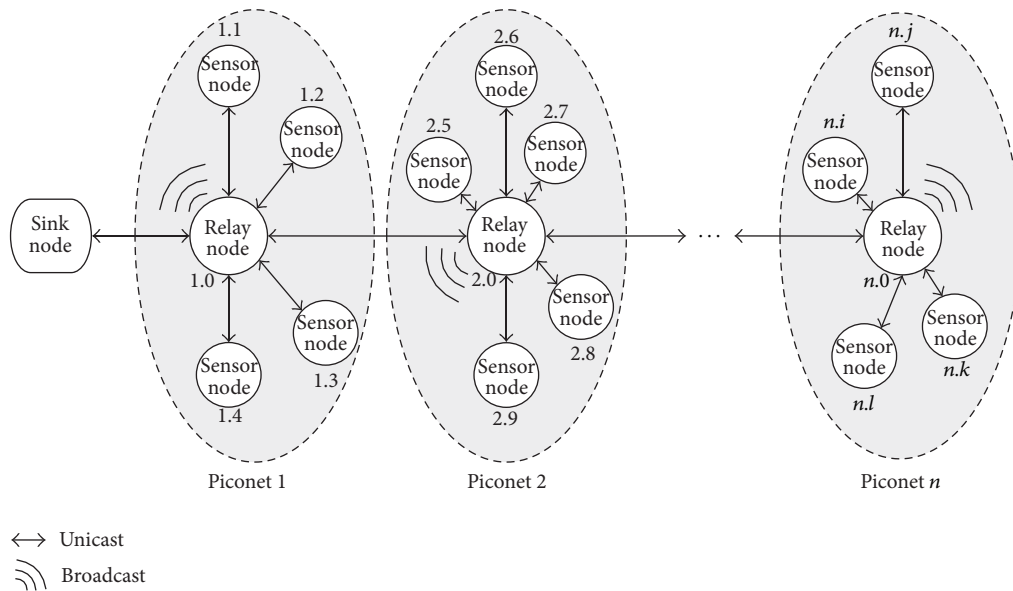


FIGURE 12: Topology of chain-type network.

and the other acts as a backup which is normally in a long-term sleep mode, as shown in Figure 13(a). When the regular one is broken, the backup could be woken up and taken over by modifying the ID address, as shown in Figure 13(b). Consequently, the robustness of the network can be secured.

Switch of Routing on Reverse Direction. In a chain-type network, if the last relay node is located in the signal scope

of the sink node, the entire chain will form a ring. The routing order could be switched into a new one on the reverse direction. This approach is very suitable for stadium buildings such as “Bird’s Nest” that has a ring shape on plan view.

Normally the chain-type network serves as regular way. When one of the relay nodes and its backup all have broken down, all relay nodes behind will switch their routing order and form another chain with the sink node, as

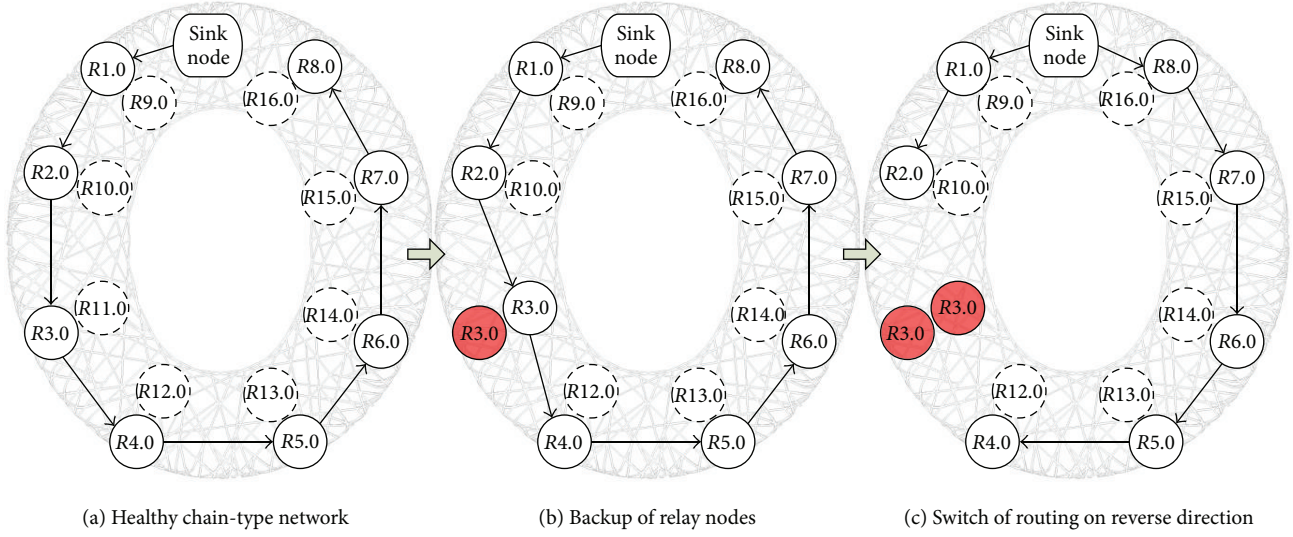


FIGURE 13: Robustness enhancement of the network.

TABLE 1: Distribution of sensor nodes on “Bird’s Nest.”

Sensor node type	Node number	Sensor amounts	Location
VWS and temperature	8, 9, 10, 11, 15, 16, 27, 31, 34, 35, 36, 44, 45, 49, 54, 65, 69, 73	36	Upper-layer tube
VWS and temperature	1, 2, 3, 4, 7, 12, 14, 17, 18, 22, 23, 24, 25, 26, 28, 33, 37, 40, 41, 42, 43, 46, 50, 51, 52, 55, 58, 59, 60, 61, 63, 64, 66, 70, 72, 74	144	Lower-layer tube
VWS and temperature	6, 13, 19, 21, 29, 32, 38, 47, 53, 56, 62, 67, 71, 75	56	Middle tube
VWS and temperature	5, 20, 30, 39, 48, 57, 68, 76	32	Column tube
Acceleration	77, 78, 79, 80, 81, 82, 83, 84, 85, 86, 87, 88, 89, 90	14	Lower-layer tube
Displacement	91, 92, 93, 94	4	Middle tube
Wind velocity and direction	95, 96, 97, 98	4	Upper-layer tube

shown in Figure 13(c). That means altogether two communication chains are set up to keep the system working except the piconet of the broken node. Therefore, the robustness of the network has been largely improved.

3.3. Application. In the case of “Bird’s Nest,” the structure has been divided into eight areas on plan view for eight piconets of the network. A relay node and a backup have been placed adjacently at the center of each area. As the root of the entire chain-type network, the sink node is in the middle of area 1 and area 8 on plan view. The field server device, a low-power industrial personal computer (IPC), receives data from the sink node. They constitute a base station together and can be controlled in various internet terminals. The base station is placed in an electrical room located on the upper level of the audience stands, which is below the steel roof and not so far from the first relay node. The layout of area division is displayed in Figure 14 and Table 2.

A graphical user interface (GUI) software has been developed for the utilization, as shown in Figure 15. All operations on WSN management including topology adjustment,

ID address reassignment, and sampling execution, could be artificially controlled.

Various internet terminals of SHM system have been set up for system controlling, data sampling, and results display. The main monitoring center is located in Zhejiang University, as shown in Figure 16(a).

At the main entrance of “Bird’s Nest,” there are also four exhibition screens displaying the statistics of the structure and environment with the latest graph. It serves as a view spot for visitors, as shown in Figure 16(b).

3.4. Workflow in Normal Process. For regular data sampling process, the first step is to wake up the relay nodes from 1.0 to 8.0 one by one by unicast way. If there is any one broken, the backup will be woken up to take over. For example, change the ID of 9.0 to 1.0. The second step is to wake up the sensor nodes and command them to start sampling in each piconet, respectively, by broadcast way. The broadcast will last 15 seconds for assurances of wakeup mode of all sensor nodes. After receiving the command of sampling, all sensor nodes start working at almost the same time. Various types of sensor

TABLE 2: Distribution of sensor nodes in eight areas.

Area number	Relay nodes (ID address)	VWS and temp. (ID address)	Acceleration (ID address)	Wind (ID address)	Displacement (ID address)
1	1.0, 9.0	1.1~1.13	1.77	1.91	1.95
2	2.0, 10.0	2.14~2.24	2.78, 2.79		
3	3.0, 11.0	3.25~3.34	3.82, 3.83	3.92	3.96
4	4.0, 12.0	4.35~4.43	4.86, 4.87		
5	5.0, 13.0	5.44~5.53	5.90	5.94	5.98
6	6.0, 14.0	6.54~6.62	6.88, 6.89		
7	7.0, 15.0	7.63~7.68	7.84, 7.85	7.93	7.97
8	8.0, 16.0	8.69~8.76	8.80, 8.81		

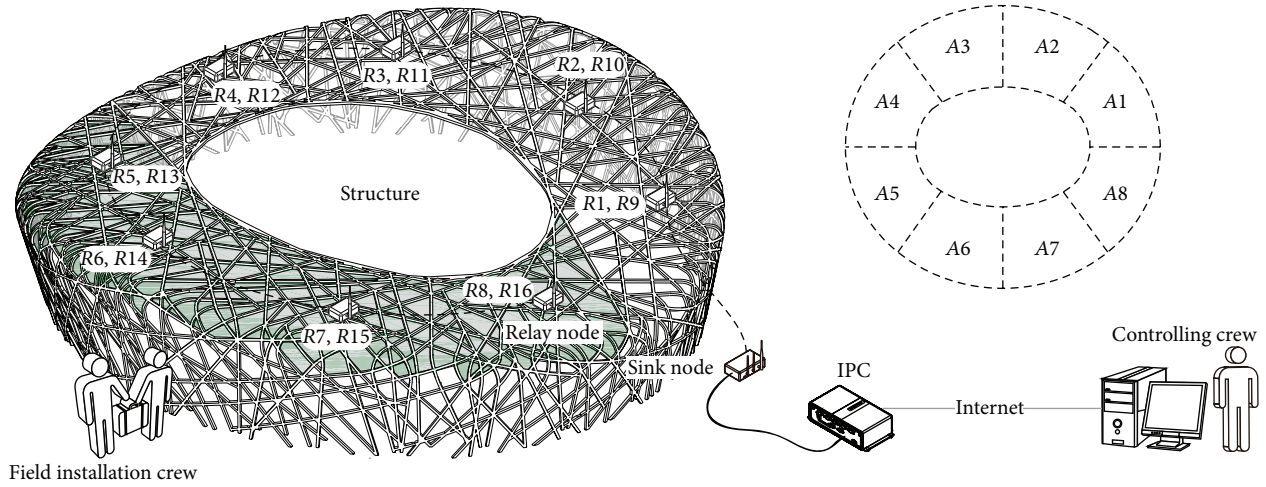


FIGURE 14: Layout of area division for chain-type network.

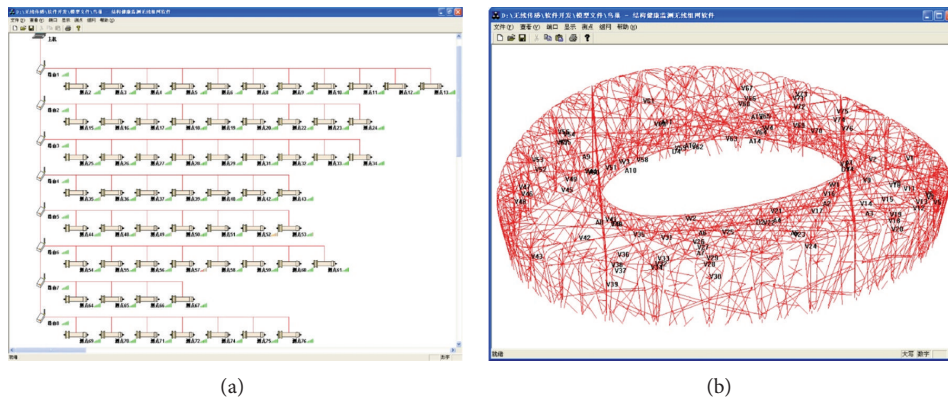


FIGURE 15: GUI software.

nodes work by specified time and frequency, respectively, and the data are saved in their SRAMs automatically. The third step is to call back the data from the sensor nodes one by one through unicast way in each piconet. The sensor nodes will be altered back to sleep mode as soon as the data has been transferred. The last step is to turn the relay node into sleep mode one by one from 8.0 to 1.0. Then, an entire work process is completed, which usually lasts 10 minutes for such scale of

a network. The work process can be artificially controlled or automatically repeated according to monitoring requirement.

4. Monitoring Data during One Year

A total of 290 sensors were installed on the stadium structure, collecting data via the WSN for more than one year. Huge amount of data have been obtained, including all kinds



FIGURE 16: Various Internet terminals of SHM system. (a) The monitoring center in Zhejiang University. (b) The exhibition screen for visitors in field.

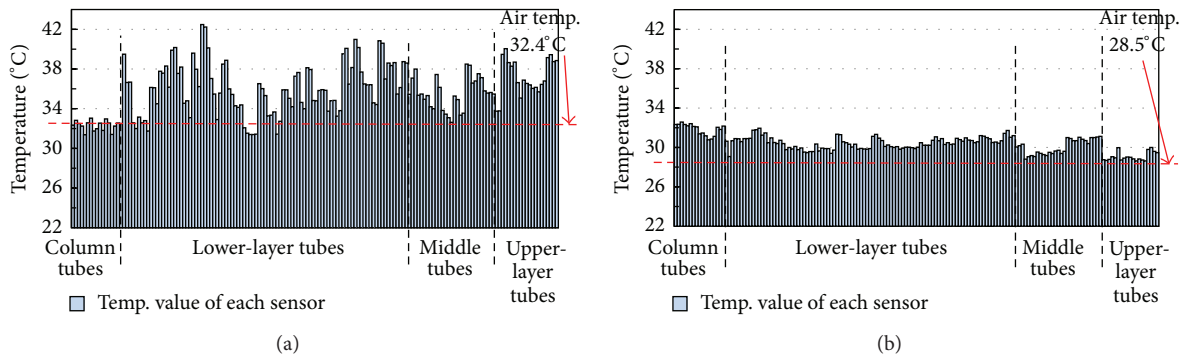


FIGURE 17: Hour-average temperature of each sensor at one hot summer day. (a) Hour-average temperature of each sensor at 14:00. (b) Hour-average temperature of each sensor at 00:00.

of parameters such as strain, temperature, displacement, acceleration, and wind. Take the data from May 1, 2011 to May 1, 2012 as examples, and the analysis work is briefly discussed in this section.

Data analysis results indicate that such super large-scale steel structure as “Bird’s Nest” is not as tough as imagined and it is very sensitive to the temperature effect. To be specific, the stress and displacement variation of the structure are correlated with the temperature. Comparatively, the wind and vibration parameters did not show particular features, so they are only briefly discussed.

4.1. Temperature. In structural analysis work on temperature effect, normally only the annual range of temperature is considered. For a specific time, the environment of an entire structure is always considered as a unified temperature field. Take the monitoring data of one hot summer day like July 17th for example. It is obvious that the structural temperature of different locations at 2:00 PM is very different from the official data of 32.4°C, as shown in Figure 17(a). Most measuring points on beams have much higher temperature due to the direct sunlight. Only points on columns are consistent with air temperature because all of them are in shadow. While at midnight, the structural temperatures of all measuring points are relatively average but still a little higher than air temperature, as shown in Figure 17(b).

4.2. Stress to Temperature. The giant “Bird’s Nest” consists of large amounts of steel tubes whose square-section measure 1 meter in side length and 40 mm in wall thickness. Supposedly, it is very rigid and can hardly be affected by conventional static loads. However, to the temperature effect, the rigidity is commonly not a beneficial factor on structural behavior. The monitoring data during one year also shows that the structure is very sensitive to temperature variation. As shown in Figure 18, take four measuring points on columns, upper-layer tubes, middle tubes and lower-layer tubes, respectively, as examples. Obviously the stress variation is related to the temperature value, and the maximum value of the entire structure could be more than 25 MPa.

4.3. Displacement to Temperature. Deformation of the structure is basically a reflection of stress distribution. From the measuring data of the displacement on cornice, it turns out that the expansion and contraction of the structure somewhat resemble the “breathing” pattern. In Figure 19, take the measuring point 1.95 of north cornice for example; the displacement value is also mainly related to the temperature variation. Specifically, the cornice moves up when the temperature increases, and the change rate is about 2.5 mm per degree Celsius.

4.4. Vibration to Performances. The acceleration data did not show particular features during regular hours. Only at

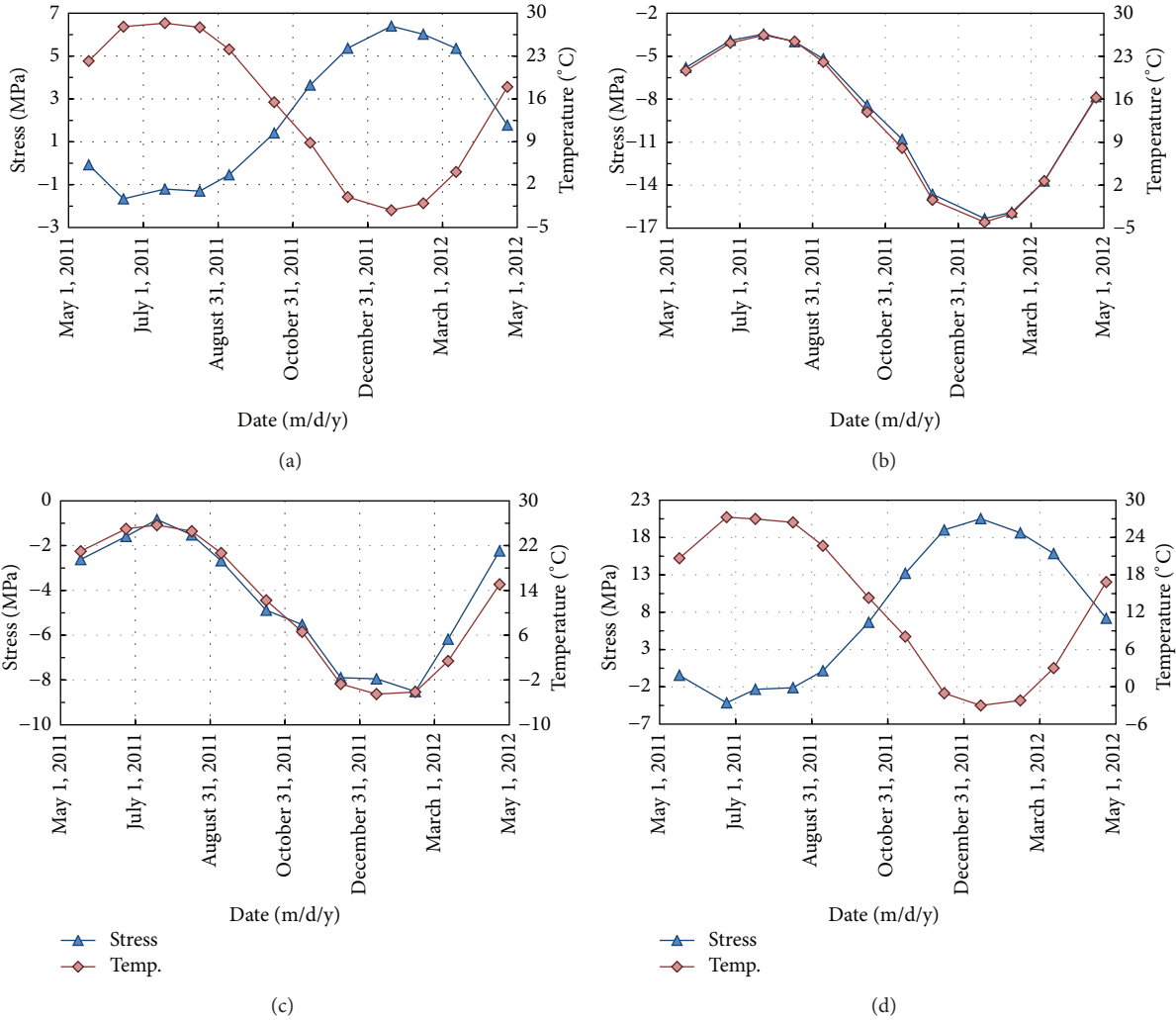


FIGURE 18: Stress variation to temperature effect during one year. (a) Sensor node 20 channel 4 at column tube. (b) Sensor node 56 channel 3 at middle tube. (c) Sensor node 8 channel 2 at upper-layer tube. (d) Sensor node 14 channel 1 at lower-layer tube.

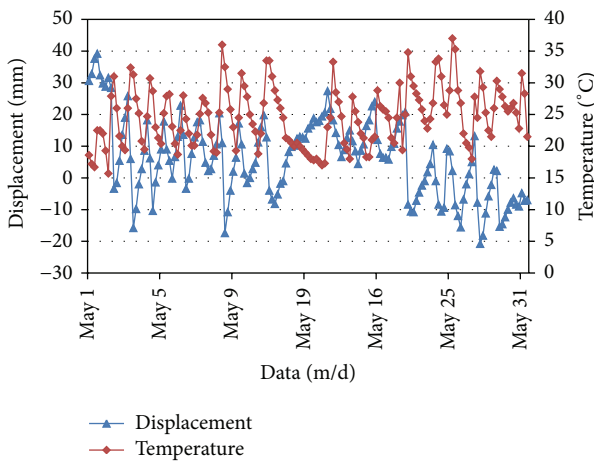


FIGURE 19: Displacement variation to temperature effect during one month.

the time of performances, the structure responds to the excitation from the audience and show. Take the data of sensor node 2.78 on April 16, 2012, for example, when there

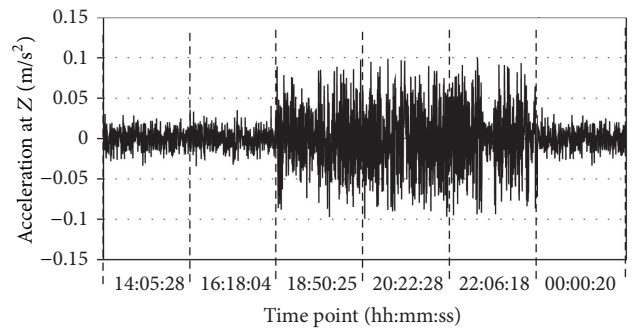


FIGURE 20: Acceleration of node 2.78 on a performance day.

is a large concert performing from 18:00 to 23:00, as shown in Figure 20, six different time points of sampling data were displayed together, and it is obvious that the structure has stronger vibration during the performance time.

4.5. *Wind Velocity and Direction.* The data of wind velocity and direction is also an integrated part of the whole monitoring database and displayable outcome on site. It helps

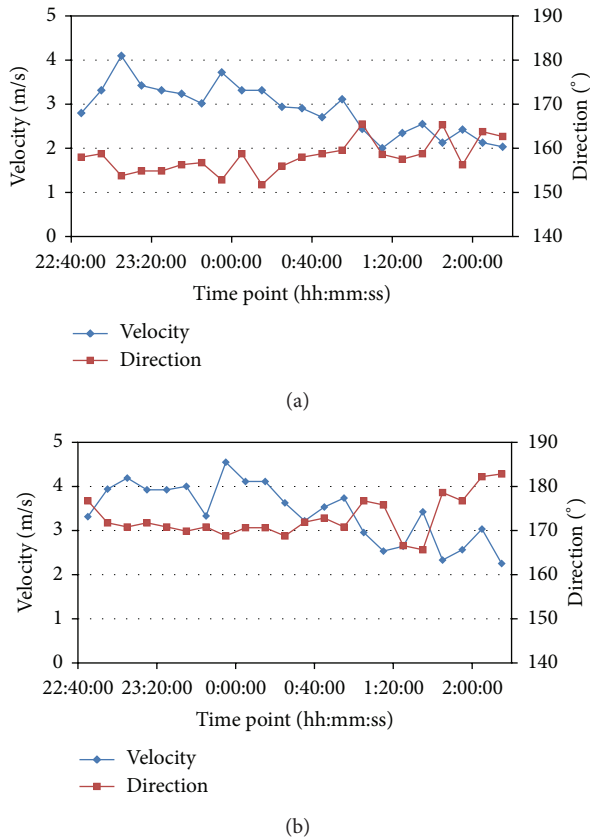


FIGURE 21: Wind velocity and direction variation during 220 minutes on September 16, 2012. (a) Wind velocity and direction variation of node 1.91. (b) Wind velocity and direction variation of node 5.94.

managers and visitors to learn the latest wind load well. Take the data of node 1.91 and 5.94 on a random date like September 16, 2012, for example, 22 times of continuous data sampling during 220 minutes are displayed in Figure 21, and the direction is indicated via the wind angle in anticlockwise direction off the north. It turns out that the wind velocity and direction at different locations of the structure are not the same due to the effect from the building itself.

5. Conclusion

The national stadium of China, generally known as “Bird’s Nest,” is deemed to be the symbol of super large-span structures in China. The integrated design and implementation of SHM systems for such an important civil infrastructure is very innovative and full of challenge. This paper introduces the development and application of a robust and efficient wireless sensor network system toward the structure. Taking the instrumented “Bird’s Nest” as a testing ground, the authors hope to generalize certain norms for health monitoring of large-area-scale structures and narrow the gap between research and application. With the case study completed, some conclusions and recommendations are summarized as follows.

- (1) To meet the monitoring requirement of the “Bird’s Nest,” the system takes multitype sensors as measurement components including stress, displacement, acceleration, wind, and temperature. In terms of hardware functional design, five modules are involved, namely, PM, RF, MCU, SRAM, and MTS. Advantages of such hardware includes (a) independent MTS module designed for multitype sensors in the same network; (b) rapid installation and low cost; (c) stable and accurate sensor measurement.
- (2) Stability and durability are mainly considered on the WSN development for real-world application of such a super large-scale structure. The customized WSN has several features as follows: adjustable chain-type topology, artificial control work mechanism, and robustness enhancement. It has been proved that the network well satisfies the requirement of plenty multitype sensors working in a large-area distribution, and the data collection work has been carried out for more than 1 year up to now.
- (3) The data analysis results reveal that the super large-scale steel structure is not as tough as supposed and it is very sensitive to the temperature effect. The variation of the deformation and stress are very relative to the temperature value, and the entire structure of “Bird’s Nest” is expanding and contracting as if it were breathing.

Acknowledgments

The authors are grateful to the National Stadium Co., Ltd. for the financial support. The work described in this paper was also supported by the National Key Technology R&D Program (2012BAJ07B03), National Science Foundation of China (Grant no. 51178415), Qianjiang Scholar Foundation of Zhejiang province (2013R10038), and the Scientific Research Foundation for the Returned Overseas Chinese Scholars, State Education Ministry.

References

- [1] D. Shi-lin, L. Yao-zhi, and Z. Yang, “The practice and development of large span space structures,” *Space Structures Symposium in China*, vol. 11, pp. 1–10, 2005 (Chinese).
- [2] Z.-D. Xu, M. Liu, Z. Wu, and X. Zeng, “Energy damage detection strategy based on strain responses for long-span bridge structures,” *Journal of Bridge Engineering*, vol. 16, no. 5, pp. 162–171, 2011.
- [3] Z.-D. Xu and W. Zhishen, “Simulation of the effect of temperature variation on damage detection in a long-span cable-stayed bridge,” *Structural Health Monitoring*, vol. 6, no. 3, pp. 177–189, 2007.
- [4] Z.-D. Xu and K.-Y. Wu, “Damage detection for space truss structures based on strain mode under ambient excitation,” *Journal of Engineering Mechanics*, vol. 138, no. 10, pp. 1215–1223, 2012.
- [5] T.-H. Yi and H.-N. Li, “Methodology developments in sensor placement for health monitoring of civil infrastructures,”

- International Journal of Distributed Sensor Networks*, vol. 2012, Article ID 612726, 11 pages, 2012.
- [6] T. H. Yi, H. N. Li, and X. D. Zhang, "Sensor placement on Canton Tower for health monitoring using asynchronous-climb monkey algorithm," *Smart Materials and Structures*, vol. 2, no. 12, pp. 1–12, 2012.
 - [7] K. R. Maser, R. Egri, A. Lichtenstein, and S. Chase, "Development of a wireless global bridge evaluation and monitoring system (WGBEMS)," in *Proceedings of the Speciality Conference on Infrastructure Condition Assessment: Art, Science, Practice*, pp. 91–100, August 1997.
 - [8] J. T. Kim, Y. S. Ryu, and C. B. Yun, "Vibration-based method to detect prestress-loss in beam-type bridges," in *The International Society for Optical Engineering*, vol. 5057 of *Proceedings of the SPIE*, pp. 559–568, 2003.
 - [9] A. J. Cardini and J. T. DeWolf, "Long-term structural health monitoring of a multi-girder steel composite bridge using strain data," *Structural Health Monitoring*, vol. 8, no. 1, pp. 47–58, 2009.
 - [10] S. Kim, S. Pakzad, D. Culler et al., "Health monitoring of civil infrastructures using wireless sensor networks," in *Proceedings of the 4th International Conference on Information Processing in Sensor Networks (IPSN '07)*, pp. 254–263, April 2007.
 - [11] J. Teng, Y. H. Zhu, W. Lu, and Y. Q. Xiao, "The intelligent method and implementation of health monitoring system for large span structures," in *Proceedings of the 12th International Conference on Engineering, Science, Construction, and Operations in Challenging Environments—Earth and Space*, pp. 2543–2552, March 2010.
 - [12] H. Li and J. Ou, "Full implementations of structural health monitoring systems for long-span bridges and large-span domes," in *The International Society for Optical Engineering*, vol. 6176 of *Proceedings of SPIE*, March 2006.
 - [13] E. G. Straser and A. S. Kiremidjian, "A modular visual approach to damage monitoring for civil structures," in *Smart Structures and Materials*, vol. 2719 of *Proceedings of SPIE*, pp. 112–122, February 1996.
 - [14] E. G. Straser and A. S. Kiremidjian, "A modular, wireless damage monitoring system for structures," Tech. Rep. 128, The John A. Blume Earthquake Engineering Center, 1998.
 - [15] E. G. Straser, A. S. Kiremidjian, T. H. Meng, and L. Redlfsen, "A Modular, wireless network platform for monitoring structures," in *The International Society for Optical Engineering*, vol. 3243 of *Proceedings of SPIE*, pp. 450–456, February 1998.
 - [16] A. S. Kiremidjian, E. G. Straser, T. H. Meng et al., "Structural damage monitoring for civil structures," in *Proceedings of the International Workshop-Structural Health Monitoring*, pp. 371–382, 1998.
 - [17] J. P. Lynch, K. H. Law, A. S. Kiremidjian et al., "The design of a wireless sensing unit for structural health monitoring," in *Proceedings of the 3rd International Workshop on Structural Health Monitoring*, pp. 1041–1050, Stanford, Calif, USA, 2000.
 - [18] J. P. Lynch and K. J. Loh, "A summary review of wireless sensors and sensor networks for structural health monitoring," *Shock and Vibration Digest*, vol. 38, no. 2, pp. 91–128, 2006.
 - [19] R. A. Swartz, D. Jung, P. J. Lynch, Y. Wang, D. Shi, and M. P. Flynn, "Design of a wireless sensor for scalable distributed in-network computation in a structural health monitoring system," in *Proceedings of the 5th International Workshop on Structural Health Monitoring*, pp. 12–14, Stanford, Calif, USA, September 2005.
 - [20] S. Cho, C.-B. Yun, J. P. Lynch, A. T. Zimmerman, B. F. Spencer Jr, and T. Nagayama, "Smart wireless sensor technology for structural health monitoring of civil structures," *Steel Structures*, vol. 8, no. 4, pp. 267–275, 2008.
 - [21] R. C. Liu, L. Zhou, X. Chen, and S. T. Mau, "Wireless sensors for structural monitoring," in *Strong Motion Instrumentation for Civil Engineering Structures*, pp. 253–266, Kluwer Academic Publishers, Dordrecht, The Netherlands, 2001.
 - [22] Y. Yu and J. Ou, "Development of a kind of multi-variable wireless sensor for structural health monitoring in civil engineering," in *Smart Structures and Materials, Sensors and Smart Structures Technologies for Civil, Mechanical, and Aerospace Systems*, M. Tomizuka, Ed., vol. 5765 of *Proceedings of SPIE*, pp. 158–166, 2005.
 - [23] L. Yaozhi, S. Yanbin, W. Bin et al., "Development of a wireless sensor system potentially applied to large-span spatial structures," in *Proceeding of the 4th China-Japan-US Symposium on Structural Control and Monitoring*, Hangzhou, China, October 2006.
 - [24] J.-H. Park, J.-T. Kim, D.-S. Hong, D. Mascarenas, and J. P. Lynch, "Autonomous smart sensor nodes for global and local damage detection of prestressed concrete bridges based on accelerations and impedance measurements," *Smart Structures and Systems*, vol. 6, no. 5–6, pp. 711–730, 2010.
 - [25] J.-T. Kim, J.-H. Park, D.-S. Hong, and D.-D. Ho, "Hybrid acceleration-impedance sensor nodes on Imote2-platform for damage monitoring in steel girder connections," *Smart Structures and Systems*, vol. 7, no. 5, pp. 393–416, 2011.
 - [26] H. M. Lee, J. M. Kim, K. Sho, and H. S. Park, "A wireless vibrating wire sensor node for continuous structural health monitoring," *Smart Materials and Structures*, vol. 19, no. 5, 2010.
 - [27] D. D. Ho, P. Y. Lee, K. D. Nguyen et al., "Solar-powered multi-scale sensor node on Imote2 platform for hybrid SHM in cable-stayed bridge," *Smart Structures and Systems*, vol. 9, no. 2, pp. 145–164, 2012.
 - [28] S. Kim, S. Pakzad, D. Culler et al., "Health monitoring of civil infrastructures using wireless sensor networks," in *Proceedings of the 6th International Symposium on Information Processing in Sensor Networks (IPSN '07)*, pp. 254–263, April 2007.
 - [29] C. B. Yun, H. Sohn, H. J. Jung, B. F. Spencer, and T. Nagayama, "Wireless sensing technologies for bridge monitoring and assessment," in *Proceedings of the 5th International Conference on Bridge Maintenance, Safety and Management, Bridge Maintenance, Safety, Management and Life-Cycle Optimization*, pp. 100–119, July 2010.
 - [30] H. Jo, S.-H. Sim, K. A. Mechitov et al., "Hybrid wireless smart sensor network for full-scale structural health monitoring of a cable-stayed bridge," in *The International Society for Optical Engineering, Sensors and Smart Structures Technologies for Civil, Mechanical, and Aerospace Systems*, vol. 7981 of *Proceedings of SPIE*, March 2011.
 - [31] S. Jang, H. Jo, K. Mechitov et al., "Autonomous structural health monitoring using wireless smart sensors on a cable-stayed bridge," in *Proceedings of the 5th International Conference on Bridge Maintenance, Safety and Management, Bridge Maintenance, Safety, Management and Life-Cycle Optimization*, pp. 185–192, July 2010.
 - [32] C.-B. Yun, S. Cho, H. -J. Park, J. Min, and J. -W. Park, "Smart wireless sensing and assessment for civil infrastructure," *Structure and Infrastructure Engineering*, 2013.
 - [33] Y. Q. Ni, B. Li, K. H. Lam et al., "In-construction vibration monitoring of a super-tall structure using a long-range wireless sensing system," *Smart Structures and Systems*, vol. 7, no. 2, pp. 83–102, 2011.

- [34] Y. Q. Ni, Y. Xia, W. Y. Liao, and J. M. Ko, "Technology innovation in developing the structural health monitoring system for Guangzhou New TV Tower," *Structural Control and Health Monitoring*, vol. 16, no. 1, pp. 73–98, 2009.
- [35] W. Qu, J. Teng, H. Xiang et al., "Intelligent health monitoring for roof space truss structure of the Shenzhen Citizen Center under wind load," *Journal of Building Structures*, vol. 27, no. 1, pp. 1–8, 2006 (Chinese).
- [36] E. Sazonov, V. Krishnamurthy, and R. Schilling, "Wireless intelligent sensor and actuator network—a scalable platform for time-synchronous applications of structural health monitoring," *Structural Health Monitoring*, vol. 9, no. 5, pp. 465–476, 2010.
- [37] S. Casciati and Z. Chen, "A multi-channel wireless connection system for structural health monitoring applications," *Structural Control and Health Monitoring*, vol. 18, no. 5, pp. 588–600, 2011.
- [38] J. A. Rice, K. A. Mechitov, S. H. Sim, B. F. Spencer Jr, and G. A. Agha, "Enabling framework for structural health monitoring using smart sensors," *Structural Control and Health Monitoring*, vol. 18, pp. 574–578, 2011.
- [39] L. E. Linderman, K. A. Mechitov, and B. F. Spencer Jr, "Tiny OS-based real-time wireless data acquisition framework for structural health monitoring and control," *Structural Control and Health Monitoring*, vol. 20, pp. 1007–1020, 2013.
- [40] I. F. Akyildiz, W. Su, Y. Sankarasubramaniam, and E. Cayirci, "Wireless sensor networks: a survey," *Computer Networks*, vol. 38, no. 4, pp. 393–422, 2002.

Research Article

Long-Term Vibration Monitoring of Cable-Stayed Bridge Using Wireless Sensor Network

Khac-Duy Nguyen,¹ Jeong-Tae Kim,¹ and Young-Hwan Park²

¹ Department of Ocean Engineering, Pukyong National University, Busan 608-737, Republic of Korea

² Structural Engineering Division, Korea Institute of Construction Technology, Gyeonggi-do 411-472, Republic of Korea

Correspondence should be addressed to Jeong-Tae Kim; idis@pknu.ac.kr

Received 5 August 2013; Accepted 17 October 2013

Academic Editor: Hong-Nan Li

Copyright © 2013 Khac-Duy Nguyen et al. This is an open access article distributed under the Creative Commons Attribution License, which permits unrestricted use, distribution, and reproduction in any medium, provided the original work is properly cited.

Wireless sensor networks provide a lot of advantages for vibration monitoring of bridges. The installation time and implementation cost of the monitoring system are greatly reduced by the adoption of this innovative technology. This paper presents a long-term vibration monitoring of the Hwamyung cable-stayed bridge in Korea using an Imote2-platformed wireless sensor network. First, the wireless vibration monitoring system of the bridge is briefly described by outlining the test history, the design of wireless sensor system, and the sensor deployment. Next, the vibration behaviors of the bridge are experimentally examined with respect to the variation of temperature, the wind loads induced by typhoons, and the change of bridge deck mass caused by pavement.

1. Introduction

Over the two past decades, the structural health monitoring has become increasingly important for the service life of civil infrastructures. In order to secure the structural integrity, many robust sensing technologies and SHM methods have been developed [1–3]. Recently, the interest in the safety assessment of cable-stayed bridges has been increasing [4]. For a cable-stayed bridge, critical damage may occur in main structural components such as a deck, cables, and pylons resulting from stiffness loss, crack growth, and concrete degradation. Critical damage in cable-anchorage subsystems may include cable force loss, anchorage damage, and anchorage force loss.

The conventional monitoring system mainly requires a number of sensors, a huge amount of signal transmitting wires, data acquisition instruments, and centralized data storage servers. Therefore, the cost associated with installation and maintenance of the monitoring system is very high. Recently, low-cost, stand-alone smart sensors have been developed by many research groups. Straser and Kiremidjian [5] proposed the design of a low-cost wireless modular monitoring system. Since then, many researchers have

developed wireless sensors based on a variety of sensor platforms [6–9].

By adopting those smart sensors for monitoring in large structures, the costs are greatly reduced and the data processing and information management will be very effective by ways of sensing and onboard computation, wireless transmission, and green energy harvesting. However, there have been a few full-scale implementations of wireless sensors for bridge monitoring so far [4, 6, 10]. Also, only a few studies have been performed on long-term monitoring using wireless sensors, which should provide solid guidelines for the practical applications.

This paper presents a long-term vibration monitoring of the Hwamyung cable-stayed bridge in Korea using an Imote2-platformed wireless sensor network. First, the wireless vibration monitoring system of the bridge is briefly described by outlining the test history, the design of wireless sensor system, and the sensor deployment. Next, the vibration behaviors of the bridge are experimentally examined with respect to the variation of temperature, the wind loads induced by typhoons, and the change of bridge deck mass caused by pavement.

TABLE I: Experiment history on the Hwamyung bridge.

Period	Work phase	Description	Event
May 2011	Wireless sensor system design	(i) Vibration sensor design (ii) Operation software design	—
June 2011	Sensor system setup	(i) Sensor placement design (ii) Internet-based remote sensing setup	—
June-July 2011	Performance evaluation	(i) Wireless communication test (ii) Solar power harvesting evaluation (iii) Response signal measurement (iv) Modal analysis and system identification	Typhoon Meari (June 2011)
August 2011–June 2013	Long-term monitoring	(i) Cable-anchorage monitoring under temperature variation (ii) Effect of dead load (iii) Bridge behavior under typhoons	(i) Asphalt pavement (February 2012) (ii) Typhoons Bolaven, Tembin, and Sanba (August-September 2012)



FIGURE 1: Hwamyung cable-stayed bridge.

2. Wireless Monitoring System of Hwamyung Cable-Stayed Bridge

2.1. Test History. Field tests were conducted on Hwamyung cable-stayed bridge, as shown in Figure 1, crossing Nakdong River between Busan and Gimhae, Korea. The bridge was constructed by Hyundai Engineering & Construction Co., Ltd., from December 2004 to July 2012. The bridge consists of three spans including a 270 m central main span between two pylons and two 115 m side spans connecting east and west approaches. The clearance of the deck is 14.7 m from the water level. The height of two pylons is 65 m from the deck level. The box girder is 27.8 m in width and 4 m in height. The bridge has a total 72 cables, positioning 36 cables at each pylon. The test history on the bridge is summarized in Table I. The research project can be outlined in four work phases: design of wireless sensor system, sensor system setup, performance evaluation, and long-term vibration monitoring.

For the design of wireless sensor system, the vibration sensor and operation software are designed during May 2011. For the sensor system setup, the location and orientation of sensor and the internet-based remote sensing schematic are designed during June 2011. For the performance evaluation, the functionality of wireless communication, the durability of solar power harvesting, the flexibility of response signal

measurement, and the feasibility of modal analysis and system identification are examined during June to July 2011. For the long-term monitoring of the bridge, several tasks such as monitoring cable-anchorage motions under temperature variation and investigating bridge behaviors under several typhoon and deck-mass changes have been performed during August 2011 to June 2013. During the entire monitoring periods, the temperature has varied in a wide range of about -10°C to 45°C .

2.2. Design of Wireless Sensor Nodes. A multiscale vibration sensor node on Imote2 platform was designed as schematized in Figure 2(a). The high performance sensor platform, Imote2, provided by Memsic Co. [11], was selected to control the operation of the sensor node. For vibration monitoring, SHM-A, SHM-AS, and SHM-H sensor boards were selected. The SHM-A and SHM-H sensor boards were developed for acceleration measurement by University of Illinois at Urbana-Champaign (UIUC) [8, 12]. The SHM-AS sensor board was modified from SHM-A sensor board in order to measure PZT's dynamic strain signal. The solar-powered energy harvesting is implemented by employing solar panel and rechargeable battery. Figure 2(b) shows a prototype of the multiscale sensor node which consists of three layers as follows: (1) X-bow battery board, (2) Imote2 sensor platform, and (3) SHM-H board or SHM-A (AS) board.

The Imote2 platform is built with 13–416 MHz PXA271 XScale processor. This processor integrates with 256 kB SRAM, 32 MB flash memory, and 32 MB SDRAM. A 2.4 GHz surface mount antenna is equipped for each Imote2 platform. For long-term operation of wireless sensor nodes, energy harvesting is employed. For powering by rechargeable battery, the hardware of X-bow battery board is modified so that a solar panel (e.g., SPE-350-6 with 9 V and 350 mA) can be integrated with the Imote2 sensor platform.

For deck's responses, SHM-H sensor board is adopted to employ a SD1221L-002 accelerometer for high-sensitivity channel, the input range $\pm 2g$, the sensitivity 2V/g , and

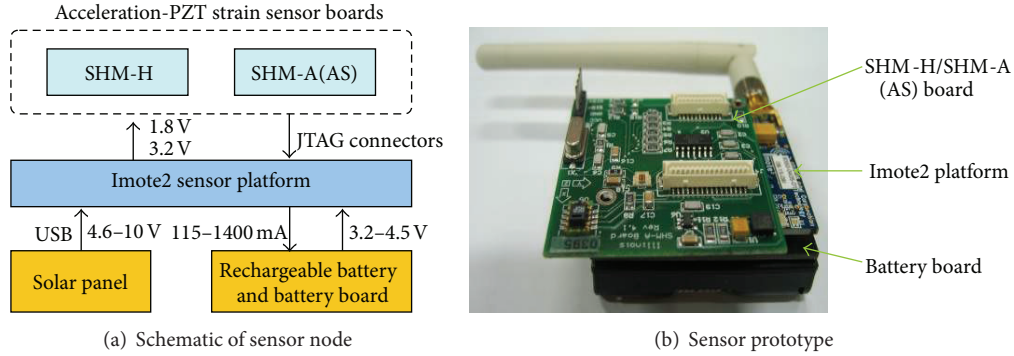


FIGURE 2: Design of wireless multiscale sensor node.

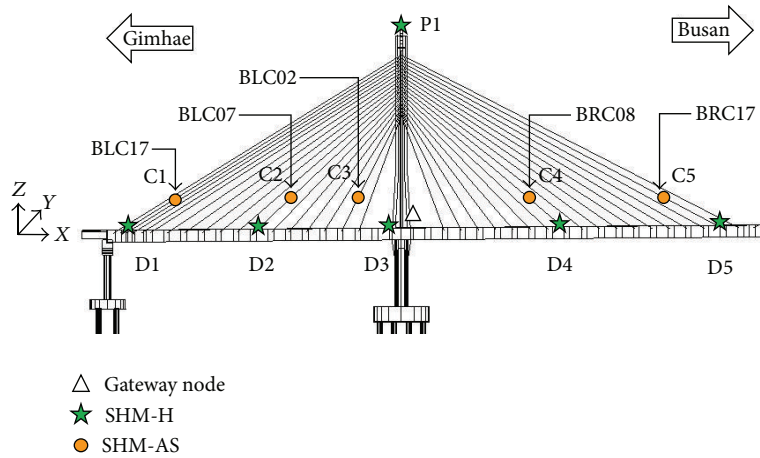


FIGURE 3: Field sensor layout on Hwamyung cable-stayed bridge.

the output noise $5 \mu\text{g}/\sqrt{\text{Hz}}$. For cable’s acceleration measurement, the SHM-A employs the triaxial LIS344ALH accelerometer whose sensitivity is relatively lower and output noise is quite higher than those of the SHM-H. In this study, a modified SHM-AS sensor board is designed to measure PZT’s dynamic strain signals. The dynamic strain signal from PZT sensor is passed through a signal conditioner circuit to produce an analog signal of $0\sim 3.3 \text{ V}$.

2.3. Sensor Deployment on the Bridge. As shown in Figure 3, wireless sensor networks were deployed on Hwamyung bridge. Two hardware configurations of Imote2-based smart sensor nodes which are gateway node and leaf node are designed to monitor the responses of the bridge. A gateway node consists of an Imote2 platform with a 2.4 GHz antenna and an IBB2400 interface board connected to the PC via a USB cable. A leaf node consists of an Imote2 platform with a 2.4 GHz antenna, a sensor board (e.g., SHM-AS and SHM-H), and an X-bow battery board powered by a Powerizer Li-ion polymer rechargeable battery with a solar panel.

For vibration monitoring, twelve sensor nodes (Imote2/SHM-AS/SHM-H) including 11 leaf nodes and 1 gateway node were installed. Among the leaf nodes, 6 Imote2/SHM-H sensors were placed at five locations of the deck and at the top

of the west pylon (i.e., D1~D5 and P1), and 5 Imote2/SHM-AS sensors were placed on five selected cables (i.e., C1~C5). For each sensor board (i.e., SHM-H or SHM-AS), three axes accelerations were measured. A spared channel in SHM-AS sensor board was used for measuring dynamic strain in cables. Also for dynamic strain measurement, five PZT patches were bonded on aluminum tubes covering the five selected cables. The vibration signals were measured in duration of 600 seconds with sampling rate 25 Hz. In summary, the total 33 channels of acceleration and 5 channels for dynamic strain were monitored in Hwamyung bridge.

All sensor nodes and base stations are placed in plastic boxes which have waterproof rubber gaskets to prevent them from sun heating, being absorbed and other damage caused by harsh environmental conditions such as rain, wind, and dust at the field site. Solar panels were mounted on the sensor boxes to harvest the solar energy for recharging the Li-ion polymer batteries embedded to the sensor boards.

3. Experimental Modal Identification of the Bridge

3.1. Modal Identification Method. In order to extract experimental natural frequencies and mode shapes of the deck

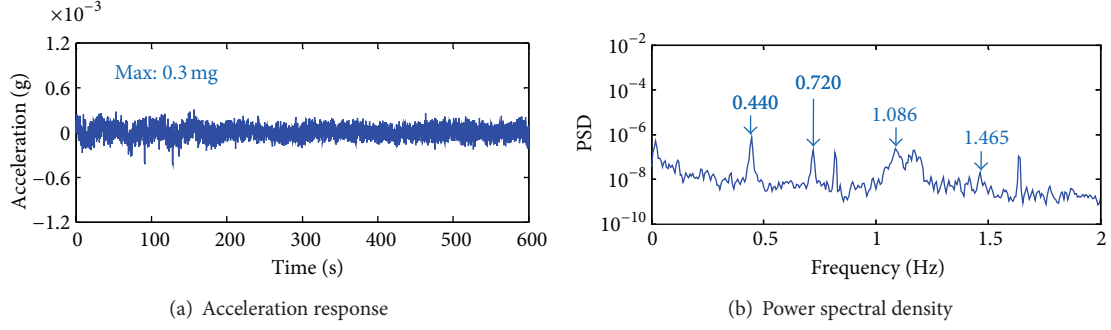


FIGURE 4: Vibration responses of the bridge: deck D2.

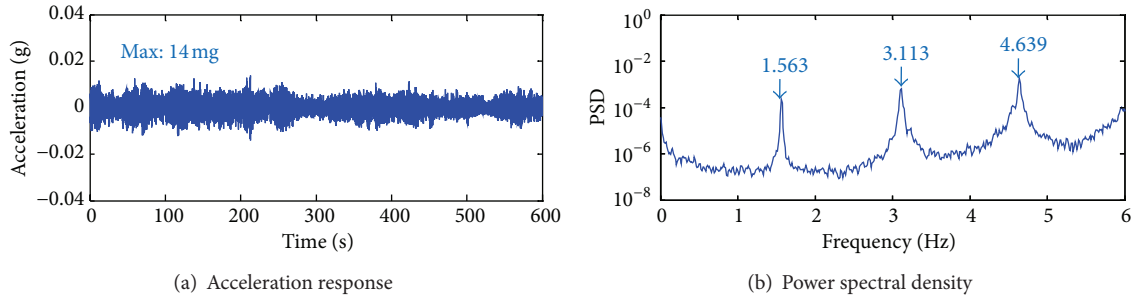


FIGURE 5: Vibration responses of the bridge: cable C4.

and the pylon, the SSI method [13] was performed. The SSI method utilizes the singular value decomposition (SVD) of a block Hankel matrix with cross correlation matrix of responses as follows:

$$\mathbf{H} = [\mathbf{U}_1 \quad \mathbf{U}_2] \begin{bmatrix} \Sigma_1 & 0 \\ 0 & 0 \end{bmatrix} \begin{bmatrix} \mathbf{V}_1^T \\ \mathbf{V}_2^T \end{bmatrix} \approx \mathbf{U}_1 \Sigma_1 \mathbf{V}_1^T, \quad (1)$$

where \mathbf{H} is the Hankel matrix; \mathbf{U} , \mathbf{V} are the unitary matrices; and Σ_1 is the singular value matrix. The modal parameters can be identified from a system matrix which is determined from the SVD algorithm. A stabilization chart is used to find a suitable system order with the criteria which classify a mode as stable mode, unstable mode, or noise mode [14]. Once the stable modes are detected, damping ratio (ξ_i) of the i th mode is identified from the eigenvalue (λ_i) as follows:

$$\xi_i = \frac{-\text{Re}(\lambda_i)}{|\lambda_i|}. \quad (2)$$

3.2. Modal Identification of the Bridge. Responses of the bridge were measured in every two-hour interval under ambient vibration condition. Figures 4 and 5 show examples of acceleration responses and the corresponding power spectral densities of the deck (i.e., sensor node D2) and the cable (i.e., sensor node C4), respectively, under normal condition without vehicle traffic on the bridge. Nevertheless,

of this low excitation condition, the maximum acceleration amplitudes are relatively high, such as 0.3 mg for the deck D2 and 14 mg for the cable C4. Also, natural frequencies of the bridge components can be well determined, which guarantees a reliable modal identification. Using the SSI method, modal parameters (natural frequency, damping ratio, and mode shape) for three vertical and three lateral bending modes (i.e., V1~V3 and L1~L3) were extracted as shown in Figure 6 and as listed in Table 2.

4. Long-Term Vibration Monitoring of the Bridge

4.1. Cable Vibration under Temperature Variation

4.1.1. Temperature Effect Estimation. For a stay cable subjected to two different temperatures, the axial extension of the cable due to temperature variation (e.g., $\Delta L_T = \alpha_T L \Delta T$) is equivalent to the deformation in the change in tension force at anchorage (e.g., $\Delta F = -EA \Delta L_T / L = -\alpha_T EA \Delta T$), where α_T is the coefficient of linear thermal expansion of the cable, ΔT is the temperature variation, and EA is the axial rigidity of the cable. The change in tension force can be simplified in a reduced order as

$$\Delta F \approx \frac{g(m, L) \Delta f_k^2}{k^2}, \quad (3)$$

where $\Delta f_k^2 = f_k^{*2} - f_k^2$ is the change in square of natural frequency; f_k and f_k^* are the k th natural frequencies of

TABLE 2: Identified natural frequencies and damping ratios.

	Vertical modes			Lateral modes		
	V1	V2	V3	L1	L2	L3
Nature frequency	0.444	0.720	1.028	0.454	0.666	1.169
Damping ratio	0.004	0.009	0.025	0.012	0.011	0.026

L indicates lateral mode; V indicates vertical mode.

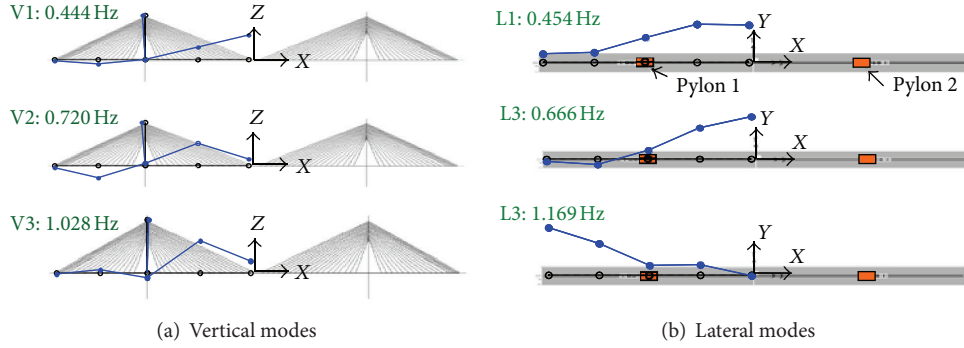


FIGURE 6: Modal parameters extracted by SSI method.

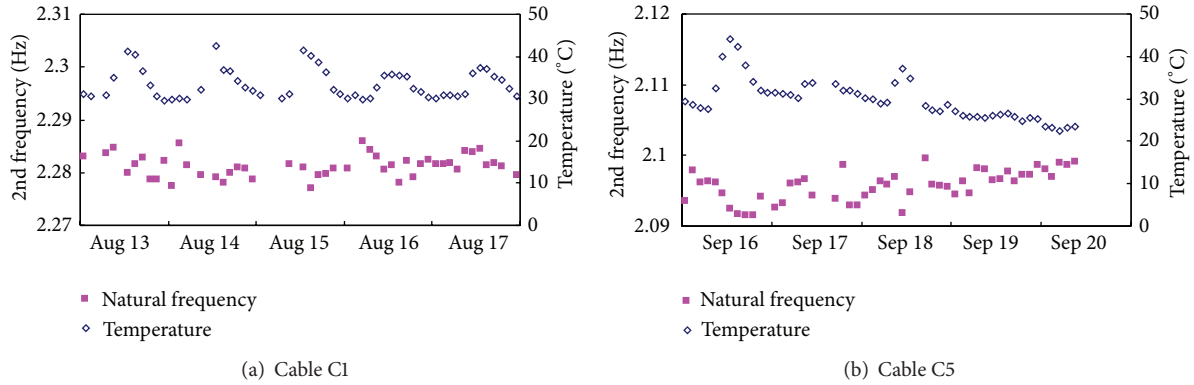


FIGURE 7: Monitoring results for long cables C1 and C5 in 5 days: 2nd natural frequency.

the cable before and after tension force change, respectively; k is the mode number; and $g(m, L)$ represents geometric and material quantities of the cable. Hence, the change in square of natural frequency due to temperature variation is expressed as follows:

$$\Delta f_k^2 \approx -\beta_k \Delta T, \quad (4)$$

where β_k is temperature correlation index which may be calculated as $\beta_k = \alpha_T E A k^2 / g(m, L)$. Since it is difficult to obtain the geometric and material quantities $g(m, L)$ theoretically, the value of β_k can be estimated from field experiment by correlating the change in natural frequency and temperature variation.

4.1.2. Natural Frequency versus Temperature Variation. The first natural frequency was monitored for the short cables C2, C3, and C4, and the second natural frequency was monitored for the long cables C1 and C5. It is worth noting

that the first natural frequency can be utilized to estimate tension force of short cables, and the second one can be used to estimate tension force of long cables, according to the method proposed by Zui et al. [15]. Figures 7 and 8 show the changes in the natural frequencies (corresponding to the first or the second mode dependent on cables) versus temperature change in 5 days. It is obvious that the natural frequencies change oppositely with temperature variation. This implies that axial stress of the cable is partially released when temperature increases and vice versa. The data in a long period of one month from August to September 2011 was utilized to construct the relationship between the natural frequencies and temperature. Figures 9 and 10 illustrate the correlations between natural frequencies and temperature. It is found that the change in the cables' natural frequencies seems to be linear with temperature variation. Those monitoring results are consistent with the analytical model of temperature variation effect on change in cables' natural frequencies (4).

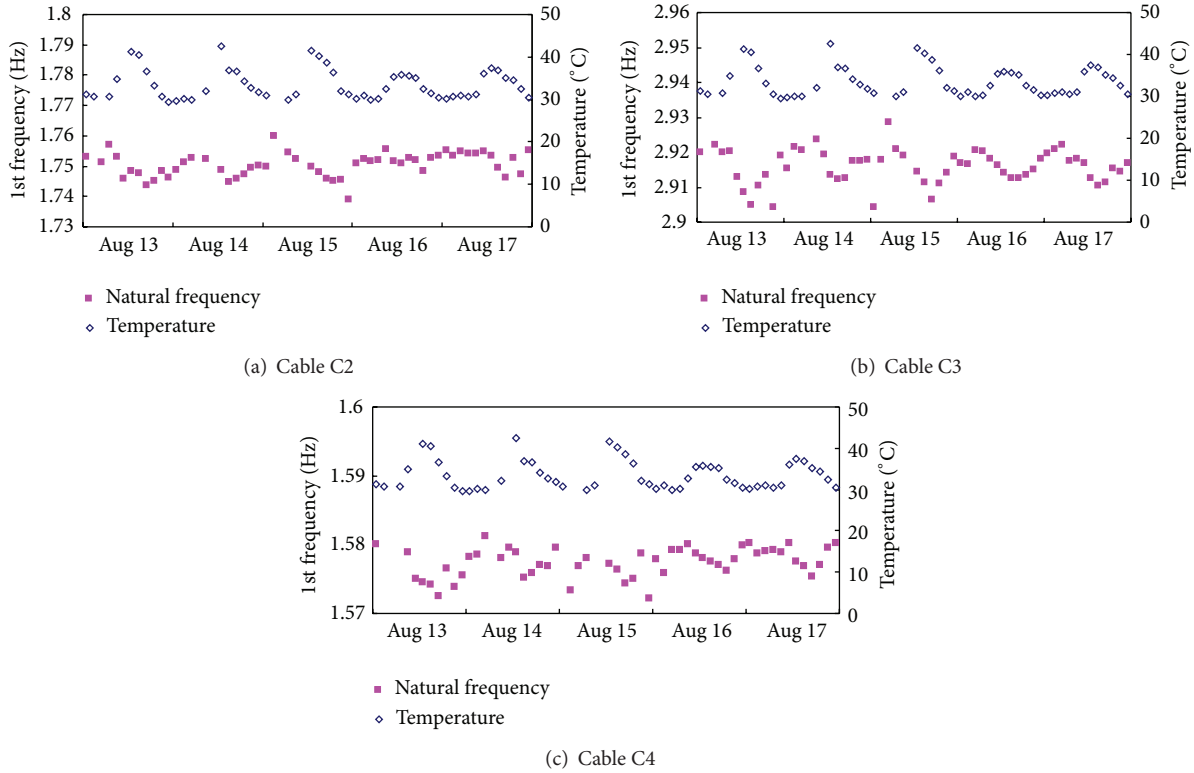


FIGURE 8: Monitoring results for short cables C2, C3, and C4 in 5 days: 1st natural frequency.

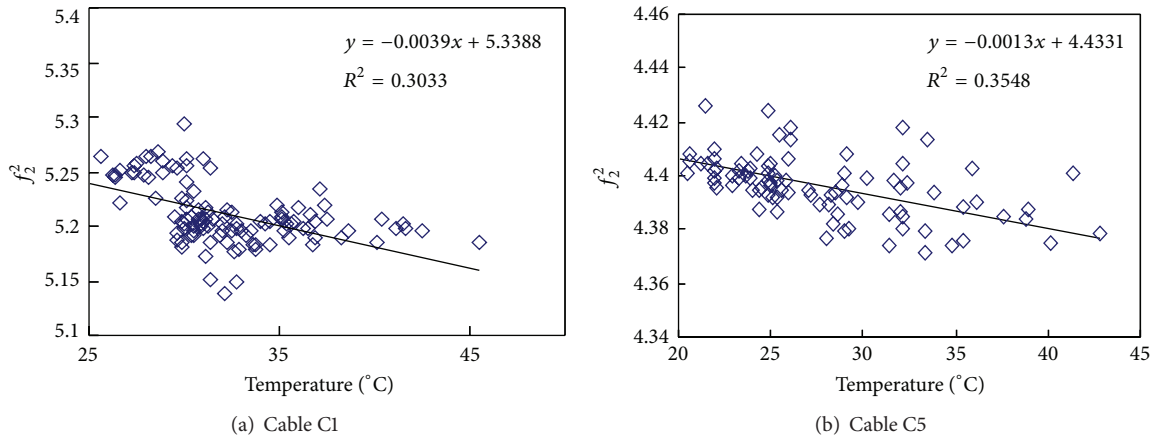


FIGURE 9: Correlation of natural frequency and temperature: long cables C1 and C5.

4.2. Bridge Behaviors under Wind Loads Induced by Typhoons. Over 2-year monitoring, there were 4 typhoons passing the Korean peninsula and directly affected the site of Hwamyung bridge, including typhoons Meari (June 2011), Bolaven (August 2012), Tembin (August 2012), and Sanba (September 2012). During typhoon Sanba, the highest wind speed was recorded on-site as 17.9 m/s. Figure 11 shows time-frequency analysis of acceleration responses of deck D2 and cable C3 during typhoon Sanba.

It is observed that the magnitudes of all vibration modes increase significantly during the attacks of the typhoon. This

implies that the typhoon gave an impact in a wide frequency range. As also shown in Figure 12, the maximum acceleration magnitude during the typhoon was much larger than that in normal wind condition. From those observations, to have a monitoring system for the internal forces of the bridge components during typhoons is found essential.

4.3. Effect of Deck Mass Change Caused by Pavement. The effect of bridge deck mass change on the change in natural frequency was examined after the asphalt pavement was laid on the bridge in February 2012. The difference in the

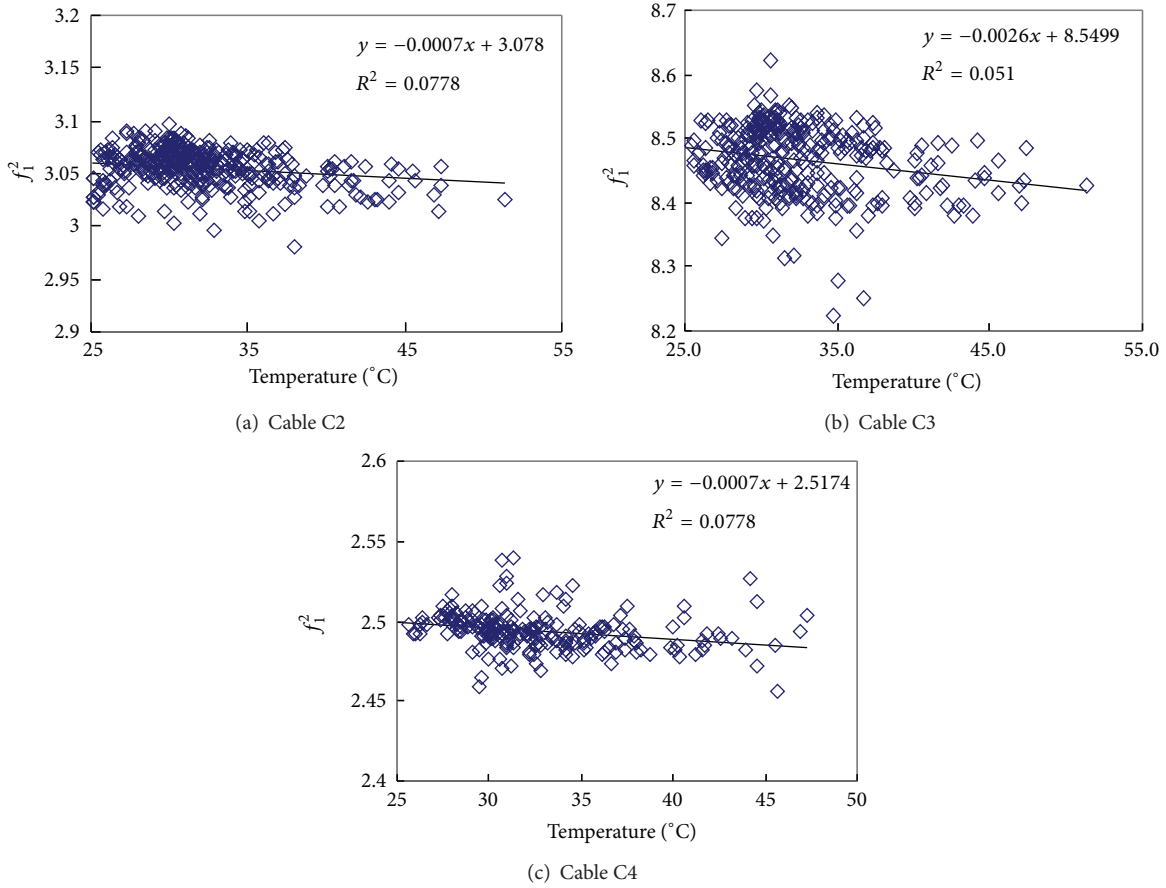


FIGURE 10: Correlation of natural frequency and temperature: short cables C2, C3, and C4.

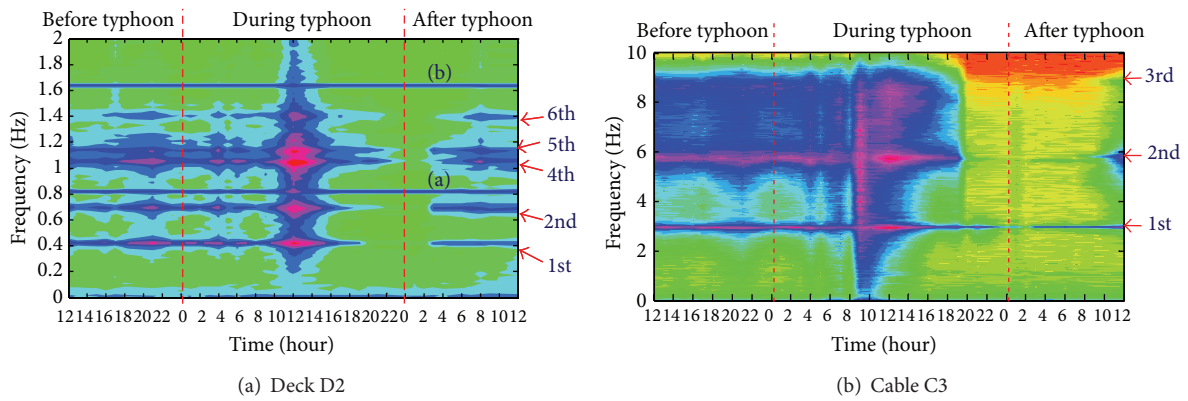


FIGURE 11: Time-frequency acceleration response of deck and cable during typhoon Sanba.

surface of the bridge deck can be clearly seen in Figures 13(a) and 13(b). For the fairness in weather condition, the data of two time periods (August 2011 and August 2012) with similar temperatures were selected as shown in Figure 13(c). Figure 14 shows the measured natural frequencies of the first mode of the deck and the five cables C1~C5 at the two periods. It is found that the natural frequency of deck decreased after laying the pavement, whereas the natural frequencies of the five cables increased after laying the pavement. These

phenomena can be explained by the following reasons: the mass of deck was increased due to the pavement’s mass, and the tension force of the cable was also increased due to the additional load from the increased weight of the deck.

5. Summary and Conclusions

A long-term vibration monitoring of the Hwamyung cable-stayed bridge in Korea using an Imote2-platformed wireless

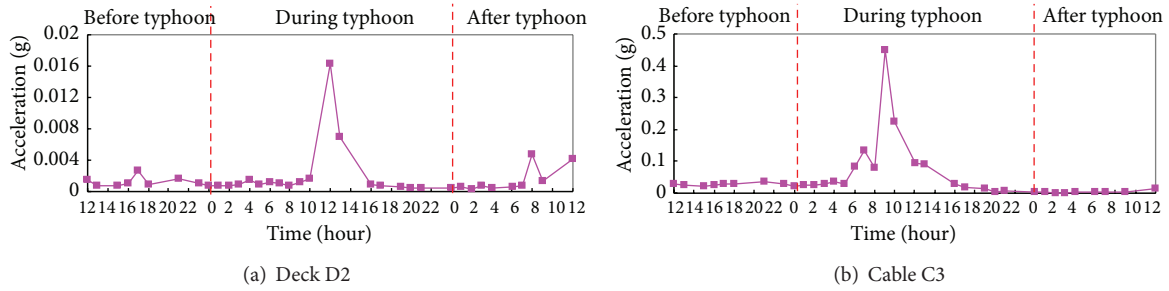
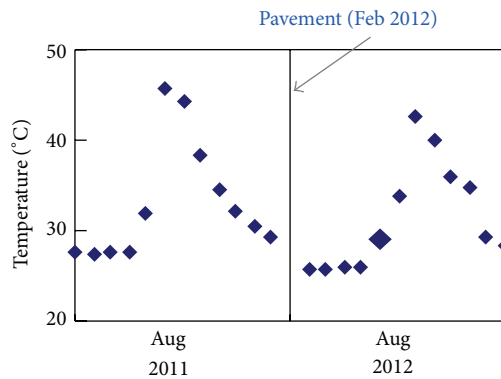


FIGURE 12: Maximum acceleration of deck and cable during typhoon Sanba.



(a) Bridge view before pavement (b) Bridge view after pavement



(c) Temperature change

FIGURE 13: Bridge conditions before and after asphalt pavement.

sensor network was presented in this study. First, the wireless vibration monitoring system of the bridge was briefly described by outlining the test history, the design of wireless sensor system, and the sensor deployment. Next, the vibration behaviors of the bridge were experimentally examined with respect to the variation of temperature, the wind loads induced by typhoons, and the change of bridge deck mass caused by asphalt pavement.

The long-term vibration monitoring of the bridge has been operated successfully via the wireless sensor network. It was found that the cables' natural frequencies varied linearly with temperature variation. Natural frequencies of the deck and the cables were found much influenced by the deck

mass change caused by the pavement, but in opposite trends. During a typhoon passing the bridge (typhoon Sanba), vibration amplitudes of the deck and the cables significantly increased, and all modal responses became more resonant. Future works remain on examining the effect of temperature variation on the deck's modal parameters and wind effect on the deck's and the cables' modal parameters.

Acknowledgment

This research was supported by a grant from a Strategic Research Project (Development of Smart Prestressing and Monitoring Technologies for Prestressed Concrete

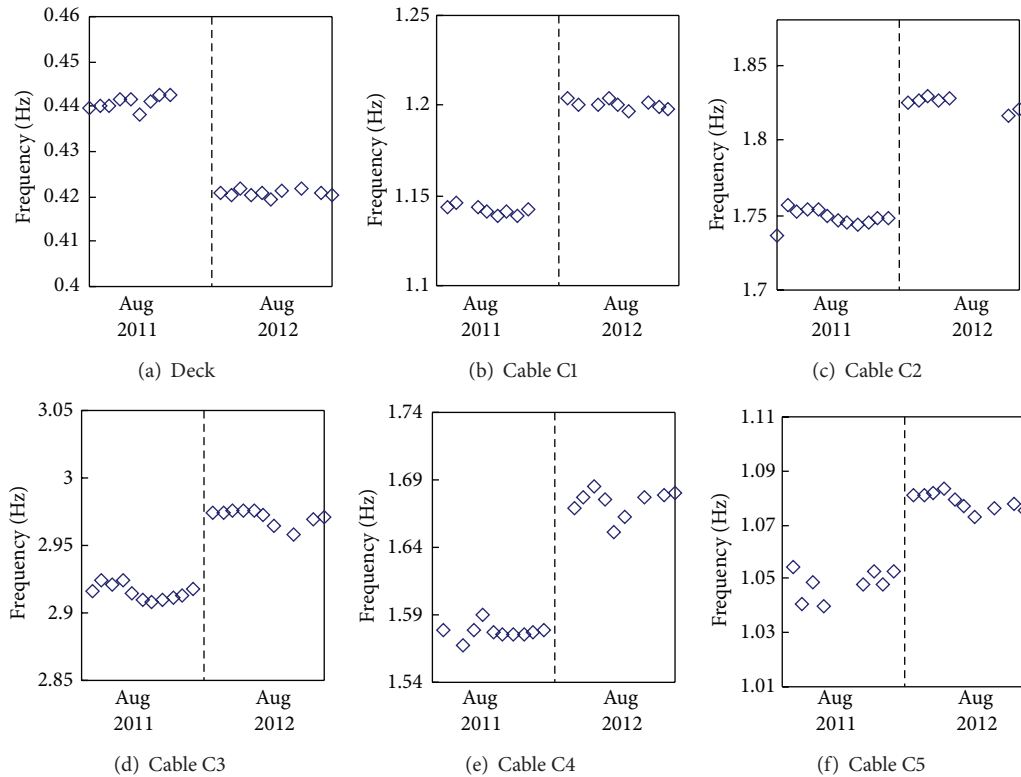


FIGURE 14: Changes in 1st natural frequencies of deck and five cables before and after asphalt pavement.

Bridges) funded by the Korea Institute of Construction Technology.

References

- [1] S. W. Doebling, C. R. Farrar, and M. B. Prime, "A summary review of vibration-based damage identification methods," *Shock and Vibration Digest*, vol. 30, no. 2, pp. 91–105, 1998.
- [2] H. Sohn, C. R. Farrar, F. M. Hemez, D. D. Shunk, D. W. Stinemates, and B. R. Nadler, *A Review of Structural Health Monitoring Literature: 1996–2001*, Los Alamos National Laboratory Report, Los Alamos, New Mexico, 2003.
- [3] J.-T. Kim, J.-H. Park, D.-S. Hong, and W.-S. Park, "Hybrid health monitoring of prestressed concrete girder bridges by sequential vibration-impedance approaches," *Engineering Structures*, vol. 32, no. 1, pp. 115–128, 2010.
- [4] B. F. Spencer and S. Cho, "Wireless smart sensor technology for monitoring civil infrastructure: technological developments and full-scale applications," in *Proceeding of the World Congress on Advances in Structural Engineering and Mechanics (ASEM '11)*, Seoul, Korea, 2011.
- [5] E. G. Straser and A. S. Kiremidjian, "A modular, wireless damage monitoring system for structure," John A. Blume Earthquake Engineering Center, Stanford University, Palo Alto, Calif, USA, 1998.
- [6] J. P. Lynch, Y. Wang, K. J. Loh, J.-H. Yi, and C.-B. Yun, "Performance monitoring of the Geumdang Bridge using a dense network of high-resolution wireless sensors," *Smart Materials and Structures*, vol. 15, no. 6, article 008, pp. 1561–1575, 2006.
- [7] D. L. Mascarenas, M. D. Todd, G. Park, and C. R. Farrar, "Development of an impedance-based wireless sensor node for structural health monitoring," *Smart Materials and Structures*, vol. 16, no. 6, pp. 2137–2145, 2007.
- [8] J. A. Rice, K. Mechitov, S.-H. Sim et al., "Flexible smart sensor framework for autonomous structural health monitoring," *Smart Structures and Systems*, vol. 6, no. 5-6, pp. 423–438, 2010.
- [9] J.-T. Kim, J.-H. Park, D.-S. Hong, and D.-D. Ho, "Hybrid acceleration-impedance sensor nodes on Imote2-platform for damage monitoring in steel girderconnections," *Smart Structures and Systems*, vol. 7, no. 5, pp. 393–416, 2011.
- [10] G. D. Zhou and T. H. Yi, "The node arrangement methodology of wireless sensor networks for long-span bridge health monitoring," *International Journal of Distributed Sensor Networks*, vol. 2013, Article ID 865324, 8 pages, 2013.
- [11] Memsic Co, 2010, Datasheet of ISM400, <http://www.memsic.com/>.
- [12] H. Jo, J. A. Rice, B. F. Spencer Jr., and T. Nagayama, "Development of high-sensitivity accelerometer board for structural health monitoring," in *Proceedings of the Sensors and Smart Structures Technologies for Civil, Mechanical, and Aerospace Systems*, San Diego, Calif, USA, March 2010.
- [13] V. P. Overschee and B. De Moor, *Subspace Identification For Linear System*, Kluwer Academic Publisher, 1996.
- [14] J.-H. Yi and C.-B. Yun, "Comparative study on modal identification methods using output-only information," *Structural Engineering and Mechanics*, vol. 17, no. 3-4, pp. 445–466, 2004.
- [15] H. Zui, T. Shinke, and Y. Namita, "Practical formulas for estimation of cable tension by vibration method," *Journal of Structural Engineering*, vol. 122, no. 6, pp. 651–656, 1996.

Research Article

Vibration Characteristics of Gravity-Type Caisson Breakwater Structure with Water-Level Variation

So-Young Lee,¹ Thanh-Canh Huynh,¹ Jeong-Tae Kim,¹
Han-Sam Yoon,² and Sang-Hun Han³

¹ Department of Ocean Engineering, Pukyong National University, Busan 608-737, Republic of Korea

² Research Center of Ocean Industrial Development, Pukyong National University, Busan 608-737, Republic of Korea

³ Coastal Engineering & Ocean Energy Research Department, KIOST, Ansan 425-600, Republic of Korea

Correspondence should be addressed to Jeong-Tae Kim; idis@pknu.ac.kr

Received 20 August 2013; Accepted 16 October 2013

Academic Editor: Ting-Hua Yi

Copyright © 2013 So-Young Lee et al. This is an open access article distributed under the Creative Commons Attribution License, which permits unrestricted use, distribution, and reproduction in any medium, provided the original work is properly cited.

Vibration characteristics of gravity-type caisson breakwater structures which have water-level variations are experimentally examined by using wave load excitations. To achieve the objective, the following approaches are implemented. Firstly, vibration analysis methods are selected to examine the dynamic characteristics of the lab-scale caisson. Secondly, vibration test on a lab-scale caisson which is installed in a two-dimensional wave flume is performed under several excitation sources and water levels. Thirdly, the compatibility of the wave-induced vibration responses is evaluated by comparison with the impact vibration responses, and the appropriate vibration analysis method is selected. Finally, the water-level effects on the caisson breakwater are examined based on the modal parameters which are experimentally measured for the 2D wave flume tests.

1. Introduction

Genesis frequency of large-scale typhoon has been increased and it results in huge losses of both life and property. In particular, coastal structures are directly faced with extreme wave loading condition. Due to these severe environmental phenomena and extreme events like typhoon or ship collision, structural integrity of harbor structure becomes a more important issue.

Most breakwater structures are constructed as gravity-type. Moreover, large gravity-type caissons become popular for constructing breakwaters. Despite the advance in the modern construction technology, damage in the harbor caisson breakwater is inevitable due to local failure or global instability problems which are mostly attributed to foundation-structure interface [1]. Goda [2] and Takahashi et al. [3] also reported that the sliding at the foundation-structure interface is the primary damage of caissons. Also, the cavity in foundation mound or the backfill makes harbor caissons weaker against extreme loads such as storm waves, mainly occurring from typhoon.

Figure 1 illustrates the local and global failures of the vertical breakwater. Oumeraci [4] has classified damage of vertical breakwater to overall failures and local failures. The overall failures such as sliding, overturning, and settlement, affect the stability of the entire structure. The local failures do not affect the structural stability as it is. The local failure, however, contributes to make unexpected water flow and it causes reduction of breaking performance of breakwater. Progress of the local failures can lead to the overall failures. It is noted that all damages of vertical breakwaters are related to integrity of the foundation mound. Therefore, the integrity monitoring of existing caisson structures is absolutely demanded.

Since the early 1980s, many researchers have studied SHM techniques in the field of civil engineering [5–9] by mainly performing vibration-based damage monitoring of civil structures. Also, many researchers have worked on developing damage detection methods such as the modal sensitivity method, modal flexibility method, genetic algorithm, and neural network [10–15]. Research studies have focused

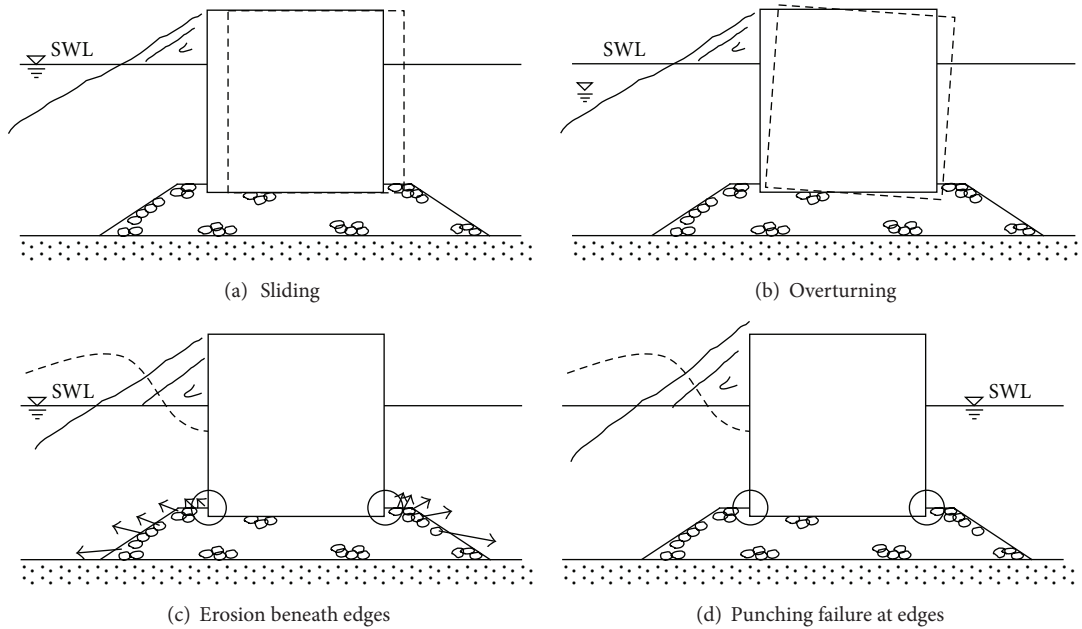


FIGURE 1: Damage types of monolithic vertical breakwaters [4].

mostly on inland structures, but only few research efforts have been made to harbor structures, including vibration response analyses of soil-structure or fluid-soil-structure interactions in harbor caisson structures [16, 17]. Also, Gao et al. [18] have studied dynamic response of caisson-type breakwater under various water levels to estimate added mass coefficient of water. On harbor caisson structures, there exist research needs to monitor their vibration responses and dynamic characteristics via the limited accessibility and to identify sensitive vibration responses of a row of caisson units which is damage in foundation or damage in interlocking members.

In this paper, vibration characteristics of gravity-type caisson breakwater structures which have water-level variations are experimentally examined by using wave load excitations. To achieve the objective, the following approaches are implemented. Firstly, vibration analysis methods are selected to examine the dynamic characteristics of the lab-scale caisson. Secondly, vibration test on a lab-scale caisson which is installed in a two-dimensional wave flume is performed under several excitation sources and water levels. Thirdly, the compatibility of the wave-induced vibration responses is evaluated by comparison with the impact vibration responses and the appropriate vibration analysis method is selected. Finally, the water-level effects on the caisson breakwater are examined based on the modal parameters which are experimentally measured for the 2-D wave flume tests.

2. Vibration Characteristics of Harbor Caisson Structure

2.1. Simplified Model-Based Vibration Monitoring. In this study, the vibration characteristics of the harbor caisson

structure are examined by identifying the equivalent vibration responses of simplified 2D models. Due to the complexity and limitations in the field monitoring of real 3D caisson breakwaters, the vibration analysis via the 2D model can be an alternative choice. Figure 2 illustrates a simplified 2D planar model and a spring-dashpot model which represent a harbor caisson structure. On assuming that the 2D model is the physical representation of the real structure, therefore, the vibration response of the 2D model provides the analysis of the structural characteristics (e.g., mass, stiffness, and damping) of the real structure.

In the vibration analysis of the caisson breakwater, the main interests are in how to excite the massive gravity-type structure and how to measure the vibration response. As shown in Figure 3, there are two alternatives for the excitation: ship collision impact load and ambient wave load. Yi et al. [14, 15] reported that the ship collision can be a very accurate shaking mechanism to measure vibration responses of caisson breakwaters. However, the ship collision test is not easy to apply in practice due to its dependability on weather conditions and potential dangers in operation. So a wave-induced loading can be an alternative choice, but there are many unanswered features related to the wave-induced vibration monitoring. Among many others, the variation of water levels and the change in incident wave characteristics are two key parameters that should be examined to prove feasibility of wave-induced vibration monitoring.

2.2. Vibration Response Analysis Method

2.2.1. Power Spectral Density. The relationship between input loads $u(t)$ applied to structure and its responses $v(t)$ can be written as [19]

$$m\ddot{v}(t) + c\dot{v}(t) + kv(t) = u(t), \quad (1)$$

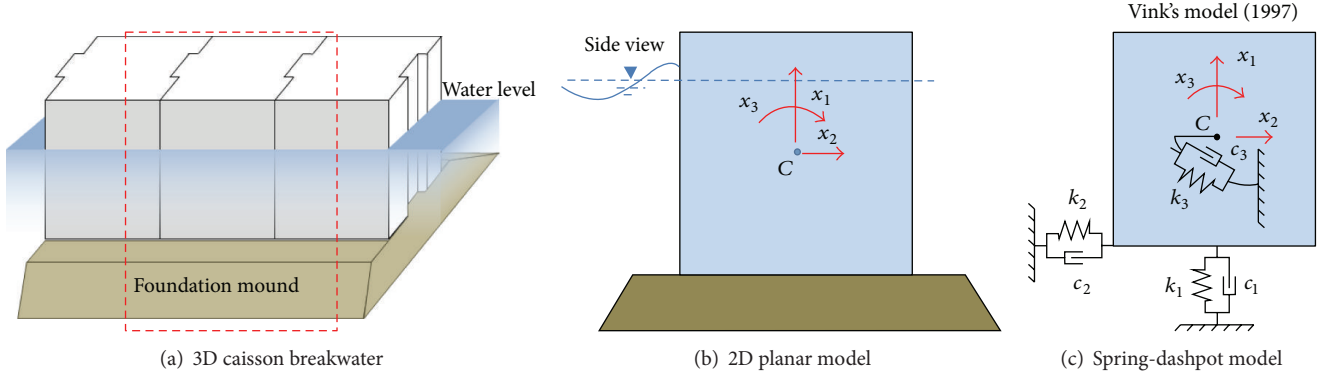


FIGURE 2: 2-D simplified model of harbor caisson breakwater.

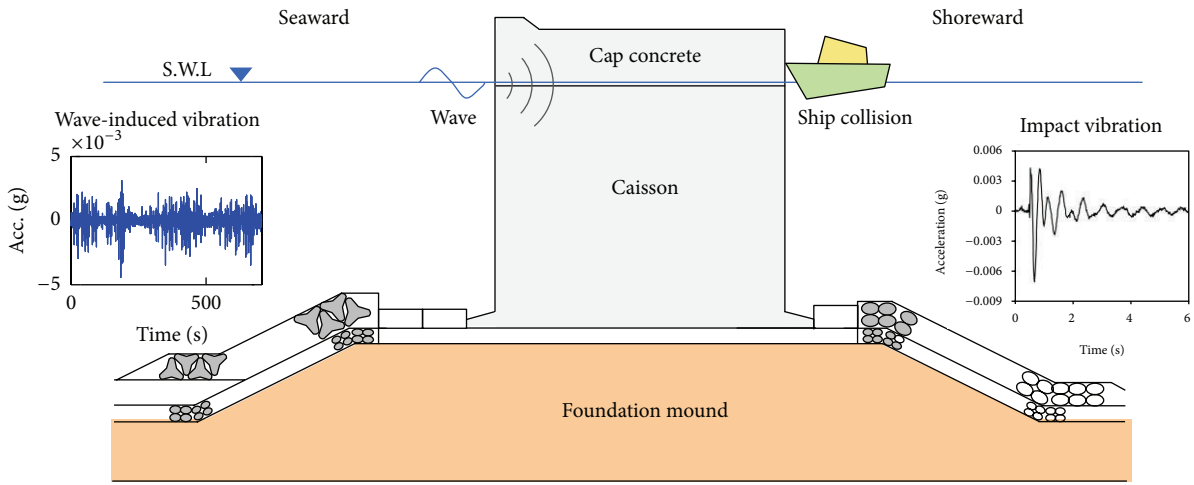


FIGURE 3: Schematic of dynamic tests on harbor caisson breakwater.

where m , c , and k are mass, damping, and stiffness, respectively. Also, $\dot{v}(t)$ and $\ddot{v}(t)$ indicate velocity and acceleration, respectively. Equation (1) can be transformed into frequency domain by the fast fourier transform. It is difficult to avoid the inclusion of noise in experimental tests. Power spectral density (PSD) is used for minimizing the noise effect. Then, PSD $S(f)$ can be calculated by Welch's procedure:

$$S(f) = \frac{1}{n_d T} \sum_{i=1}^{n_d} |Y_i(f, T)|^2, \quad (2)$$

in which $Y_i(f, T)$ is FFT result of i th acceleration signal. The calculated PSD from structural acceleration response may change according to the variation of structural condition.

2.2.2. Frequency Domain Decomposition Method. Frequency domain decomposition (FDD) method is used to extract modal parameters such as natural frequency and mode shape [20]. Singular values of the PSD function matrix $\mathbf{S}(\omega)$ are used to estimate the modal parameter instead of the PSD functions themselves as follows:

$$\mathbf{S}(\omega) = \mathbf{U}(\omega)^T \mathbf{\Sigma}(\omega) \mathbf{V}(\omega), \quad (3)$$

where $\mathbf{\Sigma}$ is the diagonal matrix consisting of the singular values (σ_i 's) and \mathbf{U} and \mathbf{V} are unitary matrices. Since $\mathbf{S}(\omega)$ is symmetric, \mathbf{U} becomes equal to \mathbf{V} . In this FDD method, the natural frequencies can be determined from the peak frequencies of the singular values and the mode shape from any of the column vectors of $\mathbf{U}(\omega)$ at the corresponding peak frequencies. Generally, the first singular value $\sigma_1(\omega)$ among σ_i 's ($i = 1, \dots, N$) is used to estimate the modal parameters except in some special cases such as with two or more identical excitations.

The decay of the amplitude of motion may be conveniently expressed by the logarithmic decrement which is defined as the natural logarithm of the ratio of any two successive peak amplitudes \ddot{u}_1 and \ddot{u}_2 . The damping ratio ξ_i can be approximated by

$$\xi_i = \frac{1}{2\pi} \ln \frac{\ddot{u}_1}{\ddot{u}_2}. \quad (4)$$

2.2.3. Stochastic Subspace Identification Method. The stochastic subspace identification (SSI) method utilizes the singular

value decomposition (SVD) of a block Hankel matrix with cross-correlation matrix of responses as follows:

$$\mathbf{H} = [\mathbf{U}_1 \ \mathbf{U}_2] \begin{bmatrix} \boldsymbol{\Sigma}_1 & 0 \\ 0 & 0 \end{bmatrix} \begin{bmatrix} \mathbf{V}_1^T \\ \mathbf{V}_2^T \end{bmatrix} \approx \mathbf{U}_1 \boldsymbol{\Sigma}_1 \mathbf{V}_1^T, \quad (5)$$

where \mathbf{H} is the Hankel matrix, \mathbf{U} , \mathbf{V} are the unitary matrices, and $\boldsymbol{\Sigma}_1$ is singular value matrix. The modal parameters can be identified from a system matrix which is determined from the SVD algorithm. A stabilization chart is used to find a suitable system order with the criteria which classify a mode as stable mode, unstable mode, and noise mode [20]. Once the stable modes are detected, damping ratio (ξ_i) of the i th mode is identified from the eigenvalue (λ_i) as follows:

$$\xi_i = \frac{-\text{Re}(\lambda_i)}{|\lambda_i|}. \quad (6)$$

3. Experiments on Lab-Scale Caisson in 2-D Wave Flume

3.1. Experimental Setup. To examine the vibration response of a submerged caisson, dynamic tests on the caisson structure are implemented. The experiments were carried out in a wave flume at the Institute of Ocean Hydraulics of Pukyong National University, Republic of Korea. The flume is 35 m long, 1 m wide, and 1 m deep with glass walls. The wave flume has a longitudinal middle wall from the half point of the flume length to the end of the flume (i.e., absorber side). Therefore, only 48.5 cm of the width is used for the experiment. The wave generator is a piston-type paddle which is capable of generating regular and irregular waves and equipped with the active absorption of reflected waves. A wave absorber is located at the end of the flume.

A real caisson breakwater located at Oh-Ryuk-do breakwater in Republic of Korea is selected as the target structure. The caisson model was designed for 2-D wave flume and all components of the test were prepared as 1/58 scale-down size. Four components of the structure include caisson body, cap concrete, and two adjacent blocks. The inner wall of the real caisson is ignored for the lab-scale caisson. All four components have shear keys to reflect interlocking effects between adjacent caissons. According to the limitation of the width of the 2-D wave flume, two concrete blocks were adopted by replacing adjacent caissons. Figure 4(a) illustrates the dimension of all components of test structure. The caisson has 34 cm of height and 34 cm of width; it also includes the empty inner space with vertical wall of 5 cm thickness. Height of the cap concrete is maximum 10 cm. Bottom dimension of the concrete is the same as that of the caisson. To make the caisson fit to the side wall of the wave flume, two adjacent blocks have 6 cm thickness except for the part of shear keys. Figure 4(b) shows the installed test structure in the 2-D wave flume. The caisson and the cap concrete were installed on the foundation mound with the adjacent block. Detailed cross-section view of the test setup is illustrated in Figure 5.

To simulate the installed condition of the real breakwater, the test structure and the foundation were set up on the 2-D wave flume. The foundation mound consists of sand layer,

gravel layer, and tetra pod (TTP) layer. The sand layer and the gravel layer represent a gravel mound and an armor gravel of the real caisson breakwater, respectively. The sand layer is approximately of maximum 10 cm thick and 1 m long. The gravel layer is mainly 2 cm thick and it covers the entire sand layer. For the wave generator side (i.e., seaward in the real), the TTP layer was set for wave energy dissipation.

Vibration responses were measured by an acceleration acquisition system which consists of accelerometers, a signal conditioner, terminal blocks, a DAQ card, and a laptop. Accelerometers used for the test are PCB 393B04 model which has ± 5 g of measureable range and 1 V/g of sensitivity. The accelerometers were installed on the cap concrete to measure the vibration response of the caisson as shown in Figure 6. Lee et al. [21] show that the rigid body motion is sensitive to the variation of foundation integrity. In this study, the rigid body motion is selected as the target motion. Also, the limited accessibility at the on-site field area was considered for the installation of the sensors for the lab tests. To extract the rigid body motion, sensors were installed in y - and z -axes for four points.

3.2. Test Scenarios. To examine the water-level effects on the caisson model by using the wave-induced vibration responses, the water level in 2-D wave flume was controlled as follows. Three water levels in 2-D wave flume were designed to give different water level conditions on the caisson. Tidal condition at the field area is reflected on the designed water levels. Three water levels are indicated in Figure 5. Water depth, h , of the highest water level (i.e., WL1) is 460 mm and that of the lowest water level (i.e., WL3) is 416 mm. The gap of each water level is 22 mm and it is 6.5% of the caisson height.

To excite the caisson, two excitation sources were employed: (1) wave load and (2) hammer impact. For the wave load excitation, the extreme waves which have 12.5 cm wave height and 1.97 seconds wave period were generated by the wave maker and applied to the model caisson. For the hammer impact, the rubber hammer was used to manually apply the impact force by a test implementer. For the wave load excitation, acceleration responses were measured during 120 seconds. It is noted that the wave generator was operated in the first half of the period and turned off in the second half. Acceleration responses were measured during 20 seconds for the hammer impact.

4. Effect of Water-Level Effect on Vibration Characteristics of Caisson Breakwater

4.1. Vibration Responses Analysis of Lab-Scale Caisson. To examine the compatibility of the wave-induced vibration responses for analyzing the vibration characteristics of the caisson, the vibration tests were performed by using the two excitation sources (i.e., the wave load and the hammer impact). Acceleration signals of the caisson structure are shown in Figure 7. As the wave load was applied to the caisson model, the maximum acceleration was 0.005 g. Even the extreme waves (which have 12.5 cm wave height and 1.97 seconds wave period) were applied to the caisson structure;

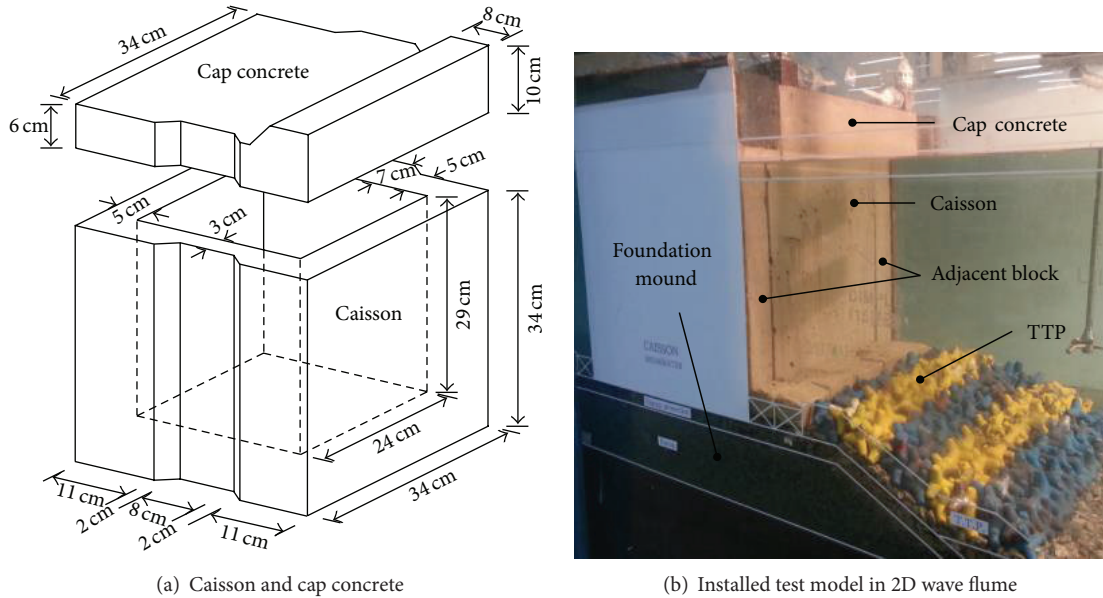


FIGURE 4: Experimental setup of lab-scale caisson model.

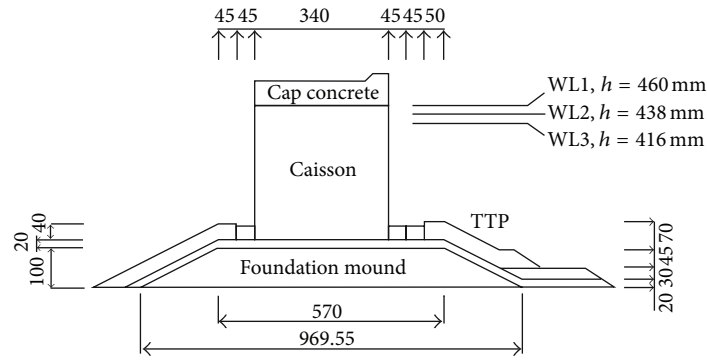


FIGURE 5: Cross section of test setup in the 2D wave flume.

relative small responses were measured as compared to that of the impact hammer excitation. Acceleration responses were rapidly decreased after turning off the wave generator. As the hammer impact was applied to the caisson model, the impact period was 1.6 seconds on average and the maximum acceleration was 0.31 g. The impact excitations were applied manually, so that all impact responses were different in magnitudes.

4.1.1. Power Spectral Density of Vibration Responses. The PSDs of the acceleration signals were calculated by using (2). In this study, the excitation was applied to the y -direction, along which vibration responses were analyzed on frequency domain. For the highest water-level (WL1), the PSDs were extracted from the y -directional response of point 1, as shown in Figure 8. The number of FFT points is 1024 for calculation of the PSD and its resolution is 0.4883 Hz.

For the wave load excitation, many peaks are observed in the frequency range of 0 to 60 Hz. For the hammer impact, only two peaks are observed in the frequency of 0 to

60 Hz. In Figure 8(b), the two peaks are the resonance peaks corresponding to the first and the second natural frequencies (i.e., 17.15 Hz and 42.50 Hz).

Next, we examined the source of many peaks of the wave load excitation in Figure 8(a). Figure 9 shows three PSDs with different measuring time sets: (1) 0–120 seconds for the entire period, (2) 0–60 seconds for the period during the operation of the wave generator, and (3) 60–120 seconds for the period after turning off the wave generator. For the PSDs corresponding to the measuring time 0–120 seconds and the measuring time 0–60 seconds, most of the peaks have relative differences in magnitudes. On the other hand, the PSD of the measuring time 60–120 seconds when the wave generator is turned off has relatively small magnitude in the frequency range higher than 10 Hz. As the incident waves repeatedly hit the caisson wall, extra random waves are generated due to the reflection, breaking, and modulation of waves. According to the wave transformation or modulation, many peaks related to the waves and structural behaviors are observed in the PSD results. The peaks corresponding to the resonance peaks of

TABLE 1: Natural frequencies and damping ratios for the highest water level.

Excitation source	Modal parameter extraction method	Natural frequency, f (Hz)		Damping ratio, ξ (%)	
		Mode 1	Mode 2	Mode 1	Mode 2
Wave load	FDD	17.08	41.5	1.28	0.58
	SSI	17.19	41.80	2.14	0.05
Hammer impact	FDD	17.09	41.99	8.34	3.45
	SSI	17.69	42.00	8.26	3.88

TABLE 2: Variation of modal parameters due to water-level changes.

Excitation source	Water-level scenarios	Natural frequency, f (Hz)		Damping ratio, ξ (%)	
		Mode 1	Mode 2	Mode 1	Mode 2
Wave load	WL1, $h = 460$ mm	17.19 (—)	41.80 (—)	2.14	0.05
	WL2, $h = 438$ mm	18.62 (8.32)	42.38 (1.39)	0.74	0.20
	WL3, $h = 416$ mm	20.98 (22.05)	41.60 (−0.48)	0.87	0.11
Hammer impact	WL1, $h = 460$ mm	17.69 (—)	42.00 (—)	8.26	3.88
	WL2, $h = 438$ mm	17.92 (1.30)	43.32 (3.14)	8.98	4.25
	WL3, $h = 416$ mm	19.55 (10.51)	42.49 (1.17)	7.85	6.29

* Parentheses indicate variation (%) of natural frequencies with respect to WL1.

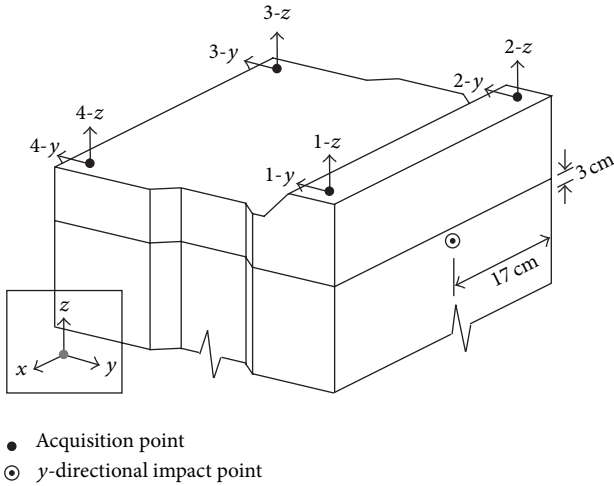


FIGURE 6: Sensor orientations and excitation points.

the hammer impact responses cannot be determined based on only the PSD results.

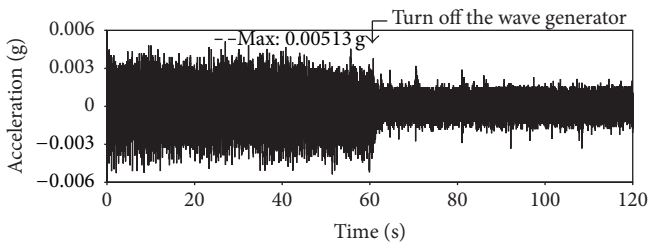
To eliminate the peaks which do not represent structural modes, the PSD analysis was performed by using the lower number of FFT points, 512, and it gives the resolution of 0.9766 Hz. Figure 10 shows the PSDs of the acceleration signals with two different resolutions. The peaks become weaker but they still exist except very small peaks. Additional future study is demanded to identify structural modes of the wave-induced vibration responses by the use of the PSD-based method.

4.1.2. Extraction of Modal Parameters. For the extraction of modal parameters such as natural frequency, damping coefficient, and mode shape, frequency domain decomposition

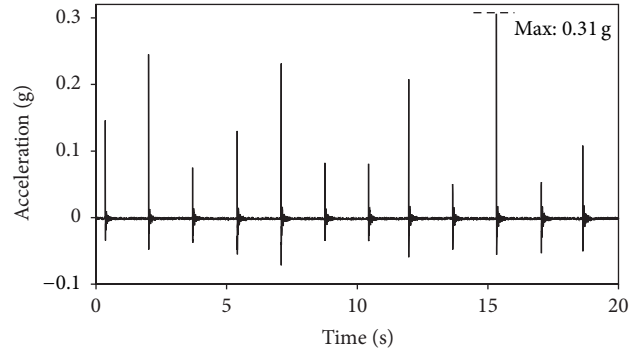
(FDD) method and stochastic subspace identification (SSI) method are selected. As previously reported by Yi and Yun [20], both methods are accurate for the extraction of modal parameters. However, their performances on gravity-type harbor structures are not reported yet. Therefore, vibration responses under the highest water level (WL1) were utilized to compare their performances on the extraction of modal parameters of harbor caisson model.

For the FDD method, the singular value matrix was extracted by using (3). Figure 11 illustrates the first columns of the singular value matrices for the highest water level, WL1. In the figure, the solid lines indicate the singular values. Also, the extracted modal parameters by the FDD method were summarized in Table 1. Two modes are observed at about 17 Hz and 42 Hz. The results of two excitation sources are shown well matched in natural frequency but different in damping ratios. The damping ratios are observed as 1.28% for mode 1 and 0.58% for mode 2 for the wave load excitation and observed as 8.34% for mode 1 and 3.45% for mode 2 for the hammer impact. The 2-D planar mode shapes are extracted as shown in Figure 12. The mode shapes are extracted from the vibration responses of the sensors installed on the top of the caisson as shown in Figure 6. Both mode shapes of mode 1 and mode 2 are the y -directional sway motions.

In the SSI method, the Hankel matrix was calculated by using (5) and the stable modes were identified by stabilization chart analysis. The stabilization charts are illustrated in Figure 11 and the extracted modal parameters are summarized in Table 1. In the figure, the grey circles indicate the stable mode. Two modes are observed at about 17 Hz and 42 Hz. Damping ratios of each mode are calculated by (6). The results of two excitation sources are shown to be well matched in natural frequency but different in damping ratios. The damping ratios are observed as 2.14% for mode 1 and 0.05% for mode 2 for the wave load excitation and observed as 8.26% for mode 1 and 3.88% for mode 2 for the hammer

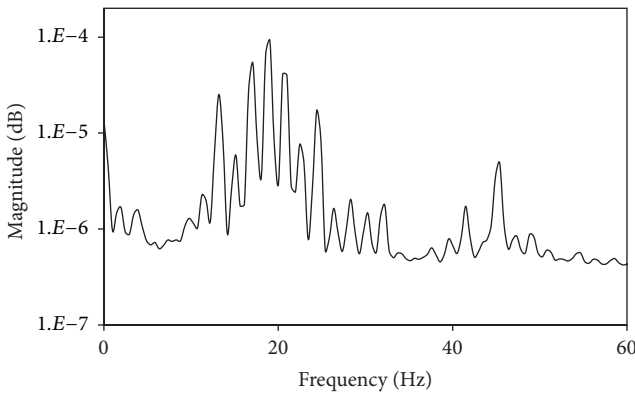


(a) Wave load

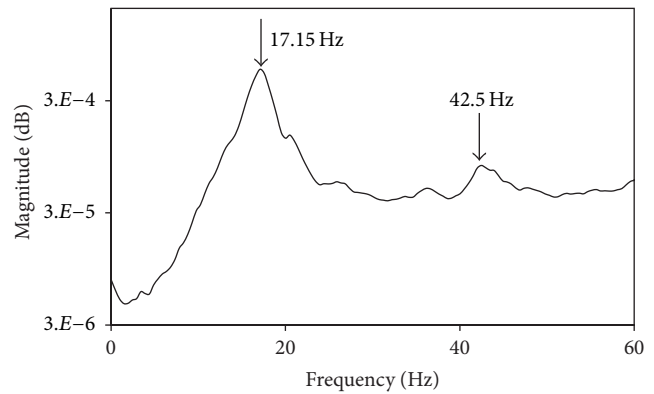


(b) Hammer impact

FIGURE 7: Vibration signals of lab-scale model.



(a) Wave load



(b) Hammer impact

FIGURE 8: Power spectral densities of vibration signals for the highest water level.

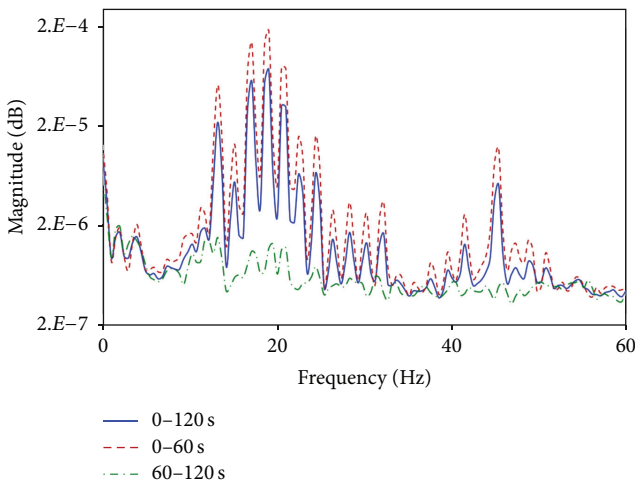


FIGURE 9: Power spectral densities for wave-induced vibration signals of different time sets.

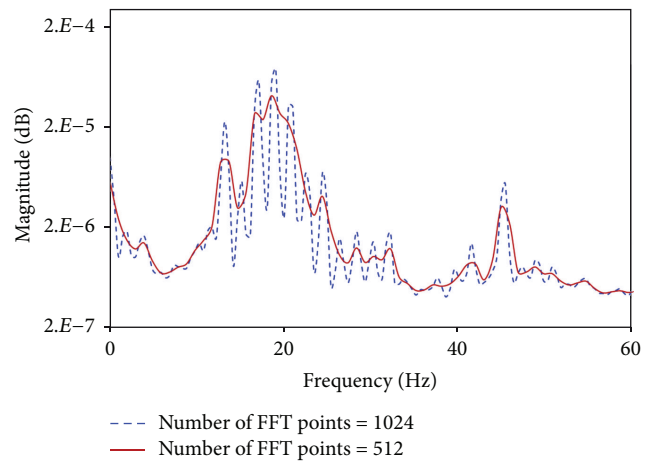


FIGURE 10: Power spectral densities for wave-induced vibration signals of two different FFT resolutions.

impact. The mode shapes are also extracted and both mode shapes of mode 1 and mode 2 are the y -directional sway motions similar to the results of the FDD method.

In case of the wave excitation, many modes are observed in the frequency range of 0 to 60 Hz. Regular waves were generated as the excitation load and it is observed not only the structural responses but also characteristics of the incident

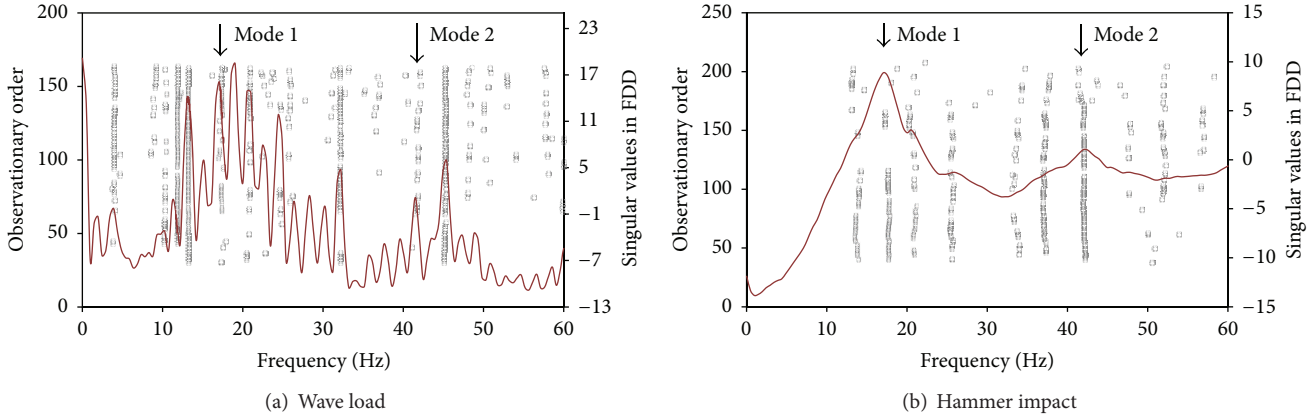


FIGURE 11: Stabilization charts of SSI method and singular values of FDD method (WL1).

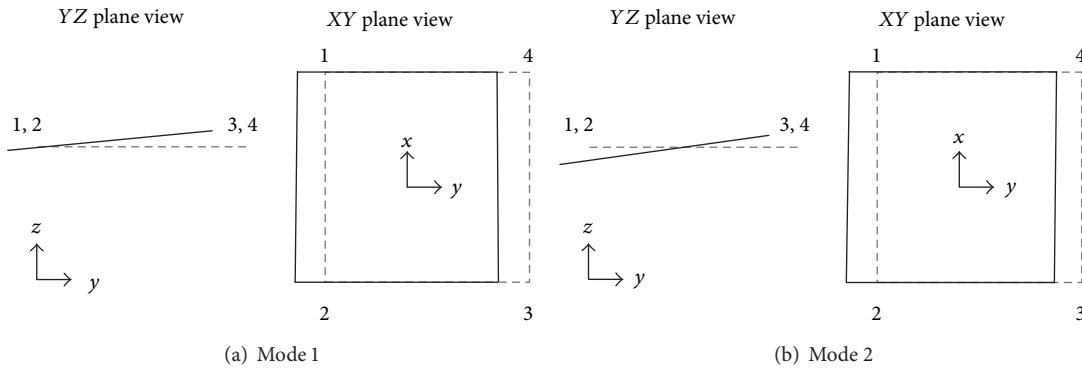


FIGURE 12: First two mode shapes of caisson structure by SSI method.

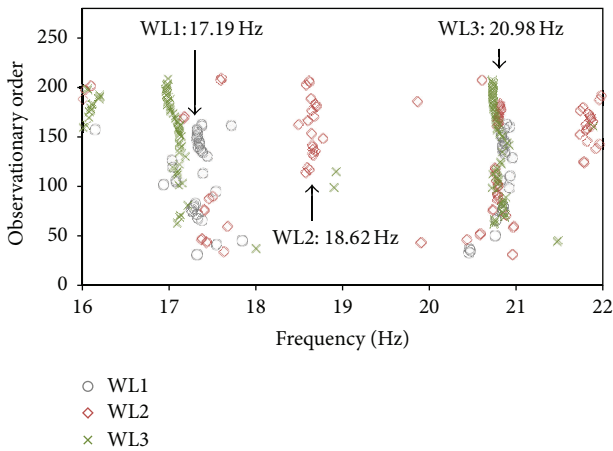


FIGURE 13: Stabilization chart of SSI method: change in natural frequency versus change in water level.

waves and its transformed waves. Therefore, it is difficult to distinguish structural modes from detected modes. As a result of hammer impact, only two structural modes are observed. It was used as the reference information of modal characteristics of caisson system. For mode 1, there are closer peaks around the peak of mode 1 in the singular values of

FDD method (see Figure 11(a)). So, we cannot make sure which one is the mode 1 from the result of the FDD method. However, mode 1 can be distinguished among the closer peaks by the use of the results from both the FDD and the SSI methods together. Note that the SSI method shows consistent results in the extraction of natural frequency and mode shape.

4.2. *Effect of Water-Level Variation on Vibration Responses.* To examine the effect of water-level variation on the caisson modal parameters, the natural frequency and the damping ratio are extracted by the SSI method, which produces more consistent results as described previously. The modal parameters were extracted for three different water levels. The natural frequencies and the damping ratios are summarized in Table 2.

As illustrated in the stabilization chart shown in Figure 13, natural frequencies of the wave-induced vibration responses are analyzed with respect to the water level changes. For the wave load excitation, the natural frequencies increase gradually as the water level decreases. In mode 1, 8.32% of natural frequency is increased when the water level decreases of 6.5% of the caisson height. Also, 22.05% of natural frequency is increased when the water level decreases of 12.9% of the caisson height. In mode 2, the changes in the natural frequencies are up and down as the water levels decrease,

which maybe partially due to measurement uncertainty. The damping ratios show the decrease tendency in mode 1 as the water levels decrease but rather in irregular pattern in mode 2.

For the hammer impact excitation, the natural frequencies of mode 1 also increase gradually as the water level decreases. In mode 1, 1.30% of natural frequency is increased when the water level decreases of 6.5% of the caisson height. Also, 10.51% of natural frequency is increased when the water-level decreases of 12.9% of the caisson height. In mode 2, the changes in the natural frequencies are up and down as the water levels decrease, which maybe partially due to measurement uncertainty. The damping ratios show the decrease tendency in mode 1 as the water levels decrease but rather in irregular pattern in mode 2.

5. Conclusion

In this paper, vibration characteristics of gravity-type caisson breakwater structures which have water level variations were experimentally examined by using wave load excitations. To achieve the objective, the following approaches were implemented. Firstly, vibration analysis methods were selected to examine the dynamic characteristics of the lab-scale caisson. Secondly, vibration test on a lab-scale caisson which is installed in a two-dimensional wave flume was performed under two excitation sources and three water levels. Thirdly, the compatibility of the wave-induced vibration responses was evaluated by comparison with the impact vibration responses, and the appropriate vibration analysis method is selected. Finally, the water-level effects on the caisson breakwater are examined based on the modal parameters which are experimentally measured for the 2-D wave flume tests.

The following observations and conclusions have been made. The vibration responses of the caisson reflect not only the caisson structural behavior but also the characteristics of the incident waves and the transformed (or modulated) waves. So, it is rather difficult to identify vibration features from the wave-induced vibration responses. However, in case of that, the information of structural modes is known and the reliable modal features can be extracted from the combined use of both SSI method and FDD method. Also, it is observed that the effect of water-level on the caisson's modal parameters can be estimated from the wave-induced vibration responses via SSI method. The effect of water level is more sensitive to the lower mode of the caisson. As the water level decreases, the natural frequency increases gradually and damping ratio decreases.

Acknowledgments

This work was supported by the Pukyong National University Research Abroad Fund in 2012 (C-D-2012-0915). The authors would like also to acknowledge the financial support of the Project "Development of inspection equipment technology for harbor facilities" funded by Korea Ministry of Land, Transportation, and Maritime Affairs.

References

- [1] S. Y. Lee, J. T. Kim, J. H. Yi, and Y. K. Kang, "Structural health monitoring of harbor caisson-type structures using harmony search method," *Journal of Ocean Engineering and Technology*, vol. 23, no. 1, pp. 122–128, 2009.
- [2] Y. Goda, "Dynamic response of upright breakwaters to impulsive breaking wave forces," *Coastal Engineering*, vol. 22, no. 1-2, pp. 135–158, 1994.
- [3] S. Takahashi, K.-I. Shimosako, K. Kimura, and K. Suzuki, "Typical failures of composite breakwaters in Japan," in *Proceedings of the 27th International Conference on Coastal Engineering (ICCE '00)*, pp. 1899–1910, July 2000.
- [4] H. Omeraci, "Review and analysis of vertical breakwater failures: lessons learned," *Coastal Engineering*, vol. 22, pp. 3–29, 1994.
- [5] R. D. Adams, P. Cawley, C. J. Pye, and B. J. Stone, "A vibration technique for non-destructively assessing the integrity of structures," *Journal of Mechanical Engineering Science*, vol. 20, no. 2, pp. 93–100, 1978.
- [6] N. Stubbs and R. Osegueda, "Global non-destructive damage evaluation in solids," *International Journal of Analytical and Experimental Modal*, vol. 5, no. 2, pp. 67–79, 1990.
- [7] D.-S. Li, H.-N. Li, L. Ren, L. Sun, and J. Zhou, "Experiments on an offshore platform model by FBG sensors," in *Smart Structures and Materials: Sensors and Smart Structures Technologies for Civil, Mechanical, and Aerospace Systems*, Proceeding of SPIE, pp. 100–106, March 2004.
- [8] S. Jang, J. Li, and B. F. Spencer Jr., "Corrosion estimation of a historic truss bridge using model updating," *ASCE Journal of Bridge Engineering*, vol. 18, no. 7, pp. 678–689, 2012.
- [9] T. H. Yi and H. N. Li, "Methodology developments in sensor placement for health monitoring of civil infrastructures," *International Journal of Distributed Sensor Networks*, vol. 2012, Article ID 612726, 11 pages, 2012.
- [10] A. E. Aktan, D. N. Farhey, A. J. Helmicki et al., "Structural identification for condition assessment: experimental arts," *Journal of Structural Engineering*, vol. 123, no. 12, pp. 1674–1684, 1997.
- [11] T. Sato and M. Sato, "Structural identification using neural network and Kalman filter algorithms," *Journal of Structural Mechanics and Earthquake Engineering*, vol. 39, no. 563, pp. 23–32, 1997.
- [12] J.-T. Kim, Y.-S. Ryu, H.-M. Cho, and N. Stubbs, "Damage identification in beam-type structures: frequency-based method vs mode-shape-based method," *Engineering Structures*, vol. 25, no. 1, pp. 57–67, 2003.
- [13] G. J. Yun, K. A. Ogorzalek, S. J. Dyke, and W. Song, "A two-stage damage detection approach based on subset selection and genetic algorithms," *Smart Structures and Systems*, vol. 5, no. 1, pp. 1–21, 2009.
- [14] J. H. Yi, W. S. Park, S. Y. Lee, J. T. Kim, and C. G. Seo, "Evaluation of vibration characteristics of caisson-type breakwater using impact vibration tests and validation of numerical analysis model," *Journal of Korean Society of Coastal and Ocean Engineers*, vol. 25, no. 1, pp. 1–10, 2013.
- [15] T. H. Yi, H. N. Li, and H. M. Sun, "Multi-stage structural damage diagnosis method based on "energy-damage" theory," *Smart Structures and Systems*, vol. 12, no. 3-4, pp. 345–361, 2013.
- [16] Z. Yang, A. Elgamel, T. Abdoun, and C. J. Lee, "A numerical study of lateral spreading Behind a caisson-type quay wall," in

Proceeding of 4th International Conference on Recent Advances in Geotechnical Earthquake Engineering and Soil Dynamics and Symposium, pp. 1–6, San Diego, Calif, USA, 2001.

- [17] D. K. Kim, H. R. Ryu, H. R. Seo, and S. K. Chang, “Earthquake response characteristics of port structure according to exciting frequency components of earthquakes,” *Journal of Korean Society of Coastal and Ocean Engineers*, vol. 17, no. 1, pp. 41–46, 2005.
- [18] M. Gao, G. Dai, and J. Yang, “Dynamic studies on caisson-type breakwaters,” in *Proceedings of the International 21st Coastal Engineering Conference*, pp. 2469–2478, 1988.
- [19] M. Paz and W. Leigh, *Structural Dynamics: Theory and Computation*, Kluwer Academic, Norwell, Mass, USA, 5th edition, 2004.
- [20] J.-H. Yi and C.-B. Yun, “Comparative study on modal identification methods using output-only information,” *Structural Engineering and Mechanics*, vol. 17, no. 3-4, pp. 445–466, 2004.
- [21] S. Y. Lee, K. D. Nguyen, T. C. Hyunh, J. T. Kim, J. H. Yi, and S. H. Han, “Vibration-based damage monitoring of harbor caisson structure with damaged foundation-structures interface,” *Smart Structures and Systems*, vol. 10, no. 6, pp. 517–546, 2012.

Research Article

A Combined Optimal Sensor Placement Strategy for the Structural Health Monitoring of Bridge Structures

Can He,¹ Jianchun Xing,¹ Juelong Li,² Qiliang Yang,¹ Ronghao Wang,¹ and Xun Zhang¹

¹ College of Defense Engineering, PLA University of Science and Technology, Nanjing 210007, China

² Technical Management Office of Naval Defense Engineering, Beijing 100841, China

Correspondence should be addressed to Can He; hecan19880828@163.com

Received 28 July 2013; Revised 4 November 2013; Accepted 5 November 2013

Academic Editor: Jeong-Tae Kim

Copyright © 2013 Can He et al. This is an open access article distributed under the Creative Commons Attribution License, which permits unrestricted use, distribution, and reproduction in any medium, provided the original work is properly cited.

Optimal sensor placement is an important part in the structural health monitoring of bridge structures. However, some defects are present in the existing methods, such as the focus on a single optimal index, the selection of modal order and sensor number based on experience, and the long computation time. A hybrid optimization strategy named MSE-AGA is proposed in this study to address these problems. The approach firstly selects modal order using modal participation factor. Then, the modal strain energy method is adopted to conduct the initial sensor placement. Finally, the adaptive genetic algorithm (AGA) is utilized to determine the optimal number and locations of the sensors, which uses the root mean square of off-diagonal elements in the modal assurance criterion matrix as the fitness function. A case study of sensor placement on a numerically simulated bridge structure is provided to verify the effectiveness of the MSE-AGA strategy, and the AGA method without initial placement is used as a contrast experiment. A comparison of these strategies shows that the optimal results obtained by the MSE-AGA method have a high modal strain energy index, a short computation time, and small off-diagonal elements in the modal assurance criterion matrix.

1. Introduction

Due to strong wind force, torrential rain, severe earthquake, explosion, and other abnormal loads, large scale civil infrastructures may be damaged in the long service period [1]. The traditional routine visual inspection usually ignores the tiny failures and the flaws inside the structures. Therefore, structural health monitoring (SHM) [2–4] has been an important research topic in the engineering protection field. A typical SHM system includes three subsystems: sensor subsystem, data processing subsystem, and condition evaluation subsystem. Optimal sensor placement (OSP) [5–7] is a critical issue in SHM research. Generally, the more sensors are placed, the more information could be obtained. Unfortunately, the number of sensors is strictly constrained by cost. For instance, there are only 23, 65, and 72 accelerometers instrumented in the Tsing Ma Bridge, the Ting Kau Bridge, and Jiangyin Bridge, respectively [8]. The sensor number is far less than the available positions. Therefore, how to set suitable sensor number and where to deploy the sensors become the challenging tasks.

Several methods have been developed to achieve OSP. Salama et al. [9] presented the modal kinetic energy method to choose the positions that have high modal energy. Deb-nath et al. [10] modified this method and used the modal contribution in output energy to evaluate sensor placement. Kammer [11] claimed that the optimal placement result was determined by minimizing the norm of the Fisher information matrix, which was obtained from the modal and measurement covariance matrices, and proposed the effective independence method. Meo and Zumpano [12] proposed the effective independence driving-point residue method. Li et al. [13] determined the existence of a relationship between the effective independence method and the modal kinetic energy method and presented a quick computation of the effective independence method through QR downdating [14]. Carne and Dohrmann [15] developed a famous method named minMAC. As known, a basic requirement in distinguishing the measured modes is that the measured modal vectors must be as linearly independent as possible. Carne considered the modal assurance criterion (MAC) matrix to be an ideal scalar constant relating the causal relationship between two modal

vectors and used the minimization of the off-diagonal terms in the MAC matrix as a measure of sensor network configuration. Li et al. [16] extended this method. In recent years, computational intelligence approaches have been applied to achieve OSP, such as genetic algorithm [17, 18] and monkey algorithm [19]. A review concerning the differences and relationships of the sensor placement methods was provided by Yi and Li [20].

Although these methods made great progress, a few defects still existed. Firstly, a suitable placement result for a real civil structure often requires multiple evaluation indexes to be optimal at the same time. To the bridge structures, the noise in the sensor signal is usually very big because of strong wind and heavy rain, so it is necessary to improve the signal to noise ratio of the collected data. A good sensor placement result for bridge structures requires both a high modal energy index and a good MAC index. A high modal energy index can ensure that the measured data have a high signal to noise ratio and a high precision. A good MAC index can guarantee the orthogonality of the measured modal vectors and increase the amount of modal information obtained from the collected data. However, most of the traditional methods were proposed for a single optimal index. This shortage leads to the fact that the traditional OSP methods cannot be used in the real bridge structures without modification. Secondly, the modal shape matrix is composed of all orders of modes, and the modes can be easily attained through modal analysis. Nevertheless, in order to reduce computation complexity, only the modes that have large dynamical response are selected to compose the modal shape matrix. How to select the modal order becomes an important problem. The modal order was selected based on experience in the traditional methods. However, Yi et al. [21] discovered that modal order selection had a strong effect on the final placement result. Therefore, the selection of modal order by expert experience is subjective and imprecise. At the same time, due to special form, size, and dynamical feature, it is very hard to obtain the optimal sensor number only by experience for a specific structure. Therefore, the determination of sensor number based on experience is also not suitable. Finally, the computation speeds of the previous methods are slow, especially with respect to the large scale bridge structures.

The objective of this study is to present a new OSP method that has multiple optimal indexes and a short computation time. A new method termed MSE-AGA is proposed to achieve this goal. First, the modal participation factor (MPF) is proposed to select the modal order. Then, the initial sensor assignment is performed using the modal strain energy (MSE) method to improve the modal energy index of the selected locations. Finally, the AGA method is adopted to determine the optimal sensor number and locations, which uses root mean square of off-diagonal elements in the modal assurance criterion matrix as the fitness function. This fitness function assists in improving the MAC index of sensor placement. At the same time, the adaptive crossover and mutation factors can improve the convergence speed and the searching efficiency of the algorithm.

The remaining parts of the paper are organized as follows. Section 2 introduces the mathematical model of OSP and

the evaluation criteria. The MSE-AGA strategy is described in Section 3. Section 4 provides a case study of sensor placement on a numerically simulated bridge structure to verify the effectiveness of the MSE-AGA method and discusses the limitations of using finite element (FE) model instead of the real structure. Section 5 is the conclusion and the future work.

2. Basic Theory

The OSP problem assumes that there are n locations where sensors can be deployed and s sensors should be placed on the structure. Therefore, the mathematical model of OSP can be described as the following optimal equation [22]:

$$\begin{aligned} \max \quad & f(n_1, n_2, \dots, n_s) \\ \text{s.t.} \quad & n_1, n_2, \dots, n_s \in N, \end{aligned} \quad (1)$$

where f is the objective function, which is determined by the selected evaluation criterion.

Several criteria, such as MAC, modal energy criterion, Fisher information matrix criterion [23], and probability-based damage detection criterion [24], are proposed to evaluate the effect of the different sensor placement methods. Due to the requirement of mode identification and the noisy environment of bridge structures, MAC and modal energy criterion are chosen as the evaluation criteria in this study.

The linearly independent of the modal vector is an essential demand to identify the modes. Carne and Dohrmann [15] considered the MAC to be an ideal criterion to evaluate the relevance of the modal vectors. In the criterion, the smaller off-diagonal elements of the MAC matrix represent better independence of the modal vectors. The MAC matrix is computed as

$$\text{MAC}_{ij} = \frac{(\phi_i^T \phi_j)^2}{(\phi_i^T \phi_i)(\phi_j^T \phi_j)}, \quad (2)$$

where ϕ_i is the i th column of the modal shape matrix.

Modal energy is an important structural feature parameter. Stubbs et al. [25, 26] determined that the MSE was an effective index to detect the structural damage. Therefore, selection of the degree of freedoms (DOFs) that have large energy is necessary to achieve condition evaluation and damage identification of the structure. The modal energy criterion selects the DOFs with high modal energy as the sensor locations. Therefore, this criterion is suitable for bridge structures with the measured data that are greatly affected by the noisy environment. The MSE matrix of the structure is defined as

$$\text{MSE} = \phi^T K \phi, \quad (3)$$

where ϕ is the modal shape matrix and K is the structural stiffness matrix.

3. Description of the MSE-AGA Method

MSE-AGA, a new OSP method, is presented in this section to address the existing problems in the previous methods.

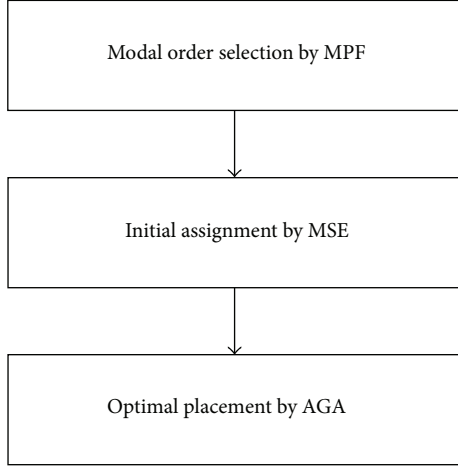


FIGURE 1: Steps of the MSE-AGA method.

The method includes three strategies. First, the suitable modal order is selected using MPF on the basis of modal analysis. Second, the initial sensor assignment is performed using the MSE method. Finally, the optimal number and locations of sensors are determined using the AGA method. The main steps of the MSE-AGA method are shown in Figure 1.

3.1. Modal Order Selection and Initial Sensor Placement

3.1.1. Modal Order Selection. Different choices of modal order result in various placement results. According to the requirement of OSP, the modal order that has a strong dynamic response should be selected. Nevertheless, modal order is selected based on experience in the traditional methods. In order to solve this problem, MPF is presented as the evaluation criterion for the modal order selection.

The equation of motion for the n DOF dynamic system is represented as

$$M\ddot{u} + C\dot{u} + Ku = -MD\ddot{u}_g, \quad (4)$$

where M is the structural mass matrix, C is the structural damping matrix, K is the structural stiffness matrix, D is the vector describing the excitation direction, u is the modal displacement vector, and \ddot{u}_g is the acceleration generated by input force.

The displacement vector u can be transformed by

$$u = \phi \cdot q, \quad (5)$$

where ϕ is the modal shape matrix and q is the modal coordinate.

If M , C , and K meet the orthogonalization of the normalization modal shape, (4) can be written as

$$\ddot{q}_i + 2\zeta_i \omega_i \dot{q}_i + \omega_i^2 q_i = -\frac{\phi_i^T MD}{\phi_i^T M \phi_i} \ddot{u}_g(t), \quad (6)$$

where q_i is the i th modal coordinate, ω_i is the natural frequency of the i th mode, and ζ_i is the fraction of critical damping of the i th mode.

The MPF is defined as (7):

$$\varphi_{ir} = \frac{\phi_i^T MD_r}{\phi_i^T M \phi_i}, \quad (7)$$

where φ_{ir} is the MPF of the i th mode in r direction.

The mass normalization for the modal shape matrix ϕ is determined by

$$\phi_i^T M \phi_i = 1. \quad (8)$$

Based on (7) and (8), the MPF can be expressed as

$$\varphi_{ir} = \phi_i^T MD_r. \quad (9)$$

D_r is a vector describing the excitation in r direction, and it can be computed as

$$D_r^T = T \cdot E_r, \quad (10)$$

where E_r is a unit vector in r direction and T is a constant matrix, which indicates the relationship between the excitation and reference points. One has the following:

$$T = \begin{bmatrix} 1 & 0 & 0 & 0 & Z - Z_0 & Y_0 - Y \\ 0 & 1 & 0 & Z_0 - Z & 0 & X - X_0 \\ 0 & 0 & 1 & Y - Y_0 & X_0 - X & 0 \\ 0 & 0 & 0 & 1 & 0 & 0 \\ 0 & 0 & 0 & 0 & 1 & 0 \\ 0 & 0 & 0 & 0 & 0 & 1 \end{bmatrix}, \quad (11)$$

where X_0 , Y_0 , and Z_0 are the global Cartesian coordinates of the reference point and X , Y , and Z are the global Cartesian coordinates of the excitation point.

MPF reflects the dynamic response amplitudes of all of the modes. Therefore, the modal order that has a bigger MPF value should be selected priorly.

Although all of the modes can be sorted based on their MPFs, there is still a question that how many modes should be selected. The modal participating mass ratio is presented as a criterion to determine the number of the modes. Modal participating mass is defined as

$$M_{pi} = \frac{(\phi_i^T MD)^2}{\phi_i^T M \phi_i}, \quad (12)$$

where M_{pi} is the modal participating mass of the i th mode.

When mass normalization has been conducted for the modal shape matrix ϕ , (12) can be transformed by:

$$M_{pi} = (\phi_i^T MD)^2. \quad (13)$$

The modal participating mass ratio of the i th mode can be expressed as

$$r_i = \frac{M_{pi}}{D^T MD}. \quad (14)$$

Wilson [27] suggested that summation of modal participating mass ratio of the selected modes should be over 90%. This criterion is employed in this study to determine the number of modes.

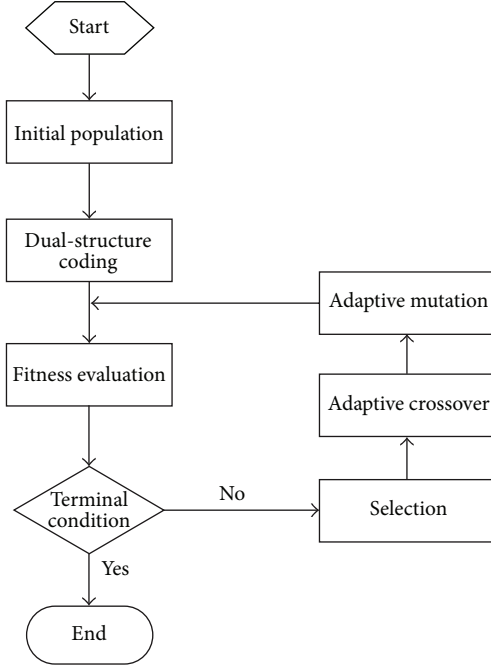


FIGURE 2: Flowchart of the AGA method.

3.1.2. *Initial Sensor Placement Using the MSE Method.* The MSE method selects the locations with large response amplitudes as sensor locations by comparing the MSE of all of the DOFs. The MSE of the i th mode can be computed as

$$\text{MSE}_i = \phi_i^T K \phi_i. \quad (15)$$

The MSE of all of the DOFs can be computed on the basis of (15):

$$\text{MSE}_i = \phi_i^T [k_1 \ k_2 \ \dots \ k_n] \phi_i = \sum_{j=1}^n \phi_i^T k_j \phi_{ji}, \quad (16)$$

$$\text{MSE}_{ji} = \phi_i^T k_j \phi_{ji}, \quad (17)$$

where MSE_{ji} is the MSE associated with the j th DOF in the i th mode.

The main idea of initial sensor placement is to select the DOFs with large MSE as the candidate locations. Therefore, this step ensures the final placement locations having big modal energy and reduces the searching space of the optimal placement.

3.2. *Final Sensor Placement Using the AGA Method.* The genetic algorithm (GA) is proven to be an effective tool for OSP. However, faults that should be improved remain. For instance, two or more sensors may be placed on one location and the searching efficiency may not be good enough. The adaptive genetic algorithm (AGA) is adopted in this study to settle the issues. The flowchart of the AGA is shown in Figure 2.

3.2.1. *Coding Method.* In the traditional coding method, the gene number of value 1 could be changed in the process of

TABLE 1: Dual-structure coding method.

Append code	$s(1)$	$s(2)$...	$s(n)$
Variable code	$Xs(1)$	$Xs(2)$...	$Xs(n)$

crossover and mutation, which may result in two or more sensors placed on one location. Therefore, the dual-structure coding method is used in this study. As shown in Table 1, the chromosome of individual is composed of two rows, where the upper row $s(i)$ named append code indicates all of the locations and the lower row $Xs(i)$ named variable code represents whether the location $s(i)$ places a sensor with the value 0 or 1.

3.2.2. *Selection, Crossover, and Mutation.* The roulette wheel selection scheme is used to select the best individual in each generation, and an elitist strategy is employed to retain the best individual for the subsequent generation.

Crossover and mutation factors have a strong influence on the efficiency of GA. In the basic genetic algorithm, these factors are set by trial and error, and they keep invariant throughout the entire iteration cycle. These defects lower the evolution velocity and the optimization ability of the algorithm. Therefore, the adaptive mechanism is introduced into this algorithm. The adaptive adjustment processes of the two factors are defined as

$$P_c = \begin{cases} p_1 - \frac{p_2(f_c - f_{\text{avg}})}{f_{\text{max}} - f_{\text{avg}}}, & f_c \geq f_{\text{avg}}, \\ p_1, & f_c < f_{\text{avg}}, \end{cases} \quad (18)$$

$$P_m = \begin{cases} p_3 - \frac{p_4(f_m - f_{\text{avg}})}{f_{\text{max}} - f_{\text{avg}}}, & f_m \geq f_{\text{avg}}, \\ p_3, & f_m < f_{\text{avg}}, \end{cases}$$

where f_{max} is the maximum of fitness value, f_{avg} is the average of population fitness value, f_c represents the bigger fitness value between the two crossover individuals, f_m is the biggest fitness value among the mutation individuals, p_1 and p_2 represent the maximum and minimum values of the crossover probability, respectively, and p_3 and p_4 are the maximum and minimum values of the mutation probability, respectively.

3.2.3. *Fitness Function.* The off-diagonal elements in the MAC matrix express the correlation between two modal vectors. Identifying the i th mode and the j th mode is easy if the value of MAC_{ij} is small. The two modal vectors are orthogonal when $\text{MAC}_{ij} = 0$. Therefore, the fitness function is constructed as

$$f = 1 - \text{RMS}, \quad (19)$$

where RMS is the root mean square of the off-diagonal elements in the MAC matrix.

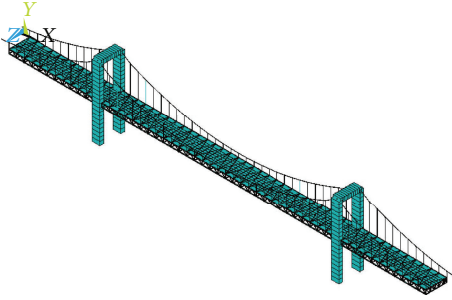


FIGURE 3: FE model of the bridge.

4. Simulation Verification of the MSE-AGA Method

In order to verify the effectiveness of the MSE-AGA method, a case study of sensor placement on a numerically simulated bridge structure is provided below.

4.1. Modeling and Modal Analysis. A three-span suspension bridge is selected in this demonstration case. The bridge has a main span of 128 m and two side spans of 46 m each. The FE model of the bridge is established using the commercial software ANSYS, and the model is shown in Figure 3.

The truss girder and main towers are modeled by beam4, the main cables and suspenders are simulated by link10, and the bridge deck is built by shell63. A total of 1276 nodes and 3381 elements are generated. The natural frequency (Table 2) and modal shape (Figure 4) of the structure are received by modal analysis.

4.2. Modal Order Selection Using MPF. The MPFs of the modes are computed using (9) to (11). The results of the first 30 modes are shown in Figures 5, 6, and 7.

As shown in Figures 5 to 7, the 2nd, 7th, 11th, and 14th modes have large MPFs in x direction. The 1st, 9th, 13th, and 22nd modes, have large MPFs in y direction, and MPFs of the 3rd, 5th, and 10th modes are big in z direction. So the 1st, 2nd, 3rd, 5th, 7th, 9th, 10th, 11th, 13th, 14th, and 22nd modes are selected as the optimal mode combination. The modal participating mass ratio of the combination in each direction is computed using (12) to (14), and the results are presented as

$$r_x = 99\%; \quad r_y = 99\%; \quad r_z = 99\%, \quad (20)$$

where r_x is the modal participating mass ratio in x direction.

The results show that r_x , r_y , and r_z are all over 90%. Therefore, the selected modal order combination is reasonable.

4.3. OSP Using MSE-AGA. The MSE of all of the DOFs in the bridge can be computed using (15) to (17). The first 1000 DOFs are selected as the candidate locations. Then, AGA is used to optimize the placement. The parameters in AGA are set as shown in Table 3.

The optimal process of AGA is executed according to Figure 2. The fitness function values with different sensors numbers are shown in Figure 8.

As shown in Figure 8, when the sensor number is set between 5 and 15, the fitness increases with sensor added. The fitness function reaches its maximum when the sensor number is set at 16. But, if the sensor number is more than 16, the fitness does not increase with sensor added. The reason for the contradiction is that the row vector determined at the newly included sensor location has a strong linear relationship with the entire previous sensor set. Therefore, sixteen is determined as the optimal sensor number in consideration of placement cost and efficiency.

AGA is used to optimize sensor placement on the basis of the initial deployment. The final optimal result is provided in Table 4.

4.4. Contrast Experiment. AGA without initial deployment is used as a contrast experiment. The optimal placement results of the two methods are provided in Figures 9 and 10.

The modal energy index and MAC indexes are selected to evaluate the placement effect of the two methods. The summations of the MSE of the selected locations are shown in Figure 11.

The MAC matrixes of the two methods are shown in Figures 12 and 13. The RMS and maximum value of the off-diagonal elements in the MAC matrix are provided in Table 5.

The two methods are calculated on the same computer with the CPU frequency of 2 GHz, and Matlab 7.0 is used as the computation software. The computation time of the two methods is shown in Table 6.

4.5. Result Analysis. As shown in Figure 11, the summation of MSE of the selected locations by MSE-AGA is evidently larger than that by AGA. The result implies that MSE-AGA is a better method than the AGA in terms of modal energy index. The reason for this result is that the MSE method is used for the initial sensor placement in the MSE-AGA method.

Table 5 shows that the off-diagonal elements in the MAC matrixes of the two methods are very small, thus suggesting that both methods are effective in terms of the MAC index. This is because AGA that is used for the final sensor placement in the two methods has a good searching ability. Comparing the two methods, the maximum value of the off-diagonal elements in MSE-AGA is 0.0826, which is smaller than that in the AGA. But the RMS of the off-diagonal elements as computed using the MSE-AGA is 0.0221, a little bigger than that computed by the AGA. A similar conclusion can be received from Figures 12 and 13. The slight difference is because the searching space of the AGA is composed of all of the structural DOFs, but the searching space of the MSE-AGA is composed of only the candidate locations selected by the MSE method.

Due to the smaller searching space, the computation time of MSE-AGA is 240 seconds as shown in Table 6. However, 3299 seconds are required to accomplish the comparison method on the same computer. Therefore, the MSE-AGA method is better than the AGA in terms of the computation time index.

TABLE 2: Natural frequency of the first 10 modes.

Modal order	1	2	3	4	5	6	7	8	9	10
Frequency (Hz)	0.539	0.733	0.934	1.143	1.173	1.294	1.477	1.680	1.735	1.810

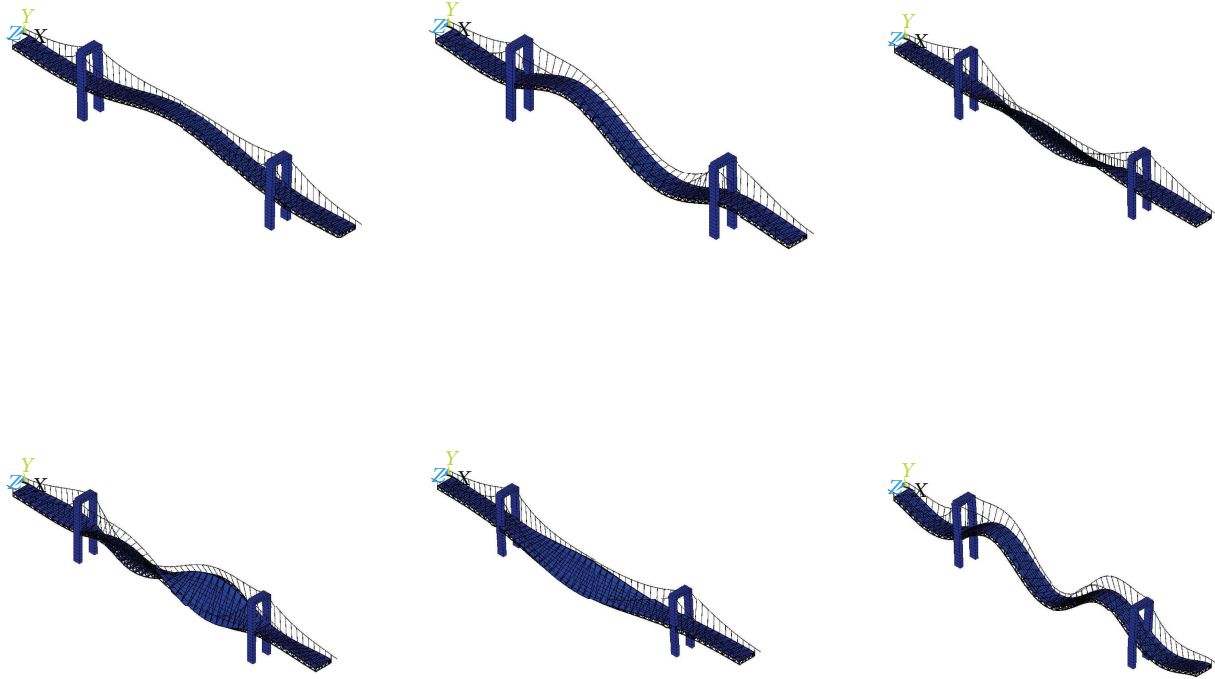


FIGURE 4: The 1st to 6th modal shapes.

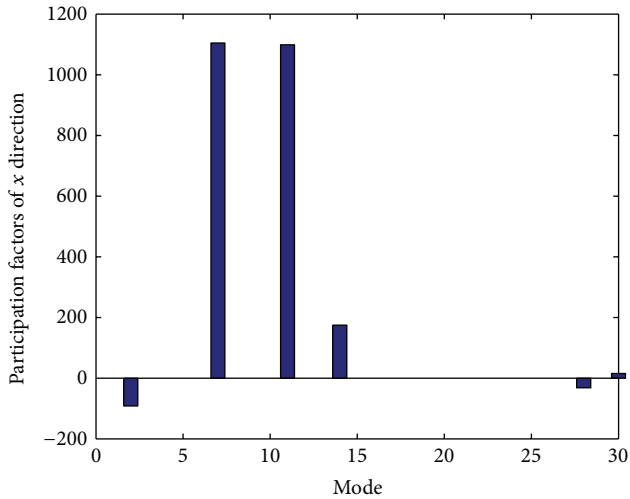


FIGURE 5: MPF of x direction.

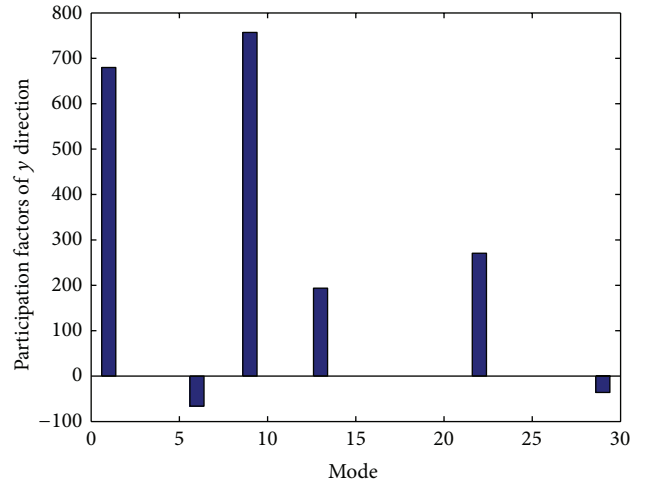


FIGURE 6: MPF of y direction.

TABLE 3: Parameter setting.

Population	Generation	P_1	P_2	P_3	P_4
80	500	0.9	0.3	0.1	0.001

4.6. Discussion. The demonstration case is based on a numerically simulated bridge structure. The FE model of the

bridge structure is built in strict accordance with the actual structure. Therefore, the numerical simulation can verify the effectiveness of the MSE-AGA method to a certain extent. Of course, the numerical FE model remains some limitations inevitably. Firstly, noise and other environmental factors, such as temperature and wind force, may impact the dynamic feature of the real bridge structure. However, these factors are

TABLE 4: Optimal sensor locations.

Sensor no.	1	2	3	4	5	6	7	8	9	10	11	12	13	14	15	16
Node	27	43	119	208	316	526	589	649	709	716	821	886	1206	1253	1258	1264
Direction	X	X	X	Y	Y	Y	Y	Y	Y	Z	Y	Y	Z	Z	X	X

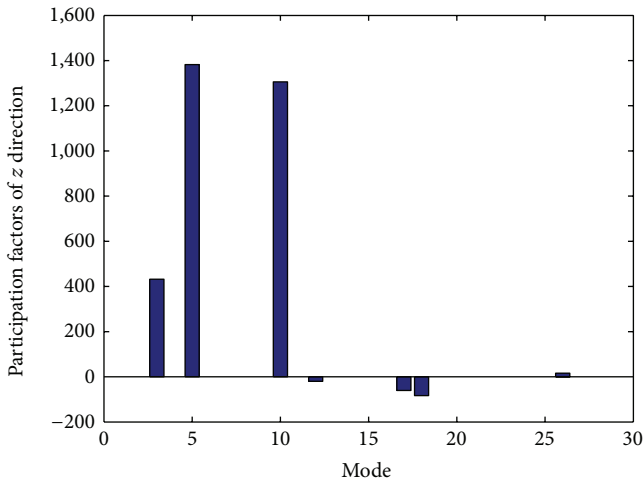


FIGURE 7: MPF of z direction.

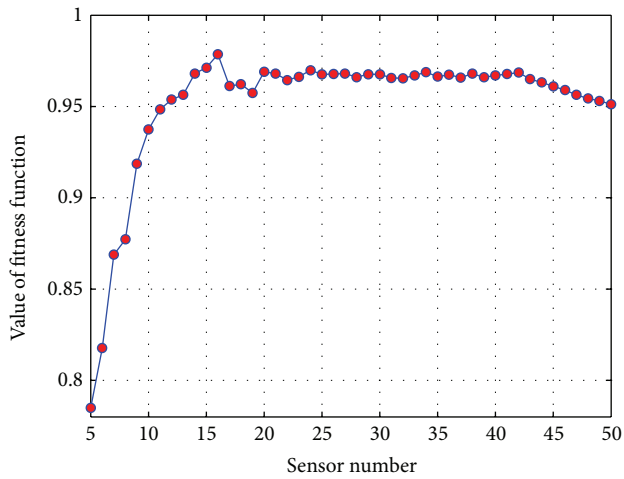


FIGURE 8: Fitness function values with different sensor numbers.

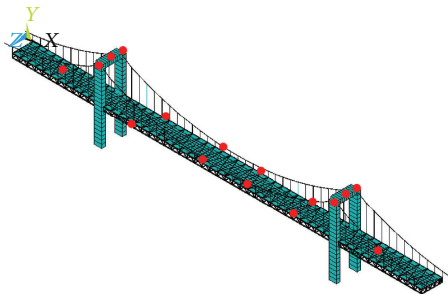


FIGURE 9: Optimal result of MSE-AGA.

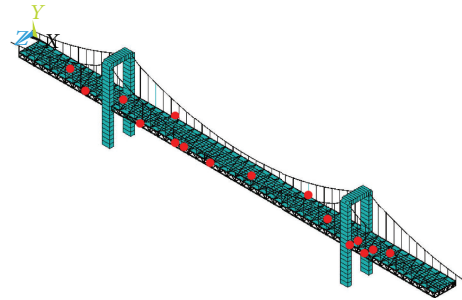


FIGURE 10: Optimal result of AGA.

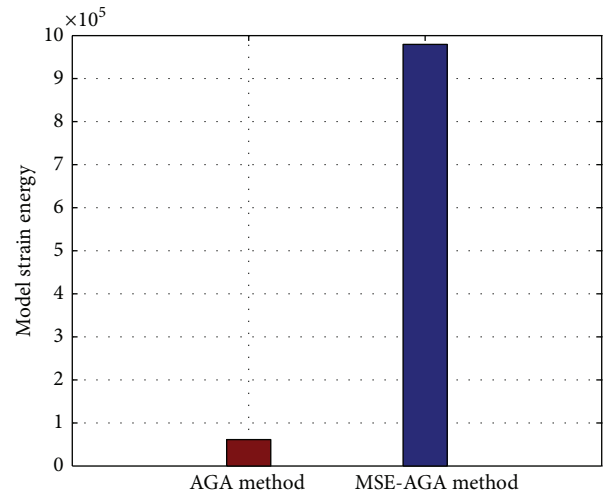


FIGURE 11: MSE indexes of the two methods.

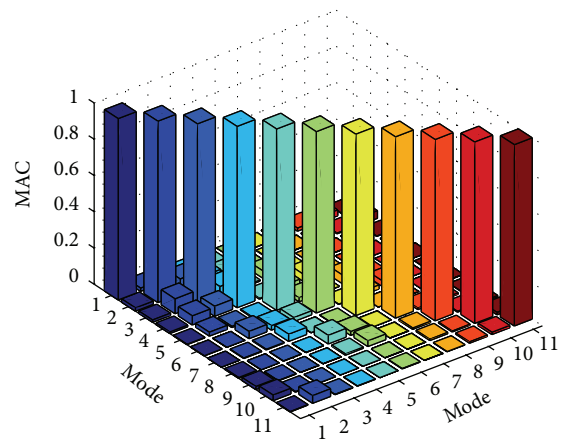


FIGURE 12: MAC matrix of MSE-AGA.

TABLE 5: MAC indexes of the two methods.

Method	RMS of the off-diagonal elements	Maximum value of the off-diagonal elements
MSE-AGA	0.0221	0.0826
AGA	0.0199	0.0855

TABLE 6: Computation times of the two methods.

Method	Computation time (second)
MSE-AGA	240
AGA	3299

not considered in the simulation experiment. Secondly, in the real structure, there are some locations that are not available to deploy the sensors. But these nodes may be selected as the optimal sensor locations in the numerical analysis.

5. Conclusions and Future Work

The traditional OSP methods are limited by the use of a single optimal index, the selection of modal order and sensor number based on experience, and the long computation time. MSE-AGA, which is a new hybrid method based on the MSE and AGA methods, is presented in this study to address these issues. In this strategy, the modal order is selected using MPF firstly. Then, the MSE method is used for the initial sensor placement. Finally, the sensor number and locations are determined using the AGA. With the case analysis, some conclusions are summarized as follows.

- (1) Using the MSE method for the initial sensor placement ensures that the optimal locations have the large MSE. Therefore, it can make the collected data have a high precision and signal to noise ratio. AGA, which uses the MAC as the fitness function, is utilized in the final sensor placement. This step guarantees that the RMS and the maximum value of the off-diagonal elements are small. Experiment results show that the combined sensor placement strategy is good in terms of both the modal energy index and the MAC index.
- (2) A new modal order selection method based on MPF is proposed as an improvement to the traditional method. MPF can reflect the dynamic response amplitudes of all modes. Therefore, it is effective to select the modes having large dynamical feature using MPF.
- (3) The optimal sensor number can be determined by computing the fitness function values with different numbers of sensors. This method can help us determine the sensor number required in the SHM and reduce cost.
- (4) Because of the additional process of the initial sensor placement, the searching space of MSE-AGA is smaller than that of AGA. This is the main reason that MSE-AGA has a short computation time.

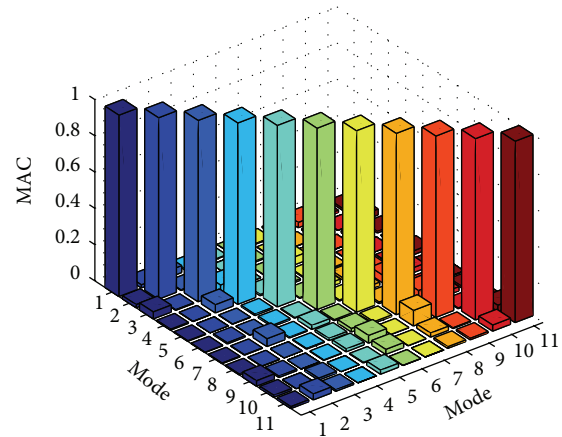


FIGURE 13: MAC matrix of AGA.

The MSE-AGA method is proved to be an effective OSP method as the numerical analysis. However, there are still some works to do. An experiment of sensor placement on a real bridge structure will be conducted by our team in further research.

Conflict of Interests

The authors declare that there is no conflict of interests regarding the publication of this paper.

References

- [1] B. Bhattacharya, "Disaster mitigation of large infrastructure systems," in *Proceedings of the International Symposium on Engineering under Uncertainty: Safety Assessment and Management (ISEUSAM '12)*, pp. 477–482, Bombay, India, 2013.
- [2] J. Ou and H. Li, "Structural health monitoring in mainland china: review and future trends," *Structural Health Monitoring*, vol. 9, no. 3, pp. 219–231, 2010.
- [3] C. Boller, F. K. Chang, and Y. Fujino, *Encyclopedia of Structural Health Monitoring*, John Wiley & Sons, New York, NY, USA, 2009.
- [4] S. Jang, H. Jo, S. Cho et al., "Structural health monitoring of a cable-stayed bridge using smart sensor technology: deployment and evaluation," *Smart Structures and Systems*, vol. 6, no. 5-6, pp. 439–459, 2010.
- [5] B. B. Li, D. S. Li, X. Zhao, and J. P. Ou, "Optimal sensor placement in health monitoring of suspension bridge," *Science China*, vol. 55, no. 7, pp. 2039–2047, 2012.
- [6] M. Meo and G. Zumpano, "On the optimal sensor placement techniques for a bridge structure," *Engineering Structures*, vol. 27, no. 10, pp. 1488–1497, 2005.
- [7] I. Bruant, L. Gallimard, and S. Nikoukar, "Optimal piezoelectric actuator and sensor location for active vibration control, using genetic algorithm," *Journal of Sound and Vibration*, vol. 329, no. 10, pp. 1615–1635, 2010.
- [8] D. Balageas and C. P. Fritzen, *Structural Health Monitoring*, ISTE, London, UK, 2006.
- [9] M. Salama, T. Rose, and J. Garba, "Optimal placement of excitations and sensors for verification of large dynamical systems,"

- in *Proceedings of the 28th Structures, Structural Dynamics, and Materials Conference*, pp. 1024–1031, 1987.
- [10] N. Debnath, A. Dutta, and S. K. Deb, “Placement of sensors in operational modal analysis for truss bridges,” *Mechanical Systems and Signal Processing*, vol. 31, no. 8, pp. 196–216, 2012.
- [11] D. C. Kammer, “Sensor placement for on-orbit modal identification and correlation of large space structures,” *Journal of Guidance, Control, and Dynamics*, vol. 14, no. 2, pp. 251–259, 1991.
- [12] M. Meo and G. Zumpano, “Optimal sensor placement on a large scale civil structure,” in *Health Monitoring and Smart Nondestructive Evaluation of Structural and Biological Systems III*, pp. 108–117, SPIE, 2004.
- [13] D. S. Li, H. N. Li, and C. P. Fritzen, “The connection between effective independence and modal kinetic energy methods for sensor placement,” *Journal of Sound and Vibration*, vol. 305, no. 4-5, pp. 945–955, 2007.
- [14] D.-S. Li, H.-N. Li, and C.-P. Fritzen, “A note on fast computation of effective independence through QR downdating for sensor placement,” *Mechanical Systems and Signal Processing*, vol. 23, no. 4, pp. 1160–1168, 2009.
- [15] T. G. Carne and C. R. Dohrmann, “A modal test design strategy for model correlation,” in *Proceedings of the 13th Proceedings of International Society for Optical Engineering*, pp. 927–933, New York, NY, USA, 1995.
- [16] D. S. Li, C. P. Fritzen, and H. N. Li, “Extended minMAC algorithm and comparison of sensor placement methods,” in *Proceedings of the 26th IMAC Conference*, pp. 248–266, Florida, USA, 2008.
- [17] Y.-J. Cha, A. K. Agrawal, Y. Kim, and A. M. Raich, “Multi-objective genetic algorithms for cost-effective distributions of actuators and sensors in large structures,” *Expert Systems with Applications*, vol. 39, no. 9, pp. 7822–7833, 2012.
- [18] K. Worden and A. P. Burrows, “Optimal sensor placement for fault detection,” *Engineering Structures*, vol. 23, no. 8, pp. 885–901, 2001.
- [19] T. H. Yi, H. N. Li, and X. D. Zhang, “A modified monkey algorithm for optimal sensor placement in structural health monitoring,” *Smart Materials and Structures*, vol. 21, no. 10, pp. 1–9, 2012.
- [20] T. H. Yi and H. N. Li, “Methodology developments in sensor placement for health monitoring of civil infrastructures,” *International Journal of Distributed Sensor Networks*, vol. 2012, Article ID 612726, 11 pages, 2012.
- [21] T.-H. Yi, H.-N. Li, and G.-X. Wang, “Optimal sensor placement for super high-rise building based on simplified finite element model,” *Chinese Journal of Computational Mechanics*, vol. 25, no. 4, pp. 417–423, 2008.
- [22] C. Papadimitriou, “Optimal sensor placement methodology for parametric identification of structural systems,” *Journal of Sound and Vibration*, vol. 278, no. 4-5, pp. 923–947, 2004.
- [23] M. Basseville, A. Benveniste, G. V. Moustakides, and A. Rougee, “Optimal sensor location for detecting changes in dynamical behavior,” *IEEE Transactions on Automatic Control*, vol. 32, no. 12, pp. 1067–1075, 1987.
- [24] E. B. Flynn and M. D. Todd, “A Bayesian approach to optimal sensor placement for structural health monitoring with application to active sensing,” *Mechanical Systems and Signal Processing*, vol. 24, no. 4, pp. 891–903, 2010.
- [25] N. Stubbs and J.-T. Kim, “Damage localization in structures without baseline modal parameters,” *AIAA Journal*, vol. 34, no. 8, pp. 1644–1649, 1996.
- [26] J.-T. Kim, Y.-S. Ryu, H.-M. Cho, and N. Stubbs, “Damage identification in beam-type structures: frequency-based method vs mode-shape-based method,” *Engineering Structures*, vol. 25, no. 1, pp. 57–67, 2003.
- [27] E. L. Wilson, “Three-dimensional static and dynamic analysis of structures,” in *Computers and Structures*, 2002.

Research Article

Multiscale Structural Health Monitoring of Cable-Anchorage System Using Piezoelectric PZT Sensors

Khac-Duy Nguyen,¹ Jeong-Tae Kim,¹ and Young-Hwan Park²

¹ Department of Ocean Engineering, Pukyong National University, Busan 608-737, Republic of Korea

² Structural Engineering Division, Korea Institute of Construction Technology, Gyeonggi-Do 411-472, Republic of Korea

Correspondence should be addressed to Jeong-Tae Kim; idis@pknu.ac.kr

Received 5 August 2013; Revised 28 October 2013; Accepted 29 October 2013

Academic Editor: Hongnan Li

Copyright © 2013 Khac-Duy Nguyen et al. This is an open access article distributed under the Creative Commons Attribution License, which permits unrestricted use, distribution, and reproduction in any medium, provided the original work is properly cited.

Structural health monitoring of the cable-anchorage system is very important to secure the integrity of the cable-stayed bridge. The cable-anchorage system carries most of the self-weight, so that any damage in the system may significantly reduce the load carrying capacity of the bridge. This study presents a multiscale structural health monitoring of the cable-anchorage system using piezoelectric PZT sensors. Firstly, the electromechanical impedance response is utilized for alerting the change in anchorage zone caused by the loss of cable force or local anchorage damage. Secondly, the dynamic strain of cable is utilized for classifying the damage type. Thirdly, the loss of cable force and the anchorage damage are quantified by a frequency-based cable force model and an impedance-based damage estimation model, respectively. The feasibility of the approach is evaluated from the experiment on a lab-scale cable-anchorage model for which several damage scenarios are simulated about cable damage and anchorage damage.

1. Introduction

Cable-supported structures such as cable-stayed bridges have been widely constructed around the world. Bridges can be larger and even slimmer thanks to prestressing techniques. Also, the risk gets worse as the failure of prestressing system could result in significant reduction of load carrying capacity and even collapse of the bridge. Damage in cable-anchorage system can be classified as cable force loss and anchorage damage. The cable force loss is caused by creep and shrinkage in concrete, relaxation of cable stress, and corrosion of tendon. The anchorage damage is mostly caused by corrosion or cracks. Therefore, the integrity of the cable and the anchorage zone is an important issue to study for the healthy status of the cable-supported structure.

The demand on structural health monitoring (SHM) has been increased in aerospace and civil infrastructures over the past two decades [1, 2]. Among a variety of SHM studies on cable-anchorage system, many researches have focused on monitoring of cable force by using vibration response of cable or impedance response of anchorage [3–6]. The

vibration-based method can give accurate estimation of cable force. However, vibration feature is not sensitive to damage in anchorage zone. On the other hand, the impedance-based method has been found sensitive to any structural change in local area like anchorage zone. By utilizing electro-mechanical impedance of anchorage zone, the loss of cable force or anchorage damage would be detected.

In this study, a multi-scale structural health monitoring of the cable-anchorage system using piezoelectric PZT sensors is presented. Firstly, the electro-mechanical impedance response is utilized for alerting the change in anchorage zone caused by the loss of cable force or local anchorage damage. Secondly, the dynamic strain of cable is utilized for classifying the damage type. Thirdly, the loss of cable force and the anchorage damage are quantified by a frequency-based cable force model and an impedance-based damage estimation model, respectively. The feasibility of the approach is evaluated from the experiment on a lab-scale cable-anchorage model for which several damage scenarios are made about cable damage and anchorage damage.

2. Multi-Scale SHM Method for Cable-Anchorage System

2.1. Design of Multi-Scale SHM. Hybrid SHM methods have been proposed by many researchers in order to examine multiple types of damage or to increase the accuracy of damage detection results. For example, Kim et al. [7] proposed a hybrid algorithm to detect different damage types in plate-girder bridges by utilizing acceleration and impedance features. Park et al. [8] has attempted to detect whether girder damage or prestress-loss occurs in prestressed concrete girders. Sim et al. [9] accommodated both acceleration and strain measurements to improve the capability of damage detection for truss structures. Also, Nguyen et al. [10] utilized both dynamic strain and impedance measured from PZT sensors to enhance the capability of damage localization for beam-type structures.

On the basis of the previous studies, a hybrid SHM method is proposed for detecting the multiple damage types in cable-anchorage systems such as anchorage damage and cable force-loss. The method utilizes the active and passive responses of piezoelectric sensors at anchorage zone and cable body, respectively. The hybrid SHM scheme is performed in 3 major steps. In step 1, the occurrence of damage is alerted by monitoring electro-mechanical (E/M) impedance of the anchorage zone. In step 2, the alerted damage is classified into cable damage or anchorage damage by monitoring PZT dynamic strain of the cable. Finally, in step 3, damage estimation is performed for the classified damage type. If cable damage is specified, the amount of cable force change is estimated. If anchorage damage is specified, the severity of damage is evaluated.

2.2. Damage Occurrence Alert. Both the loss of cable force and anchorage damage causes the change in structural characteristics of the anchorage zone. Then, inversely, the electro-mechanical impedance signature of anchorage zone can be utilized to detect the occurrence of those damage types. The impedance response is based on the coupling of mechanical and electrical characteristics [11]. In this method, a piezoelectric (PZT) patch is usually surface-bonded to a host structure. The electrical signals of the PZT are partly controlled by mechanical effect of the host structure. By actuating the PZT with a voltage and measuring the current, the impedance can be obtained as a combined function of mechanical impedance of the host structure, $Z_s(\omega)$, and that of the PZT patch, $Z_a(\omega)$, as follows:

$$Z(\omega) = \left[j\omega \frac{w_p l_p}{t_p} \left(\left(\overline{e_{33}^\sigma} - d_{31}^2 \overline{Y_{11}^E} \right) + \frac{Z_a(\omega)}{Z_a(\omega) + Z_s(\omega)} d_{31}^2 \overline{Y_{11}^E} \left(\frac{\tan kl_p}{kl_p} \right) \right) \right]^{-1}, \quad (1)$$

where $\overline{Y_{11}^E} = (1 + j\eta)Y_{11}^E$ is the complex Young's modulus of the zero-electric field; $\overline{e_{33}^\sigma} = (1 - j\delta)e_{33}^\sigma$ is the dielectric constant of piezoelectric wafer; d_{31} is the piezoelectric coupling constant

in the direction-1 at zero stress; $k = \omega \sqrt{\rho/Y_{11}^E}$ is the wave number that depends on mass density ρ and Young's modulus Y_{11}^E of the piezoelectric material; and w_p , l_p , and t_p are the width, length, and thickness of the piezoelectric transducer, respectively. The parameters η and δ are structural damping loss factor and dielectric loss factor of piezoelectric material, respectively. The first term of (1) is the capacitive admittance of the free PZT patch, and the second term includes the mechanical impedance of both the PZT patch and the host structure. The mechanical impedance of the host structure can be expressed in term of mass (m), stiffness (k), and damping (c) as

$$Z_s(\omega) = m\omega j + c - \frac{k}{\omega} j. \quad (2)$$

Equations (1) and (2) show that any change in dynamic characteristic of the host structure can be represented by the change in E/M impedance. In this study, the change in E/M impedance is quantified by root mean square deviation (RMSD) index as

$$\text{RMSD}(Z, Z^*) = \sqrt{\frac{\sum_{i=1}^N [Z^*(\omega_i) - Z(\omega_i)]^2}{\sum_{i=1}^N [Z(\omega_i)]^2}}, \quad (3)$$

where $Z(\omega_i)$ and $Z^*(\omega_i)$ are the impedances measured before and after damage for the i th frequency, respectively; and N denotes the number of frequency points in the sweep. Basically, the RMSD has equal to 0 if no damage and larger than 0 if damage occurs. However, due to experimental and environmental errors, the RMSD may be larger than 0 although damage is not occurred. To deal with the uncertain conditions, the control chart analysis is used for decision-making out of RMSD values. In this study, the upper control limit (UCL_{RMSD}) is adopted for alarming damage occurrence, as follows:

$$\text{UCL}_{\text{RMSD}} = \mu_{\text{RMSD}} + 3\sigma_{\text{RMSD}}, \quad (4)$$

where μ_{RMSD} and σ_{RMSD} are mean and standard deviations of RMSD data set at undamaged condition, respectively. The calculation of UCL_{RMSD} is outline in three steps: firstly, n impedance signals are measured at undamaged condition; secondly, RMSD values for n impedance signals are computed by (3), then a set of RMSD values is obtained; and finally, UCL_{RMSD} of the RMSD value is calculated using (4). The occurrence of damage is indicated when the RMSD values are larger than the UCL. Otherwise, there is no indication of damage occurrence.

2.3. Damage-Type Classification. Once the damage is alerted, it should be classified as cable damage or anchorage damage using PZT dynamic strain response of cable. The fundamental of PZT dynamic strain has been studied by Sirohi and Chopra [12]. It is based on the direct effect of piezoelectric materials that an electrical field is produced due to mechanical strain of a PZT patch. When a PZT is bonded to the cable, strain

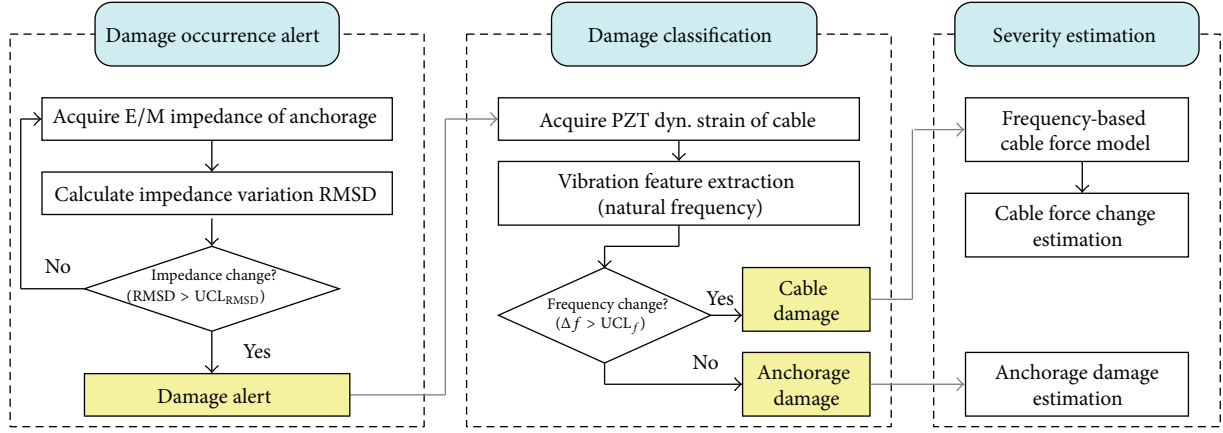


FIGURE 1: Schematic of multi-scale SHM for cable-anchorage system.

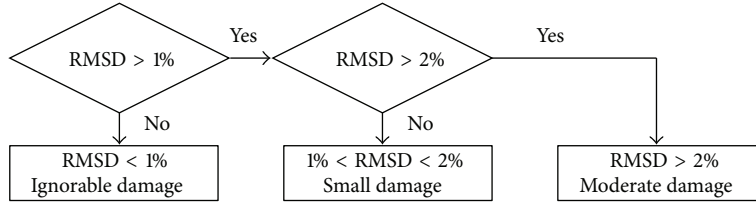


FIGURE 2: Damage severity assessment for anchorage damage.

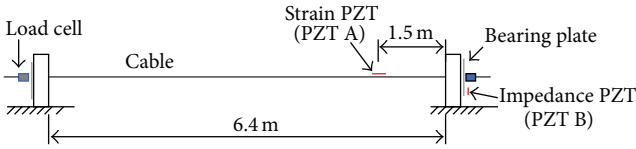


FIGURE 3: Schematic of cable-anchorage system.

response of cable can be expressed in term of the differential voltage measured between the PZT's terminals as

$$\varepsilon = \left(\frac{\overline{e_{33}^\sigma}}{d_{31} t_p Y^E} \right) V, \quad (5)$$

where ε is the strain of the cable; V is output voltage across the terminals of the PZT patch; t_p is thickness of the PZT patch; $\overline{e_{33}^\sigma}$ is the dielectric constant of the PZT patch; and d_{31} is the piezoelectric coupling constant. The natural frequencies of the cable are extracted by using power spectral density of the PZT strain signal as follows [13]:

$$S_\varepsilon(f) = \frac{1}{n_d T} \sum_{i=1}^{n_d} |\varepsilon_i(f)|^2, \quad (6)$$

where $\varepsilon_i(f)$ is dynamic responses transformed into frequency domain (FFT of a time history of dynamic strain $\varepsilon_i(t)$); n_d is the number of divided segments in the time history; and T is the data length of a divided segment.

If the change in cable's natural frequency is observed, the damage in cable is alerted. Otherwise, the damage is specified

to anchorage zone. Due to experimental and environmental errors, the upper control limit (UCL_f) is defined as a threshold for indicating the change in natural frequencies, as follows:

$$UCL_f = \mu_{\Delta f} + 3\sigma_{\Delta f}, \quad (7)$$

where $\mu_{\Delta f}$ and $\sigma_{\Delta f}$ are mean and standard deviations of change in natural frequency data set at undamaged condition, respectively. The calculation of UCL_f includes the following three steps: firstly, n PZT strain signals are measured at undamaged state; secondly, the natural frequencies of cable are extracted using power spectral densities of n strain signals by (6), then a set of the i th natural frequency of cable is obtained; and finally, UCL_f of change in the i th natural frequency is calculated using (7).

2.4. Damage Severity Estimation

2.4.1. Frequency-Based Cable Force Estimation. Once cable damage is alerted, tension force of the cable is estimated and the amount of cable force loss is calculated. In this study, the method proposed by Zui et al. [4] which considers effects of both flexural rigidity and cable-sag is used for estimating cable force by the following practical formulas.

Case 1. Cable with small sag ($\Gamma \geq 3$):

$$F = 4m(f_1 L)^2 \left[1 - 2.2 \frac{C}{f_1} - 0.55 \left(\frac{C}{f_1} \right)^2 \right]; \quad \xi \geq 17, \quad (8a)$$

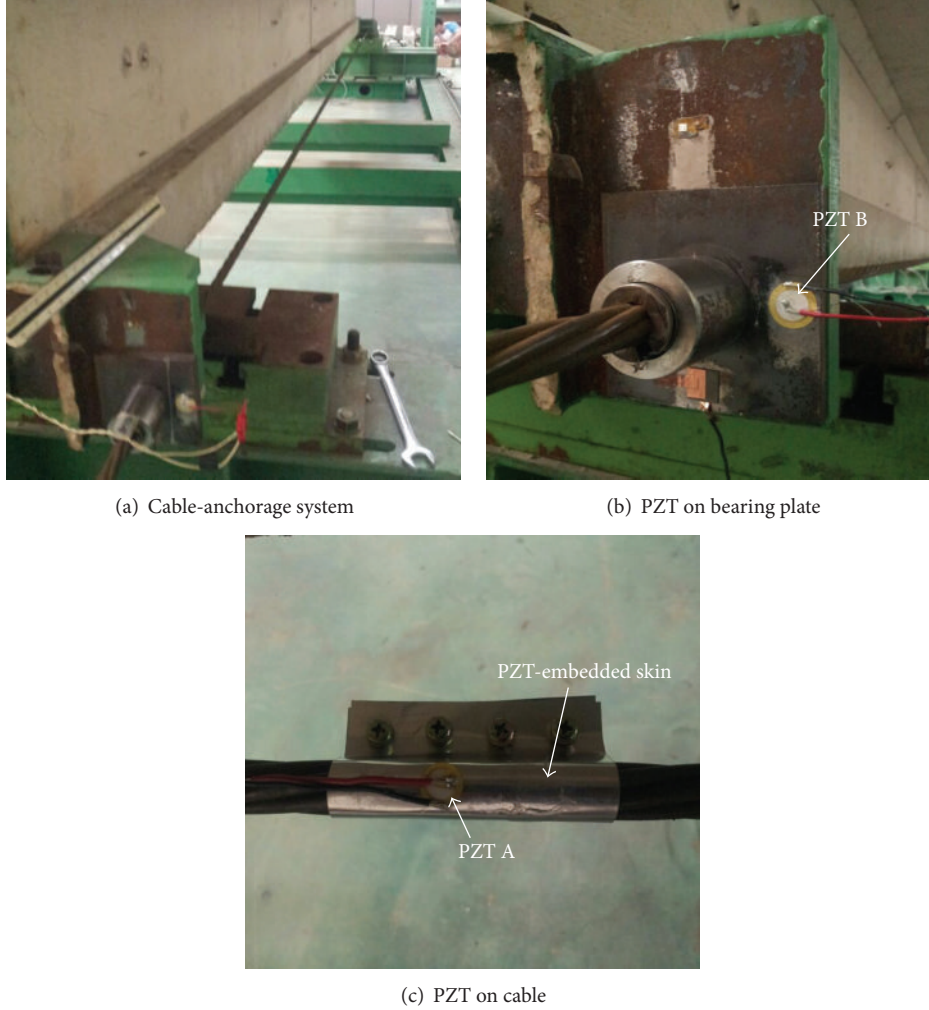


FIGURE 4: Experimental setup.

$$F = 4m(f_1L)^2 \left[0.865 - 11.6 \left(\frac{C}{f_1} \right)^2 \right]; \quad 6 \leq \xi \leq 17, \quad (8b)$$

$$F = 4m(f_1L)^2 \left[0.828 - 10.5 \left(\frac{C}{f_1} \right)^2 \right]; \quad \xi \leq 6. \quad (8c)$$

Case 2. Cable with large sag ($\Gamma \leq 3$):

$$F = m(f_2L)^2 \left[1 - 4.4 \frac{C}{f_2} - 1.1 \left(\frac{C}{f_2} \right)^2 \right]; \quad \xi \geq 60, \quad (9a)$$

$$F = m(f_2L)^2 \left[1.03 - 6.33 \frac{C}{f_2} - 1.58 \left(\frac{C}{f_2} \right)^2 \right]; \quad 17 \leq \xi \leq 60, \quad (9b)$$

$$F = m(f_2L)^2 \left[0.882 - 85 \left(\frac{C}{f_2} \right)^2 \right]; \quad \xi \leq 17. \quad (9c)$$

Case 3. Very long cable:

$$F_n = \frac{4m}{n^2} (f_nL)^2 \left[1 - 2.2n \frac{C}{f_n} \right]; \quad \xi > 200, \quad (10)$$

where f_1 , f_2 , and f_n are, respectively, measured natural frequencies corresponding to first, second, and n th modes ($n \geq 2$); $C = \sqrt{EI/(mL^4)}$; $\xi = \sqrt{F/(EI)} \cdot L$; $\Gamma = \sqrt{(mgL)/(128EA\delta^3 \cos^5 \theta [(0.31\xi + 0.5)/(0.31\xi - 0.5])}$; EI is the flexural rigidity of cable; L is the span length of cable; m is the mass of cable per unit length; δ is sag-to-span ratio which can be calculated as: $\delta = mgL/(8F)$ and θ is inclination angle of cable.

2.4.2. Anchorage Damage Estimation. The impedance-based monitoring technique may not quantitatively estimate the change in structural properties via the change in impedance signatures [14]. Many researchers have reported that the change in impedance signature is generally increased with damage growth [15, 16]. In this study, anchorage damage is specified into ignorable, small, or moderate damage based on

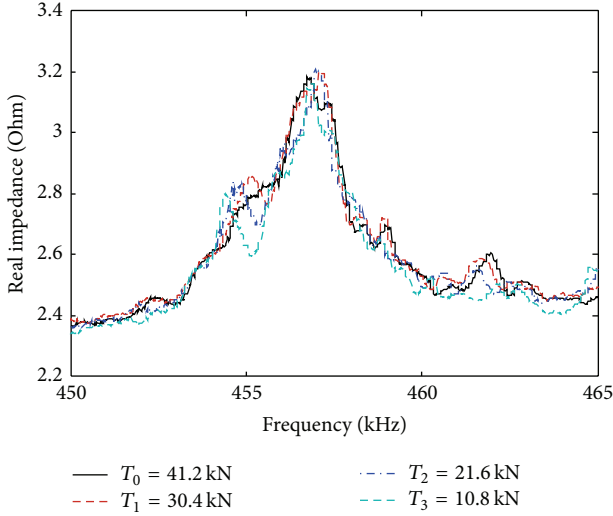


FIGURE 5: Impedance signatures for 4 cable force levels.

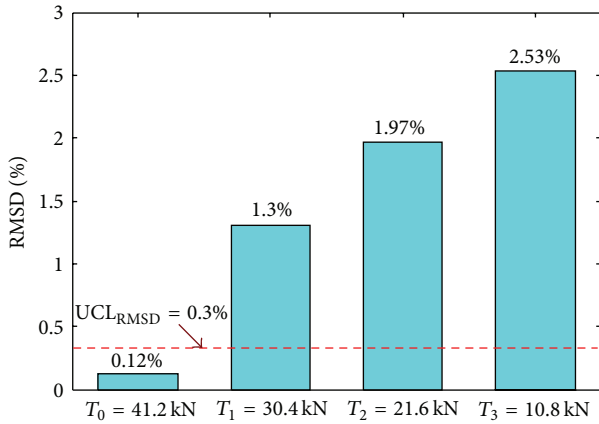


FIGURE 6: Damage occurrence alert for cable force-loss.

TABLE I: Specifications of cable.

	Nominal diameter (mm)	15.2
	Nominal are (mm ²)	138.7
	Tensile strength (kN)	260
	Elastic modulus (kN/m ²)	190
	Unit mass (kg/m)	1.37

the RMSD level as shown in Figure 2. Two threshold values, Threshold 1 and Threshold 2, are, respectively, set as 1% and 2% for indicating small damage and moderate damage.

3. Experimental Verification

3.1. Description of Test Structure. As shown in Figure 3, an experiment was carried out for a lab-scale cable-anchorage

model. The cable was comprised of 7 stainless steel ropes. The experimental setup is also described in Figure 4. The length of the cable was 6.4 m. The cable was anchored by two bearing plates at two ends. Detailed specifications of the cable are given in Table 1. For measurement of the cable's strain, a PZT sensor of 1 cm in diameter (PZT A) was bonded on a smart skin which tightly covers the cable at location 1.5 m from one cable end. The smart skin was designed to overcome the problem of bonding condition between the PZT sensors and cable surfaces. The deformation of the smart skin is secured by static friction in the interface between the skin and the cable. The skin plate should be flexible and should have low mass in order not to affect the response of the cable. Also, its thickness should be small enough compared to the cable section and its surface should have large frictional coefficient in order to guarantee the accuracy of strain measurement. The data acquisition system for PZT dynamic strain consisted of a NI-6036E DAQ card, a BNC-2090 terminal block and a PC with MATLAB. The NI-6036E DAQ card has the input impedance of up to 100 G Ω and the input data rates of up to 200 K samples/s which can ensure the proper sampling of the PZT sensor. The strain signals were recorded for 50 seconds with a sampling frequency of 500 Hz. For measurement of anchorage impedance, another PZT sensor of 1.5 cm in diameter (PZT B) was bonded on to one bearing plate. The E/M impedance signatures were measured by a commercial HIOKI 3532 impedance analyzer. The signatures between 450 kHz and 465 kHz were recorded with 801 interval points. During the test, room temperature was kept as close as constant of 23–24°C by air conditioners.

3.2. Damage Monitoring Case 1: Cable Damage. Cable tension force was introduced into the cable by a hydraulic jack as the cable was anchored at one end and pulled out at the other. A load cell was installed at one cable anchorage to measure the actual cable force. Each test was conducted after the desired cable force has been applied and the cable has been anchored. During the measurement, the hydraulic jack was removed from the cable-anchorage system to avoid the influence of the jack weight on dynamic characteristics of the cable. The cable was first pretensioned to $T_0 = 41.2$ kN which is considered as the healthy state. For cable damage simulation, the tension force was reduced to $T_1 = 30.4$ kN, $T_2 = 21.6$ kN, and $T_3 = 10.8$ kN.

The multi-scale damage detection is carried out in three steps as previously schematized in Figure 1. In the first step, the occurrence of damage is alerted using RMSD of impedance as described in (3). For each of the four tension force levels, impedance signatures were measured up to 4 ensembles from PZT B (on bearing plate as shown in Figure 4). As shown in Figure 5, impedance signatures were obtained for four cable force levels. By setting the impedance signature for the maximum tension force level, T_0 , as the undamaged state, RMSD values between the reference and other cable force levels are calculated as shown in Figure 6. It is observed that the RMSD values increase with the loss of cable force. For the three cable force-loss cases,

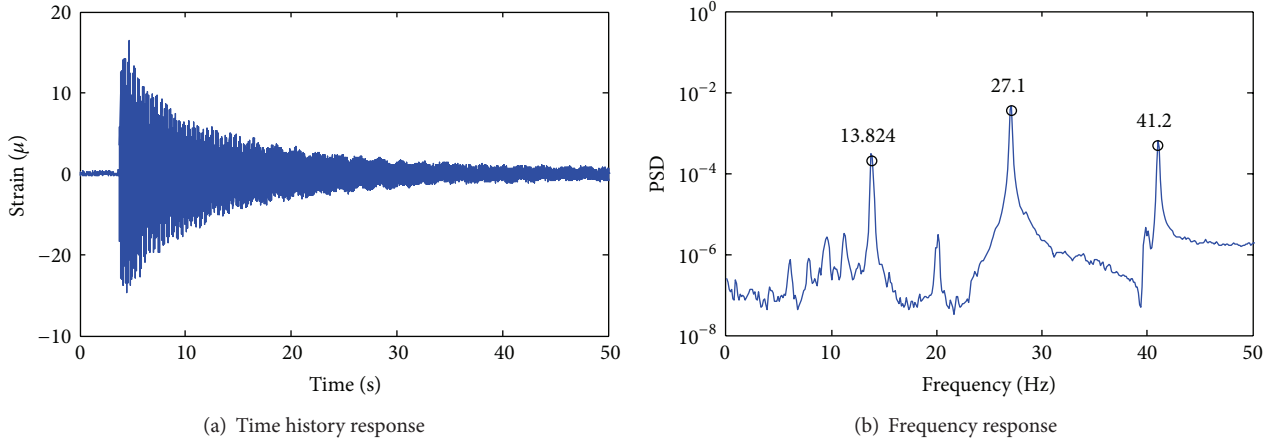


FIGURE 7: PZT dynamic strain of cable for case T_0 .

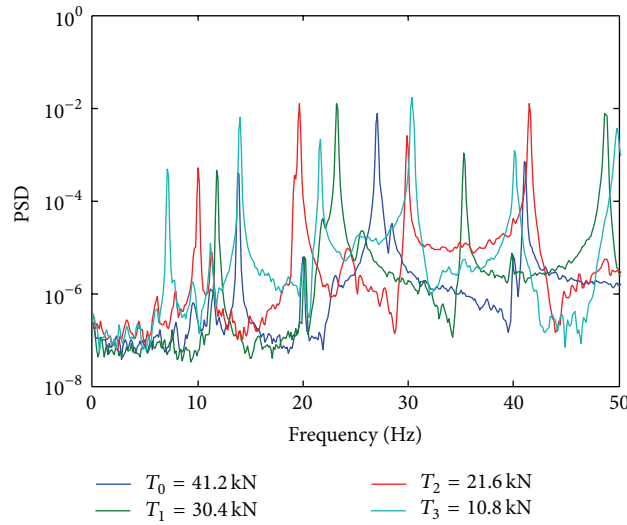


FIGURE 8: PSD of cable strain for 4-cable force levels.

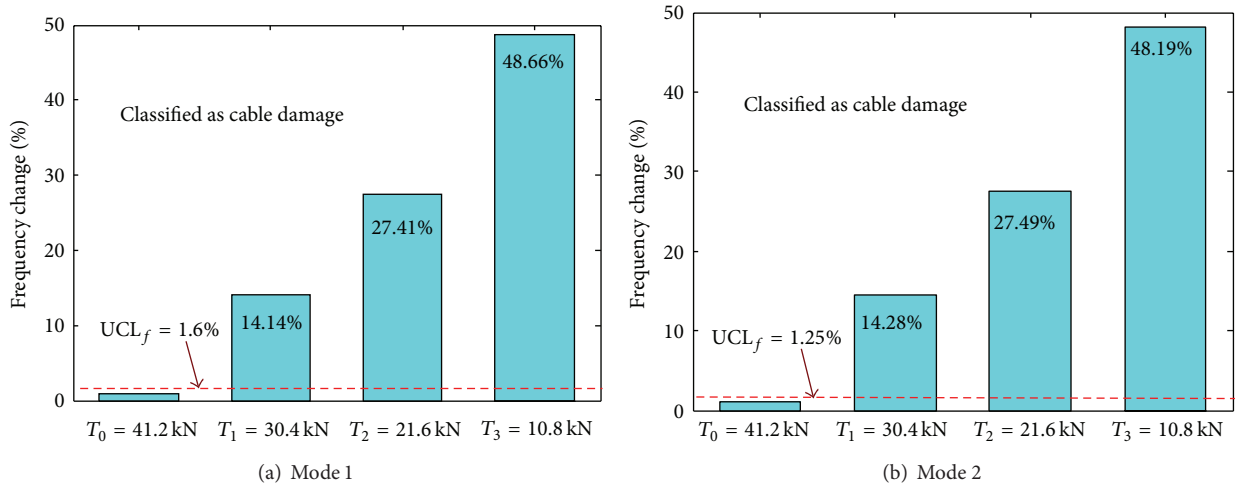


FIGURE 9: Change in natural frequency for cable damage.

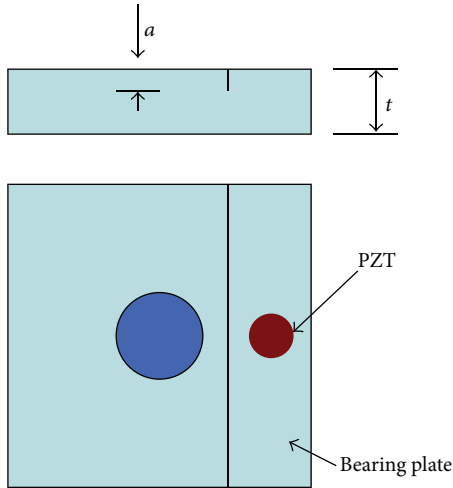


FIGURE 10: Simulated crack on bearing plate.

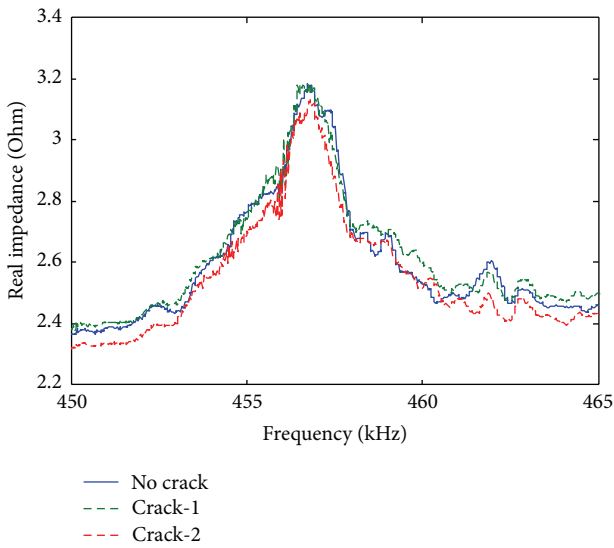


FIGURE 11: Impedance signatures for anchorage damage.

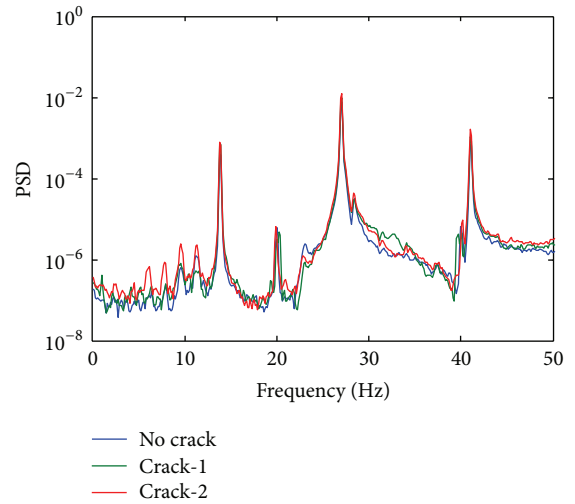


FIGURE 13: PSD of cable strain for anchorage damage.

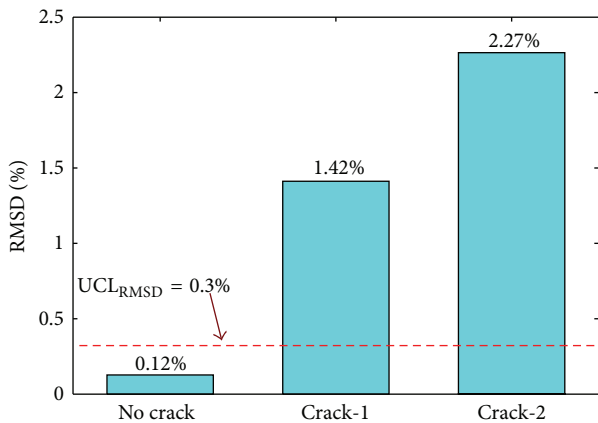


FIGURE 12: Damage alarming for anchorage damage.

the occurrence of damage is successfully alerted by the change in RMSD values.

In the next step, the alerted damage is classified by identifying the change in natural frequency of cable. For each of the four tension force levels, PZT dynamic strain responses of the cable were measured up to 4 ensembles from PZT A (on cable body as shown in Figure 4). Figure 7 shows a sample signal of PZT dynamic strain of cable. Figure 8 shows the change in power spectral densities of cable's strain for the four cable force levels. It can be seen that the power spectral densities shift left when the cable force decreases. The change in natural frequency is utilized to decide the damage type of the alerted damage. As shown in Figure 9, the changes in the first and second frequencies are larger than the control limit of about 1.6% and 1.25%, respectively. These results indicate that the alerted damage is cable-force loss, according to the multi-scale logics described in Figure 1.

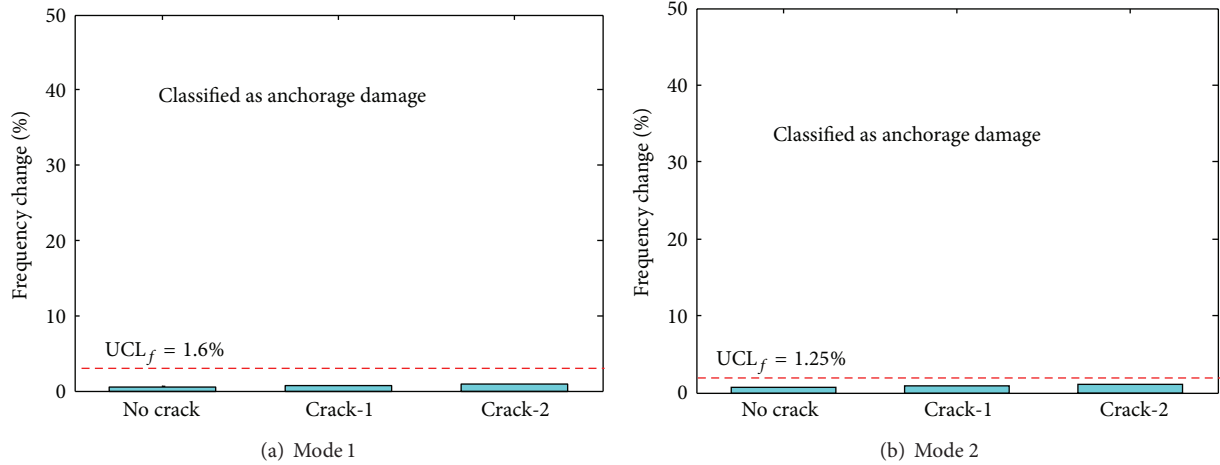


FIGURE 14: Change in natural frequency for anchorage damage.

TABLE 2: Cable force-loss monitoring results.

Tension level	Inflicted cable force		Impedance RMSD (%)	Natural frequency		Estimated cable force	
	T (kN)	Change (%)		f_1 (Hz)	f_2 (Hz)	T (kN)	Change (%)
T_0	41.2	0	0.12	13.824	27.1	41.26	—
T_1	30.4	26.2	1.3	11.856	23.19	30.28	24.9
T_2	21.6	47.6	1.97	10.045	19.65	21.6	47.5
T_3	10.8	73.8	2.53	7.128	14.04	10.97	73.4

As the damage type is classified as the loss of cable force, the amount of cable force-loss is estimated from (8a)–(10). The cable force and the amount of loss are calculated as listed in Table 2. Both the estimated cable force and the loss show good match with the inflicted ones.

3.3. Damage Monitoring Case 2: Anchorage Damage. As shown in Figure 10, a crack was introduced into the bearing plate by saw cut for simulating the damage in anchorage zone. The crack was simulated with two levels corresponding to the ratio of crack depth to the bearing plate's thickness: $a/t = 5\%$ (Crack-1) and $a/t = 10\%$ (Crack-2). During the test, the cable force was set as the maximum tension force T_0 (41.2 kN).

The multi-scale damage detection is carried out again in three steps as previously schematized in Figure 1. In the first step, the occurrence of damage is alerted using RMSD of impedance as described in (3). For each of the four tension force levels, impedance signatures were measured up to 4 ensembles from PZT B (on bearing plate as shown in Figure 3). As shown in Figure 11, impedance signatures were obtained for reference case and the two crack levels. The RMSD values between the reference and the two crack levels are calculated as shown in Figure 12. It is observed that the RMSD values increase with the growth of crack. For the two anchorage damage cases, the occurrence of damage is successfully alerted by the change in RMSD values.

In the next step, the alerted damage is classified by identifying the change in natural frequency of cable. For each of the reference case and two crack levels, PZT dynamic strain responses of the cable were measured up to 4 ensembles from

PZT A. Figure 13 shows the power spectral densities of cable's strain for the reference case and the two crack cases. It can be seen that the power spectral densities do not shift when the crack increases. As shown in Figure 14, the changes in the first and second natural frequencies are smaller than the control limit. These results indicate that the alerted damage belong to anchorage damage, according to the multi-scale logics previously described in Figure 1.

As the damage type is classified as the anchorage damage, the severity of damage is examined by using the thresholds of impedance RMSD as previously described in Figure 2. The changes in impedance signatures for the two damage cases are quantified by RMSD index as listed in Table 3. According to the damage assessment logics for anchorage zone (Figure 2), the damage case Crack-1 is estimated as small damage since the corresponding RMSD index (1.42%) is larger than 1%. Meanwhile, the damage case Crack-2 is recognized as moderate damage since the corresponding RMSD index (2.27%) is larger than 2%.

4. Conclusions

In this study, a multi-scale structural health monitoring of the cable-anchorage system using piezoelectric PZT sensors was presented. In this approach, the PZT impedance response of anchorage was utilized for alerting the change in anchorage zone caused by cable tension force-loss or anchorage damage. Meanwhile, the PZT dynamic strain of cable was utilized for classifying the damage type. The amount of cable tension force-loss was estimated by a frequency-based cable force

TABLE 3: Anchorage damage monitoring results.

Crack level	Inflicted crack size a/t (%)	Impedance RMSD (%)	Natural frequency		Damage severity evaluation
			f_1 (Hz)	f_2 (Hz)	
No crack	—	0.12	13.824	27.1	Ignorable damage
Crack-1	5	1.42	13.824	27.0	Small damage
Crack-2	10	2.27	13.694	26.8	Moderate damage

model, and the anchorage damage was evaluated by setting RMSD thresholds of impedance signatures.

The feasibility of the proposed system was evaluated on a lab-scale cable-damage model with several damage scenarios of cable damage and anchorage damage. The occurrence of either cable damage or anchorage damage was successfully alerted by monitoring electro-mechanical impedance of the bearing plate. Then the damage type was successfully classified into cable damage or anchorage damage. For the cable damage cases, the loss of cable tension force was accurately estimated. For the anchorage damage cases, the damage severity was specified into small or moderate damage, and the damage growth was successfully indicated by the increase of RMSD.

The future works are remained to examine the combination of cable damage and anchorage damage for multi-scale SHM. Also, temperature-compensated models should be studied to improve the accuracy of damage detection results.

Acknowledgment

This research was supported by a grant from a Strategic Research Project (Development of Smart Prestressing and Monitoring Technologies for Prestressed Concrete Bridges) funded by the Korea Institute of Construction Technology.

References

- [1] H. Sohn, C. R. Farrar, F. M. Hemez, D. D. Shunk, D. W. Stinemates, and B. R. Nadler, "A review of structural health monitoring literature: 1996–2001," Los Alamos National Laboratory Report LA-13976-MS, Los Alamos National Laboratory, Los Alamos, NM, USA, 2003.
- [2] C. B. Yun and J. Min, "Smart sensing, monitoring, and damage detection for civil infrastructures," *KSCE Journal of Civil Engineering*, vol. 15, no. 1, pp. 1–14, 2010.
- [3] T. Shimada, *A study on the maintenance and management of the tension measurement for the cable of bridge [Ph.D. thesis]*, Kobe University, Kobe, Japan, 1995.
- [4] H. Zui, T. Shinke, and Y. Namita, "Practical formulas for estimation of cable tension by vibration method," *Journal of Structural Engineering*, vol. 122, no. 6, pp. 651–656, 1996.
- [5] B. H. Kim and T. Park, "Estimation of cable tension force using the frequency-based system identification method," *Journal of Sound and Vibration*, vol. 304, no. 3–5, pp. 660–676, 2007.
- [6] J. T. Kim, J. H. Park, D. S. Hong, H. M. Cho, W. B. Na, and J. H. Yi, "Vibration and impedance monitoring for prestress-loss prediction in PSC girder bridges," *Smart Structures and Systems*, vol. 5, no. 1, pp. 81–94, 2009.
- [7] J. T. Kim, W. B. Na, D. S. Hong, and J. H. Park, "Global and local health monitoring of plate-girder bridges under uncertain temperature conditions," *Steel Structures*, vol. 6, pp. 369–376, 2006.
- [8] J. H. Park, J. T. Kim, D. S. Hong, D. Mascarenas, and J. P. Lynch, "Autonomous smart sensor nodes for global and local damage detection of prestressed concrete bridges based on accelerations and impedance measurements," *Smart Structures and Systems*, vol. 6, no. 5–6, pp. 711–730, 2010.
- [9] S. H. Sim, B. F. Spencer, and T. Nagayama, "Multimetric sensing for structural damage detection," *Journal of Engineering Mechanics*, vol. 137, no. 1, pp. 22–30, 2010.
- [10] K. D. Nguyen, D. D. Ho, and J. T. Kim, "Damage detection in beam-type structures via PZT's dual piezoelectric responses," *Smart Structures and Systems*, vol. 11, no. 2, pp. 217–240, 2013.
- [11] C. Liang, F. P. Sun, and C. A. Rogers, "Electro-mechanical impedance modeling of active material systems," *Smart Materials and Structures*, vol. 5, no. 2, pp. 171–186, 1996.
- [12] J. Sirohi and I. Chopra, "Fundamental understanding of piezoelectric strain sensors," *Journal of Intelligent Material Systems and Structures*, vol. 11, no. 4, pp. 246–257, 2000.
- [13] J. S. Bendat and A. G. Piersol, *Engineering Applications of Correlation and Spectral Analysis*, Wiley-Interscience, New York, NY, USA, 1993.
- [14] G. Park, H. H. Cudney, and D. J. Inman, "Feasibility of using impedance-based damage assessment for pipeline structures," *Earthquake Engineering and Structural Dynamics*, vol. 30, no. 10, pp. 1463–1474, 2001.
- [15] S. Park, S. Ahmad, C. B. Yun, and Y. Roh, "Multiple crack detection of concrete structures using impedance-based structural health monitoring techniques," *Experimental Mechanics*, vol. 46, no. 5, pp. 609–618, 2006.
- [16] Y. Yang, H. Liu, V. G. M. Annamdas, and C. K. Soh, "Monitoring damage propagation using PZT impedance transducers," *Smart Materials and Structures*, vol. 18, no. 4, Article ID 045003, 9 pages, 2009.

Research Article

Near-Field Ultrasonic Phased Array Deflection Focusing Based CFRP Wing Box Structural Health Monitoring

Yajie Sun, Yonghong Zhang, Chengshan Qian, and Zijia Zhang

School of Information and Control, Nanjing University of Information Science and Technology, No. 219, Ningliu Road, Nanjing 210044, China

Correspondence should be addressed to Yajie Sun; syj@nuist.edu.cn

Received 5 June 2013; Revised 7 September 2013; Accepted 7 October 2013

Academic Editor: Gangbing Song

Copyright © 2013 Yajie Sun et al. This is an open access article distributed under the Creative Commons Attribution License, which permits unrestricted use, distribution, and reproduction in any medium, provided the original work is properly cited.

Near-field ultrasonic phased array theory is researched and utilized in the carbon-fiber wing box to identify the damage in the structure. Near-field ultrasonic phased array based structural health monitoring is researched to overcome the limitation of the far-field ultrasonic phased array in monitoring scope. The time delay of the theory and the process of the damage identification method are researched in detail. The recognition result is shown in a mapped image. The proposed method is applied in carbon fiber-reinforced polymer (CFRP) wing box to monitor the load in the structure. The experimental results show that the near-field ultrasonic phased array based structural health monitoring method is effective to identify the load position in the structure.

1. Introduction

Lamb wave can propagate a long distance in plate-like and shell-like structures [1, 2]. Hence, the structural health monitoring (SHM) [3–9] based on Lamb wave has emerged as a promising technique by using piezoelectric (PZT) actuators/receivers to generate/receive the signals for monitoring the structural damage. Ultrasonic phased array based structural health monitoring [10–15] can control the Lamb wave beam steering to scan the structure in a certain direction to identify the damage in the structure by controlling the time delay of transmitting and receiving for each PZT element in the PZT sensor array. Previous researches on ultrasonic phased array were carried out under the condition of the monitoring target in the PZT sensor array far-field [16–19]. In this condition, the monitoring method cannot exactly identify the damage of the structure in PZT sensor array near-field area. For the far-field ultrasonic phased array structural health monitoring, the Lamb wave beams connecting the PZT sensors with the monitoring target are parallel each other. But in the near-field, the Lamb wave beams from PZT elements to monitoring target are not parallel with each other. They focus on the monitoring target. The formulas used in the far-field ultrasonic phased array based structural health

monitoring become invalid in near-field ultrasonic phased array.

In this paper, the near-field ultrasonic phased array based structural health monitoring is researched. The time delay used in near-field ultrasonic phased array and the damage identification process using near-field ultrasonic phased array theory are researched. The damage identification result is shown on a mapped image. The proposed method is verified by experiments on the wing box and the results show that it is effective to identify the damage position of structure.

2. Near-Field Ultrasonic Phased Array Theory

Near-field ultrasonic phased array principle is shown in Figure 1. The PZT linear sensor array consists of M PZT elements with each PZT element acting as a transmitter and receiver. The PZT elements in the array are equally spaced at the distance d . The coordinate system origin is set to the most left point of the PZT sensor array and the 0° direction is consistent with the alignment of the PZT sensor array. The coordinate in cartesian coordinate system of i th PZT element is $(x_i, 0)$, $i = 0 \sim M - 1$, where $x_i = i \cdot d$.

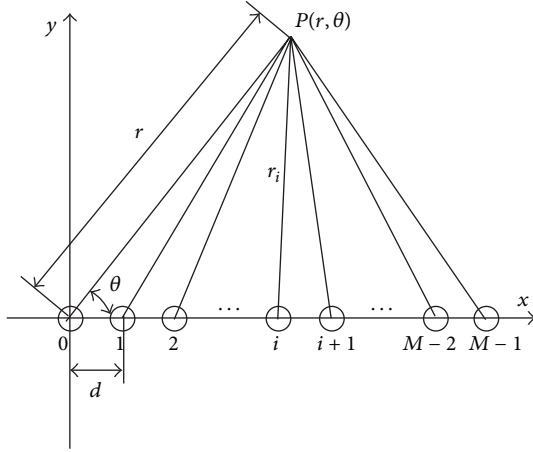


FIGURE 1: Near-field ultrasonic phased array theory.

The near-field ultrasonic phased array principle is applied to generate and receive Lamb waves. For a near-distance point $P(r, \theta)$, the rays connecting the point P with the sensors are focused on the point P . Coordinate system origin is acted as a reference point. For the i th PZT element, the distance from the point P to the sensor will be shortened by

$$\Delta r_i(\theta) = r - r_i = r - \sqrt{r^2 + (i \cdot d)^2 - 2 \cdot r \cdot i \cdot d \cdot \cos \theta}. \quad (1)$$

The signal from the i th PZT element will arrive at point P quicker than the point P to coordinate system origin by

$$\Delta t_i(r, \theta) = \frac{\Delta r_i(\theta)}{c} = \frac{r - \sqrt{r^2 + (i \cdot d)^2 - 2 \cdot r \cdot i \cdot d \cdot \cos \theta}}{c}, \quad (2)$$

where c is the Lamb wave speed traveling in the structure.

The total signal received at point P will be

$$\begin{aligned} S_P(r, \theta) &= K_1 \sum_{i=0}^{M-1} S_e \left(t - \frac{r_i}{c} \right) = K_1 \sum_{i=0}^{M-1} S_e \left(t - \frac{r - \Delta r_i(\theta)}{c} \right) \\ &= K_1 \sum_{i=0}^{M-1} S_e \left(t - \frac{r}{c} + \Delta t_i(r, \theta) \right), \end{aligned} \quad (3)$$

where K_1 is the amplitude attenuation coefficient in signal emission process, S_e represents excitation signal, and r/c is the time due to the travel distance between the coordinate system origin and the point P . Here, wave-energy conservation is assumed.

If the PZT elements are not excited simultaneously, but with specific time delays $\Delta t(r, \theta)$ for each PZT element, the total signal received at point P will be

$$S_P(r) = K_1 \cdot M \cdot S_e \left(t - \frac{r}{c} \right). \quad (4)$$

According to the principle of reciprocity, the receiving process is consistent with exciting process under the same

conditions. The point $P(r, \theta)$ acts as a new wave source reflecting the signal to all the PZT elements. The signal arrives the i th PZT element quicker by $\Delta t_i(r, \theta)$. Its expression is

$$S_i(r, \theta) = K_2 S_P \left(t - \frac{r}{c} + \Delta t_i(r, \theta) \right), \quad (5)$$

where K_2 is the amplitude attenuation coefficient in signal reception process. S_P represents the signal that the point P received.

Hence, with specific time delays $\Delta t_i(r, \theta)$ for the i th PZT element, the signal that reached the PZT element will be

$$S_i(r) = K_2 S_P \left(t - \frac{r}{c} \right). \quad (6)$$

The total signals received from the beam-steering of θ will be

$$\begin{aligned} S(r) &= \sum_{i=0}^{M-1} K_2 S_P \left(t - \frac{r}{c} \right) = K_2 \cdot M \cdot S_P \left(t - \frac{r}{c} \right) \\ &= K_1 \cdot K_2 \cdot M^2 \cdot S_e \left(t - \frac{2r}{c} \right) = K \cdot M^2 \cdot S_e \left(t - \frac{2r}{c} \right), \end{aligned} \quad (7)$$

where $K = K_1 \cdot K_2$ is the amplitude attenuation coefficient.

The signal amplitude increases M^2 times in comparison with a single PZT element. The signal-to-noise ratio (SNR) is enhanced. The beam steering of Lamb wave is controlled well to the desired directions by near-field ultrasonic phased array theory.

Assume that damage exists at angle θ_0 and distance R in the structure. The signals scan the structure in increasing angles θ and the PZT elements receive the largest reflection signal from the damage when $\theta = \theta_0$.

By analyzing the signal in the damage direction, the distance R of the damage can be calculated as

$$R = \frac{c\tau}{2}, \quad (8)$$

where τ is the time of arrival of the signal in the damage direction.

3. Near-Field Ultrasonic Phased Array Implementations

In time delay equation (2), there are five parameters. They are the distance r , angle θ , PZT element number i , PZT element spacing d , and Lamb wave speed c . The PZT element number i is predefined. PZT element spacing d is related to the arrangement of the PZT sensor array. Once the arrangement is fixed, the spacing d is known. Lamb wave speed c in carbon-fiber box structure is determined by experiment. Both the distance r and the angle θ are unknown. So the time delay of the near-field ultrasonic phased array theory is not only related to the angle θ , but also related to the distance r . In the near-field ultrasonic phased array structural health monitoring implementation process, the distance r and the angle θ in equation (2) need to be controlled simultaneously. In the angle monitoring range $\theta \in [0^\circ, 180^\circ]$ and the distance

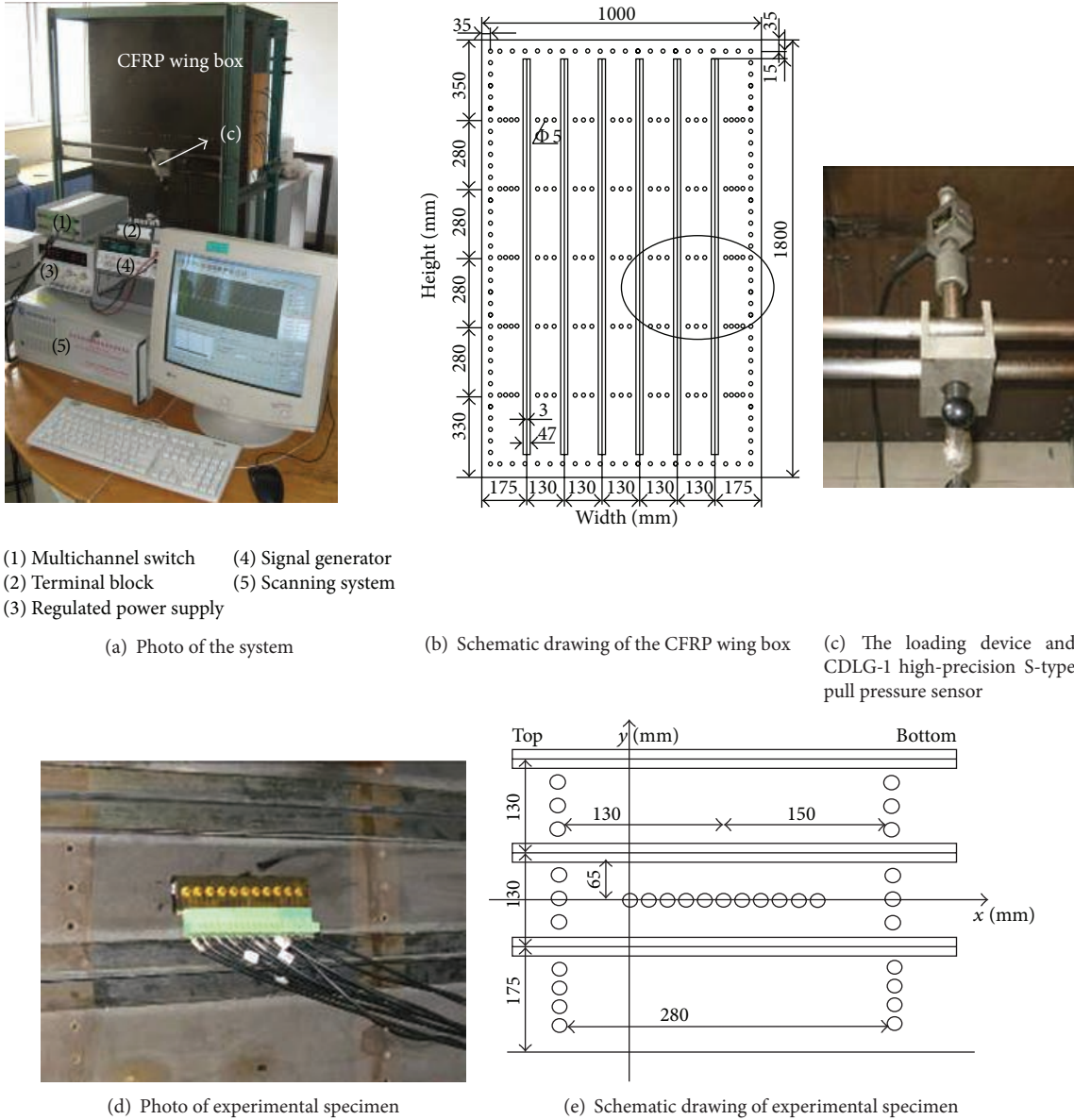


FIGURE 2: Experiment system.

monitoring range $r \in [0 \text{ cm}, 16 \text{ cm}]$, the step of the angle θ is 1° and the step of the distance r is 1 mm. Every angle and distance are corresponding with a time delay. And every time delay is added to response signal to get delayed signals in different distances and in different angles. The signals at the same angle and the same distance are cumulated to get the synthetic signal in a special angle and distance. The angle where the signal of the max amplitude lies in is the polar angle of the damage, and the polar radius of the damage is calculated from the signal that damage lies in.

4. Experimental Research

4.1. Experimental System. Experiment is conducted on a carbon fiber composite wing box to verify the theoretical results. The experimental system is shown in Figure 2. Figure 2(a) is the photo of the experimental system that

includes the carbon fiber composite wing box, loading device and CDLG-1 high-precision S-typed pull pressure sensor, and the experimental setup. The main material of wing box is carbon fiber-reinforced polymers (CFRP). Figure 2(b) is the schematic drawing of the wing box that gives a specific size of every part of the structure. The dimension of the structure is $1.8 \text{ m} \times 1 \text{ m} \times 2.84 \text{ mm}$. One side of the structure has strengthened T-shaped stringers. There are threaded holes in the structure. The structure consists of 22 layers and the layer thickness is 0.12 mm. The upper and lower boards are interlayer plates and the ply sequence is $[45^\circ / -45^\circ / 0^\circ / -45^\circ / 0^\circ / 45^\circ / 90^\circ / 45^\circ / 90^\circ / -45^\circ / 0^\circ / 0^\circ / -45^\circ / 90^\circ / 45^\circ / 90^\circ / 45^\circ / 0^\circ / -45^\circ / 0^\circ / -45^\circ / 45^\circ]$. The T-shaped stringer consists of 10 layers and the layer thickness is 0.12 mm. The ply sequence of the T-shaped stringer is $[45^\circ / -45^\circ / 0^\circ / 90^\circ / 0^\circ / 0^\circ / 90^\circ / 0^\circ / -45^\circ / 45^\circ]$. The blue oval marked region in Figure 2(b) is the experimental area for near-field

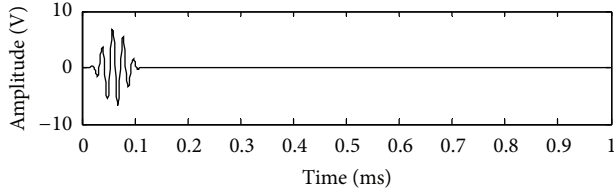


FIGURE 3: Excitation signal.

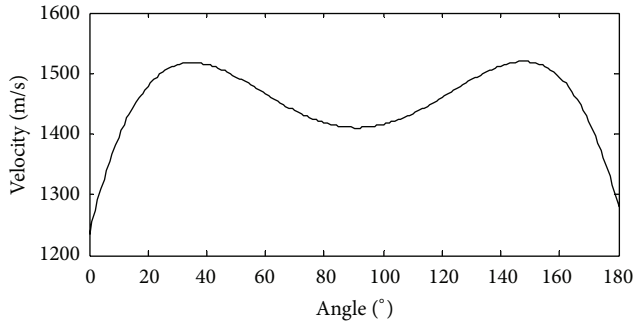


FIGURE 4: The speed of Lamb wave in CFRP wing box.

phased-array principle based load monitoring in structure. The load is used in the experiment to simulate the damage in the structure. Figure 2(c) is the loading device and CDLG-1 high-precision S-typed pull pressure sensor. The experimental setup includes integrated scanning system, multichannel switch, terminal block, regulated power supply, and signal generator. The integrated scanning system includes industrial personal computer, data acquisition card, and charge amplifier. Its details are described in [20]. The regulated power supply can provide the power for S-type pull pressure sensor. The experimental specimen of using near-field phased-array method to monitor the load location in the structure is shown in Figures 2(d) and 2(e). Figure 2(d) is the photo of the structure that shows the layout of the PZT sensor array in the structure. Figure 2(e) is the schematic drawing of Figure 2(d). There are 11 PZT elements in PZT sensor array, that is, arranged in linear array with 1 cm spacing. The diameter of each PZT element is 8 mm and its thickness is 0.48 mm. The coordinate system origin is set to the most left point of the PZT sensor array and the 0° direction is consistent with the alignment of the PZT sensor array. The load location in the structure is $(92^\circ, 5.8 \text{ cm})$ and the payload is 35 Kg.

4.2. Experimental Verification and Analysis. The excitation signal is narrowband modulation sine signal. Its waveform is shown in Figure 3. The amplitude of the signal is 7 V. The central frequency is 50 KHz. The number of wave peak is 5. The time of arrival of the excitation signal is 0.064 ms.

Because of the anisotropy of composite material, the Lamb wave speed travelling in the CFRP wing box in different directions is different. The wave speed in CFRP wing box structure gotten by the experiment is shown in Figure 4.

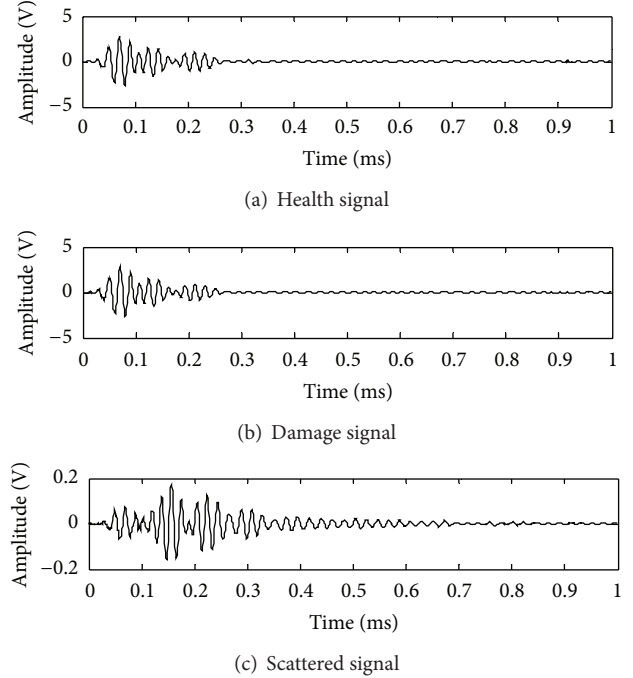


FIGURE 5: The health signal damage signal and scattered signal.

Each element in PZT sensor array can act as both transmitter and receiver because of its piezoelectric effect. The sensing signal is collected in round-robin pattern. In turns, one PZT sensor is the transmitter to generate the excitation signal and the others are receivers to collect the sensing signals. The next PZT sensor in the array becomes transmitter and the process is repeated. Thus, a total of $M \times (M - 1) = 11 \times 10 = 110$ signals are collected in each direction. Data acquisition is carried out to get the sensing signals collected in structural health state and in structural damage state, respectively. The sensing signals collected in structure health state is named health signal and the sensing signals collected in structure damage state is named damage signal. The health signal acts as a reference signal and the damage signal is compared with the reference signal to get the damage scattered signal. The sensing signals and the damage scattered signal in the angle of 0° in which the sensor 0 is actuator and the sensor 1 is receiver are shown in Figure 5. The damage scattered signals are caused by the damage in the structure. That is to say, the damage scattered signals can explain whether the structure is healthy or not. The energy of the signal caused by damage is weak and it is aliasing in other signals.

The damage scattered signals are processed with the time delay $\Delta t_i(r, \theta) = [r - \sqrt{r^2 + (i \cdot d)^2} - 2 \cdot r \cdot i \cdot d \cdot \cos \theta] / c$ at interval of 1° in the angle $[0^\circ, 180^\circ]$ and at interval of 1 mm in the distance $[0 \text{ cm}, 16 \text{ cm}]$ to get delayed signals at each angle-distance. For example, the time delay in the distance of 1 mm and in the angle of 0° for actuator 0 and transducer 1 is $\Delta t(1, 0^\circ) = \Delta t_0(1, 0^\circ) + \Delta t_1(1, 0^\circ) = 0 + 0.0081 = 0.0081 \text{ ms}$ which means that the signal moves to the right 0.0081 ms. The Lamb wave speed in carbon-fiber wing box in direction

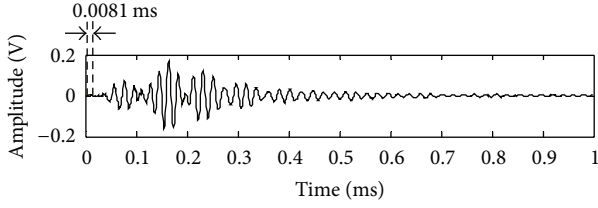


FIGURE 6: The delayed signal.

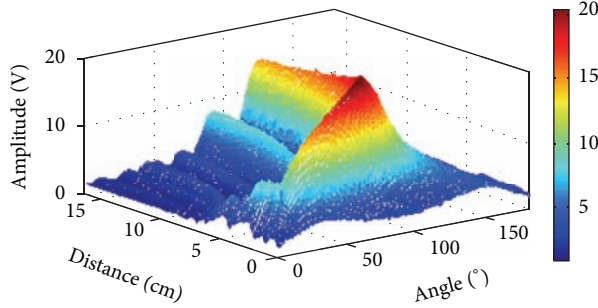


FIGURE 7: The max amplitude of synthetic signals.

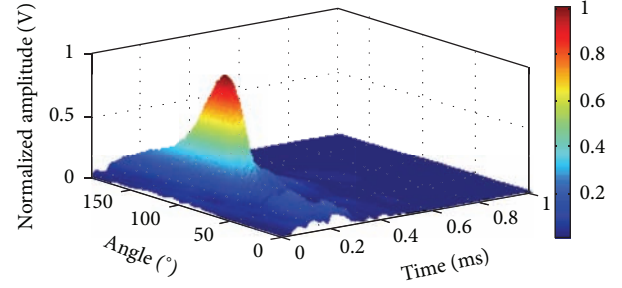


FIGURE 8: The synthetic signals.

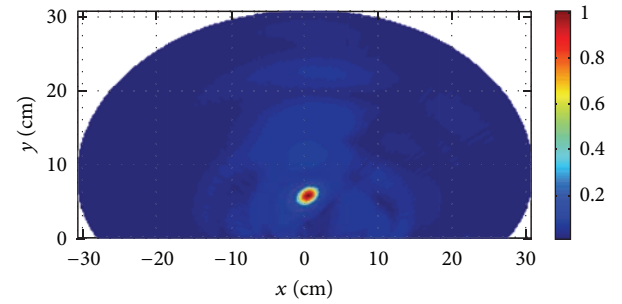


FIGURE 9: The mapped image of the near-field ultrasonic phased array.

of 0° used in the expression is 1235.3 m/s, which is gotten from Figure 4. This time delay is added to the corresponding scattered signal (Figure 5(c)) to get the delayed signal, which is shown in Figure 6.

All the delayed signals at the same angle-distance are cumulated to get the synthetic signal. Figure 7 is the max amplitude of the synthetic signals at every angle-distance. The synthetic signal amplitude is compared with the max amplitude of all signals to get its relative amplitude. The angle where the signal of the max amplitude lies in is the polar angle of the damage and the polar radius of the damage is calculated from the signal that damage lies in. Figure 8 is the normalized synthetic signals in the angle $[0^\circ, 180^\circ]$ where the synthetic signal with max amplitude lies in. These signals are described on distance-direction two-dimensional plane in the gray form to get a mapped image. The horizontal axis and vertical axis of the mapped image represent the horizontal and vertical coordinates of the monitoring scope. The pixel value of each point in the mapped image is corresponding to the normalized amplitude of the signal point. The mapped image of damage identification is shown in Figure 9. The monitoring scope is not a semicircle, because the experimental specimen is anisotropic CFRP. That is to say, in every direction of the structure, the signal collection points are equal, but the wave speed in different directions is different. Therefore, the monitoring distances in different angles are different. The max amplitude of the mapped image (Figure 9) is the damage location of the structure. The location of identification damage is $(89^\circ, 5.78 \text{ cm})$. The location of the actual damage is $(92^\circ, 5.8 \text{ cm})$. Their angle error is 3° and the distance error of two points between identification damage and actual damage is 0.3 cm. The angle error is the absolute difference between two angles. The

distance error is calculated by the law of cosines. They are expressed as

$$\Delta\theta = |\theta_i - \theta_0|,$$

$$\Delta r = \sqrt{r_i^2 + r_0^2 - 2 \cdot r_i \cdot r_0 \cdot \cos(\Delta\theta)}, \quad (9)$$

where $\Delta\theta$ is the angle error, Δr is the distance error, θ_i is the angle of identification damage location, θ_0 is the angle of actual damage location, r_i the distance of identification damage location, and r_0 is the distance of actual damage location.

5. Summary and Conclusions

The near-field ultrasonic phased array theory based structural health monitoring is researched to overcome the limitation of the far-field ultrasonic phased array theory in monitoring scope. This method controls the beam steering by controlling the time delay of the signals to focus on the structure and to detect the damage in the structure. The proposed method is verified by the experiment on CFRP wing box. The results show that the method is effective to identify the damage position of structure. In addition, the damage in the test structure was clearly presented by the mapped image.

Acknowledgments

This work is supported by National Natural Science Foundation of China (Grant No. 51305211), Nanjing University of Information Science and Technology Research Start-up

Foundation (Grant No. 20100385), and Industry-Academia Cooperation Innovation Fund Projects of Jiangsu Province (Grant No. 2012s028).

References

- [1] B. C. Lee and W. J. Staszewski, "Lamb wave propagation modelling for damage detection: i. two-dimensional analysis," *Smart Materials and Structures*, vol. 16, no. 2, article 3, pp. 249–259, 2007.
- [2] X. Y. Zhang, S. F. Yuan, and M. L. Liu, "Analytical modeling of lamb wave propagation in composite laminate bonded with piezoelectric actuator based on mindlin plate theory," *Journal of Vibroengineering*, vol. 14, no. 4, pp. 1681–1700, 2012.
- [3] K. P. Lonkar, V. Janapati, S. Roy, and F. K. Chang, "A Model-assisted integrated diagnostics for structural health monitoring," in *Proceedings of the 53rd AIAA/ASME/ASCE/AHS/ASC Structures, Structural Dynamics and Materials Conference*, pp. 1–14, Honolulu, Hawaii, USA, April 2012.
- [4] L. Qiu, S. F. Yuan, X. Y. Zhang, and Y. Wang, "A time reversal focusing based impact imaging method and its evaluation on complex composite structures," *Smart Materials and Structures*, vol. 20, no. 10, Article ID 105014, 2011.
- [5] J. Cai, L. Shi, S. F. Yuan, and Z. Shao, "High spatial resolution imaging for structural health monitoring based on virtual time reversal," *Smart Materials and Structures*, vol. 20, no. 5, Article ID 055018, 2011.
- [6] M. A. De Oliveira and J. V. Filho, "Structural health monitoring based on AR models and PZT sensors," *IEEE Sensors Journal*, pp. 1–4, 2012.
- [7] F. G. Baptista, J. V. Filho, and D. J. Inman, "Sizing PZT transducers in impedance-based structural health monitoring," *IEEE Sensors Journal*, vol. 11, no. 6, pp. 1405–1414, 2011.
- [8] Q. Wang and S. F. Yuan, "Baseline-free imaging method based on new PZT sensor arrangements," *Journal of Intelligent Material Systems and Structures*, vol. 20, no. 14, pp. 1663–1673, 2009.
- [9] Y. J. Sun, S. F. Yuan, and B. F. Wang, "Research on using extreme value theory to recognize damage in structural health monitoring for composite materials," *Chinese Journal of Astronautics*, vol. 28, no. 5, pp. 1366–1370, 2007.
- [10] American Society of Nondestructive Testing, *American Nondestructive Testing Manual (Ultrasonic)*, WPC, Shanghai, China, 1996.
- [11] F. Yan and J. L. Rose, "Guided wave phased array beam steering in composite plates," in *Proceedings of the Health Monitoring of Structural and Biological Systems*, San Diego, Calif, USA, March 2007.
- [12] P. Malinowski, T. Wandowski, I. Trendafilova, and W. Ostachowicz, "A phased array-based method for damage detection and localization in thin plates," *Structural Health Monitoring*, vol. 8, no. 1, pp. 5–15, 2009.
- [13] G. Srinivasan, D. R. Mahapatra, and N. Chakraborty, "Ultrasonic guided wave characterization and damage detection in foam-core sandwich panel using PWAS and LDV," in *Health Monitoring of Structural and Biological Systems*, vol. 8348 of *Proceedings of SPIE*, pp. 1–10, San Diego, Calif, USA, 2012.
- [14] M. Engholm and T. Stepinski, "Adaptive beamforming for array imaging of plate structures using lamb waves," *IEEE Transactions on Ultrasonics, Ferroelectrics, and Frequency Control*, vol. 57, no. 12, pp. 2712–2724, 2010.
- [15] G. Giridhara, V. T. Rathod, S. Naik, D. Roy Mahapatra, and S. Gopalakrishnan, "Rapid localization of damage using a circular sensor array and lamb wave based triangulation," *Mechanical Systems and Signal Processing*, vol. 24, no. 8, pp. 2929–2946, 2010.
- [16] A. S. Purekar and D. J. Pines, "Damage detection in thin composite laminates using piezoelectric phased sensor arrays and guided lamb wave interrogation," *Journal of Intelligent Material Systems and Structures*, vol. 21, no. 10, pp. 995–1010, 2010.
- [17] L. Y. Yu, S. G. Bottai, and V. Giurgiutiu, "Shear lag solution for tuning ultrasonic piezoelectric wafer active sensors with applications to lamb wave array imaging," *International Journal of Engineering Science*, vol. 48, no. 10, pp. 848–861, 2010.
- [18] V. Giurgiutiu, "Development and testing of high-temperature piezoelectric wafer active sensors for extreme environments," *Structural Health Monitoring*, vol. 9, no. 6, pp. 513–525, 2010.
- [19] D. Kim and M. Philen, "Guided wave beamsteering using mfc phased arrays for structural health monitoring: analysis and experiment," *Journal of Intelligent Material Systems and Structures*, vol. 21, no. 10, pp. 1011–1024, 2010.
- [20] L. Qiu and S. F. Yuan, "On development of a multi-channel PZT array scanning system and its evaluating application on UAV wing box," *Sensors and Actuators A*, vol. 151, no. 2, pp. 220–230, 2009.

Research Article

Active Sensing Based Bolted Structure Health Monitoring Using Piezoceramic Transducers

R. L. Wang,¹ H. Gu,² and G. Song^{2,3}

¹ School of Civil Engineering, Wuhan University, Wuhan, Hubei 430072, China

² Department of Mechanical Engineering, University of Houston, Houston, TX 77204, USA

³ School of Civil Engineering, Dalian University of Technology, Dalian, Liaoning 116024, China

Correspondence should be addressed to G. Song; gsong@uh.edu

Received 6 July 2013; Accepted 15 September 2013

Academic Editor: Hong-Nan Li

Copyright © 2013 R. L. Wang et al. This is an open access article distributed under the Creative Commons Attribution License, which permits unrestricted use, distribution, and reproduction in any medium, provided the original work is properly cited.

Bolted structures are commonly used in civil infrastructure. It is important to perform bolt inspection regularly to ensure the safety of structures. Traditional bolt inspection methods are time-consuming; moreover, bulky instruments are needed in these methods. In this paper, a piezoceramic based active sensing approach is developed to perform the health monitoring of bolted structures. Surface-bonded piezoceramic patches are used as health monitoring transducers. Wavelet packet analysis is used to analyze the sensor data to extract the features that indicate bolt looseness. Based on wavelet packet analysis results, a damage index is developed to quantitatively evaluate the damage status. To verify the effectiveness of the proposed method, a bolted connection experiment with piezoceramic transducers was performed. In the experiment, the looseness of the bolt is adjusted by a torque wrench. Experimental results show that the proposed approach is effective to detect and evaluate bolt looseness.

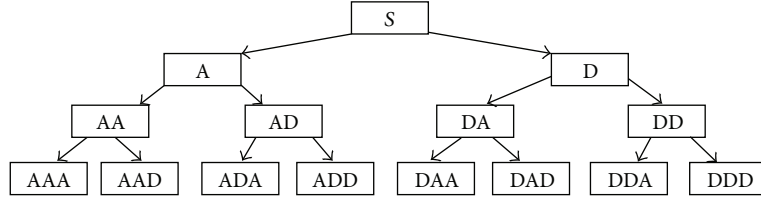
1. Introduction

Bolts are commonly used in civil infrastructure where the inspection of bolts is extremely labor intensive. To reduce inspection labor and enhance safety, real-time health monitoring technologies have been recently researched for bolt inspection, such as an impedance based method [1–4], a vibration or ultrasonic based method [5, 6], and an electric conductivity based method [7]. Due to the advantages of low cost, quick response, and solid-state actuation, piezoceramic materials have been used as transducers for health monitoring purposes. In addition, an active sensing approach has been used in the health monitoring of various civil infrastructures [8–13]. Recently, a proof-of-concept study of monitoring bolt connection status using a piezoelectric based active sensing method was conducted [14]. The proof-of-concept study only involves a pair of bolt-and-nut that connect two small metal plates. No meaningful structure was involved in the proof-of-concept study. In this paper, using piezoceramic materials, an active sensing based approach is further developed and applied to perform health monitoring

of a bolted connection in light pole structure. During the experiment, different torque values were applied to tighten a bolt connection on the structure to simulate the damage of different degrees of looseness. The proposed health monitoring approach was performed to evaluate the health status of the bolt connection on a real structure. A damage index was developed to quantitatively evaluate the severity of the bolt looseness. Experimental results verified the effectiveness of the proposed approach.

2. Monitoring Principle and Algorithm

For various degrees of looseness of a bolt, the stiffness around the screwed area and the boundary conditions of the bolt are different. The changes in the stiffness and boundary conditions result in the alternation in the wave propagation. Thus, the bolt inspection can be performed by analyzing the wave responses across the bolted connection. In the proposed research, the active sensing approach is used; that is, a piezoceramic transducer bonded on the surface of a bolt is used as an actuator to generate the stress wave, while



$$S = AAA + AAD + ADA + ADD + DAA + DAD + DDA + DDD$$

FIGURE 1: Decomposition of wavelet packet analysis.

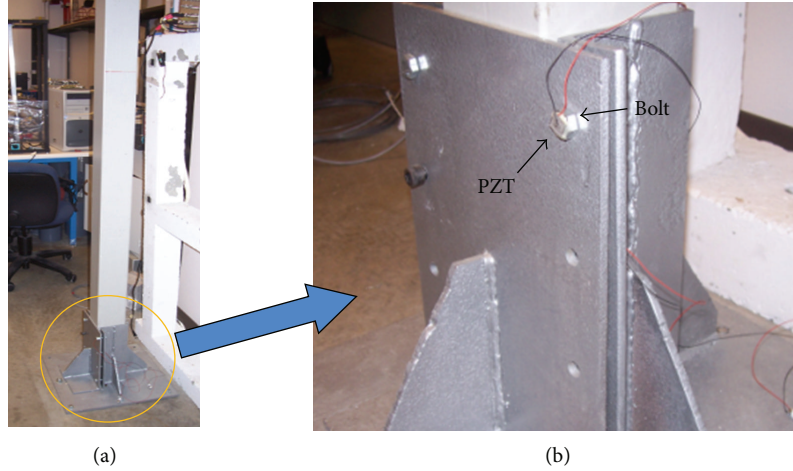


FIGURE 2: Piezoceramic transducer (actuator) bonded on the bolt cap.

another piezoceramic transducer bonded on the other side of the screwed area is used as the sensor to detect the responses. By analyzing the response signals, the health status of the bolt is evaluated. Wavelet packet analysis is used as the signal processing tool due to the fact that it enables the inspection of relatively narrow frequency bands over a relatively short time window. In wavelet analysis, a signal is split into an approximation (low frequency information) and a detail (high frequency information). The approximation is then itself split into a second-level approximation and its detail, and then the process is repeated. In wavelet packet analysis, not only the approximations are decomposed into the next level's approximations and details but also the details are decomposed into the next level's approximations and details. This process is repeated as shown in the decomposition tree in Figure 1. In Figure 1, the letter "A" stands for "Approximation" and the letter "D" stands for "Detail."

In the proposed health monitoring algorithm, the sensor signal S is decomposed by an n -level wavelet packet decomposition into 2^n signal subsets $\{X_1, X_2, \dots, X_{2^n}\}$ and the decomposed subset X_j is written as

$$X_j = [x_{j,1}, x_{j,2}, \dots, x_{j,m}], \quad (j = 1, 2, \dots, 2^n), \quad (1)$$

where m is the amount of sampling data. The decomposed subset for the health state (where the bolt is fully tightened) is written as

$$X_{jh} = [x_{jh,1}, x_{jh,2}, \dots, x_{jh,m}], \quad (j = 1, 2, \dots, 2^n). \quad (2)$$



FIGURE 3: Piezoceramic transducer (sensor) bonded on the other side.

The damage index for the decomposed signal at the j th frequency band is defined as

$$I_j = \sqrt{\frac{\sum_{i=1}^m (x_{jh,i} - x_{j,i})^2}{\sum_{i=1}^m x_{jh,i}^2}}. \quad (3)$$

The proposed damage index I_j shows the wave transmission energy ratio at the j th frequency band compared with the transmission energy when the bolt is fully tightened.

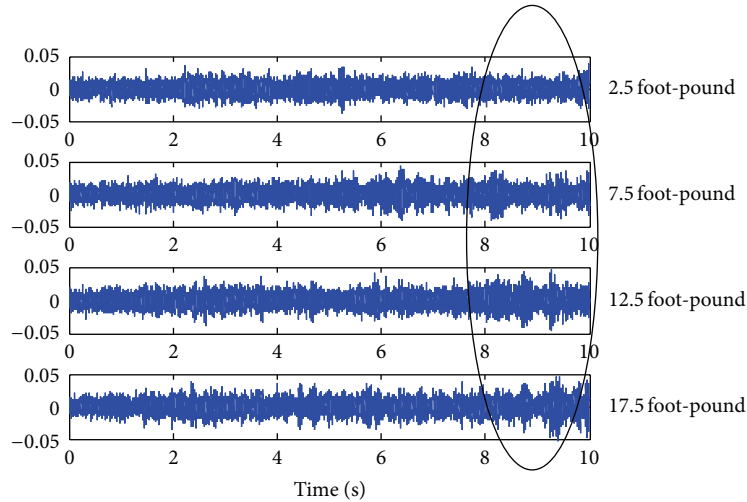


FIGURE 4: Time response comparison for sweep sine wave responses.

3. Experimental Setup and Testing Program

In this health monitoring test, a bolt connection that joins two plates in a pole structure was used as a testing object, as shown in Figure 2(a). Different values of torque were applied to gradually tighten the bolt and piezoceramics were used as health monitoring transducers. The proposed active sensing approach was implemented to evaluate the health status of the bolt during the tightening process. At present, the most widely used piezoceramic material is the lead zirconate titanate (PZT) due to its strong piezoelectric effect and wide availability. In this experiment, one PZT patch is attached on the bolt as an actuator as shown in Figure 2(b), and another PZT patch is attached on the other side of the plate as a sensor, as shown in Figure 3. The dSPACE 1104 is used as the data acquisition system. During the experiment, the bolt looseness was controlled by a torque wrench. In the experiment, the torque was gradually increased from 2.5 foot-pounds to a maximum allowable value of 17.5 foot-pounds. The proposed active sensing based health monitoring approach was implemented to evaluate the bolt looseness.

4. Experimental Results

During the health monitoring test, a sweep sine wave was used as the excitation source for the PZT patch bonded on the surface of the bolt. The PZT patch bonded on the surface of the plate on the other side of the connection was used as a sensor. The sweep sine wave starts at 100 Hz and ends at 12 KHz with a period of 10 seconds. Wavelet packet analysis is used as the signal processing tool to extract the damage features. Daubechies wavelet (db10) is used as the mother wavelet. The decomposition level for the wavelet packet analysis is 3 and the sensor signals are decomposed into 8 subsets in different frequency bands. The proposed damage index is used to evaluate the damage status on the bolt.

From the time response comparison, shown in Figure 4, it is observed that there are some differences around 8–10 seconds for different torque cases; however, the differences are not very obvious. The wavelet packet analysis will be used here to further analyze the data. To extract more detailed damage information, the time responses were decomposed into 8 subsets by wavelet packet analysis. Figure 5 shows the decomposed signals in 8 frequency bands, respectively. It is noted from Figure 5 that the time responses in the frequency bands DAA (5th), DDA (6th), and DDD (8th) have very low energy levels as compared to the rest the frequency bands and will not be used for further consideration. For the frequency bands that have much higher energy levels, that is, the 1st, 2nd, 3rd, 4th, and 7th frequency bands (AAA, AAD, ADA, ADD, and DDA), a comparison of the decomposed signals reveals that there is an obvious difference between each case. During the process of tightening the bolt with increasing torque, the stiffness and boundary conditions changed significantly, which resulted in the change of wave propagation at different frequency ranges. To visually show the damage development, damage indices of different frequency bands are shown in Figure 6. The damage index figure quantitatively reveals the damage severities under different degrees of bolt looseness. From the experimental results shown in Figure 6, it is clear that the damage becomes more severe with less torque applied on the bolt, which means that the proposed wavelet packet based damage index can be used to represent the severity of bolt looseness.

5. Conclusion

In this paper, using piezoceramic patch transducers, an innovative active sensing approach was developed to perform bolt inspection in a structure. To simulate different damage severities, the looseness of a bolt was adjusted by a torque wrench with various torque values. In order to quantitatively evaluate the damage, a wavelet packet based damage index was developed. Experimental results show that damage

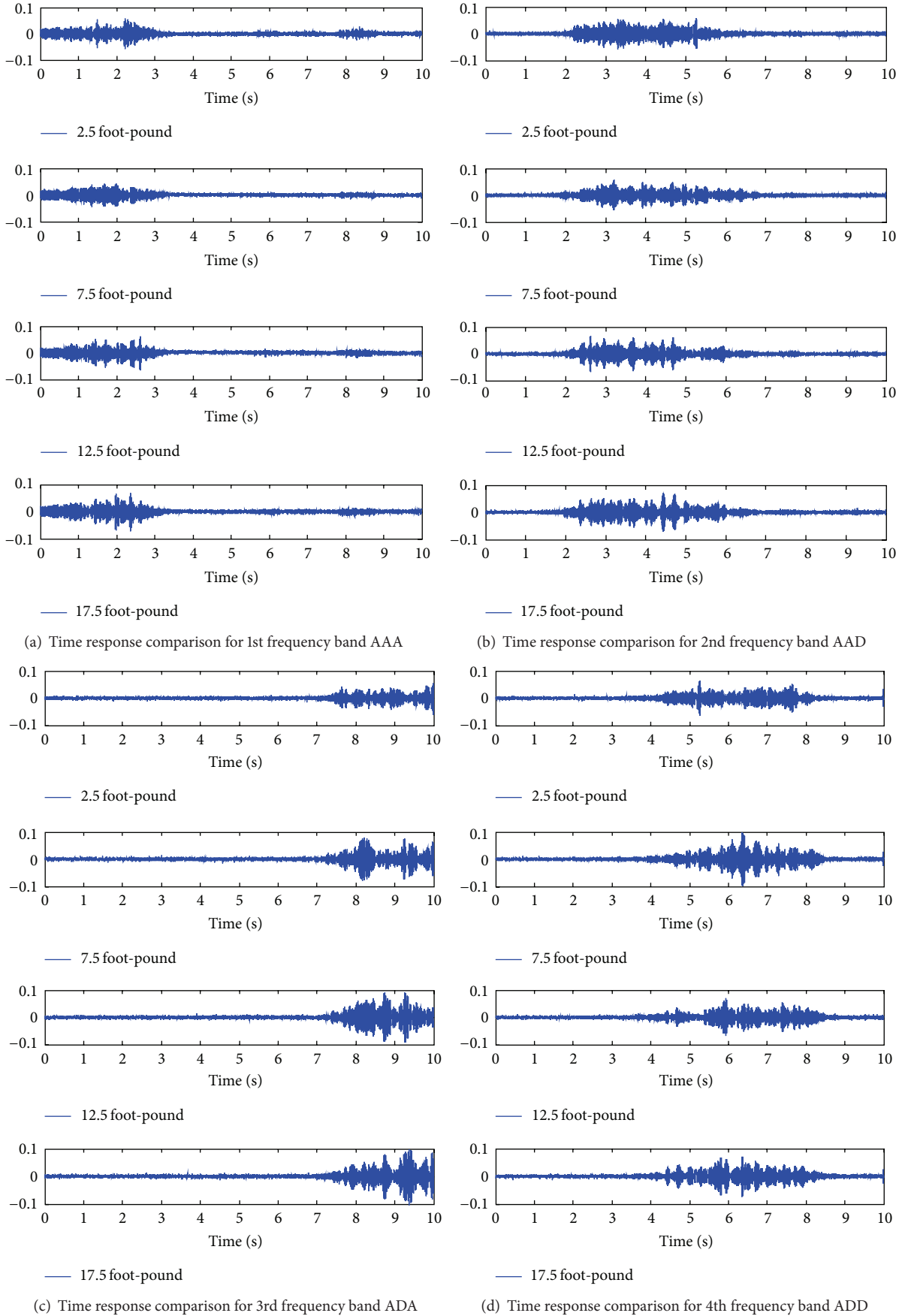
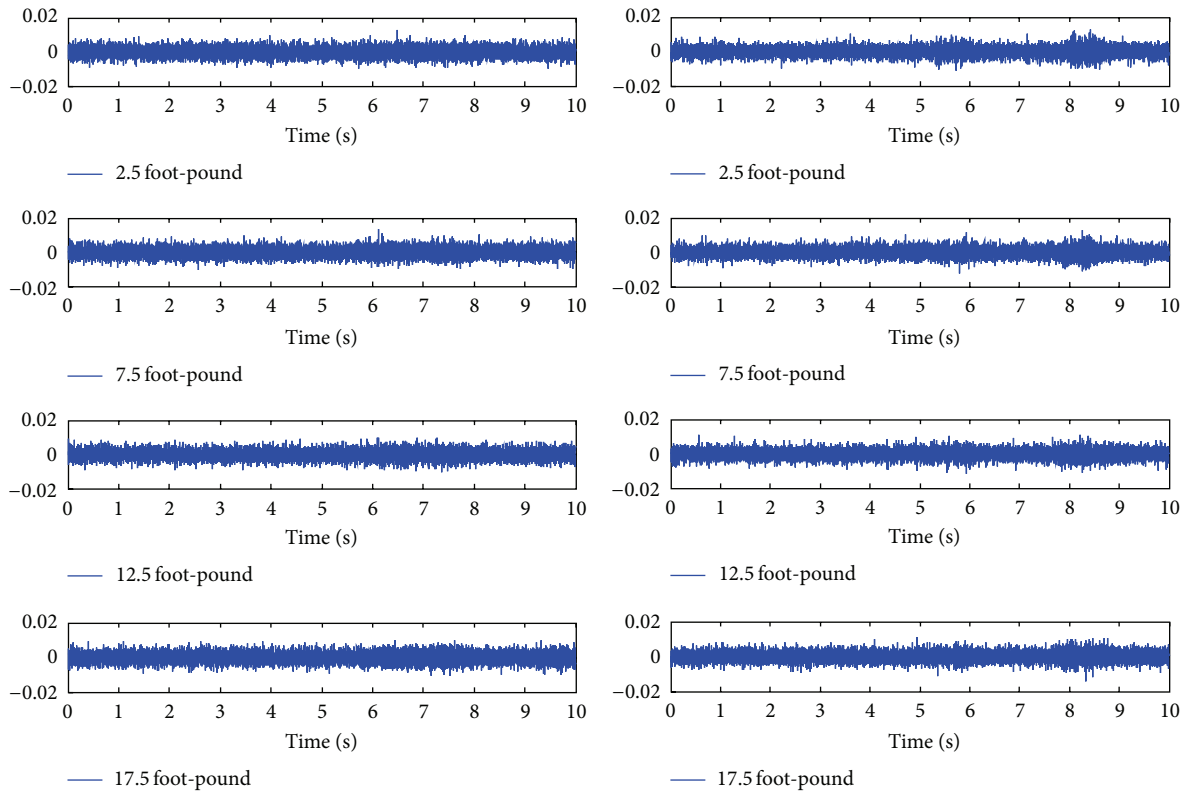
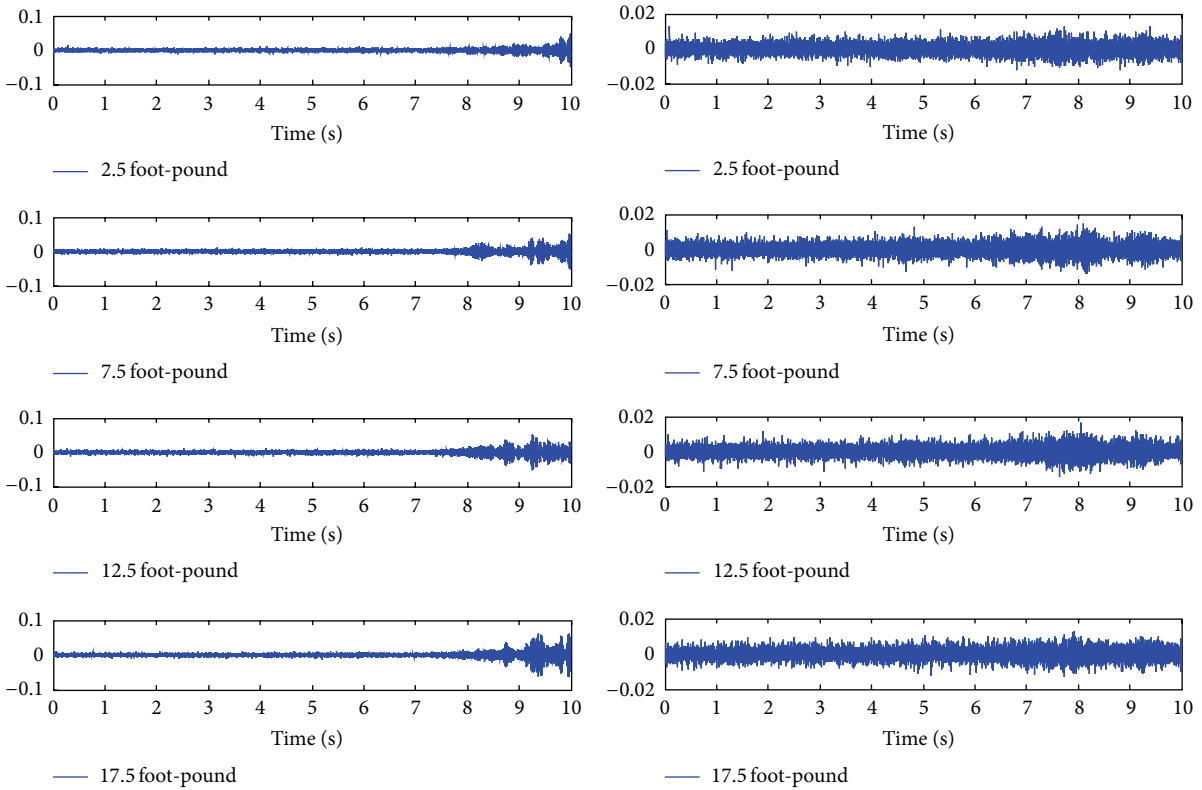


FIGURE 5: Continued.



(e) Time response comparison for 5th frequency band DAA

(f) Time response comparison for 6th frequency band DAD



(g) Time response comparison for 7th frequency band DDA

(h) Time response comparison for 8th frequency band DDD

FIGURE 5: Time response comparison for different frequency bands.

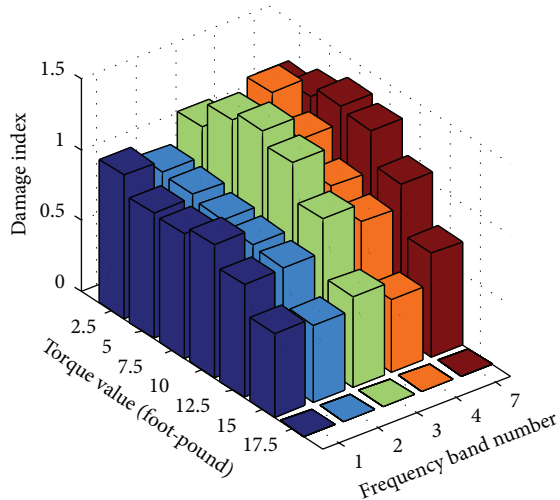


FIGURE 6: Damage indices of interested frequency bands.

indices captured damage features and the damage index values matched the damage development. The proposed approach has the ability to detect the loosening bolt at its incipient stage and has the potential to perform real-time inspection of bolted structures. Please note that a “calibration” process that uses different levels of applied torque is needed to establish the damage index of the bolt connection prior to field deployment. Since multiple bolt-nut pairs are often employed in a single connect, our future work will involve optimization algorithms [15, 16] to determine optimal sensor numbers and locations. In addition, the time reversal method will be explored in our future work to increase the sensitivity of the proposed method.

Acknowledgment

This research was partially supported by Grant nos. 51278387, 51278084, and 51121005 (Science Fund for Creative Research Groups) from the National Science Foundation of China (NSFC).

References

- [1] G. Park, H. Sohn, C. R. Farrar, and D. J. Inman, “Overview of piezoelectric impedance-based health monitoring and path forward,” *The Shock and Vibration Digest*, vol. 35, no. 6, pp. 451–463, 2003.
- [2] D. M. Peairs, G. Park, and D. J. Inman, “Improving accessibility of the impedance-based structural health monitoring method,” *Journal of Intelligent Material Systems and Structures*, vol. 15, no. 2, pp. 129–140, 2004.
- [3] S. Ritdumrongkul, M. Abe, Y. Fujino, and T. Miyashita, “Quantitative health monitoring of bolted joints using a piezoceramic actuator-sensor,” *Smart Materials and Structures*, vol. 13, no. 1, pp. 20–29, 2004.
- [4] A. C. Rutherford, G. Park, and C. R. Farrar, “Non-linear feature identifications based on self-sensing impedance measurements for structural health assessment,” *Mechanical Systems and Signal Processing*, vol. 21, no. 1, pp. 322–333, 2007.
- [5] J. S. Heyman, “A CW ultrasonic bolt-strain monitor—a new sensitive device is reported for the measurement of stress-related strain as well as stress-related change in velocity of sound,” *Experimental Mechanics*, vol. 17, no. 5, pp. 183–187, 1977.
- [6] F. Amerini and M. Meo, “Structural health monitoring of bolted joints using linear and nonlinear acoustic/ultrasound methods,” *Structural Health Monitoring*, vol. 10, no. 6, pp. 659–672, 2011.
- [7] I. Argatov and I. Sevostianov, “Health monitoring of bolted joints via electrical conductivity measurements,” *International Journal of Engineering Science*, vol. 48, no. 10, pp. 874–887, 2010.
- [8] S. Yan, W. Sun, G. Song et al., “Health monitoring of reinforced concrete shear walls using smart aggregates,” *Smart Materials and Structures*, vol. 18, no. 4, Article ID 047001, 2009.
- [9] A. Laskar, H. Gu, Y. L. Mo, and G. Song, “Progressive collapse of a two-story reinforced concrete frame with embedded smart aggregates,” *Smart Materials and Structures*, vol. 18, no. 7, Article ID 075001, 2009.
- [10] H. Gu, Y. Moslehy, D. Sanders, G. Song, and Y. L. Mo, “Multi-functional smart aggregate-based structural health monitoring of circular reinforced concrete columns subjected to seismic excitations,” *Smart Materials and Structures*, vol. 19, no. 6, Article ID 065026, 2010.
- [11] Y. Moslehy, H. Gu, A. Belarbi, Y. L. Mo, and G. Song, “Smart aggregate based damage detection of circular RC columns under cyclic combined loading,” *Smart Materials and Structures*, vol. 19, no. 6, Article ID 065021, 2010.
- [12] G. Song, H. Gu, Y. L. Mo, T. T. C. Hsu, and H. Dhonde, “Concrete structural health monitoring using embedded piezoceramic transducers,” *Smart Materials and Structures*, vol. 16, no. 4, article 003, pp. 959–968, 2007.
- [13] H. Gu, G. Song, and P. Qiao, “Delamination detection of composite plates using piezoceramic patches and wavelet packet analysis,” in *Proceedings of the International Society for Optical Engineering (SPIE '04)*, pp. 220–230, San Diego, Calif, USA, March 2004.
- [14] T. Wang, G. Song, Z. G. Wang, and Y. R. Li, “Proof-of-concept study of monitoring bolt connection status using a piezoelectric based active sensing method,” *Smart Materials and Structures*, vol. 22, no. 8, Article ID 087001.
- [15] T.-H. Yi, H.-N. Li, and M. Gu, “Optimal sensor placement for structural health monitoring based on multiple optimization strategies,” *The Structural Design of Tall and Special Buildings*, vol. 20, no. 7, pp. 881–900, 2011.
- [16] Y. Ting-Hua, L. Hong-Nan, and Z. Xu-Dong, “A modified monkey algorithm for optimal sensor placement in structural health monitoring,” *Smart Materials and Structure*, vol. 21, no. 10, pp. 1–9, 2012.

Research Article

Evaluation of Vibration Characteristics of an Existing Harbor Caisson Structure Using Tugboat Impact Tests and Modal Analysis

Jin-Hak Yi,¹ Woo-Sun Park,¹ So-Young Lee,² Thanh-Canh Huynh,²
Jeong-Tae Kim,² and Chun-Kyo Seo³

¹ Coastal Development and Ocean Energy Research Division, Korea Institute of Ocean Science and Technology, Ansan, Gyeonggi 426-744, Republic of Korea

² Department of Ocean Engineering, Pukyong National University, Busan 608-737, Republic of Korea

³ KEPCO E&C, Yongin, Gyeonggi 446-713, Republic of Korea

Correspondence should be addressed to Jeong-Tae Kim; idis@pknu.ac.kr

Received 26 August 2013; Accepted 17 October 2013

Academic Editor: Hong-Nan Li

Copyright © 2013 Jin-Hak Yi et al. This is an open access article distributed under the Creative Commons Attribution License, which permits unrestricted use, distribution, and reproduction in any medium, provided the original work is properly cited.

Ambient and forced vibration tests are proposed to evaluate dynamic characteristics of a caisson-type breakwater, including natural frequencies and modal damping ratios. The feasibility of a numerical analysis model with fluid-structure-soil interaction effects, which play an important role in evaluating structural performance and safety, was investigated by comparing the numerical results with experimental results. The Oryukdo breakwater in Busan, Republic of Korea, was employed as the target structure. This breakwater was once heightened by installing additional parapet structures of about 4 m tall to improve the harbor tranquility in 2005. Vibration tests were carried out in 2000 (before heightening) and in 2011 (after heightening). Most caissons were tested in the first test, while only one caisson was tested in 2011. It was found that natural frequencies were reduced by 1.7%–4.3% after heightening, and similar results were observed from the numerical analysis. It was also found that forced vibration tests can yield more reasonable results than ambient vibration tests. Even though there is some discrepancy between experimental and numerical results, numerical analysis can be carried out to analyze dynamic characteristics and evaluate structural performance and safety.

1. Introduction

In the recent years, strong typhoons (e.g., Typhoon Maemi in 2003 and Typhoon Bolaven in 2012) have slammed into the Korean Peninsula. Tremendous economic losses were incurred, including the severe damage to harbor structures. To protect harbor infrastructures and facilities from future typhoons and storms, design specifications for breakwaters should be revised to take into account gradually increasing extreme wind speed and wave height during typhoons due to climate change in the northeast Asian region [1]. Accordingly, existing structures designed to old design specifications need to be upgraded to meet the recently revised design codes based on performance evaluations.

It is possible to evaluate existing structures by carrying out numerical analysis with simulation models based on

design drawings. However, it would be very difficult or infeasible to quantitatively evaluate structural performance when design drawings are unclear or when the structure is modified without documentation. In such cases, the structural performance can be evaluated using nondestructive techniques or loading tests, which can also be applied to assess the reusability of deteriorated facilities (e.g., armor blocks, tetrapods, and caissons) in harbor remodeling projects. Among available methods, visual inspection is a practical and widely applied means of inspecting caisson-type breakwaters and can be supplemented with nondestructive evaluation when necessary. Loading tests such as static and dynamic tests allow for loading conditions similar to service loading states and hence can more accurately evaluate structural performance. However, such tests require a lot of time and expense to be carried

out and are very difficult or impossible to apply to large infrastructures like caisson-type breakwaters. Alternatively, ambient and forced vibration tests (AVTs and FVTs), which are actively applied to large inland infrastructures such as bridges and buildings, can be also applied for performance evaluations of caisson-type breakwaters.

Vibration tests on caisson-type breakwaters were previously reported by many researchers [2–5]. Boroschek et al. [6] evaluated a pile-supported breakwater using AVTs and FVTs to identify the dynamic characteristics of a pile-supported breakwater. Gao et al. [2] analyzed dynamic characteristics such as natural frequencies in the 0–30 Hz range for a newly constructed caisson-type breakwater in Shandong Province, China, using six tons of exciter, and identified two rigid body modes at about 3.8 Hz and 8.0 Hz. Lamberti and Martinelli [3] carried out FVTs using impact loading on two breakwaters in Genoa Voltri Port and Punta Riso Port in Italy using a sand bag of 2 tons and tugboats of 100 and 500 tons as a part of PROVERBS, a research project to develop reliability-based design guidelines. It was found that the estimated natural frequencies, that is, 1.4–1.8 Hz for the first mode and 2.3–3.6 Hz for the second mode, were very close to the numerically calculated values. Furthermore, it was observed that the horizontal and rotational modes are highly correlated. Boroschek et al. carried out similar vibration tests on a pile-supported breakwater in Ventanas Port, Chile, through pull-back tests (a type of FVTs) and AVTs. It was reported that clearer and more distinct peaks were observed from FVTs than AVTs, and the first and second natural frequencies were estimated to be around 1.6 Hz and 2.7 Hz, respectively. They also investigated the effects of the external loading level (i.e., pull-back force) on natural frequencies, damping ratios, and initial deflections.

In this study, vibration tests were performed on the caisson-type Oryukdo breakwater in Busan, Republic of Korea, which was heightened about 4 m by installing additional parapet structures to increase harbor tranquility. Two rounds of tests were carried out: in 2000 before heightening and in 2011 after heightening. The first tests were FVTs via tugboat and were conducted to investigate the structural safety of most of the caissons. The stochastic subspace identification method was applied to estimate natural frequencies and modal damping ratios of the caissons. The more recent vibration tests were carried out to investigate the effect of the additionally installed parapets. The practicality of the numerical analysis model was then investigated by comparing the analysis results with experimental results.

2. Theoretical Background

2.1. Experimental Modal Analysis Method. The stochastic subspace identification method utilizes the singular value decomposition of a block Hankel matrix with a cross-correlation matrix of responses. The fundamental basis is the stochastic state-space equation, which expresses the system dynamics under the stochastic random excitation as

$$\begin{aligned} \mathbf{z}(k+1) &= \mathbf{A}\mathbf{z}(k) + \mathbf{w}(k), \\ \mathbf{y}(k) &= \mathbf{C}\mathbf{z}(k) + \mathbf{v}(k), \end{aligned} \quad (1)$$

where $\mathbf{z}(k)$ and $\mathbf{y}(k)$ are the state and observation vectors at k th time step, respectively, and $\mathbf{w}(k)$ and $\mathbf{v}(k)$ are statistically uncorrelated Gaussian random vector sequences with zero means representing the process and measurement noises, respectively. \mathbf{A} and \mathbf{C} are the system and observation matrix, respectively. Then, the cross-correlation function $\mathbf{R}(k)$ can be calculated as

$$\begin{aligned} \mathbf{R}(k) &= E[\mathbf{y}(k+m)\mathbf{y}(m)^T] \\ &= \mathbf{C}\mathbf{A}^{k-1}E[\mathbf{z}(m+1)\mathbf{y}(m)^T] \\ &= \mathbf{C}\mathbf{A}^{k-1}\mathbf{G}, \end{aligned} \quad (2)$$

where $\mathbf{G} \triangleq E[\mathbf{z}(m+1)\mathbf{y}(m)^T]$. Constructing the block Hankel matrix with the cross-correlation matrix $\mathbf{R}(k)$, this block Hankel matrix (\mathbf{H}_{n_1, n_2}) can be decomposed into an observability matrix (\mathcal{O}_{n_1}) and an extended controllability matrix ($\mathcal{C}_{n_2}^{\text{ext}}$) as follows:

$$\begin{aligned} \mathbf{H}_{n_1, n_2} &= \begin{bmatrix} \mathbf{R}_1 & \cdots & \mathbf{R}_{n_2} \\ \vdots & \ddots & \vdots \\ \mathbf{R}_{n_1} & \cdots & \mathbf{R}_{n_1+n_2-1} \end{bmatrix} \\ &= \begin{bmatrix} \mathbf{C}\mathbf{G} & \cdots & \mathbf{C}\mathbf{A}^{n_2-1}\mathbf{G} \\ \vdots & \ddots & \vdots \\ \mathbf{C}\mathbf{A}^{n_1-1}\mathbf{G} & \cdots & \mathbf{C}\mathbf{A}^{n_1+n_2-2}\mathbf{G} \end{bmatrix} \\ &= \begin{bmatrix} \mathbf{C} \\ \vdots \\ \mathbf{C}\mathbf{A}^{n_1-1} \end{bmatrix} \begin{bmatrix} \mathbf{G} & \cdots & \mathbf{A}^{n_2-1}\mathbf{G} \end{bmatrix} = \mathcal{O}_{n_1} \mathcal{C}_{n_2}^{\text{ext}}, \end{aligned} \quad (3)$$

where $\mathcal{O}_{n_1} \triangleq \begin{bmatrix} \mathbf{C}^T & \cdots & (\mathbf{C}\mathbf{A}^{n_1-1})^T \end{bmatrix}^T$, $\mathcal{C}_{n_2}^{\text{ext}} \triangleq \begin{bmatrix} \mathbf{G} & \cdots & \mathbf{A}^{n_2-1}\mathbf{G} \end{bmatrix}$, and n_1 and n_2 are the numbers of the cross-correlation matrix in rows and columns in the block Hankel matrix. Then, the system matrix \mathbf{A} can be obtained using the upper $(n_1 - 1)$ block matrix deleting the last block row of \mathcal{O}_{n_1} and the lower $(n_1 - 1)$ block matrix of the upper shifted matrix by one block row as

$$\mathcal{O}_{n_1-1}^\dagger = \mathcal{O}_{n_1-1}\mathbf{A}, \quad (4)$$

where $\mathcal{O}_{n_1-1}^\dagger \triangleq \begin{bmatrix} (\mathbf{C}\mathbf{A})^T & \cdots & (\mathbf{C}\mathbf{A}^{n_1-1})^T \end{bmatrix}^T$, and $\mathcal{O}_{n_1-1} \triangleq \begin{bmatrix} \mathbf{C}^T & \cdots & (\mathbf{C}\mathbf{A}^{n_1-2})^T \end{bmatrix}^T$. The eigenvalues and vectors of the discrete system can be calculated from the eigenvalue decomposition of the system matrix \mathbf{A} as follows:

$$\begin{aligned} \mathbf{A}\Psi &= \Psi\mathbf{M} \left(\mathbf{M} = \text{diag}(\mu_1, \dots, \mu_N) \in \mathbf{R}^{N \times N}, \right. \\ \Psi &= [\psi_1 \ \cdots \ \psi_N] \in \mathbf{R}^{N \times N} \left. \right). \end{aligned} \quad (5)$$

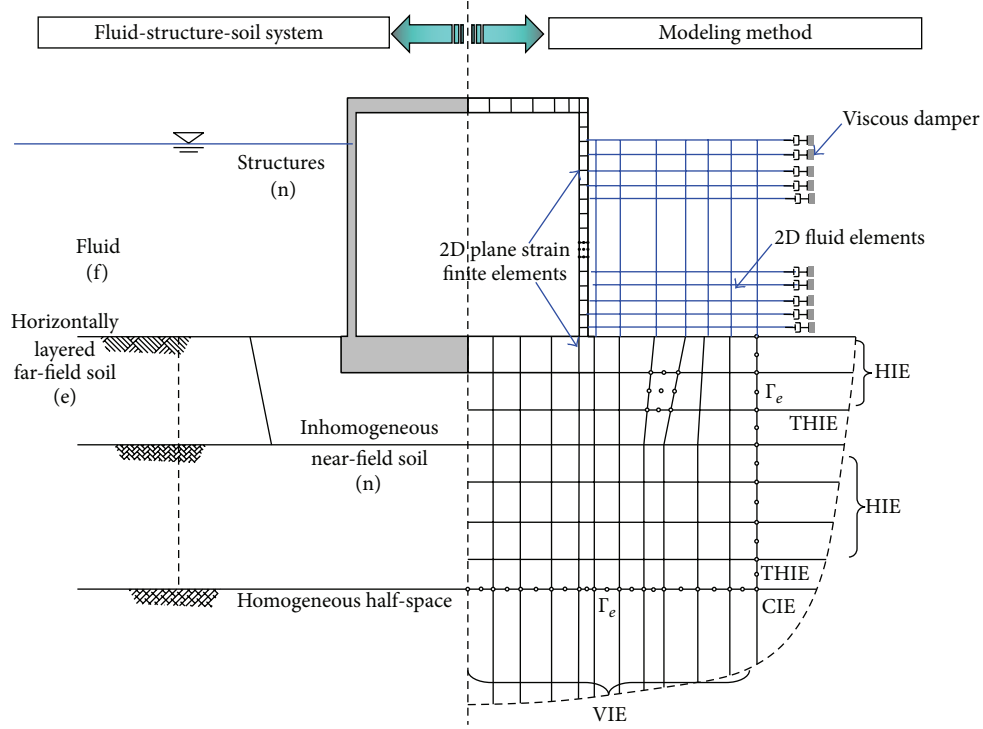


FIGURE 1: Modeling of fluid-structure-soil interaction system.

Finally, the eigenvalue, modal damping ratio, natural frequency, and modal vector for the physical system can be obtained as follows:

$$\begin{aligned}\lambda_k &= \frac{1}{\Delta t} \ln \mu_k, \\ \xi_k &= -\frac{\text{Re}(\lambda_k)}{|\lambda_k|}, \\ \omega_k &= -\frac{\text{Im}(\lambda_k)}{\sqrt{1 - \xi_k^2}}, \\ \phi_k &= \mathbf{C}\psi_k.\end{aligned}\quad (6)$$

2.2. Numerical Modal Analysis Method. Dynamic analysis with fluid-structure-soil interactions was carried out to analyze the dynamic characteristics of a caisson-type breakwater. In this method, the region of the structure and near-field soil is modeled using finite elements, and the far-field soil medium is modeled using infinite elements as shown in Figure 1. The fluid region is modeled with inviscid and incompressible fluid elements for the near-field region and viscous dampers at the interface between the near-field and far-field regions.

The dynamic stiffness matrix for structure and near-field soil medium ($\mathbf{S}^{\text{SN}}(\omega)$) can be obtained using the stiffness matrix (\mathbf{K}^{FE}) and mass matrix (\mathbf{M}^{FE}) for 2D plane strain finite elements as follows:

$$\mathbf{S}^{\text{SN}}(\omega) = (1 + i2h)\mathbf{K}^{\text{FE}} - \omega^2\mathbf{M}^{\text{FE}}, \quad (7)$$

where $i = \sqrt{-1}$, h is the hysteretic damping ratio, and ω is the circular frequency. The modeling procedure for structure and near-field soil using finite elements is almost the same as the procedure used in finite element analysis except in the case of saturated soil. For saturated soil with a Poisson ratio of 0.5, the selective reduced integration technique was applied in this study to avoid the locking phenomenon on volumetric deflection and to simulate saturated soil behavior accurately. The dynamic stiffness matrix for far-field soil ($\tilde{\mathbf{S}}^{\text{F}}(\omega)$) can be obtained using stiffness and mass matrices for dynamic infinite elements as follows [7–10]:

$$\tilde{\mathbf{S}}^{\text{F}}(\omega) = (1 + i2h)\tilde{\mathbf{K}}^{\text{IE}}(\omega) - \omega^2\tilde{\mathbf{M}}^{\text{IE}}(\omega), \quad (8)$$

where the stiffness and mass matrices for dynamic infinite elements are obtained as follows [11]:

$$\begin{aligned}\tilde{\mathbf{K}}^{\text{IE}}(\omega) &= \iint_{\Omega^{(e)}} \tilde{\mathbf{B}}^T(\omega) \mathbf{D} \tilde{\mathbf{B}}(\omega) dx dy, \\ \tilde{\mathbf{M}}^{\text{IE}}(\omega) &= \iint_{\Omega^{(e)}} \tilde{\mathbf{N}}^T(\omega) \rho \tilde{\mathbf{N}}(\omega) dx dy.\end{aligned}\quad (9)$$

In (9), $\tilde{\mathbf{B}}(\omega)$ and \mathbf{D} are the strain-displacement and stress-strain matrices, respectively, and ρ and $\tilde{\mathbf{N}}(\omega)$ are the mass density and shape function vectors, respectively, for an infinite element with complex wave functions. In the far-field region, horizontally layered soil and infinite half-space soil were modeled using horizontal infinite elements (HIEs) and vertical infinite elements (VIEs), respectively. The soil medium at the corner was modeled using corner infinite

elements (CIEs). Transitional horizontal infinite elements (THIEs) were also employed to satisfy the continuity of the displacement by linearly varying the wave numbers associated with body waves in the vertical direction. For modeling the fluid, the fluid was assumed to be shear-free, inviscid, and incompressible. Hence, it was modeled based on the following Navier equation [12]:

$$K_f \nabla \nabla^T \mathbf{u}_f - \rho_f \ddot{\mathbf{u}}_f = 0 \quad \text{in } \Omega, \quad (10)$$

where \mathbf{u}_f , ρ_f , and K_f are, respectively, the displacement vector, mass density, and bulk modulus of the fluid. Equation (10) can be transformed into the weak form using the natural and essential boundary conditions as follows:

$$\begin{aligned} & \int_{\Omega} \left\{ \rho_f \mathbf{w}^T \ddot{\mathbf{u}}_f + K_f (\nabla^T \mathbf{w})^T (\nabla^T \mathbf{u}_f) \right\} d\Omega \\ & + \rho_f g \int_{\Gamma_f} (\mathbf{w}^T \mathbf{n}) (\mathbf{n}_g^T \mathbf{u}_f) d\Gamma \\ & = - \int_{\Gamma_p} (\mathbf{w}^T \mathbf{n}) \bar{p} d\Gamma, \end{aligned} \quad (11)$$

where \mathbf{w} and \bar{p} are the virtual displacement field and prescribed pressure at the interface (Γ_p), respectively; \mathbf{n} and \mathbf{n}_g are the direction vector normal to the boundary and the gravitational direction vector at the interface, respectively; and g denotes the gravitational acceleration. The matrix equation can be expressed by imposing variational formulation as follows:

$$\mathbf{M} \ddot{\mathbf{d}}_f + (\mathbf{K} + \mathbf{S}) \mathbf{d}_f = \mathbf{f}, \quad (12)$$

where \mathbf{M} , \mathbf{K} , and \mathbf{S} are the mass matrix of fluid, stiffness matrix associated with volumetric deflection, and stiffness matrix against sloshing motion, respectively, and \mathbf{f} denotes the external loading vector. Modeling the fluid using four-node quadrilateral displacement-type fluid elements, the stiffness and mass matrices of the fluid medium can be obtained by combining the constant-strain mode (\mathbf{K}_0^e and \mathbf{M}_0^e) and bending mode (\mathbf{K}_B^e and \mathbf{M}_B^e) as follows:

$$\mathbf{K}^e = \mathbf{K}_0^e + \mathbf{K}_B^e, \quad \mathbf{M}^e = \mathbf{M}_0^e + \mathbf{M}_B^e. \quad (13)$$

Herein, because the bending mode can reduce the accuracy of the fluid element associated with volumetric deflection, (1×1) -reduced integration and mass projection techniques were applied for constructing stiffness and mass matrices, respectively, to resolve the accuracy problem. The spurious zero-energy modes in rotational displacement were solved by forcing a rotational penalty method with irrotational flow conditions. Finally, the stiffness and mass matrices for the four-node quadrilateral displacement-type fluid element can be obtained as follows [12]:

$$\mathbf{K}^e = \mathbf{K}_0^e + \mathbf{K}_R^e, \quad \mathbf{M}^e = \mathbf{M}_0^e + \mathbf{M}_R^e. \quad (14)$$

By using the mass and stiffness matrices obtained through the previously mentioned formulation procedure, the equation of

motion for the fluid-structure-soil interaction system can be expressed by the following:

$$\begin{aligned} & \begin{bmatrix} \mathbf{S}_{ff}(\omega) & \mathbf{S}_{fn}(\omega) & \mathbf{0} & \mathbf{0} & \mathbf{0} \\ \mathbf{S}_{nf}(\omega) & \mathbf{S}_{nn}(\omega) & \mathbf{S}_{ns}(\omega) & \mathbf{0} & \mathbf{0} \\ \mathbf{0} & \mathbf{S}_{ss}(\omega) & \mathbf{S}_{ff}(\omega) & \mathbf{S}_{si}(\omega) & \mathbf{0} \\ \mathbf{0} & \mathbf{0} & \mathbf{S}_{is}(\omega) & \mathbf{S}_{ii}(\omega) + \tilde{\mathbf{S}}_{ii}(\omega) & \tilde{\mathbf{S}}_{ie}(\omega) \\ \mathbf{0} & \mathbf{0} & \mathbf{0} & \tilde{\mathbf{S}}_{ei}(\omega) & \tilde{\mathbf{S}}_{ee}(\omega) \end{bmatrix} \\ & \times \begin{Bmatrix} \mathbf{d}_f(\omega) \\ \mathbf{d}_n(\omega) \\ \mathbf{d}_s(\omega) \\ \mathbf{d}_i(\omega) \\ \mathbf{d}_e(\omega) \end{Bmatrix} = \begin{Bmatrix} \mathbf{0} \\ \mathbf{f}_n(\omega) \\ \mathbf{0} \\ \mathbf{0} \\ \mathbf{0} \end{Bmatrix}, \end{aligned} \quad (15)$$

where subscripts f , n , s , i , and e denote the fluid region, interface between the fluid and structure, region of the structure and near-field soil, interface between the near-field and far-field regions, and far-field region, respectively. $\mathbf{S}(\omega)$ and $\tilde{\mathbf{S}}(\omega)$ denote the dynamic stiffness matrices for finite elements and infinite elements, respectively, and $\mathbf{f}_n(\omega)$ represents the external loading vector. For simulating the radiational energy dissipation effect in the fluid region, the viscous damper was added at the interface between the near-field and far-field regions, and the damping parameter (C_p) was calculated using the p -wave propagation velocity (V_p), mass density (ρ), and projection area (A) as follows [13]:

$$C_p = \rho V_p A. \quad (16)$$

3. Dynamic Characteristics by Forced Vibration Tests

3.1. Layout of Target Structure and Experimental Setups. Vibration-based structural tests were carried out on the Oryukdo breakwater in Busan, Republic of Korea, in 2000, as a part of a structural safety assessment project on that breakwater. At that time, FVTs using impact loading applied by a tugboat were carried out on most of the caissons. Three successive caissons were combined into one test case, and 14 test cases were conducted as shown in Table 1. The center caisson in each group was excited with a tugboat, and impulse responses were measured using eight accelerometers, as shown in Figure 3(a). The caisson IDs and case numbers are indicated in Figure 2(a) and Table 1. The accelerometers were installed on the top surface of the cap concrete, as shown in Figure 3(a). Meanwhile, in 2005, the height of this breakwater was increased by constructing additional parapet structures of 4 m to protect naval facilities in the harbor. To investigate the effect of the additional parapet structures on the dynamic characteristics, AVTs and FVTs were performed in 2011 using the experimental setup shown in Figure 3(b). Details of the setup are described in Yoon et al. [14].

3.2. Vibration Tests in 2000 before Parapet Installation. Figures 4(a)–4(c) show impulse responses for Cases 3 and 4, and Figure 4(d) shows the stabilization chart for selecting stable modes and an appropriate model order [15] by stochastic subspace identification during the experimental modal analysis.

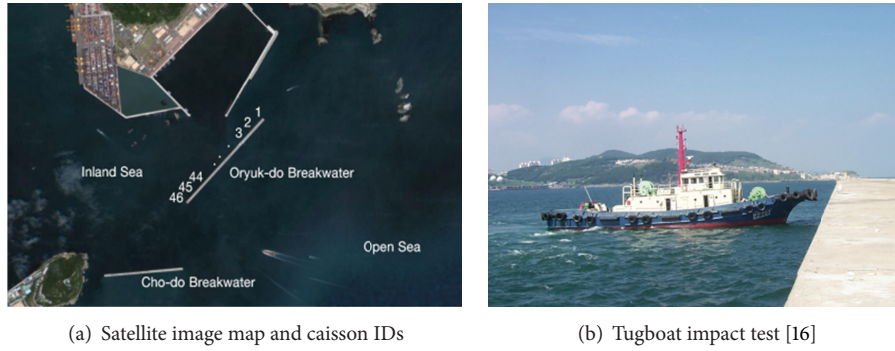


FIGURE 2: Location of target breakwater and impact vibration test.

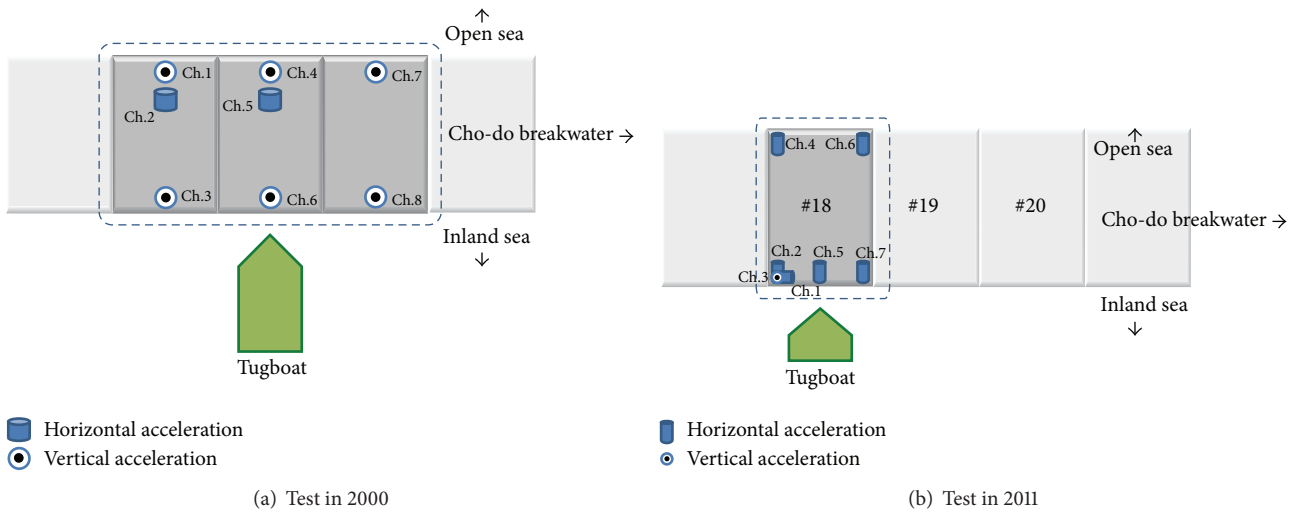


FIGURE 3: Experimental setups.

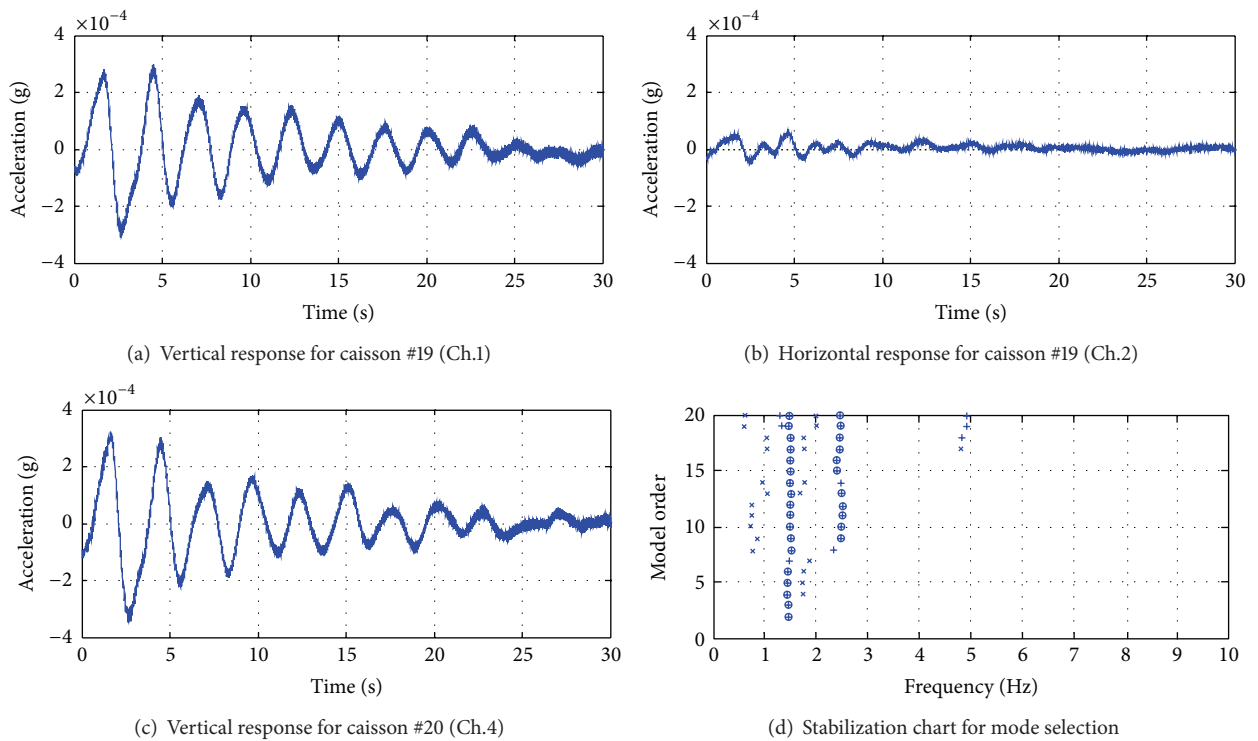


FIGURE 4: Measured impulse responses and stabilization chart.

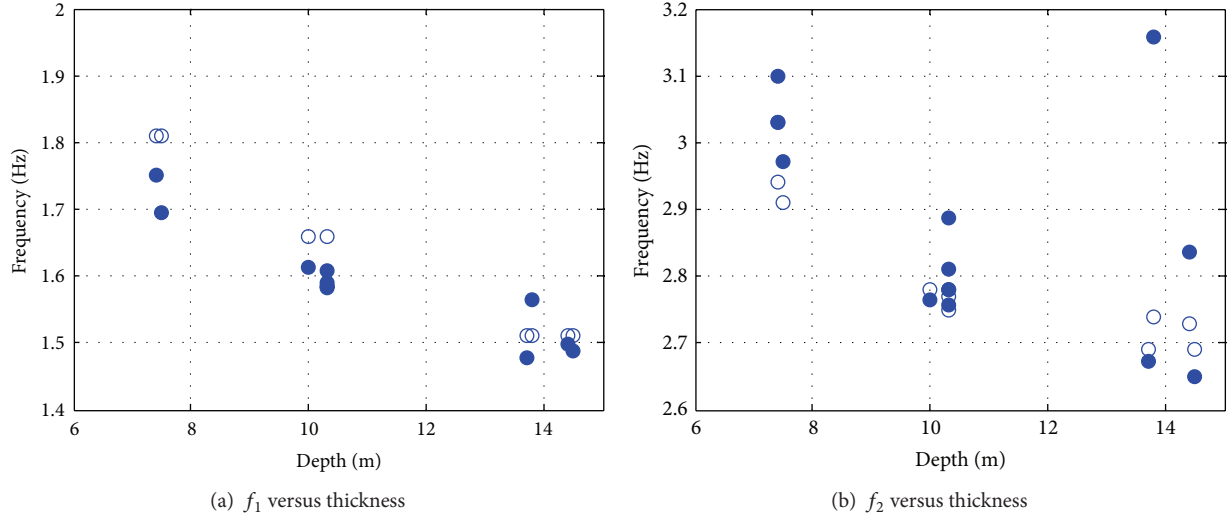


FIGURE 5: Estimated natural frequencies and thickness of sand-fill.

TABLE 1: Test cases and caisson IDs.

Test cases	Caisson IDs
Case 1	1, 2, 3
Case 2	7, 8, 9
Case 3	15, 16, 17
Case 4	19, 20, 21
Case 5	25, 26, 27
Case 6	31, 32, 33
Case 7	32, 33, 34
Case 8	33, 34, 35
Case 9	35, 36, 37
Case 10	36, 37, 38
Case 11	39, 40, 41
Case 12	41, 42, 43
Case 13	42, 43, 44
Case 14	44, 45, 46

TABLE 2: Experimental natural frequencies from vibration tests in 2000.

	Experimental natural frequency (Hz)		Caisson size and depth of sand-fill	
	f_1	f_2	Size	Depth (m)
Case 1	1.982	3.720	A	11.5
Case 2	1.748	3.351	B	13.8
Case 3	1.499	2.835	B	14.4
Case 4	1.488	2.651	B	14.5
Case 5	1.477	2.672	B	13.7
Case 6	1.608	2.886	B	10.3
Case 7	1.586	2.811	B	10.3
Case 8	1.582	2.758	B	10.3
Case 9	1.590	2.781	B	10.3
Case 10	1.613	2.765	B	10.0
Case 11	1.695	2.972	B	7.5
Case 12	1.750	3.031	B	7.4
Case 13	1.752	3.510	B	7.4
Case 14	1.957	4.122	A	5.0

From this stabilization chart, it can be seen that there are two clear and distinct modes around 1.5 Hz and 2.7 Hz. The estimated natural frequencies are listed in Table 2 along with the modal damping ratios.

From Table 2, it can be observed that the estimated natural frequencies are obviously reduced as the sand-fill layer is thickened as shown in Figure 5. It means that the structural system becomes more flexible as the thickness of the sand-fill layer increases. This is because of the larger flexibility of the sand-fill layer (shear wave velocity of about 250 m/s) compared to that of the bedrock (shear wave velocity of about 400 m/s). Figure 6 shows the estimated modal damping ratios. Although there is no clear relationship between the damping ratios and depth of the sand-fill layer, it can be observed that the modal damping ratios for the second mode are generally higher than those for the first mode. Furthermore, the estimated damping ratios are in the range of

4%–15%, which is relatively higher than the range for general concrete structures. This is attributed to the additional hydrodynamic damping effects owing to the adjacent sea water in this structural system.

3.3. Vibration Tests in 2011 after Parapet Installation. Figures 7 and 8 show the measured acceleration responses and their corresponding stabilization charts for the 18th caisson structure, with the results of AVTs shown in Figure 7 and the results of FVTs shown in Figure 8. For the field works, wireless system is good to reduce installation time and cost [17]. Therefore, instead of the wired system used in the earlier test in 2000, wireless sensors were used in the tests. Seven high-sensitivity ICP-type accelerometers with

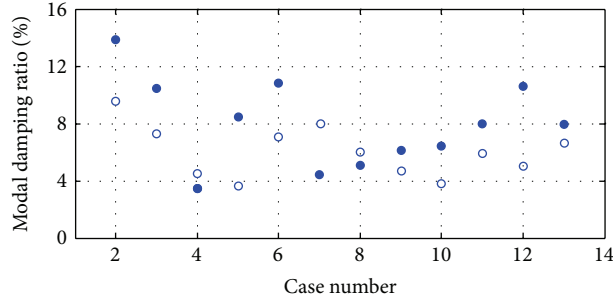


FIGURE 6: Estimated modal damping ratios and thickness of sand-fill.

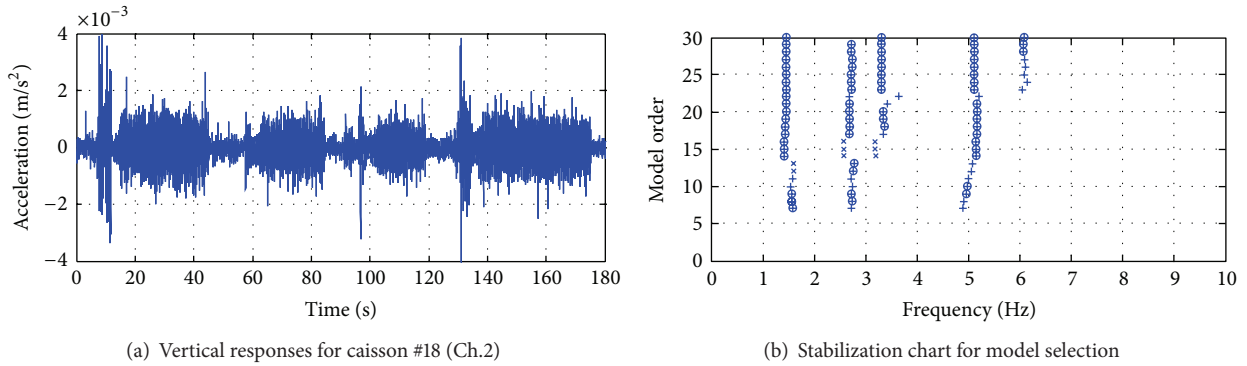


FIGURE 7: Measured responses and stabilization chart for AVTs.

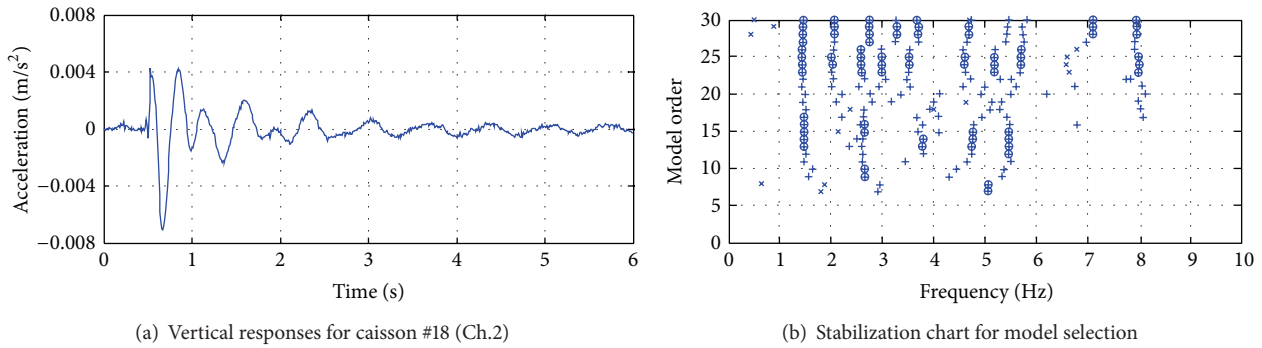


FIGURE 8: Measured responses and stabilization chart for FVTs.

a measurement range of $\pm 0.5g$ were used, and the acceleration responses were sampled at 100 Hz. Ambient vibration responses were also measured for three minutes after impact-based FVTs. The estimated dynamic characteristics are listed in Table 3.

The natural frequencies for the first and second modes are estimated to be 1.471 Hz and 2.753 Hz, respectively, from AVTs; they are estimated to be 1.430 Hz and 2.695 Hz, respectively, from FVTs. From the results, it is observed that the estimated natural frequencies from FVTs are lower than those from AVTs by 2.1%–2.8%. This can be explained by considering the level of external forces: in the case of AVTs, the external force is relatively small, and, hence, the responses are also very small and the soil behaves relatively stiffer owing to the initial stiffness effects. Similar trends were found in the

research by Boroscchek et al. [6], who reported that the estimated natural frequencies from a pull-back test were 1.63 Hz and 2.74 Hz for the first and second modes, respectively, and that these values were lower than those from AVTs (1.68 Hz and 2.82 Hz) by 2.8%–2.9%. Considering these observations, it can be preliminarily concluded that the natural frequencies estimated from FVTs are slightly lower than those obtained from AVTs by about 2%–3%. Considering that strong typhoons generate high levels of external loads, FVTs can exert more realistic loading conditions. In other words, the structural stiffness can be overestimated by AVTs. Compared with the previous results obtained in 2000, the first and second natural frequencies decreased by about 1.7%–4.3% after heightening owing to the additional mass effects as shown in Table 4.

TABLE 3: Experimental natural frequencies from vibration tests in 2011.

Modes	AVTs		FVTs	
	Frequency (Hz)	Damping ratio (%)	Frequency (Hz)	Damping ratio (%)
1st	1.471	4.536	1.430	2.760
2nd	2.753	6.183	2.695	0.888

TABLE 4: Changes in natural frequencies after parapet installation.

	1st mode	2nd mode
Test in 2000 without parapet (Hz)	1.493	2.743
Test in 2011 with parapet (Hz)	1.430	2.695
Rate of change (%)	-4.30	-1.70

4. Numerical Modal Analysis Results

4.1. Layout of Numerical Analysis. Figure 9(a) shows the sectional dimension of the Oryukdo breakwater after it was heightened, and Figure 9(b) represents the corresponding numerical analysis model using finite, infinite, and viscous damper elements. This numerical analysis model built for the heightened structure was constructed by simply adding the installed parapet (circled in Figure 9(b)) to the model of the unheightened breakwater. In 2011, only one caisson (the 18th) was tested among the 46 total caissons for the purpose of this comparison study. It is noted that the sand-fill depth is 14.8 m, the region of the structure and near-field soil was modeled using 2D plane finite elements, the fluid region was modeled using quadrilateral four-node displacement-type fluid elements, and the horizontal infinite far-field soil region was modeled using 2D dynamic infinite elements. A viscous damper was also added for simulating the radiational energy dissipation.

The material properties used in the numerical analysis are listed in Table 5, with general concrete properties, assigned to the cap concrete, caisson, and concrete block, and ordinary sea water properties used for the fluid region. The soil properties listed in Table 5 were assigned for the armor blocks, sand-fill, and infinite homogenous half-space region.

4.2. Analysis Results. In this study, the KIESSI-2D software (a computer program for soil-structure interactions using finite and infinite element techniques) was used for forced vibration analysis on the breakwater structure considering fluid-structure-soil interactions [18]. The dynamic characteristics were analyzed using numerical models of the structure before and after parapet installation, and the results were compared with experimentally evaluated natural frequencies.

To excite this structural system, impulse loading was applied, where the loading spectrum has unit amplitude at all frequencies ($1(\omega)$) and the frequency response function (FRF) can be obtained by dividing the dynamic response ($U(\omega)$) with the static response ($U(0)$) as follows:

$$H(\omega) = \frac{U(\omega)}{U(0)}. \quad (17)$$

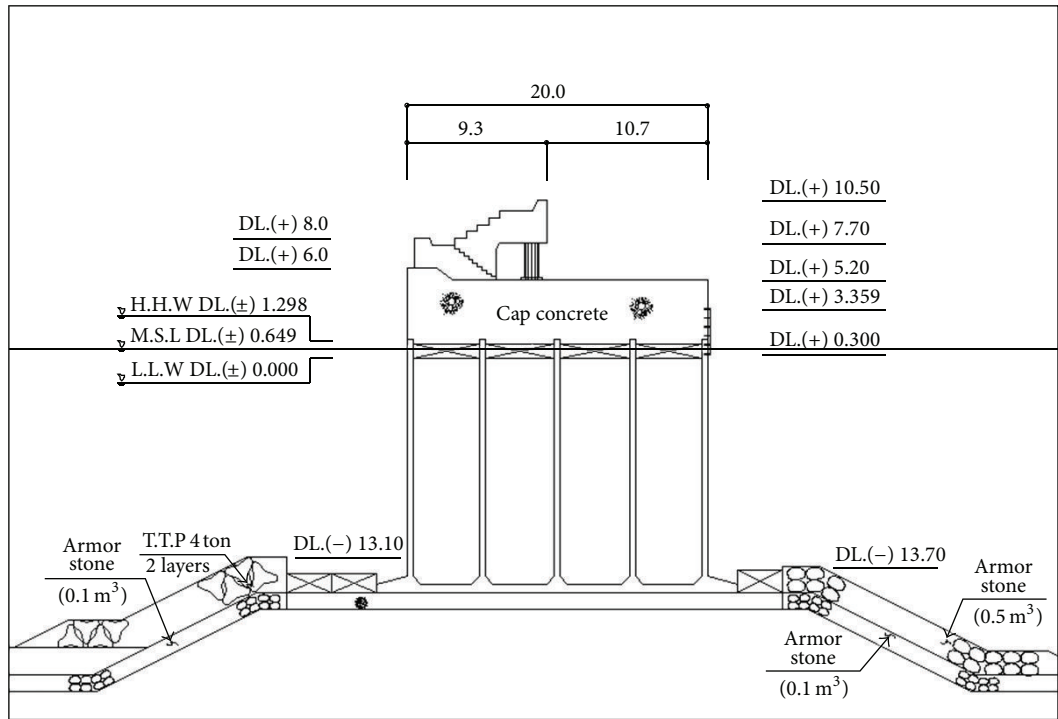
The impulse loading was horizontally applied at the upper-left corner of the cap concrete from the inner harbor side (i.e., point A in Figure 9(b)), and the vertical and horizontal responses were obtained at the upper-right corner of the cap concrete in the outer harbor side (i.e., point B in Figure 9(b)). The displacement ($u(t)$), velocity ($\dot{u}(t)$), and acceleration ($\ddot{u}(t)$) were obtained using the inverse Fourier transform of responses in the frequency domain.

Figures 10 and 11 show the calculated horizontal and vertical responses and the corresponding FRFs, respectively. The resonant frequencies obtained for the first and second modes are 1.514 Hz and 2.441 Hz, respectively, for the cases of the unheightened breakwater. The frequencies are 1.416 Hz and 2.344 Hz for the heightened case. Compared with the measured values shown in Table 6, the natural frequencies of the first mode are closely matched, while the second mode frequencies deviate by about 10%. Moreover, the frequency changes after structural heightening were 1.7%–4.3% in the experimental tests and about 4.6%–6.5% in the numerical tests. Hence, further studies are recommended for reducing discrepancies between experimental and numerical results to some extent.

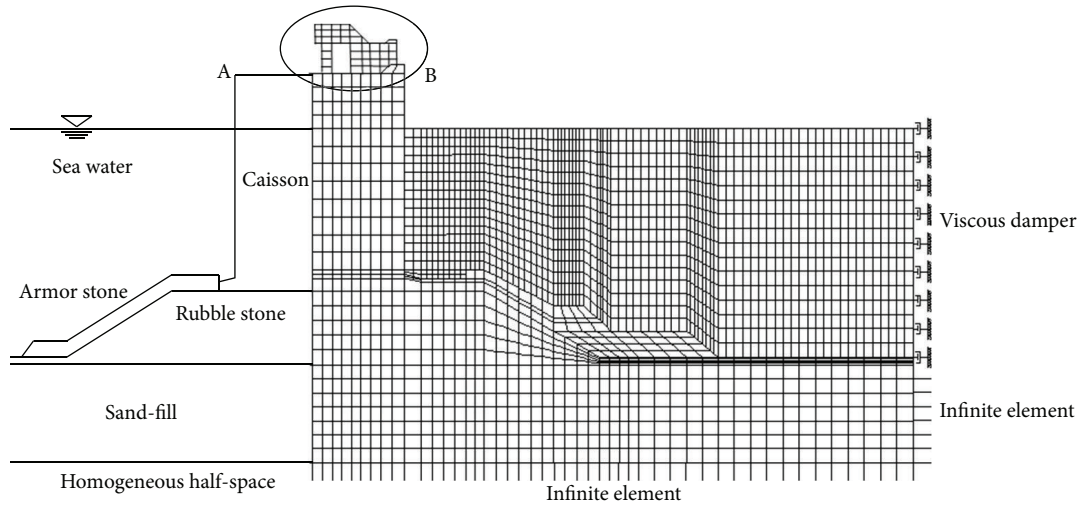
5. Conclusions

Dynamic characteristics were analyzed using experimental and numerical tests for the caisson-type Oryukdo breakwater, in Busan, Republic of Korea, and the practical applicability of a numerical analysis model was investigated by a comparison study. From the tests, it was found that the natural frequencies decrease as the sand-fill layer is thickened as a result of the lower shear wave velocity of sand-fill ($V_s = 250$ m/s) compared to that of bedrock ($V_s = 400$ m/s). Consequently, the entire structural system becomes more flexible as the sand-fill layer becomes thicker. Recently, AVTs and FVTs were also conducted to analyze dynamic characteristics after heightening by parapet installation. It was found that the natural frequencies estimated from FVTs are lower owing to the high level of external loads. Therefore, it is recommended that FVTs be applied when possible for more accurate evaluation of practical cases.

It was also found that the estimated natural frequencies after heightening are lesser by 1.7%–3.7% compared to those before heightening owing to the additional mass effect to the parapet structure, which is not affected by stiffness change. A similar trend was found from numerical analysis as well. However, there is some degree of discrepancy (about 2%–3%) between the experimental and numerical results. Hence, further studies are recommended to investigate the source of this



(a) Sectional dimension of target breakwater



(b) Model of fluid-structure-soil interaction analysis

FIGURE 9: Sectional dimension and numerical model of breakwater after parapet installation.

TABLE 5: Material properties of caisson and soil for numerical analysis.

	Elastic modulus (kN/m ²)	Poisson's ratio	Density (×10 ³ kg/m ³)	Shear wave velocity (m/s)
Cap concrete	2.800 × 10 ⁷	0.20	2.50	—
Caisson concrete	2.800 × 10 ⁷	0.20	2.50	—
Sea water	1.967 × 10 ⁶	0.49	1.02	—
Armor stone	2.800 × 10 ⁶	0.20	2.00	—
Rubble stone	7.450 × 10 ⁴	0.40	2.20	—
Sand-fill soil	—	0.43	2.00	250.0
Bedrock soil	—	0.45	2.40	400.0

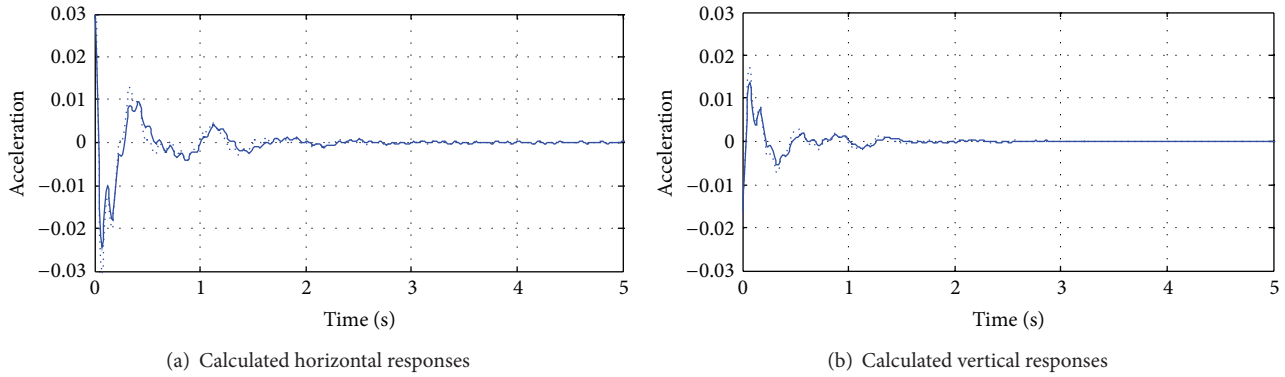


FIGURE 10: Impulse responses at upper-right corner of cap concrete by FSSI analysis (Dotted line: before installation, solid line: after installation).

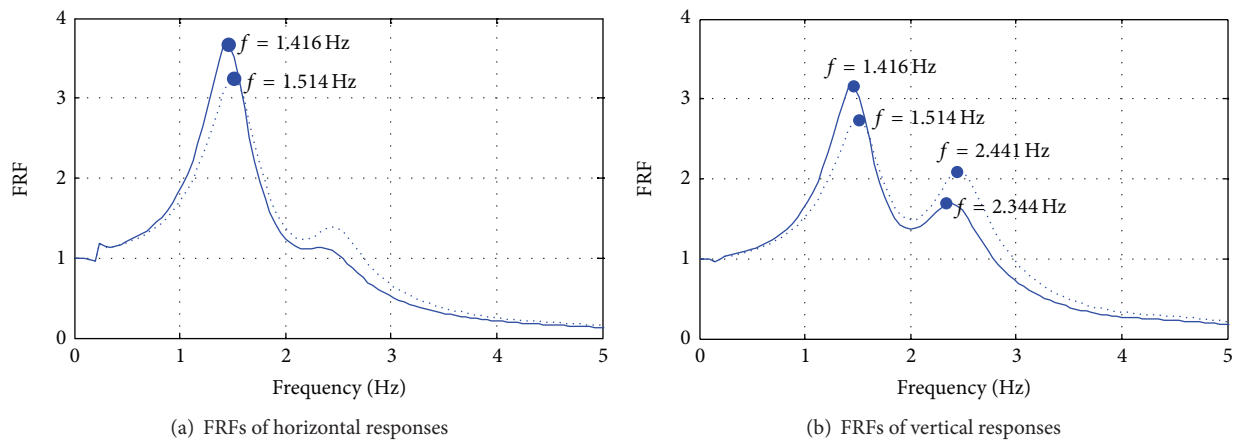


FIGURE 11: FRFs of responses at upper-right corner of cap concrete by FSSI analysis (dotted line: before installation; solid line: after installation).

TABLE 6: Experimental and numerical natural frequencies before and after parapet installation.

Modes	Vibration tests		Numerical analysis	
	1st	2nd	1st	2nd
No parapet (Hz)	1.494	2.743	1.514	2.441
With parapet (Hz)	1.430	2.695	1.416	2.344
Change rate (%)	-4.3	-1.7	-6.5	-4.0

discrepancy and identify effective remedies. It is noteworthy that the methods presented in this study can be applied in the global monitoring of damage such as scouring at the foundation of caisson-type structures. Moreover, vibration tests can be a good alternative to the visual inspections popularly performed by divers, which are generally time-consuming and dangerous.

Acknowledgments

This work was supported by the KIOST Research Program (PE98974) and Basic Science Research Program through the National Research Foundation of Korea funded by

the Ministry of Education, Science and Technology (NRF-2013RIA1A2A10012040). The authors would like to express their appreciation for the financial support.

References

- [1] E. Vanem, B. Natvig, and A. B. Huseby, "Modelling the effect of climate change on the wave climate of the world's oceans," *Ocean Science Journal*, vol. 47, no. 2, pp. 123–145, 2012.
- [2] M. Gao, G. Dai, and J. Yang, "Dynamic studies on caisson-type breakwaters," in *Proceedings of the International Twenty-first Coastal Engineering Conference*, pp. 2469–2478, 1988.
- [3] A. Lamberti and L. Martinelli, "Prototype measurements of the dynamic response of caisson breakwaters," in *Proceedings of the 26th International Conference on Coastal Engineering (ICCE '98)*, pp. 1972–1985, June 1998.
- [4] S.-Y. Lee, K.-D. Nguyen, T.-C. Huynh, J.-T. Kim, J.-H. Yi, and S.-H. Han, "Vibration-based damage monitoring of harbor caisson structure with damaged foundation-structure interface," *Smart Structures and Systems*, vol. 10, no. 6, pp. 517–546, 2012.
- [5] T.-C. Huynh, S.-Y. Lee, J.-T. Kim, W.-S. Park, and S.-H. Han, "Simplified planar model for damage estimation of interlocked caisson system," *Smart Structures and Systems*, vol. 12, no. 3, pp. 441–463, 2013.

- [6] R. L. Boroschek, H. Baesler, and C. Vega, "Experimental evaluation of the dynamic properties of a wharf structure," *Engineering Structures*, vol. 33, no. 2, pp. 344–356, 2011.
- [7] S.-C. Yang, *Development of dynamic infinite element for soil-structure interaction analysis [Ph.D. dissertation]*, KAIST, 1992.
- [8] J.-M. Kim, *Development of axisymmetric dynamic infinite elements based on multiple wave functions and its application to solid-structure interaction analysis [Ph.D. dissertation]*, KAIST, 1995.
- [9] D.-K. Kim, *Analytical frequency-dependent infinite elements for soil-structure interaction analysis in time domain [Ph.D. dissertation]*, KAIST, 1999.
- [10] C.-K. Seo, *Three dimensional elasto-dynamic infinite elements for soil-structure interaction analysis [Ph.D. dissertation]*, KAIST, 2007.
- [11] C.-B. Yun, D.-K. Kim, Y.-J. Kim, and J.-W. Lee, "Vibration analysis of strip foundations in layered soils using infinite elements," *Journal of Korea Society of Civil Engineers*, vol. 17, no. 1-2, pp. 271–282, 1997, Korean.
- [12] Y.-S. Kim and C.-B. Yun, "A spurious free four-node displacement-based fluid element for fluid-structure interaction analysis," *Engineering Structures*, vol. 19, no. 8, pp. 665–678, 1997.
- [13] J. Lysmer and R. L. Kuhlemeyer, "Finite dynamic model for infinite media," *Journal of Engineering Mechanics*, ASCE, vol. 95, pp. 859–887, 1969.
- [14] H.-S. Yoon, S.-Y. Lee, J.-T. Kim, and J.-H. Yi, "Field implementation of wireless vibration sensing system for monitoring of harbor caisson breakwaters," *International Journal of Distributed Sensor Networks*, vol. 2012, Article ID 597546, 9 pages, 2012.
- [15] B. Peeters and G. De Roeck, "Reference-based stochastic subspace identification for output-only modal analysis," *Mechanical Systems and Signal Processing*, vol. 13, no. 6, pp. 855–878, 1999.
- [16] KORDI, Final Report on Precision Survey on Oryukdo Breakwater in Busan Port and Precision Inspection for Outlying Facilities, Busan Regional Maritime Affairs and Port Office, (Korean), 2001.
- [17] G.-D. Zhou and T.-H. Yi, "The node arrangement methodology of wireless sensor networks for long-span bridge health monitoring," *International Journal of Distributed Sensor Networks*, vol. 2013, Article ID 865324, 8 pages, 2013.
- [18] J.-M. Kim, S.-H. Jang, C.-B. Yun, and Y. S. Kim, "A computer program for 2-D fluid-structure-soil interaction analysis," in *Proceedings of EESK Spring Conference*, Seoul, Korea, 2000, (Korean).

Research Article

Development and Application of Structural Health Monitoring System Based on Piezoelectric Sensors

Shi Yan,¹ Jianxin Wu,² Wei Sun,¹ Haoyan Ma,¹ and Han Yan²

¹ School of Civil Engineering, Shenyang Jianzhu University, Shenyang, Liaoning 110168, China

² Liaoning Electric Power Survey & Design Institute, Shenyang, Liaoning 110179, China

Correspondence should be addressed to Shi Yan; syan1962@163.com

Received 4 July 2013; Revised 22 September 2013; Accepted 27 September 2013

Academic Editor: Jeong-Tae Kim

Copyright © 2013 Shi Yan et al. This is an open access article distributed under the Creative Commons Attribution License, which permits unrestricted use, distribution, and reproduction in any medium, provided the original work is properly cited.

Structural health monitoring (SHM) can enhance the functionality of structures, improve its safety and reliability, reduce maintenance costs, and increase the service life. A new kind of SHM technology based on piezoelectric ceramic transducers is an effective way to realize the prospective functions. However, many of piezoelectric ceramic SHM systems, which are complicated, weighty, and having much equipment, are mainly used for laboratory researches. In order to meet the needs of engineering applications, a portable piezoelectric concrete SHM system which uses the virtual instrument technology is proposed and produced in this paper. The developed system which is based on piezoelectric transducers can be realized to monitor online vibration accelerations, dynamic stresses, concrete cracks, and so forth. The function of this integrated system has been effectively proved in test and in an engineering application. The experimental and applied results show that the system is reliable, of high degree of automation, and portable. The work provides important technical support for improvement of structure design and monitoring of structural health status.

1. Introduction

In the field of civil engineering, the security issue for concrete structures as one of the most widely used form of structure has always been concerned because of significant shortcomings of the concrete structure such as easily cracking. The appearance of cracks not only weakens the bearing capacity of the member, but also enables the reinforcement to expose in the air then makes the reliability of the structure greatly reduce. Therefore, the health monitoring technology of concrete structures has become one of the research focuses in recent years. The SHM is the use of on-site nondestructive sensing technology, through the analysis of the structure system characteristics including structural responses, to achieve the purpose of detection of structural damage or degradation [1]. Among them, the use of piezoelectric ceramic transducers for health monitoring of concrete structures has achieved initial results.

At present, the piezoelectric concrete structural health monitoring technology has two main categories: active monitoring technology and passive monitoring one. According

to the damage diagnosis methods, the active monitoring technology is divided into the wave-based method and the mechanical impedance method. For the wave-based method, the basic principle is the use of inverse piezoelectric effect of piezoelectric ceramic which was used to produce transducers, which are arranged in the structure as a certain array, so as to establish the actuator-sensor channel to realize the component interval scanning, through the analysis of the difference of signal to achieve identification and diagnosis of structural damage [2–10]. In recent years, a new technology called smart aggregate that uses embedded piezoceramic has been used to monitor cracks in concrete structures [11–16]. Electro-mechanical impedance method by comparing the mechanical impedance value of the structure to judge whether it is damaged or not [17–21]. The passive monitoring method mainly measures dynamic responses of the structure which refers to the high-impedance characteristics of piezoelectric ceramics. At present, applications using the passive monitoring method are mainly concerned with structural vibration condition monitoring, impact load monitoring, and structural monitoring based on acoustic

emission technique. In 2006, Yang from Tianjin University used this method to experimentally monitor the deformation of a two-story reinforced concrete frame structure under earthquake ground motion [22]. The test results showed that the piezoelectric ceramic can effectively monitor stress changes of the structure. In 2007, Song et al. carried out tests of an overloaded truck hitting the high-speed bridge, using piezoelectric ceramic sensors to monitor the impact load of the structure. The results showed that the piezoelectric ceramic transducer can correctly reflect the impact load value [23].

The technology achieves good results in the laboratory research stage however, due to the lack of development of the corresponding monitoring equipment system, its application in engineering field is greatly limited. The monitoring system for laboratory research use is often realized by the signal generator, power supply, charge amplifier, oscilloscope, and other independent instruments. Many of these systems are complicated and weighty, and data processing and further damage identification are mostly offline manual processing; it is inconvenient to be used in engineering applications. Sun et al. [24, 25] have built piezoelectric monitoring systems that rely on offline manual data processing. Massive data caused a huge amount of work, and many devices limit the system application environments. Therefore, the development of a set of portable piezoelectric health monitoring systems for the real-time and online monitoring of concrete structures is imperative. It is of great significance to promote the application of the technology in the practical engineering. Development of structural health monitoring system based on virtual instrument technology can make good use of the software on hardware for unified management and enhance real-time data acquisition and processing. The flexible graphical software interface is user-friendly. In recent years, the technology in the field of health monitoring has a certain development. In 2008, Qiu and Yuan used LabVIEW to develop an integrated health monitoring piezoelectric scanning system [26]. Myer Charles stadium in Milan developed a distributed health monitoring system with LabVIEW and CompactRIO platform by the Polytechnic University of Milan.

In this paper, a multifunctional integrated piezoelectric health monitoring system was developed to meet the need of engineering application. Relying on NI CompactRIO embedded platform as the core, it is convenient to the corresponding ancillary equipment and platform configurations to meet different functional requirements. Using the LabVIEW graphical software for integrated management of the hardware can make full use of hardware resources and provide the user with easy operation, flexible graphical user interface. The function of the proposed system is verified by both experiments in laboratory and the engineering application of wind turbines concrete foundation. The validation studies have shown that the integrated system, developed in this paper for high precision, good reliability, compact structure, and being scalable and highly available, can be effectively applied for the health monitoring of concrete structures. In the later, the user also can expand the system according to the increasing demand.

2. The Description of the System

Currently, a variety of piezoelectric sensor health monitoring systems often consist of the independent instruments, and software compatibility between each other is poor. Especially, for the use of piezoelectric monitoring technology to build the monitoring system, the hardware such as oscilloscope and signal generator is independent and of low degree of automation, and data processing also relies on artificial offline processing, resulting in a heavy workload, and this cannot meet the need of engineering applications.

The system is based on piezoelectric health monitoring technology, and the original monitoring system was optimally designed by using the virtual instrument technology. By adding a series of hardware or software, a reconfigurable test instrumentation system which is based on software and hardware supplemented with good interactive interface is formed. Based on NI CompactRIO embedded platform, users can achieve a variety of applications on a single system through modular configurations. By taking advantage of LabVIEW graphical programming software for unified management of various software modules, simple operation and easy extension, and function can be defined by the user.

The overall structural design of the system is divided into hardware configuration and software design [27]. The hardware configuration of the system mainly consists of the selection of sensors, data acquisition instrument, and other ancillary equipment. The logical relationship configuration diagram of the system is shown in Figure 1. The system's hardware core is the United States NI company's CompactRIO embedded platform (including NI 9263, NI 9221, and NI 9234). By configuring different sensor platforms and associated ancillary equipment to achieve different application functions on the CompactRIO embedded platform.

The software design of the system is based on the LabVIEW graphical programming environment by choosing the United States NI LabVIEW 2010 development software, LabVIEW RT 2010 and LabVIEW FPGA 2010 toolkits, to develop the program code of modules. The main function modules have active monitoring module, passive monitoring module, and acceleration monitoring module. Among them, the active monitoring module mainly uses the active monitoring technique of piezoelectric ceramics for crack online monitoring of concrete structures, the passive monitoring module can be used in the dynamic impact load collection, and the acceleration monitoring module is applied to achieve structural vibration monitoring information collection.

3. System Hardware Realization

3.1. Sensor Configuration. Sensors of the system mainly include piezoelectric smart aggregates which can be sensors and actuators in the active monitoring module. Piezoelectric smart aggregates by calibration can be made into force sensors, which are used to collect pressure in the passive monitoring module. The acceleration module uses the built-in IC piezoelectric acceleration sensor of Lance.

The piezoelectric smart aggregate production principle, shown in Figure 2, mainly uses positive inverse piezoelectric

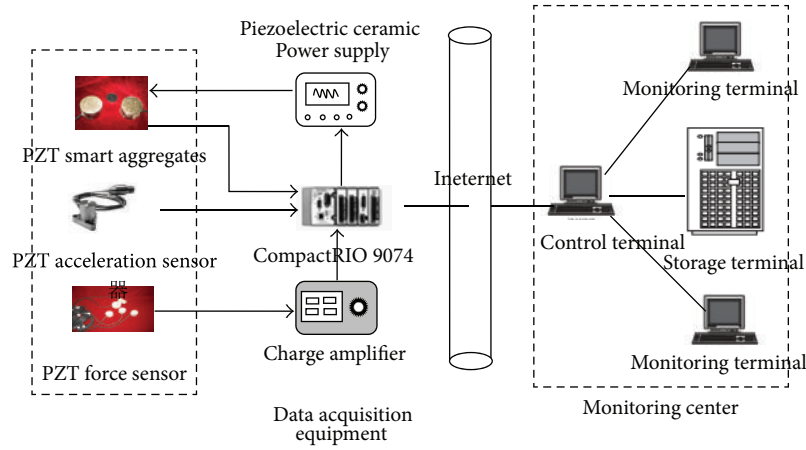


FIGURE 1: Logical relationship configuration diagram of the system.

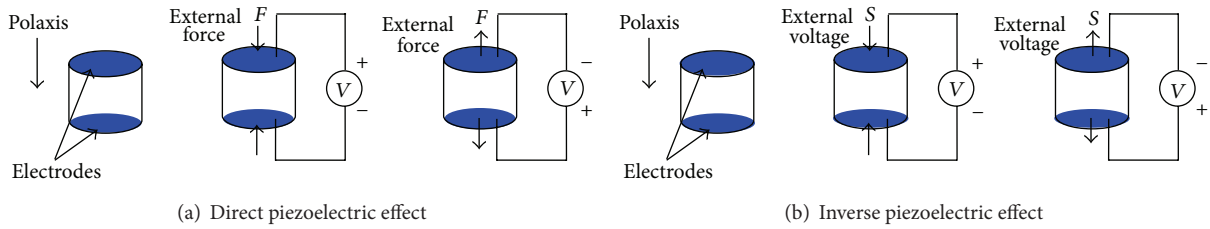


FIGURE 2: Piezoelectric effects.

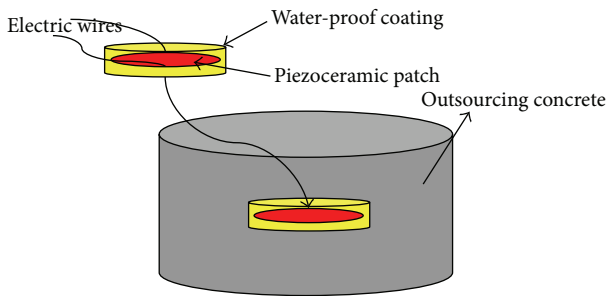


FIGURE 3: Illustration of a smart aggregate.



FIGURE 4: Two smart aggregates.

effect of the piezoelectric ceramic. When the piezoelectric ceramic is forced, the mechanical energy will transfer to electrical energy, and the use of the piezoelectric effect can be made into sensors. On the contrary, under the action of an electric field, the piezoelectric ceramic can also convert the electric energy into mechanical one, which is the inverse piezoelectric effect and can be used to make actuators.

Because of the frangible material of the piezoelectric ceramic such as lead zirconate titanate (PZT), it can be embedded into a small volume of concrete to make a smart aggregate encapsulated into a cylindrical shape after a certain processing method, shown in Figure 3, and a photo of the piezoelectric smart aggregate is shown in Figure 4. The developed piezoelectric smart aggregates can fasten to the

given places before casting concrete to establish a monitoring array for the SHM use.

The piezoelectric force sensor is based on the piezoelectric smart aggregate, shown in Figure 5. The PZT force sensor works as a capacitor, and the vertical surface will produce charges when it is applied by a force. According to the longitudinal piezoelectric effect, the amount of charges generated by the piezoelectric ceramic sheets will be proportional to the force; then the relationship of the force and the charge can be established, shown in

$$Q = d_{ij}F, \tag{1}$$



FIGURE 5: Piezoelectric force sensor.



FIGURE 6: LC0101 piezoelectric acceleration sensor.

where Q is electric charge (pC); F is force (N); d_{ij} is piezoelectric modulus (pC/N).

The piezoelectric acceleration sensor of LC0101 is selected, shown in Figure 6. Its main parameters include the sensitivity of 100 mV/g; the acceleration range of 50 g; frequency range of 0.5–15000 Hz ($\pm 10\%$).

3.2. Data Acquisition Devices. In order to meet the needs of SHM system, the NI CompactRIO 9074 embedded platform, the NI 9263 analog output card, and the NI 9221 and NI 9234 analog signal input cards are selected for the system.

The CompactRIO embedded platform, which integrates the embedded real-time controller, programmable hardware logic (FPGA), and reconfigured I/O module, was developed by American National Instrument Company (NI) for the test and measurements. The I/O module of the CompactRIO embedded platform can finish the input, output, and control for all kinds of digital/analog signals (such as voltage, current, and resistance), and the researcher can hot-swap, plug, and play to meet the different needs of engineering applications. The NI 9221 and NI 9263 modules are chosen as the active and passive monitoring modules for the system, and the NI 9234 is used for the acceleration acquisition module. Composition diagram of the data acquisition equipment and its main technical parameters are shown in Figure 7.

3.3. Other Ancillary Equipment. The system according to the needs of different monitoring module is also equipped with a number of auxiliary equipments, mainly used for signal amplification, A/D conversion, and conditioning, which mainly include the driving power for piezoelectric ceramics, charge amplifier, signal conditioning, and UPS power.

The main function of the piezoelectric ceramic power is using it as the power amplifier of piezoelectric ceramic driver to generate signals in the active monitoring module, and the charge amplifier is mainly applied for the pressure acquisition in the passive monitoring module. Because the piezoelectric force sensor can receive the charge signal and the signal acquisition card is suitable for the voltage signal and the sensor output signal is very weak, the transformation of the signal amplification and charge voltage realized by a charge amplifier is required. Due to the built-in IC piezoelectric acceleration sensor works need motivation, so the signal conditioner should be configured. Considering the fact of

no power in the actual monitoring field, the system is also equipped with a number of independent UPS power supplies.

4. System Software Design

The system modular design is applied for the software part of the system, and the main advantage is convenient for expanding the function of the system according to actual needs. According to the different functions of each module, the system is divided into the active monitoring module, the passive monitoring module, and the acceleration monitoring module. The active monitoring module can realize the signal transmission, acquisition, the crack damage identification, and sound and light warning. The passive monitoring module can complete the real-time acquisition of dynamic responses of the structure and a series of data processing. The acceleration acquisition module can accomplish the real-time acquisition and filtering of data and the spectrum analysis of the acceleration signal.

4.1. Active Monitoring Module. The active monitoring module mainly monitors cracks of the concrete structure, based on the wave-based method of the active monitoring technology. The basic principle is that piezoelectric smart aggregates, which are used as transducers, are embedded in the given places of the concrete structure. The actuator emits signal and the sensor receives signal, resulting in establishing an actuator-sensor scanning channel. Based on the analysis of changes in the signal and the extraction of the damage factor, the on-line system for monitoring crack damages of concrete structures can be realized. The hardware of the module mainly includes piezoelectric smart aggregates, piezoelectric ceramic drive power, the CompactRIO platform, the NI 9263, the NI 9221 card, and computer. The diagram is shown in Figure 8.

According to the results of research by our group [24], in the concrete structure, the amplitude of the signal analysis is sensitive to the crack damage, and with the injury increases, the more severe attenuation of the amplitude. So we selected the signal amplitude as the damage characteristic parameter, and through the further quantification of the characteristic parameter, referred to as the energy value. The energy value is the amplitude of the signal after discretization and the

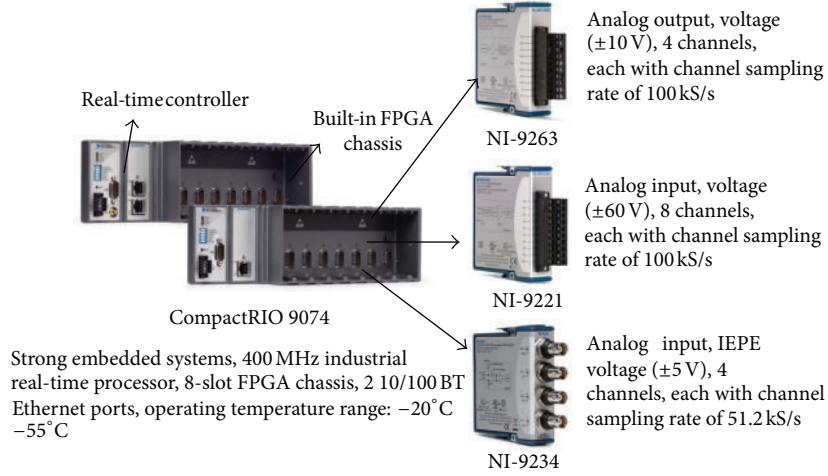


FIGURE 7: Architecture of CompactRIO embedded system.

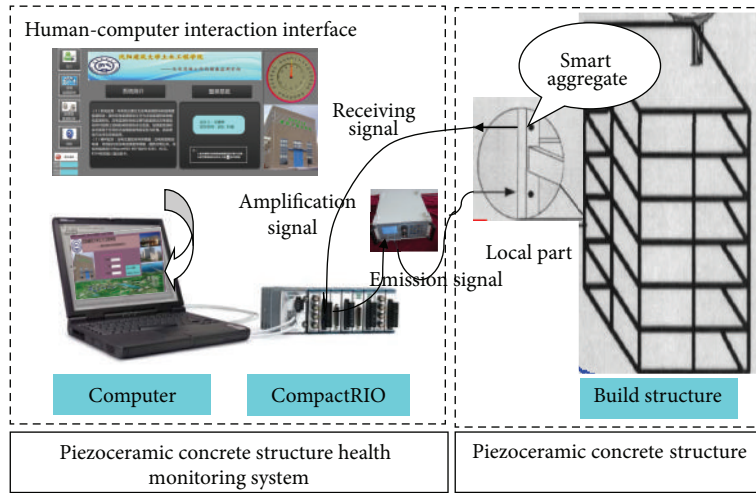


FIGURE 8: Physical structure diagram of the active monitoring module.

absolute value of the square integral. For E_i as a moment, the energy value is as follows:

$$E_i = \sum_{i=m} |x_i|^2 = x_1^2 + x_2^2 + \dots + x_m^2, \quad (2)$$

where x_i is the single point discrete signal which is collected by the sensors.

If E_h is the health state of the energy value, then the relative health of the structure can be expressed as

$$H_i = \frac{E_i}{E_h} = \frac{\sum_{n=0}^{\infty} |x_i(n)|^2}{\sum_{n=0}^{\infty} |x_h(n)|^2} \times 100\%, \quad (3)$$

where $x_h(n)$ and $x_i(n)$ are discrete signal in health state and damage state which are collected by the sensor.

It is not difficult to see that, when the structure is in a healthy condition, $H_i = 1$, and when the structure is

completely failure, $H_i = 0$. In the actual health monitoring, the index is higher when the structural damage is more serious, so this paper puts the DI value as damage index. Consider the following:

$$\text{DI} = 1 - H_i = 1 - \frac{E_i}{E_h} = 1 - \frac{\sum_{n=0}^{\infty} |x_i(n)|^2}{\sum_{n=0}^{\infty} |x_h(n)|^2} \times 100\%. \quad (4)$$

The software of the active monitoring module can realize the signal transmission and acquisition, signal processing and analysis, damage identification, warning, and data storage. The man-machine interface is shown in Figure 9. The workflow of the software is, first of all, for the module to provide the sweep wave and sine wave pulse signal according to the actual need. Then, the NI 9263 emits a signal and the NI 9221 receives the signal by the program control of CompactRIO embedded platform. Next, after the real-time acquisition original signal is filtered and denoised, the signal can be

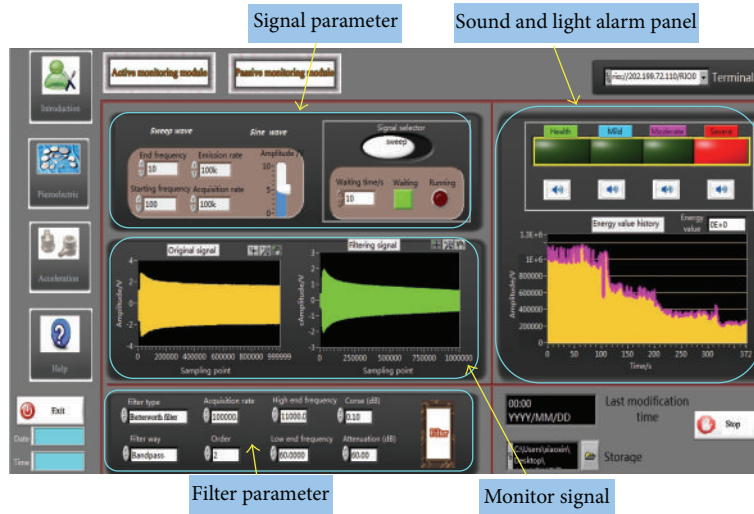


FIGURE 9: The human-machine interface of active monitoring module.

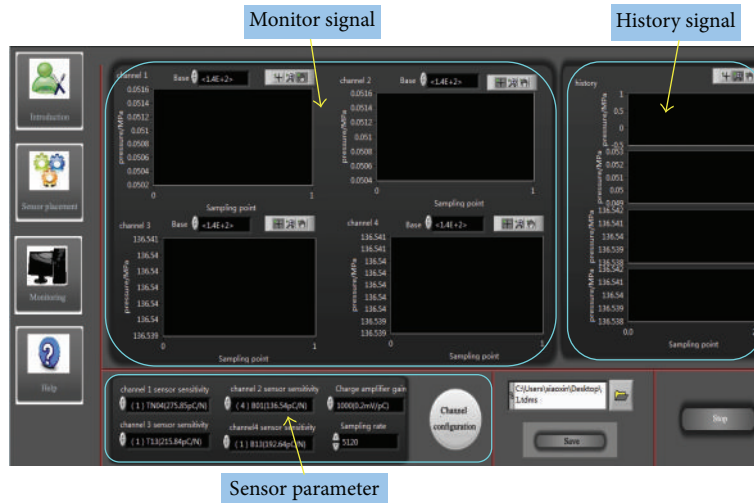


FIGURE 10: The human-machine interface of passive monitoring module.

processed for the damage identification. The determination of the structural crack damage can be made based on the energy attenuation identification algorithm. The energy value obtained from the response time historical curve is used to characterize the structural health state from a macrostandpoint. Finally, the system will automatically compare the damage index with the corresponding threshold and achieve sound and light warning on the status of the structure.

4.2. Passive Monitoring Module. The passive monitoring module is developed based on the active monitoring module. When the passive monitoring of structures is needed, the system signal source is closed, and the piezoelectric smart aggregates are used as sensors to achieve the related physical quantity acquisition. Compared to the active monitoring module, the passive monitoring module in terms of equipment or software is relatively and greatly simplified. Due to having no excitation source, the passive monitoring module is mainly composed of sensors and the data acquisition system.

In practical engineering, data acquisition systems often collect voltage signals. In general, the charge signals from sensors need to be transformed into voltage signals. To establish the correspondence between voltage and pressure, the data acquisition system often needs to be equipped with a charge amplifier.

The passive monitoring module in the system can realize the synchronous acquisition and online processing of four channel data. The software interface is shown in Figure 10.

4.3. Acceleration Monitoring Module. The acceleration monitoring module utilizes piezoelectric acceleration sensors to measure the dynamic acceleration response signal of the structures during an earthquake or wind loads [28, 29]. The system mainly includes acceleration sensors, signal conditioning, data acquisition platform (CompactRIO embedded platform and NI 9234 module), and PC control module. The workflow is that, first of all, the sensors need to be arranged in the structure according to the measurement

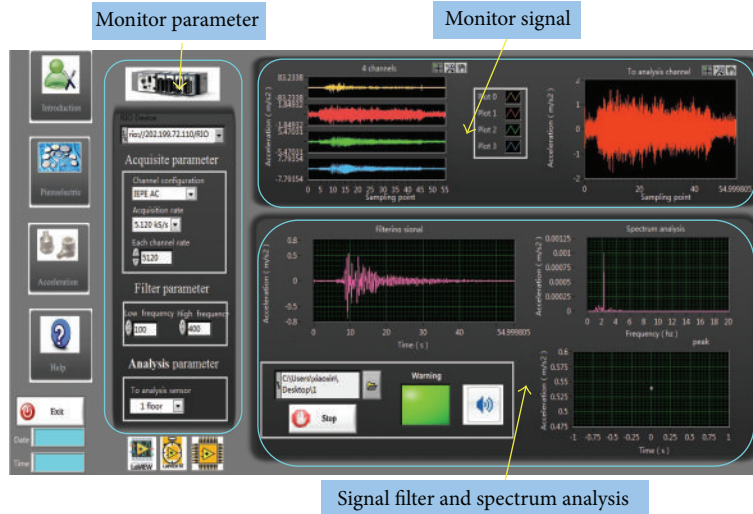


FIGURE 11: The human-machine interface of acceleration monitoring module.

requirement. The sensors can put into normal work by conditioning supply power, and the sensor signal is transformed into a voltage signal, transmitting into the data acquisition module. The PC control module controls the data acquisition platform for collection and processing as well as analysis of data.

The module interface is shown in Figure 11. The developed software can realize four channel data, acquisition, filtering, spectrum analysis, data storage, and other functions. It can monitor the peak of signals to achieve sound and light warning when the acceleration exceeds the given threshold.

5. Test Validation and Application of the System

Because the development of the system is a process, according to different needs, the several modules are developed individually. In the later use of software integration for each module of the system, the testing and engineering application of each module introduced below will be separated.

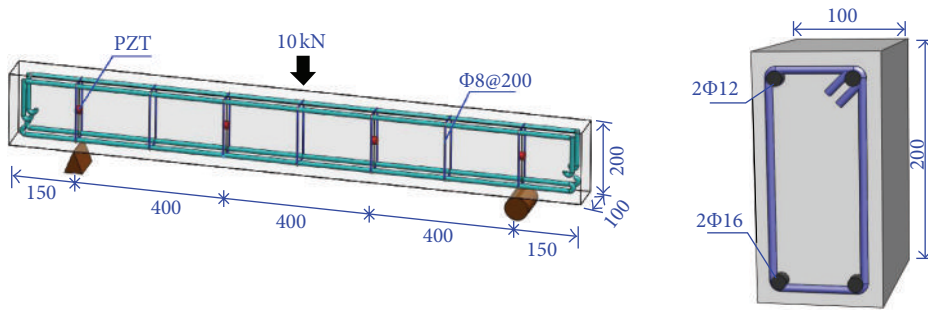
5.1. Experimental Verification of the Active Monitoring Module. In the whole function test of the module, a reinforced concrete beam element as the monitoring object is selected, shown in Figure 12(a). The size of the model is $1500 \times 100 \times 200$ mm, approximately the ratio of 1:3. Piezoelectric smart aggregates are embedded in the beam before casting concrete. One smart aggregate is placed at the position of 150 mm from the end and the other from the other end. The distance between the two transducers is 1200 mm. The process of crack damages is simulated through loading. The loading device of hydraulic jacks can provide 10 kN load. The active monitoring module test site is shown in Figure 12(b).

The test adopts a gradual loading plan, and the states of the tested concrete structure are divided into the health state (no cracks), slight damage (initial crack), moderate damage (cracks significantly increased), and severe damage (structural failure). Each damage state is shown in Figure 13.

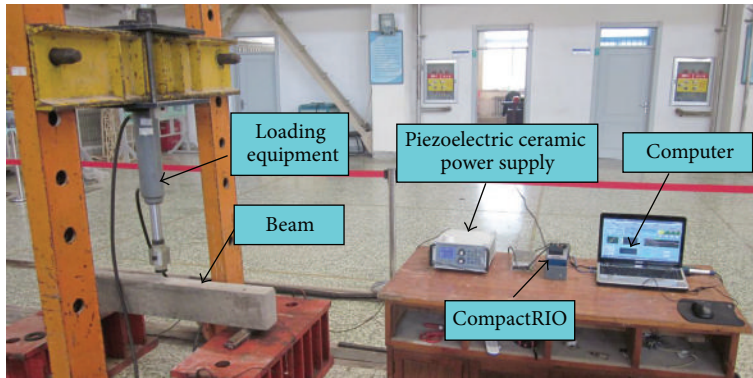
The developed system is used in the experiment for real-time online monitoring. The signal transmission and data acquisition are performed for every time interval of 10 s. To eliminate noise interference caused by external factors such as local data instability, the test for each state continuously scans 100 times. The damage index of each state is shown in Figure 14. The state of the damage index is at a different level, showing that the structure damage is in different states. The damage index is growing with the increase of the degree of damage. Meanwhile, the warning module can achieve a sound and light warning for different damage states. The results show that the system can efficiently monitor and identify the process of concrete crack damage and it achieves the design goal.

5.2. Engineering Application of the Passive Monitoring Module. A new kind of steel bolt RC foundations for rock soil is used for the wind drive generators constructed in 2012 in Guodian Tieling wind farms which are located at the Development Zone of Tieling city, China. In order to study the interaction of new rock bolts and concrete foundation which influences the force performance of wind turbine foundation, the passive monitoring module is developed on the basis of established system, through which you can understand the real-time status of the internal stress distribution, and the work also can put forward the reasonable proposals for design and construction.

In view of the load of wind turbine foundation composed by the static and dynamic loads, the project will use the piezoelectric sensors to obtain the dynamic stress inside the foundation, through a combination of theoretical calculations that show the actual internal stress of foundation. The structural health monitoring system is established by placing the developed smart aggregates in the foundation. The sensors are distributed at the horizontal direction along the circumferential uniform layout, divided into inside and outside layers, and relatively closely placed at the main wind direction, and the vertical direction is divided into two layers.



(a) Beam size and sensors arrangement



(b) Test field

FIGURE 12: The active monitoring module test.



(a) Health status



(b) Mild damage



(c) Moderate damage



(d) Severe damage

FIGURE 13: The different damage states of the components.

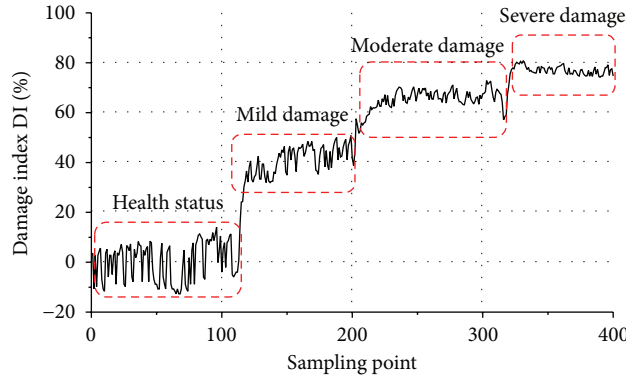
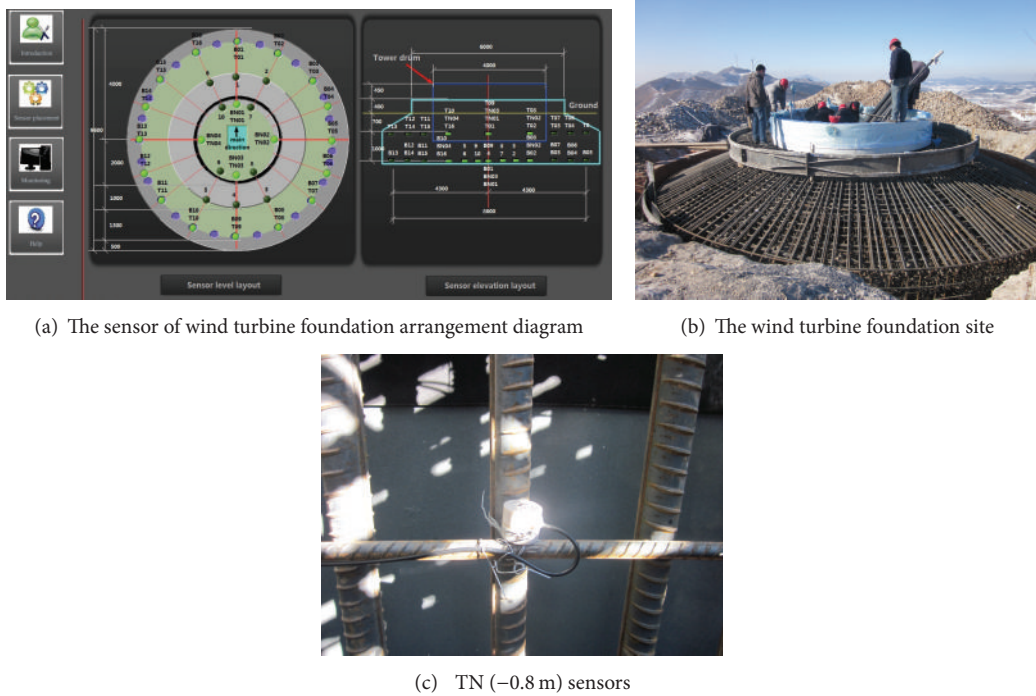


FIGURE 14: Monitoring data in four different conditions.



(a) The sensor of wind turbine foundation arrangement diagram

(b) The wind turbine foundation site

(c) TN (-0.8 m) sensors

FIGURE 15: Layout of sensors in field.

Each sensor is numbered, and B, T, BN, and TN denote the bottom, the upper, the bottom inner ring, and the upper inner ring, respectively. The layout of sensors in site of the project is shown in Figure 15.

Sensors were arranged in the wind turbine foundation before pouring the concrete. In May 9, 2012, the first field testing of the wind turbine foundation is completed, and fans condition is shutdown. In order to facilitate inspection and checking of the results, the stress of different locations on-site monitoring was extracted from sensors, to compare with the numerical simulation results.

The comparison between calculated and monitored values is shown in Figure 16 [30]. The monitoring results show that the stress of different positions inside the wind turbine foundation has the consistent change with numerical

simulation. However, due to the difference of the actual load with respect to the numerical calculation, there are some differences between the two values. For this project, under the action of moment generated in the wind loading, the leeward side of wind turbine foundation is mostly in the state of compression and the windward side of ring outside and the anchor position are in tension. It can be concluded that the system is running well and work in a stable way.

5.3. The Experimental Validation for Acceleration Monitoring Module. In order to test the reliability of the acceleration monitoring module, a three-layer steel frame model is used in the paper as an experimental monitoring object. The model height is 500 mm, and the slab thickness is 5 mm. The beams and columns adopt the round steel tube whose outer diameter

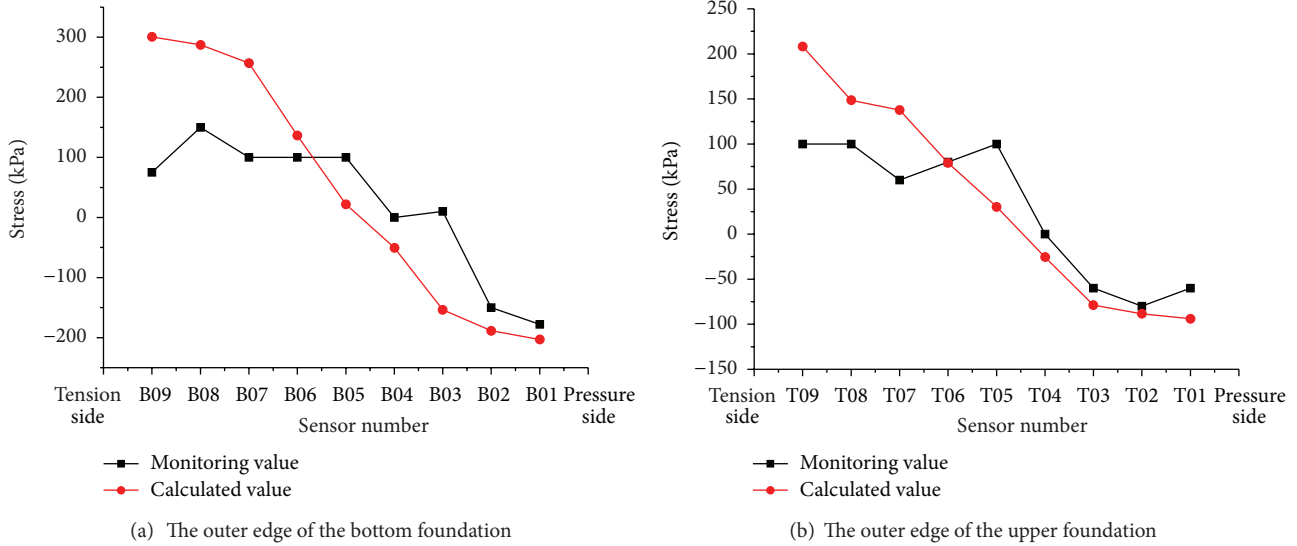


FIGURE 16: Measured stress and calculation analysis of stress.

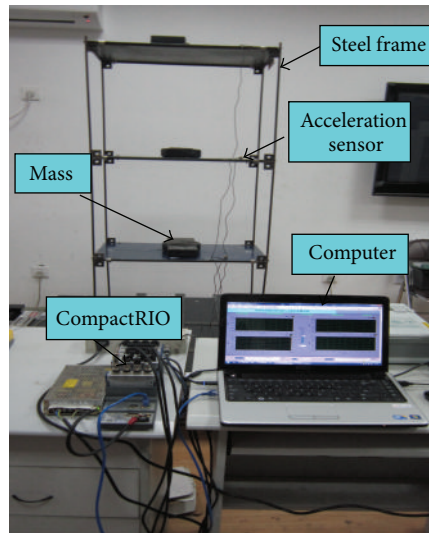


FIGURE 17: Field test equipment.

is 8 mm, and the inner diameter is 4 mm. The overall size of the model is 500 mm × 400 mm × 400 mm, and the 10 kg mass is placed on each floor.

In order to simulate the real acceleration response of the structure under earthquake, a shaking table test is chosen and performed in Structural Engineering Laboratory of Shenyang Jianzhu University, China. The Shake Table II - 240 produced by Canada QUANSER company is used. Four acceleration sensors are placed at each layer; the sampling frequency of 5.12 kS/s is selected. At the same time, the traditional acquisition equipment is chosen to synchronously collect the same parts of the acceleration signal, which is used for the comparison of test data and verification of the accuracy of the data. Field test equipment of the system is shown in Figure 17.

The Northridge wave record whose maximum acceleration is 0.1 g is used as excitation seismic waves of vibrating

table during the test selects. The acceleration signal of the first layer of the frame structure is selected as an example for analysis. In Figure 18(a), the time-history curve of the original acceleration signal of the frame structure at the first layer collected by the system is shown. Due to the interference of noises in the testing site, the collected signals by the sensor cannot completely represent the structure vibration characteristics. Therefore, the original signals need to be performed for noise filtering. By analyzing the frequency spectrum of the signal, the acceleration signal spectrum curve of the structure at the first layer can be obtained, shown in Figure 18(b), showing that the fundamental frequency of the structure is 2.2 Hz. Therefore, this system chooses the Butterworth band-pass filter, and the filtered signal frequency is greater than 5 Hz and less than 1 Hz. Finally, the acceleration signal at the first layer after filtering is shown in

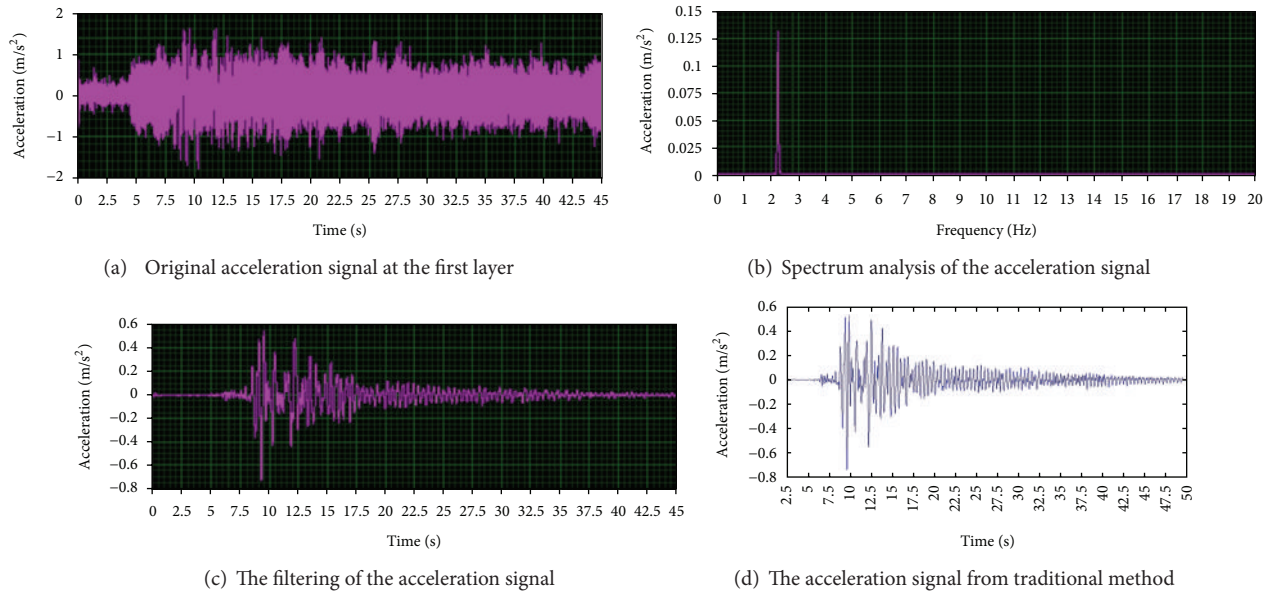


FIGURE 18: Comparison and analysis of acceleration signal at the first floor.

Figure 18(c). In Figure 18(d) the acceleration signal at the first layer after filtering is shown, which is synchronously collected by dynamic signal analyzer TST5912. From the comparative analysis between Figures 18(c) and 18(d), it can be seen that the time-history curve of vibration signal collected by this system is nearly the same as the acceleration time-history curve collected by traditional instruments, the maximum acceleration of both is 0.74 m/s^2 . Therefore, we can conclude that this system can effectively collect structure vibration signal and its data is accurate and reliable.

6. Conclusions

The advantage of virtual instrument technology is taken in the paper to develop a concrete structural health monitoring system which is based on piezoelectric sensors. Through the test and engineering application, it shows that the system can not only realize the damage identification and sound-light alarm but also can achieve the online monitoring of acceleration, stress state, and other physical quantities. Using the graphical programming software LabVIEW to develop the structural health monitoring system, it has a good human-computer interaction interface and short development time. It is suitable for nonprofessional engineer to complete project development. At the same time, CompactRIO embedded platform with a compact and rugged feature, which is very suitable for complex and bad environments of construction site. It achieves the leap from stationary health monitoring system to the portable the health monitoring system. The work provides a good technical support to solve practical problems and has a good foundation for piezoelectric health monitoring technology from the laboratory research to the engineering application.

Acknowledgments

This work was financially supported in part by the National Natural Science Foundation of China (51278313), the Natural Science Foundation of Liaoning Province (201202180), the Science Foundation of Liaoning Education Department (L2012214), Key Laboratory Foundation of Liaoning Province (JG2009-18), and Liaoning Electric Power Survey & Design Institute Foundation.

References

- [1] G. W. Housner, L. A. Bergman, T. K. Caughey et al., "Structural control: past, present, and future," *Journal of Engineering Mechanics*, vol. 123, no. 9, pp. 897–971, 1997.
- [2] Y. S. Roh and F. K. Chang, *Built in diagnostics for identifying an anomaly in plates using wave scattering [Ph.D. thesis]*, University of Stanford, 1999.
- [3] C. S. Wang and F. K. Chang, "Built-in diagnostics for impact damage identification of composite structures," in *Proceedings of the 3rd International Workshop on Structural Health Monitoring*, pp. 612–621, Stanford, Calif, USA, 1999.
- [4] G. Kawiecki, "Feasibility of applying distributed piezotransducers to structural damage detection," *Journal of Intelligent Material Systems and Structures*, vol. 9, no. 3, pp. 189–197, 1998.
- [5] C. S. Wang, F. Wu, and F. K. Chang, "Structural health monitoring from fiber-reinforced composites to steel-reinforced concrete," *Smart Materials and Structures*, vol. 10, no. 3, pp. 548–552, 2001.
- [6] M. M. Saafi and T. Sayyah, "Health monitoring of concrete structures strengthened with advanced composite materials using piezoelectric transducers," *Composites B*, vol. 32, no. 4, pp. 333–342, 2001.

- [7] M. Q. Sun, W. J. Staszewski, R. N. Swamy, and Z. Q. Li, "Surface wave method in piezoceramic patches/concrete smart structure," *Journal of Building Materials*, vol. 7, no. 2, pp. 145–149, 2004.
- [8] J. Sirohi and I. Chopra, "Fundamental understanding of piezoelectric strain sensors," *Journal of Intelligent Material Systems and Structures*, vol. 11, no. 4, pp. 246–257, 2000.
- [9] S. Yan and W. Sun, "Erical simulation for concrete structural health monitoring based on smart piezoelectric transducer array," *Advances in Science and Technology*, vol. 56, pp. 469–476, 2008.
- [10] S. Yan, W. Sun, G. Song et al., "Health monitoring of reinforced concrete shear walls using smart aggregates," *Smart Materials and Structures*, vol. 18, no. 4, Article ID 047001, 2009.
- [11] G. B. Song, Y. L. Mo, K. Otero, and H. Gu, "Health monitoring and rehabilitation of a concrete structure using intelligent materials," *Smart Materials and Structures*, vol. 15, no. 2, pp. 309–314, 2006.
- [12] G. Song, H. Gu, Y. L. Mo, T. T. C. Hsu, and H. Dhonde, "Concrete structural health monitoring using embedded piezoceramic transducers," *Smart Materials and Structures*, vol. 16, no. 4, pp. 959–968, 2007.
- [13] G. Song, H. C. Gu, and Y. L. Mo, "Smart aggregates: multi-functional sensors for concrete structures—a tutorial and a review," *Smart Materials and Structures*, vol. 17, no. 3, Article ID 033001, 2008.
- [14] A. Laskar, H. Gu, Y. L. Mo, and G. Song, "Progressive collapse of a two-story reinforced concrete frame with embedded smart aggregates," *Smart Materials and Structures*, vol. 18, no. 7, Article ID 075001, 2009.
- [15] H. Gu, Y. Moslehy, D. Sanders, G. Song, and Y. L. Mo, "Multi-functional smart aggregate-based structural health monitoring of circular reinforced concrete columns subjected to seismic excitations," *Smart Materials and Structures*, vol. 19, no. 6, Article ID 065026, 2010.
- [16] W. I. Liao, J. X. Wang, G. Song et al., "Structural health monitoring of concrete columns subjected to seismic excitations using piezoceramic-based sensors," *Smart Materials and Structures*, vol. 20, no. 1, Article ID 125015, 2011.
- [17] F. P. Sun, Z. Chaudhry, C. Liang, and C. A. Rogers, "Truss structure integrity identification using PZT sensor-actuator," *Journal of Intelligent Material Systems and Structures*, vol. 6, no. 1, pp. 134–139, 1995.
- [18] C. K. Soh, K. K. Tseng, S. Bhalla, and A. Gupta, "Performance of smart piezoceramic patches in health monitoring of a RC bridge," *Smart Materials and Structures*, vol. 9, no. 4, pp. 533–542, 2000.
- [19] S. Bhalla and C. K. Soh, "Structural impedance based damage diagnosis by piezo-transducers," *Earthquake Engineering and Structural Dynamics*, vol. 32, no. 12, pp. 1897–1916, 2003.
- [20] D. S. Wang, *Structural damage detection based on the anti-resonant frequency and piezoelectric impedance [Ph.D. thesis]*, University of Science & Technology, 2006.
- [21] J. T. Kim, K. D. Nguyen, and T. C. Huynh, "Wireless health monitoring of stay cable using piezoelectric strain response and smart skin technique," *Smart Structures and Systems*, vol. 12, no. 3-4, pp. 381–397, 2013.
- [22] X. M. Yang, *Research on performance monitoring system and damage identification method for civil engineering structures [Ph.D. thesis]*, University of Tianjin, 2006.
- [23] G. B. Song, C. Olmi, and H. Gu, "An overheight vehicle-bridge collision monitoring system using piezoelectric transducers," *Smart Materials and Structures*, vol. 16, no. 2, pp. 462–468, 2007.
- [24] Y. Y. Meng, S. Yan, and W. Sun, "Experimental research on active health monitoring of PZT concrete beam," *Journal of Shenyang Jianzhu University (Natural Science)*, vol. 27, no. 2, pp. 253–259, 2011.
- [25] W. Sun, *Health monitoring technology for smart concrete structures using piezoelectric ceramic [Ph.D. thesis]*, Dalian University of Technology, 2009.
- [26] L. Qiu and S. F. Yuan, "Research and application of integrated health monitoring scanning system based on PZT sensor array," *Piezoelectrics and Acoustooptics*, vol. 30, no. 1, pp. 39–41, 2008.
- [27] D. D. Ho, K. D. Nguyen, H. S. Yoon, and J. T. Kim, "Multiscale acceleration-dynamic strain-impedance sensor system for structural health monitoring," *International Journal of Distributed Sensor Networks*, vol. 2012, Article ID 709208, 17 pages, 2012.
- [28] J. T. Kim, J. Park, D. Hong, H. Cho, W. Na, and J. Yi, "Vibration and impedance monitoring for prestress-loss prediction in PSC girder bridges," *Smart Structures and Systems*, vol. 5, no. 1, pp. 81–94, 2009.
- [29] J. H. Park, J. Kim, D. Hong, D. Mascarenas, and J. Peter Lynch, "Autonomous smart sensor nodes for global and local damage detection of prestressed concrete bridges based on accelerations and impedance measurements," *Smart Structures and Systems*, vol. 6, no. 5-6, pp. 711–730, 2010.
- [30] H. Yan, J. X. Wu et al., "Concrete stress monitoring and numerical analysis on new type rock bolt foundation of wind turbine generator," *Concrete*, no. 5, pp. 9–12, 2013.

Research Article

Feasibility Study of Stress Measurement in Prestressing Tendons Using Villari Effect and Induced Magnetic Field

Changbin Joh, Jung Woo Lee, and Imjong Kwahk

Korea Institute of Construction Technology, Goyang, Gyeonggi 411-712, Republic of Korea

Correspondence should be addressed to Changbin Joh; cjoh@kict.re.kr

Received 20 August 2013; Accepted 16 October 2013

Academic Editor: Jeong-Tae Kim

Copyright © 2013 Changbin Joh et al. This is an open access article distributed under the Creative Commons Attribution License, which permits unrestricted use, distribution, and reproduction in any medium, provided the original work is properly cited.

This paper investigates experimentally the feasibility of estimating the stress in the prestressing tendons of prestressed concrete bridges using the magnetic field induced by an electromagnet and the Villari effect in which the magnetic susceptibility or permeability of a ferromagnetic material changes when subjected to a mechanical stress. The test results show the good linearity between the stress in the prestressing tendon and the induced magnetic flux density within the practical stress range of the tendons. In addition, the induced magnetic flux density in the tendon appears to depend on the intensity of the electromagnet and the distance between the electromagnet and the tendon regardless of the concrete cover. Accordingly, although further studies are needed for practical applications, the stress in the prestressing tendon of a prestressed concrete bridge can be estimated by measuring the induced magnetic flux density generated in the tendon and by using the linear relationship between this induced magnetic flux density and the stress in the prestressing tendon.

1. Introduction

Prestressed concrete bridges started to be erected effectively worldwide in the 1980s to achieve bridges with spans longer than concrete bridges. The prestressed concrete bridge is a structure in which the deflection or the cracks are reduced by introducing prestress forces through the use of prestressing tendons. Owing to such structural characteristics, the prestress force introduced by means of the tendons has significant effect on the performance of the prestressed concrete bridge. The prestress force of the prestressing tendons experiences changes immediately after its introduction due to not only the loss of prestress but also due to other various reasons during the lifespan of the structure like creep, drying shrinkage, relaxation, and corrosion, which should be managed appropriately through evaluation all along the service life [1]. Failing in the management of the prestress force will result in the increase of the deflection or cracks according to the loss of prestress and lead to severe degradation of the performance or, in worst case, to the collapse of the prestressed concrete bridge [2]. In view of this necessity, diversified nondestructive test (NDT) methods have been

studied to estimate the prestress force of the prestressing tendons during the lifespan of prestressed concrete bridges but without successful application on site. In particular, there is practically no example in which economically efficient estimation of the prestress force has been realized for the bonded prestressing tendons applied in existing prestressed concrete bridges.

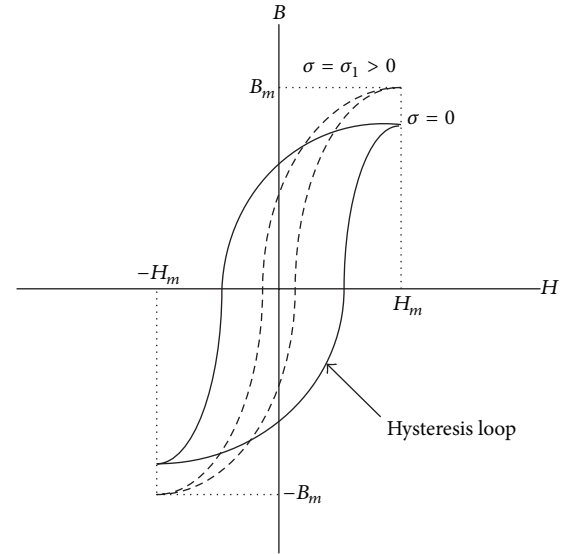
Research for the estimation of the prestress force in the bonded prestressing tendons applied in existing prestressed concrete bridges can be subdivided into those using system identification (SID), those using guided ultrasonic waves, and those using stress waves. The SID method monitors the change in modal properties in relation to the change in prestress forces. Kim et al. [3] and Ho et al. [4] developed a multiphase SID scheme to detect the occurrence of prestress loss systematically. Kim et al. [5] proposed the vibration and impedance monitoring method to improve the detection of occurrence and location of prestress loss. In general, the SID method has a strong point for overall structural health monitoring but has still limits to estimate the prestress forces locally and directly.

The guided ultrasonic wave method is a NDT method using the vibrational characteristics or propagation velocity characteristics of the ultrasonic wave varying with the stress of the prestressing tendon [6, 7]. This method is widely adopted for the inspection of the cracks or corrosion of pipelines but presents limitations when applied on bonded prestressing tendons. This means that the guided ultrasonic wave experiences loss when penetrating concrete, which makes it difficult to measure the guided wave at distance of merely 1.5 m from the anchorage of the prestressed concrete bridge [6]. Recently, Salamone et al. [7] found out experimentally that the vibrational frequency ratio of the prestressing tendon is proportional to the stress rather than the wave propagation velocity, but this result could not be considered as having solved the loss of the guided wave due to grouting since the experiences were conducted only on specimens shorter than 1.5 m. Considering that most of the prestressed concrete bridges in Korea are longer than 40 m and were erected with bonded prestressing tendons, need is for further research to exploit the guided ultrasonic wave method for the estimation of the stress in prestressing tendons.

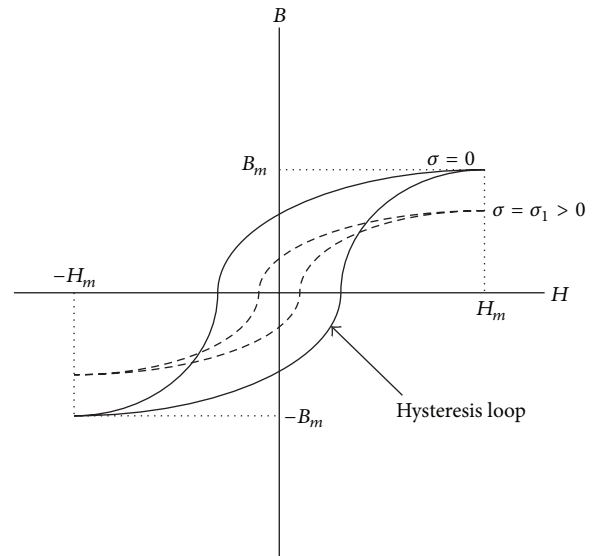
Kim et al. [8] estimated the stress in prestressing tendons using the increase of the velocity of the longitudinal stress wave along the tendon according to the prestress force. Differently to the guided wave method, this method enables to measure the stress wave at any position even in bonded prestressing tendons longer than 40 m. However, the sensitivity of the stress to the velocity of the stress wave shows significant degradation at stress level larger than 40% of the yield stress of the tendon. Jang et al. [9] applied successfully this method to estimate the residual stress of the bonded prestressing tendons in the containment structure of nuclear power plants, but this method also necessitates additional improvement to measure accurately the stress in the tendon accounting that the stress in the tendon reaches 50 to 60% of the yield stress under the service load of the prestressed concrete bridge.

The method using the magnetic field can be envisaged for overcoming the disadvantages encountered in the methods using SID, ultrasonic wave, or stress wave. This method uses an external magnetic field to generate an induced magnetic field in the prestressing tendon adopted as magnetic body and applies the Villari effect. The Villari effect, also known as the inverse magnetostriction, was discovered in 1865 by Villari and describes the phenomenon by which the magnetic characteristics like the permeability, μ , of the magnetic body changes according to its stress [10]. Conceptually, the method forms a closed magnetic circuit including the prestressing tendon of the prestressed concrete bridge by means of an external electromagnet and exploits the change in the magnetic flux density, B , of the induced magnetic field flowing in the prestressing tendon according to the stress.

This paper derives a method measuring the prestress force of bonded prestressing tendons in prestressed concrete bridge using the Villari effect and the induced magnetic field generated by an electromagnet. The feasibility of the method is verified experimentally through scaled models.



(a) Positive magnetostriction



(b) Negative magnetostriction

FIGURE 1: B - H hysteresis loop and concept of Villari effect.

2. Estimation of the Stress of Prestressing Tendon Using the Villari Effect and Induced Magnetic Field

The relation between the intensity, H , of the magnetic field and the magnetic flux density, B , can be defined by the magnetic permeability, μ , as expressed in the following:

$$B = \mu H. \quad (1)$$

In the physics of magnetic material, the Villari effect, also known as the inverse magnetostrictive effect, is the name given to the change of the magnetic permeability, μ , of a magnetic material when subjected to a mechanical stress [11]. Figure 1 describes conceptually the Villari effect. This is due to the rearrangement of the magnetic domains within

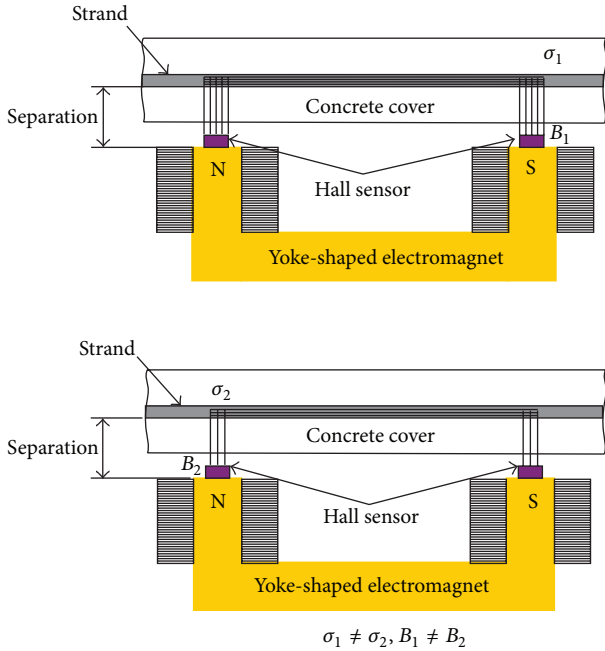


FIGURE 2: Illustration of induced magnetic fields in tendons of different stresses.

the structure of the material. The Villari effect can be either positive or negative depending on the specific material and the intensity of magnetic field (H).

This phenomenon is very effective in amorphous alloys and exhibits outstanding thermal characteristics and durability, which boosted research dedicated to strain gages and torsion gages using such properties [12]. As a typical example, Baudendistel and Turner [13] investigated the change in the permeability, μ , with respect to the stress and temperature of a Fe-Ni alloy and used it to propose an innovative strain gage concept.

As shown in Figure 2, an induced magnetic field is generated in the magnetic body that is the prestressing tendon when a yoke-shaped electromagnet is disposed below the prestressed concrete structure including the prestressing tendon. This layout forms a magnetic circuit in which a magnetic flux, Φ , flows through the electromagnet and the prestressing tendon. The magnetic flux density, B , representing the size of this induced magnetic field in the prestressing tendon depends on the permeability, μ , and the cross-sectional area of the magnetized prestressing tendon and the continuity of the magnetic circuit (closed magnetic circuit). The magnetic flux density, B , crossing the prestressing tendon is measured by a Hall sensor installed on the pole face. The accurate measurement necessitates near magnetic saturation of the prestressing tendon. The continuity of the magnetic circuit depends on the separation between the prestressing tendon and the pole face. Since larger separation results in larger loss of the magnetic flux forming the closed magnetic circuit, a relatively strong electromagnet is required to magnetize the prestressing tendon. In addition, according to Bozorth [14], the intensity of magnetic field (H) changes the sign of

magnetostriction of ferromagnetic material and, accordingly, the sign of variation of permeability under stress. So, this effect should be considered for a prestressing tendon, one of ferromagnetic materials. Considering that concrete is a non-magnetic material, concrete does not disperse the magnetic flux flowing in the prestressing tendon and the concrete cover has practically no effect. Fernandes et al. [15, 16] exploited the fact that the magnetic flux density of the magnetic field is influenced by the cross sectional area of the prestressing tendon to measure the degree of corrosion of the tendon in a prestressed concrete structure.

Therefore, since the permeability, μ , of the prestressing tendon subjected to stress varies according to the stress when the tendon is magnetized by means of a permanent magnet or an electromagnet with a magnetic field intensity, H , the density, B , of the magnetic flux flowing in the tendon will vary with respect to the stress owing to the Villari effect. Even if the cross sectional area of the tendon decreases under larger stress due to the Poisson's effect, this effect can be assumed to be relatively insignificant. Consequently, the measurement of the magnetic flux density, B , flowing in the tendon will enable to estimate the stress of the tendon by comparison with the stress of the tendon that has been preliminary measured and the magnetic hysteresis loop $B-H$. To that goal, need is to collect a database by measuring in advance the $B-H$ hysteresis loop according to the stress of the prestressing tendon used in the prestressed concrete structure. In this process, the effects of the intensity of an electromagnet, the concrete cover, the separation, and temperature must be considered.

3. Model Test for the Proposed Method

3.1. Summary of Test. The feasibility of the method measuring the stress of the prestressing tendon by means of the Villari effect and the induced magnetic field is examined experimentally by measuring the relation between the stress of the tendon and the induced magnetic flux density.

Figure 3 illustrates the concept underlying the test. A loading device and a frame are prepared so as to vary the stress of the tendon during the test, and an electromagnet is disposed at a position below the tendon to secure definite separation. Two Hall sensors are installed on the face poles of the electromagnet to measure the magnetic flux density, B .

The loading frame for the prestress of the tendon was fabricated using 100×100 mm H-beam (Figure 4). Loading was applied by means of a hydraulic nut (Figure 5). The introduced prestress force was measured using a center holed load cell with capacity of 50 ton disposed between the loading frame and the hydraulic nut (Figure 5). The temperature of the tendon during the test was measured by a thermosensor attached to the tendon and the ambient temperature by a digital thermometer.

The electromagnet used to induce the magnetic field in the tendon was fabricated to provide a maximum magnetic induction of 4000 Gauss at the pole face (Figure 6). Two Hall sensors (model WSH135 of Winson) are attached at the centers of N-pole and S-pole for measuring the magnetic flux density (Figure 7). The voltage occurring at the Hall sensor

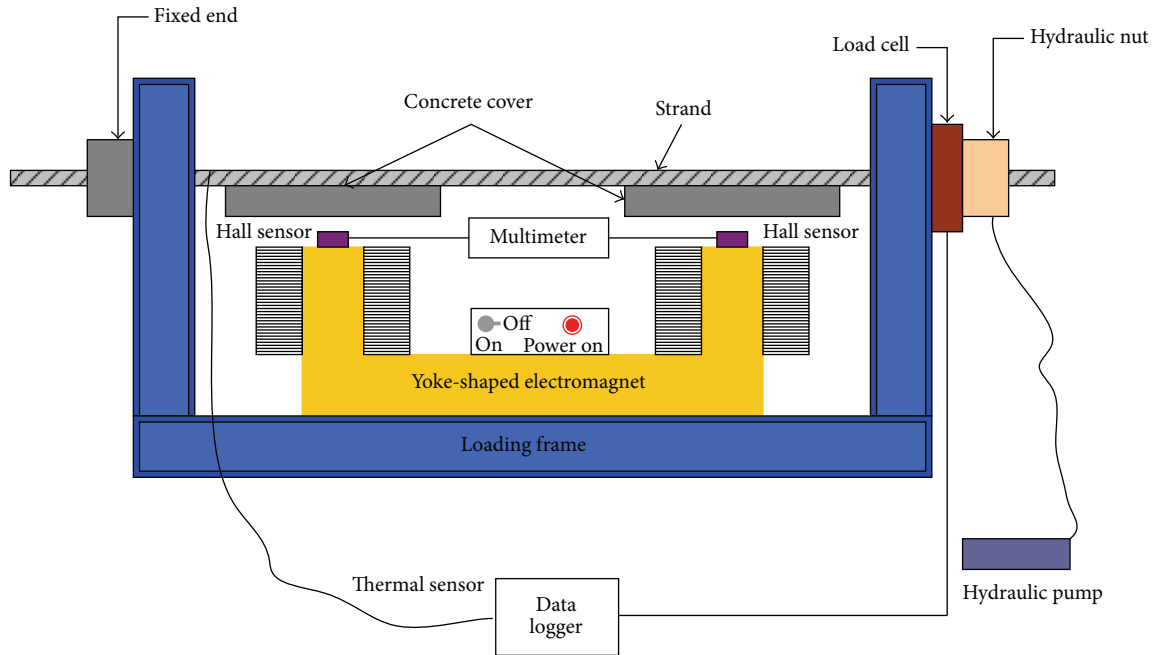


FIGURE 3: Illustrative layout for the test.



FIGURE 4: Test setup.



FIGURE 6: Prestressing tendon and installed Hall sensor, thermosensor, and electromagnet.

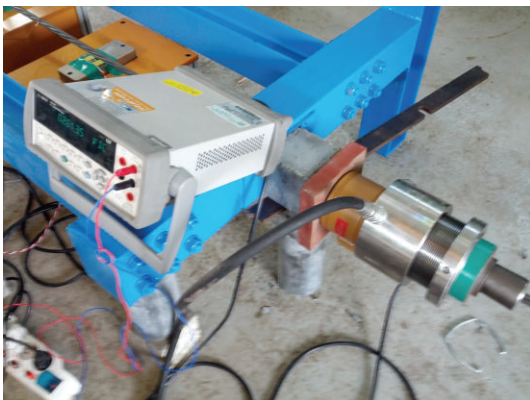


FIGURE 5: Multimeter, load cell, and hydraulic nut.

is measured by means of a multimeter (model 34410A of Agilent) (Figure 5).

In order to examine the effect of the concrete cover on the magnetic flux density, tests were performed using a movable concrete plate disposed at the bottom of the tendon (Figures 8 and 9). The thickness of the concrete plate is 22.7 mm.

Using this experimental setup, the magnetic flux density or magnetic induction, B , induced in the tendon by the electromagnet was measured by varying the stress of the prestressing tendon. Referring to the Korean Highway Bridge Design Code (2010) [17], the stress of the prestressing tendon was varied from 14% of the yield stress to a value of 80% of the yield stress close to the tensile allowable stress of the tendon



FIGURE 7: Hall sensor installed at the N-pole of the electromagnet.

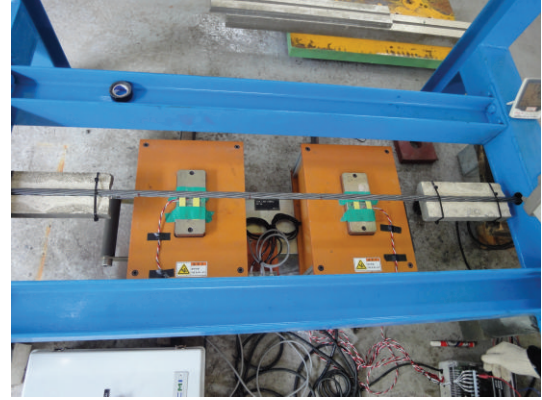


FIGURE 9: Case with removed concrete cover.



FIGURE 8: Case with concrete cover.

TABLE 1: Test variables for the test.

Variable	Values	Remarks
Input current of electromagnet (A)	4, 5	See Figure 10
Stress of prestressing tendon (f_y)	0.14, 0.27, 0.41, 0.54, 0.68, 0.81	$f_y = 1600$ MPa (SWPC7B 15.2 mm 7-strand)
Separation between the tendon and the electromagnet (mm)	25, 46	See Figure 2

immediately after the introduction of prestress. The tendon adopted for the test is SWPC7B tendon (7 strands of 15.2 mm) widely used for prestressed concrete structures. The input current determining the intensity of the magnetic field and the separation, which is the distance between the pole face of the electromagnet and the bottom of the prestressing tendon, was decided so as to magnetize the tendon to near saturation level. The variables used in the test are arranged in Table 1.

3.2. Measurement of Magnetic Saturation of Prestressing Tendon. Prior to investigate the relation between the stress and induced magnetic flux density in the prestressing tendon, the input current of the electromagnet was varied to find the input current and separation enabling to magnetize

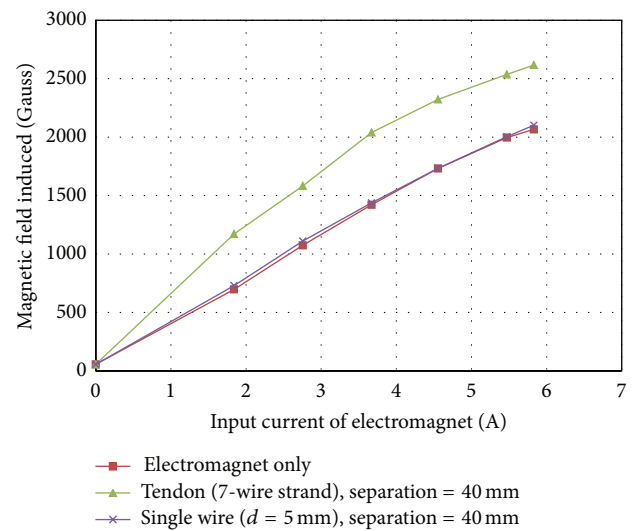


FIGURE 10: Magnetization of the prestressing tendon to near saturation.

the tendon to near saturation level. Comparison of the magnetic flux densities of the electromagnet was conducted for the cases corresponding to the absence of tendon and corresponding to the tendon without prestress. In addition, the induced magnetic flux density of 1 wire of 5 mm diameter composing the tendon was also measured to test the effect of the cross sectional area of the tendon on the magnetic induction. For both cases, the separation was set to 40 mm.

In view of the test results in Figure 10, when the input current of the electromagnet ranges between 0 to 3.67 A, the difference between magnetic flux densities of electromagnet and the prestressing tendon, that is, the increased magnetic flux density due to the presence of the prestressing tendon, tends to increase with the varying input current. However, for input currents larger than 3.67 A, this increase converges to a constant value. This means that near magnetic saturation of the tendon can be achieved for input current larger than 3.67 A in the case of a separation of 40 mm. Besides, for the wire with diameter of 5 mm, difference could practically not be observed between the cases where there was only

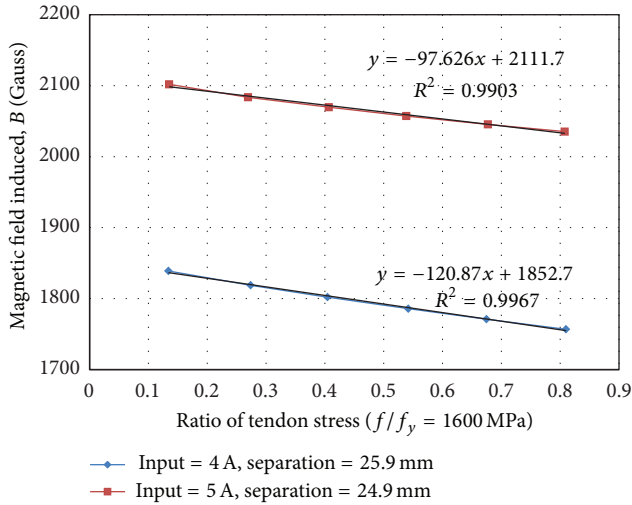


FIGURE 11: Stress of prestressing tendon versus magnetic induction B (separation of 25 mm).

the electromagnet and where the wire was present. This observation can be attributed to the fact that near magnetic saturation is easily achieved for small cross sectional areas.

3.3. Measurement of the Induced Magnetic Field of the Prestressing Tendon. Referring to Figure 10, the input current of the electromagnet was set to 4 A and 5 A. The separation was decided as 25 mm and 46 mm (practically close to 25 mm and 46 mm, resp.) considering the cover thickness in real concrete structures. During the tests, the variation of temperature remained insignificant. During the tests with separation of 25 mm, the ambient temperature was 23.5°C (4 A) and 23.7°C (5 A), and the temperature of the tendon ranged between 22.6 and 23.3°C for input currents of 4 A and between 22.9 and 23.8°C for input currents 5 A. During the tests with separation of 46 mm, the ambient temperature was 21.8°C (4 A) and 22.9°C (5 A), and the temperature of the tendon ranged between 21.4 and 21.8°C for input current of 4 A and between 22.6 and 22.8°C for input current of 5 A.

In view of the test results for a separation of 25 mm in Figure 11, a highly linear relationship can be observed between the stress of the tendon and the induced magnetic induction B for both input currents. The linear regression of the relation between the stress of the tendon and the induced magnetic induction reveals a coefficient of determination (R^2) of 0.9967 for the input current of 4 A and of 0.9903 for 5 A. Besides, the size of the magnetic flux density induced in the tendon increases when the input current rises from 4 A to 5 A.

From the test results for a separation of 46 mm in Figure 12, the highly linear relationship between the stress of the tendon and the induced magnetic induction appears also for the input currents of 4 A and 5 A with coefficients of determination (R^2) of 0.9964 (4 A) and 0.9982 (5 A).

The relation between the separation and magnetic flux density induced in the tendon for the input current of 5 A was examined (Figure 13). The magnetic induction is seen to

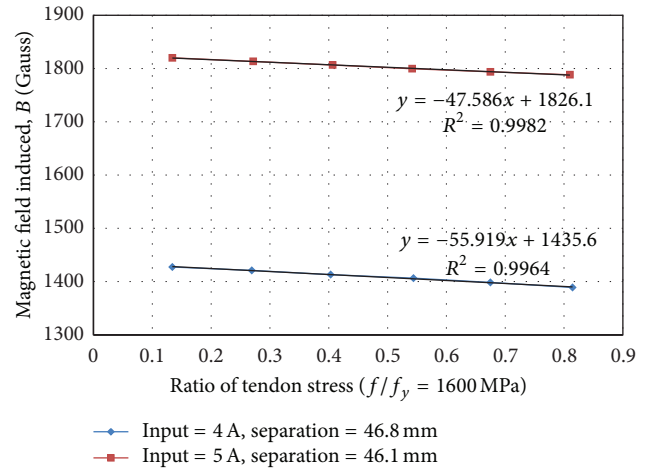


FIGURE 12: Stress of prestressing tendon versus magnetic induction B (separation of 50 mm).

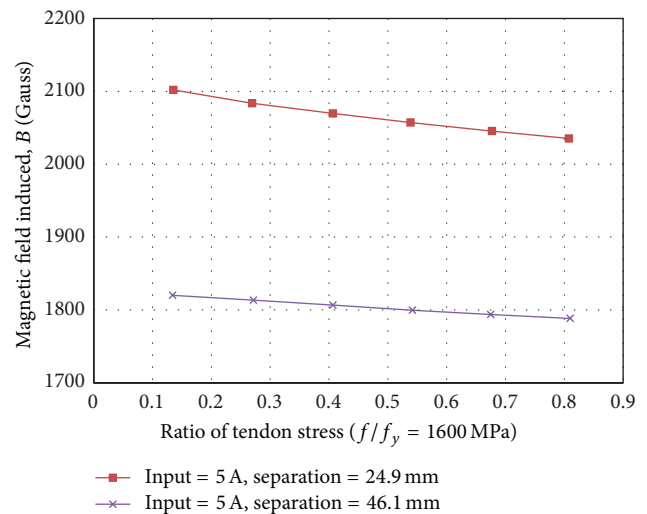


FIGURE 13: Reduction of the magnetic induction according to the separation.

reduce by 281 Gauss in average according to the increase of the separation from 25 mm to 46 mm.

Figure 14 plots the results of the tests investigating the relation between the thickness of the concrete cover and the induced magnetic induction for the input current of 4 A and separation of 46 mm. It appears that the cover made of nonmagnetic concrete has practically no effect on the magnetic flux density induced in the tendon. Despite of slight change in the magnetic induction B due to the concrete cover, this change remained within the measurement error occurring during the measurement of the voltage of the Hall sensors, which means that the concrete cover has practically no effect on the magnetic flux density.

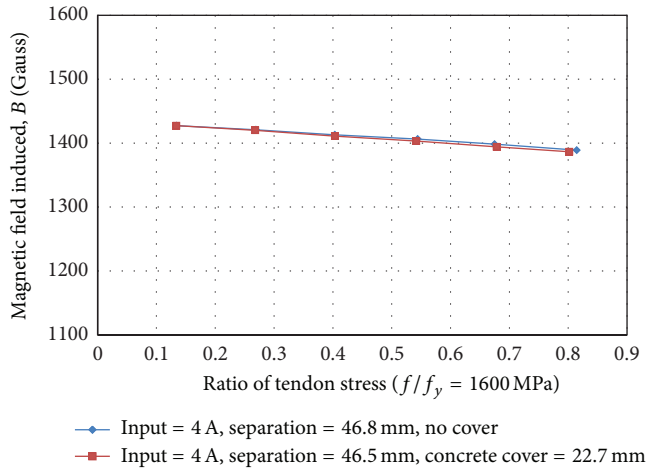


FIGURE 14: Relation between the concrete cover and the induced magnetic induction B .

4. Conclusions

This paper investigated the feasibility of the method estimating the stress in the bonded tendon of prestressed concrete bridge using the Villari effect and the induced magnetic field. To that goal, a magnetic field was generated in the prestressing tendon by means of an electromagnet and the relation between the stress of the tendon and the so-induced magnetic flux density was observed. The test results revealed that, within the stress range (from $0.14 f_y$ to $0.81 f_y$) of the prestressing tendon used in field, there is a linear relationship between the stress of the tendon and the induced magnetic induction. Moreover, the magnetic flux density induced in the tendon depended on the intensity of the electromagnet and the separation but was not affected by the concrete cover.

Accordingly, this linear relation between the stress of the tendon and the induced magnetic flux density can be used to estimate the stress of the bonded prestressing tendon in existing prestressed concrete bridges. This means that if Hall sensors are used to measure the magnetic flux density induced in the prestressing tendon by an external electromagnet attached to the prestressed concrete bridge, the stress of the tendon can be estimated by the Villari effect in which the magnetic permeability varies according to the stress of the magnetic body. However, additional studies should be conducted for further practical application of the method. Concretely, the magnetic B - H hysteresis loops should be constructed per stress of the prestressing tendon, and study should be performed to examine systematically the effect of the separation and the intensity of the electromagnet on the magnetic flux density induced and the sign of magnetostriction in the prestressing tendon. In addition, methods enabling to consider the effects of the diverse details in actual prestressed concrete bridges like the effect of longitudinal and transverse reinforcements, the case of prestressing tendons arranged in bundles, and the ordinary use of metallic sheath shall also be investigated.

Acknowledgment

This research was supported by a grant from a Strategic Research Project (Diagnostic Techniques for the Prestressing System in Concrete Bridges) funded by the Korea Institute of Construction Technology.

References

- [1] M. K. Tadros, N. A. Omaishi, S. J. Seguirant, and J. G. Gallt, "Prestress losses in pretensioned high-strength concrete bridge girders," Transportation Research Board, NCHRP Report 496, 2001.
- [2] R. Woodward and F. Williams, "Collapse of the Ynys-y-Gwas bridge, West Glamorgan," in *Proceedings of the Institution of Civil Engineers*, vol. 84, pp. 635–669, London, UK, August 1988.
- [3] J.-T. Kim, C.-B. Yun, Y.-S. Ryu, and H.-M. Cho, "Identification of prestress-loss in PSC beams using modal information," *Structural Engineering and Mechanics*, vol. 17, no. 3-4, pp. 467–482, 2003.
- [4] D. D. Ho, J. T. Kim, N. Stubbs, and W. S. Park, "Prestress-force estimation in PSC girder using modal parameters and system identification," *Advances in Structural Engineering*, vol. 15, no. 6, pp. 997–1012, 2012.
- [5] J.-T. Kim, J.-H. Park, D.-S. Hong, H.-M. Cho, W.-B. Na, and J.-H. Yi, "Vibration and impedance monitoring for prestress-loss prediction in PSC girder bridges," *Smart Structures and Systems*, vol. 5, no. 1, pp. 81–94, 2009.
- [6] M. D. Beard, M. J. S. Lowe, and P. Cawley, "Ultrasonic guided waves for inspection of grouted tendons and bolts," *Journal of Materials in Civil Engineering*, vol. 15, no. 3, pp. 212–218, 2003.
- [7] S. Salamone, I. Bartoli, R. Phillips, C. Nucera, and F. L. di Scalea, "Health monitoring of prestressing tendons in posttensioned concrete bridges," *Journal of the Transportation Research Record*, no. 2220, pp. 21–27, 2011.
- [8] B. H. Kim, J. B. Jang, H. P. Lee, and I. K. Lee, "Estimation of prestressed tension on grouted PSC tendon using measured elastic wave velocity," *Journal of Korean Society of Civil Engineers A*, vol. 32, no. 5, pp. 289–297, 2012 (Korean).
- [9] J. B. Jang, K. M. Hwang, H. P. Lee, and B. H. Kim, "Assessment of the prestress force on the bonded tendon using the strain and the stress wave velocity," *Journal of Korean Society of Civil Engineers A*, vol. 32, no. 3, pp. 183–188, 2012 (Korean).
- [10] E. Villari, "Change of magnetization by tension and by electric current," *Annual Review of Physical Chemistry*, vol. 126, pp. 87–122, 1865.
- [11] B. D. Cullity and C. D. Graham, *Introduction to Magnetic Materials*, IEEE Press, 2005.
- [12] D. Son, S. J. Lim, and C. S. Kim, "Non-contact torque sensor using the difference of maximum induction of amorphous cores," *IEEE Transactions on Magnetics*, vol. 28, no. 5, pp. 2205–2207, 1992.
- [13] T. A. Baudendistel and M. L. Turner, "A novel inverse-magnetostrictive force sensor," *IEEE Sensor Journal*, vol. 7, no. 2, pp. 245–250, 2007.
- [14] R. M. Bororth, *Ferromagnetism*, IEEE Press, 1993.
- [15] B. Fernandes, J. D. Wade, D. K. Nims, and V. K. Devabhaktuni, "A new magnetic sensor concept for nondestructive evaluation of deteriorated prestressing strand," *Research in Nondestructive Evaluation*, vol. 23, no. 1, pp. 46–68, 2012.

- [16] B. Fernandes, M. D. Titus, D. K. Nims, A. Ghorbanpoor, and V. K. Devabhaktuni, "Practical assessment of magnetic methods for corrosion detection in an adjacent precast prestressed concrete box-beam bridge," *Nondestructive Testing and Evaluation*, vol. 28, no. 2, pp. 99–118, 2012.
- [17] Korea Road & Transportation Association, *Highway Bridge Design Code*, 2010, (Korean).

Research Article

Microseismic Monitoring and Numerical Simulation of Rock Slope Failure

Zhengzhao Liang,^{1,2} Nuwen Xu,³ Ke Ma,¹ Shibin Tang,¹ and Chunan Tang¹

¹ School of Civil Engineering, Dalian University of Technology, Dalian 116024, China

² The Key Laboratory of Safety for Geotechnical and Structural Engineering of Hubei Province, Wuhan University, Wuhan 430072, China

³ College of Water Resource & Hydropower, Sichuan University, Chengdu 610065, China

Correspondence should be addressed to Zhengzhao Liang; z.z.liang@163.com

Received 9 July 2013; Accepted 28 September 2013

Academic Editor: Hong-Nan Li

Copyright © 2013 Zhengzhao Liang et al. This is an open access article distributed under the Creative Commons Attribution License, which permits unrestricted use, distribution, and reproduction in any medium, provided the original work is properly cited.

A numerical code with an elastic-brittle failure model has been developed to simulate the seismic activities in rock failure problems. The feasibility in principle of monitoring and prediction of rock failure was numerically simulated. The heterogeneity was considered to be the main reason for the existence of slope failure precursors. Seismic events could be observed in heterogeneous rock, whereas the homogeneous rocks showed an abrupt fracture mode without any early seismic precursors. The failure process of a slope was numerically investigated by using a gravity increase method (centrifugal loading method), and the application of the microseismic monitoring system in the slope was introduced. The numerical results showed that the fracture of the main faults caused the slope slide, and the microcracking caused by the heterogeneity in the faults prior to the landslide could be considered as the precursors of the slope failure, which were captured by the microseismic monitoring system. The microseismic monitoring technique was proved to be successful in predicting the failure in the slope, and the numerical results will be helpful in interpreting the microseismic monitoring results.

1. Introduction

Microseismic monitoring technique has been used to predict rock burst in mining engineering for many years. Rock burst is a catastrophic phenomenon triggered by a progressive failure process of rocks, which has extremely complex mechanical mechanisms. The present studies are mostly based on hypotheses or experiences. Hoek and Brown also pointed out that this type of progressive failure process was still not clearly understood up to now [1]. At present, many rock burst theories were proposed, using mainly the strength theory, the energy theory, the burst liability theory, the stiffness theory, and the instability theory. Unfortunately, although all of these methods have been used, none is proved to be adequately reliable, and almost no successful application has been reported.

In recent years, many monitoring sensors have been widely used in civil engineering [2, 3] and microseismic

monitoring technique has been developed rapidly and widely used to capture the microcracking in underground tunnel engineering and mining engineering [4–6]. The microseismic monitoring technique can be used to obtain the time, location, and magnitude by acoustic analysis. Currently, advanced rock burst monitoring network systems have been established for many deep mines in Canada, the United States, South Africa, and Australia. In China, many sets of monitoring equipment were imported by a few large coal mines and metal mines to monitor rock burst hazards.

Similar to rock burst problems, slope instability and landslides have always been one of the most significant subjects of slope engineering. How to monitor and predict rock slope failure hazards has been one of the hottest topics in rock engineering in recent years. Successful application of microseismic monitoring on rock slope failure prediction has not been found up to now.

With the rapid development of the deep mines and particularly large hydroelectric projects in southwest China, rock slope failure seems to be the most challenging problem. In these large hydroelectric projects, the rock slopes are often characterized by deep cracks and faults, high stress levels, intense weathering, unloading fractures, and so forth. Extensive use of the new measurement techniques and the traditional techniques, such as Global Positioning System (GPS), Synthetic Aperture Radar (SAR) Interferometry, Time Domain Reflect meter (TDR), multiple position extensometers, convergence meters, and surface subsidence monitoring, is currently found to be very useful in surface deformation monitoring of civil engineering [7–12]. However, it is unrealistic for them to effectively monitor the occurrence of microcracking in deep rock masses prior to the formation of a macroscopic rock fracture outside slope surface [13–16].

It is well known that rock slopes have smaller deformation before slip failure than soil slopes. Rock slope failure often happens in a more abrupt way, which is hard to be captured by surface deformation monitoring techniques. Microseismic monitoring technique seems to be a better way to capture the internal microcracking, which may often cause macroslide of rock slopes gradually.

Rocks loaded in testing machine and rock masses that are stressed near underground excavations emit detectable acoustic or seismic signals. If these signals can be captured sufficiently clearly as seismograms by a number of sensors nearby, the origin time of seismic events, their location, and other source parameters such as source radius, static stress drop, dynamic stress drop, and apparent stress can be estimated. In rock engineering practice, the microcracking or microfracturing can be located by microseismic monitoring system, and the local damage can be determined by analyzing the time of seismic events, magnitude of energy release, and the stress drop. The damage zone and the parameters of seismic events can be employed to predict rock slope failure.

However, the results of microseismic monitoring can only provide information of stress drop and seismic energy. How to utilize this seismic information becomes much significant in rock slope failure analysis. Therefore, a proper model revealing the relation between damage evolution and stress variation, such as the phenomena of stress buildup, stress shadow, and stress transfer, is helpful for rock slope failure prediction.

In order to understand the failure mechanism of rock engineering structures, numerical methods, such as the FEM, boundary element method (BEM), and discrete element method (DEM), have been developed, and they have become increasingly popular for the stability analysis of the structures. It has been shown that the numerical methods have a number of advantages over the traditional limit equilibrium approaches for stability analysis of rock engineering. Most importantly, the critical failure surface can be found automatically. Nevertheless, the currently widely accepted numerical methods do not take into account the heterogeneity of rock masses at macroscopic levels under complicated geological conditions. The heterogeneity plays an important role in determining the fracture paths and fracture patterns of rock masses [13].

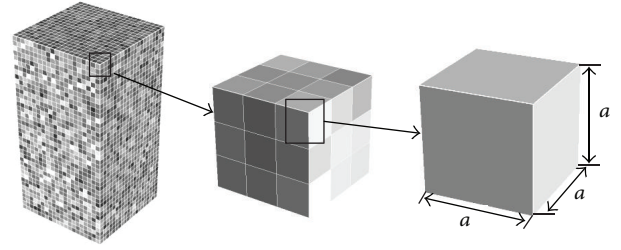


FIGURE 1: Mesh generation in RFPA^{3D}. Heterogeneity is introduced into the numerical specimen by following a statistical distribution. However, the mechanical properties in each element are homogeneous.

In this study, the microseismic monitoring technique and a numerical code RFPA^{3D} with an elastic-brittle constitutive law were applied to the right slope stability analysis of Dagangshan Hydropower Station. The influence of the heterogeneity on seismic events was simulated by a numerical model to discuss the feasibility of slope failure prediction by using microseismic monitoring.

2. Numerical Modelling

2.1. Mesh Generation and the Heterogeneity Index. As shown in Figure 1, the model in RFPA^{3D} is meshed into brick elements with randomly distributed mechanical properties. When a heterogeneous material is simulated, disorder should be implemented. In the lattice model, all elements of the mesh have different lengths and different stiffness. In order to deal with real random microstructures in numerical simulation, rock heterogeneity can be characterized better with statistical approaches. In RFPA^{3D}, since the numerical specimens consist of the elements of the same shape and size, there is no priority geometrically in any orientation in the specimen. Disorder can be obtained by means of random distributions of the mechanical properties of the elements. The statistical distribution of elastic modulus can be described by Weibull distribution function (1), even distribution function (2), or normal distribution function (3) as follows:

$$W(x) = \frac{m}{x_0} \left(\frac{x}{x_0}\right)^{m-1} \exp\left[-\left(\frac{x}{x_0}\right)^m\right], \quad (1)$$

$$E(x) = \begin{cases} 0, & x \leq a, \\ \frac{1}{(b-a)}, & a \leq x \leq b, \\ 1, & x \geq b, \end{cases} \quad (2)$$

$$N(x) = \frac{1}{\sqrt{2\pi}s} \exp\left[-\frac{(x-x_0)^2}{2s^2}\right]. \quad (3)$$

In these equations, x can be the elemental mechanical parameter, such as uniaxial compressive strength, elastic modulus, Poisson's ratio, or specific weight. The parameters a and b in (1) are the minimal value and the maximal value of x , respectively, and in (3), x_0 and s are the mean value and the variance of x , respectively. In (1), m defines the shape of

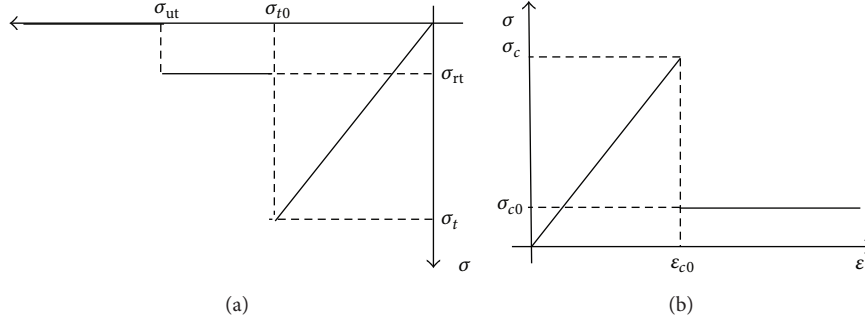


FIGURE 2: The stress-strain relation of the element for two different failure modes.

the Weibull distribution function. According to the Weibull distribution and the definition of homogeneity index, a larger m implies that more elements with the mechanical properties approximated to the mean value and a more homogeneous rock specimen.

In Figure 1, the gray color represents the value of the parameters relatively. Even though mechanical parameters in each element are different from each other, which make the specimen heterogeneous, the mechanical properties throughout a single element are assumed to be homogeneously distributed. It should be noted that the elemental mechanical parameters, such as uniaxial compressive strength, elastic modulus, Poisson's ratio, and weight, are distributed throughout the specimen independently.

2.2. Constitutive Law. The elastic modulus of the damaged element is defined as follows:

$$E = (1 - D) E_0, \quad (4)$$

where E represents the damage variable and E and E_0 are the elastic modulus of the damaged and undamaged elements, respectively. It must be noted that the element and its damage are assumed to be isotropic, and therefore E , E_0 , and D are all scalar.

It was assumed that each element may fail in either tensile failure mode or shear failure mode. If the elemental stress state satisfies both the tensile failure criterion and shear failure criterion, the tensile failure mode takes the higher priority. Figure 2 shows the elemental stress-strain relation for the two failure modes. If the element is subjected to uniaxial tensile stress, before the tensile stress (the minimal principal stress) of the element reaches its tensile strength, the element keeps linear elastic. When the minimal principal stress increases beyond the tensile strength, the element fails and the elastic modulus changes to a small value and its strength falls to residual tensile strength. When the tensile strain increases to a more large value, the strength of the element falls to a much smaller value that can be ignored approximately, which we can call the ultimate tensile strength, and the element loses its capability of loading. Accordingly, the element keeps linear elastic before the uniaxial compressive stress reaches the uniaxial compressive strength. When the elemental stress meets the shear failure criterion, the element will damage gradually.

The damage variable D can be described as follows when the element is subjected to uniaxial tension:

$$D = \begin{cases} 0, & (\epsilon_3 > \epsilon_{t0}), \\ 1 - \frac{\sigma_{rt}}{\epsilon_3 E_0}, & (\epsilon_{t0} \geq \epsilon_3 \geq \epsilon_{ut}), \\ 1, & (\epsilon_3 \leq \epsilon_{ut}), \end{cases} \quad (5)$$

where σ_{rt} is the residual strength of the element and $\sigma_{rt} = -\lambda|\sigma_t|$. ϵ_{t0} is the tensile strain at the point of failure. ϵ_{ut} is the ultimate tensile strain and can be described as $\epsilon_{ut} = \eta\epsilon_{t0}$. η is the ultimate tensile strain coefficient and λ is the coefficient of residual strength.

The damage evolution function mentioned above only considers the tensile failure mode of the mesoscopic elements. Compressive softening induced by shear damage at mesoscopic level is also assumed to exist when the mesoscopic element is under compressive and shear stress. In shear failure mode, the damage variable D can be described as follows:

$$D = \begin{cases} 0, & \epsilon_1 < \epsilon_{c0}, \\ 1 - \frac{\sigma_{rc}}{E_0 \epsilon_1}, & \epsilon_1 \geq \epsilon_{c0}, \end{cases} \quad (6)$$

where σ_{rc} is the peak strength of the element subjected to uniaxial compression and ϵ_{c0} is the compressive strain at the point of shear failure.

2.3. Failure Criterion. One of the basic goals of rock mechanics has been to provide useful methods for predicting failure strength and associated parameters. In three-dimensional studies, the traditional Mohr-Coulomb strength criterion or Hoek-Brown strength criterion is not valid any longer since the effect of intermediate principal stress is not taken into consideration. The strength increases considerably in excess of its corresponding value for standard triaxial tests with an increasing value of the intermediate principal stress. The Drucker-Prager strength criterion and unified strength criterion proposed by Yu [17], which consider all of the three principal stresses, are also provided in RFPA^{3D}. The criterions mentioned above are all of shear failure criterions, and the tensile failure is not considered. As we know, many fractures are induced by tensile stress and even some shear failures are found in shear zones. Therefore, the maximal

tension strength criterion is introduced into the shear failure criterions in RFPA^{3D}. The Mohr-Coulomb strength criterion with tension cutoff is incorporated into the model as follows:

$$\begin{aligned} \sigma_1 - \frac{1 + \sin \phi}{1 - \sin \phi} \sigma_3 &\geq \sigma_c, & \sigma_1 &> \sigma_c - \lambda \sigma_t, \\ \sigma_3 &\leq -\sigma_t, & \sigma_1 &\leq \sigma_c - \lambda \sigma_t, \end{aligned} \quad (7)$$

where $\lambda = (1 + \sin \phi)/(1 - \sin \phi) = \tan^2 \theta$.

The Drucker-Prager strength criterion with tension cutoff can be described as follows:

$$\begin{aligned} f = \alpha I_1 + \sqrt{J_2} - K &> 0, \\ \sigma_3 &\leq -\sigma_t. \end{aligned} \quad (8)$$

The twins shear criterion with tension cutoff can be expressed as follows:

$$\begin{aligned} \sigma_3 &\leq -\sigma_t, \\ F = \alpha \sigma_1 - \frac{1}{2} (\sigma_2 + \sigma_3) - \sigma_t &\geq 0, & \sigma_2 &\leq \frac{\sigma_3 + \alpha \sigma_1}{1 + \alpha}, \\ F' = \frac{\alpha}{2} (\sigma_1 + \sigma_2) - \alpha \sigma_3 - \sigma_t &\geq 0, & \sigma_2 &> \frac{\sigma_3 + \alpha \sigma_1}{1 + \alpha}. \end{aligned} \quad (9)$$

2.4. Microseismic Events and Energy. It is assumed that the number of microseismic events or acoustic emission (AE) is proportional to the number of failure elements. Thus, by recording the counts of failed elements, the microseismic events associated with the progressive failure process can be simulated. Therefore, as an approximation, it is assumed that the strain energy released by damaged elements is all in the form of the microseismic events:

$$\begin{aligned} E_e &= \frac{1}{2E} (\sigma_1^2 + \sigma_2^2 + \sigma_3^2 - \sigma_1 \sigma_2 - \sigma_1 \sigma_3 - \sigma_3 \sigma_2) V, \\ E_r &= \frac{1}{2E'} (\sigma_1'^2 + \sigma_2'^2 + \sigma_3'^2 - \sigma_1' \sigma_2' - \sigma_1' \sigma_3' - \sigma_3' \sigma_2') V', \end{aligned} \quad (10)$$

where V is the volume of the element, σ_1 , σ_2 , and σ_3 are the maximal principal stress, intermediate principal stress, and minimal principal stresses before failure, respectively, and σ_1' , σ_2' , and σ_3' are the maximal principal stress, intermediate principal stress, and minimal principal stresses after failure, respectively. The energy of the failure element can be determined by the difference of the strain energy stored in the element before failure and after failure as follows:

$$E_\Delta = E_e - E_r. \quad (11)$$

By using a three-dimensional graphic library, OpenGL, each microseismic event can be presented as a 3D ball in the postprocessing picture. Two different colors are selected to draw the balls to distinguish the failure modes of each element subjected to stresses.

2.5. Gravity Increase Method. In order to solve the stability problem related to rock engineering structures, the

fundamental principle of gravity increase method (GIM) is introduced into the RFPA. The code considers the deformation of a heterogeneous material containing randomly distributed microfractures. As loads are applied, the fractures will grow, interact, and coalesce, resulting in nonlinear rock behavior and formation of macroscopic fractures. The codes not only satisfy the global equilibrium, strain-consistent, and nonlinear constitutive relationship of rock and soil materials but also take into account the heterogeneous characteristics of materials at microscopic and macroscopic levels. The code has been successfully applied in failure process analysis of rock material. For the RFPA-GIM, the critical failure surface of slopes is obtained by gradually increasing the gravity while keeping material properties constant. In the RFPA-GIM, the gravitation of the elements increases linearly. For each loading step, there is a corresponding trial gravitational acceleration. Referring to the definition of factor of safety in the finite element strength reduction technique, the safety repertory factor F is defined as the ratio of the element gravitation in the failure state to the initial element gravitation, which can be written as follows:

$$F = \frac{g_0 + (n-1) \cdot \alpha \cdot g_0}{g_0} = 1 + (n-1) \alpha, \quad (12)$$

where g_0 is the initial gravitational acceleration (m/s^2), α is the coefficient of the gravitational acceleration increment, and n is the calculating step. The gravitational acceleration will be increased step by step.

In the RFPA-GIM, slope stability analysis is run with the trial gravitational acceleration until the critical failure surface in the slope is determined. Several possible techniques can be used to define slope failure, including the formation of critical failure surface and nonconvergence of the finite element solution. In the RFPA-GIM, the maximum microseismic event rate is used as the criterion of slope failure.

Monitoring microseismic event rates seems to be a good way of identifying the initiation and propagation of cracks and fractures in rocks. In quasi-brittle materials, such as rocks, the microseismic events are predominantly related to the release of elastic energy. It is assumed that if the microseismic event rate reaches the maximum value, a macroscopic failure surface forms and slope failure occurs. More details about RFPA^{3D} can be found in [16, 18].

3. Microseismic Activity Modes

According to the homogenous degree, three basic modes of seismic activities are found: swarm shocks, fore-main-after shocks, and main shock. Figure 3 shows the microseismic events that occurred in the heterogeneous rock specimen ($m = 1.1$), and Figure 4 shows the sequences of acoustic emission of the specimens with $m = 1.1, 3$, and 10 subjected to uniaxial compression until failure. Swarm shock can be found in much heterogeneous rocks ($m = 1.1$). Microfractures and microseismic events scattered throughout the specimen and acoustic emission could be detected at initial stage. Fore-main-after shocks could be found in more homogenous rocks and both acoustic emissions can be detected before and after

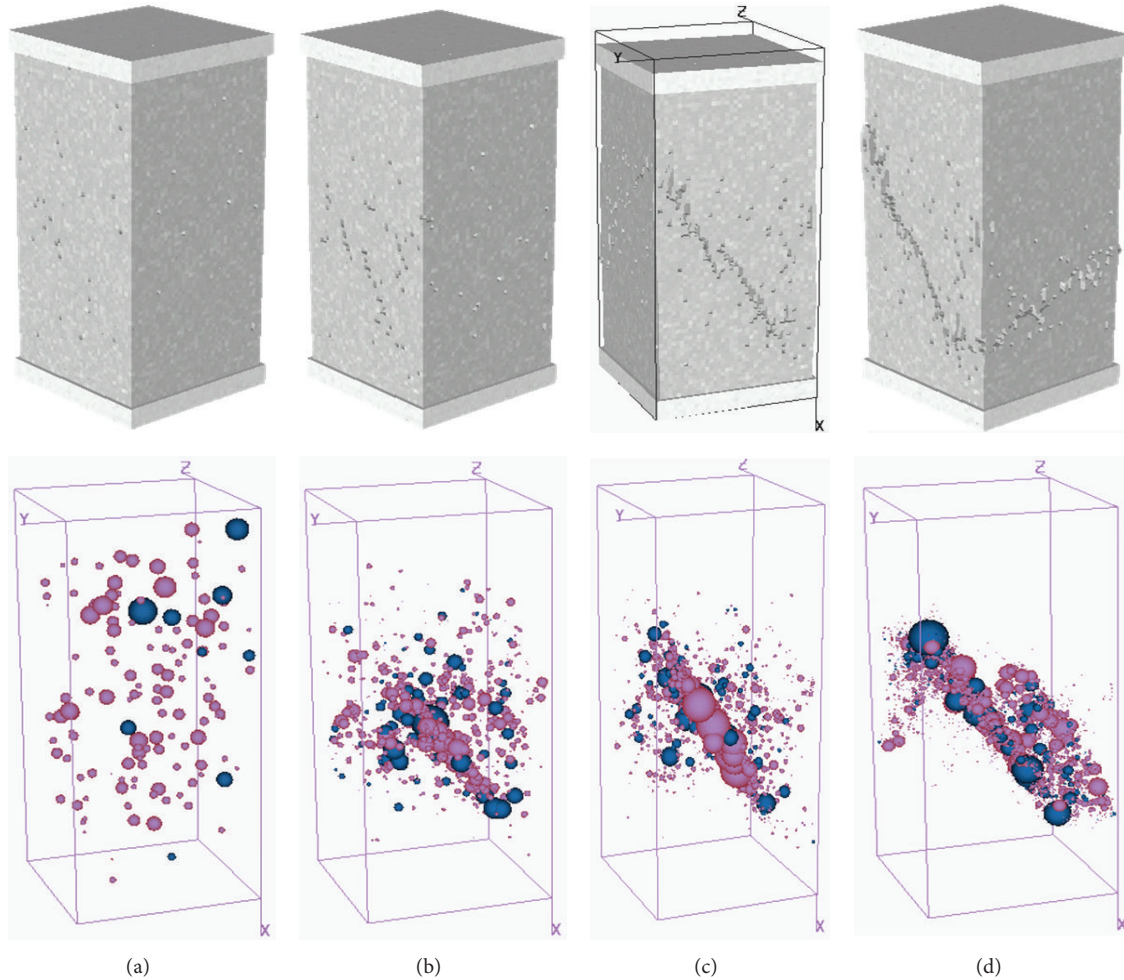


FIGURE 3: Plots of the microseismic events occurred in the heterogeneous rock specimen ($m = 1.1$). The balls in the microseismic event pictures represent microseismic events.

the main macrofractures were formed. Main shock could be found in most homogenous rocks. In more homogenous rocks, it is hard to predict the precursors because they showed only a small number of acoustic emissions. The results showed that relatively heterogeneous specimens emitted more acoustic emission as precursors of macrofractures than relatively homogenous specimens at the first loading stage. A greatly larger number of acoustic emissions were recorded in homogenous numerical rock specimens than in heterogeneous ones when the specimen reached its peak strength.

4. Seismic Events Monitoring of the Right Bank Slope at Dagangshan Hydroelectric Station

Dagangshan Hydropower Station is located at Dadu River in Sichuan province in southwestern China. It is one of the largest hydroelectric power stations which are currently developed in China. It has a double-curvature dam with a maximum height of 210 m and a total installed capacity of

2,600 MW. The maximal water head is 178.0 m, the minimal water head is 156.8 m, and the standard rated water head is 160 m. The slopes at the two sides of the mountain are very high and steep with exposed bedrocks. The inclination of the right bank slope is about 40 degrees to 65 degrees, and the relative height is above 600 m. The right bank has complicated geological conditions such as faults, unloading cracks zones, and joints with cracks development. In particular, faults X316-1 and f231 are the most significant to influence the stability of the rock slope. A microseismic monitoring system was applied to capture microseismic events for slope stability analysis in June, 2010.

The microseismic monitoring systems are manufactured by the Engineering Seismology Group (ESG) in Canada. The seismic monitoring network consists of Hyperion digital signal processing system, Paladin digital signal acquisition system, and a number of uniaxial/triaxial acceleration transducers deployed in boreholes drilled from rock mass in rock slopes or tunnels. Accelerometers are connected to the Paladins acquisition system using copper twisted-pair cables. The Paladins acquisition system is connected in series to the central system using optical fiber cables and network cables.

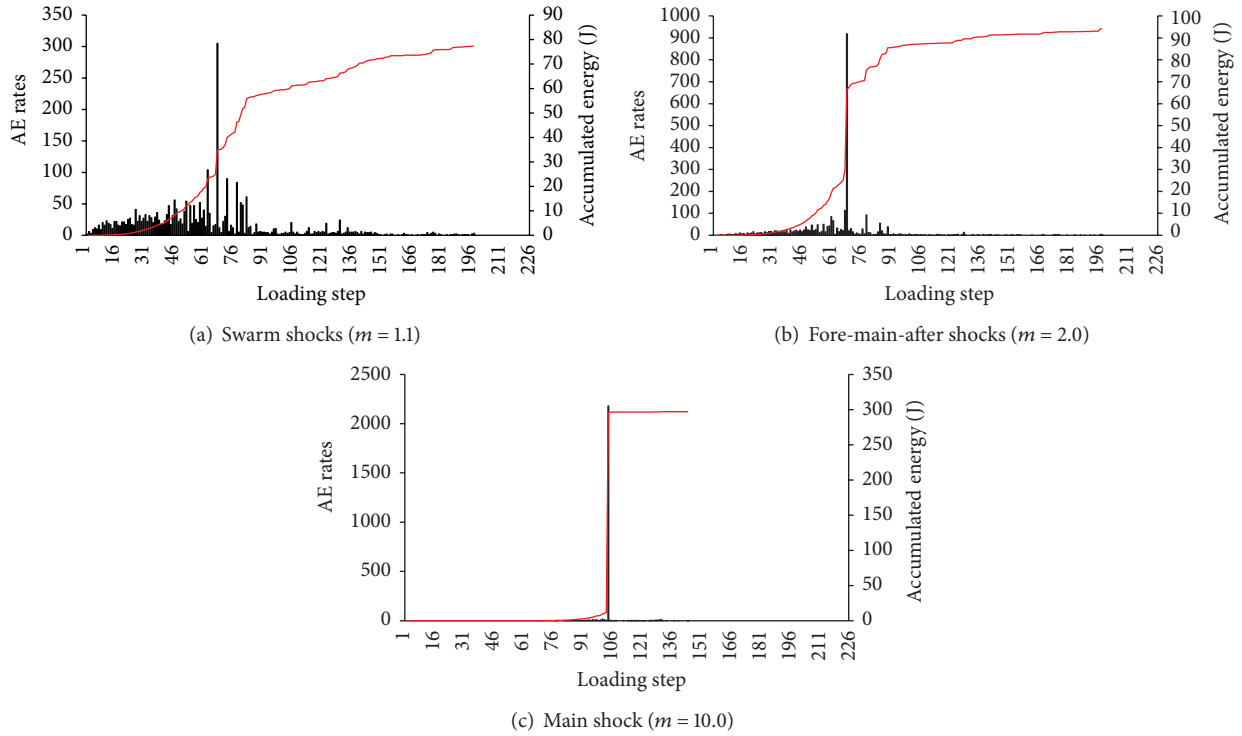


FIGURE 4: Three modes of microseismic activities in rock failure process.

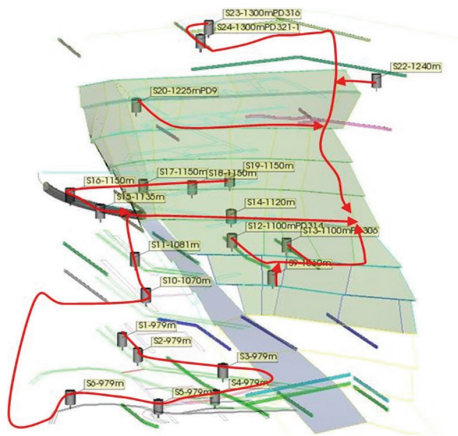


FIGURE 5: The layout of the sensor location in the slope.

Paladin units rely on a pulse-per-second (PPS) signal that originated from the Paladin Timing Source over the network. The seismic data recorded are transmitted from the on-site center to the office by GPRS for further analysis.

The spatial layout of sensors at eleven elevations is shown in Figure 5. Totally, 22 channels and 22 sensors were distributed in the slope and an area of $600\text{ m} \times 400\text{ m} \times 600\text{ m}$ was monitored. The sensors were connected to the data acquisition units by electric cable, and the seismic events were collected and uploaded to the acquisition data server when converted to digital format by optical fiber. The digital data were transmitted to the computing center and the clients in

3D figures. The topological diagram of the ESG monitoring system is shown in Figure 6.

The microseismic events were increased gradually when the rock slope was excavated continuously from the level 1070 m to 980 m. Figure 7 shows the evolution of the microseismic events during this period. Due to the excavation induced unloading, some microseismic events with small energy release appeared randomly distributed in the slope. More microseismic events were observed when the excavation proceeded. It could be found that the color of the balls changed from green to orange and red, which represented greater energy. When the excavation moved to 980 m, the microseismic events were distributed in a larger zone. However, most of the events were captured along the main faults (X316-1 and f231) that developed along the slope surface. The compressive stress on the faults was reduced due to the excavation upside. The tensile stress concentrated along the faults. The microseismic event locations show that hypocenters are concentrated on these excavation zones. The hypocenters follow the working faces and they are located where the excavation is carried out.

With the process of the shear elevation tunnel excavation, backfilling, and grouting at 1135~1240 m level, the microseismic events gradually reduced and the slope still remained stable. Actually, slope slip plane will be formed with the development of microfractures within rock mass, and the microseismic monitoring results can indicate the damage zones and then predict the potential slip plane. The monitoring results of the right bank slope, including the microseismic events and the energy loss density, showed the slope was much stable. Large external excavation, which

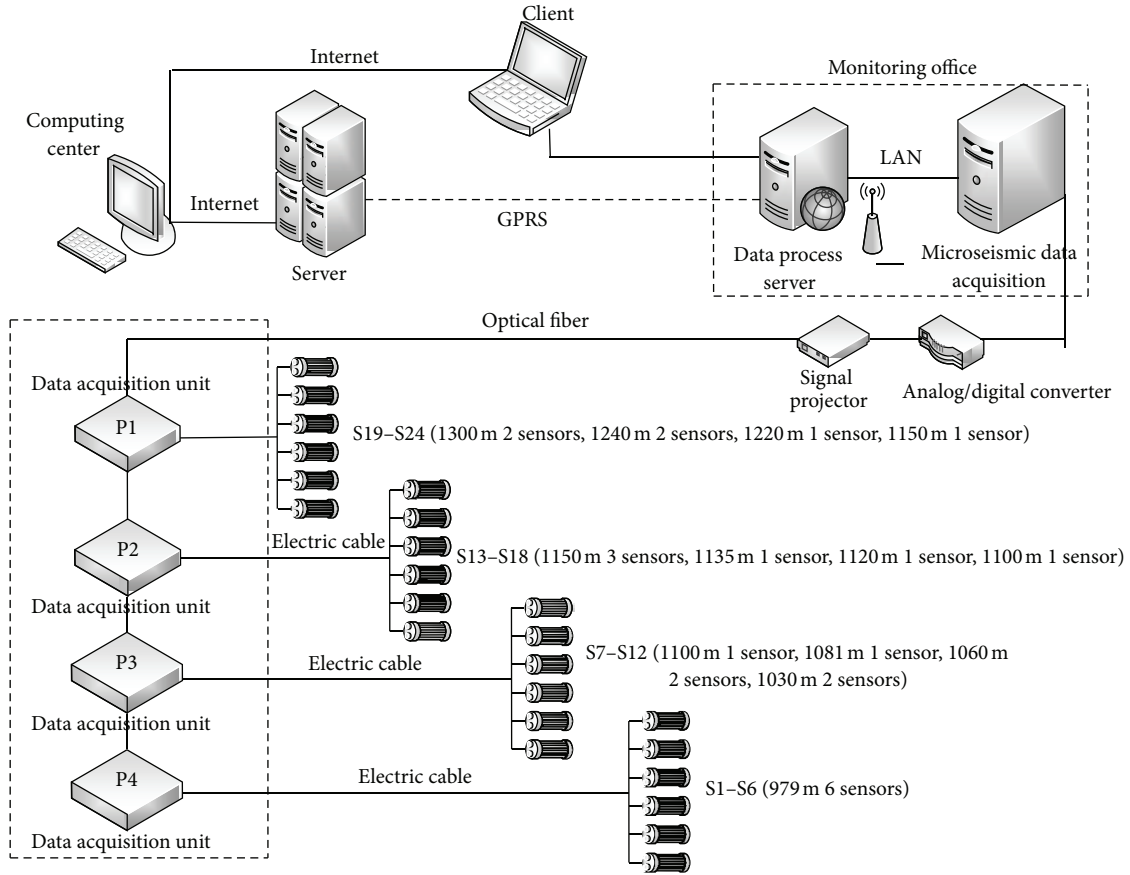


FIGURE 6: The topological graph of the microseismic monitoring system.

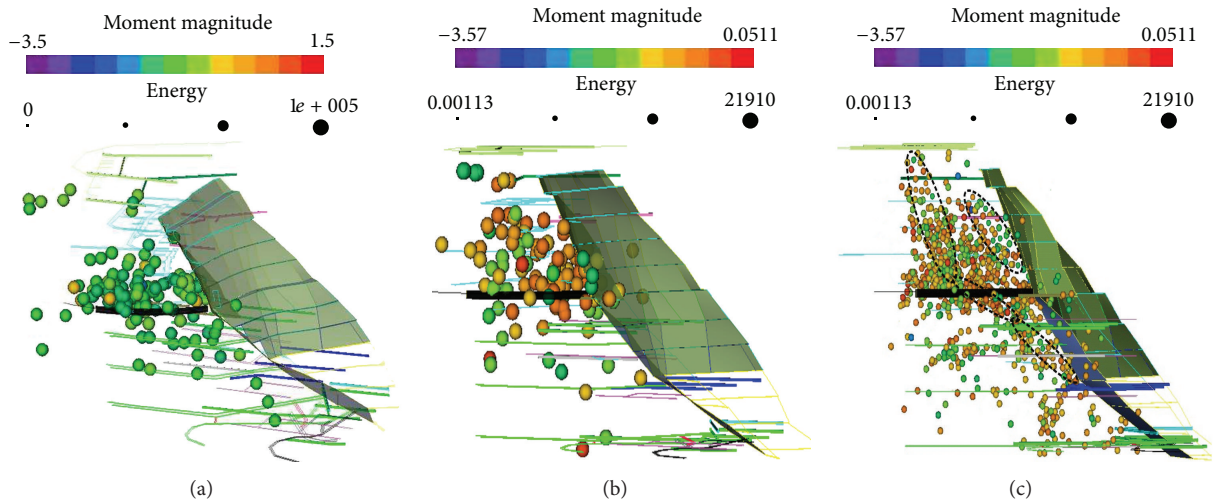


FIGURE 7: The distribution of the microseismic events in the slope during the excavation.

would lead to the increase of the microseismic events and energy loss, may cause slope instability and failure.

5. Rock Slope Failure Process Analysis

The failure process of the right bank slope of Dagangshan Hydroelectric Station was simulated by the RFPA^{3D} code.

The elastic-brittle model was considered for modeling the slope failure by using the centrifuge loading method. The homogeneity index for the rock mass was set 2.0.

When the acceleration of gravity increased from 1.0 g to 1.25 g, microseismic events were observed randomly distributed in the slope. The released energy of the microseismic events at this stage was much relatively smaller. When the

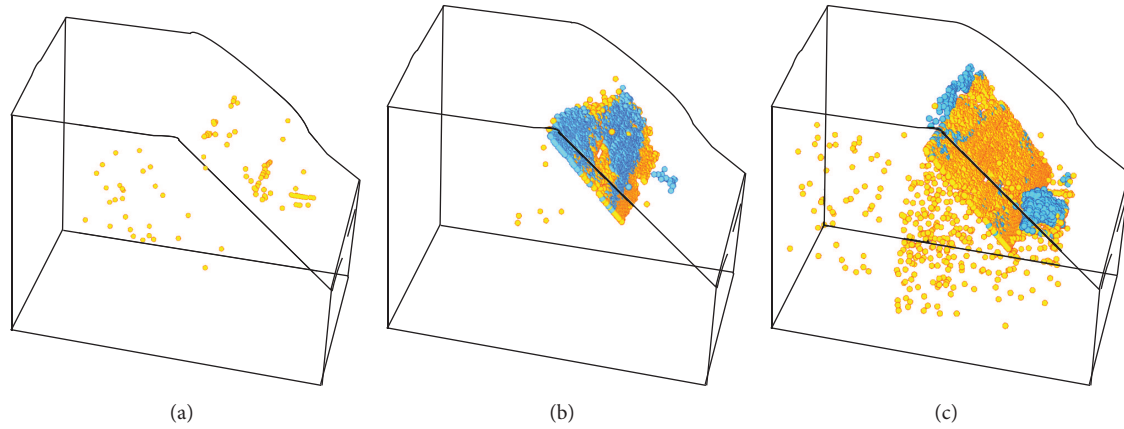


FIGURE 8: The simulated distribution of the microseismic events by RFPA^{3D} code.

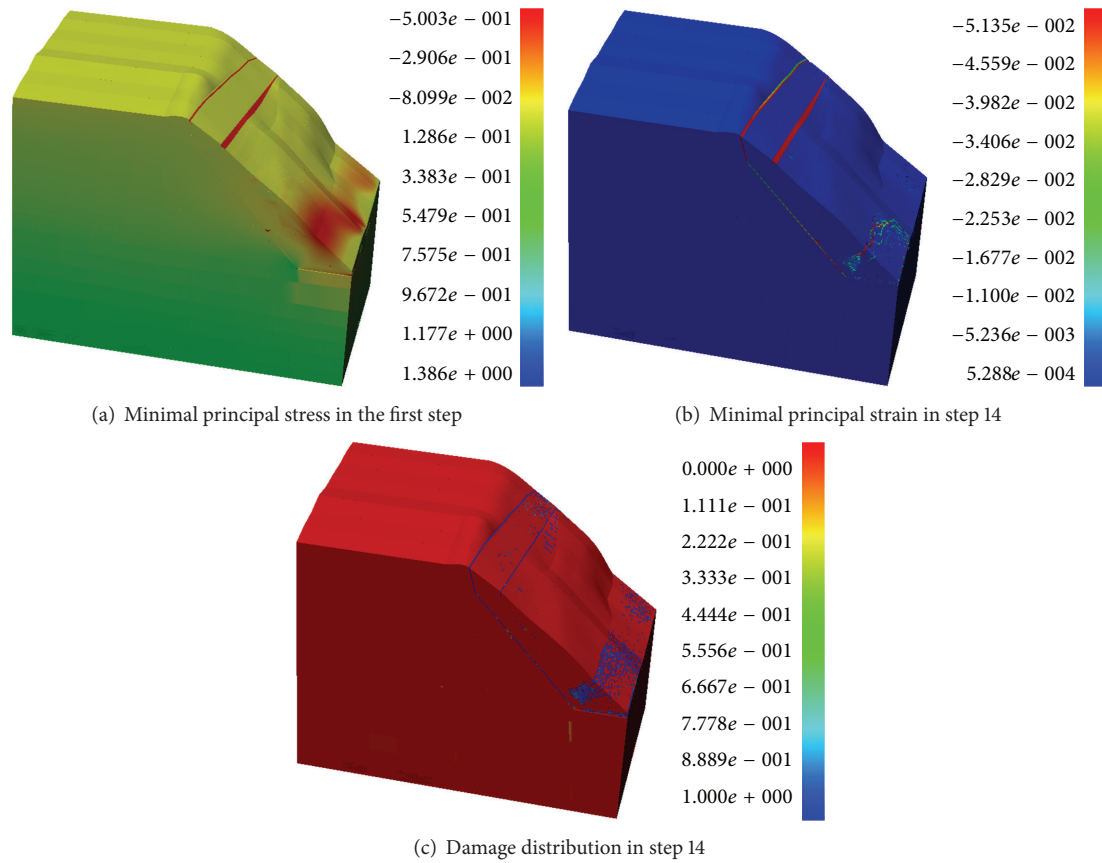


FIGURE 9: The distribution of the minimal principal stress, minimal principal strain, and the damage.

gravity acceleration increased to 1.50 g, more microcracking events concentrated along the fault zone. The slip plane was formed when the acceleration increased to 1.75 g. A large number of microseismic events appeared around the slip plane and deep into the slope under the left side of the slip plane. The spatial distribution of the microseismic events was shown in Figure 8.

The simulated results also revealed that most of the microcracking existed close to the faults (X316-1 and f231).

The minimal principal stress, the minimal principal strain, and the damage distribution were shown in Figures 9(a), 9(b), and 9(c), respectively. When the acceleration coefficient was 1.0, the minimal principal stress (tensile stress) was observed on the upper side of the two faults where microseismic events occurred. The slip plane was formed gradually with the acceleration coefficient increasing step by step. The concentrated tensile stress along the slip plane was released when the gravity acceleration coefficient increased to 1.5.

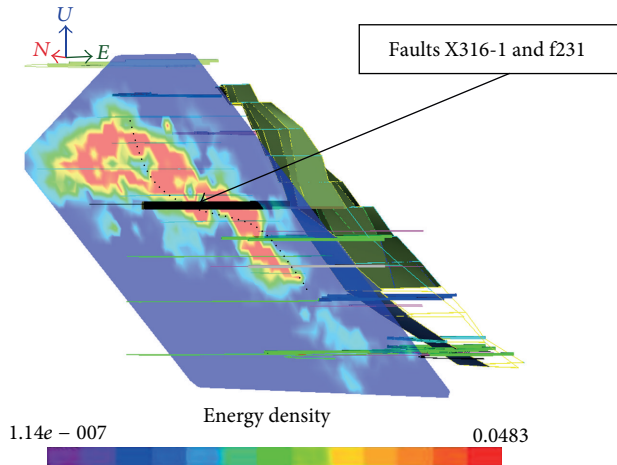


FIGURE 10: The microseismic energy density in the slope. The red color represented the highest energy zone.

However, the compressive stress concentrated at the bottom of the slope where the stress transformation led to a great number of microseismic events. The final gravity acceleration is 1.75 g, so the safety factor of the slope is 1.75. It should be noted that the numerical model only considered the natural slope without excavation.

The released energy density obtained from the microseismic monitoring system was shown in Figure 10. The red zone indicated the highest energy density. It was obvious that the red zones were located near the faults and merged with each other to form a possible slip plane. The numerical results agreed well with the monitoring results.

By comparison with the elastic-brittle model, an ideal elastic-plastic model was also applied in the simulation. In RFPA^{3D} code, the residual strength coefficient was set 1.0. Because the stress would never decrease when the stresses of the elements satisfied the failure criterion, the failure of elements would never release any energy. From this point of view, the ideal elastic-plastic model in the numerical code was not reasonable for microseismic activity modelling.

6. Conclusions

The microseismic monitoring system was set up to predict the failure of the right bank slope of Dagangshan Hydroelectric Power Station, and the numerical code RFPA^{3D} with an elastic-plastic model was applied to simulate failure process of the slope. The following conclusions can be drawn.

- (1) The heterogeneity in rocks provides the feasibility to predict the failure of rock slope. The numerical results showed that the homogeneous rock specimen demonstrated an abrupt failure mode, and no microseismic events prior to the failure could be observed. However, in the heterogeneous rock specimens, a great number of microseismic events provided the damage information, including the stress concentration and failure location. This will be helpful in predicting rock slope failure.

- (2) Ideal elastic-plastic model is not reasonable for microseismic problem modelling. The stress will never be released in ideal elastic-plastic model, and no energy will be released.
- (3) The application of the microseismic monitoring technique on the right bank slope of Dagangshan Hydroelectric Power Station was successful in analyzing slope stability and in predicting the failure in the slope. Rock slope failure often happens in an abrupt manner, which is hard to be captured by surface deformation monitoring techniques. Microseismic monitoring technique seems to be a better way to capture the internal microcracking, which may often result in macroslide of rock slopes gradually.
- (4) The numerical results, including the stress concentration, stress release, and microfailure location in numerical model, will be helpful in explaining the microseismic monitoring results.

Acknowledgments

This work was supported by the National Program on Key Basic Research Project of China (973 Program) (Grant no. 2014CB047100), the National Natural Science Foundation of China (Grant nos. 51121005, 51079017, and 51274053), the Open Research Fund Program of the Key Laboratory of Safety for Geotechnical and Structural Engineering of Hubei Province, the Foundation for the Author of National Excellent Doctoral Dissertation of China (no. 200960), and the Program for New Century Excellent Talents in University (NECT-09-0253).

References

- [1] E. Hoek and E. T. Brown, *Underground Excavation in Rock*, The Institute of Mining and Metallurgy, London, UK, 1980.
- [2] T. H. Yi, H. N. Li, and G. U. Ming, "Recent research and applications of GPS-based monitoring technology for high-rise structures," *Structural Control & Health Monitoring*, vol. 20, no. 5, pp. 649–670, 2013.
- [3] H. F. Bai, T. H. Yi, H. N. Li, and R. Liang, "Multisensors on-site monitoring and characteristic analysis of UHV transmission tower," *International Journal of Distributed Sensor Networks*, vol. 2012, Article ID 545148, 10 pages, 2012.
- [4] N. Dixon and M. Spriggs, "Quantification of slope displacement rates using acoustic emission monitoring," *Canadian Geotechnical Journal*, vol. 44, no. 8, pp. 966–976, 2007.
- [5] D. Arsoasio, L. Longoni, and M. Papini, "Towards rockfall forecasting through observing deformations and listening to microseismic emissions," *Natural Hazards and Earth System Sciences*, no. 9, pp. 1119–1131, 2009.
- [6] M. Cai, P. K. Kaiser, and C. D. Martin, "Quantification of rock mass damage in underground excavations from microseismic event monitoring," *International Journal of Rock Mechanics and Mining Sciences*, vol. 38, no. 8, pp. 1135–1145, 2001.
- [7] M. K. Abdul-Wahed, M. A. Heib, and G. Senfaute, "Mining-induced seismicity: seismic measurement using multiplet approach and numerical modeling," *International Journal of Coal Geology*, vol. 66, no. 1-2, pp. 137–147, 2006.

- [8] T. H. Yi, H. N. Li, and G. U. Ming, "Optimal sensor placement for structural health monitoring based on multiple optimization strategies," *The Structural Design of Tall and Special Buildings*, vol. 20, no. 7, pp. 881–900, 2011.
- [9] M. Cai and P. K. Kaiser, "Assessment of excavation damaged zone using a micromechanics model," *Tunnelling and Underground Space Technology*, vol. 20, no. 4, pp. 301–310, 2005.
- [10] A. Hirata, Y. Kameoka, and T. Hirano, "Safety management based on detection of possible rock bursts by AE monitoring during tunnel excavation," *Rock Mechanics and Rock Engineering*, vol. 40, no. 6, pp. 563–576, 2007.
- [11] P. Lin, Q. B. Li, and H. Hu, "A flexible network structure for temperature monitoring of a super high arch dam," *International Journal of Distributed Sensor Networks*, vol. 2012, Article ID 917849, 10 pages, 2012.
- [12] C. A. Tang, H. L. Fei, and X. H. Xu, "Application of modern system theory to rock unstable failure (part 2)," *Journal of Northeastern University (Natural Science)*, vol. 15, no. 2, pp. 124–127, 1994 (Chinese).
- [13] C. A. Tang, "Preliminary engineering application of microseismic monitoring technique to rockburst prediction in tunneling of Jinping II project," *Journal of Rock Mechanics and Geotechnical Engineering*, vol. 2, no. 3, pp. 193–208, 2010.
- [14] N. W. Xu, C. A. Tang, H. Li, and S. H. Wu, "Optimal design of micro-seismic monitoring array and seismic source location estimation for rock slope," *Open Civil Engineering Journal*, vol. 5, no. 1, pp. 36–45, 2011.
- [15] N. W. Xu, C. A. Tang, L. C. Li et al., "Microseismic monitoring and stability analysis of the left bank slope in Jinping first stage hydropower station in southwestern China," *International Journal of Rock Mechanics and Mining Sciences*, vol. 48, no. 6, pp. 950–963, 2011.
- [16] Z. Z. Liang, H. Xing, S. Y. Wang et al., "A three-dimensional numerical investigation of the fracture of rock specimens containing a pre-existing surface flaw," *Computers and Geotechnics*, vol. 45, pp. 19–33, 2012.
- [17] M. H. Yu, *Unified Strength Theory and Its Applications*, Springer, 2004.
- [18] Z. Z. Liang, C. A. Tang, H. X. Li, and Y. B. Zhang, "Numerical simulation of the 3D failure process in heterogeneous rocks," *International Journal of Rock Mechanics and Mining Sciences*, vol. 41, no. 3, p. 419, 2003.

Research Article

A SA-Based Wireless Seismic Stress Monitoring System for Concrete Structures

S. Hou,¹ Y. Yu,² H. B. Zhang,¹ X. Q. Mao,² and J. P. Ou^{1,3}

¹ School of Civil Engineering, Dalian University of Technology, Dalian 116024, China

² School of Electronic Science and Technology, Dalian University of Technology, Dalian 116024, China

³ School of Civil Engineering, Harbin Institute of Technology, Harbin 150090, China

Correspondence should be addressed to S. Hou; hous@dlut.edu.cn

Received 29 July 2013; Accepted 6 October 2013

Academic Editor: Gangbing Song

Copyright © 2013 S. Hou et al. This is an open access article distributed under the Creative Commons Attribution License, which permits unrestricted use, distribution, and reproduction in any medium, provided the original work is properly cited.

A PZT-based smart aggregate (SA) is capable of full process stress monitoring during earthquakes. A wired seismic monitoring system is prone to failure during earthquakes. Therefore, it is extremely necessary to use the wireless monitoring technique in the SA-based monitoring system. In this paper, the SA is integrated with the ZigBee wireless network which consists of a charge-to-voltage converter, a microprocessing unit, a wireless transmission unit, a base station, and a host computer. The dynamic loading scheme is applied on the SA and the output signal is measured by the wireless system and the wired system in parallel. The performance of the proposed wireless monitoring system is validated by comparing the wired and wireless signals. It is anticipated that this research will demonstrate the potential of using wireless monitoring systems for full damage process monitoring of concrete structures.

1. Introduction

In seismically active regions, acquisition of structural response data during earthquakes is essential to assist the evaluation of the current design practices [1]. Most of the existing seismic monitoring systems are based on the accelerometers [1–6]. However, damage detection using acceleration information is impractical due to the very heavy computational demands and the need for a detailed and accurate three-dimensional finite element model [2]. Thus, sensors that provide local damage information supplement the existing seismic monitoring systems nicely.

Traditional strain gauges like fiber Bragg Grating sensors and foil strain gauges, when embedded in a concrete structure, cannot measure the damage process reliably because their bondages with concrete tend to become loose. A commercially available load cell is able to measure the internal stress directly, but issues such as the size of the cell, its bondage with concrete, the interference it produces to the local stress field, and the cost hinder its application. The cement-based strain/stress sensors, which take advantage of the piezoresistivity effect developed by various researchers for

internal stress/strain measurement [7–10], unfortunately can only be used when the building structure is in a uniaxial and elastic stress/strain state. A cement-based smart aggregate (SA) with a d_{33} -mode lead zirconate titanate (PZT) patch embedded in it was proposed by Song et al. [11]. By evaluating the wave propagation among SAs, it can detect the cracking level of the structure in a qualitative manner [12–15]. The application of SA has also been extended to measure the compressive stress monitoring by calibrating the SA to only relatively low stress levels [16, 17]. To monitor the full damage process of concrete structures, Hou et al. proposed a novel SA which uses a marble material as the supporting structure [18].

All the above-mentioned monitoring systems are generally the wired system. However, this kind of system itself is also subject to failure during strong ground motions since it has many independent components, such as data loggers, sensors, and long cabling, which are very fragile. Thus, to acquire the full damage process information of a concrete structure during an earthquake event, it is extremely necessary to use the wireless monitoring system. Although many wireless monitoring systems have been developed for different types of structures [19–24], the architecture

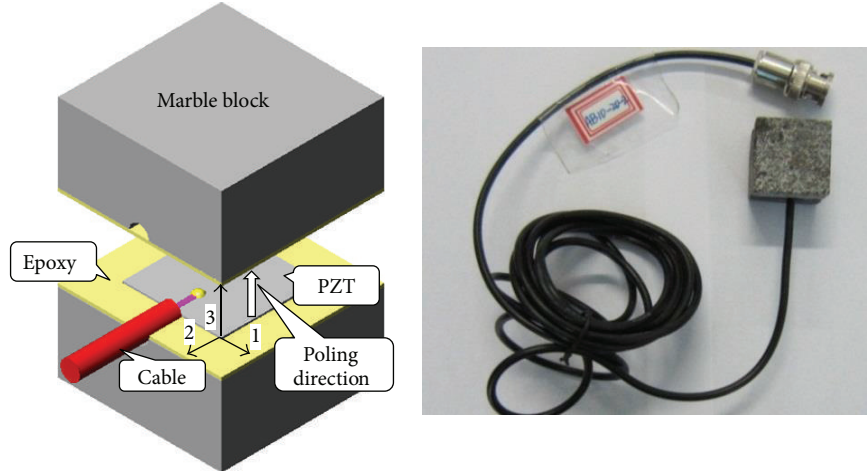


FIGURE 1: Structure of the smart aggregate and its photo.

TABLE 1: Typical properties of the selected PZT P-5H.

PZT property	Value
Young's modulus (GPa)	46
Density (kg/m^3)	745
d_{31}, d_{32} (pC/N)	-186
d_{33} (pC/N)	670
d_{15} (pC/N)	660

of the mentioned network differs greatly when the monitored structure types and structural parameters are different. Therefore, it is still worthy of a trial to integrate the SA with the existing wireless monitoring system.

2. Introduction of the Smart Aggregate

The structure of the SA used in this paper has been presented in the previous work of [18]. Figure 1 demonstrates its structure. The proposed SA consists of a piece of PZT patch connected with a piece of two-wire cable and a pair of marble blocks. The commercially available soft PZT ceramic referred to as P-5H with a major composition of $\text{Pb}(\text{TiZr})\text{O}_3$ was chosen. The PZT's properties, measured by the supplier, are listed in Table 1. Young's modulus of the marble and the epoxy was 51.5 GPa and 2.5 GPa, respectively, as supplied by the manufacturer. The size of the PZT patch was 15×15 mm, and the thickness was 0.3 mm. The marble blocks were $25 \times 25 \times 12$ mm in size. When the marble blocks were aligned together along the 12 mm long edge, a hole with a diameter of 3 mm and depth of 10 mm was bored to accommodate the cable and the soldering points on the PZT patch. Then the PZT patch was sandwiched between the marble-block pair with epoxy. The calibration test had been conducted and showed that the SA had constant sensitivity at a relatively high stress level. Sensitivity obtained from the calibration test was 1.23×10^5 pC/MPa.

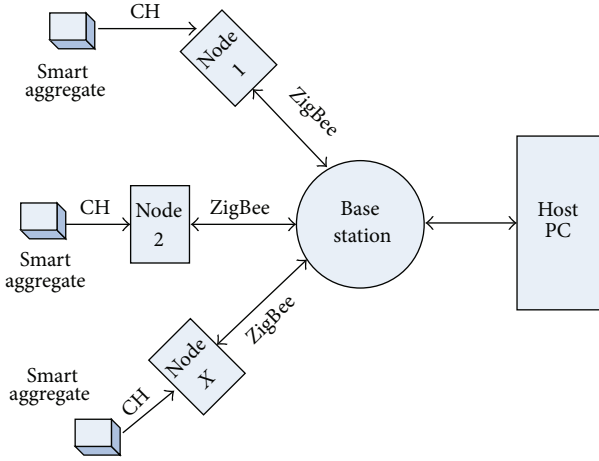
3. Hardware of the Wireless Acquisition System

3.1. The Overall Architecture of the System. The charge signal generated by the SA was collected by the wireless monitoring system as shown in Figure 2. The system consists of a base station, a host personal computer, and several wireless nodes. The wireless network structure of this acquisition system used a star topology. Each node of the network was connected to the base station in a point-to-point manner. The communication among any two nodes in the star network was subject to the control of the base station. With such a system structure, it was easy to implement centralized control and, due to this characteristic, it also brought the advantages of safety and ease of maintenance.

3.2. Design of Wireless Node. The wireless node collected the generated charge signals and transmitted them to the base station. Its structure is shown in Figure 3. The node used a modular design method, which included the flash storage unit, a wireless transmission unit, a microprocessing unit, and a power management unit.

3.3. Microprocessing Unit. The microprocessing unit that contains the analog-to-digital (AD) converter, timer function, channel selection, and other modules' drivers was also responsible for data preprocessing and system activation or hibernation. In addition, it also integrated embedded programs used to transfer data and commands between the node and the coordinator. In this design, TI high-performance 16 bit MSP430 was used in the microprocessing unit. Not only did it run efficiently, but also the power consumption was very low, which met the power requirements of the wireless network system.

3.4. Flash Storage. The storage used Nand flash which has the advantages of large capacity and can be read and written at a fast speed. In this system, it could be used to store the data



CH: Data acquisition channels

FIGURE 2: Architecture of the SA-based wireless seismic monitoring system.

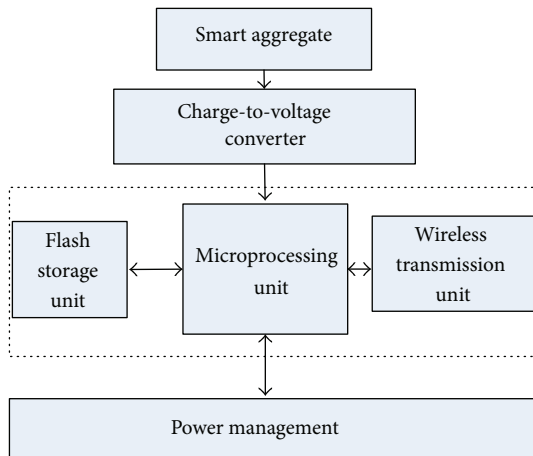


FIGURE 3: Structure of wireless node.

obtained by timing acquisition and also could be used for the interim storage of other data.

3.5. Wireless Transmission Unit. The wireless transmission unit was in charge of sending and receiving orders or data. It used the CC2520 + CC2951 modules that can realize a long-distance data transmission, where the CC2520 chip is the second generation ZigBee/IEEE802.15.4 radio frequency transceiver that has a wide supply range of 1.8–3.8 V and excellent link budget of 103 dB. The CC2951 chip was a cost-effective and high-performance RF Front End for low-power and low-voltage 2.4 GHz wireless applications, which could increase the link budget by providing a power amplifier for increased output power and a LNA with low noise feature for improved receiver sensitivity.

3.6. Power Management Block. A 24 V large-capacity lithium battery was used as the power source of the entire node. In order to meet the different supply needs of each chip and

circuit unit, the 24 V lithium battery output voltage could be transformed as ± 15 V, ± 12 V, and ± 3.3 V outputs after the conversion of the DC-DC and LDO chips.

4. Design of Application Software for Data Acquisition and Analysis

The application software was developed by the C++ language, using object-oriented programming and full plug-in architecture, which featured reliable and highly scalable performance. It supported two working conditions: the signal acquisition and postprocessing analysis. The software architecture is shown in Figure 4. It mainly consisted of parameter settings, acquisition mode, waveform display, data processing and analysis, and data conversion and storage.

The parameter setting module sets the input signal type, input range, sensor sensitivity, bias, and other functions. The data processing and analysis block conducted modal analysis, power spectrum analysis, and Lissajous pattern analysis, and it also had access to a variety of statistical information, such as maximum, minimum, peak-to-peak, and RMS.

5. Performance of the SA-Based Wireless Monitoring System

5.1. Experimental Setup. The performance of the integrated wireless monitoring system was evaluated by the dynamic loading test. The test configuration is shown in Figure 5. The dynamic stress was applied on the SA by the servo-hydraulic test machine (MTS 810). The high-impedence charge signal was converted to the low-impedence voltage signal by a charge-to-voltage converter (HK9209, Hengke Tech. Co., China). The capacitance of the converter was set to 5000 nF. The converted voltage signals then were measured by the wireless system and the wired system in parallel (NI-4472 module, National Instruments). The sampling frequencies of both the wireless and wired system were all set to 100 Hz. The wired system also measured the load signal applied by the servo-hydraulic test machine. Figure 6 shows a photo of the test.

The loading scheme applied on the SA is shown in Figure 7. Firstly, a static compressive stress of 24 MPa was applied on the SA, which lasted for 15 minutes to allow the exhaustion of the depolarization process of the PZT material [18]. Then, a dynamic stress in a cosine wave form with a frequency of 3 Hz and stress range of 1.6–16 MPa was applied. The picked loading frequency was within the resonant frequency of general earthquake ground motions. The highest loading stress of about 40 MPa corresponded to the crushing strength of commonly used concrete. The test aimed to evaluate the performance of the wireless monitoring system in measuring the structure’s response during full damage processes under strong earthquake ground motions.

The profile of the applied alternating stress and the SA output voltage measured by the wired and the wireless monitoring system are depicted in Figure 8. It can be seen that the two measurements are quite close and their waveforms are close to the applied stresses. This test indicates that

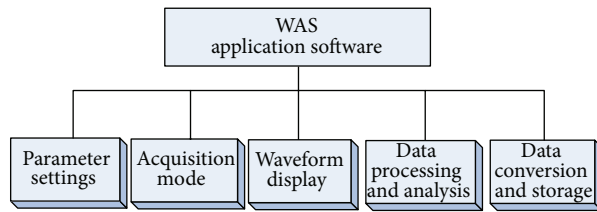


FIGURE 4: Architecture of the application software.

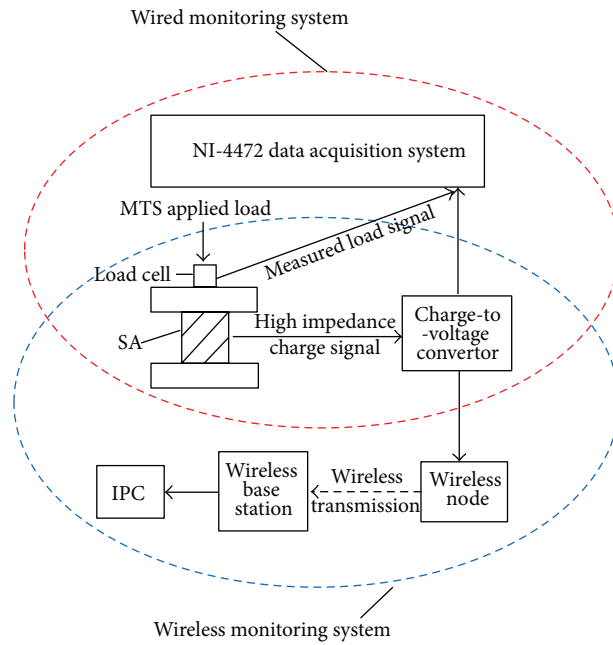


FIGURE 5: Configuration of the test system.

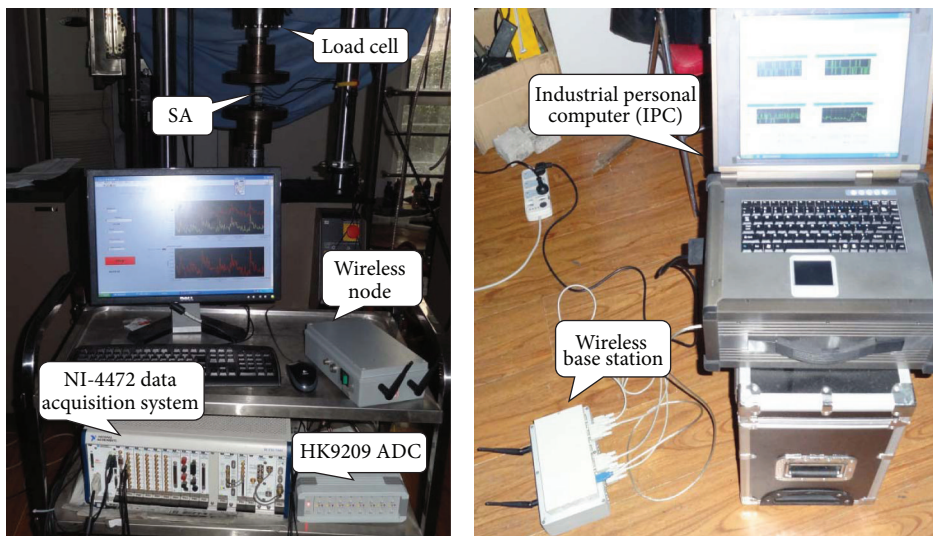


FIGURE 6: A photo of the test system to measure the dynamic excitation.

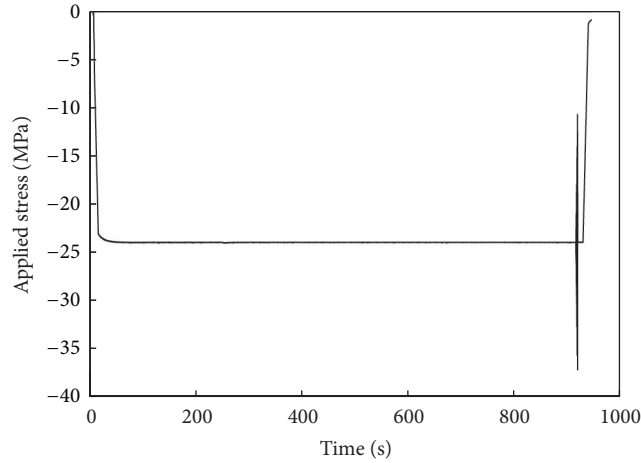


FIGURE 7: Loading scheme.

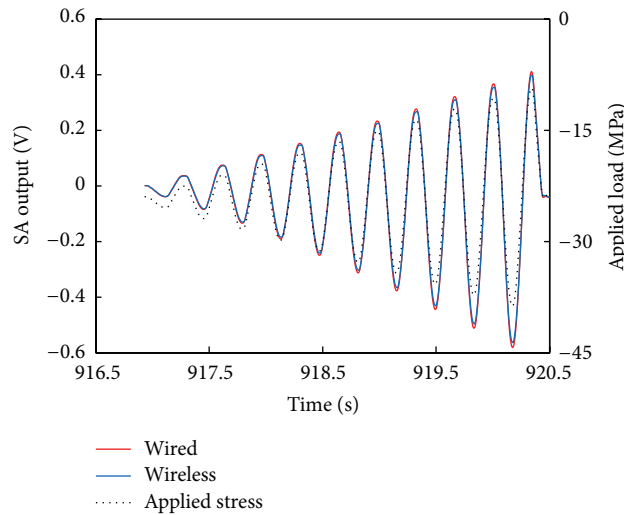


FIGURE 8: Applied stresses and the SA output voltage measured by the wireless and the wired monitoring systems.

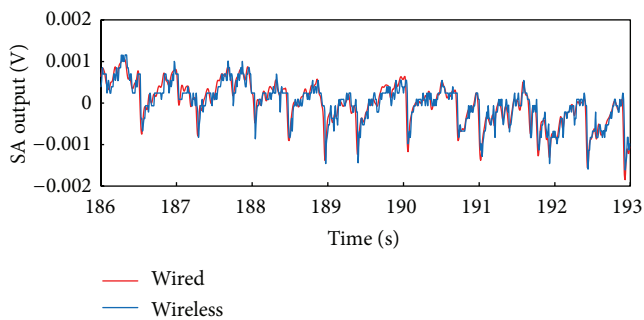


FIGURE 9: SA output measured by the wireless and wired monitoring system.

the wireless system is able to accurately measure the full damage process of the concrete structures under strong earthquake ground motions.

5.2. Measurement of Tiny Random Excitation. When the static stress applied to the SA was maintained constant, tiny

random vibrations still existed due to the perturbation of the servo-hydraulic system. The tiny variations of the output voltage from the SA were also measured by both the wired and the wireless monitoring system. These results allow us to evaluate the resolution of the integrated wireless monitoring system. The resolution of the system determines the weakest detectable response of the concrete structures resulting from minor earthquakes that are much more likely to occur than the strong earthquakes. Although it is unlikely that structural damage will occur during a minor earthquake, the structural response is still useful to improve human understanding of the structures global behaviors.

The results are compared as shown in Figure 9. It can be seen that the results of the two measurements are very close during 917 s to 920.5 s. The amplitude of the output voltage is 0.001 V, which corresponds to the stress of 0.04 MPa. This indicates that the wireless monitoring system has a high resolution and is capable of monitoring the response of the structure under minor earthquakes. The FFT results of these two measurements are also compared in Figure 10. It can be

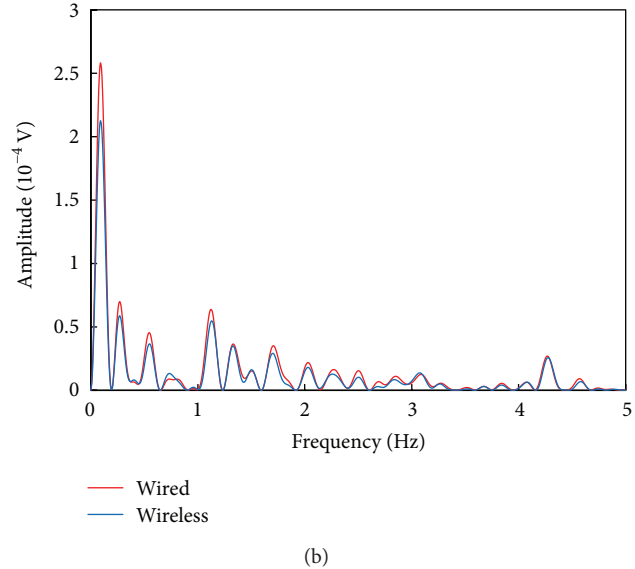
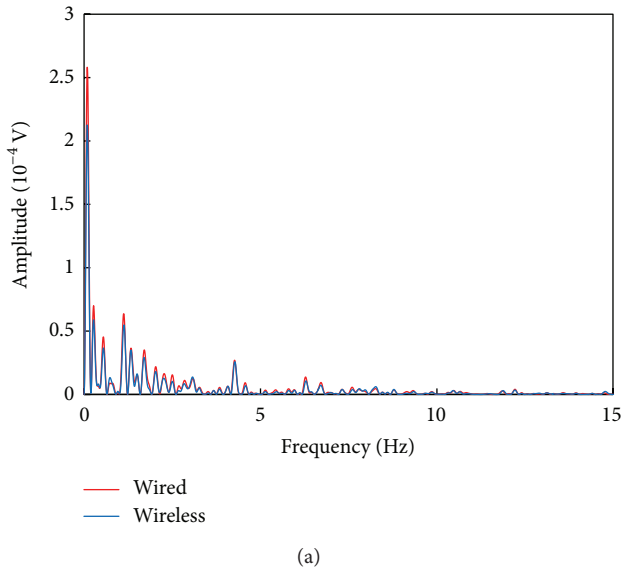


FIGURE 10: FFT results of the wired and wireless measurements in the frequency range of (a) 0–15 Hz and (b) 0–5 Hz.

seen that the frequency components are distributed in the low-frequency range of 0–5 Hz, which is similar to that of the earthquake ground motions. The frequency spectra of these two measurements are almost the same, reconfirming that the integrated wireless monitoring system is also capable of seismic monitoring in terms of frequency response.

6. Conclusions

The smart aggregate has been integrated with a charge-to-voltage converter, a microprocessing unit, a wireless transmission unit, a base station, and a host personal computer to form a wireless seismic monitoring system. The performance of the wireless monitoring system is evaluated through a dynamic loading test. The output voltage of the smart aggregate is measured by the wireless monitoring system and a wired monitoring system in parallel. The test results show that the SA-based wireless seismic monitoring is able to reliably measure the dynamic stress of up to 40 MPa with resolution of 0.04 MPa. This implies that it will measure both the full damage process of concrete structures under strong earthquake ground motions and the dynamic response under minor earthquakes. This study initiates the application of the SA-based wireless networks for full damage process monitoring of concrete structures under strong earthquake ground motion.

Acknowledgments

This paper received financial support (Grants 50908031, 51161120359, and 51108060) from the National Science Foundation of China and the Provincial Education Department of Liaoning Province (Grant no. L2013020).

References

- [1] M. Çelebi, “Real-time seismic monitoring of the New Cape Girardeau Bridge and preliminary analyses of recorded data: an overview,” *Earthquake Spectra*, vol. 22, no. 3, pp. 609–630, 2006.
- [2] J. E. Rodgers and M. Çelebi, “Seismic response and damage detection analyses of an instrumented steel moment-framed building,” *Journal of Structural Engineering*, vol. 132, no. 10, pp. 1543–1552, 2006.
- [3] M. Çelebi, “Recorded earthquake responses from the integrated seismic monitoring network of the Atwood Building, Anchorage, Alaska,” *Earthquake Spectra*, vol. 22, no. 4, pp. 847–864, 2006.
- [4] E. Miranda and V. V. Bertero, “Seismic performance of an instrumented ten-storey reinforced concrete building,” *Earthquake Engineering and Structural Dynamics*, vol. 25, no. 10, pp. 1041–1059, 1996.
- [5] F. Naeim, “Performance of 20 extensively-instrumented buildings during the 1994 Northridge earthquake,” *Structural Design of Tall Buildings*, vol. 7, no. 3, pp. 179–194, 1998.
- [6] C.-M. Uang, Q.-S. Yu, A. Sadre, D. Bonowitz, N. Youssef, and J. Vinkler, “Seismic response of an instrumented 13-story steel frame building damaged in the 1994 Northridge earthquake,” *Earthquake Spectra*, vol. 13, no. 1, pp. 131–149, 1997.
- [7] B. G. Han, B. Z. Han, and J. P. Ou, “Experimental study on use of nickel powder-filled Portland cement-based composite for fabrication of piezoresistive sensors with high sensitivity,” *Sensors and Actuators A*, vol. 149, no. 1, pp. 51–55, 2009.
- [8] B. Han and J. Ou, “Embedded piezoresistive cement-based stress/strain sensor,” *Sensors and Actuators A*, vol. 138, no. 2, pp. 294–298, 2007.
- [9] H. Xiao, H. Li, and J. Ou, “Modeling of piezoresistivity of carbon black filled cement-based composites under multi-axial strain,” *Sensors and Actuators A*, vol. 160, no. 1-2, pp. 87–93, 2010.
- [10] H. Xiao, H. Li, and J. Ou, “Strain sensing properties of cement-based sensors embedded at various stress zones in a bending concrete beam,” *Sensors and Actuators A*, vol. 167, no. 2, pp. 581–587, 2011.

- [11] G. Song, H. Gu, Y. L. Mo, T. Hsu, H. Dhonde, and R. R. H. Zhu, "Health monitoring of a concrete structure using piezoceramic materials," in *Smart Structures and Materials 2005: Sensors and Smart Structures Technologies for Civil, Mechanical, and Aerospace Systems*, vol. 5765 of *Proceedings of SPIE*, pp. 108–119, March 2005.
- [12] S. Yan, W. Sun, G. Song et al., "Health monitoring of reinforced concrete shear walls using smart aggregates," *Smart Materials and Structures*, vol. 18, no. 4, Article ID 047001, 2009.
- [13] H. Gu, Y. Moslehy, D. Sanders, G. Song, and Y. L. Mo, "Multi-functional smart aggregate-based structural health monitoring of circular reinforced concrete columns subjected to seismic excitations," *Smart Materials and Structures*, vol. 19, no. 6, Article ID 065026, 2010.
- [14] A. Laskar, H. Gu, Y. L. Mo, and G. Song, "Progressive collapse of a two-story reinforced concrete frame with embedded smart aggregates," *Smart Materials and Structures*, vol. 18, no. 7, Article ID 075001, 2009.
- [15] Y. Moslehy, H. Gu, A. Belarbi, Y. L. Mo, and G. Song, "Smart aggregate based damage detection of circular RC columns under cyclic combined loading," *Smart Materials and Structures*, vol. 19, no. 6, Article ID 065021, 2010.
- [16] X. Yang, Z. Li, Y. Ding, and Z. Li, "Test on sensor effect of cement matrix piezoelectric composite," *Transactions of Tianjin University*, vol. 11, no. 2, pp. 133–136, 2005.
- [17] Z. Li, X. Yang, and Z. Li, "Application of cement-based piezoelectric sensors for monitoring traffic flows," *Journal of Transportation Engineering*, vol. 132, no. 7, pp. 565–573, 2006.
- [18] S. Hou, H. B. Zhang, and J. P. Ou, "A PZT-based smart aggregate for compressive seismic stress monitoring," *Smart Materials and Structures*, vol. 21, no. 10, Article ID 105035, 2012.
- [19] Y. Yu, J. Ou, J. Zhang, C. Zhang, and L. Li, "Development of wireless MEMS inclination sensor system for swing monitoring of large-scale hook structures," *IEEE Transactions on Industrial Electronics*, vol. 56, no. 4, pp. 1072–1078, 2009.
- [20] W. -S. Jang, D. -E. Lee, and J. -H. Choi, "Ad-hoc performance of wireless sensor network for large scale civil and construction engineering applications," *Automation in Construction*, vol. 26, pp. 32–45, 2012.
- [21] M. J. Chae, H. S. Yoo, J. Y. Kim, and M. Y. Cho, "Development of a wireless sensor network system for suspension bridge health monitoring," *Automation in Construction*, vol. 21, pp. 237–252, 2012.
- [22] P. Katsikogiannis, E. Zervas, and G. Kaltsas, "A wireless sensor network for building structural health monitoring and seismic detection," *Physica Status Solidi C*, vol. 5, no. 12, pp. 3834–3838, 2008.
- [23] J. P. Lynch, Y. Wang, K. J. Loh, J.-H. Yi, and C.-B. Yun, "Performance monitoring of the Geumdang Bridge using a dense network of high-resolution wireless sensors," *Smart Materials and Structures*, vol. 15, no. 6, article 008, pp. 1561–1575, 2006.
- [24] T. Nagayama, M. Ushita, and Y. Fujino, "Suspension bridge vibration measurement using multihop wireless sensor networks," *Procedia Engineering*, vol. 14, pp. 761–768, 2011.

Research Article

Mechanism of a Hair Cell Bioinspired Sensor with Ultrasensitivity to Weak and Low Frequency Vibration Signals

L. J. Liu^{1,2} and Y. Lei²

¹ Department of Mechanical and Electrical Engineering, Xiamen University, Xiamen 361005, China

² Department of Civil Engineering, Xiamen University, Xiamen 361005, China

Correspondence should be addressed to Y. Lei; ylei@xmu.edu.cn

Received 6 July 2013; Accepted 24 September 2013

Academic Editor: Ting-Hua Yi

Copyright © 2013 L. J. Liu and Y. Lei. This is an open access article distributed under the Creative Commons Attribution License, which permits unrestricted use, distribution, and reproduction in any medium, provided the original work is properly cited.

Although significant progresses have been made in sensor technology, it is still a challenging task to develop ultrasensitive sensors to monitor very weak and low frequency vibration signal for early warning of natural disasters and efficient structural health monitoring of infrastructures. It has been reported from previous experiments that some fishes have acute sensitivities to extremely low frequency linear acceleration due to the otolith organs of the inner ear. In this paper, based on the experimental results and qualitative mechanism of the infrasound sensitivity of some fishes conducted by other researchers, a bioinspired gating spring model with negative stiffness is established to simulate the mechanical-electricity transduction of the hair cell in fish ear. Then, numerical analyses of the mechanical model subject to static and dynamic loading are conducted, respectively. It is shown that the gating model has adaptive amplification capability to weak and low frequency excitation compared with the corresponding linear model. This mechanism can be used for the design of bioinspired ultrasensitive sensors for monitoring weak and low frequency vibration signal.

1. Introduction

It is essential to develop high sensitive sensors for early warning of natural disasters and efficient health monitoring of infrastructures [1, 2]. Nowadays, infrastructures are large in size. Ambient vibration signals of these large scale infrastructures including tall buildings and long span bridges are weak, low-frequency dominated with frequencies less than 1 Hz and sometimes around 0.1 Hz, and flooded in the ambient noise as the spectra of typical ambient noise grow toward the lower frequencies [3]. Also, structural damage is essentially a local phenomenon; thus only high sensitive sensors near the site of damage can sense the minor changes of vibration signal caused by damage. Moreover, weak and low frequency vibration signals can also be used to monitor natural hazards other than earthquakes, such as rock avalanches, debris flow, and flooding [4]. Amitrano et al. [5] indicated that the frequency range of 0.1–1 Hz is the most sensitive to mudslide velocity and that the frequency range of 0.01–10 Hz is associated with landslide deformation. Kao et al. [6] found

two distinct seismic signatures of landslides with tremor-like waveforms and a predominant frequency band of 0.5–5 Hz. Feng [7] indicated that the frequency range of 0.5 to 1.5 Hz is the main frequency of the seismic signal of the Shiaolin landslide occurring in Taiwan in 2009. Dammeier et al. [8] showed that it is possible not only to locate the landslides to within a few kilometers but also to extract information about the characteristics of the landslide from the seismic signals. Thus, seismic signals may be abnormal and in the range of infrasound during geological disasters, such as landslides, and spread to the surrounding air medium. Velocity of infrasound is much larger than that of landslide, so imminent landslides can be forecasted through infrasound monitoring by advancements in ultrasensitive low frequency sensors.

Although a lot of advanced sensors have been developed for monitoring weak and low frequency vibration signal, these sensors are too bulky, large energy consuming, and expensive; for example, a Streckeisen STS-2 seismometer weights 9 kg and costs more than 10 k US dollars, which can

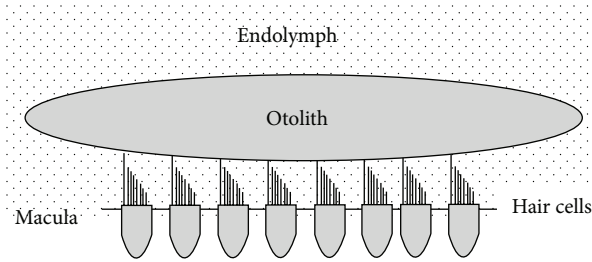


FIGURE 1: Schematic of the hair cells in relation to the otolith, redrawn from Popper [9].

hardly meet the demands on a large number of sensitive sensors for monitoring large size structures and natural disasters. Also, current sensors do not have adaptive sensitivity; that is, sensors with high sensitivity to weak signals, intended for ambient monitoring, will saturate during strong excitation.

On the other hand, former experiments have shown that some fishes, such as teleost species, can detect very weak and low frequencies motion. At 0.1 Hz, the particle acceleration threshold of Atlantic cod was about 10^{-5} m/s^2 [10, 11]. All plaice readily responded to infrasound down to 0.1 Hz with threshold of approximately $4 \cdot 10^{-5} \text{ m/s}^2$ [11, 12]. The infrasound sensitivity observed in these experiments depends on the otolith organs and not the lateral line [11]. The experimental research also found that blocking the lateral-line system did not affect the sensitivity to the infrasound stimulation [13].

The otolith organs contain a dense calcified matrix (the otolith) overlying a sensory epithelium (or macula) containing hair cells as shown in Figure 1 redrawn from Popper [9]. The basic structure of the otolith organs of fishes closely resembles that of an accelerometer—a mass that moves in a relative manner to some kind of receptor. The otolith serves as the mass, whereas the sensory hair cells serve as the receptors [16]. Sand and Karlsen [17] indicated an otolith organ as a simple harmonic oscillator. The unaided otolith organs of the inner ear are not sensitive to sound pressure but to linear accelerations, which is the more relevant stimulus parameter at very low frequencies [11]. Actually, the hair cells display adaptive signal amplification to mechanical stimuli, leading to high sensitivity to weak input and low sensitivity to high input, thus expanding the dynamic range through adaptive amplification [18].

Recently, some researchers have studied ultrasensitive low frequency sensors using the high sensitivity of fish's hearing ability to infrasound. Lim and Park [21] investigated the mechanical model of gating spring mechanism of stereocilia. Zhang et al. [22] simulated the octopus' hearing system as dynamic oscillating system. The modeling results agree reasonably well with the experimental audiograms (acceleration threshold, velocity threshold, and sound pressure level) of the three cephalopod species. Zheng et al. [23] developed capacitive accelerometer incorporating positive and negative feedbacks into the system, inspired by the operation mechanisms of the inner ear hair cells. Lee and Park [24] developed a mechanical model consisting of an inverted

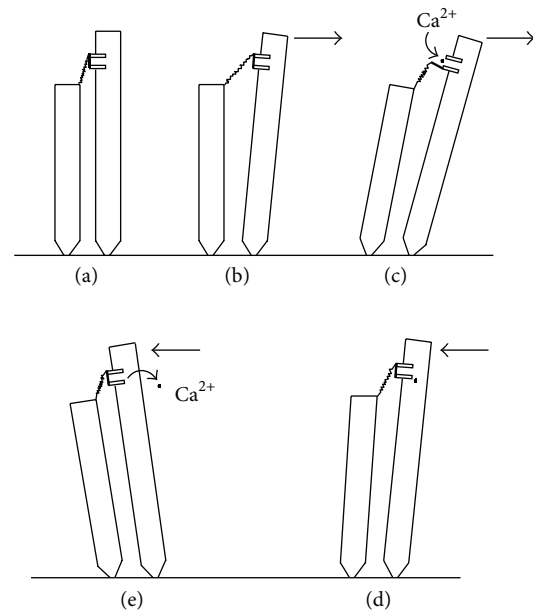


FIGURE 2: Mechanical behaviors of a hair bundle, redrawn from Hudspeth [14, 15].

pendulum and a fixed T-bar that mimic the interaction of two adjacent stereocilia, and a magnet pair was attached to the top of the inverted pendulum and the fixed T-bar to emulate the negative resistance of the tip link due to the transient stiffness softening by the gating ion channel. The authors have also studied the mechanism of gating model of hair cell subject to static and dynamic loading at the tip of the tallest stereocilia [25].

In this paper, based on observed experimental results from other researchers [10–13] on the mechanism of the sensitivity of fish's inner ear to extremely weak low frequency motion, a bioinspired mechanical model with gating spring for simulating the mechanical-electricity transduction of fish's hair cell is established. Then, numerical responses of the mechanical model subject to static loading and ground motion are analyzed by the Open System for Earthquake Engineering Simulation (OpenSees), a popular software for simulating the seismic response of structural systems. Finally, mechanical functions of the proposed mechanical model on the design of new high sensitive bioinspired low frequency sensors for effective monitoring the vibration signals of civil infrastructures and early warning of natural disasters are addressed.

2. Mechanical Behaviors of Fish's Hair Bundle

A fish's hair cell bundle may contain from 20 to 300 stereocilia aligned in the order of height, which are interconnected by long protein strings called tip links. Stereocilia are relatively stiff and pivot at a tapered base. In hair cells of the inner ear, mechanical stimulation supplies the work necessary to open transduction channels. The dense otolith provides a stimulus for the hair cells, which results in the shear deformations of the hair cell [11]. In Figure 2(a), Stereocilia

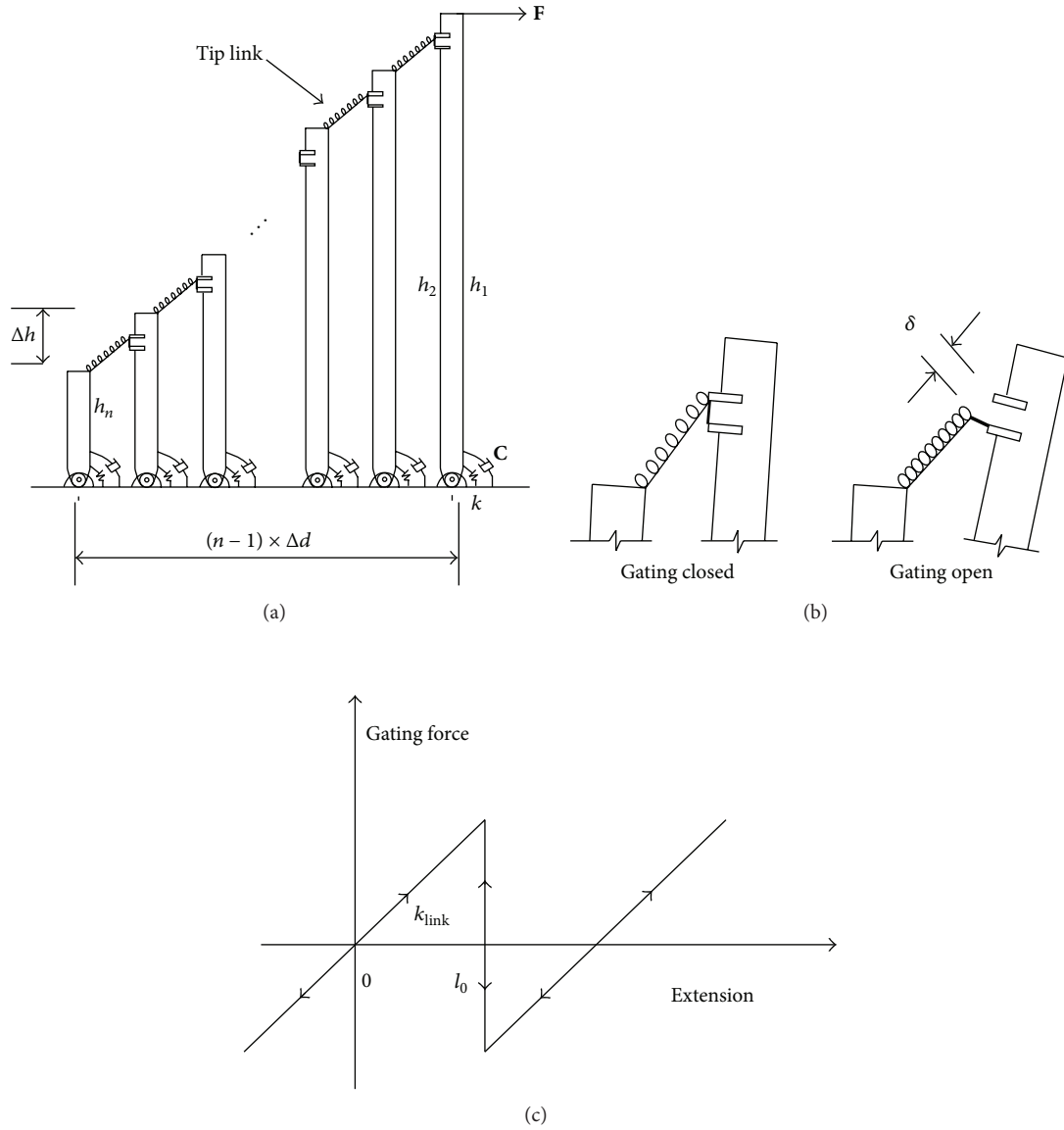


FIGURE 3: Simulation model of stereocilia bundle. (a) Stereocilia bundle; (b) gating spring (tip link) and ion channel; (c) sketch of stiffness of the gating spring.

bundles are in resting state and ion channels are closed. When a hair bundle is deflected by the positive phase of a sinusoidal stimulus (Figure 2(b)), increased tension of tip link opens the ion channels at the tip of the stereocilia, and Ca^{2+} enters through the transduction channel (Figure 2(c)). Then the associated tip link shortens, and the tension in the link falls. Relaxation of the tip link acts like an external force in the positive direction, causing the bundle to move still further. The reduced tension in the tip link then permits the channel to reclose (Figure 2(d)). As the channel shuts, the increased tension in the tip link exerts a force that moves the bundle in the negative direction. When the ion is extruded by a membrane Ca^{2+} pump, the hair bundle is primed to repeat the cycle (Figure 2(e)) [14, 15].

3. A Bioinspired Mechanical Model

3.1. *Modeling.* Based on the mechanical behaviors of fish's hair bundle and the bioinspired mechanism, an electromechanical model that extends the gating-spring model described by Lim and Park [21] is established to simulate the adaptive signal amplification functions of the auditory hair cells of fish. This model consists of an inverted pendulum array of 21 stereocilia bundles supported by pivotal springs at the base and interconnected by tip link springs. Each stereocilium is modeled as a rigid bar with a hinge joint at its base that approximates the nonbending, rotational motion of a stereocilia's tapered base, as shown in Figure 3(a). Based on the biomechanics characteristics of tip link and ion channel described in Figure 2, the gating

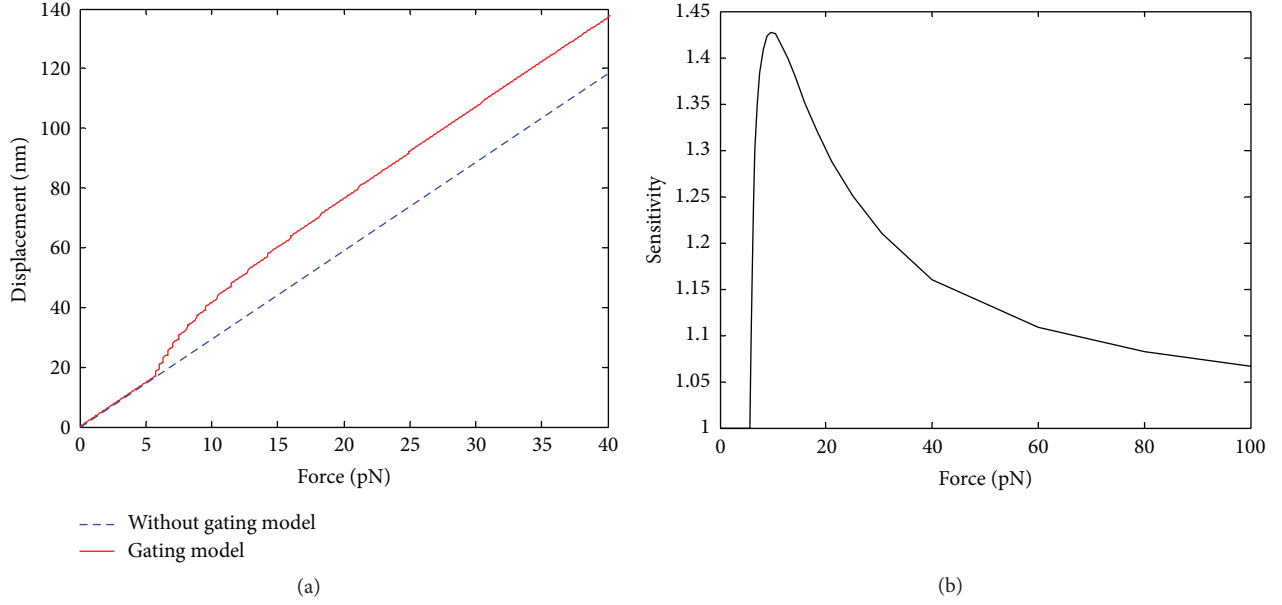


FIGURE 4: Analysis result of the two models subject to static loading. (a) Comparisons of displacement at the tip of the tallest stereocilium under static loading. (b) The sensitivity of the gating model subject to static loading.

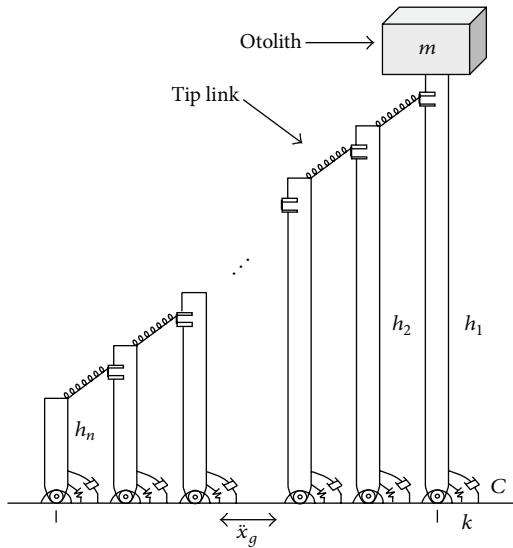


FIGURE 5: Model subject to ground acceleration motion.

spring is modeled by the nonlinear spring characteristics to simulate the tip-link and ion gating channel and connects the tip of the adjacent stereocilium, as shown in Figure 3(b).

The gating spring is defined as a nonlinear elastic spring with variational stiffness shown in Figure 3(c). The gating force f_i applied between the two adjacent stereocilia (the i th and the $(i + 1)$ th stereocilia) can be described as follows [21]:

$$\begin{aligned} x &\leq l_0, \text{ closed, } f_i = k_{\text{link}}x, \\ x &> l_0, \text{ open, } f_i = k_{\text{link}}(x - \delta), \end{aligned} \quad (1)$$

where x is the extension of the tip link, k_{link} is the linear stiffness of the gating spring, and δ is the gating displacement shown in Figure 3(b), and l_0 is the critical tip link extension between gate closed and open, defined by (2) [21]:

$$l_0 = \frac{\Delta E}{k_{\text{link}}\delta} + \frac{\delta}{2}, \quad (2)$$

$$\Delta E = \Delta E_{\text{closed}} - \Delta E_{\text{open}} = \frac{1}{2} \times k_{\text{link}} \times [l_0^2 - (l_0 - \delta)^2]$$

in which ΔE is energy difference before and after channel opening.

Mechanical model of the above stereocilia bundles is established by OpenSees with the parameters of mechanical model shown in Table 1. Detailed explanations of the parameters in the table are shown after Table 1.

3.2. Analyses of the Model Subject to Static Loading. A static external force \mathbf{F} is applied at the top of the tallest stereocilium shown in Figure 3(a). The governing equation of the stereocilia array can be obtained as follows:

$$\mathbf{K}\boldsymbol{\theta} = \mathbf{T}_{\text{link}} + \mathbf{T}_{\text{ext}}, \quad (3)$$

where $\boldsymbol{\theta}$ is the vector of angular displacement of the stereocilia bundles and \mathbf{K} is the tensional stiffness matrix defined by:

$$\mathbf{K} = \begin{bmatrix} k_{11} & & \\ & k_{ii} & \\ & & k_{nn} \end{bmatrix}, \quad i = 1, \dots, n, \quad n = 21 \quad (4)$$

in which k_{ii} is the pivotal stiffness of the i th stereocilium, $k_{11} = k_{22} = \dots = k_{ii} = \dots = k_{nn} = k$, n is the number of stereocilia, $n = 21$.

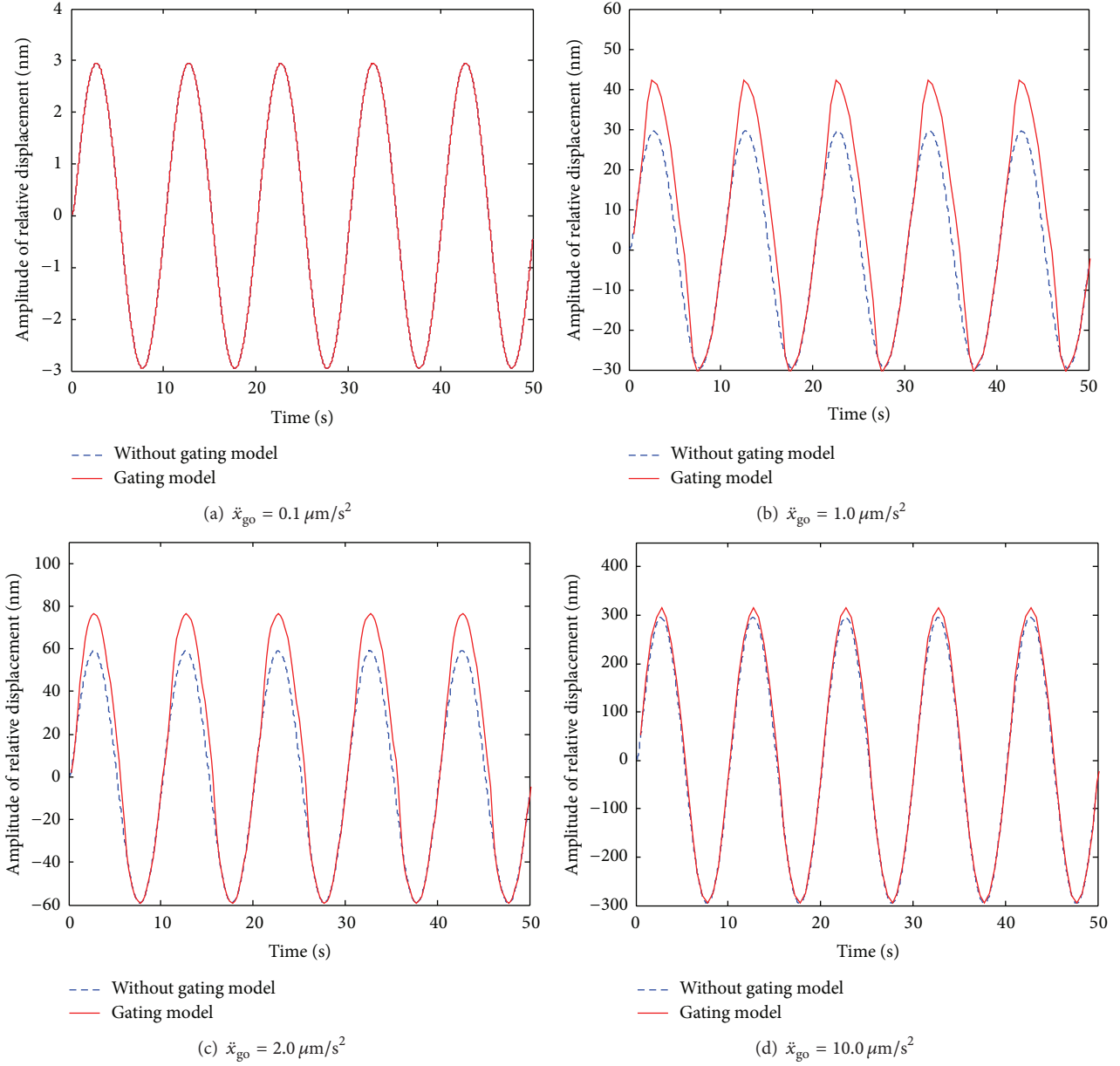


FIGURE 6: The time history chats on displacement at the tip of the tallest stereocilium of two models under ground motion at 0.1 Hz.

\mathbf{T}_{ext} is the vector of external torque defined as

$$\mathbf{T}_{\text{ext}} = [\mathbf{F}h_1, \mathbf{0}, \mathbf{0}, \dots, \mathbf{0}]_{1 \times n}^T. \quad (5)$$

\mathbf{T}_{link} is the vector of torque exerted by the tip link defined by

$$\mathbf{T}_{\text{link}} = [\mathbf{T}_1 \ \mathbf{T}_2 \ \dots \ \mathbf{T}_i \ \dots \ \mathbf{T}_n]^T, \quad i = 1, \dots, n,$$

$$\mathbf{T}_i = \begin{cases} -\mathbf{f}_i (h_{i+1} + \Delta) \cos \alpha, & i = 1 \\ [\mathbf{f}_{i-1}h_i - \mathbf{f}_i (h_{i+1} + \Delta)] \cos \alpha, & i = 2, \dots, n-1 \\ \mathbf{f}_{i-1}h_i \cos \alpha, & i = n, \end{cases} \quad (6)$$

where \mathbf{T}_i is the vector of torque of i th stereocilium exerted by the adjacent tip link and \mathbf{f}_i is the vector of gating force applied

between the i th and the $(i+1)$ th stereocilium, defined as (1). h_i is the height of i th stereocilium, α is the angle of gating force \mathbf{f}_i with respect to the horizontal, and Δ is the height difference between each end of the tip link springs.

The magnitudes of the static external load range from 0 to 100 pN with an interval of 0.02 pN. The displacements at the tip of the tallest stereocilium in the two models with gating and without gating are calculated by OpenSees, respectively.

Figure 4(a) shows the comparisons of displacements at the tip of the tallest Stereocilia in the two models subject to variation of static loading. The threshold force required to open the first gate spring is 5.76 pN, which is a very small value. It is clear that twenty gates are opened sequentially one by one. The amplification of gating model is defined as the

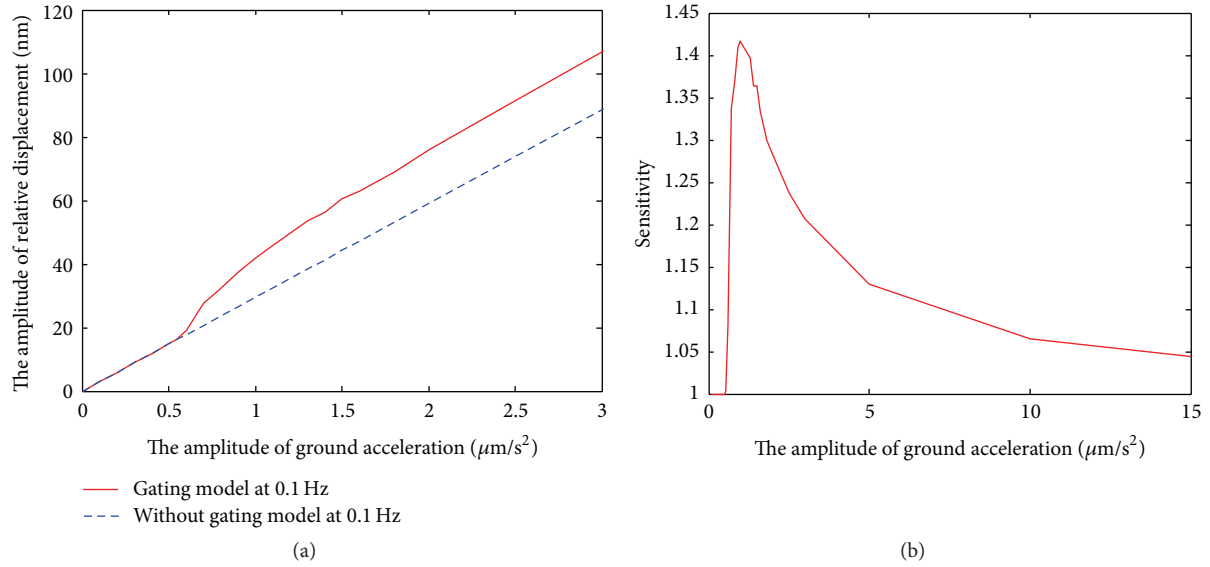


FIGURE 7: Analysis result of the two models subject to ground acceleration motion. (a) Comparisons of the amplitudes of relative displacements at the tip of the tallest stereocilium in the two models subject to ground acceleration motion. (b) The sensitivity of the gating model subject to ground acceleration motion.

TABLE 1: Parameters of simulation model.

Item	Value	Definition	Reference
D	$0.24 \mu\text{m}$	Diameter of the stereocilia	[19]
h_1	$2.34 \mu\text{m}$	Height of the tallest stereocilium	[20]
Δh	90 nm	Height difference of stereocilia	[21]
Δd	40 nm	Spacing between the stereocilia	[19]
D	10 nm	Diameter of the tip link	[19]
L	57 nm	Length of the tip link	[19]
α	45°	Angle of tip link with respect to the horizontal direction.	[19]
Δ	40 nm	Height difference between each end of the tip link spring	[19]
E_s	$3 \times 10^9 \text{ N/m}^2$	Young's modulus of Stereocilia	[19, 20]
E_t	$1 \times 10^7 \text{ N/m}^2$	Young's modulus of tip link	[20]
K	100 pN· $\mu\text{m}/\text{rad}$	Pivotal stiffness of the stereocilia	Estimated
k_{link}	13.7 pN/nm	Stiffness of the tip link	Calculated
ΔE	65 zJ	Energy difference after channel opening	[21]
Δ	1.14 nm	Gating distance of tip link	Calculated
l_0	$l \times 1\%$	The critical tip link extension between gate closed and open	Estimated
ζ	0.7	Damping ratio of model	Estimated

Details of some parameters are listed below:

- (1) E_s —Young's modulus of Stereocilia, measured value for actin filaments by Cotton and Grant [19, 20].
- (2) E_t —Young's modulus of tiplink. The table value shown was determined to be the lowest value which will allow tip links to carry a significant percentage of bundle stiffness [20].
- (3) α —angle of tiplink with respect to the horizontal direction, estimated from TEM and SEM by Cotton and Grant [19].
- (4) k —pivotal stiffness of a single stereocilia; the table value shown was determined to make the stereocilia bundles have sufficient stiffness.
- (5) k_{link} —stiffness of the tiplink, calculated from parameters E_t , A_t , and l_0 . A_t is the sectional area of tip link calculated from diameter of the tip link d .
- (6) ζ —damping ratio of model. The otolith and hair cells are surrounded by endolymph, the larger damping of the each stereocilia is simplified as the viscous damping, and damping ratio $\zeta = 0.7$.

ratio of the amplitude of displacement of gating model and that of the model of without gating. As shown in Figure 4(b), the amplification is in rising tendency with the increasing of external load for small values of loading and trends to decrease for larger values of external loading. Therefore, the model is highly sensitive to weak external loading and lowly

sensitive to large external loading, due to the negative stiffness of gating spring.

3.3. *Analyses of the Model Subject to Ground Motion.* The whole stereocilia bundles and the otolith are subject to the ground acceleration motion as shown in Figure 5. The mass

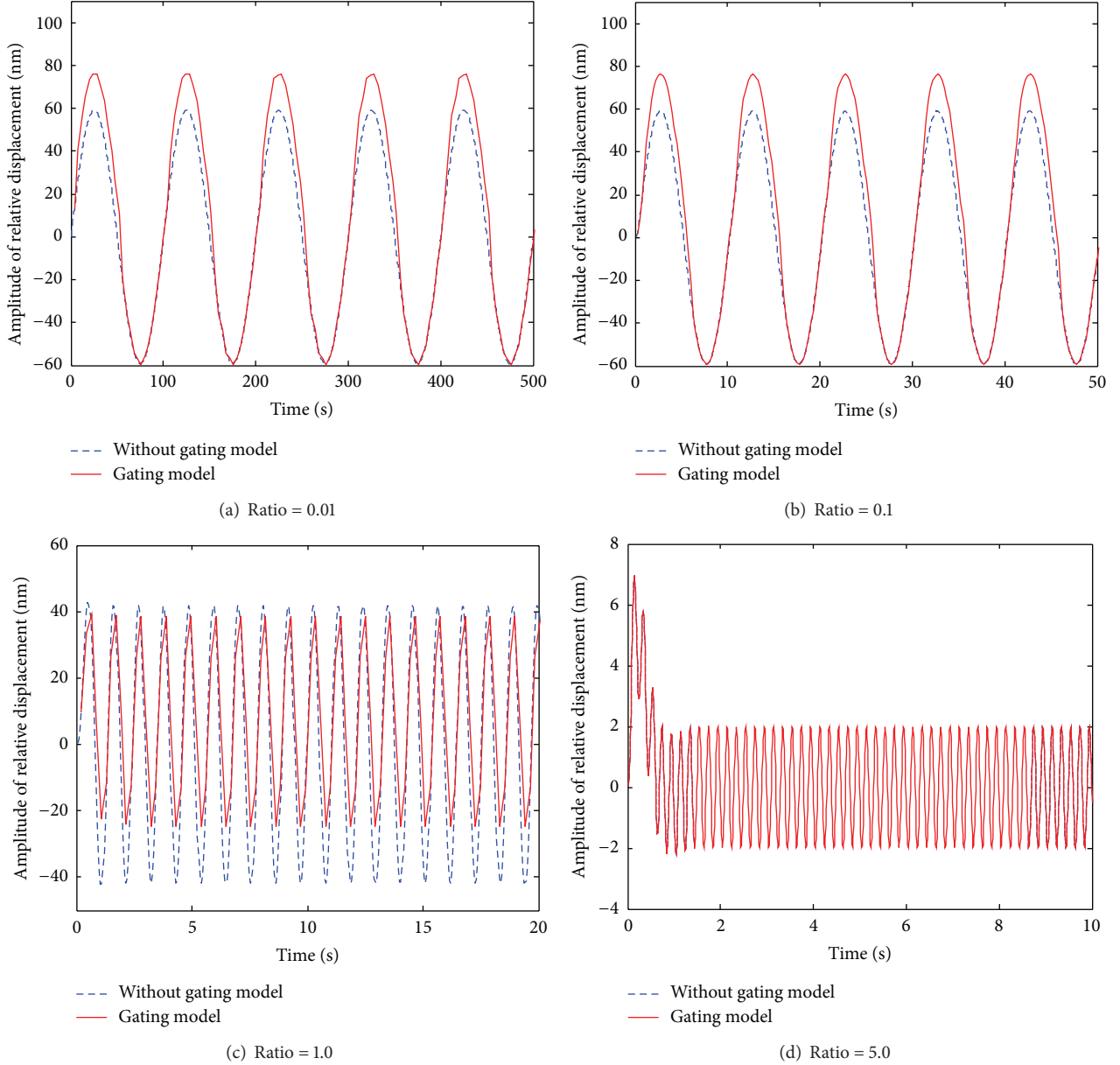


FIGURE 8: The time history chats on relative displacements of two models to frequency ratio.

of each stereocilia bundle is ignored because it is negligible when compared with that of the otolith.

The governing equation of the stereocilia array and the otolith can be obtained as follows:

$$\mathbf{J}\ddot{\boldsymbol{\theta}} + \mathbf{C}\dot{\boldsymbol{\theta}} + \mathbf{K}\boldsymbol{\theta} = \mathbf{T}_{\text{link}} - \mathbf{T}_g, \quad (7)$$

where $\ddot{\boldsymbol{\theta}}$, $\dot{\boldsymbol{\theta}}$, and $\boldsymbol{\theta}$ are the angular acceleration, angular velocity, and angular displacement of the stereocilia bundles relative to the ground motion, respectively, \mathbf{K} is the tensional stiffness matrix defined by (4), and \mathbf{J} is the mass moment of inertia matrix for the stereocilia bundles defined as:

$$\mathbf{J} = \frac{1}{3} \begin{bmatrix} m_1 h_1^2 & & \\ & m_i h_i^2 & \\ & & m_n h_n^2 \end{bmatrix}, \quad i = 1, \dots, n \quad (8)$$

in which h_i is the height of i th stereocilium, and m_i is the mass of the i th stereocilia, $m_i/h_i = 10^{-15}$ g/nm. \mathbf{C} is the viscous damping coefficient matrix. Because the whole hair bundle and otolith are surround with endolymph, the damping of the each stereocilium is simplified as lager viscous damping ratios $\zeta = 0.7$. \mathbf{T}_{link} is the vector of torque exerted by the tip link defined by (6) and \mathbf{T}_g is the vector of torque exerted by ground motion:

$$\mathbf{T}_g = [m\ddot{x}_g h_1, 0, 0, \dots, 0]_{1 \times n}^T \quad (9)$$

in which m is the mass of the otolith, $m = 10$ mg [26], and $\ddot{x}_g(t)$ is the ground acceleration.

To examine the adaptive amplification of the gating model to the amplitude of external excitation, it is assumed that

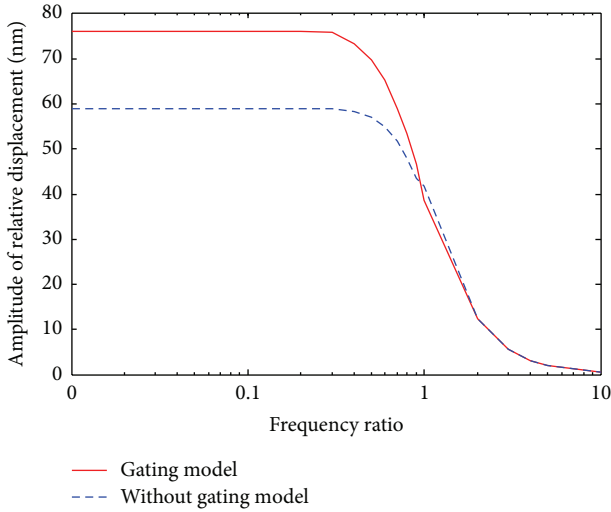


FIGURE 9: The comparisons of relative displacements to frequency ratio of two models.

the gating model and model without gating are subject to the ground acceleration motion in sinusoidal wave; that is, $\ddot{x}_g(t) = \ddot{x}_{go} \sin \omega t$, respectively. The amplitude of ground acceleration \ddot{x}_{go} ranges from 0 to $15.0 \mu\text{m/s}^2$. The nature frequency of the two models of gating model and linear model without gating is 0.927 Hz.

The displacement responses at the tip of the tallest stereocilium in the two models (with gating spring and without gating spring) are calculated by OpenSees. Figure 6 shows the time history of the relative displacement responses of the tip of the tallest stereocilium of the two models subjected to sinusoidal ground motion with a different amplitude \ddot{x}_{go} . Figure 7(a) shows the comparisons of the amplitudes of displacement response at the tip of the tallest stereocilium (or the otolith) in the two models subjected to ground acceleration motion with variations of amplitudes \ddot{x}_{go} . The threshold amplitude of acceleration required to open the first gate spring is $0.58 \mu\text{m/s}^2$ at 0.1 Hz. As shown in Figure 7(b), the amplification is in highly rising tendency at the weak amplitude of the ground acceleration and is in descent tendency at the larger amplitude of the ground acceleration. This conforms that the hair cell model has adaptive amplification capability and is more sensitive to weak motion, due to the negative stiffness of gating spring.

To examine the adaptive amplification of the gating model to the frequency of external excitation, the gating model and model without gating are subject to sinusoidal ground acceleration motion with variational frequency ω . The amplitude of ground acceleration \ddot{x}_{go} is assumed as $2.0 \mu\text{m/s}^2$, which exceeds the threshold amplitude. Figures 8(a)–8(d) show the time history of the relative displacement responses of the tip of the tallest stereocilium of the two models subjected to ground motion with different sets of excitation frequency ratios ω/ω_n . The comparisons of the amplitudes of relative displacements of two models subject to sinusoidal ground acceleration motion with variational

excitation frequency ratios ω/ω_n are shown in Figure 9. For ground acceleration at low frequency ($0 \leq \omega/\omega_n \leq 0.6$), larger amplitude is clearly shown in the gating model than that of the model without gating, due to adaptive amplification caused by gating spring. However, the amplitudes of the responses of two models are almost the same for high frequency excitation ($\omega/\omega_n > 0.6$).

3.4. Low Frequency Thresholds for Gating Hair Cell Model.

Low frequency thresholds for gating hair cell model are defined as the amplitude of ground motion required to open the first gate spring; that is, the first ion channels is opened, because opening the transduction channel in the cilia and allowing the entry of calcium ions into the cell result in a cascade of events that leads to the release of chemical neurotransmitters from the base of the cell. The neurotransmitter crosses a small gap between cells and excites the endings of the nerve that innervates the cell. This, in turn, results in an electrical potential (the action potential) in the nerve that is carried to the brain.

Acceleration threshold of ground motion for gating hair cell model is shown in Figure 10(a). The thresholds at 0.01 Hz and 0.1 Hz are all approximately $0.58 \mu\text{m/s}^2$ (or $-11 \text{ dB re: } 1 \mu\text{m/s}^2$). It is shown clearly that acceleration threshold is in sharp increase with the rise of frequency when the exciting frequency exceed the nature frequency (0.927 Hz). Meanwhile, below the upper frequency cutoff, the acceleration thresholds audiogram is virtually flat, as predicted by Sand and Karlsen [17]. The acceleration thresholds audiogram of gating hair cell model is also similar with that of perch tested by Karlsen shown in Figure 10(b) [13]. These two figures both depict that when thresholds are related to particle acceleration, which is the relevant stimulus parameter at very low frequencies, the apparent drop in sensitivity towards low frequencies disappears.

4. Conclusions

In this paper, based on the experimental results of the infrasound sensitivity of some fishes from other researchers, a bioinspired gating spring model with negative stiffness is established to simulate the mechanical-electricity transduction of the hair cell in fish inner ear. Through numerical analyses of the model by OpenSees, it is shown that the gating model is more sensitive to weak excitation and low frequency ground acceleration motion due to the negative stiffness of whole stereocilia bundles caused by the opening of gating spring.

The gating model simulating the mechanical-electricity transduction of hair cell and its mechanical function can be used as the theoretical basis for the design of bioinspired sensors with adaptive amplification capability and ultrasensitivity to weak and low vibration signals for efficient monitoring of infrastructures and early warning of natural disasters.

This paper only conducts numerical analyses of the mechanism of a hair cell bioinspired sensor. Further experiment validation work of presented mechanism is necessary.

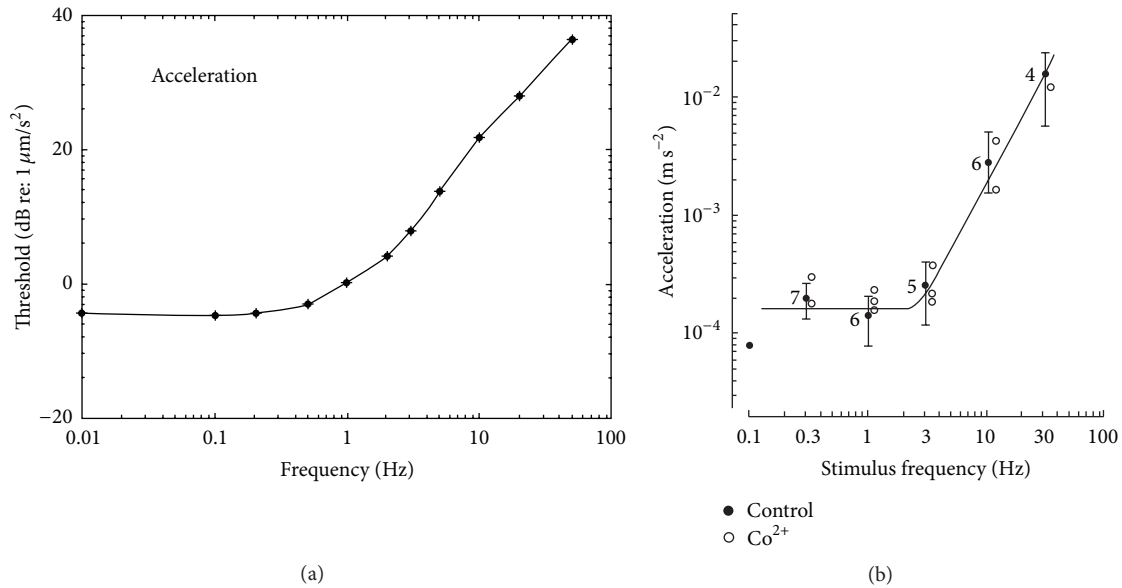


FIGURE 10: Acceleration threshold of fish ear. (a) Acceleration threshold for gating hair cell model; (b) acceleration thresholds for perch stimulated at different frequencies from Karlsten [13].

Acknowledgments

This work is sponsored by the Natural Science Foundation of China (no. 51308482) and by the Key Project of Fujian Province of China (no. 2013Y0079). The authors are also grateful to Professor Y. F. Zhang of University of Maryland for his great contributions to the research project.

References

- [1] S. D. Glaser, M. Li, M. L. Wang, J. Ou, and J. Lynch, "Sensor technology innovation for the advancement of structural health monitoring: a strategic program of US-China research for the next decade," *Smart Structures and Systems*, vol. 3, no. 2, pp. 221–244, 2007.
- [2] T. H. Yi and H. N. Li, "Methodology developments in sensor placement for health monitoring of civil infrastructures," *International Journal of Distributed Sensor Networks*, vol. 2012, Article ID 612726, 11 pages, 2012.
- [3] T. H. Yi, H. N. Li, and X. Y. Zhao, "Noise smoothing for structural vibration test signals using an improved wavelet thresholding technique," *Sensors*, vol. 12, no. 8, pp. 11205–11220, 2012.
- [4] Z.-Y. Feng, "The seismic signatures of the surge wave from the 2009 Xiaolin landslide-dam breach in Taiwan," *Hydrological Processes*, vol. 26, no. 9, pp. 1342–1351, 2012.
- [5] D. Amitrano, S. Gaffet, J.-P. Malet, and O. Maquaire, "Understanding mudslides through micro-seismic monitoring: the Super-Sauze (South-East French Alps) case study," *Bulletin de la Societe Geologique de France*, vol. 178, no. 2, pp. 149–158, 2007.
- [6] H. Kao, C. Kan, R. Chen et al., "Locating, monitoring, and characterizing typhoon-induced landslides with real-time seismic signals," *Landslides*, vol. 9, no. 4, pp. 557–563, 2012.
- [7] Z. Feng, "The seismic signatures of the 2009 Shiaolin landslide in Taiwan," *Natural Hazards and Earth System Science*, vol. 11, no. 5, pp. 1559–1569, 2011.
- [8] F. Dammeier, J. R. Moore, F. Haslinger, and S. Loew, "Characterization of alpine rockslides using statistical analysis of seismic signals," *Journal of Geophysical Research F*, vol. 116, no. 4, Article ID F04024, 2011.
- [9] A. N. Popper, "Final Report: effects of exposure to seismic air-guns on the ears of Atlantic cod (*Gadus morhua*)," 2006, <http://www.cnsopb.ns.ca/pdfs/HuntAtlanticCodReport.pdf>.
- [10] O. Sand and H. E. Karlsten, "Detection of infrasound by the Atlantic cod," *Journal of Experimental Biology*, vol. 125, pp. 197–204, 1986.
- [11] A. N. Popper, R. R. Fay, C. Platt, and O. Sand, "Sound detection mechanisms and capabilities of teleost fishes," in *Sensory Processing in Aquatic Environments*, S. Collin and N. Marshall, Eds., pp. 3–38, Springer, New York, NY, USA, 2003.
- [12] H. E. Karlsten, "Infrasound sensitivity in the plaice (*Pleuronectes platessa*)," *The Journal of Experimental Biology*, vol. 171, pp. 173–187, 1992.
- [13] H. E. Karlsten, "The inner ear is responsible for detection of infrasound in the perch (*Perca fluviatilis*)," *The Journal of Experimental Biology*, vol. 171, pp. 163–172, 1992.
- [14] A. J. Hudspeth, Y. Choe, A. D. Mehta, and P. Martin, "Putting ion channels to work: mechano-electrical transduction, adaptation, and amplification by hair cells," *Proceedings of the National Academy of Sciences of the United States of America*, vol. 97, no. 22, pp. 11765–11772, 2000.
- [15] A. J. Hudspeth, "How the ear's works work: mechano-electrical transduction and amplification by hair cells," *Comptes Rendus Biologies*, vol. 328, no. 2, pp. 155–162, 2005.
- [16] A. N. Popper and R. R. Fay, "Rethinking sound detection by fishes," *Hearing Research*, vol. 273, no. 1-2, pp. 25–36, 2011.
- [17] O. Sand and H. E. Karlsten, "Detection of infrasound and linear acceleration in fishes," *Philosophical Transactions of the Royal Society B*, vol. 355, no. 1401, pp. 1295–1298, 2000.
- [18] A. J. Hudspeth, "Mechanical amplification of stimuli by hair cells," *Current Opinion in Neurobiology*, vol. 7, no. 4, pp. 480–486, 1997.

- [19] J. Cotton and W. Grant, "Computational models of hair cell bundle mechanics: II. Simplified bundle models," *Hearing Research*, vol. 197, no. 1-2, pp. 105-111, 2004.
- [20] J. Silber, J. Cotton, J.-H. Nam, E. H. Peterson, and W. Grant, "Computational models of hair cell bundle mechanics: III. 3-D utricular bundles," *Hearing Research*, vol. 197, no. 1-2, pp. 112-130, 2004.
- [21] K. Lim and S. Park, "A mechanical model of the gating spring mechanism of stereocilia," *Journal of Biomechanics*, vol. 42, no. 13, pp. 2158-2164, 2009.
- [22] Y. F. Zhang, F. Shi, J. K. Song, and X. G. Zhang, "Hearing characteristics of cephalopod: modeling and environmental impact study," in *Proceedings of the International Conference of Environmental Changes on the Sensory World of Fish/Aquatic Animals and Fisheries*, Shanghai, China, October-November 2012.
- [23] Q. Zheng, Y. Zhang, Y. Lei, J. Song, and Y. Xu, "Haircell-inspired capacitive accelerometer with both high sensitivity and broad dynamic range," in *Proceedings of the 9th IEEE Sensors Conference (SENSORS '10)*, pp. 1468-1473, Waikoloa, Hawaii, USA, November 2010.
- [24] C. Lee and S. Park, "A mechanical model of stereocilia that demonstrates a shift in the high-sensitivity region due to the interplay of a negative stiffness and an adaptation mechanism," *Bioinspiration & Biomimetics*, vol. 7, no. 4, Article ID 046013, 2012.
- [25] L. J. Liu and Y. Lei, "Mechanism of bio-inspired ultrasensitive low frequency sensor with mechanics analysis," *Applied Mechanics and Materials*, vol. 252, pp. 162-166, 2013.
- [26] J. Z. Shen, W. X. Cao, Y. B. Cui, and J. Chang, "The relationship between otolith-weight and age with reference to its use in age determination for *Carassius auratus*," *Acta Hydrobiological Sinica*, vol. 26, no. 6, pp. 662-668, 2002.

Research Article

A Revised Counter-Propagation Network Model Integrating Rough Set for Structural Damage Detection

Shao-Fei Jiang,¹ Chun Fu,^{1,2} Chun-Ming Zhang,³ and Zhao-Qi Wu¹

¹ College of Civil Engineering, Fuzhou University, Fuzhou 350108, China

² College of Petroleum Engineering, Liao Ning Shihua University, Fushun, Liaoning 113001, China

³ College of Resources and Civil Engineering, Northeastern University, Shenyang, Liaoning 110004, China

Correspondence should be addressed to Shao-Fei Jiang; cejsf@163.com

Received 30 June 2013; Accepted 20 September 2013

Academic Editor: Gangbing Song

Copyright © 2013 Shao-Fei Jiang et al. This is an open access article distributed under the Creative Commons Attribution License, which permits unrestricted use, distribution, and reproduction in any medium, provided the original work is properly cited.

This paper proposes a revised counter-propagation network (CPN) model by integrating rough set in structural damage detection, applicable for processing redundant and uncertain information as well as assessing structural health states. Firstly, rough set is used in the model to deal with a large volume of data; secondly, a revised training algorithm is developed to improve the capabilities of the CPN model; and lastly, the least input vectors are input to the revised CPN (RCPN) model, hence the rough set-based RCPN is proposed in the paper. To validate the model proposed, numerical experiments are conducted, and, as a result, six damage patterns have been successfully identified in a steel frame. The influence of measurement noise, the network models adopted, and the data preprocessing methods on damage identification is also discussed in the paper. The results show that the proposed model not only has good damage detection capability and noise tolerance, but also significantly reduces the data storage requirement and saves computing time.

1. Introduction

The Structural Health Monitoring (SHM) issue has attracted more and more attention, largely due to the rapid increase in the number of deteriorated and damaged structures, especially tall buildings, long span bridges, and large spatial structures [1, 2]. Great efforts have been made to develop SHM techniques and damage detection methods, some of which have been applied to practical engineering problems to some extent in the past two decades [3, 4]. Although the number of permanent structural health monitoring systems installed in various kinds of structures is increasing, it is still of an emergency and constitutes a big challenge as to how to deal effectively with the uncertainties inherent in the great volume of measured data from the health monitoring systems [5].

Recently, neural networks are becoming increasingly popular with data processing and damage detection due to their powerful nonlinear modeling capability and high fault tolerance [1, 6–11]. Although such methods are available and applicable for processing of uncertain data from SHM systems in some cases, these neural network models also have

some disadvantages, for instance, local optimal solution and poor extrapolation for a BP network, complex network architecture for a fuzzy neural network structure, and difficult determination of the parameter σ of Gaussian kernel function in a probabilistic neural network [9]. The counter-propagation network (CPN) began to be adopted in pattern classification, function approximation, and statistical analysis not very long ago [10, 11], because it has a relatively simple network structure and does not have an error criterion for convergence owing to its combination of the Kohonen self-organizing map and Grossberg competitive learning network model [12, 13]. Nevertheless, the CPN model often requires higher data storage memory and more runtime than other neural network models [10, 11]. Consequently, for any CPN model which is applied to practical engineering problems, it is becoming increasingly urgent and vital to develop efficient learning algorithms and reduce the spatial dimensions of the measured data from the SHM systems of large and complex structures.

Numerous techniques have been developed to extract feature parameters and reduce the spatial dimensions of the

great quantities of data, for example, principal component analysis (PCA) and kernel principal component analysis [3, 4, 14, 15]. These multivariate statistics-based methods are efficient for some problems that are involved with dimension reduction, but in other cases, they either cause key information loss or fail the precise physical interpretation of results. When this happens, intelligent information techniques, such as neural networks, fuzzy logic, data fusion, and rough set, are usually needed for solving uncertainty and imprecision as well as dealing with the large amount of data concerning feature extraction and damage detection [2, 8, 9]. Compared with multivariable statistical analysis methods, intelligent information techniques are considered to be more efficient in solving the above problems, because (1) they can treat both numerical data and linguistic data taken together in an uncertain and imprecise situation, (2) they can allow for nonlinear relationships in the analysis, and (3) they lead to more precise physical interpretation. As a consequence, there has been a rapid growth in interest in rough set theory and its applications recently [7–9, 16, 17]. Some scholars have tried to combine rough set with other intelligent methods in order to reduce uncertainty and spatial dimension of data, thereby to improve pattern recognition and damage diagnosis accuracy [7–9, 16, 17]. To date, in spite of great efforts on developing integrating methodologies, few of them seem to be successful in dealing with great quantities of noisy measured data.

In view of the abovementioned description, it is no denying that it is necessary and significant to develop efficient data processing and damage detection methods. In the following sections, the training algorithm of a CPN model is revised firstly, and then the revised CPN model and rough set are integrated to address the processing of great quantities of information with uncertainty, as well as to detect damages in a structure. Finally, a novel damage detection model is presented, which is especially suitable for structural damage detection with noisy data and/or a great volume of measured data. In the validation of the proposed model, both single- and multidamage patterns of a 7-story steel frame are detected, and its effects on the performance of the model are investigated as well.

The rest of the paper is organized as follows. The principles of counter-propagation network are briefly reviewed in Section 2. In Section 3, we propose a revised counter-propagation network (CPN) model by integrating rough set for structural damage detection. In Section 4, six damage patterns from a steel frame are identified firstly, and then the effects of measurement noise, network models, and data preprocessing methods on damage detection results are also discussed, respectively. Finally, Section 5 draws some conclusions and remarks.

2. Counter-Propagation Network (CPN)

The counter-propagation neural network (CPN) has been described in great detail in relevant textbooks and articles [10, 11, 18]. Its applications in damage detection and fault diagnosis are also reported in the literature [14, 18–20]. Therefore, only a brief introduction of CPN is given in the paper as for how the CPN works.

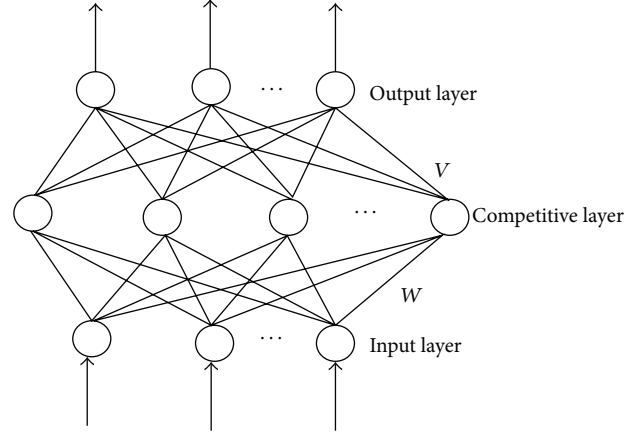


FIGURE 1: Architecture of a CPN model.

In general, a CPN model consists of three layers (as shown in Figure 1), specifically, input layer, competitive layer, and output layer [10, 18, 19]. The first two layers constitute self-organising maps (SOMs). The SOM performs the mapping of input data into two-dimensional plane, and in most cases, neurons are ordered in a rectangular or hexagonal matrix. The last two layers form a Grossberg network [10, 11, 18], which is a general competitive network model.

From the input layer to the output layer, the winning neuron of competitive layer is obtained in accordance with the self-organization mapping (SOM) learning norm, and then the connecting weights between the input layer and the competitive layer are adjusted using the following learning rule:

$$W_g(\text{new}) = W_g(\text{old}) + \alpha [A - W_g(\text{old})], \quad (1)$$

where W_g is the weight connecting the winning neuron g in the competitive layer to each neuron in the input layer; α is the learning rate; A is the input vector.

From the competitive layer to the output layer, the actual output value of each output neuron is attained in accordance with the learning rule of a general competitive network, and the connecting weights between them are adjusted according to the supervised learning algorithm. Then the weight vectors are modified by the following equation:

$$V_g(\text{new}) = V_g(\text{old}) + \beta b_g [C - V_c(\text{old})], \quad (2)$$

where V_g is the weight connecting the winning neuron g in the competitive layer to neurons in the output layer; b_g is the output value of neuron g , with a value of 1; C is the desired output vector corresponding to the input vector A ; β is the learning rate.

CPN has been widely used in the fields of pattern recognition, decision-making optimization, and robot intelligence for its adaptability and robustness. In addition, CPN is a hybrid network, which combines unsupervised learning with supervised learning and thus enjoys the advantages of both teacher type and nonteacher type networks, such as simple structure, less iterations of data set, and no error criterion for convergence. However, the CPN model often requires

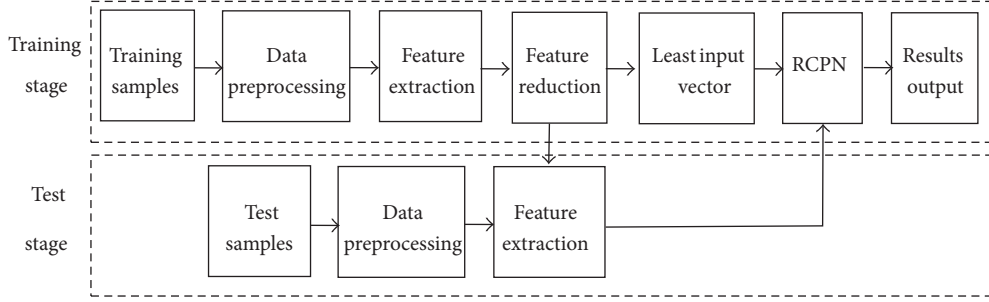


FIGURE 2: Structural damage detection method.

much larger storage memory and more computing time than other neural network models, and it might fail in its learning process when the same weight value is adjusted for samples with similar values. So we hereby propose a novel revised CPN (RCPN) to address the abovementioned problems, and more details can be seen in Section 3.4.

In recent years, rough set has attracted increasingly more attention and has been applied to structural health monitoring and damage detection owing to its capability of processing the data uncertainty and reducing the space dimension of data [21, 22]. To take advantage of both rough set and neural network methods, a novel damage detection method based on the CPN model combined with rough set is proposed in this paper, and a comparison of different methods' performance is also conducted.

3. Structural Damage Detection Methods

To improve the capabilities of damage detection methods in dealing with massive data redundancy and noise, rough set is used for reducing redundant data and a revised counter-propagation neural network (RCPN) is adopted for damage detection. Thereby, a 6-phase structural damage detection method based on rough set and RCPN is proposed, which involves data preprocessing, feature extraction, feature reduction, least input vector, RCPN, and results output as shown in Figure 2.

3.1. Data Preprocessing and Feature Extraction. On account of environment variations, measurement errors, the skills of erectors, and so forth, measurement noise and errors are inevitably introduced along with the true data acquired from multisensors in structural damage detection and health monitoring. As a consequence, the digitized raw data must be preprocessed to eliminate noise and errors using threshold, averaging, and image processing techniques before it goes through subsequent phases.

3.2. Feature Extraction. Feature extraction plays an important role in damage detection and structural health monitoring because it has a remarkable impact on processing efficiency and detection results. Frequency, mode shape, and the combined feature indices of structures are used to detect the damages of structures, because it is easy to

extract this information from structural responses. In doing so, the normalized damage signature index (NDSI) and the normalized frequency change ratio (NFCR) are employed as features in this study, which are denoted as follows [7, 9]:

$$\begin{aligned} \text{NFCR}_i &= \frac{\text{FFC}_i}{\sum_{j=1}^m \text{FFC}_j}, \\ \text{NDSI}_i &= \frac{\text{DSI}_i(k)}{\sum_{j=1}^n |\text{DSI}_j(k)|}, \end{aligned} \quad (3)$$

where FFC_i ($\text{FFC}_i = (f_{ui} - f_{di})/f_{ui}$) and DSI_i ($\text{DSI}_i = (\{\Phi_{ui}\} - \{\Phi_{di}\})/(f_{ui}^2 - f_{di}^2)$) are the fractional frequency change and damage signature index of the i th mode, respectively; m is the number of modes with measured frequencies; n is the total number of normalized damage indices; f_{ui} and f_{di} are the frequencies of the i th mode of the structure in the undamaged and damaged states; $\{\Phi_{ui}\}$ and $\{\Phi_{di}\}$ are the modal vector values of the i th mode in the undamaged and damaged states, respectively.

3.3. Feature Reduction and Least Input Vector. Rough set is employed to implement the feature reduction. Attribute discretization and reduction are two key aspects of the rough set theory. Attribute reduction mainly refers to the reduction of condition attributes in a decision table. When the rough set theory is employed to process data for a training sample, all data must be discretized before the reduction of condition attributes can be performed on the decision table created.

3.3.1. Discretization of Continuous Attribute Values. Rough set analysis is a symbolized analysis method where the continuous variable must be discretized. K -means are used to discretize condition attribute values.

K -means clustering is a partitioning method that treats observations in data as objects having locations and distances from each other. It partitions the objects into k mutually exclusive clusters so that objects within each cluster are as close to each other as possible and as far as possible from objects in other clusters. Each cluster is characterized by its centroid or centre point. The K -means function in MATLAB is employed to analyze condition attributes, and the function `KMEANS` is called to complete K -means clustering, using an iterative algorithm that assigns objects to clusters so that the

sum of distances from each object to its cluster centroid, over all clusters, is a minimum.

3.3.2. Constructing the Decision Table. On the basis of the rough set theory, a two-dimensional table, known as a decision table, is created, where each row describes an object while each column describes an attribute of the object. Decision pertains mainly to decision attributes. Discretized features are condition attributes, and damage patterns are decision attributes.

3.3.3. Reduction of Attributes. Reduction of attributes is implemented by removing all redundant condition attributes, meanwhile keeping indispensable attributes in the decision table, which is governed by reduction rules. During the process of attribute reduction, there are numerous types of reduction rules [7, 8, 20], and the importance of attribute is selected as a reduction rule owing to its precision and convenience. The reduced decision table has the same function as the original decision table but contains fewer condition attributes. A computer program developed is finally run to achieve the reduction of condition attributes in this study [20].

3.3.4. Least Input Vectors. The least input vectors are created with the least condition attributes for both training samples and test samples. Then these feature parameters, which are mutually independent, are input to the input layer of a revised CPN for structural damage detection purposes.

3.4. Revised Counter-Propagation Network (RCPN). Network structure and learning algorithm are two key issues to a neural network model. For the learning algorithm of a CPN model, all training samples are used to train the network, and the connecting weights are adjusted simultaneously during one training echo. The training phase will stop until the network output error is less than the allowable error or it achieves the maximum training echo. In doing so, the CPN model needs to adjust the connecting weights between the neurons for each sample in each training echo. This not only leads to adjusting the connecting weights every now and then in each iterative step, but also costs longer time in the training phase. Furthermore, the CPN model will not converge in some cases when two samples are very similar [19].

In order to solve the abovementioned problems, a revised CPN learning algorithm is addressed in this study. With the revised learning algorithm, a sample is used to train the CPN model firstly. Only when the network output error is less than the allowable error value or the network reaches the maximum iterative steps will the next sample be continued to train the CPN model. This process is repeated until all samples are done with the training, and the training phase is over finally. It is noted that the trained weights using certain sample will keep unchangeable and will not be adjusted in the training of the next sample [19].

Besides the learning algorithm, another important but difficult task is to determine the architecture of a CPN. Generally, the numbers of neurons in the input layer and output

layer are in accordance with the numbers of least input vectors and pattern classes, respectively. The most difficult issue is to determine the appropriate neuron number of the competitive layer. However, there is no guideline in theory, so it is set by trial and error in this study.

After the architecture of the RCPN model is constructed, the above revised learning algorithm is used to train the RCPN model. A training sample is input to the network, and the weighted input summation of each neuron in the competitive layer is obtained. The winning neuron is the one with the maximum value. Then the connecting weights are trained in accordance with the abovementioned learning algorithm. The training is over when the network output error is up to the allowable error or the network achieves the maximum echo for all training samples.

3.5. Results Output. In the last phase, new test samples are input to the trained RCPN model, and the output of the competitive layer is obtained as follows:

$$b_g = \max_{j=1,2,\dots,Q} \left(\sum_{i=1}^N w_{ji} a_i \right), \quad (4)$$

where b_g is the output of the competitive layer; w_{ji} is the connecting weight between the input layer and competitive layer; a_i is the test sample value; Q is the number of neurons in the competitive layer; N is the number of neurons in the input layer.

The output value of the winning neuron g is 1 in the competitive layer, and the output values of the others are 0. The output of neurons in the output layer is represented as follows:

$$c_j = V_{jg} b_g, \quad (5)$$

where c_j is the output of neurons in the output layer, which indicates the pattern class; V_{jg} is the connecting weight between the competitive layer and output layer.

4. Simulation Examples

4.1. Structural Model and Damage Simulation. To check the applicability and performance of the proposed method, a numerical simulation study is carried out on examples with known values. A scaled 7-story shear-beam type building model with known damages is used to observe the performance of the damage detection method based on RCPN. For comparison purpose, a probabilistic neural network (PNN) model is also applied to detect the damages.

Details of a 7-story shear-beam type steel frame model are as follows: the stiffnesses of all stories are identical; that is, $k_1 = \dots = k_7 = 375$ KN/m. The masses of all stories are also the same, $m_1 = \dots = m_6 = 3.78$ kg, except for the 7th story where $m_7 = 3.31$ kg. According to the solution method of the eigenvalue problem, the natural frequencies and mode shapes of the healthy structural building model can be easily obtained as long as stiffness and mass matrices are known. Damage scenarios were simulated by reduction of the stiffness in each story. Two magnitudes of

TABLE 1: Damage extent and location of each damage pattern.

Pattern class	Small damage	Large damage
Pattern 1	4th story	—
Pattern 2	—	4th story
Pattern 3	6th story	4th story
Pattern 4	3rd and 6th stories	4th story
Pattern 5	3rd story	4th and 6th stories
Pattern 6	—	3rd, 4th, and 6th stories

damage and four damage locations were used to validate the proposed approach. The damage magnitudes were classified quantitatively as small (4.1%) and large (16.7%), while the damage locations were denoted by their corresponding story numbers. Thus six damage patterns were simulated (as shown in Table 1) and are discussed further next.

The numerically simulated response is obtained for 1 s at time step of 0.002 s (500 steps) by using Newmark's constant-acceleration method, and random noise is added. As the natural frequencies and first mode shape could be measured easily and accurately, just as in the healthy building model, natural frequencies of the first four modes and the components of the first mode vector at 7 stories were calculated. In addition, as the noise is inevitable, each set of the analytical computed modal parameters for both healthy and damage scenarios were then added by a random sequence to simulate the measured data; that is,

$$y_i = y_i^a \times (1 + \varepsilon R), \quad (6)$$

where y_i is the measured modal parameter polluted by noise (i.e., natural frequency or modal vector); y_i^a is the analytically computed modal parameter for healthy or a certain damage scenario; R is a normally distributed random variable with zero mean and a derivation of 1; ε is an index representing the noise level; here ε is set to 0.1%, 0.2%, and 0.3%, respectively.

For each noise level, 200 sets were randomly produced for each damage scenario, and thus there were 200 sets of measured data. In these data sets for each scenario, the first 100 sets were used to create training samples, and the others were used to create test samples. As there were totally six damage scenarios, thus a total of $100 \times 6 = 600$ measured data sets were created for training along with a total of 600 measured data sets for test.

4.2. Damage Detection

4.2.1. Damage Detection Model. In order to construct the rough set-based RCPN model (RSRCPN), some work had to be done in advance, such as extracting feature parameters, producing training and test samples, and determining the structure of the network model. Here the model was taken as an example to describe the process of constructing the network model when $\varepsilon = 0.1\%$.

(1) *Feature Extraction.* NFCR and NDSI were taken as feature parameters in this example; thus 7 NDSIs for the components of the first mode vector at 7 stories and 4 NFCRs for the natural frequencies of first four modes were computed by (3).

Six hundred training samples and another six hundred test samples different from the training samples were produced. Each feature parameter was regarded as a condition attribute, so there were $7 + 4 = 11$ condition attributes for each sample.

(2) *Cluster Analysis.* The function KMEANS in MATLAB was used to analyze cluster condition attributes. Herein 4 clusters were set to 4 by trial and error, which means that the feature parameter data would be classified into 4. This was done using two-phase iterative analysis so that the sum of the distances from each object to its cluster centroid, over all clusters, was minimized. Consequently attribute values could be replaced with the clusters to which that data is affiliated, and the feature parameters for all samples were discretized into discrete data represented with 1, 2, 3, and 4.

(3) *Decision-Table Reduction.* Discretized feature parameters were used to construct the decision table for damage detection, where condition attributes included NFCR1, NFCR2, NFCR3, NFCR4, and NDSI1, NDSI2, ..., NDSI7, and decision attributes consisted of the damage pattern that could be represented by a number ranging from 1 to 6. The rough set-based attribute reduction program [20] was run to reduce the decision table; accordingly, the core sets of feature parameters were NFCR1, NFCR2, NFCR3, NFCR4 and NDSI2, ..., NDSI7, which meant that the feature parameter NDSI1 was redundant and therefore eliminated.

(4) *RCPN Calculation.* In correspondence with the new set of feature parameters of the training and test samples that was produced by the reduction process, the least input vectors were reextracted and subsequently fed to the input layer of the RSRCPN. Thus the number of neurons in the input layer was equal to the number of least condition attributes; that is, $4 + 6 = 10$. The number of neurons in the output layer was six, which meant one neuron corresponded to one damage pattern. The study [23] showed that the number of neurons in the competitive layer had little impact on a CPN model, when it was more than twice that of training samples. As the number of training samples was 600, the number of neurons in the competitive layer was set to 2000. Thus the structure of the rough set-based RCPN (RSRCPN) was represented by 10-2000-6.

After the RSRCPN was configured, the model was trained by the abovementioned revised learning algorithm, wherein both α and β were set to 0.1 in (1) and (2). Once the RSRCPN reached the allowable error or the maximum echo, the training was over.

(5) *Results Output.* Given a sample (or test sample) to the trained RSRCPN, the winning neuron g in the competitive layer and the output values corresponding to output neurons were obtained using (4) and (5), and the classification result was finally attained.

4.2.2. Damage Detection Results. Here the identification accuracy (IA) is defined as the ratio of the total number of correct identification samples to the number of total test samples. Table 2 and Figure 3 show the identification results of test samples.

TABLE 2: Identification results of test samples by using different models.

Method	ε (%)	The number of correct pattern identification						Average IA (%)
		Pattern 1	Pattern 2	Pattern 3	Pattern 4	Pattern 5	Pattern 6	
RSRCPN	0.1	86	93	96	100	100	100	95.83
	0.2	90	81	83	90	100	100	90.67
	0.3	89	67	70	83	96	100	84.17
PCARCPN	0.1	84	97	97	100	100	100	96.33
	0.2	89	79	81	91	100	100	90.00
	0.3	88	66	69	86	97	100	84.33
RCPN	0.1	86	97	97	100	100	100	96.67
	0.2	89	79	81	91	100	100	90.00
	0.3	87	66	69	85	97	100	84.00
RSPNN [7]	0.1	35	95	98	98	100	100	88.00
	0.2	79	50	80	97	100	100	84.33
	0.3	86	44	55	86	99	100	78.33
PNN	0.1	35	95	99	100	100	100	88.17
	0.2	79	53	81	97	100	100	85.00
	0.3	84	43	57	88	99	100	78.50

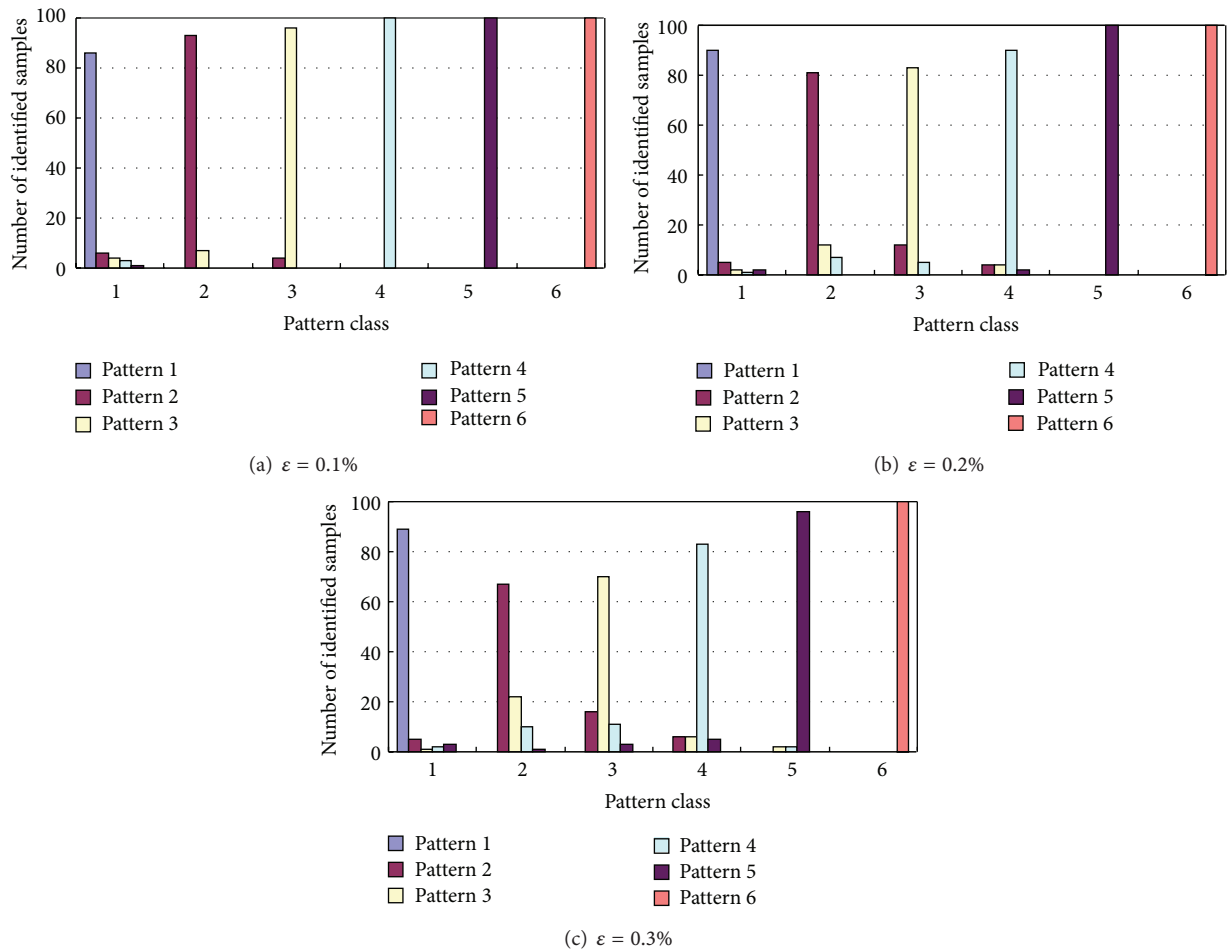


FIGURE 3: Identification results using RSRCPN.

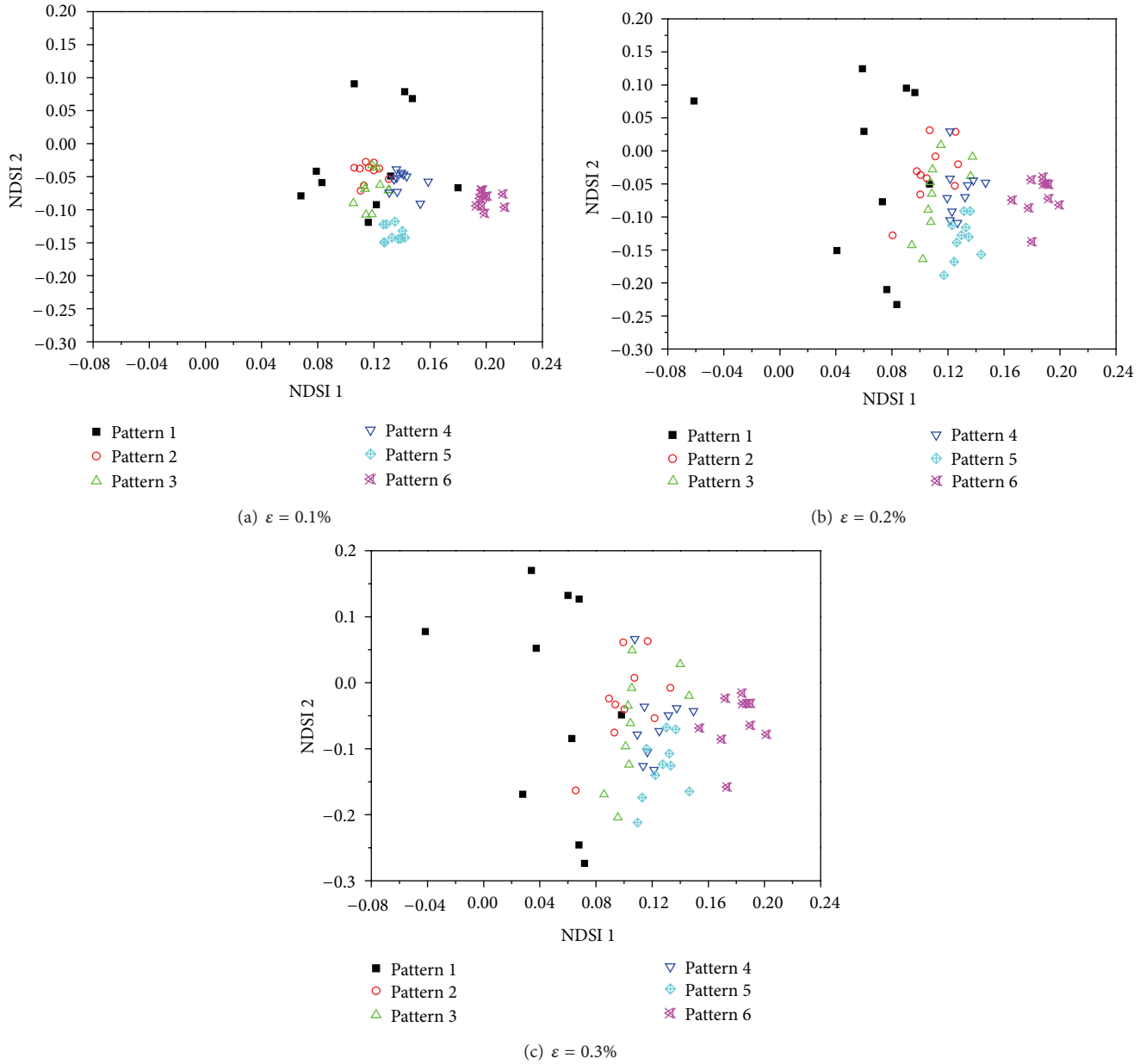


FIGURE 4: The projection diagram of features for each pattern.

It is found that the average IA of RSRCPN is 95.83% for all patterns when $\varepsilon = 0.1\%$. Even in pattern 1, the IA value is the lowest and amounts to 86%. Some samples from pattern 1 are misclassified into other patterns (as shown in Figure 3(a)); that is, 6, 4, 3, and 1 samples belonging to pattern 1 are classified into patterns 2, 3, and 4, respectively. The reason for this is that Pattern 1 has only a small damage extent on the 4th story, whilst patterns 2, 3, and 4 all have large damage extents on the 4th story, and apart from that, pattern 3 has one more small extent damage on the 6th story, and Pattern 4 has additional small extent damages on both the 3rd and 6th stories. Because of the similarity in location and damage extent, the changes in modal parameters for patterns 1, 2, 3, and 4 also look similar, as shown in Figure 4(a).

Apparently, small extent damages result in slight changes of modal parameters. Most of the projection points of pattern 1 are located nearby the point clusters of patterns 2, 3, and 4 (see Figure 4), as a result of which they are misidentified as patterns 2, 3, and 4, hence a low IA for pattern 1. Although some samples belonging to patterns are misclassified into other patterns, such as pattern 2, IA for pattern 2 is not affected since IA is defined as the ratio of the number of correctly identified samples (matching the predefined pattern 2) to the number of total test samples. It is why the model proposed still enjoys high identification accuracy greater than 93% for pattern 2.

Except for patterns 1 and 2, the IA values of other patterns are over 96%; even the IA values of patterns 4, 5, 6 are all up

TABLE 3: Runtime and memory usage comparison of RCPN using different models.

Models	ϵ (%)	Training phase		Test phase	
		Runtime (s)	Memory usage (kB)	Runtime (s)	Memory usage (kB)
RSRCPN	0.1	585.58	664	1.37	384
	0.2	584.16	756	1.38	480
	0.3	589.81	797	1.30	576
PCARCPN	0.1	579.39	544	1.29	356
	0.2	581.94	668	1.33	412
	0.3	584.11	712	1.28	474
RCPN	0.1	612.13	5688	1.46	506
	0.2	611.80	5736	1.44	688
	0.3	612.67	5976	1.42	753

to 100%. As patterns 1, 2, and 3 have larger extent of damage, the samples can be correctly identified from the above three patterns (as shown in Table 2 and Figure 3). It is also observed that the projection points of feature data from patterns 4, 5, and 6 are clearly classified into three different clusters as shown in Figure 4(a); thus none of samples are misclassified for these three patterns. The results indicate that the proposed model has a good damage detection capability.

4.3. Comparison and Discussion. In an attempt to prove the applicability and efficiency, we investigated the effects of measurement noise, network models, and data preprocessing methods on the performance of the RSRCPN model.

4.3.1. Noise Level. Just as $\epsilon = 0.1\%$, the RSRCPN models with other noises, that is, $\epsilon = 0.2\%$ and 0.3% , were constructed, and both structures of RSRCPN models were also 10-2000-6. Then both models were trained and stopped just as the case when $\epsilon = 0.1\%$. The identification results are also shown in Table 2 and Figure 3. Some phenomena are found and deductions are made herein.

First, the average IA value decreases with the increase of noise level, just as expected. As shown in Table 2, the average IA is 95.83% when $\epsilon = 0.1\%$ and still as high as 90.67% when $\epsilon = 0.2\%$. Even when the noise level is up to 0.3% , the average IA is 84.17%. This indicates that the proposed model has good damage detection capability, noise tolerance, and robustness.

Second, it is remarkable that the IA value of pattern 1 does not change or slightly increase with the increase of noise level, contrary to common knowledge. There are three reasons for this [7]: (1) the changes in modal parameters induced by noise are comparatively more significant than those by small extent damage; (2) the number of projection points of pattern 1 located nearby the point clusters of patterns 2, 3, and 4 decreases with noise level (as shown in Figure 4); consequently, the number of samples identified correctly as pattern 1 increases with noise level (as shown in Figure 3 and Table 2); and (3) the neural networks have good tolerance, noise-resistance, and self-learning capabilities. Furthermore, neural network models have better pattern recognition and generality capabilities in noisy environment than in noise-free environment to some extent.

4.3.2. Data Processing Method. We also studied the effects of data processing methods on damage detection using the RCPN model, and the same method as that used in RSRCPN was adopted to construct new classifiers with different data processing methods. Equation (3) were employed to extract features; 4 NFCRs and 7 NDSIs were chosen as inputs. The extracted feature data were directly input to the RCPN model, while the extracted feature data were processed with the principal component analysis and then input to the proposed RCPN model so as to identify damage. It is noted that the components whose contribution ratio is less than 2% are removed. The two models were represented with RCPN and PCARCPN, respectively; thus a comparison study of different models' performance was conducted. The results are listed in Tables 2 and 3, respectively.

In contrast with the RCPN, the average IA changes from 96.67% to 95.83% with a decrease of 0.84% using RSRCPN when $\epsilon = 0.1\%$, and the average IA value rises from 90% to 90.67% with an increase of 0.67% when $\epsilon = 0.2\%$, whilst the average IA is from 84.0% to 84.17% with an increase of only 0.17% when $\epsilon = 0.3\%$. The results show that the proposed model has good damage detection capability and noise tolerance.

Except the identification accuracy, a comparison of different identification models is made in the runtime and memory usage (as shown in Table 3). It is shown that both RSRCPN and PCARCPN models use less time and memory usage than the RCPN model in both training and test phases. For example, the training time of RSRCPN decreases from 612.13 seconds with RCPN to 585.58 seconds, a decrease of 27 seconds when $\epsilon = 0.1\%$, while the training time of PCARCPN decreases from 612.13 seconds with RCPN to 579.39 seconds, a decrease of 32 seconds; with regard to the memory usage, in the training phase, the memory usage decreases from 5688 kB with RCPN to 664 kB with RSRCPN when $\epsilon = 0.1\%$, while the memory usage decreases from 5688 kB with RCPN to 544 kB with PCARCPN. The same phenomenon can be found in the test stage.

All in all, these facts have proven that the proposed model cannot only have good damage detection capability and noise tolerance, but also reduces spatial data dimensions and the memory requirements for data storage without sacrificing identification accuracy.

4.3.3. Network Model. In order to illuminate the advantages of RSRCPN model, the probabilistic neural network (PNN) based on rough set (RSPNN) [9], RCPN, and PNN were employed to identify the above structural model and damage patterns. These models were constructed in a similar way, in which the number of neurons in the input layer was equal to the number of feature vectors, the number of neurons in the output layer was six, each of which corresponded to a damage pattern, the number of training samples was 600, and $\sigma = 0.25$. It is noted that the data used by the RSPNN model were preprocessed using rough set, while the data used by other two models were not preprocessed. The identification results are also shown in Table 2.

As shown in Table 2, the neural network models have a great impact on the results of damage identification. The IA of RCPN is apparently higher than that of PNN at each noise level. For example, when $\varepsilon = 0.1\%$, 0.2% , and 0.3% , the average IA values of RCPN are higher than PNN by 8.5%, 5.00%, and 5.50%, respectively. The largest difference in IA is seen in pattern 1 when $\varepsilon = 0.1\%$, and the IA of RCPN is 51% greater than PNN. When $\varepsilon = 0.2\%$, the IA of RCPN in pattern 2 was greater than PNN by 26%. Similarly, the difference between the RSRCPN and the RSPNN is similar to the case of RCPN and PNN. In a word, the RCPN has better damage detection capability than that of PNN.

In summary, rough set or principal component analysis can be used to reduce the redundant information, the spatial dimension, and data storage space. This not only saves the running time, but also improves the damage detection capabilities and robustness. This implies that the proposed model is feasible and effective in structural damage detection.

5. Conclusions

This paper presents a revised CPN model by integrating rough set for damage detection, which is suitable for dealing with redundant and uncertain information in structural damage detection. Furthermore, a numerical example has proved the effectiveness of the proposed method. The results show that excellent performances are achieved with this model in comparison with different network models and data processing methods. That is, the presented method not only has good damage detection and noise-resistant capabilities, but also significantly reduces the memory requirements for data storage and saves runtime as a consequence of the rough set technique and RCPN model processing.

The study shows that the integration of rough set processing and a revised CPN has great potential in the field of structural damage detection. However, it is noted that the proposed model has been proved feasible and efficient only in the case of numerical examples. Its actual performance in experimental work needs to be studied in the coming investigations.

Acknowledgments

The work is supported by the National Natural Science Foundation of China (nos. 51278127 and 50878057), the National

12th Five-Year Research Program of China (Grant no. 2012BAJ14B05), and Research Plan for Minjiang Scholar of Fujian Province, China. Many thanks are given to Mr. Jie Lin for his simulation and analysis.

References

- [1] H. N. Cho, Y. M. Choi, S. C. Lee, and C. K. Hur, "Damage assessment of cable stayed bridge using probabilistic neural network," *Structural Engineering and Mechanics*, vol. 17, no. 3–4, pp. 483–492, 2004.
- [2] M. A. K. Jaradat and R. Langari, "A hybrid intelligent system for fault detection and sensor fusion," *Applied Soft Computing Journal*, vol. 9, no. 1, pp. 415–422, 2009.
- [3] S. W. Doebbling and C. R. Farrar, "The state of the art in structural identification of constructed facilities," Los Alamos National Laboratory Report Draft, Los Alamos, NM, USA, 1999.
- [4] H. Sohn, C. R. Farrar, and F. M. Hemez, "A review of structural health monitoring literature: 1996–2001," Los Alamos National Laboratory Report LA-13976-MS, 2003.
- [5] Y. L. Xu, X. L. Ding, J. N. Cao et al., "Performance-based health monitoring of large civil structures," in *Proceedings of the 14th Asia-Pacific Vibration Conference*, pp. 69–83, Hong Kong, 2011.
- [6] N. Bakhary, H. Hao, and A. J. Deeks, "Damage detection using artificial neural network with consideration of uncertainties," *Engineering Structures*, vol. 29, no. 11, pp. 2806–2815, 2007.
- [7] J. Shao-Fei, Z. Chun-Ming, and Y. Juan, "Eigen-level data fusion model by integrating rough set and probabilistic neural network for structural damage detection," *Advances in Structural Engineering*, vol. 14, no. 2, pp. 333–349, 2011.
- [8] Y. K. Liu, H. Xia, C. L. Xie, Z. H. Chen, and H. X. Chen, "Study on intelligence fault diagnosis method for nuclear power plant equipment based on rough set and fuzzy neural network," *Journal of Nuclear Power Engineering*, vol. 28, no. 1, pp. 110–114, 2007.
- [9] S.-F. Jiang and Z.-Q. Wu, *Intelligent Information Processing and Its Application in Structural Health Monitoring*, China Building Industry Press, Beijing, China, 2011.
- [10] I. Kuzmanovski, M. Novič, and M. Trpkovska, "Automatic adjustment of the relative importance of different input variables for optimization of counter-propagation artificial neural networks," *Analytica Chimica Acta*, vol. 642, no. 1–2, pp. 142–147, 2009.
- [11] I. Kuzmanovski and M. Novič, "Counter-propagation neural networks in Matlab," *Chemometrics and Intelligent Laboratory Systems*, vol. 90, no. 1, pp. 84–91, 2008.
- [12] K. L. Du, "Clustering: a neural network approach," *Neural Networks*, vol. 23, no. 1, pp. 89–107, 2010.
- [13] D. Ballabio, M. Vasighi, V. Consonni, and M. Kompany-Zareh, "Genetic algorithms for architecture optimisation of counter-propagation artificial neural networks," *Chemometrics and Intelligent Laboratory Systems*, vol. 105, no. 1, pp. 56–64, 2011.
- [14] I. Lopez and S. K. Nesrin, "Distance similarity matrix using ensemble of dimensional data reduction techniques: vibration and aerocoustic case studies," *Mechanical Systems and Signal Processing*, vol. 23, no. 7, pp. 2287–2300, 2009.
- [15] K. Worden and G. Manson, "Damage identification using multivariate statistics: kernel discriminant analysis," *Inverse Problems in Engineering*, vol. 8, no. 1, pp. 25–46, 2000.

- [16] R. W. Swiniarski and A. Skowron, "Rough set methods in feature selection and recognition," *Pattern Recognition Letters*, vol. 24, no. 6, pp. 833–849, 2003.
- [17] Y. Qian, J. Liang, W. Pedrycz, and C. Dang, "An efficient accelerator for attribute reduction from incomplete data in rough set framework," *Pattern Recognition*, vol. 44, no. 8, pp. 1658–1670, 2011.
- [18] C. Guang, Q. Li, and L. Yang, "Research on application of CPN neural network to fault diagnosis of analog circuits," *Ship Electronic Engineering*, vol. 28, no. 5, pp. 5–7, 2008.
- [19] L. Jie, *Study on structural damage detection method based on revised CPN and data fusion with incomplete information [Dissertation]*, Fuzhou University, Fuzhou, China, 2010.
- [20] D. Y. Xue and Y. Q. Chen, *Application MATLAB To Solve Higher Applied Mathematics Problems*, Tsinghua University Press, Beijing, China, 2004.
- [21] S.-F. Jiang, C.-M. Zhang, and J. Yao, "Eigen-level data fusion model by integrating rough set and probabilistic neural network for structural damage detection," *Advances in Structural Engineering*, vol. 14, no. 2, pp. 333–349, 2011.
- [22] L.-A. Chen, M.-Q. Xiao, and X. Zhao, "Fault diagnosis under condition of incomplete test information based on rough set and information entropy," *Journal of Vibration and Shock*, vol. 3122, pp. 24–28, 2012.
- [23] W. Peng, X. Luo, and P. Lu, "A study of vibration fault diagnosis of hydro-turbine generating unit based on the CPN network," *Journal of Xi'an University of Technology*, vol. 22, no. 4, pp. 365–368, 2006.

Research Article

Measurement of Additional Strains in Shaft Lining Using Differential Resistance Sensing Technology

Guangsi Zhao,^{1,2,3} HuaFu Pei,⁴ and Hengchang Liang^{1,3}

¹ State Key Laboratory for Geomechanics and Deep Underground Engineering, China University of Mining & Technology, Xuzhou 221116, China

² Department of Civil and Environmental Engineering, The Hong Kong Polytechnic University, Hong Kong, China

³ School of Mechanics and Civil Engineering, China University of Mining & Technology, Xuzhou 221116, China

⁴ Harbin Institute of Technology Shenzhen Graduate School, Department of Civil and Environmental Engineering, Shenzhen 518055, China

Correspondence should be addressed to Guangsi Zhao; zgscumt@126.com

Received 4 July 2013; Accepted 15 September 2013

Academic Editor: Hong-Nan Li

Copyright © 2013 Guangsi Zhao et al. This is an open access article distributed under the Creative Commons Attribution License, which permits unrestricted use, distribution, and reproduction in any medium, provided the original work is properly cited.

As is well known, shaft lining fracture is the main disaster resulting in a large amount of fatalities and property loss. Thus, the additional strain is a key parameter to evaluate the safety condition of existing shaft linings. In this study, a new type of safety monitoring system based on differential resistance sensing technology is developed to measure the additional strain in shaft linings. In this paper, the theoretical study, the working principle, and the function of the newly developed monitoring system are fully presented. To investigate the reliability and effectiveness of the monitoring system, the differential resistance sensors are used to measure the horizontal and vertical strains at different elevations in a shaft lining during reinforcing the fracture inside the shaft lining. It can be found that from the test results the monitoring system based on differential resistance sensing technology can measure the deformation of the existing wall lining during stratum grouting. Therefore, it can be concluded that the newly developed monitoring system is significant for fracture warning and reinforcement engineering.

1. Introduction

Nowadays, more and more large-scale civil infrastructures are being constructed in prosperous cities [1]. These structures are susceptible to random vibrations in their long service period whether they are from changes in temperature, severe wind gusts, torrential rain, strong earthquake tremors, or abnormal loads such as explosions. The coupling effects between these natural or man-made factors make the problem even more complicated. Although the routine visual inspection is effective in some cases, its effectiveness in finding the possible defects in time is questionable. Therefore, it is imperative that a continuous structural health monitoring (SHM) system be developed [1, 2]. Shaft lining is one kind of large-scale civil infrastructures. Since 1980s, the disasters of shaft lining fracture have repeatedly taken place at digging in east China, which greatly threatened the

production and safety of collieries. According to the data, there are more than 100 shaft linings with similar fracture, which has caused a large amount of property loss and remains a great deal of potential troubles. The depth of these vertical shaft linings is commonly ranging from 400 to 1000 meters. When the fracture happened, the falling of broken concrete caused casualties and damage to equipments. According to the existing results, the mechanism of shaft lining fracture had been found. China University of Mining and Technology puts forward the vertical additional stress theory on the shaft fracture, which can describe the main characters of the shaft fracture and is gradually accepted by the specialists and scholars home and abroad because it has been supported by many results from theories, experiments, and practical researches [3–5]. Because mining leads to the drainage of the bed of aquifer at bottom of overburden and the dropping of water table, the effective stress of the aquifer increases. These

cause the settlement of strata and axial additional force acting on the shaft lining. It is proved that the axial additional force is a main factor leading to the fracture of shaft lining [6, 7].

According to the additional stress theory, to achieve the early warning of fracture, it is important to measure the additional strain and additional stress of shaft lining and get the information of its stress state and trends real time dynamically. Based on the fracture mechanism, it can be found that grouting certain range soil around the lining is an effective reinforcement technique, as shown in Figure 1. In the grouting reinforcement process, the injection pressure can cause the alluvium uplift, which may result in lining subjected to vertical tensile stress and fracture even, and the concrete lining is also susceptible to compress fracturing along the ring. In order to avoid secondary lining fracture, to ensure the normal mine production, real-time monitoring of the stress is needed. From the literatures, it can be found that the frequency strain gage had been tested and utilized in shaft lining engineering, but the effect and durability are poor. In this paper, the authors describe the application of the differential resistance strain gauges in shaft lining safety monitoring system including system components, basic principles, system advantages, and wide applications, and this distributed automatic monitoring system has made a solid foundation for the realization of lining fracture hazard warning; finally, some prospects about this system needed for further study have also been presented.

2. Composition of Shaft Lining Health Monitoring System (SLHMS)

2.1. The Differential Resistance Sensors. The sensors are important to the safety monitoring system of shaft lining. The differential resistance sensor has inherent advantages over other electric sensors including high sensitivity, large measurement range, high accuracy, and good stability in long-term monitoring. In addition, the differential resistance sensor with small size ($\phi 30 \times 100$ mm) is suitable for lining monitoring without damage to the structure.

As shown in Figure 2, the sensing unit of the differential resistance sensor consists of two pretension steel wires connected with two ceramic blocks. The tensile force can be determined by the maximum tensile strain and the strength of steel wire. R_1 will increase and R_2 will decrease once the tensile force is applied. The resistance ratio $Z = R_1/R_2$ will increase once the sensor is subjected to tensile force; otherwise, the resistance ratio will decrease.

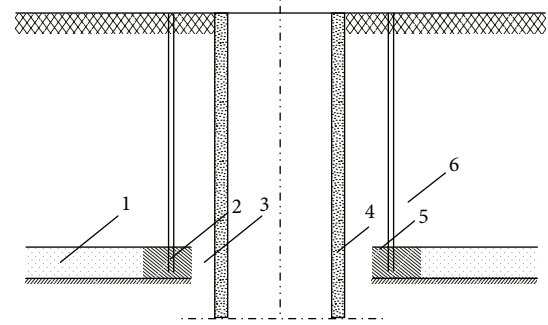
The colors, black, red and white, of cables are designed respectively. Their arrangements are shown in Figure 3. So the resistance R_1 and R_2 can easily be distinguished, and the sensors can be installed in-site conveniently.

In order to decrease the resistance of sensor's extending cable, we used the following scheme, as shown in Figure 4.

The measured strain can be expressed by

$$\varepsilon = f(Z - Z_0) + b(t - t_0), \quad (1)$$

where ε is the measured strain, f is the sensitivity, b is the modification coefficient for temperature, Z is the electric



(1) Aquifer (2) Grouting piles (3) Bedrock (4) Shaft lining (5) Reinforced area (6) Alluvium

FIGURE 1: Stratum reinforced by grouting.

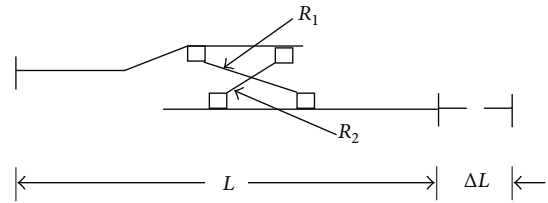


FIGURE 2: Working principle of the differential resistance sensor.

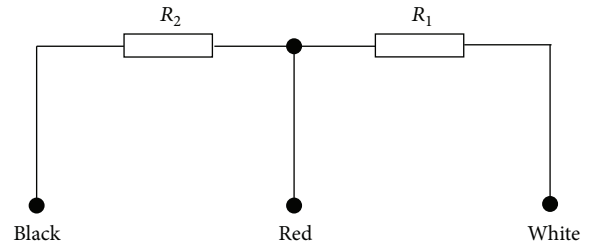


FIGURE 3: Resistance effect of the differential resistance sensor.

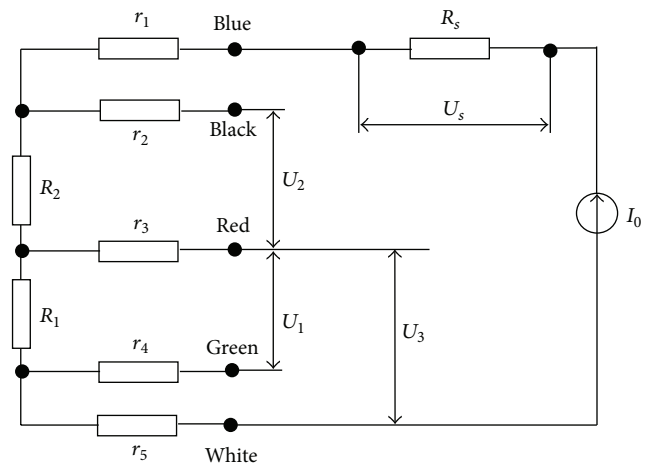


FIGURE 4: Sensing principle of the differential resistance sensor.

resistance ratio, $Z = (R_1 + \Delta R_1)/(R_2 - \Delta R_2)$, Z_0 is the initial value of electric resistance, $Z_0 = R_1/R_2$, t is the actual measured temperature, and t_0 is the datum value of temperature.

2.2. Arrangement of the SLHMS. To mine the potential of sensors, the optimization of sensor placement is a hot issue for structural health monitoring especially for high rise buildings [8, 9]. In this study, four measurement points at four elevations as shown in Figure 5 were monitored according to the geological investigation. Three measurement points were in the soil mass while one point was at the interface between soil mass and rock bed. As shown in Figures 6 and 7, two differential sensors were used to measure the displacements in two directions at one measurement point.

The sensors were buried in the shaft lining at different levels along the vertical directions. The size of the sensor $\phi 30 \times 100$ mm is small; thus, the influence of the differential resistance sensors on the integrity of shaft lining can be neglected. As shown in Figure 6, four measuring points were uniformly arranged along the circle of the shaft lining, and at each point two sensors are buried vertically and tangentially. Eight sensors were buried in the shaft lining at the same elevation. Finally, all the sensors were connected to the junction box and computer through the armored cables. In this case, the strain values of shaft lining can be collected automatically. As shown in Figure 8, the measured strains were computed by the software in the computer. SLHMS consists of sensor, electric cables, junction box, measurement unit, and computer.

3. Advantages of the SLHMS

All of the sensors data collection was based on computer controlling system. The results can be displayed on the computer screen after data processing software was programed by the computer. It can get the developing status and tendency at any time as the system can maintain 24-hour continuous monitoring. The sensing system possesses features of stability behavior, high precision, and reliability for long term, and each sensor can measure strain and temperature simultaneously, which can simplify the system. It has several advantages such as electromagnetic interference resistance, stability for long-term monitoring, and large working temperature range (from -25°C to $+60^\circ\text{C}$). The sensors buried in the wall can have more than 10-year service life, especially suitable for long-term monitoring.

Based on theoretical analysis, numerical simulation, model test and field measurement conducted by China University of Mining and Technology, the monitoring system can automatically give an alarm once the actual value overrides the set value. System has the function of data remote transmission and the realization of data exchange between single user and data analysis center.

4. Applications of the SLHMS

4.1. Monitoring of Anomalies and Possible Damage/Deterioration. A coal mine has the depth of 462.1 m and the diameter of 6.0 m. The overburden section was excavated by freezing method and the shaft concrete. The inner layer has the

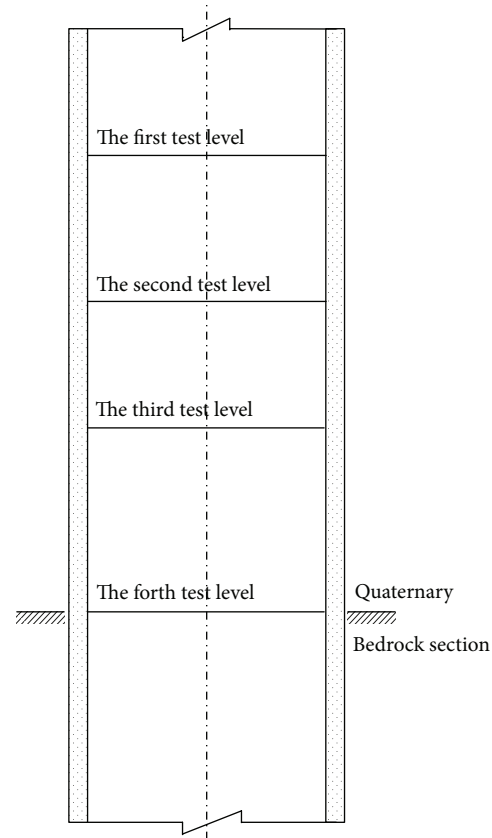


FIGURE 5: Schematic illustration of the measurement project.

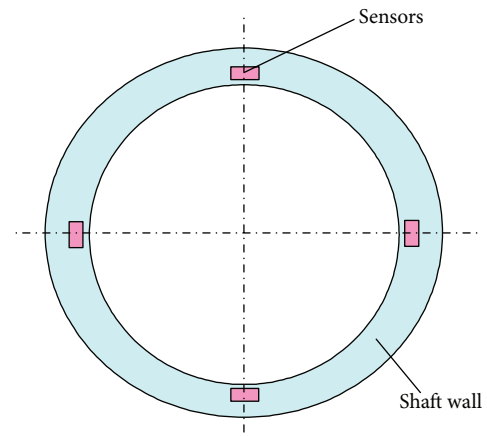


FIGURE 6: Layout of measurement points at the same elevation.

thickness of 0.4 m and the outer one has the thickness of 0.4 m too. For the bedrock section, the shaft lining was composed of one-layer concrete with thickness of 0.4 m.

In its long service period, the shaft lining's stress state has been changing. As shown in Figure 9, we have obtained the evolution of the additional strain in 3 years. According to the curve, especially the substantial changes of additional strain and its evolution trend, we can judge whether the shaft lining is safe or not.

Hurst obtained the explanation to H based on a series of studies: (1) when $H = 0.5$, the sequence is Brownian movement; variables are independent; the corresponding coefficient is 0; it will not affect the future; therefore, the time series is random. (2) When $0 \leq H < 0.5$, it indicates that time series presents long-term correlation, but the future overall trend is contrary to the past, the process is antisustainability. (3) When $0.5 < H < 1$, it indicates that the time series present the characteristic of long-term correlation; that is to say, the process is sustainable.

Generally speaking, the shaft additional forces variation consisted with the past variation, and the maintenance is stronger with the increase of the H .

4.2. Process Control during Stratum Grouting for Ensuring the Safety of Shaft Lining. Once a circumferential microcrack appears in the shaft lining, it is on the verge of fracture. To avoid further destruction, the stratum grouting method is used to prevent the shaft lining from fracture as follows [11–13].

The reinforcing engineering is to change the stratum characters by means of grouting and consolidating the bed of aquifer. The purpose is to use the grouting with consolidation performance pouring into holes, cracks in the stratum directly, and squeezing or replace the water in strata in order to compact and raise the stratum. This method can decrease the settlement of the stratum, while the water table is decreasing, and eliminate the additional force. Stratum grouting can not only reduce the additional strain of lining caused by stratum, but also release the existing vertical strain slowly.

Although stratum grouting for the bed of the aquifer has the advantage of restraining and releasing additional strain, it brings the weak side, that is, the stability of shaft lining during stratum-grouting. The improper range, techniques, and parameters of grouting may cause damage to the shaft lining. For example, because the grouting pressure may lead the horizontal pressure acted on lining to exceed the designed one, the shaft lining can be damaged. Due to the excessive stratum uplifted and the excessive release of additional strain, the shaft lining will be tensioned in the vertical direction, and its stability will be threatened. So the parameters of stratum grouting must be adjusted in time and the grouting process must be controlled through monitoring the change of the additional strain of shaft lining.

In order to ensure the stability of shaft lining during stratum grouting and to inspect the grouting effect, it is necessary to monitor timely and dynamically the shaft lining stability by setting up a health monitoring system to gather the additional strain values. Based on the evolution of additional strain, the stratum grouting process can be controlled by adjusting the grouting parameters. The controllable parameters in grouting process include the grouting position, pressure, volume, and the density of grout.

Figure 10 is its principle. The stress condition will be changed after stratum-grouting. Because the consolidation of cement slurry entering strata will uplift the stratum, there will be the relatively compressive and tensile strain in the shaft lining, which is the additional strain. By monitoring the additional strain of the key points of shaft lining, we can

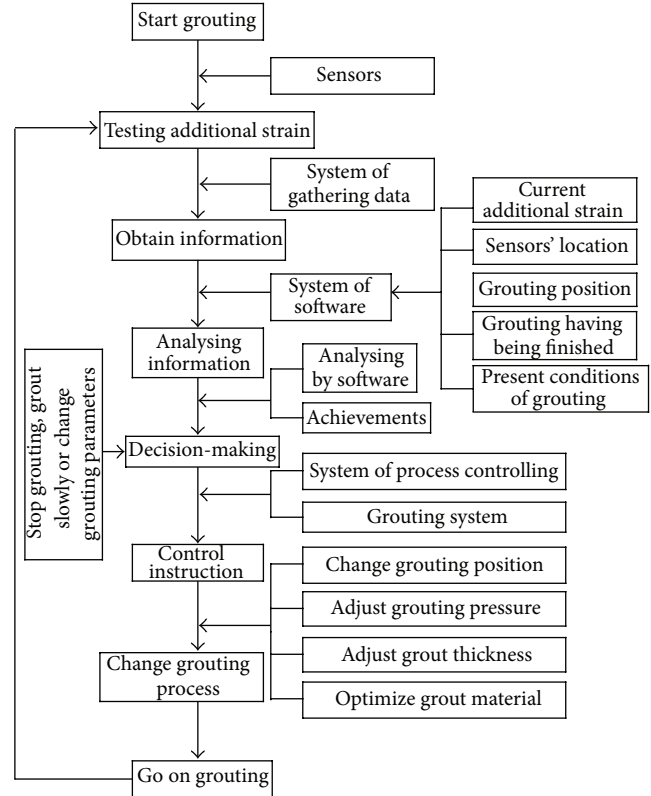


FIGURE 10: Working principle of controlling stratum grouting process.

obtain the changing law of the additional strain and judge duly the stability of the shaft lining. So we can effectively control stratum grouting process.

Based on the analysis of the strain state at different points of the shaft lining, we can determine the allowable value of the additional strain $[\Delta\varepsilon]$ at each grouting stage. When the additional strain near the hole reaches the allowable value, we must take the following measures: “Stop”—stop grouting; “Slow”—slow down the grouting; “Shift”—shift the hole or grouting level; “Change”—change the parameters of grouting.

During grouting, we must always comply with the principle of timing, quantification, and interval. According to the evolution of additional strain of shaft lining, we must duly change the parameters of grouting process, such as the grouting order, pressure, volume, and the density of grout, so as to make sure the stratum around shaft lining lifts uniformly.

4.3. Monitor the Repair with the View of Evaluating the Effectiveness of Maintenance and Repair Work. Based on the measured data, we can evaluate the effectiveness after grouting. Figure 11 is a duration curve of shaft lining’s additional strain increasing during grouting. According to the shaft concrete properties and strain increment, especially its changing trend, we can also evaluate its safety and service life. Generally, the much flatter the curve is, the longer the service life of the shaft lining could be obtained.

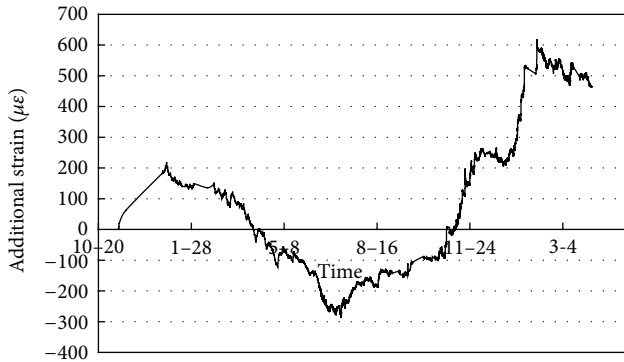


FIGURE 11: Variation of additional strain in shaft lining during grouting.

5. Conclusions

In this study, the following conclusions can be drawn.

- (a) Differential resistance sensor is reliable and efficient for measuring the additional strain in shaft lining, especially for long-time monitoring.
- (b) The safety monitoring system is necessary for the shaft lining in thick alluvium. The case study presented that the stress of shaft lining measured by the monitoring system can measure the stress changes in shaft lining.
- (c) The monitoring results show that grouting for reinforcing stratum can effectively reduce the axial additional strain of shaft lining. It can prevent and cure the fracture of shaft lining. According to the evolution of additional strain, it is feasible and effective to control the grouting process and ensure the safety of shaft lining.
- (d) Further study is needed to study the relationship between the additional strains and related various parameters.

Acknowledgments

The financial supports from the Major State Basic Research Development Program of China (973 Program) no. 2012CB026103, the National Natural Science Foundations of China no. 51104149, and Postdoctoral Special Fund of China no. 2012T50532 are acknowledged. The authors would like to express their deepest gratitude to Professor Guoqing Zhou and all his group members for their great contribution to the work.

References

- [1] T. H. Yi and H. N. Li, "Methodology developments in sensor placement for health monitoring of civil infrastructures," *International Journal of Distributed Sensor Networks*, vol. 2012, Article ID 612726, 11 pages, 2012.
- [2] T. H. Yi, H. N. Li, and M. Gu, "Recent research and applications of GPS-based monitoring technology for high-rise structures,"

Structural Control and Health Monitoring, vol. 20, no. 5, pp. 649–670, 2013.

- [3] X. L. Cheng and G. Q. Zhou, "Study on the stress calculation of shaft lining surrounded by special strata," in *Proceedings of the 2nd International Symposium on Mining Technology & Science*, X. Zhou, Ed., 1990.
- [4] X. L. Cheng, W. H. Yang, G. Q. Zhou et al., "Predicting the stress state of shaft lining lying in thick overburden by simulation test," in *Proceedings of the International Symposium on Application of Computer Methods in Rock Mechanics and Engineering*, pp. 703–709, Science and Technology Press, Shanxi, China, 1993.
- [5] W. H. Yang, G. X. Cui, and G. Q. Zhou, "Fracture Mechanism of shaft lining under special strata condition and the technique preventing the shaft from fracturing (part one)," *Journal of China University of Mining and Technology*, vol. 25, no. 4, pp. 1–5, 1996.
- [6] G. Q. Zhou, X. L. Cheng, and G. X. Cui, "Simulation study on the additional stress of the shaft lining in clay," *Journal of China University of Mining and Technology*, vol. 20, no. 3, pp. 86–91, 1991.
- [7] G. X. Cui and X. L. Cheng, "Primary study on the reason of the rupture of the shaft lining in the xu-huai region," *Mining Science and Technology*, no. 8, pp. 46–50, 1991.
- [8] T. H. Yi, H. N. Li, and X. D. Zhang, "Sensor placement on Canton Tower for health monitoring using asynchronous-climb monkey algorithm," *Smart Materials and Structures*, vol. 21, no. 12, Article ID 125023, 2012.
- [9] T. H. Yi, H. N. Li, and M. Gu, "Optimal sensor placement for structural health monitoring based on multiple optimization strategies," *Structural Design of Tall and Special Buildings*, vol. 20, no. 7, pp. 881–900, 2011.
- [10] G. Zhao, G. Q. Zhou, X. D. Zhao, Y. Z. Wei, and L. J. Li, "R/S analysis for stress evolution in shaft lining and fracture prediction method," *Advanced Materials Research*, vol. 374–377, pp. 2271–2274, 2012.
- [11] G. Q. Zhou, G. S. Zhao, Z. Q. Liu et al., "Study on the stratum-grouting control according to the evolution of additional strain of shaft lining," in *Mining Science and Technology*, A. A. Balkema, Ed., pp. 357–361, 2004.
- [12] G. S. Zhao, G. Q. Zhou, X. Y. Bie et al., "Application of the shaft lining curing technology of cement grouting for reinforcing soil," *Ground Pressure and Strata Control*, no. 2, pp. 109–111, 2004.
- [13] Z. Q. Liu, G. Q. Zhou, G. S. Zhao, H. Liang, and J. Zhou, "Control method and its application about the soil grouting reinforcement process in vertical shaft," *Journal of the China Coal Society*, vol. 30, no. 4, pp. 472–475, 2005.

Research Article

Measurement Model for the Maximum Strain in Beam Structures Using Multiplexed Fiber Bragg Grating Sensors

Se Woon Choi,¹ Jihoon Lee,¹ Bo Hwan Oh,² and Hyo Seon Park¹

¹ Department of Architectural Engineering, Yonsei University, 134 Shinschon-dong, Seoul 120-749, Republic of Korea

² Daewoo Institute of Construction Technology, 60 Songjuk-dong, Suwon 440-210, Republic of Korea

Correspondence should be addressed to Hyo Seon Park; hspark@yonsei.ac.kr

Received 12 July 2013; Revised 6 September 2013; Accepted 8 September 2013

Academic Editor: Hong-Nan Li

Copyright © 2013 Se Woon Choi et al. This is an open access article distributed under the Creative Commons Attribution License, which permits unrestricted use, distribution, and reproduction in any medium, provided the original work is properly cited.

This study develops a strain measurement model for beam structures subjected to multiloading conditions by defining the strain-shape function and participation factors to overcome the limitations of strain measurements using fiber Bragg grating (FBG) strain sensors. Using the proposed model, the maximum strain in a beam is obtained by the sum of the strains caused by the different loadings acting separately. In this paper, the strain-shape functions for various loading and support conditions are provided, and a system of equations is defined to calculate the participation factors. Furthermore, the influence ratio is defined to identify the influence of each loading on the value of the total strain. The measurement model is applied to the monitoring of the maximum strain in a 4 m long steel beam subjected to two concentrated loads. For measurements during the test, seven FBG sensors and nine electric strain gauges (ESGs) were attached on the surface of the bottom flange. The experimental results indicate a good agreement between the estimated strains based on the model and the measured strains from ESGs. Furthermore, the dependency of the locations for the FBG sensors installed at the beam structure on the selection can be avoided using the measurement model.

1. Introduction

Structural members in buildings or infrastructures experience various loads, such as gravity-induced loads, earthquake, wind, or unexpected loads. To secure the safety of a structure, the maximum stresses in the members due to various loads must not exceed the allowable stress of a member [1, 2]. For this reason, strain-based structural health monitoring (SHM) has been widely used to assess the structural states of the members by sensing the maximum stresses [3–8].

Various types of point sensors, including fiber optic sensors and electric strain gauges (ESGs), are applied to measure the maximum stresses. However, point sensors used to measure strains can cover only a relatively small range of structural members because they can measure the strain only at a local point of a member. Thus, many difficulties exist when determining the maximum stress in a member with point sensors because the actual strain distribution of a member is nonuniform. In this case, the reliability of the safety of a member based on the measured maximum strain depends on the number and location of the sensors. However, when

attempting to overcome these limitations, the number of sensors may not be increased to cover the entire length of a member because of practical problems related to maintenance and installation.

Various techniques to estimate the maximum strain based on the measured strains have been reported [5, 7] because the measured strains from point sensors cannot be directly considered when evaluating the safety of a member. To cover a relatively long length of a member, the average strains from long-gauge fiber optic sensors (LGFOSS) or vibrating wire strain sensors (VWSGs) have been used to estimate the maximum strains of a member subjected to a single loading condition. However, the techniques are rather impractical because structural members in real building structures or infrastructures are subjected to multiple loading conditions.

Considering the limits of point sensors and long-gauge sensors, fiber Bragg grating (FBG) strain sensors are suitable for measuring the maximum strain of a beam. Although an FBG sensor is a point sensor with a relatively short-gauge length, it can measure the maximum strains with a minimum

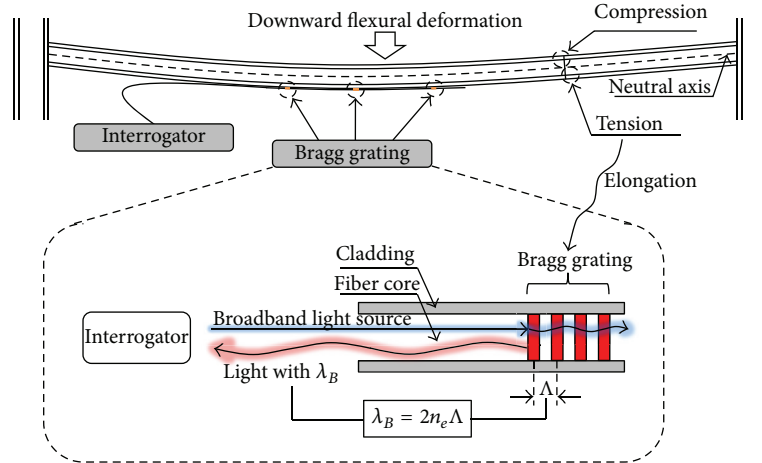


FIGURE 1: Measurement principle of the strain using an FBG sensor.

number of sensors because of the multiplexing technology in FBG [9]. Multiplexing is a method by which multiple signals are combined into one signal, and only a single cable suffices for a certain number of sensors. In addition, FBG strain sensors have high resolution and are convenient to install compared to long-gauge sensors.

However, to date, no research regarding point sensors, including FBG sensors, has been reported on the measurement or sensing method for the maximum strains in a structural member subjected to real multiple loading conditions. Therefore, in this paper, a maximum strain measurement model based on point sensors is developed for the FBG sensor to be applied to find the maximum strain in a steel beam structure subjected to multiple loading conditions. In addition to the maximum strain, a distribution of the strains along the length of a member is provided by the measured local strains from the minimum number of FBG sensors. To evaluate the performance of the model, an experiment has been conducted on a 4 m long steel beam to compare the maximum strain directly obtained from ESGs and the maximum strain from the model with the strains measured from FBG sensors.

2. FBG Sensors

In FBG sensors, a Bragg grating is introduced to the core of a fiber [10]. If the broadband light source collides against the Bragg grating, a light with a particular wavelength, called the Bragg wavelength λ_B , satisfying the relationship shown in (1) is reflected:

$$\lambda_B = 2n_e\Lambda, \quad (1)$$

where Λ is the period of Bragg grating and n_e is the effective refractive index. Because the Bragg grating period varies according to the elongation, a strain can be calculated by detecting the change of the Bragg wavelength that reflects an elongation.

As shown in Figure 1, the longitudinal strain of a beam member subjected to multiple loadings can be measured by

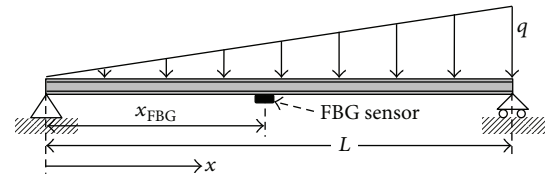


FIGURE 2: Simply supported beam subjected to a linearly varying load.

typical FBG sensors attached to the face of the member. Especially from the aspect of SHM, the multiplexing technology in an FBG sensor makes strain-based SHM more reliable and practical because of the convenience with which such sensors can be managed and installed. A variety of applications can be found in the field of SHM, including building, civil, and infrastructure [11–15].

3. Maximum Strain Measurement Model

In this paper, the strain measurement model is presented to estimate the maximum strain of a beam structure using local strains measured from FBG sensors. For a beam structure subjected to multiple loading conditions simultaneously, the total strain at a specific point can be found by superimposing the strains due to separate loadings. However, to find the maximum strain of a beam structure instead of the strain value at a point, the deformed shape caused by the multiple loadings must be defined by superimposing the distribution shape of the strains along the length of a beam for each loading separately. The total strain at an arbitrary point in a beam structure can be estimated using the deformed shape.

3.1. Shape Function for the Distribution of Strains Caused by a Single Load. Based on general concepts in engineering mechanics, as shown in Figure 2, the longitudinal strain $\varepsilon(x)$ of a beam subjected to a linearly varying distributed load of

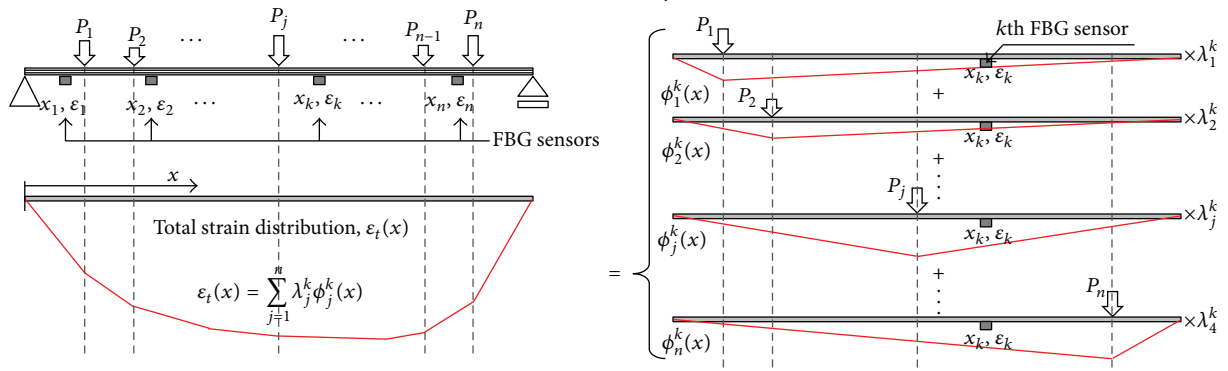


FIGURE 3: Decomposition of the strain distribution caused by multiple loadings into individual effects.

q can be expressed as a function of the distance x from the left-hand support:

$$\varepsilon(x) = \frac{M(x)}{EZ}, \quad (2)$$

where $M(x)$ is the bending moment, E is the modulus of elasticity, Z is the elastic section modulus, and L is the length of the beam. For a FBG sensor installed at a length of x_{FBG} in Figure 2, the strain measured from the FBG strain sensor ε_{FBG} is expressed as

$$\varepsilon_{\text{FBG}} = \frac{1}{EZ} \left(\frac{qL}{6} x_{\text{FBG}} - \frac{q}{6L} x_{\text{FBG}}^3 \right). \quad (3)$$

From (3), the intensity of the distributed load q can be expressed as

$$q = \frac{2EZL\varepsilon_{\text{FBG}}}{x_{\text{FBG}}(L^2 - x_{\text{FBG}}^2)}. \quad (4)$$

Then, the general form for the longitudinal $\varepsilon(x)$ at an arbitrary point x can be defined by

$$\varepsilon(x) = \varepsilon_{\text{FBG}} \frac{x(L^2 - x^2)}{x_{\text{FBG}}(L^2 - x_{\text{FBG}}^2)} = \varepsilon_{\text{FBG}} \phi(x), \quad (5)$$

where $\phi(x)$ is defined as a shape function for the distribution of strains along the length of the beam. The strain-shape function $\phi(x)$ for the distribution of strains in (5) depends on the loading and support conditions of a beam structure. For convenience, nine typical shape functions for the distribution of strains in beam structures subjected to various loading and support conditions are derived in Tables 1 and 2.

As given in (5), the general form of $\varepsilon(x)$ for a beam subjected to a loading can be defined by the strain measured from an FBG sensor at an arbitrary location of x_{FBG} multiplied by the shape function $\phi(x)$ for the distribution of strains in Table 1.

3.2. Superposition of Shape Functions Caused by Multiple Loadings. For a beam structure subjected to n different point loadings of P_j ($j = 1$ to n) in Figure 3, the general form for

the total strain $\varepsilon_t(x)$ of a beam at a distance x from the left-hand support can be expressed as the sum of the strains due to n different point loadings acting separately:

$$\varepsilon_t(x) = \sum_{j=1}^n \lambda_j^k \phi_j^k(x), \quad (6)$$

where λ_j^k is the participation factor for the j th strain-shape function $\phi_j^k(x)$. The superscript k in (6) is the FBG sensor number selected to calculate the strain-shape functions and the participation factors. The calculation of the participation factors is not dependent on the selection of an FBG sensor, as with other types of sensors. Thus, the value of the total strain in (6) does not vary with the selection of the FBG sensor used to calculate the factors.

For the k th FBG sensor selected for the calculation of the factors, a system of n simultaneous equations in (7) can be expressed in matrix notation as follows:

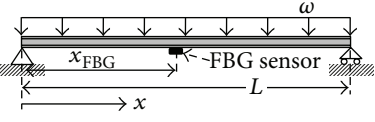
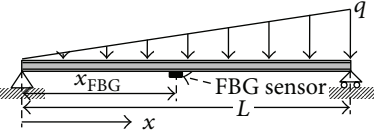
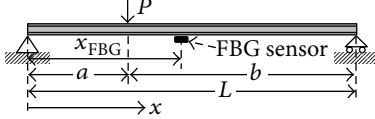
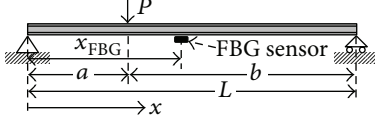
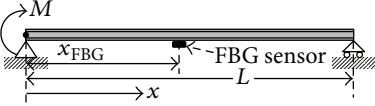
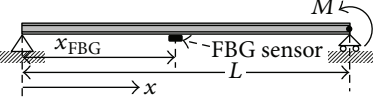
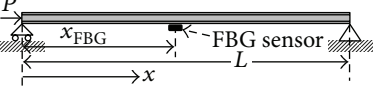
$$\begin{Bmatrix} \varepsilon_1 \\ \varepsilon_2 \\ \vdots \\ \varepsilon_j \\ \vdots \\ \varepsilon_n \end{Bmatrix} = \begin{bmatrix} \phi_{11}^k & \phi_{12}^k & \cdots & \phi_{1j}^k & \cdots & \phi_{1n}^k \\ \phi_{21}^k & \phi_{22}^k & \cdots & \phi_{2j}^k & \cdots & \phi_{2n}^k \\ \vdots & \vdots & \ddots & \vdots & \ddots & \vdots \\ \phi_{j1}^k & \phi_{j2}^k & \cdots & \phi_{jj}^k & \cdots & \phi_{jn}^k \\ \vdots & \vdots & \ddots & \vdots & \ddots & \vdots \\ \phi_{n1}^k & \phi_{n2}^k & \cdots & \phi_{nj}^k & \cdots & \phi_{nn}^k \end{bmatrix} \begin{Bmatrix} \lambda_1^k \\ \lambda_2^k \\ \vdots \\ \lambda_j^k \\ \vdots \\ \lambda_n^k \end{Bmatrix}, \quad (7)$$

where $\phi_{ij}^k = \phi_j^k(x_i)$ is the value of the j th strain-shape function at the position of x_i . Then, the participation factors can be found as the solution to (7):

$$\{\lambda^k\} = [\phi^k]^{-1} \{\varepsilon_{\text{FBG}}\}, \quad (8)$$

where $\{\lambda^k\}$ is a column vector of the participation factors, $[\phi^k]$ is a square matrix of ϕ_{ij}^k , and $\{\varepsilon_{\text{FBG}}\}$ is a column vector of the measured strains. Then, using the total strain obtained by the superposition of n shape functions for strains due to the multiple loadings in (6), the location for the maximum

TABLE 1: Distributional strain-shape function $\phi(x)$: simply supported beam.

Loading condition	Condition of FBG sensor location	$\phi(x)$
	$0 < x_{\text{FBG}} < L$	$\frac{x(L-x)}{x_{\text{FBG}}(L-x_{\text{FBG}})}$
	$0 < x_{\text{FBG}} < L$	$\frac{x(L^2-x^2)}{x_{\text{FBG}}(L^2-x_{\text{FBG}}^2)}$
	$0 < x_{\text{FBG}} \leq a$	$\begin{cases} \frac{x}{x_{\text{FBG}}}, & (0 < x \leq a), \\ \frac{a(L-x)}{bx_{\text{FBG}}}, & (a \leq x \leq L) \end{cases}$
	$a \leq x_{\text{FBG}} < L$	$\begin{cases} \frac{bx}{a(L-x_{\text{FBG}})}, & (0 < x \leq a), \\ \frac{L-x}{L-x_{\text{FBG}}}, & (a \leq x \leq L) \end{cases}$
	$0 \leq x_{\text{FBG}} < L$	$\frac{L-x}{L-x_{\text{FBG}}}$
	$0 < x_{\text{FBG}} \leq L$	$\frac{x}{x_{\text{FBG}}}$
	$0 < x_{\text{FBG}} \leq L$	-1

strain caused by multiple loadings can be found by setting the derivative of (6) equal to zero:

$$\frac{d}{dx} \left(\sum_{j=1}^n \lambda_j^k \phi_j^k(x) \right) = 0. \quad (9)$$

3.3. Example Case: Simply Supported Beam Subjected to Three Types of Loads. To measure the strains in the beam structure subjected to a uniformly distributed load F_1 and two end moments F_2 and F_3 , three FBG sensors are attached at three different locations, as shown in Figure 4.

3.3.1. Strain-Shape Functions and Total Strain. The total strain distribution of the beams in Figure 4 is found by superimposing the strains caused by the three different loadings acting separately. If the first FBG sensor is selected to calculate the strain-shape functions and participation factors, the strain-shape functions for the three different loadings of F_1 , F_2 , and

F_3 can be found in the first, fourth, and fifth rows of Table 1, respectively. The strain-shape functions are given by

$$\begin{aligned} \phi_1^1(x) &= \frac{x(L-x)}{x_1(L-x_1)}, \\ \phi_2^1(x) &= \frac{L-x}{L-x_1}, \\ \phi_3^1(x) &= \frac{x}{x_1}. \end{aligned} \quad (10)$$

From (8), the participation factors for the three loadings λ_1^1 , λ_2^1 , and λ_3^1 can be found by

$$\begin{Bmatrix} \lambda_1^1 \\ \lambda_2^1 \\ \lambda_3^1 \end{Bmatrix} = \begin{bmatrix} \frac{x_1(L-x_1)}{x_1(L-x_1)} & \frac{L-x_1}{L-x_1} & \frac{x_1}{x_1} \\ \frac{x_2(L-x_2)}{x_1(L-x_1)} & \frac{L-x_2}{L-x_1} & \frac{x_2}{x_1} \\ \frac{x_3(L-x_3)}{x_1(L-x_1)} & \frac{L-x_2}{L-x_1} & \frac{x_3}{x_1} \end{bmatrix}^{-1} \begin{Bmatrix} \varepsilon_1 \\ \varepsilon_2 \\ \varepsilon_3 \end{Bmatrix}. \quad (11)$$

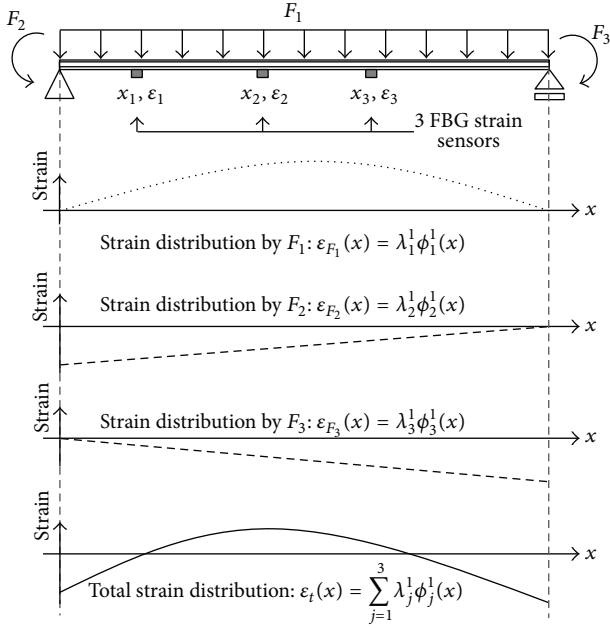


FIGURE 4: Distribution of the strain-shape functions for a beam subjected to three different loadings.

Then, the total strain $\varepsilon_t(x)$ at an arbitrary location is found by substituting $\lambda_1^1, \lambda_2^1, \lambda_3^1, \phi_1^1(x), \phi_2^1(x)$, and $\phi_3^1(x)$ into (6):

$$\varepsilon_t(x) = \sum_{j=1}^3 \lambda_j^1 \phi_j^1(x) = \lambda_1^1 \frac{x(L-x)}{x_1(L-x_1)} + \lambda_2^1 \frac{L-x}{L-x_1} + \lambda_3^1 \frac{x}{x_1}. \quad (12)$$

3.3.2. Maximum Strain. Using the total strain distribution along the length of a beam structure in (12), the location for the maximum strain caused by the three loadings can be found by setting the derivative of (12) equal to zero:

$$\frac{d}{dx} \varepsilon_t(x) = \lambda_1^1 \frac{L-2x}{x_1(L-x_1)} - \lambda_2^1 \frac{1}{L-x_1} + \lambda_3^1 \frac{1}{x_1} = 0. \quad (13)$$

Then, the solution of (13), x^* , is found by

$$x^* = \frac{L}{2} - \frac{\lambda_2^1 x_1 (L-x_1)}{\lambda_1^1 2(L-x_1)} + \frac{\lambda_3^1 x_1 (L-x_1)}{\lambda_1^1 2x_1}. \quad (14)$$

Therefore, the maximum strain can be obtained by comparing (1) the strain calculated by substituting x^* into x in (12) and (2) the strains at both ends of the beam.

3.3.3. Simulation of the Example Case. To test the performance of the measurement model, the intensities of the three loadings F_1, F_2 , and F_3 acting on the steel beam in Figure 4 are set to 37.1, -636.0 , and 636.0 kNm, respectively. For the simulation, H-708 \times 302 \times 15 \times 28 was used for the section of the beam structure, and three FBG sensors were attached 3, 6, and 9 m from the left-hand end of the beam. From the structural analysis for the beam structure, the strains for FBG #1, #2, and #3 were found to be 23.2, 266.6, and 266.6 $\mu\varepsilon$, respectively.

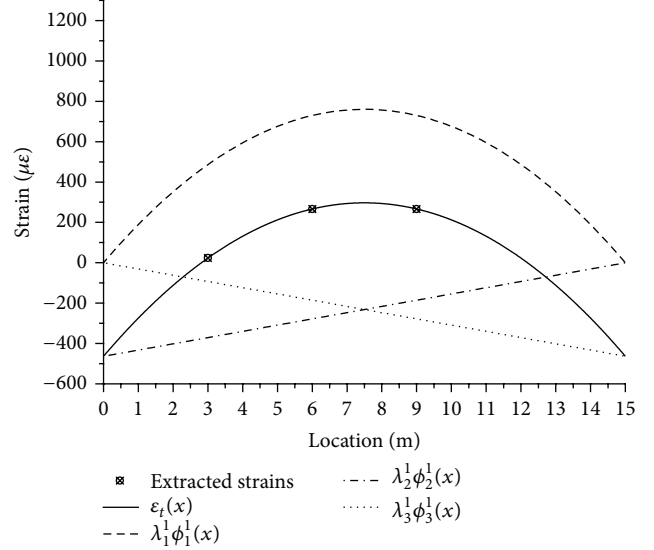


FIGURE 5: Composition of the total strain distribution.

Using the values of the strains for FBG #1, #2, and #3, the participation factors of λ_1^1, λ_2^1 , and λ_3^1 in (11) were calculated as 486.6, -370.7 , and -92.7 , respectively. Thus, the total strain of the beam $\varepsilon_t(x)$ in (12) is expressed as

$$\varepsilon_t(x) = \sum_{j=1}^3 \lambda_j^1 \phi_j^1(x) = (486.6) \left(-\frac{x^2 + 15x}{36} \right) + (-370.7) \left(-\frac{x-15}{12} \right) + (-92.7) \left(\frac{x}{3} \right). \quad (15)$$

The distributions of the total strains and the strains caused by the three loadings are plotted in Figure 5, which illustrates that the strain values for FBG #1, #2, and #3 obtained from the structural analyses are identical to those estimated by the measurement model.

The influence ratio R_j is defined in (16) to identify the influence of each loading on the value of the total strain:

$$R_j = \frac{\int_0^L \lambda_j^k \phi_j^k(x) dx}{\sum_{i=1}^n \sqrt{\left(\int_0^L \lambda_i^k \phi_i^k(x) dx \right)^2}}. \quad (16)$$

The influence ratio R_j indicates a ratio of the area of the strain distribution caused by the j th loading to the sum of the areas of the strain distributions caused by n different loadings. If the influence ratio R_j has a positive sign, then R_j has the same sign as the total strain distribution. Furthermore, the sum of the absolute values of the influence ratios must be one. Thus, the influence of each loading on the total strain distribution can be checked by the influence ratio proposed here. Table 3 presents the strain-shape functions, participation factors, and influence ratios for this simulation for three different FBG sensor numbers ($k = 1, 2$, and 3). For this example case, the most active loading is the uniformly distributed loading of F_1 .

TABLE 2: Distributional strain-shape function $\phi(x)$: cantilever beam.

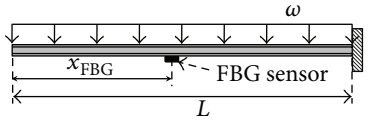
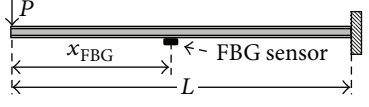
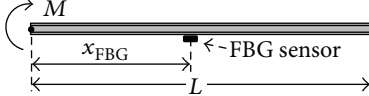
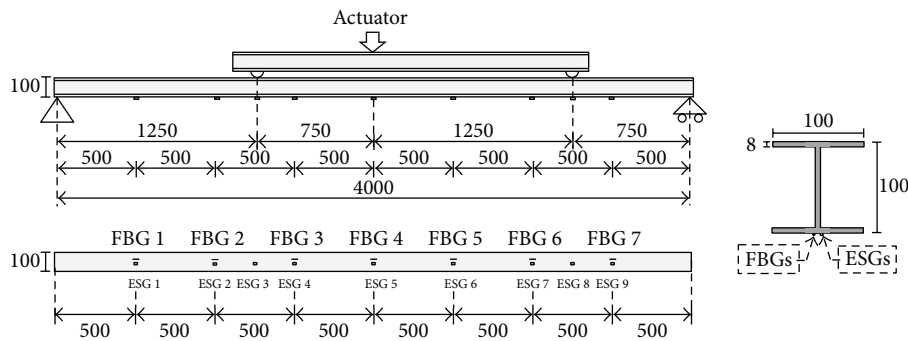
Loading condition	Condition of FBG sensor location	$\phi(x)$
	$0 < x_{\text{FBG}} \leq L$	$\frac{x^2}{x_{\text{FBG}}^2}$
	$0 < x_{\text{FBG}} \leq L$	$\frac{x}{x_{\text{FBG}}}$
	$0 < x_{\text{FBG}} \leq L$	1

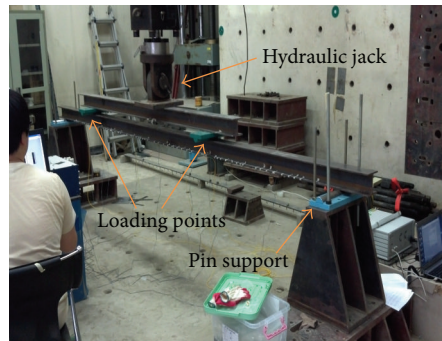
TABLE 3: The function of the total strain distribution and its components.

Load	$k = 1$		$k = 2$		$k = 3$		$\lambda_j^k \phi_j^k(x)$	R_j
	λ_j^k	$\phi_j^k(x)$	λ_j^k	$\phi_j^k(x)$	λ_j^k	$\phi_j^k(x)$		
F_1	486.6	$-(x^2 - 15x)/36$	730.0	$-(x^2 - 15x)/54$	730.0	$-(x^2 - 15x)/54$	$-13.52(x^2 - 15x)$	0.522
F_2	-370.7	$-(x - 15)/12$	-278.0	$-(x - 15)/9$	-185.4	$-(x - 15)/6$	$-30.89(x - 15)$	-0.239
F_3	-92.7	$x/3$	-185.4	$x/6$	-278.0	$x/9$	$-30.89(x)$	-0.239

$$\varepsilon_t = \sum_{j=1}^3 \lambda_j^k \phi_j^k(x) = -13.52(x^2 - 15x) - 30.89(x - 15) + 30.89(x)$$



(a) Side and bottom views for the test model subjected to two point loadings



(b) Overall view of the test model

FIGURE 6: Test model setup.

4. Application to Measurements of the Maximum Strain of a Steel Beam

The proposed measurement model could evaluate the maximum strain in beam structures subjected to multiple loading conditions using the strain-shape functions for various loadings, including point loading, distributed loading, and bending moment loading, as shown in Tables 1 and 2. The proposed measurement model was demonstrated for distributed loading and bending moment loading by a numerical simulation in Section 3.3. In this chapter, the experimental test is conducted to evaluate the performance of the proposed measurement model for the point loading condition.

4.1. Test Setup. In the bending test of the simply supported steel beam in Figure 6, a concentrated load was applied on the upper steel beam by a hydraulic jack. The load was increased in two steps, 7.4 and 12.9 kN. The concentrated load was split into two concentrated loads applied 1.25 and 3.25 m from the left end of the beam. The section of the beams was $H-100 \times 100 \times 6 \times 8$ with a length of 4 m. Figure 6(a) shows that the measurements during the bending test were performed with both seven FBG sensors with a 10 mm grating length and nine ESGs with a 5 mm gauge length attached to the surface of the bottom flange. IS 7000, which is manufactured by Fiberpro, was used for the interrogation system. The major specifications of IS 7000 are listed in Table 4. The grating lengths of the seven FBG sensors are 1,540–1,560 nm, in accordance with the wavelength tuning range of IS 7000. The sampling rate for the strain measurement was set as 0.1 per second.

4.2. Results. During the test, the beam deflected downward and tensile longitudinal strains occurred at the outer surface of the bottom flange. Before testing the measurement model, the strains obtained from the FBGs and ESGs were compared to verify the quality of the value by the FBGs. Table 5 indicates that the strain measured by FBGs could be assessed as reliable values for sensing beam members. The maximum difference between the two measurements was found to be less than 1.34% for each load step.

To measure the maximum strain of the test model subjected to two different point loads, two FBG sensors were required to estimate the maximum strain of the beam based on the model proposed in (6). Among the 21 possible combinations when choosing two of the seven FBG sensors without repetition, the combination of the first and second FBG sensors attached 0.5 and 1.0 m from the left end of the beam is not valid for the estimation because the matrix $[\phi^k]$ in (8) based on the combination is singular.

To test the dependency on the selection of the locations for FBG sensors in the measurement of the maximum strain, all 20 FBG sensor combinations in Table 6 were used in the measurements. The numbers for the FBG sensors are shown in Figure 6(a). Figure 7 compares the estimated distributions of strains from the 20 FBG sensor combinations with the strains measured directly from the nine ESGs for each loading step. Furthermore, the dependency of the locations for

TABLE 4: Major specifications of the interrogator (IS 7000).

Laser module (wavelength swept laser)	
Wavelength tuning range	1,533.7–1,569.5 nm
Sensor module	
Repeatability	± 2 pm
Wavelength accuracy	$< \pm 10$ pm
Sampling frequency	200 Hz

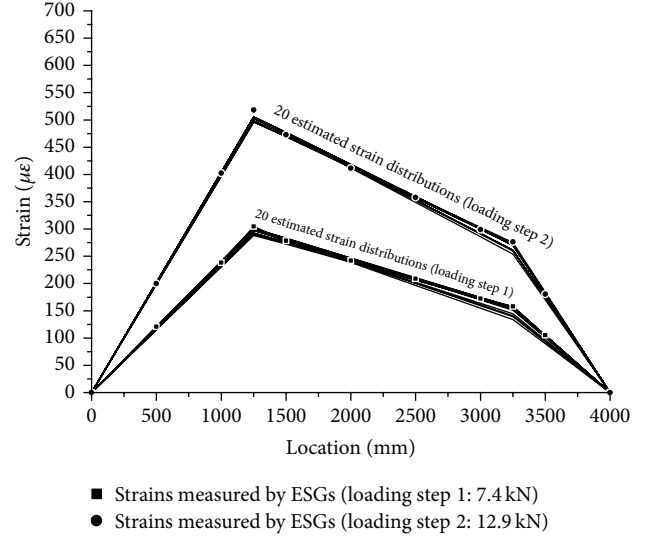


FIGURE 7: Estimated strain distributions from different combinations of FBG sensors for two.

the FBG sensors installed at the beam structure on the selection can be avoided using the measurement model in (5).

To evaluate the performance of the measurement model, the relative error in the estimated strain distributions was calculated by

$$\text{relative error of strain distribution (\%)} = \frac{\|\epsilon_{\text{est}} - \epsilon_{\text{ESG}}\|}{\|\epsilon_{\text{ESG}}\|} \times 100, \quad (17)$$

where ϵ_{ESG} is a vector of the strains measured directly from nine ESGs and ϵ_{est} is a vector of the estimated strains from the model. Figure 8 indicates that the average relative errors for the 20 possible combinations of strain distributions are 2.37% and 1.84% for loading steps 1 and 2, respectively. The maximum of the relative errors for all combinations was approximately 6% for the first combination in load step 2. The estimated maximum strains based on the 20 combinations are compared with the maximum directly measured from ESG #3 in Figure 9. The average relative errors for the 20 possible combinations in the maximum strain are 2.54% and 2.74% for loading steps 1 and 2, respectively. The experimental results indicate good agreement between the estimated strains based on the model and the strains measured from the ESGs.

TABLE 5: Measured strain by the FBG sensors and ESGs.

Sensing location (mm)	First step (7.4 kN)			Second step (12.9 kN)		
	FBG ($\mu\epsilon$)	ESG ($\mu\epsilon$)	Relative error (%)	FBG ($\mu\epsilon$)	ESG ($\mu\epsilon$)	Relative error (%)
500	120.5	120.9	0.36	202.2	199.6	1.34
1,000	238.4	238.3	0.01	405.2	402.6	0.64
1,250	—	304.6	—	—	518.1	—
1,500	280.3	278.3	0.74	474.9	472.8	0.45
2,000	240.4	241.8	0.57	413.8	411.4	0.59
2,500	207.2	208.7	0.69	358.3	357.9	0.10
3,000	172.7	172.3	0.22	299.7	299.0	0.24
3,250	—	157.9	—	—	276.5	—
3,500	104.1	105.3	1.16	181.0	180.6	0.21

TABLE 6: Number alignment of the combinations.

Combination number	1	2	3	4	5	6	7	8	9	10
Combination of sensors	(1,3)	(1,4)	(1,5)	(1,6)	(1,7)	(2,3)	(2,4)	(2,5)	(2,6)	(2,7)
Combination number	11	12	13	14	15	16	17	18	19	20
Combination of sensors	(3,4)	(3,5)	(3,6)	(3,7)	(4,5)	(4,6)	(4,7)	(5,6)	(5,7)	(6,7)

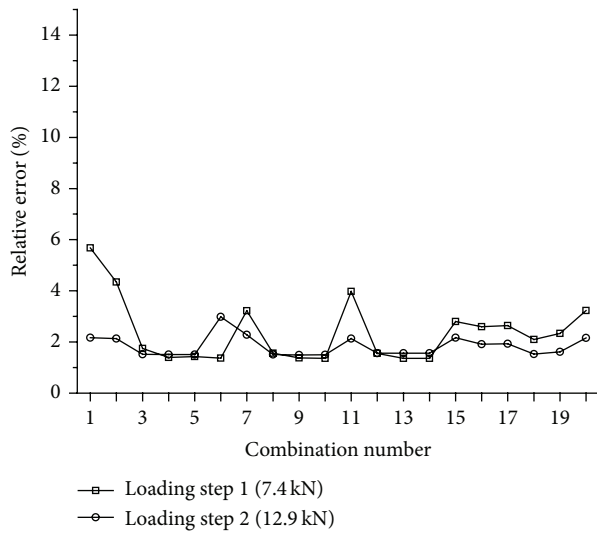


FIGURE 8: Relative errors of the estimated strain distributions.

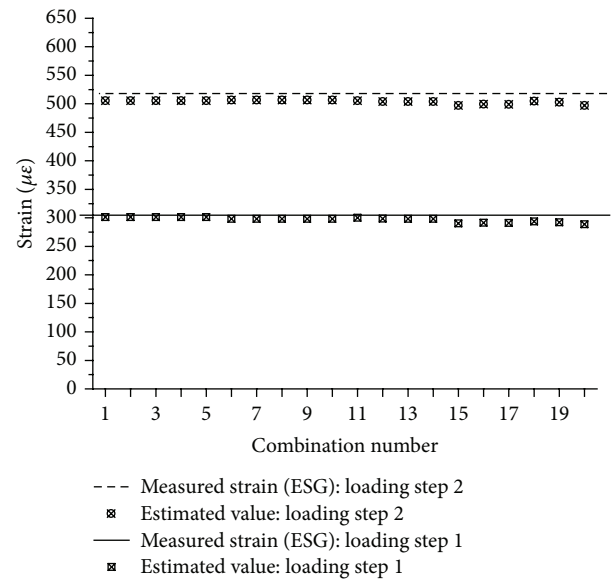


FIGURE 9: Maximum strains estimated from the estimated strain distributions.

5. Conclusion

In this paper, a maximum strain measurement model for beam structures subjected to multiple loading conditions is developed by defining the strain-shape function and participation factors. The maximum strain in a beam is found by the sum of the strains caused by the different loadings acting separately. The strain-shape functions for various loading and support conditions are derived, and a system of equations is defined to calculate the participation factors. The influence of each loading on the value of the total strain can be identified using the influence ratio defined here.

The measurement model is applied to monitor the maximum strain in a 4 m long steel beam subjected to two

concentrated loads. Seven FBG sensors and nine ESGs were attached on the surface of the bottom flange to obtain measurements during the test. The estimated maximum strain and distribution of strains along the length of the beam were compared with those obtained directly from the ESGs. The experimental results indicate good agreement between the strains that were estimated based on the model and the strains measured by the ESGs. Furthermore, the dependency of the locations for the FBG sensors installed on the beam structure on the selection can be avoided using the measurement model.

Acknowledgments

This research is supported by Grant (code #09 R&D A01) from High-Tech Urban Development Program funded by the Ministry of Land, Infrastructure and Transport.

References

- [1] AISC, *Manual of Steel Construction, Allowable Stress Design*, American Institute of Steel Construction, Chicago, Ill, USA, 1989.
- [2] H. S. Park, H. M. Lee, H. Adeli, and I. Lee, "A new approach for health monitoring of structures: terrestrial laser scanning," *Computer-Aided Civil and Infrastructure Engineering*, vol. 22, no. 1, pp. 19–30, 2007.
- [3] Y. Wang, Y. Wang, Y. Li, J. Ran, and M. Cao, "Experimental investigation of a self-sensing hybrid GFRP-concrete bridge superstructure with embedded FBG sensors," *International Journal of Distributed Sensor Networks*, vol. 2012, Article ID 902613, 10 pages, 2012.
- [4] T. H. Yi and H. N. Li, "Methodology developments in sensor placement for health monitoring of civil infrastructures," *International Journal of Distributed Sensor Networks*, vol. 2012, Article ID 612726, 11 pages, 2012.
- [5] H. S. Park, H. S. Jung, Y. H. Kwon, and J. H. Seo, "Mathematical models for assessment of the safety of steel beams based on average strains from long gage optic sensors," *Sensors and Actuators A*, vol. 125, no. 2, pp. 109–113, 2006.
- [6] T. A. Hampshire and H. Adeli, "Monitoring the behavior of steel structures using distributed optical fiber sensors," *Journal of Constructional Steel Research*, vol. 53, no. 3, pp. 267–281, 2000.
- [7] H. S. Park, S. M. Jung, H. M. Lee, Y. H. Kwon, and J. H. Seo, "Analytical models for assessment of the safety of multi-span steel beams based on average strains from long gage optic sensors," *Sensors and Actuators A*, vol. 137, no. 1, pp. 6–12, 2007.
- [8] H. M. Lee and H. S. Park, "Gage-free stress estimation of a beam-like structure based on terrestrial laser scanning," *Computer-Aided Civil and Infrastructure Engineering*, vol. 26, no. 8, pp. 647–658, 2011.
- [9] K. T. V. Grattan and T. Sun, "Fiber optic sensor technology: an overview," *Sensors and Actuators A*, vol. 82, no. 1, pp. 40–61, 2000.
- [10] S. W. James, M. L. Dockney, and R. P. Tatam, "Simultaneous independent temperature and strain measurement using in-fibre Bragg grating sensors," *Electronics Letters*, vol. 32, no. 12, pp. 1133–1134, 1996.
- [11] H. Li, D. Li, and G. Song, "Recent applications of fiber optic sensors to health monitoring in civil engineering," *Engineering Structures*, vol. 26, no. 11, pp. 1647–1657, 2004.
- [12] D. Luo, Z. Ibrahim, Z. Ismail, and B. Xu, "Optimization of the geometries of biconical tapered fiber sensors for monitoring the early-age curing temperature of concrete specimens," *Computer-Aided Civil and Infrastructure Engineering*, vol. 28, no. 7, pp. 531–541, 2013.
- [13] M. Mieloszyk, L. Skarbek, M. Krawczuk, W. Ostachowicz, and A. Zak, "Application of fibre Bragg grating sensors for structural health monitoring of an adaptive wing," *Smart Materials and Structures*, vol. 20, Article ID 125014, 12 pages, 2011.
- [14] R. C. Tennyson, A. A. Mufti, S. Rizkalla, G. Tadros, and B. Benmokrane, "Structural health monitoring of innovative bridges in Canada with fiber optic sensors," *Smart Materials and Structures*, vol. 10, no. 3, pp. 560–573, 2001.
- [15] W. Chung and D. Kang, "Full-scale test of a concrete box girder using FBG sensing system," *Engineering Structures*, vol. 30, no. 3, pp. 643–652, 2008.

Research Article

Study on the Stress Relaxation Behavior of Large Diameter B-GFRP Bars Using FBG Sensing Technology

Li Guo-wei,^{1,2} Pei Hua-Fu,³ and Hong Cheng-yu⁴

¹ Key Laboratory of Ministry of Education for Geomechanics and Embankment Engineering, Hohai University, Nanjing, Jiangsu 210098, China

² Highway and Railway Engineering Institute, Hohai University, Nanjing, Jiangsu 210098, China

³ Harbin Institute of Technology Shenzhen Graduate School, Department of Civil and Environmental Engineering, Shenzhen 518055, China

⁴ Department of Civil Engineering, Shantou University, Shantou 515063, China

Correspondence should be addressed to Pei Hua-Fu; 08902616r@connect.polyu.hk

Received 19 June 2013; Accepted 31 August 2013

Academic Editor: Hong-Nan Li

Copyright © 2013 Li Guo-wei et al. This is an open access article distributed under the Creative Commons Attribution License, which permits unrestricted use, distribution, and reproduction in any medium, provided the original work is properly cited.

Corrosion of steel tendons in certain aggressive environments could lead to durability problems of civil engineering. More recently, fiber-reinforced polymer (FRP) rods have been introduced in the market as tendons for prestressed concrete structures because of their lower modulus behavior. However, previous studies on the FRP mechanical time dependent behavior regarding the stress relaxation of large diameter GFRP have not been well understood. This paper investigates the influence of stress levels on the relaxation behavior of a GFRP bar gripped with a seamless pipe under sustained deformations ranging from 30% to 60% of its ultimate strain. In order to study the behavior of stress relaxation, two basalt-glass fiber hybrid composite (B-GFRP) bars were developed and instrumented with fiber Bragg grating (FBG) strain sensors. It can be found that the test results reveal that the seamless pipe grip method can undertake 70% of ultimate tensile load of the B-GFRP bar, which can satisfy the requirement of stress relaxation of B-GFRP bar subjected to prestress. The model proposed for evaluating stress relaxation ratio can reflect the influences of the nature of B-GFRP bar and the property of grip method.

1. Introduction

The use of ground anchors has been a common practice in civil and mining engineering. Ground anchors function as temporary or permanent structural members to ensure the stability of various structural systems. In general terms, a grouted anchor is a bar that is inserted and grouted into a hole drilled in rock/concrete. Steel strands and wires have been used as anchor tendons for many years, but in certain aggressive environments, corrosion of steel tendons leads to durability problems [1]. In mainland China, anchor bolt structures were widely used for engineering reinforcement in the 1960s. The problem of low durability in reinforced structures also exists [2]. More recently, fiber-reinforced polymer (FRP) rods have been introduced in the market as

tendons for prestressed concrete structures and prestressed ground anchors [3].

Glass FRP (GFRP) bar is the currently available product which is becoming more and more popular in the constructions of concrete structures owing to its low cost compared to CFRP reinforcement. Compared with prestressing steel, the advantages of FRP tendons are (1) high corrosion resistance, (2) high tensile strength, (3) light weight, (4) insensitivity to electromagnetic fields, (5) excellent fatigue behavior, and (6) possible incorporation of optical fiber sensors.

GFRP bar has higher strength and smaller Young's modulus than conventional steel bar [4–6]. The lower modulus of elasticity of an FRP reinforcement may lead to larger deflection of a concrete member after cracking. On the other hand, in prestressed beams, it will lead to a lower loss of



FIGURE 1: B-GFRP bar used in this study.

prestress due to the shrinkage and creep of concrete [7]. If the FRP bar embedded in reinforced concrete is not prestressed, it will not reinforce the structures subjected to slight deformation. Therefore, the prestress is essential for FRP bars used in structural reinforcement.

In the past few decades, the durability of the GFRP materials was recognized as the most critical issue of research. Extensive studies were conducted on the durability of the GFRP material in the 1990s [8–10], including the behavior of GFRP materials and the bond characteristics of GFRP bars in concrete [11–13]. A few studies on time dependent mechanical characteristics of GFRP bars were found in the literature [14–18]. The creep behaviors of GFRP bars obtained from different studies are not consistent such as the review of Laoubi et al. [17] which is different from that of Al-Salloum and Almusallam [18].

For the prestressed or passive FRP ground anchors, reinforced bar produces creep that could cause the stress relaxation. According to the creep behavior of reinforce FRP bar individually, it would be difficult to predict the future stress reduction of the FRP bar subjected to a tensile loading, because its relaxation is related to not only its creep behavior but also the grip method [7]. The grip method of FRP bar is a key technique for pre-stressed FRP reinforced structures. Different grip methods for FRP bars subjected to a tensile force will lead to different slip deformations between the grip body and the FRP bar.

In order to grip the FRP tendons tightly, the methods to grip FRP bar in the structure usually are that (a) the FRP bar was gripped on the press with steel pipe anchors [19]; (b) the FRP bar was gripped with a steel pipe filled with expansive cement material or paste material [7, 20]; and (c) the FRP bar was gripped with a concrete block casted in advance.

Previous research results revealed that a larger diameter GFRP bar has the lower bonding strength than the smaller size [13, 21, 22]. As almost all of the previous researches of GFRP bar durability are for small-sized (diameter less than 20 mm) specimens, the behavior and endurance of larger size GFRP bar are still not well understood, and further research in this aspect is required. Furthermore, ACI 440.1R-01 [23] acknowledged that the creep of GFRP bars and the long-term

deflection behavior of concrete members reinforced with FRP need further research to provide information in areas that are still unclear or in need of additional evidence to validate performance.

However, few studies have been conducted on the stress relaxation in GFRP bar. In this paper, the main objective is to examine the effect of stress level on the relaxation behavior of a GFRP bar gripped with a seamless pipe under sustained deformations of about 30–60% of its ultimate strain.

2. Experimental Study

The experimental program in this study aims to investigate the effect of stress levels on the relaxation behavior of the GFRP bar gripped with a seamless pipe under sustained deformation in laboratory.

2.1. Properties of B-Glass FRP Sand-Coated Bars. The FRP bars used in this study are made of epoxy resin and two types of fibers including basalt and glass fibers. To improve the resistance of pure glass fiber composite to corrosion in alkaline environment, these two types of fibers were used to fabricate a new type of FRP materials. To produce basalt-glass fiber hybrid composites, inner cores of glass fiber are covered by the basalt fibers with better alkali resistance. As shown in Figure 1, the reinforcement materials used in the tests are the basalt-glass fiber hybrid composites with a diameter of 25 mm produced by Zhongshan Pulwell Composites Co., Ltd., in Guangdong Province, China; the basic body is a thermosetting epoxy resin, and the contents of each component (by weight) are resin for 19%, basalt fiber for 10%, glass fiber for 65%, and fine sand for 6%. The mechanical test of the reinforcement material was carried out. The details for physical and mechanical properties of FRP bars used in this study are listed in Tables 1 and 2, respectively.

2.2. Devices for the Stress Relaxation Test of FRP Bar Gripped with Seamless Pipe. If an FRP bar is loaded using traditional wedge-shaped frictional grips, the combination of high compressive stresses and mechanical damage caused by



FIGURE 2: Centralizer used for fixing FRP bar in the anchorage pipe.

TABLE 1: Properties of FRP rebars used in this study.

Diameter (mm)		Ratio of fiber weight of basalt to total fiber (%)	Density (g/cm ³)	Content (weight ratio%)			
Basalt	Glass			Basalt	Glass	Resin	Fine sand
2.10	25.35	13.16	2.07	10	65	19	6

TABLE 2: Properties of FRP rebars.

Item	Calculation method	Value
Ultimate tensile load	$P_{u,ave}$	536.29 ± 6.74 kN
Ultimate tensile strength	$f_{u,ave}$	906.40 ± 11.29 MPa
Guaranteed tensile strength	$f_{fu}^* = f_{u,ave} - 3\sigma$	872.53 MPa
Design tensile strength	$f_{fu} = C_E * f_{fu}^*, C_E = 0.7$	610.77 MPa
Modulus of elasticity	$E_{f,ave}$	52.26 ± 0.87 GPa
Ultimate tensile strain	$\epsilon_{f,ave}$	1.73 ± 0.04%
Guaranteed strain	$\epsilon_u^* = \epsilon_{u,ave} - 3\sigma$	1.62%
Design strain	$\epsilon_u = C_E * \epsilon_u^*$	1.13%
Allowable strain for creep	20% ϵ_u	0.23%

the serrations on the wedge surface will lead to premature failure of the grip zone. Gripping the FRP bar with a device which could undertake the tensile load for any measurement of mechanical properties is a key technique. In this study, the seamless steel pipe was used to grip the FRP bar by filling the binding agent which could expand by itself to create compressive stress gradually. In order to fix the FRP bar at the centre of grip pipe precisely, the centralizer was designed to keep the FRP bar specimen for the tensile property test, as shown in Figure 2. Firstly, Fix the two half centralizers at the tail tip of the pipe, then put the pipe wrapped with the centralizers vertically, and insert the FRP bar into the pipe until the head of FRP bar crosses through the hole of the centralizers, (Figure 3(a)). Secondly, pour the binding agent liquid into the pipe; the binding agent liquid was made from cement, expansible materials, and water by certain ratio (Figure 3(b)). Thirdly, set up two half centralizers at another end of the pipe, and then put the grip pipe of FRP bar specimen into the water to cure the binding agent for 24 hours (Figure 3(c)). Another end of the specimen was gripped as described previously. When all grip actions for FRP bar specimen were ready, these specimens were stored in the

normal room temperature (23°C–26°C) and humidity (35%–60%) situation for 28 days, (Figure 3(d)).

The main advantage of this setup is that it can produce a tensile stress that can reach 70% of its ultimate tensile strength for the large diameter FRP bar at the condition of constant deformation. This setup can satisfy the requirements of the durability test of FRP bar simulated to the actual carry processes of pre-stressed structures reinforced with FRP bar. Furthermore, it does not require a large counter weight and large space, and it is easy to operate.

The expansible material chosen was a highly effective soundless cracking agent (HSCA) which was made in the factory of expanding agents of Hezhou city, Guangxi province, China, and it could create a significant expanding force to press the FRP bar body and lead to enough resistant force for preventing the bar body from sliding out of the pipe. The binding agent consisted of cement, HSCA, and water by the weight ratio 0.5 : 0.5 : 0.3.

The principle of anchoring FRP bar inside the seamless pipe is shown in Figure 4(a). A binding agent could expand to create the compressive stress f_{ep} which leads to tensile stress f_T in the pipe wall, Figure 4(b).

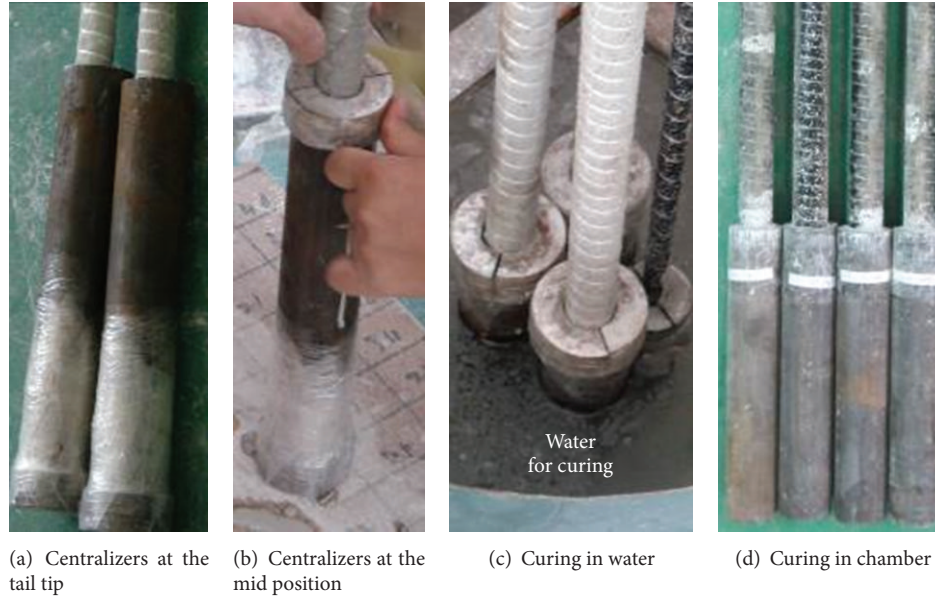


FIGURE 3: Specimens producing process for FRP bar tensile test.

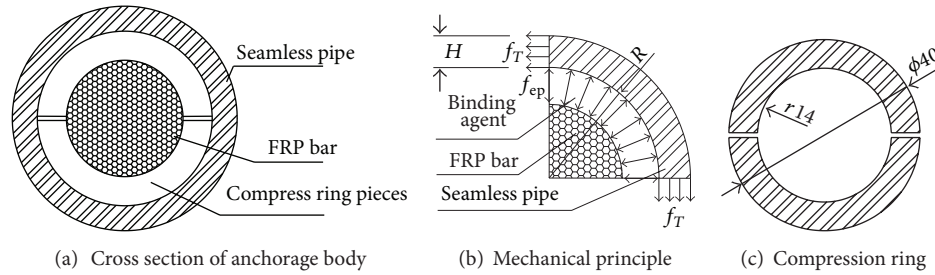


FIGURE 4: Schematic illustration of anchorage pipe of FRP bar specimen for stress relaxation test.

In order to retain the expanding force at the top of the pipe, two compress ring pieces were used to cover on the binding agent and locate between FRP bar and pipe wall, Figure 4(c). Bearing steel plate could stop the ring piece from moving outside during the binding agent expanding and also could close the top binding agent, as shown in Figure 5.

The loading system for the FRP bar relaxation test consisted of hollow jack, bearing plate, load cell, loading pads, and bed plates which could move with the bearing plate during the hollow jack loading, as shown in Figures 6 and 7. The bearing plates could fix the specimen at the suitable position by locking the pipe end of gripping pipe in the groove located on the plate, and the optic fiber wires for monitoring could be connected to the outside by crossing the U gap, as shown in Figure 8. When the piston of the hollow jack pushes the bearing plate to move, it could create the space between the bearing plate and the shell of the hollow jack, and then the loading pads are put in the gap to keep the space constant. As shown in Figure 9, corresponding pads were used at different loading stages. The surfaces of pad are smooth enough to keep the load distributing on the bearing plate uniform. Optic fiber Bragg grating (FBG) sensors were installed at the centre of the

FRP bar body; FBG sensors were mounted diametrically on the FRP bar.

2.3. Strain Monitoring Method of Fiber Bragg Grating (FBG) Sensors. In the past few decades, structural health monitoring as a key technique for evaluating the performance of geotechnical structures is becoming more and more popular. A variety of instruments including GPS [24, 25] and fiber optic sensors [26] have been widely employed and applied in laboratory tests and engineering projects. The conventional instruments used in the test of the FRP bars include the extensometer, strain gauge, and dial gauge. The test for the FRP bars stress relaxation requires high accuracy, stable signal in long-term monitoring, and small volume suitable for FRP bar. Therefore, conventional instruments cannot satisfy the requirements of the stress relaxation test.

Fiber grating technology is achieved by using the characteristics of the light reflected from grating with a specific wavelength [27]. When the incident light is injected into the fiber, the grating will reflect the light with specific wavelength, the value $\Delta\lambda_B$ of the wavelength shift of this reflected light has linear relationship with the applied strain and temperature changes simultaneously. The wavelength will be changed



FIGURE 5: Compression ring and location.

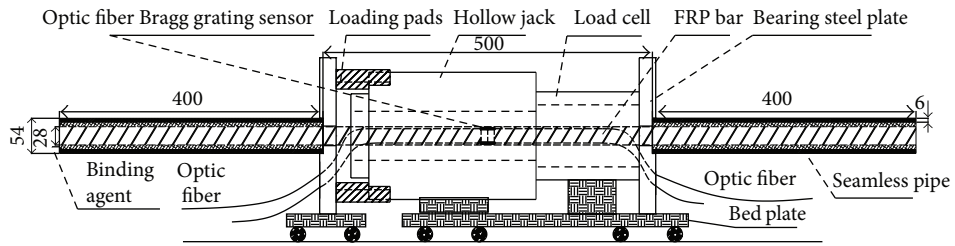


FIGURE 6: Diagram of the loading system for stress relaxation test.

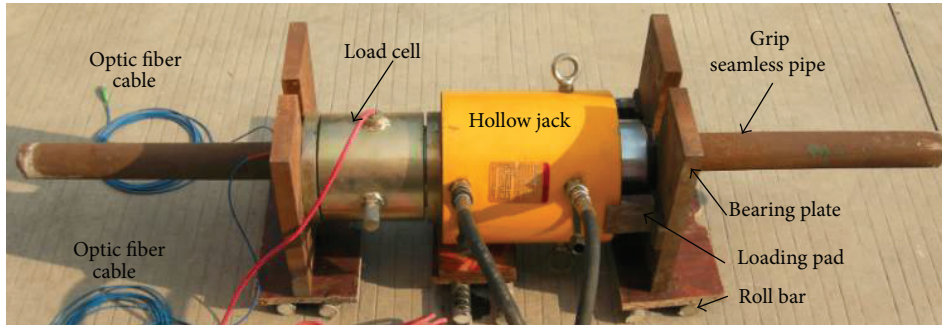


FIGURE 7: Photo of the loading system for stress relaxation test.

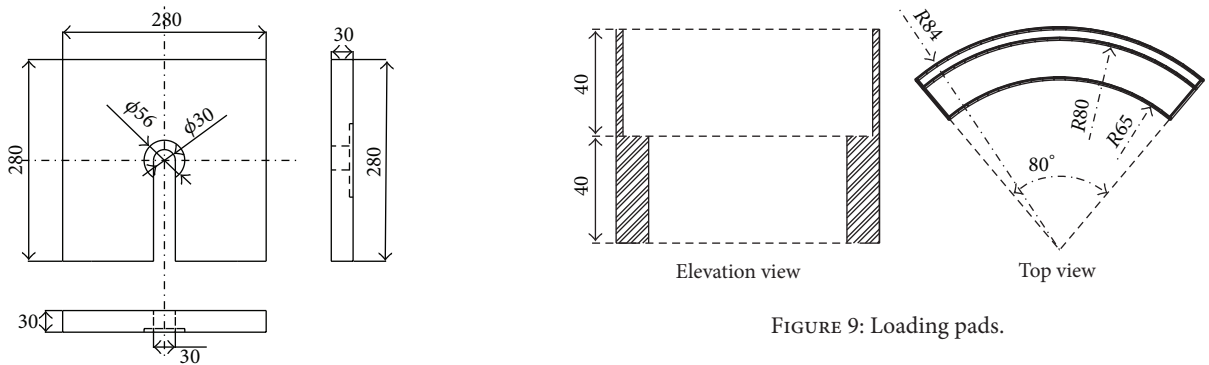


FIGURE 9: Loading pads.

FIGURE 8: Bearing plate for the tensile loading system.

when the grating is subjected to strain or temperature change. This linear relationship can be expressed as

$$\frac{\Delta\lambda_B}{\lambda_B} = c_\epsilon \cdot \Delta\epsilon + c_T \cdot \Delta T, \quad (1)$$

where λ_B is the initial peak wavelength of the reflected light; $\Delta\lambda_B$ is the wavelength shift of peak wavelength; $\Delta\epsilon$ and ΔT are the strain and temperature, respectively; c_ϵ and c_T are coefficients for strain and temperature. The main advantages of FBG sensing technology are the clear mechanism of grating sensor and high detection accuracy. Based on the current demodulation technique, the accuracy of fiber grating sensor

TABLE 3: Summary of relaxation test results for the B-GFRP bar gripped with seamless pipes.

Measured data	Phase 1	Phase 2	Phase 3	Phase 4	Phase 5	Phase 6
Max. load stress (MPa)	385.04	425.54	530.42	570.69	649.97	676.13
Ratio of max. load to ultimate strength (%)	42.48	46.95	58.52	62.96	71.71	74.60
Initial stress of relaxation procedure (MPa)	278.17	302.06	365.27	453.34	507.76	Slippage
Ratio of initial stress to ultimate strength (%)	30.69	33.33	40.30	50.02	56.02	Slippage
Initial strain of the centre of bar ($\mu\epsilon$)	5613.17	5959.42	7316.05	8978.92	10367.79	Slippage
Ratio of initial strain to ultimate strain (%)	32.45	34.45	42.29	51.90	59.93	Slippage
Temperature range ($^{\circ}\text{C}$)	23.1~25.5	16.8~18.9	15.1~17.8	14.5~18.5	13.5~16.8	/
Period of time (hour)	240	142	206	276	191	/
Modulus of elasticity at loading (GPa)	50.5	51.4	48.7	49.7	50.6	/

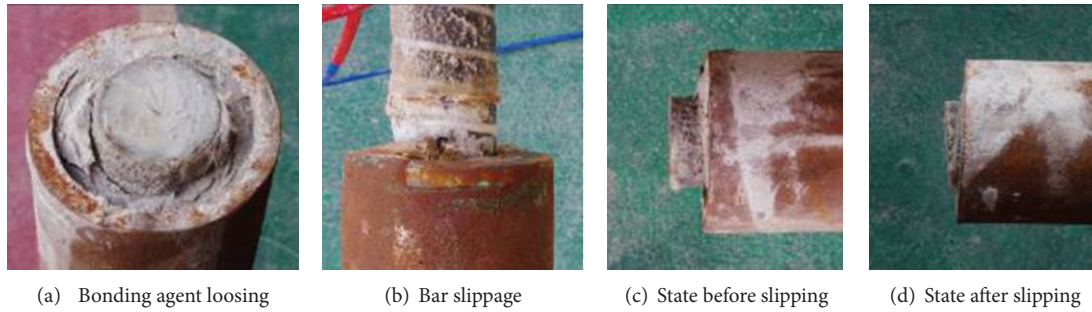


FIGURE 10: The damage phenomenon of B-GFRP bar specimen at stress relaxation processes.

in temperature and strain is up to 0.1°C and $1\mu\epsilon$, the data acquisition frequency is up to 5 kHz, and the sensors spacing can be designed and welded according to the test requirements, which can achieve the long-term monitoring.

3. Test Results

In this study, there are many different optimization strategies for sensors distribution [28–30]. Researchers [31–34] conducted a series of GFRP soil nails pullout tests on site. However, the mechanical behavior of GFRP has not been fully investigated in their study. In this experiment, the FBG sensors were uniformly mounted along the tested FRP bars. Based on the strains measured by FBG strain sensors, stress relaxation tests were conducted on two specimens of the B-GFRP bar gripped with a seamless pipe at different loading stages in laboratory. The test results were summarized in Table 3.

The load was applied on the specimen by hydraulic jack in stages. To keep the space constant, two specific pads were installed between the bearing plate and the jack shell. The stress and strain at different loading levels were recorded. When the piston returns back, the load applied to the bearing plate decreases immediately and arrives to the initial value of stress because of the gaps being closed. The loading pads were used to fill the space between jack shell and the bearing plate as far as possible to avoid too much loss of stress after unloading. The procedure from the maximum to the initial value of stress for specimen was carried out as fast as possible not more than the actual prestress applying actions period of time. When the initial stress relaxes for a period of time

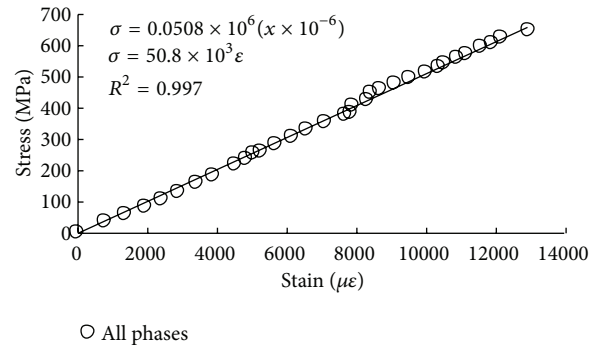


FIGURE 11: B-GFRP bar Young's modulus in all loading phases.

(approximately 7 days), the rate of stress decreasing becomes smaller, and the trend of stress relaxation appears clearly; it is the time to close the current phase and start the next phase of test.

Six phases of loading were conducted for the specimen, and the related test data were recorded, and some of these were presented in Table 3. The 6th phase only obtained the maximum value of stress because of the B-FRP bar slipping out of the grip pipe during the stress relaxation, as shown in Figure 10.

Test results regarding Young's modulus of B-GFRP bar in all phases, stress relaxation processes, and strain change in every phase are presented in terms of stress versus strain, stress versus elapsed time, and strain versus elapsed time for different conditioning schemes, as shown in Figures 11–14.

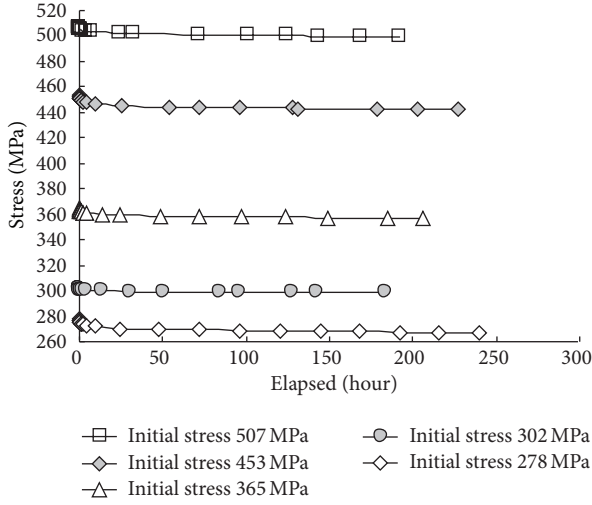


FIGURE 12: Axial stress of the B-GFRP bar versus elapsed time.

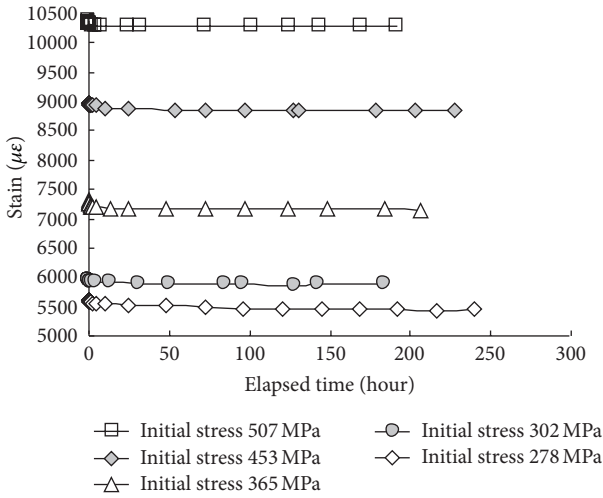


FIGURE 13: Axial strain of B-GFRP bar versus elapsed time.

4. Analysis of the Behavior of Stress Relaxation

4.1. Behavior of Stress Relaxation of the B-GRP Bar Gripped with a Seamless Pipe. Figure 12 shows that the B-GFRP bar gripped with a seamless pipe has a stress relaxation attribution. In all phases of test, the stress of B-GFRP bar decreases with elapsed time at different rates.

In order to compare the difference of stress relaxation rate of B-GFRP bar subjected to different stress increments at different initial stress levels, the ratio of relaxation for increment of stress was defined as

$$r_{\sigma_i, \Delta\sigma} = \frac{\Delta R_{\Delta\sigma}}{\sigma_i}, \quad (2)$$

where $r_{\sigma_i, \Delta\sigma}$ is the ratio of stress relaxation at a certain initial stress σ_i and a certain stress increment $\Delta\sigma$; $\Delta R_{\Delta\sigma}$ is the variation of stress relaxation at σ_i and $\Delta\sigma$.

Figure 15(a) shows the relationship between the variation of ratio of stress relaxation and elapsed time, which was

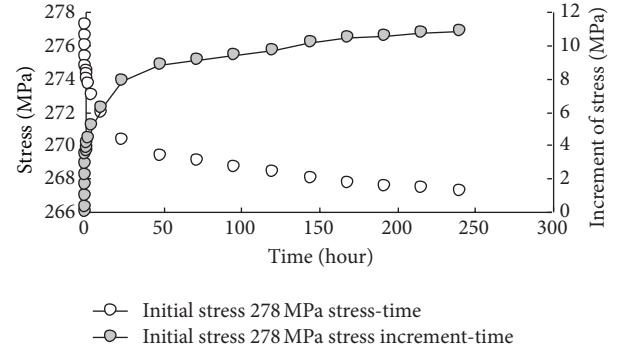


FIGURE 14: Axial stress decreasing process at an initial stress of 278 MPa.

obtained from all phases tests carried out on the B-GFRP bar specimen gripped with a seamless pipe subjected to a constant deformation. It can be found that the relationship of variation of ratio of stress relaxation and elapsed time is similar to a logarithm curve in every phase which has different initial stress and different stress increments. In order to describe test curves, the horizontal coordinate is shown in logarithmic scale. This change makes the curves straight with different intercepts and slopes, as shown in Figure 15(b). Even though the correlation of model for test data is very high, it is difficult to find a unified linear relationship between the parameters of models and the test conditions.

It should be noticed that the variation of stress relaxation ratio (2) was defined without considering the effect of stress history. It does not consider the quantities of stress relaxation produced in the previous procedure in which the initial stress is less than that of the current. In order to consider the effect of stress history, the definition of variation of stress relaxation is defined as

$$R_{\sigma_i} = R_{\sigma_{i-1}} + \Delta R_{\Delta\sigma}, \quad (3a)$$

$$\sigma_i = \sigma_{i-1} + \Delta\sigma, \quad (3b)$$

where R_{σ_i} is the total variation of stress relaxation at a certain initial stress; $R_{\sigma_{i-1}}$ is the total variation of stress relaxation at a certain initial stress σ_{i-1} ; and $\Delta R_{\Delta\sigma}$ is the variation of stress relaxation at a certain increment of stress started at initial stress σ_i .

According to test results, it can be found that

$$R_{\sigma_{i-1}} = A_{\sigma_{i-1}} \cdot \ln(t) + B_{\sigma_{i-1}}, \quad (4)$$

$$\Delta R_{\Delta\sigma} = A_{\Delta\sigma} \cdot \ln(t) + B_{\Delta\sigma},$$

where $A_{\sigma_{i-1}}$ and $B_{\sigma_{i-1}}$ are the slope and intercept of the straight line of stress relaxation at a previous class of initial stress level, respectively; and $A_{\Delta\sigma}$ and $B_{\Delta\sigma}$ are the slope and intercept of straight line of stress relaxation variation at an increment of stress started at present initial stress, respectively.

Assuming that the procedure of stress relaxation for all phase starts at the same time, (3a) can be expressed as

$$R_{\sigma_i} = A_{\sigma_{i-1}} \cdot \ln(t) + B_{\sigma_{i-1}} + A_{\Delta\sigma} \cdot \ln(t) + B_{\Delta\sigma}. \quad (5)$$

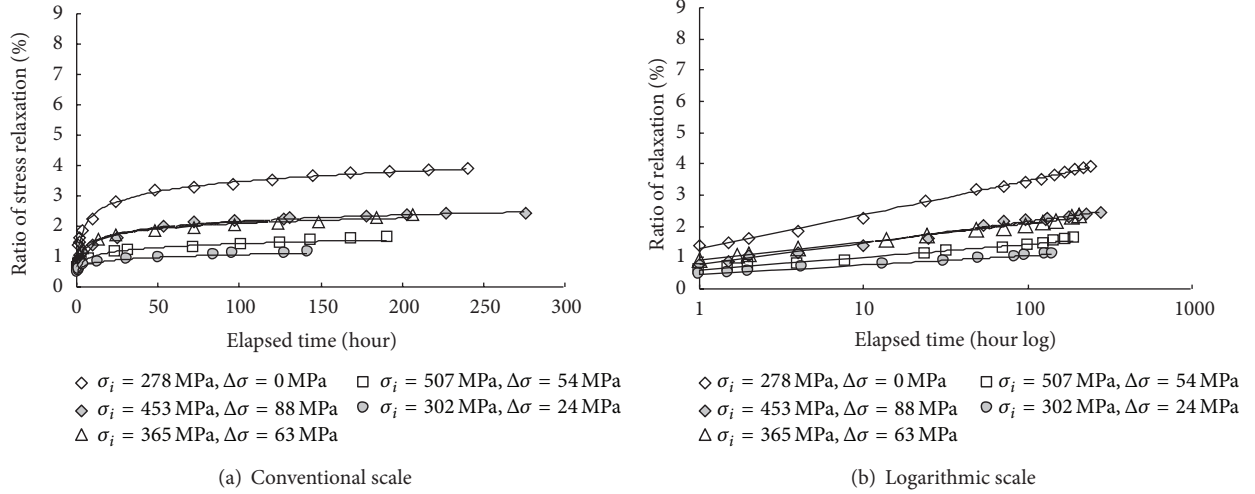


FIGURE 15: Ratio of relaxation versus elapsed time.

TABLE 4: Parameters of stress relaxation variation and ratio for the B-GFRP bar.

Parameters	Phase 1	Phase 2	Phase 3	Phase 4	Phase 5
Initial stress (MPa)	278	302	365	453	507
Increment of stress (MPa)	0	24	63	88	54
Slope of stress relaxation variation, A	1.3025	0.3918	0.8955	1.3887	0.9096
Intercept of stress relaxation variation, B	3.596	1.4041	3.3873	3.4474	2.975
Slope of stress relaxation ratio, a	0.47	0.56	0.71	0.88	0.96
Intercept of stress relaxation ratio, b	1.29	1.66	2.30	2.61	2.92

The accumulated ratio of stress relaxation can be expressed by

$$r_{\sigma_i} = \frac{R_{\sigma_i}}{\sigma_i}, \quad (6)$$

where r_{σ_i} is the accumulated ratio of stress relaxation at initial stress; R_{σ_i} is the accumulated variation of stress relaxation; and σ_i is the initial stress.

Substituting (5) into (6)

$$r_{\sigma_i} = \frac{A_{\sigma_{i-1}} + A_{\Delta\sigma}}{\sigma_i} \cdot \ln(t) + \frac{B_{\sigma_{i-1}} + B_{\Delta\sigma}}{\sigma_i}. \quad (7)$$

By substituting $a_{\sigma_i} = (A_{\sigma_{i-1}} + A_{\Delta\sigma})/\sigma_i$, $b_{\sigma_i} = (B_{\sigma_{i-1}} + B_{\Delta\sigma})/\sigma_i$ to (7), (7) can be expressed by

$$r_{\sigma_i} = a_{\sigma_i} \cdot \ln(t) + b_{\sigma_i}. \quad (8)$$

The test data were reorganized according to (7). Parameters a and b are calculated and listed in Table 4. The stress relaxation ratio curves are plotted in Figure 16(a), and the shape of curves is highly different from before, as shown in Figure 16(a). The straight lines show a clear relationship between slopes and intercepts with initial stress of the relaxation procedure, as shown in Figure 16(b).

It can be found that the slope a_{σ_i} and intercept b_{σ_i} increase with the initial stress simultaneously. The correlation of a_{σ_i} and b_{σ_i} with the initial stress is shown in Figures 17 and 18.

The two parameters of α and β are obtained for the slope by fitting in the relationship about slope and initial stress, as shown in Figure 17. The other two parameters of κ and λ are obtained for the intercept by fitting the relationship between intercepts and initial stress levels, as shown in Figure 18.

Consider

$$a_{\sigma_i} = \alpha \cdot \ln(\sigma_i) + \beta, \quad (9)$$

$$b_{\sigma_i} = \kappa \cdot \ln(\sigma_i) + \lambda.$$

Substituting (9) to (8),

$$r_{\sigma_i} = (\alpha \cdot \ln(\sigma_i) + \beta) \cdot \ln(t) + \kappa \cdot \ln(\sigma_i) + \lambda. \quad (10)$$

Equation (10) is the final unified model describing the stress relaxation procedure of the B-GFRP bar gripped with a seamless pipe, which is obtained from the relaxation test carried out in accordance with step by step loading. α and β all reflect the effect of elapsed time of stress relaxation, which are called delay relaxation parameters. κ and λ reflect the extent of instant relaxation of stress. Thus, they are called instant relaxation parameters.

If $a_{\sigma_i} = 0$, a new parameter σ_{ID} can be obtained. σ_{ID} is the minimum value of the initial stress which can cause delay relaxation of stress, which should be associated with the nature of the B-GFRP bar. Also, if $b_{\sigma_i} = 0$, another parameter σ_{II} can be obtained, which is the minimum value of initial stress which can cause instant relaxation of stress which should be associated with gripping method.

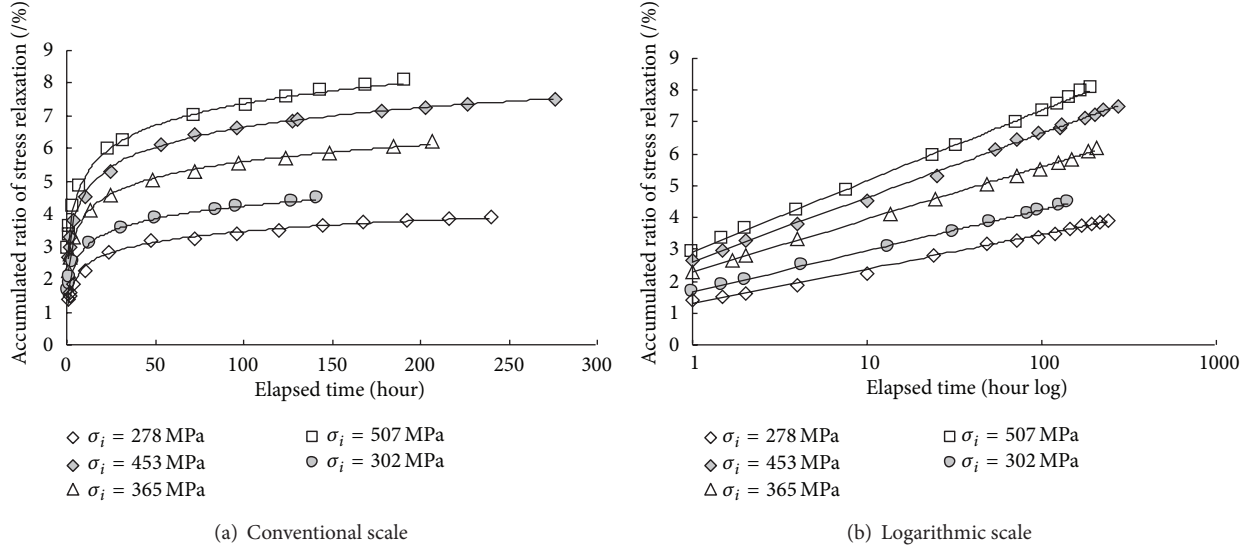


FIGURE 16: Accumulated ratio of stress relaxation versus elapsed time.

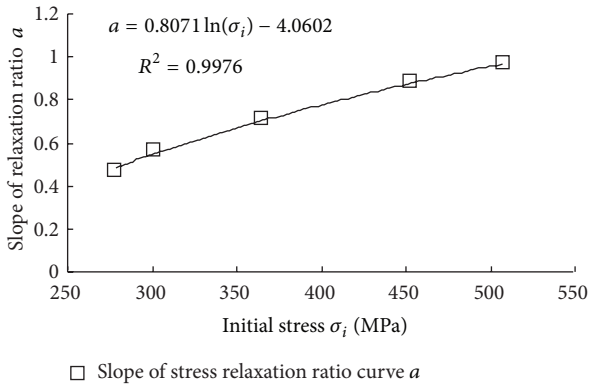


FIGURE 17: Slopes versus initial stress.

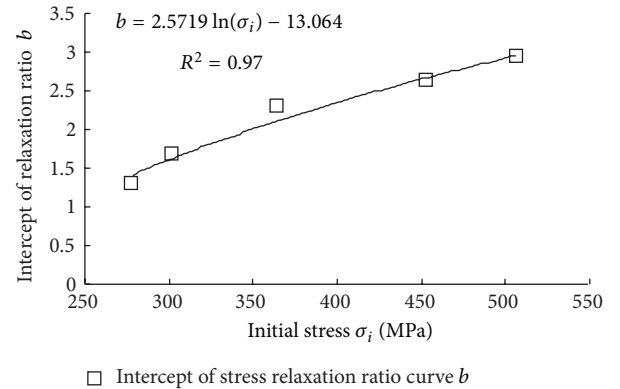


FIGURE 18: Intercepts versus initial stress.

Consider

$$\sigma_i = \exp\left(-\frac{\beta}{\alpha}\right) = \sigma_{ID}, \quad (11)$$

$$\sigma_i = \exp\left(-\frac{\lambda}{\kappa}\right) = \sigma_{II}.$$

To sum up, six relaxation parameters obtained from the test about the B-GFRP bar gripped with seamless pipe are listed in Table 5. These parameters are substituted into (10) and obtain model curves in Figure 19. It can be found that the model curves fit well with the test curves.

It can be found that a little difference exists between the minimum value σ_{ID} of stress causing delay relaxation and the minimum value σ_{II} of stress causing instant relaxation, and σ_{ID} is less than σ_{II} . These test results mean that the procedure of stress relaxation for a B-GFRP bar gripped with seamless pipe can be described precisely by the presented model with 4 parameters, and producing the instant stress relaxation needs larger initial stress relative to the delay relaxation of stress.

TABLE 5: Parameters of stress relaxation for the B-GFRP bar gripped with seamless pipes.

α	β	κ	λ	σ_{ID} (MPa)	σ_{II} (MPa)
0.81	-4.06	2.57	-13.06	153.03	160.70

TABLE 6: Ratio of stress relaxation for the B-GFRP soil nail element at a duration of million hours.

Initial stress/ultimate strength	30%	40%	50%	60%	70%
Ratio of stress relaxation at a					
period of time (%)					
10 years	6.81	10.21	12.84	14.99	16.80
114 years					
1,000,000 hours	7.98	11.94	15.01	17.52	19.64

According to the newly developed stress relaxation model, the ratios of stress relaxation in 10 years and one million hours at different initial stress are calculated in Table 6.

4.2. Behavior of Young's Modulus of the B-GFRP Bar in that Procedure of Stress Relaxation. Figure 13 shows that the

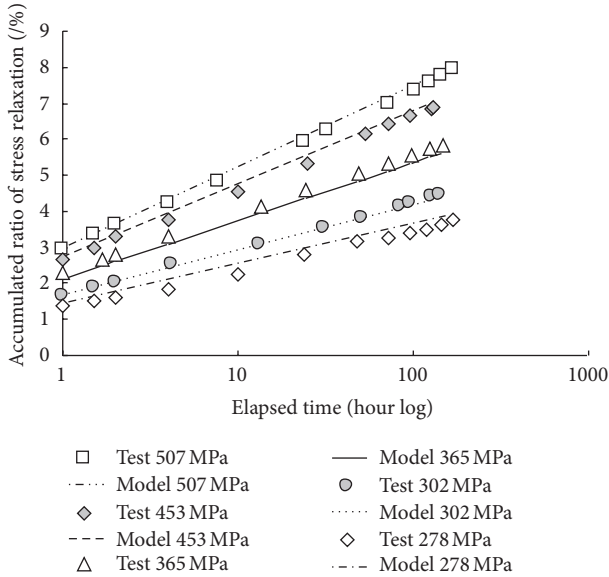


FIGURE 19: Test curves and model curves of stress relaxation for B-GFRP bars gripped with seamless pipes.

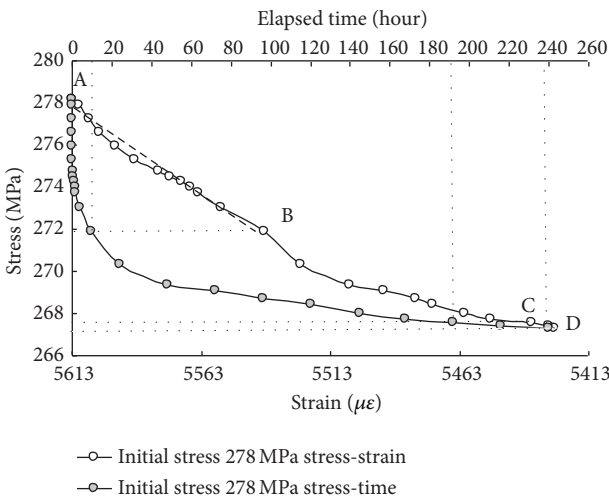


FIGURE 20: Stress versus strain during stress relaxation process for B-GFRP bar gripped with seamless pipe.

relationship between stress and strain of the B-GFRP bar gripped with a seamless pipe is linear. From these, it can be concluded that the stress relaxation over a long period of time at a lower stress level can not change the slope of linear relationship between stress and strain at a higher stress level for B-GFRP bar. That can be said that the Young's modulus of B-GFRP bar can not be impacted by stress relaxation at lower stress level.

Figure 20 shows the relationship between stress and strain during the stress relaxation for a B-GFRP bar gripped with a seamless pipe. It can be seen that the procedure of stress relaxation can be divided into three periods. In the first period AB, approximately 10 hours, the rate of stress relaxing is very fast and the relationship between stress and strain approaches a

straight line. For the second period BC, over a longer time, the rate of stress relaxing becomes slower and the relationship between stress and strain is nonlinear. In the last period CD, the stress and strain change slowly and almost reach a constant value, and the curve approaches a point. Thus, the relationship of stress versus strain of B-GFRP bar is variable during stress relaxation processes, which is a nonlinear relationship and can not be described by a constant modulus.

5. Conclusion

The objectives of this research program are to evaluate the behavior of stress relaxation of a large diameter B-GFRP bar. Two experiments were conducted on the model of stress relaxation of B-GFRP bar in a specialized grip method at different stress levels. Based on the experimental results and analytical studies on sand-coated B-GFRP bar under the described test conditions, the following conclusions can be drawn.

- (a) For the large diameter B-GFRP bar (27.45 mm), it can be gripped with seamless pipe by filling a binding agent, which can undertake 70% of its ultimate tensile load. This gripped method can satisfy the requirements for the testing the behavior of stress relaxation of pre-stressed B-GFRP.
- (b) The behavior of stress relaxation of B-GFRP bar gripped with seamless pipe subjected to prestress is related to the elapsed time and the initial stress level. A model of stress relaxation ratio was obtained, which has four parameters reflecting the influences of the nature of B-GFRP bar and the property of grip method. It can be concluded that the model is in good agreement with the experimental results.
- (c) According to the newly developed stress relaxation model, the ratios of stress relaxation in ten years and one million hours at an initial stress of 30% ultimate strength are 6.81% and 7.98%, respectively.
- (d) The stress relaxing over a long period at a lower stress level cannot change the slope of the linear relationship between stress and strain at a higher stress level for the B-GFRP bar.

Acknowledgments

The authors wish to express their gratitude and sincere appreciation for the financial support received from the government of Guangdong province and Ministry of education of China (Project no. 2009B09060011). The help received from the technical staff of the Rock and Soil Mechanics Laboratory in the College of Civil and Transportation Engineering at the Hohai University is also acknowledged.

References

[1] G. H. Koch, M. P. H. Brongers, N. G. Thomson, Y. P. Virmanio, and J. H. Payer, *Cost of Corrosion in the United States, Handbook*

- of Environmental Degradation of Materials*, William Andrew, Norwich, NY, USA, 2005.
- [2] X. Zeng, Z. Chen, J. Wang, and Y. Du, "Research on safety and durability of bolt and cable-supported structures," *Chinese Journal of Rock Mechanics and Engineering*, vol. 23, no. 13, pp. 2235–2242, 2004.
 - [3] B. Zhang, B. Benmokrane, A. Chennouf, P. Mukhopadhyaya, and A. El-Safy, "Tensile behavior of FRP tendons for prestressed ground anchors," *Journal of Composites for Construction*, vol. 5, no. 2, pp. 85–93, 2001.
 - [4] G. W. Li, W. M. Ge, C. Ni, J. Dai, and C. L. Mu, "Effect of loading rate on tensile properties of full-scale specimen of larger-diameter glass fiber reinforced polymer (GFRP) bar," *Chinese Journal of Rock Mechanics and Engineering*, vol. 31, no. 7, pp. 1469–1477, 2012.
 - [5] F. Katsuki and T. Uomoto, "Prediction of deterioration of FRP rods due to alkali attack," in *Proceedings of the 2nd International Conference on Non-Metallic Reinforcement for Concrete Structures*, L. Taewer, Ed., pp. 82–89, (FRPRSC-2), Ghent, Belgium, E&FN Spon, London, UK, 1995.
 - [6] F. E. Tannous and H. Saadatmanesh, "Durability of AR glass fiber reinforced plastic bars," *Journal of Composites for Construction*, vol. 3, no. 1, pp. 12–19, 1999.
 - [7] P. X. W. Zou, "Long-term properties and transfer length of fiber-reinforced polymers," *Journal of Composites for Construction*, vol. 7, no. 1, pp. 10–19, 2003.
 - [8] Y. Chen, J. F. Davalos, I. Ray, and H.-Y. Kim, "Accelerated aging tests for evaluations of durability performance of FRP reinforcing bars for concrete structures," *Composite Structures*, vol. 78, no. 1, pp. 101–111, 2007.
 - [9] A. S. M. Kamal and M. Boulfiza, "Durability of GFRP rebars in simulated concrete solutions under accelerated aging conditions," *Journal of Composites for Construction*, vol. 15, no. 4, pp. 473–481, 2011.
 - [10] S. Alsayed, Y. Al-Salloum, T. Almusallam, S. El-Gamal, and M. Aqel, "Performance of glass fiber reinforced polymer bars under elevated temperatures," *Composites B*, vol. 43, no. 5, pp. 2265–2271, 2012.
 - [11] R. Masmoudi, A. Masmoudi, M. B. Ouezdou, and A. Daoud, "Long-term bond performance of GFRP bars in concrete under temperature ranging from 20°C to 80°C," *Construction and Building Materials*, vol. 25, no. 2, pp. 486–493, 2011.
 - [12] J. Zhou, X. Chen, and S. Chen, "Durability and service life prediction of GFRP bars embedded in concrete under acid environment," *Nuclear Engineering and Design*, vol. 241, no. 10, pp. 4095–4102, 2011.
 - [13] J. Alves, A. El-Ragaby, and E. El-Salakawy, "Durability of GFRP bars' bond to concrete under different loading and environmental conditions," *Journal of Composites for Construction*, vol. 15, no. 3, pp. 249–262, 2011.
 - [14] Z. Wang, O. Joh, and Y. Goto, "Bond creep behavior of FRP rods and their bond strength after sustained loading," *Concrete Engineering Annual Collected Papers*, vol. 21, no. 3, pp. 1513–1518, 1999.
 - [15] H. Saadatmanesh and F. E. Tannous, "Relaxation, creep, and fatigue behavior of carbon fiber reinforced plastic tendons," *ACI Materials Journal*, vol. 96, no. 2, pp. 143–153, 1999.
 - [16] B. Benmokrane, P. Wang, T. M. Ton-That, H. Rahman, and J.-F. Robert, "Durability of glass fiber-reinforced polymer reinforcing bars in concrete environment," *Journal of Composites for Construction*, vol. 6, no. 3, pp. 143–153, 2002.
 - [17] K. Laoubi, E. El-Salakawy, and B. Benmokrane, "Creep and durability of sand-coated glass FRP bars in concrete elements under freeze/thaw cycling and sustained loads," *Cement and Concrete Composites*, vol. 28, no. 10, pp. 869–878, 2006.
 - [18] Y. A. Al-Salloum and T. H. Almusallam, "Creep effect on the behavior of concrete beams reinforced with GFRP bars subjected to different environments," *Construction and Building Materials*, vol. 21, no. 7, pp. 1510–1519, 2007.
 - [19] A. Nanni, T. Utsunomiya, H. Yonekura, and M. Tanigaki, "Transmission of prestressing force to concrete by bonded fiber reinforced plastic tendons," *ACI Structural Journal*, vol. 89, no. 3, pp. 335–344, 1992.
 - [20] D. Schesser, Q. D. Yang, A. Nanni, and J. W. Giancaspro, "Expansive grout-based gripping systems for tensile testing of large diameter composite bars," *Journal of Materials in Civil Engineering*, 2013.
 - [21] A. Nanni, M. M. Al-Zaharani, S. U. Al-Dulaijan, C. E. Bakis, and T. E. Boothby, "Bond of FRP reinforcement to concrete-Experimental results," in *Proceedings of the 2nd International RILEM Symposium on Nonmetallic FRP Reinforcement for Concrete Structures (FRPRCS-2)*, L. Taerwe, Ed., pp. 135–145, E&FN Spon, Ghent, Belgium, 1995.
 - [22] B. Benmokrane, B. Tighiouart, and O. Chaallal, "Bond strength and load distribution of composite GFRP reinforcing bars in concrete," *ACI Materials Journal*, vol. 93, no. 3, pp. 246–253, 1996.
 - [23] A. C. I. Committee 440, *Guide for the Design and Construction of Concrete reinforced with FRP Bars*, ACI 440.1R-06, American Concrete Institute, Farmington Hills, Mich, USA, 2006.
 - [24] T.-H. Yi, H.-N. Li, and M. Gu, "Recent research and applications of GPS-based monitoring technology for high-rise structures," *Structural Control and Health Monitoring*, vol. 20, no. 5, pp. 649–670, 2013.
 - [25] T.-H. Yi, H.-N. Li, and M. Gu, "Characterization and extraction of global positioning system multipath signals using an improved particle-filtering algorithm," *Measurement Science and Technology*, vol. 22, no. 7, Article ID 075101, pp. 1–11, 2011.
 - [26] H. F. Pei, J. H. Yin, H. H. Zhu, and C. Y. Hong, "Monitoring performance of a glass fiber reinforced polymer soil nail during laboratory pullout test using FBG sensing technique," *International Journal of Geomechanics*, vol. 13, no. 4, pp. 467–472, 2013.
 - [27] H. F. Pei, J. H. Yin, H. H. Zhu, C. Y. Hong, W. Jin, and D. S. Xu, "Monitoring of lateral displacements of a slope using a series of special FBG based in-place inclinometers," *Measurement Science and Technology*, vol. 23, no. 2, Article ID 025007, 2012.
 - [28] T.-H. Yi, H.-N. Li, and M. Gu, "A new method for optimal selection of sensor location on a high-rise building using simplified finite element model," *Structural Engineering and Mechanics*, vol. 37, no. 6, pp. 671–684, 2011.
 - [29] T.-H. Yi, H.-N. Li, and M. Gu, "Optimal sensor placement for structural health monitoring based on multiple optimization strategies," *Structural Design of Tall and Special Buildings*, vol. 20, no. 7, pp. 881–900, 2011.
 - [30] T. H. Yi, H. N. Li, and X. D. Zhang, "Sensor placement on Canton Tower for health monitoring using asynchronous-climbing monkey algorithm," *Smart Materials and Structures*, vol. 21, no. 12, pp. 1–12, 2012.
 - [31] H.-H. Zhu, J.-H. Yin, A. T. Yeung, and W. Jin, "Field pullout testing and performance evaluation of GFRP soil nails," *Journal of Geotechnical and Geoenvironmental Engineering*, vol. 137, no. 7, pp. 633–642, 2011.

- [32] W.-H. Zhou and J.-H. Yin, "A simple mathematical model for soil nail and soil interaction analysis," *Computers and Geotechnics*, vol. 35, no. 3, pp. 479–488, 2008.
- [33] W.-H. Zhou, J.-H. Yin, and C.-Y. Hong, "Finite element modelling of pullout testing on a soil nail in a pullout box under different overburden and grouting pressures," *Canadian Geotechnical Journal*, vol. 48, no. 4, pp. 557–567, 2011.
- [34] J.-H. Yin and W.-H. Zhou, "Influence of grouting pressure and overburden stress on the interface resistance of a soil nail," *Journal of Geotechnical and Geoenvironmental Engineering*, vol. 135, no. 9, pp. 1198–1208, 2009.

Research Article

Feasibility Study on Crack Detection of Pipelines Using Piezoceramic Transducers

Guofeng Du,^{1,2} Qingzhao Kong,² Timothy Lai,² and Gangbing Song²

¹ School of Urban Construction, Yangtze University, Jingzhou, Hubei 434023, China

² Department of Mechanical Engineering, University of Houston, Houston, TX 77204, USA

Correspondence should be addressed to Guofeng Du; gfd.1125@126.com

Received 5 July 2013; Accepted 5 September 2013

Academic Editor: Ting-Hua Yi

Copyright © 2013 Guofeng Du et al. This is an open access article distributed under the Creative Commons Attribution License, which permits unrestricted use, distribution, and reproduction in any medium, provided the original work is properly cited.

Damage detection of pipelines is of great significance in terms of safety in the oil and gas industry. Currently, lead zirconate titanates (PZTs) are the most popular piezoceramic materials and show great potential in the applications of structural health monitoring. In this paper, the authors present a feasibility study on the crack detection and severity monitoring of pipelines using PZT transducers. Due to their electromechanical properties, the piezoceramic transducers can be either as an actuator or a sensor to generate or detect the stress wave. The active sensing approach was applied to monitor the crack severity of pipelines. The crack in the stress wave propagation path can be regarded as a stress relief, which reduces the received energy by the sensors. In the test, eight different operating conditions were tested in which one artificial crack was created ranging from 0 mm to 10.5 mm. A wavelet packet-based crack severity index was also built to quantitatively identify the pipeline damage condition at various crack depths.

1. Introduction

Pipelines consistently experience complications in service, with some examples being stress corrosion and excessive external forces, which cause the pipelines to form cracks. These cracks, if not detected in a timely fashion, may lead to catastrophic events with severe economic losses and environmental pollution. The study on damage detection of pipelines is of great significance to ensure their safe operation and receives increasing attention in the literature. Methods for pipeline damage detection include the fiber optic sensor based method [1–3], the acoustic emission method [4–6], the ultrasonic method [7–10], the eddy current method [11–13], and piezoelectric impedance method [14–17].

In recent years, the piezoceramic transducer based active-sensing approach has been developed and demonstrated its promises in real-time damage detection and health monitoring of civil infrastructures [18–28]. Due to its advantages of both actuation and sensing capacities, wide bandwidth, fast response, and low cost, piezoceramic based transducers are used in the active sensing approach to structural damage detection. In the active sensing approach, one piezoceramic

transducer is used as an actuator to generate the desired wave to propagate through the host structure, and other distributed piezoceramic transducers are used as sensors to detect the wave response. Cracks or damages inside the structure act as a stress relief in the wave propagation path. The amplitude of wave and the transmission energy will decrease due to the existence of cracks or damages. The decrease of the transmission energy can be correlated with the degree of the structural damage. In general, the active sensing approach has the advantages of real time and distributed monitoring.

In this paper, the authors explore the feasibility of applying the active sensing approach to crack detection and crack severity monitoring of pipelines using piezoceramic transducers. The lead zirconate titanate (PZT) type of piezoceramic material is adopted in this paper due to its strong piezoelectric effect. In this research, an experimental setup involving a pipe segment with an artificial crack is fabricated. On the pipe segment, one PZT is used as the actuator in order to generate the swept sine wave signal. Meanwhile, three PZTs are set up at different locations on the pipe as sensors to receive the excitation signal from the actuator. Since all structures have their own unique initial and boundary

TABLE 1: Pipeline dimensions and Q235 steel properties.

Steel grade	Density (kg/m ³)	Elastic modulus (MPa)	Poisson ratio	Wall thickness (mm)	Pipe length (mm)
Q235	7850	205,000	0.30	10.5	100

TABLE 2: Main properties of PZT patches.

Density (g/cm ³)	Dielectric constant	Electromechanical coupling coefficient	Capacitance (nF)	Piezoelectric coefficient (C/N)	Curie temperature (°C)
7.50	1600 ± 10%	0.65	3.77	450	350

conditions (including different sensor locations), the severity of structural damage will be assessed by the changes in the damage indexes as monitored by the sensors. With this approach, the severity of the pipeline crack can be monitored by tracing and analyzing the amplitude of the response signal. In addition, the wavelet packet-based crack severity index is implemented to quantify the severity of the crack detected via the active sensing approach.

2. Wavelet Packet-Based Crack Severity Index

When piezoelectric materials are subjected either to a stress or strain, they will generate an electric charge. Similarly, the opposite is also true—when subject to electric charges, piezoelectric materials are able to produce a stress or strain. Due to this special piezoelectric property, PZT transducers can be used interchangeably either as actuators or as sensors. This research takes advantage of these properties in the active sensing approach. One PZT is set up as an actuator to generate a guided electrical signal, while additional distributed PZTs are set up elsewhere to receive this signal. Since the stress wave propagation is highly dependent on the wave path's medium, the characteristics of the received signal can be used as an indicator for the structural health monitoring.

In this research, the basic experimental approach is related to the above principles. The crack in the stress wave propagation path functions as a stress relief. Furthermore, the loss of energy received by the sensors is correlated with the severity of the crack. These phenomena are then quantified with wavelet packet analysis, which is used as a signal-processing tool for analysis. The wavelet transform technique is widely used in engineering structural analysis. For example, the wavelet energy method was used to search the critical incidence of earthquake excitation in multidimensional seismic response of offshore platforms [29]. Wavelet denoising has been used for bridge health monitoring using GPS and the characterization of multipath signals and techniques for their removal by improved particle filtering [30, 31]. In this paper, indicators of damage to the pipeline will be extracted from data using wavelet analysis techniques. Because of the complexity of the tested structure, the frequency response can be observed by a guided swept sine wave input and the energy obtained by wavelet packet analysis from the response is compared to the baseline, thereby increasing the accuracy when judging whether structure damage has occurred. The basic principles of this analysis technique are as follows.

In the proposed health monitoring algorithm, the sensor signal V is decomposed by an n -level wavelet packet decomposition into 2^n signal subsets $\{X_1, X_2, \dots, X_{2^n}\}$ and j is the frequency band. The decomposed subset X_j is written as

$$X_j = [x_{j,1} \ x_{j,2}, \dots, x_{j,m}], \quad (j = 1, 2, \dots, 2^n), \quad (1)$$

where m is the amount of sampling data. Additionally, the energy of the decomposed signal at time index i can be defined as

$$E_{i,j} = x_{j,1}^2 + x_{j,2}^2 + \dots + x_{j,m}^2. \quad (2)$$

The energy vector at time index i can be defined as

$$E_i = [E_{i,1}, E_{i,2}, \dots, E_{i,2^n}]. \quad (3)$$

Based on the calculation of energy vectors (E_i), the crack severity index for the sensor signal at time index i can be expressed as

$$I(i) = \sqrt{\frac{\sum_{j=1}^{2^n} (E_{i,j} - E_{1,j})^2}{\sum_{j=1}^{2^n} E_{1,j}^2}}. \quad (4)$$

Since crack severity may be described by depth, $I(i)$ can be an approximate indicator of the crack size (although it cannot be used to exactly calculate the dimensions). The deeper the crack, the larger the index becomes.

3. Experimental Setup and Testing Procedures

3.1. Pipeline Specimen and PZT Locations. One section of a pipeline sample was used in this experiment. The pipeline was constructed from Q235 steel. The dimensions and material properties of the pipeline are shown in Table 1. The outer and inner diameters of the pipeline are 101 mm and 80 mm, respectively.

Four PZT patches were fixed on the pipeline surface using Epoxy (LOCTITE EPOXY). The locations of PZT patches are shown in Figure 1. It should be noted that PZT-1, PZT-2, and PZT-3 are equidistant from each other along the length of the pipe. Also seen in Figure 1, the location of PZT-4 is rotated 90 degrees counterclockwise from PZT-3. A third point to note is that an artificial crack was cut approximately halfway between PZT-1 and PZT-2. Figure 2 shows the actual specimen with the aforementioned PZT locations and the artificial crack.

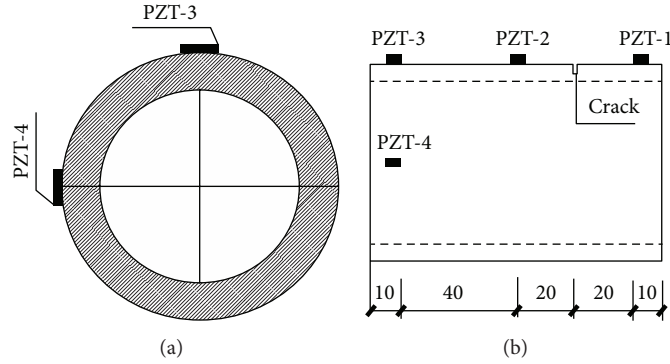


FIGURE 1: Locations of PZT sensors.

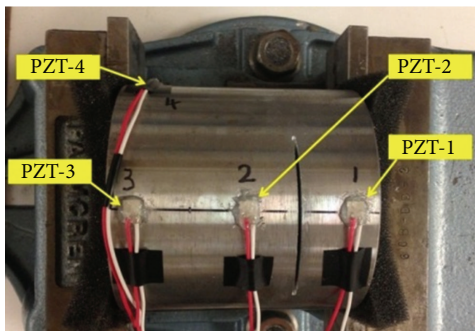


FIGURE 2: Pipeline specimen with PZT patches.

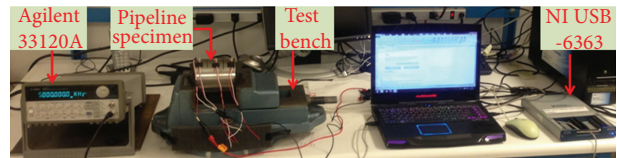


FIGURE 3: Experimental setup.

TABLE 3: Test operating conditions (OCs).

Operating condition	1	2	3	4	5	6	7	8
Crack depth (mm)	0	1.5	3.0	4.5	6.0	7.5	9.0	10.5

As mentioned previously, the PZTs display special electromechanical properties, such as density and capacitance. Some of these properties are presented in Table 2. Many factors will influence the detection of pipeline damage, such as piezoelectric ceramic sensor types and properties, the thickness of the bonding layer, the quality of bonding, the material, and size of pipeline. On the other hand, since the proposed method compares the damage indexes of the structure during healthy and damaged states, the above factors will not affect the damage identification results.

During the test, eight operating conditions correlating to different crack depths (0 mm–10.5 mm) were investigated. Table 3 depicts each operating condition with its corresponding crack depth. It should be noted that the crack depth increased by 1.5 mm for each operating condition starting from condition 1 and the crack width was always 1.2 mm.

3.2. *Experimental Setup.* In the presented test system, the PZT actuator (PZT-1) is connected with a function generator (Agilent 33120A). The PZT sensors (PZT-2, PZT-3, and PZT 4) are connected with a data acquisition system (NI USB-6363). The sampling rate of the data acquisition system for

each channel is 1Ms/S. The entire experimental setup is shown in Figure 3.

3.3. *Testing Procedures.* During the test, PZT-1 was used as an actuator and PZT-2, PZT-3, and PZT-4 were used as sensors. A swept sine wave signal from 60 kHz to 200 kHz was generated by PZT-1, as shown in Figure 4. The amplitude of the excitation signal is 10 V and the period is 2 s. During each operating condition, PZT-1 produced the guided swept sine wave to all the other sensors and the response signal were recorded by the sensors. Since the pipeline crack was regarded as a stress relief which affected the performance of the stress wave propagation between the actuator and sensors, the sensor signals accurately reflected the pipeline crack severity for each operating condition.

4. Experimental Results and Analysis

The received signals of PZT-2, PZT-3, and PZT-4 in each operating condition are shown below in Figures 5, 6, and 7. Each signal was subjected to several resonance frequencies within the range of 60 kHz to 200 kHz. Each plot reflects the sensor signal response from one period of the swept sine wave signal, which is equal to 2 seconds in the time domain. From the plots, several resonance peaks can be observed, especially towards the end of the period (i.e., after 1.8 seconds). Through the analysis of these peaks, the same general trend can be identified for each of the PZTs. This trend shows that the amplitudes of the resonance peaks decrease with an increase of the crack depth. This trend indicates that less energy is collected by the sensors with increasing crack depth. Ultimately when the crack is of a depth near 10.5 mm, the entire signal response is extremely weak, which indicates that

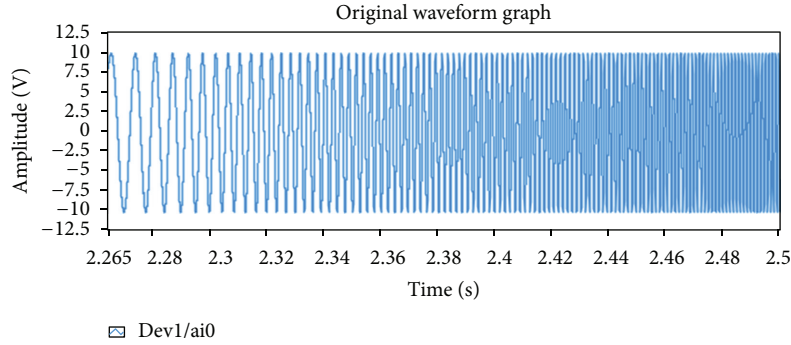


FIGURE 4: One section of the swept sine wave signal.

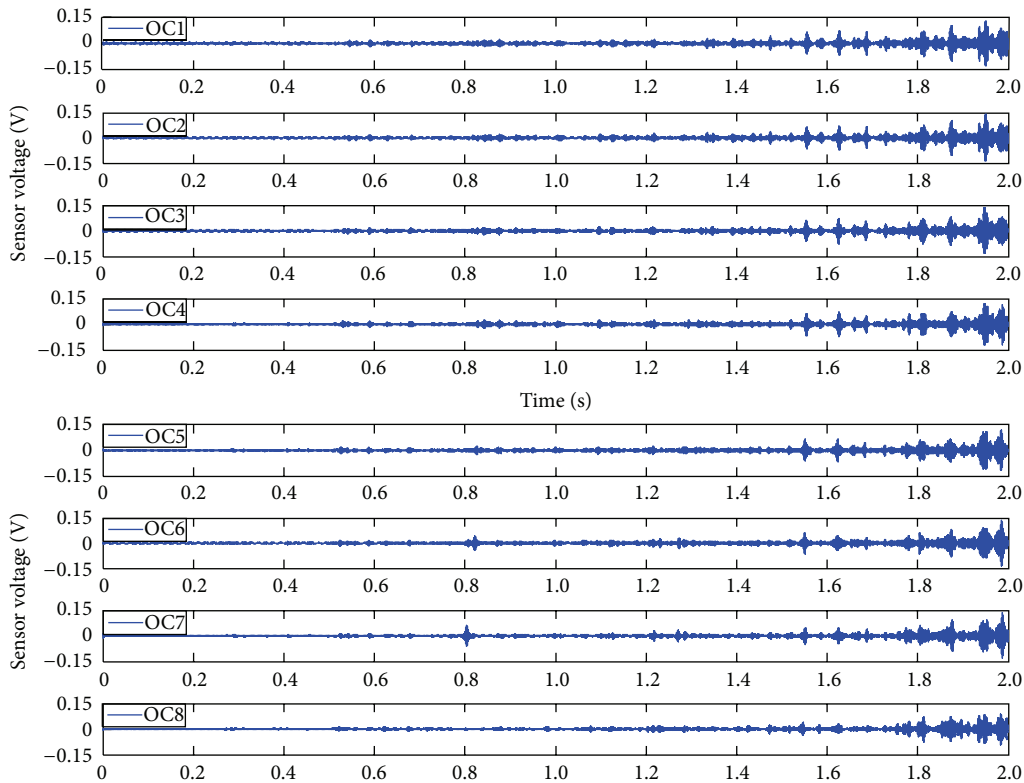


FIGURE 5: Sensor 2 signal response for each operating condition.

the crack almost fully blocks the stress wave propagation from the actuator to sensors.

The signals received by sensors are different for the same stress wave propagating through different crack depths. It is from these differences that the method can determine the location and severity of cracks in the structure. As the method only compares two states (healthy versus damaged), differences in materials, size, and so forth across samples/structures will not affect the performance or requirements of the method. In addition, the vibration response of the structure in a very wide frequency range is calculated by the energy method, and it is more sensitive to minor damage identification.

In order to quantitatively analyze the crack severity on the pipe, the wavelet packet-based crack severity index is developed, as shown in Figure 8. The height of the bars indicates the damage degree collected by the each corresponding sensor. Based on the principle of the crack severity index, 0 is the health status of the structure corresponding to a crack depth of 0 mm (operating condition no. 1). It can be seen that the heights of the bars increase for each incremental operating condition that corresponds to an increase of the crack depth. For Sensor 2, the most distinguishable changes in crack severity index are observed due to the increases in bar height up to the value of 0.4 for operating condition no. 8. This can be attributed to Sensor 2's close proximity to

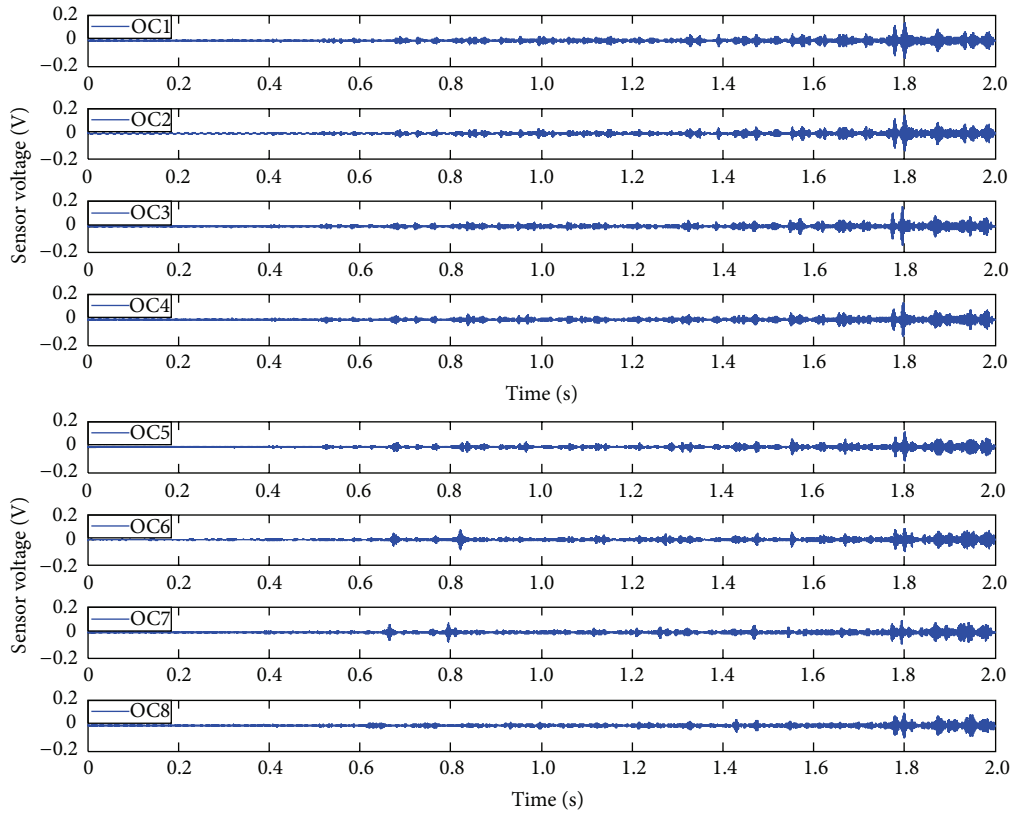


FIGURE 6: Sensor 3 signal response for each operating condition.

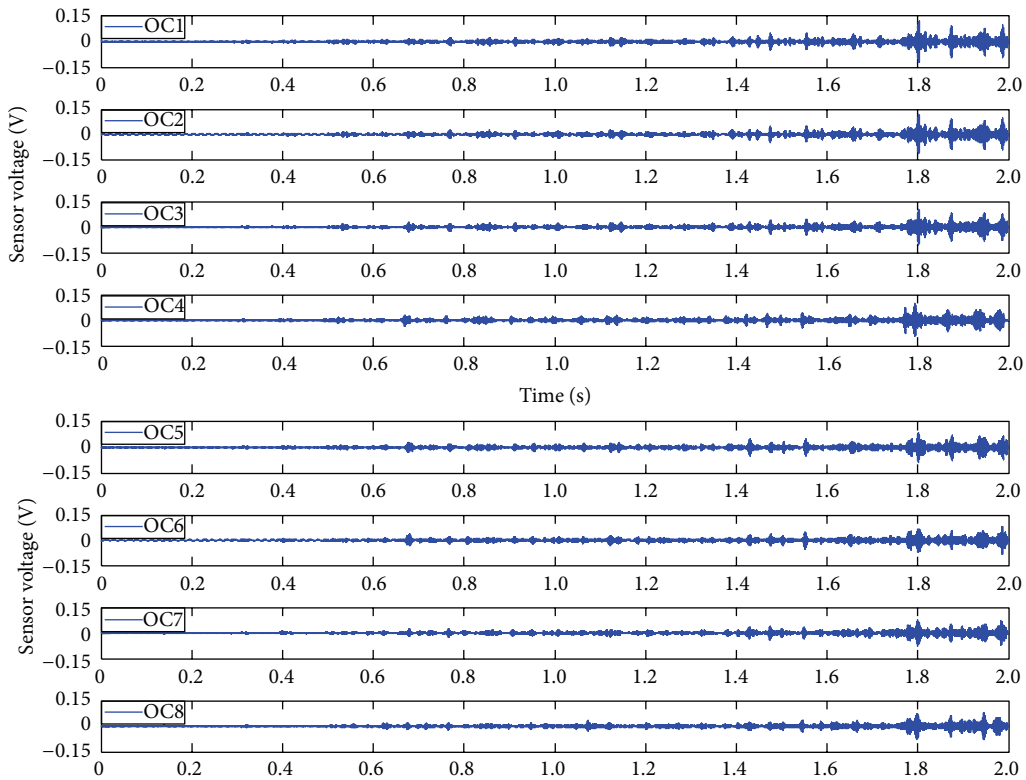


FIGURE 7: Sensor 4 signal response for each operating condition.

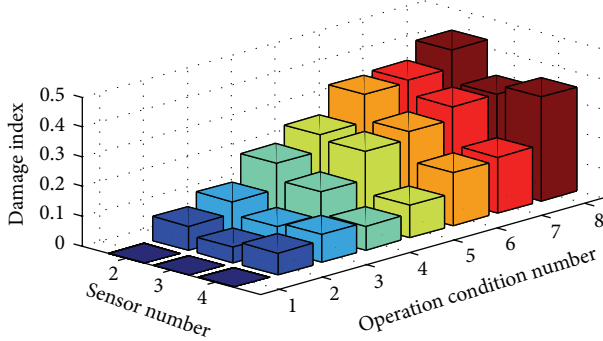


FIGURE 8: Pipeline crack severity index.

the artificial crack location on the pipe (as seen in Figure 2). The same trend is also observed for Sensors 3 and 4, which confirms that the crack functions as a stress relief in the wave propagation path.

5. Conclusion

In this paper, the active sensing based crack severity detection of pipelines was verified. Since the crack functions as a stress relief in the wave propagation path, the signal response of the sensors reports a decreasing trend with the increasing depth of the crack. From the wavelet packet-based crack severity index, the crack severity for each operating condition was quantitatively identified by the values indicated by the heights of the index bars. As the cracks developed, the damage index for all sensors increased. In addition, the energy loss phenomenon directly correlated to the locations of the sensors with respect to the crack and the sensitivity of the sensors. It was then identified that the sensor the closest to the crack was subjected to a largest energy loss. Since the damage index value of the sensors is highly dependent upon sensor locations, the proposed crack severity index presents great potential to locate cracks with distributed sensors. Compared to the engineering applications for pipelines, the principles and methods of damage detection are identical. To better understand the performance of the active sensing based crack detection system shown in this paper, location detection for multiple cracks on longer pipelines will be studied in future work.

Acknowledgments

This research reported in this paper was partially supported by The National Natural Science Foundation of China (no. 51378077), the Petro China Innovation Foundation (2011D-5006-0605), and the Scientific Research Project Foundation of Hubei Provincial Department of Education (D20131205).

References

[1] E. Tapanes, "Fibre optic sensing solutions for real-time pipeline integrity monitoring," *Australian Pipeline Industry Association National Convention*, 2001.

[2] H.-N. Li, D.-S. Li, and G.-B. Song, "Recent applications of fiber optic sensors to health monitoring in civil engineering," *Engineering Structures*, vol. 26, no. 11, pp. 1647–1657, 2004.

[3] S. Z. Yan and L. S. Chyan, "Performance enhancement of BOTDR fiber optic sensor for oil and gas pipeline monitoring," *Optical Fiber Technology*, vol. 16, no. 2, pp. 100–109, 2010.

[4] A. Anastasopoulos, D. Kourousis, and K. Bollas, "Acoustic emission leak detection of liquid filled buried pipeline," *Journal of Acoustic Emission*, vol. 27, pp. 27–39, 2009.

[5] D. Ozevin and J. Harding, "Novel leak localization in pressurized pipeline networks using acoustic emission and geometric connectivity," *International Journal of Pressure Vessels and Piping*, vol. 92, pp. 63–69, 2012.

[6] A. Mostafapour and S. Davoodi, "Analysis of leakage in high pressure pipe using acoustic emission method," *Applied Acoustics*, vol. 74, no. 3, pp. 335–342, 2013.

[7] J. Okamoto, J. C. Adamowskia, M. S. G. Tsuzukia, F. Buiochia, and C. S. Camerinib, "Autonomous system for oil pipelines inspection," *Mechatronics*, vol. 9, no. 7, pp. 731–743, 1999.

[8] E. Pan, J. Rogers, S. K. Datta, and A. H. Shah, "Mode selection of guided waves for ultrasonic inspection of gas pipelines with thick coating," *Mechanics of Materials*, vol. 31, no. 3, pp. 165–174, 1999.

[9] H. Ravanbod, "Application of neuro-fuzzy techniques in oil pipeline ultrasonic nondestructive testing," *NDT & E International*, vol. 38, no. 8, pp. 643–653, 2005.

[10] B. Hertlein, "Stress wave testing of concrete: a 25-year review and a peek into the future," *Construction and Building Materials*, vol. 38, pp. 1240–1245, 2013.

[11] D. Vasić, V. Bilas, and D. Ambruš, "Pulsed eddy-current nondestructive testing of ferromagnetic tubes," *IEEE Transactions on Instrumentation and Measurement*, vol. 53, no. 4, pp. 1289–1294, 2004.

[12] J. B. Nestleroth and R. J. Davis, "Application of eddy currents induced by permanent magnets for pipeline inspection," *NDT & E International*, vol. 40, no. 1, pp. 77–84, 2007.

[13] R. Keshwani and S. Bhattacharya, "Design and optimization of eddy current sensor for instrumented pipeline inspection gauge," *Sensor Review*, vol. 28, no. 4, pp. 321–325, 2008.

[14] G. Park, H. H. Cudney, and D. J. Inman, "Feasibility of using impedance-based damage assessment for pipeline structures," *Earthquake Engineering and Structural Dynamics*, vol. 30, no. 10, pp. 1463–1474, 2001.

[15] D. M. Peairs, G. Park, and D. J. Inman, "Improving accessibility of the impedance-based structural health monitoring method," *Journal of Intelligent Material Systems and Structures*, vol. 15, no. 2, pp. 129–140, 2004.

[16] K. K. Tseng and L. Wang, "Smart piezoelectric transducers for in situ health monitoring of concrete," *Smart Materials and Structures*, vol. 13, no. 5, pp. 1017–1024, 2004.

[17] G. F. Du, J. J. Hu, and C. Wan, "The study situation and analysis of oil & gas pipeline health detection," in *Proceedings of the International Conference on Pipelines and Trenchless Technology*, pp. 551–560, 2012.

[18] G. Song, Y. L. Mo, K. Otero, and H. Gu, "Health monitoring and rehabilitation of a concrete structure using intelligent materials," *Smart Materials and Structures*, vol. 15, no. 2, pp. 309–314, 2006.

[19] G. Song, H. Gu, Y. L. Mo, T. T. C. Hsu, and H. Dhonde, "Concrete structural health monitoring using embedded piezoceramic transducers," *Smart Materials and Structures*, vol. 16, no. 4, pp. 959–968, 2007.

- [20] L. Jun, "Scattering of harmonic anti-plane shear stress waves by a crack in functionally graded piezoelectric/piezomagnetic materials," *Acta Mechanica Sinica*, vol. 20, no. 1, pp. 75–86, 2007.
- [21] G. Song, H. Gu, and Y.-L. Mo, "Smart aggregates: multi-functional sensors for concrete structures—a tutorial and a review," *Smart Materials and Structures*, vol. 17, no. 3, Article ID 033001, 2008.
- [22] A. Laskar, H. Gu, Y. L. Mo, and G. Song, "Progressive collapse of a two-story reinforced concrete frame with embedded smart aggregates," *Smart Materials and Structures*, vol. 18, no. 7, Article ID 075001, 2009.
- [23] S. Yan, W. Sun, G. Song et al., "Health monitoring of reinforced concrete shear walls using smart aggregates," *Smart Materials and Structures*, vol. 18, no. 4, Article ID 047001, 2009.
- [24] P. Li, H. Gu, G. Song, R. Zheng, and Y. L. Mo, "Concrete structural health monitoring using piezoceramicbased wireless sensor networks," *Smart Structures and Systems*, vol. 6, no. 5-6, pp. 731–748, 2010.
- [25] H. Gu, Y. Moslehy, D. Sanders, G. Song, and Y. L. Mo, "Multi-functional smart aggregate-based structural health monitoring of circular reinforced concrete columns subjected to seismic excitations," *Smart Materials and Structures*, vol. 19, no. 6, Article ID 065026, 2010.
- [26] Y. Moslehy, H. Gu, A. Belarbi, Y. L. Mo, and G. Song, "Smart aggregate based damage detection of circular RC columns under cyclic combined loading," *Smart Materials and Structures*, vol. 19, no. 6, Article ID 065021, 2010.
- [27] W. Liao and J. Wang, "Application of piezoceramic-based sensors to the structural health monitoring of bridge piers," *China Civil Engineering Journal*, vol. 45, no. 2, pp. 197–201, 2012.
- [28] X. Hong, H. Wang, T. Wang, G. Liu, Y. Li, and G. Song, "Dynamic cooperative identification based on synergetics for pipe structural health monitoring with piezoceramic transducers," *Smart Materials and Structures*, vol. 22, no. 3, pp. 1–13, 2013.
- [29] H.-N. Li, X.-Y. He, and T.-H. Yi, "Multi-component seismic response analysis of offshore platform by wavelet energy principle," *Coastal Engineering*, vol. 56, no. 8, pp. 810–830, 2009.
- [30] T.-H. Yi, H.-N. Li, and M. Gu, "Characterization and extraction of global positioning system multipath signals using an improved particle-filtering algorithm," *Measurement Science and Technology*, vol. 22, no. 7, Article ID 075101, 2011.
- [31] T. H. Yi, H. N. Li, and M. Gu, "Wavelet based multi-step filtering method for bridge health monitoring using GPS and accelerometer," *Smart Structures and Systems*, vol. 11, no. 4, pp. 331–348, 2013.

Research Article

Health Condition Evaluation of Cable-Stayed Bridge Driven by Dissimilarity Measures of Grouped Cable Forces

Dan-Hui Dan,¹ Yi-Ming Zhao,² Tong Yang,¹ and Xing-Fei Yan³

¹ Department of Bridge Engineering, Tongji University, Shanghai 200092, China

² Technology Center of Shanghai Construction Group, Co., Ltd., Shanghai 200431, China

³ Shanghai Urban Construction Design Research Institute, Shanghai 200125, China

Correspondence should be addressed to Dan-Hui Dan; dandanhui@tongji.edu.cn

Received 28 May 2013; Revised 25 August 2013; Accepted 26 August 2013

Academic Editor: Ting-Hua Yi

Copyright © 2013 Dan-Hui Dan et al. This is an open access article distributed under the Creative Commons Attribution License, which permits unrestricted use, distribution, and reproduction in any medium, provided the original work is properly cited.

An index system for the health-status evaluation of cable-stayed bridges is presented based on a set of dissimilarity measures (DMs) of the cable force of grouped cables. The DMs and their labels corresponding to health status derived by the serviceability limit states of a bridge are determined by the combination of the finite element method and the influence matrix method. The Monte-Carlo method is used to determine the rational values of thresholds of proposed DMs. By comparing the indices with the thresholds, the holistic health status assessment of a cable-stayed bridge can be easily and reasonably determined. Based on eight years of historical data on the cable forces investigated from a real cable-stayed bridge, the proposed methods are applied to evaluate the health status of this cable-stayed bridge. The results show the validity of the proposed methods.

1. Introduction

The relationship between the current internal force state (action effects) and the structure's limit state (resistance forces) bridges the gap between measurable quantities and structural health status. Thus, the availability of these quantities can facilitate the evaluation of the health status of the long-span cable-stayed bridges [1]. Stayed cables comprise the main structural components of a cable-stayed bridge, and the changes in inclined cable force significantly affect the state of the whole structure [2]. After years of bridge service, deviation attributed to tower-top displacement, foundation settlement, shrinking and creeping, and so on are likely to occur between real and designed cable forces [3]. These deviations are apparently linked to specific and holistic working statuses when the structure is in service. To detect and explore the deviation of grouped cable forces rationally, the changes in the corresponding internal force state of the whole structure can be determined [4, 5]. By associating these changes in the internal force state with the known relationships between such changes and a certain structural limit states, the health status of a cable-stayed bridge structure

could be evaluated. Therefore, monitoring the grouped cable forces of long-span cable-stayed bridges and developing a safety evaluation method based on such monitoring data have become important tasks in bridge structural safety evaluation.

A simple comparison method continues to be widely used for the evaluation of cable forces. By computing the relative changes in single-cable force over time to reflect the state of cable forces, such state can be considered normal when the relative change value is less than a certain value (e.g., 5%) [6]. This estimation method has several limitations. On one hand, a rational threshold system has never been built, which makes quantitative evaluation impossible; on the other hand, considering the stress redistribution in the cable plane, the significant changes in single-cable force may not directly affect the safety of the whole structure. However, even when the cable force deviations occurred in each cable is inconsiderable and hereby jumped to a positive conclusion, the holistic cable forces would sometimes fail to meet the safety requirements of the whole structure. Therefore, to evaluate bridge safety based on cable force monitoring data, the whole cable group should be considered simultaneously.

The present synthetic evaluation methods like variable weight method [6] and gray related degree method [7] continue to be the most commonly used in evaluation of grouped cable forces. The two methods rely on certain parameters with poor physical significance, thus yielding unsatisfactory results. The former method depends on a balance coefficient representing the degree of correlation of structural components, whereas the latter is constrained by the correlation of the cable forces, where all such methods have no significant relationship with the structures' working state and thus have the disadvantage of poor interpretability. The statistical methods and pattern recognition methods recently are used in structural status evaluation [8] and health monitoring [9, 10], with a capacity of dealing with multiple quantities measured by integrated monitoring system or comprehensive bridge detection project synchronously, and so the ability to conduct synthetic evaluation of bridge condition can therefore be expected. For lack of effective channel of communication between patterns and the definition of health status of target structures, the interpretability of these kinds of methodologies still are unsatisfactory. Thus, developing a rational and interpretable technology for the evaluation of the working state of whole structures based on grouped cable forces is necessary.

Based on a comprehensive analysis of grouped cable forces, this paper proposes a rational evaluation method that considers the dissimilarity measure (DM) of grouped cable forces. The threshold system of DMs can then be obtained by using the Monte-Carlo method. Finally, based on the historical measurement data of cable forces of a long-span, cable-stayed bridge located in Guangdong, China, this paper conducts a health evaluation for same bridge and confirms the validity of the evaluation method.

2. Measure of Grouped Cable Forces

A holistic assessment of structural health status can be achieved by analyzing the data samples of grouped cable forces. However, two issues must be addressed: first, the assumption that grouped cable forces are directly related to structural health status should be proven. Second, valid measures of grouped cable forces should be determined to achieve an accurate assessment.

2.1. Correlation of Grouped Cable Forces and Structural Inner Force. As a space-stressed system, a cable-stayed bridge is characterized by a condition wherein loads are borne by the combination of the main girder and the cable tower as well as the stayed cables. Among all loads, vertical loads are primarily balanced by the vertical component of the cable forces. Considering that all cables are anchored to the same tower and main girder, the functionality of a single cable is restricted by that of other cables. All cables are closely related and thus serve a joint function of balancing the loads. Therefore, the inner force of structural components aside from the cables correlates with the holistic cable forces but not with the force of a single cable. Changes in single-cable force, whether present or not, have a negligible effect on the inner force of the whole structure.

The relationship between the distribution of grouped cable forces and the behavior of the structure is significantly affected by factors such as traffic loads, uneven settlement, and temperature. The effects of wind load and nonlinear factors on the internal forces of grouped cables are negligible [11]. Thus, the influence matrix method based on linear theory can be used to describe the effect of grouped cable forces on the behavior of the bridge structure [12].

Figure 1 shows that if the effect of wind load is disregarded, the relationship between the grouped cable forces and the target mechanical variables of the bridge structure (e.g., external load, inner force, stress, or displacement) could be described as

$$S = C \cdot D, \quad (1)$$

where $S = S_G + S_{\text{config}} + S_{\text{tr}} + S_{\text{us}} + S_t$ is a column vector of the grouped cable forces of a finished bridge. S_G , S_{tr} , S_{us} , and S_t , respectively, denote the cable forces produced by the dead loads, traffic loads, uneven settlement, and temperature; S_{config} stands for the additional cable forces of the group cables that emerge after reaching the destination through cable force adjustment. S is used to denote the passive controlled vectors.

$D = \{D_G, D_{\text{config}}, D_{\text{tr}}, D_{\text{us}}, D_t\}^T$ stands for the actions applied to the structure. Index G represents the dead loads, tr represents the traffic loads, us represents the uneven settlement, and t represents the temperature effect. D_{config} represents the initial cable force obtained after cable force is adjusted. All elements in D are row vectors, and D is column vector, which is used to denote the comprehensive active controlled vectors.

C stands for the influence matrix and is a constant under the linear hypothesis. $C = [C_G, C_{\text{config}}, C_{\text{tr}}, C_{\text{us}}, C_t]$, and the submatrices in C relate some factors to corresponding cable forces. The referred factors contain dead loads, initial cable force after cable force adjustment, traffic loads, uneven settlement, temperature effect, and corresponding cable forces. The size of first dimension of C is equal to the number of grouped cables, and the size of second dimensions is equal to that of D .

In the same way, the relationship between the target mechanical variables and the comprehensive active controlled vectors under the ultimate limit state (ULS) and serviceability limit state (SLS) is given by

$$S_{\text{tar}} = C_{\text{tar}} \cdot D, \quad (2)$$

where S_{tar} is column vector of the target mechanical variables, generally refers to typical mechanical variables in typical sections of a cable-stayed bridge, including internal forces, stress and displacement; C_{tar} is the influence matrix between the comprehensive active controlled vectors and the target mechanical variables. The target mechanical variables are typically used in function equations which describe a certain conditions under the ULS and SLS in the design stage. Let Z represent the function equation Z or function margin, which is given by

$$Z = [S_{\text{tar}}] - S_{\text{tar}}, \quad (3)$$

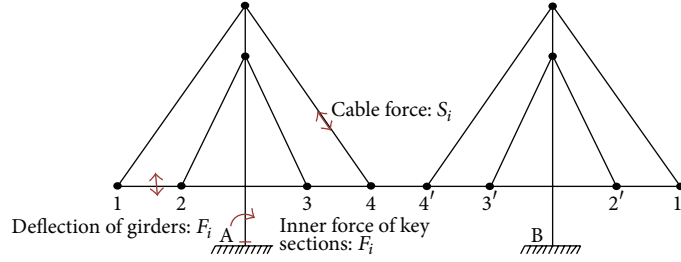


FIGURE 1: Simplified model of a cable-stayed bridge.

where $[S_{\text{tar}}]$ denotes the thresholds or resistance column vectors of the corresponding target mechanical variables.

According to the influence matrix features, (1) could be rewritten as follows:

$$\begin{aligned} S &= S_D + S_Q + S_R, \\ S_D &= C_G D_G + C_{\text{config}} D_{\text{config}}, \\ S_Q &= C_{\text{us}} D_{\text{us}} + C_{t,a} D_{t,a}, \\ S_R &= C_{\text{tr}} D_{\text{tr}} + C_{t,i} D_{t,i}, \end{aligned} \quad (4)$$

where S_D refers to the grouped cable forces under the combination of the permanent loads; S_Q denotes the grouped cable forces under the combination of quasipermanent loads; and S_R stands for the grouped cable forces under the combination of live loads, which has a random value. “ t, a ” and “ t, i ”, respectively, represent the average annual temperature effects and the momentary temperature effects of the structure. The former is recognized as a quasipermanent load and has high periodicity and certainty, whereas the latter is characterized by randomness.

The target mechanical variables S_{tar} , which reflect the structure state, can also be rewrite as

$$\begin{aligned} S_{\text{tar}} &= S_{\text{tar},D} + S_{\text{tar},Q} + S_{\text{tar},R}, \\ S_{\text{tar},D} &= C_{\text{tar}} D_G + C_{\text{tar}} D_{\text{config}}, \\ S_{\text{tar},Q} &= C_{\text{tar}} D_{\text{us}} + C_{\text{tar}} D_{t,a}, \\ S_{\text{tar},R} &= C_{\text{tar}} D_{\text{tr}} + C_{\text{tar}} D_{t,i}. \end{aligned} \quad (5)$$

Thus, the relationship between the target mechanical variables and the grouped cable forces could be written as the following linear combination:

$$S_{\text{tar}} = C_{\text{tar}} \cdot C^{-1} \cdot S. \quad (6)$$

Equations (1) to (6) show that the state of the inner forces of the structure is closely related to the grouped cable forces. Moreover, the target mechanical variables that reflect the state of the structure can be approximately expressed as a linear combination of grouped cable forces. Thus, through the grouped cable forces, the condition of the target mechanical variables can be obtained; moreover, the function margin Z can be expressed by the following equation:

$$Z = [S_{\text{tar}}] - C_{\text{tar}} \cdot C^{-1} \cdot S. \quad (7)$$

The resistance $[S_{\text{tar}}]$ and the effects S_{tar} in (3) are difficult to monitor, but the grouped cable forces in (7) can be measured easily and thus can serve as an agent in function equation. Thus, the original function equation based on resistance and effects is transformed into one that is based on the agent of grouped cable forces, which facilitates to form a structural reliability evaluation frame based on aforementioned monitored measurement agent.

2.2. DMs of Grouped Cable Forces. To determine structure’s states accurately, rational measures should be given for the vectors of grouped cable forces. Grouped cable forces are high dimensional and are thus difficult to deal with. Therefore, low-dimensional measures of the vectors should be introduced to simplify the analysis.

In practical applications, the most common method used for vector measurement is DM. DM determines the dissimilarity among multidimension data samples, which are essentially a group of special dissimilar functions. The differences between two sample vectors can possibly be transformed into scalars. Common DM functions include Euclidian distance, street block distance, Chebyshev distance, Canberra distance, angle separation degree, and correlation coefficient [13, 14]. The two data sample vectors can be set as

$$\begin{aligned} x &= [x_1 \ x_2 \ \cdots \ x_i \ x_{i+1} \ \cdots \ x_n]^T, \\ y &= [y_1 \ y_2 \ \cdots \ y_i \ y_{i+1} \ \cdots \ y_n]^T. \end{aligned} \quad (8)$$

Thus, $\text{DM}(x, y)$ could be written as shown in Table 1.

All DMs could constitute the index system used to evaluate the health status of a structure. When using the given DMs to measure grouped cable forces, observations S_0 under specific conditions could be selected as the reference, and together with the rest observations S , DMs can be derived via operation on DM operators, that is, $\text{DM}(S_0, S)$. Designed cable forces and finished-bridge cable forces could both be used as S_0 .

DMs are used to classify the data points and to identify the boundaries between data points under different categories. Their capability to distinguish such categories could be measured based on the value of the criteria J_1 , J_2 , and J_3 . The given criteria are defined in (9) [14]. A larger value of these criteria denotes a smaller within-class spread and a larger

TABLE 1: Functions of dissimilarity measures [6].

Euclidian distance	$DM(x, y) = \sqrt{\sum_{i=1}^n (x_i - y_i)^2}$
Street block distance	$DM(x, y) = \sum_{i=1}^n x_i - y_i $
Chebyshev distance	$DM(x, y) = \max_i x_i - y_i $
Canberra distance	$DM(x, y) = \sum_{i=1}^n \frac{ x_i - y_i }{x_i + y_i}$
Angle separation degree	$DM(x, y) = \frac{\sum_{i=1}^n x_i y_i}{\sqrt{\sum_{i=1}^n x_i^2 \sum_{i=1}^n y_i^2}}$
Correlation coefficient	$DM(x, y) = \frac{\sum_{i=1}^n (x_i - \bar{x})(y_i - \bar{y})}{\sqrt{\sum_{i=1}^n (x_i - \bar{x})^2 \sum_{i=1}^n (y_i - \bar{y})^2}}$

between-class spread of DMs. And a larger between-class spread of DMs results in better classification performance:

$$J_1 = \text{Tr} \{Q_W^{-1} Q_B\}, \quad J_2 = \frac{|\hat{\Sigma}|}{|Q_W|}, \quad J_3 = \frac{\text{Tr} \{Q_B\}}{\text{Tr} \{Q_W\}}, \quad (9)$$

where Q_W is the within-class scatter matrix. Q_B is the sample between-class covariance matrix,

$$Q_W = \sum_{i=1}^C \frac{n_i}{n} \hat{\Sigma}_i, \quad (10)$$

$$Q_B = \sum_{i=1}^C \frac{n_i}{n} (m_i - m)(m_i - m)^T,$$

where Σ is the population covariance matrix, and Σ_i is the covariance matrix of class w_i . The maximum likelihood estimates of Σ and Σ_i are, respectively, $\hat{\Sigma}$ and $\hat{\Sigma}_i$:

$$\hat{\Sigma} = \frac{1}{n} \sum_{j=1}^n (x_j - m)(x_j - m)^T, \quad (11)$$

$$\hat{\Sigma}_i = \frac{1}{n_i} \sum_{j=1}^n z_{ij} (x_j - m_i)(x_j - m_i)^T,$$

where

$$z_{ij} = \begin{cases} 1, & x_j \in w_i, \\ 0, & \text{otherwise,} \end{cases} \quad (12)$$

$$n_i = \sum_{j=1}^n z_{ij},$$

m_i is the sample mean of the class w_i , which is given by

$$m_i = \frac{1}{n_i} \sum_{j=1}^n z_{ij} x_j, \quad (13)$$

m is the sample population mean

$$m = \sum_{i=1}^C \frac{n_i}{n} m_i. \quad (14)$$

3. Threshold Systems of DMs

To achieve an accurate and rational evaluation of the health status of bridge structures, the threshold system of the DMs of grouped cable forces should be determined. From (7), it is known that the thresholds of DMs can be obtained by comparing the real-time target mechanical variables of the significant sections with its corresponding thresholds under two limit states: the ULS and SLS [15]. The solving method is given in the following subsections.

3.1. Definition of Threshold Systems of DMs. The threshold systems of the DMs of grouped cable forces can be obtained by using (3), (6), and (7). Cable-stayed bridges typically have two limit states, and each limit state has upper and lower limits in real conditions. Equation (3) could thus be rewritten as

$$[S_{\text{tar}}]_{u,f} \leq S_{\text{tar},u} \leq [S_{\text{tar}}]_{u,c}, \quad (15)$$

$$[S_{\text{tar}}]_{s,f} \leq S_{\text{tar},s} \leq [S_{\text{tar}}]_{s,c},$$

where $[S_{\text{tar}}]_{u,f}$, $[S_{\text{tar}}]_{u,c}$ denote the lower and upper limit thresholds of the target mechanical variables under ULS, respectively, whereas $[S_{\text{tar}}]_{s,f}$, $[S_{\text{tar}}]_{s,c}$ denote the same thresholds under SLS, respectively. The four limit thresholds can be obtained based on structure design specifications or through finite element analysis. $S_{\text{tar},u}$, $S_{\text{tar},s}$ stand for the target mechanical variables calculated with grouped cable forces under conditions of ULS and SLS, which can be obtained as follows:

$$S_{\text{tar},u} = C_{\text{tar},u} \cdot C^{-1} \cdot S, \quad (16)$$

$$S_{\text{tar},s} = C_{\text{tar},s} \cdot C^{-1} \cdot S.$$

For a cable-stayed bridge, the target mechanical variables that have clear design limits include the displacement of tower top, deflection in the middle of the main span, rotation angle of the girder beam end, and bending moment of the significant girder sections, as well as the bending moment of the tower and pylon-beam junction. These target mechanical variables could be set as an index for evaluation, whereas their design limits can be set as thresholds.

It should be mentioned that if the direct measurement is good enough, it is a more accurate way to monitor and evaluate the status of the bridge. It is reported by Yi et al. that the GPS techniques can help to get the accurate deformation information of bridge; so if there have GPS devices in the monitoring system, it is valuable to use these direct deformation data to evaluate the bridge [15, 16]. However, by now, the price of GPS monitoring system is so expensive that some bridge health monitoring systems do not adopt this technique [17, 18]. In our study, we consider this situation and build our condition evaluation framework on the basis of these two quantities measured indirectly.

Equations (6), (7), and (15) show that the threshold systems of grouped cable force could be indirectly obtained

based on the target mechanical variables that reflect the structure state, that is,

$$[S]_i = C \cdot (C_{\text{tar},u})^{-1} \cdot [S_{\text{tar}}]_i, \quad (17)$$

where subscript “ i ” represents the indexes u, f, u, c, s, f , and s, c . The thresholds of the DMs of grouped cable forces can then be derived as

$$[\text{DM}(\cdot)]_i = \text{DM}([S]_i, S_0), \quad (18)$$

where S_0 is a specific vector of grouped cable forces used as the reference, typically the design cable force or finished-bridge cable force.

Therefore, the evaluation of grouped cable forces S could be converted to the comparison of the DMs with its corresponding thresholds,

$$\text{DM}(S, S_0) \begin{cases} > \\ = \\ < \end{cases} [\text{DM}(\cdot)]_i. \quad (19)$$

$[S_{\text{tar}}]_i$, which is the threshold of the structural target mechanical variable S_{tar} , is usually a scalar or low-dimensional vector with dimensions that are far less than the number of group cables. Given that (17) does not have a definite solution, it cannot be used to calculate the thresholds. In practical applications, the Monte-Carlo methods can be used to generate mass of samples of grouped cable forces, and then all samples can be labeled into two classes: the safe and unsafe label classes. Subsequently, by distinguishing these labeled DMs samples, the boundary of safe and unsafe samples can be derived, and the threshold system of DMs can be further obtained.

3.2. Flowchart for Threshold Solving Using the Monte-Carlo Method. The initial comprehensive active controlled vectors D_0 and the comprehensive influence matrix $[C, C_{\text{tar},u}, C_{\text{tar},s}]$ are obtained through cable force adjustment process firstly, which is operated under the combinations of action effects under SLS, including dead loads, traffic loads, temperature, uneven settlement, and so on. Then, the values of the comprehensive active controlled subvectors corresponding to dead loads, initial cable force, uneven settlement, and global temperature effect are fixed as constants; the values of comprehensive active controlled subvectors, D_{tr} and D_{t} , corresponding to traffic loads and transient temperature effect, are varied within a rational range randomly, which are then determined using the Monte-Carlo method [7]. The random comprehensive active controlled vectors D are then established and used to calculate the random grouped cable force vectors and target mechanical variables via influence matrix method. The DMs of all cable forces vectors are calculated against its references, and (15) is used to determine the sample labels of all cable force vectors by comparing the target mechanical variables with their limits or thresholds. Finally, the threshold system of the DMs of grouped cable forces is determined according to the boundaries between DMs with different labels.

The steps employed by the Monte-Carlo method to determine the threshold system of DMs are shown in Figure 2.

TABLE 2: Threshold of target variables.

Mechanical variables	Floor threshold	Ceiling threshold	Limit state
Bending moment (tonf-m)	-52292.62	32908.08	Ultimate
Mid-span deflection (m)	-0.738	0.116	Serviceability

4. Engineering Application

4.1. Engineering Background. Taking a long-span cable-stayed bridge with two towers in China’s Guangdong province as a case study, seen in Figure 3, the feasibility of the method discussed above will be verified in these sections. The bridge has four cable planes, with 40 cables in each plane for a total of 160 cables. Considering that cable force detection has been conducted eight times and that the bridge is not entirely longitudinally symmetrical, the cable forces of the 80 cables of two cable planes at the upstream side are selected as data samples. Totally 16 data samples can be gathered.

All cable forces are regularly detected by the same bridge detection organization and thus the consistency and credibility of the data are guaranteed. Through an analysis of the variation of single cable force, the results show significant similarities. Except for the variations of a few cable forces of nearly $\pm 10\%$ in the previous year, the range of changes of rest cable forces was within -5% to 5% . At present, there are not apparent indications of abnormality occurred during its service history, which means the bridge is in a good condition.

As previously mentioned, the key to apply the Monte-Carlo method to obtain the threshold values of grouped cable force is to bond the class label to a certain limit state. This paper uses Midas Civil Software to build the finite element model (FEM) of the bridge, as shown in Figure 4. In this model, the living loads are arranged at the most unfavorable position. The bending moment of the unilateral bottom section of the tower is chosen as the mechanical variable to calculate the ultimate limit state and the mid-span deflection of girders is taken as the mechanical variable to calculate the serviceability limit state. The bending moment arrives at its ceiling with counterclockwise direction and floor value with clockwise direction when the two limit live load distributions are applied to the girder. While, for serviceability limit state, the two extremes live loads distributions are arranged in this way that the deflection of middle span has exceeded the design specifications or codes both upward and downward. The threshold values of the two mechanical variables are shown in Table 2. From the FEM model of the bridge, the initial active controlled vectors of cable force and the influence matrix can also be obtained. The two limit states are shown in Figure 5.

4.2. Monte-Carlo Statistical Test. To obtain the mass of samples of grouped cable forces and to ensure that the samples can fully reflect the structural behavior of the target bridge under real operation conditions, a traffic load model must

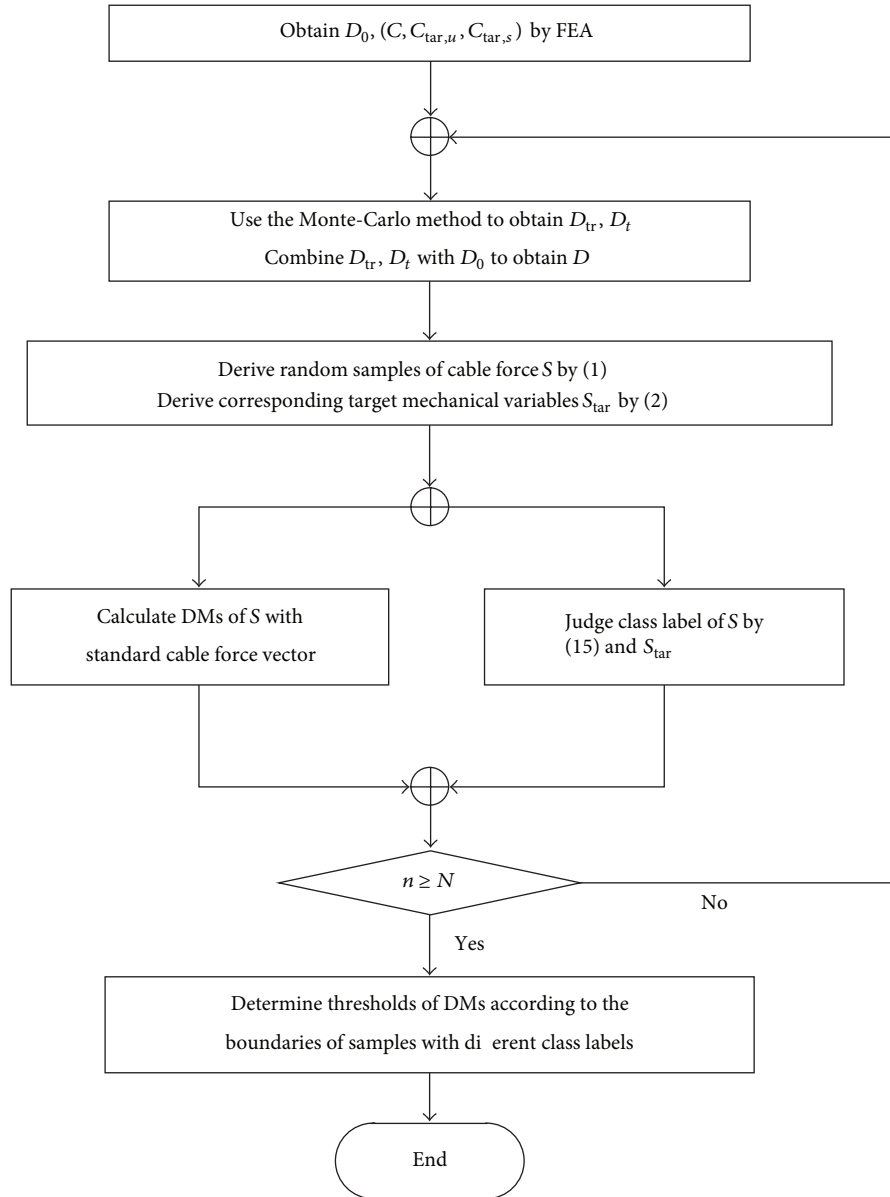


FIGURE 2: Flowchart of Monte-Carlo method for threshold of dissimilarity measures of grouped cable forces.



FIGURE 3: Case study for cable-stayed bridge (Guangdong, China).

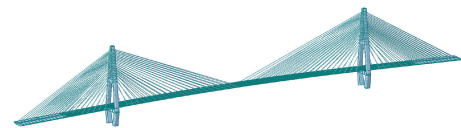


FIGURE 4: FEM model of target bridge by Midas Civil.

be properly built. In order to simplify the calculation, such modeling should differ from lane load modeling in terms of

design specification in that it should be randomly distributed on the deck, but it should not stand on any certain vehicle loading manners or any random distribution types of traffic loads.

Therefore, a model of traffic with 80 independent concentrated loads located on the anchorages of the cables and girder are built and applied to the bridge FEM models. Considering

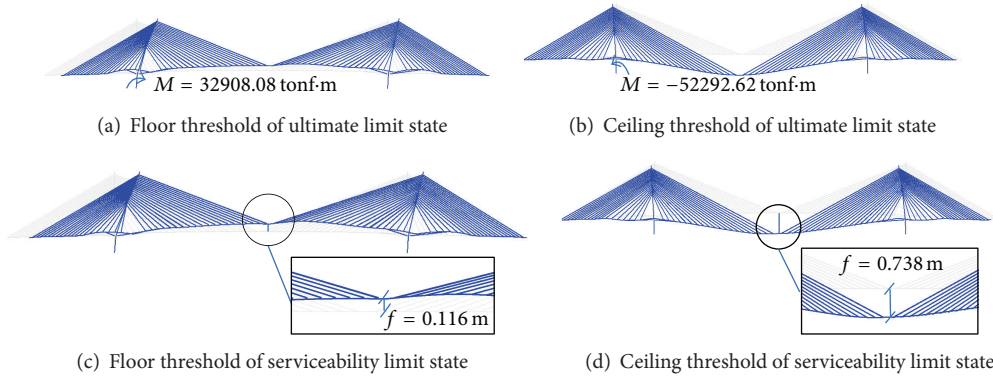


FIGURE 5: Limit state deformed configuration of target bridge.

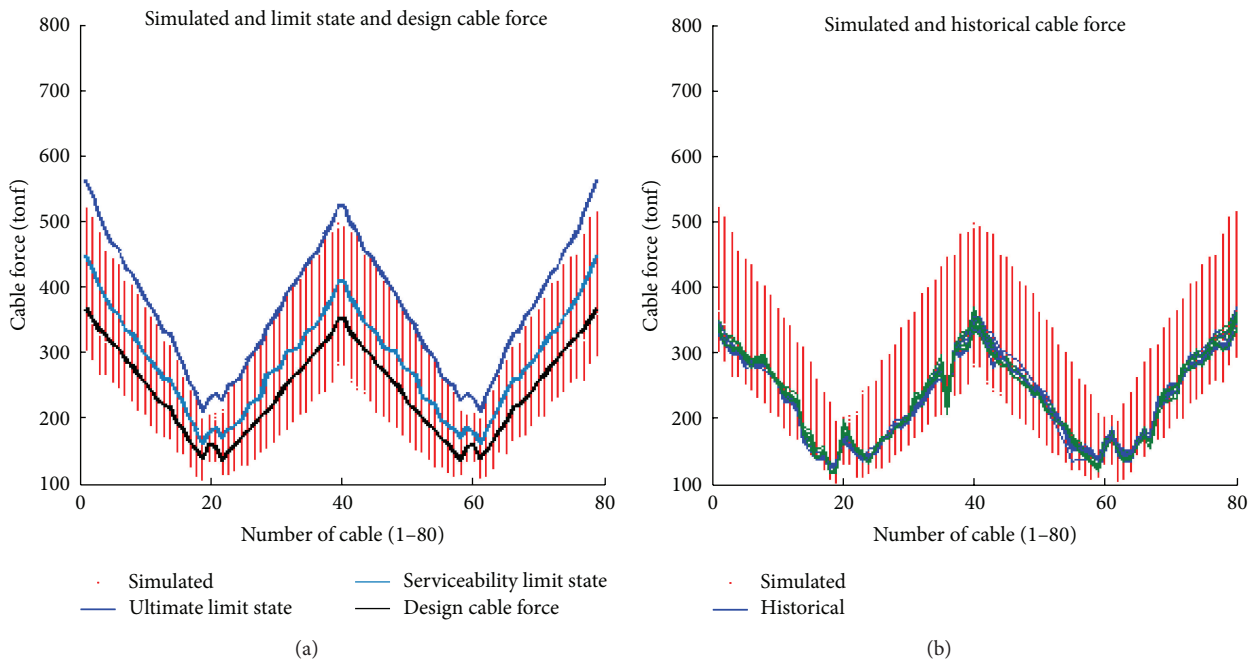


FIGURE 6: Samples of grouped cable forces obtained by MC simulation ((a) samples versus limit state and designed cable forces; (b) samples versus historical measurements).

the short-term temperature effect, the lower limit of loads should be negative. Thus, the preliminary design is that each concentrated load is evenly distributed within an interval of -70 and 210 tons. To avoid mass repetition of the FEM calculations, the influence matrix method is used to derive the cable forces in the Monte-Carlo simulations operation, under the postulate that the influence matrix can properly represent the complex functional relations among random live loads, grouped cable forces, and target mechanical variables. A total of 180,000 rounds of simulation are conducted, and the same number of cable force samples was obtained. To simplify the illustration, 5000 samples are randomly selected from the population. For every sample, the corresponding values of the target mechanical variables are also derived from the simulation simultaneously.

Figures 6 and 7 show that the grouped cable forces provided by the simulation cover the design cable forces, the

region of cable forces of determined by the SLS, as well as the historical cable forces and the scope of these samples approached to the limit determined by ULS. It can be concluded that the parameters used in the simulation have good representativeness and can reflect the possible conditions of real cable forces. Similarly, the simulation values of target mechanical variables overspread the feasible engineering region, and the sample set contains the full information on structural behavior.

4.3. Comparison of DMs and Determination of Threshold System. It is reasonable to designate the finished-bridge state as the reference, which implies that the target bridge is in a health status at the very beginning of its service history; choosing the grouped cable forces on phase of finished bridge as standard, the DM of the samples of cable forces are calculated. The corresponding class labels can then be

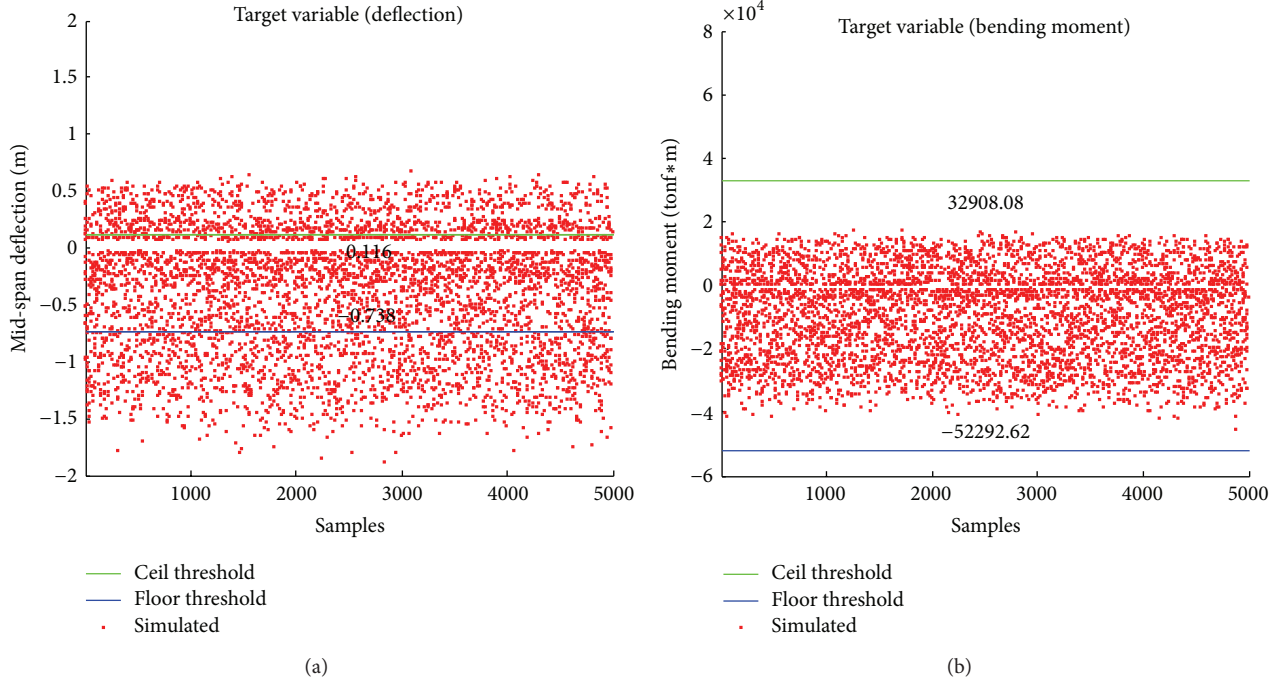


FIGURE 7: Samples of target variables obtained by MC simulation ((a) deflection in middle span of mid-span, upward values take positive signs; (b) bending moment of bottom of pylon, clockwise values take positive signs).

determined based on the comparison between the simulation values and the SLS threshold values of the target mechanical variables. Therefore, when using DMs to describe grouped cable force samples, each DM is related to a class label.

According to (9), we can assess the classification capacity of DMs based on their corresponding class labels, and as shown in Table 3, it can be seen from that the best DM is Canberra distance, followed by street block distance, and Euclidean distance. However, the J_3 values of Chebyshev distance, angular separation, and correlation coefficient are extremely small and are thus inappropriate for classifications.

Figure 8 shows that two clear distinctions exist between the points of DMs with two different class labels in Figure 8(a) Canberra distance, Figure 8(b) street block distance, and Figure 8(c) Euclidean distance, which divides the whole measurement space into three regions: completely safe region, completely unsafe region, and mixed region. For Figure 8(d) Chebyshev distance, the completely unsafe line is clear, but the completely safe line is difficult to identify. For Figure 8(e) angular separation and Figure 8(f) correlation coefficient, the points with safe and unsafe labels are fully mixed, and almost the entire measurement space is a mixed area. Thus, the two DMs lose the capability of classification.

In Figures 8(a)–8(d), the boundaries of different regions can be determined by the following equations:

$$\begin{aligned}
 [DM(\cdot)]_{\text{safety}} &= \min \left(DM(S_{\text{unsafety}}, S_0) \right), \\
 [DM(\cdot)]_{\text{unsafety}} &= \max \left(DM(S_{\text{safety}}, S_0) \right).
 \end{aligned} \tag{20}$$

Based on the formulas of DMs, a lesser similarity of the samples denotes larger values of Euclidean distance, street

block distance, Chebyshev distance, and Canberra distance but smaller values of angular separation and correlation coefficient. Combined with the J_3 criterion, the maximum of DMs with safe labels and the minimum of DMs with unsafe labels are chosen as the thresholds, as shown in Table 4.

4.4. Health Status Evaluation. To validate the rationality and validity of the given threshold system, the DMs in practical application are derived by samples of historical measured cable forces and finished-bridge cable forces. With eight years' measurement results and considering 160 cables divided into two samples (80 upstream cables as the first sample and 80 downstream cables as the second), the number of samples of historical measured cable forces comes up to 16. Thus, 16 results can be obtained for each DM, which are drawn in scatter plots in Figure 9. The green points are DMs of the measures at the finished-bridge state (given that they are compared with themselves, DMs equal zero), whereas the red points are the maximum DMs, which are the closest points to the safe boundaries. The results show that all data are located at the safe region of the corresponding measurement space. This demonstrates that both the safety requirements and serviceability requirements of the bridge are met. This deduction from these three figures is consistent with the current service status of the bridge.

Figures 9(a)–9(c) show that whether Canberra distance, street block distance, or Euclidean distance, the maximum values of DMs occur in the most recent monitoring year (2010). With the increasing lifespan of the bridge, each DM value gradually increases and approximates the upper limit of the safe region. The tendency discovered by DM history

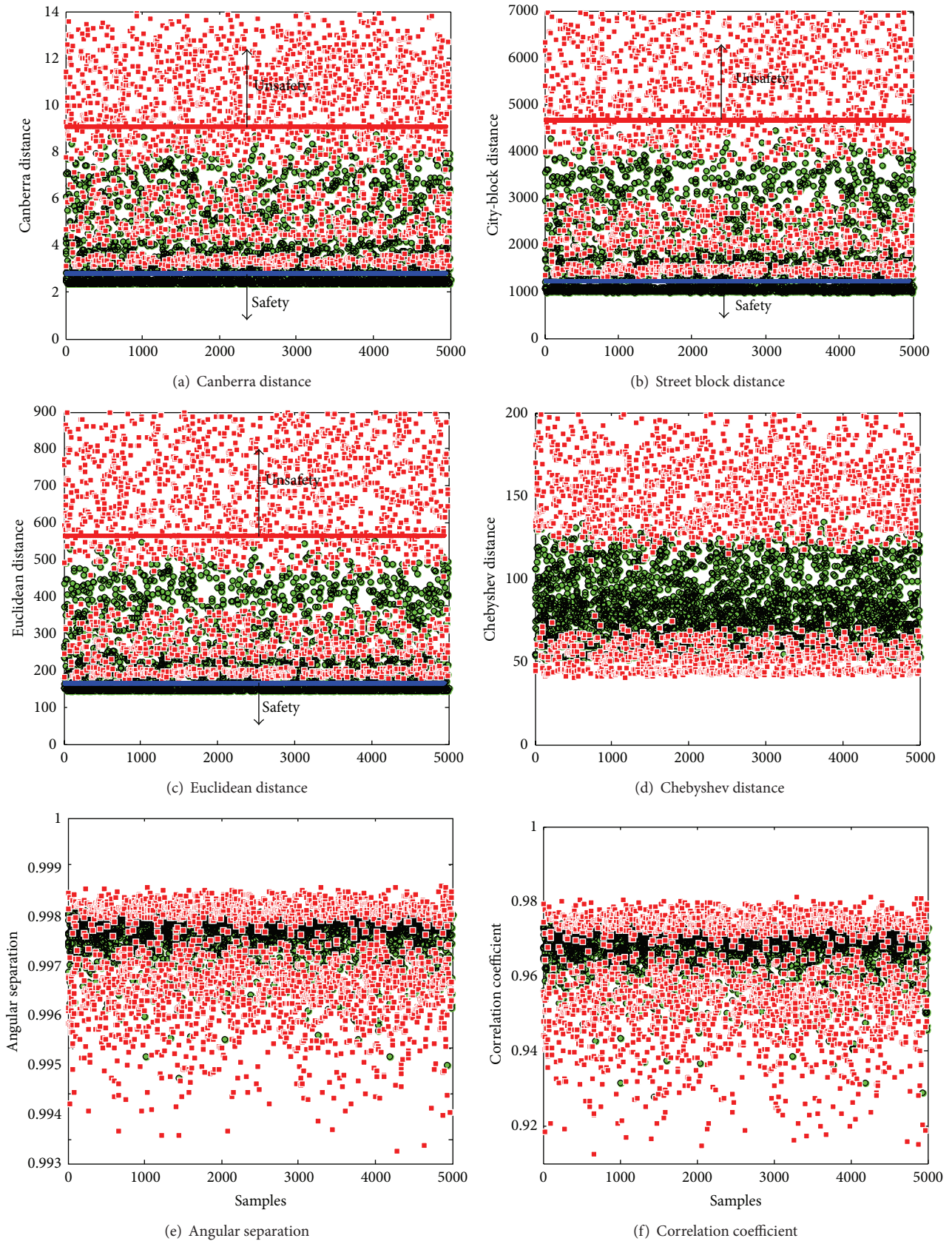


FIGURE 8: DMs scatter plots of grouped cable forces from Monte-Carlo simulation (green points are labeled as a class meeting requirement of SLS, whereas red points are labeled as a class dissatisfying it).

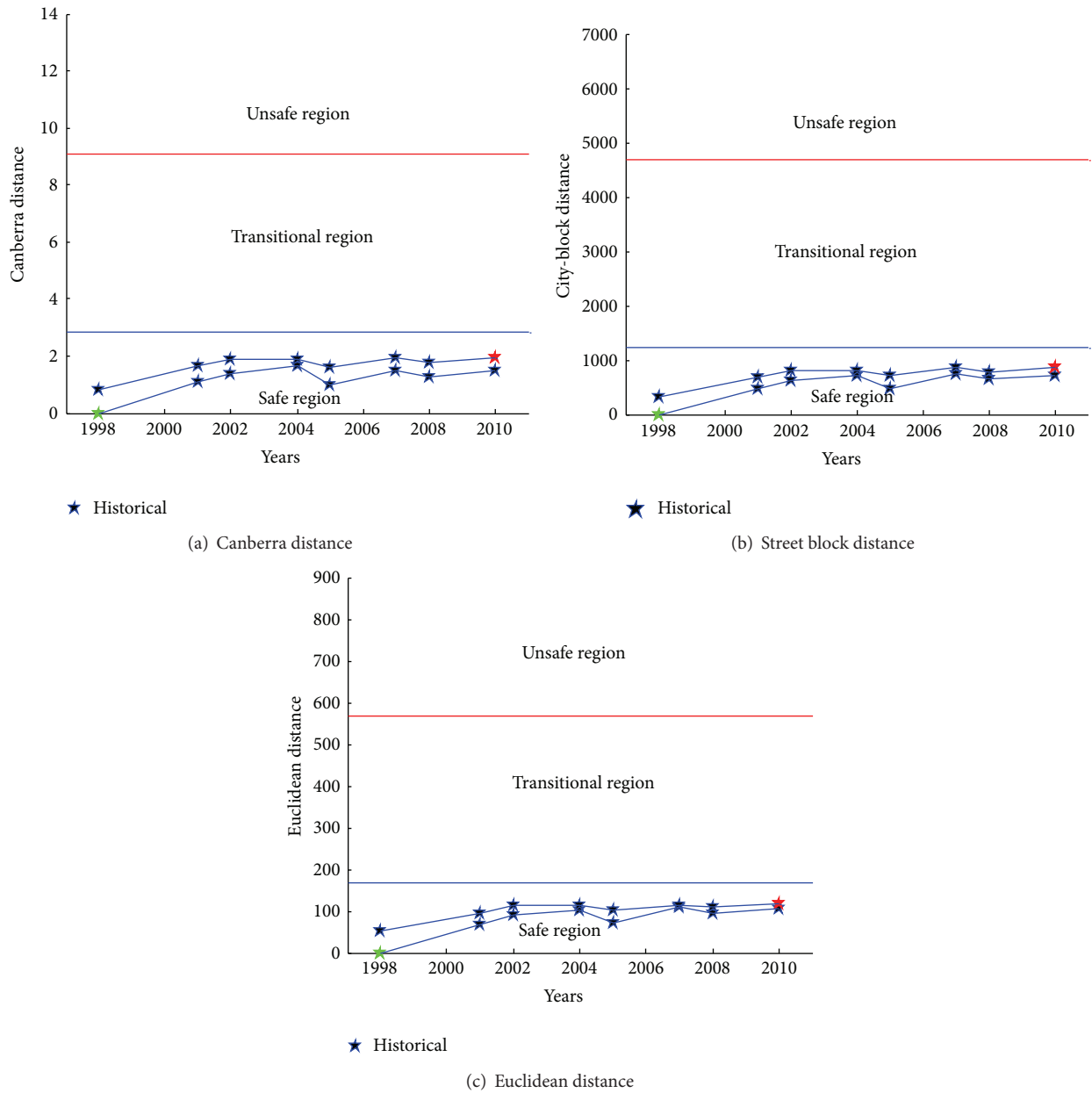


FIGURE 9: Health status evaluation driven by DMs of historical real data on grouped cable forces.

TABLE 3: Comparison of classification capacities of DMs.

DMs	Between-class spread	Within-class spread	Total spread	J_3 value
Euclidean distance	30867.8	21905.21	52773	0.7096
Street block distance	2217641	1680175	3897816	0.7576
Chebyshev distance	1446.89	332.481	1779.37	0.2298
Canberra distance	6.0993	5.0901	11.1894	0.8345
Angular separation	$6.90E - 7$	$1.31E - 7$	$8.21E - 07$	0.1905
Correlation coefficient	$1.15E - 4$	$2.00E - 5$	$1.35E - 4$	0.1744

TABLE 4: Threshold of dissimilarity measures.

DM(·)	[DM(·)] _{unsafety}	[DM(·)] _{safety}
Euclidean distance	566.7726	168.0435
Street block distance	4679.68	1227.92
Canberra distance	9.0863	2.8368

curves demonstrates that the overall performance of the bridge is gradually degrading and the disquieting departure from baseline status is increasing continuously, which should call the attention of the bridge owner.

5. Conclusions

This paper proposed an evaluation method for the health status of a cable-stayed bridge based on a set of DMs of grouped cables forces. By mapping the relationship between grouped cable forces and health status and building the measure space of grouped cable forces, the evaluation of structure health status is realized. Likewise, the structure's health status can be grasped in a macro sense. The main research conclusions are as follows.

(1) The status of grouped cable forces corresponds to the specific inner force state of a bridge. Thus, a holistic state evaluation of bridge health can be accomplished by evaluating the state of grouped cable forces as the agent, and the measure of grouped cable forces, which are DMs, can further service for this evaluation.

(2) Based on the Monte-Carlo method and combined with the threshold of target mechanical variables under the bridge limit state, a threshold system of the DMs of grouped cable forces can be established.

(3) Among all the DMs, Canberra distance, street block distance, and Euclidean distance exhibit better classification performance and can thus be used for similar cases.

(4) With increasing service time, the DMs values of the grouped cable forces continuously increase, which indicates that the performance of the bridge structure degrades annually.

Based on the finding of this paper, historical data on cable forces can be used to establish a safety evaluation system for cable-stayed bridges. Likewise, the data can also be used to facilitate the functions of online early warning and real-time evaluation of bridges based on the fact that the health monitoring system of bridges can acquire sufficient real-time data on cable forces.

However, this paper does not consider the influence of nonlinear factors in calculating the influence matrix. Relevant research considering more other factors will be conducted in the future.

Acknowledgments

This paper was sponsored by the project of the National Key Technology R&D Program in the 12th Five Year Plan of China (Grant no. 2012baj11b01), the National Natural Science Foundation of China (Grant no. 50978196), the Key State Laboratories Freedom Research Project (Grant no. sldrc09-d-01), the Fundamental Research Funds for the Central Universities, the State Meteorological Administration Special Funds

of Meteorological Industry Research (Grant no. 201306102), and Research of the Provincial Department of the Ministry of Education of Guangdong Province (2008b090500222).

References

- [1] D. F. Wisniewski, J. R. Casas, and M. Ghosn, "Codes for safety assessment of existing bridges—current state and further development," *Structural Engineering International*, vol. 22, no. 4, pp. 552–561, 2012.
- [2] H. M. Irvine, *Cable Structures*, Dover Publications, New York, NY, USA, 1991.
- [3] F. N. Catbas and A. E. Aktan, "Condition and damage assessment: issues and some promising indices," *Journal of Structural Engineering*, vol. 128, no. 8, pp. 1026–1036, 2002.
- [4] N. Wang, C. O'Malley, B. R. Ellingwood, and A.-H. Zureick, "Bridge rating using system reliability assessment. I: assessment and verification by load testing," *Journal of Bridge Engineering*, vol. 16, no. 6, pp. 854–862, 2011.
- [5] N. Wang, B. R. Ellingwood, and A.-H. Zureick, "Bridge rating using system reliability assessment. II: improvements to bridge rating practices," *Journal of Bridge Engineering*, vol. 16, no. 6, pp. 863–871, 2011.
- [6] H. Wu, Y. Xiang, and Y. Li, *Research on Safety Evaluation of Large Span Cable Stayed Bridge*, China Municipal Engineering, 2006, Chinese.
- [7] X. Shang and Y. Xu, "Safety-based cables' condition evaluation of cable stayed bridge with grey theory," *Journal of Chang'an University*, vol. 24, no. 1, p. 52, 2004.
- [8] M. Gul and F. N. Catbas, "Identification of structural changes by using statistical pattern recognition," in *Proceedings of the 6th International Workshop on Structural Health Monitoring, Stanford*, 2007.
- [9] H. Sohn, C. R. Farrar, N. F. Hunter, and K. Worden, "Structural health monitoring using statistical pattern recognition techniques," *Journal of Dynamic Systems, Measurement and Control, Transactions of the ASME*, vol. 123, no. 4, pp. 706–711, 2001.
- [10] M. Gul and F. Necati Catbas, "Statistical pattern recognition for Structural Health Monitoring using time series modeling: theory and experimental verifications," *Mechanical Systems and Signal Processing*, vol. 23, no. 7, pp. 2192–2204, 2009.
- [11] X. Hua and G. Xu, *Nonlinear Analysis of Bridge Structure*, vol. 6, People's Communication Press, 1997.
- [12] R. Xiao and H. Xiang, "Influence matrix optimization method on cable force of cable stayed bridge," *Journal of Tongji University*, no. 3, pp. 235–240, 1998.
- [13] P. C. Mahalanobis, "On the generalized distance in statistics," in *Proceedings of the National Institute of Sciences of India*, pp. 49–55, 1936.
- [14] R. W. Andrew, *Statistical Pattern Recognition*, 2nd edition, 2004.
- [15] T. Yi, H. Li, and M. Gu, "Full-scale measurements of dynamic response of suspension bridge subjected to environmental loads using GPS technology," *Science China Technological Sciences*, vol. 53, no. 2, pp. 469–479, 2010.
- [16] T. H. Yi, H. N. Li, and M. Gu, "Recent research and applications of GPS based technology for bridge health monitoring," *Science China Technological Sciences*, vol. 53, no. 10, pp. 2597–2610, 2010.
- [17] T.-H. Yi, H.-N. Li, and M. Gu, "Experimental assessment of high-rate GPS receivers for deformation monitoring of bridge," *Measurement*, vol. 46, no. 1, pp. 420–432, 2013.

- [18] T.-H. Yi, H.-N. Li, and M. Gu, "Wavelet based multi-step filtering method for bridge health monitoring using GPS and accelerometer," *Smart Structures And Systems, An International Journal*, vol. 11, no. 4, pp. 331-348, 2013.

Research Article

Real-Time Monitoring System for Workers' Behaviour Analysis on a Large-Dam Construction Site

Peng Lin,¹ Qingbin Li,¹ Qixiang Fan,² and Xiangyou Gao¹

¹ State Key Laboratory of Hydrosience and Hydraulic Engineering, Tsinghua University, Beijing 100084, China

² China Yangtze Three Gorges Group Corporation, Beijing 100038, China

Correspondence should be addressed to Peng Lin; celinpe@tsinghua.edu.cn

Received 21 June 2013; Accepted 26 July 2013

Academic Editor: Ting-Hua Yi

Copyright © 2013 Peng Lin et al. This is an open access article distributed under the Creative Commons Attribution License, which permits unrestricted use, distribution, and reproduction in any medium, provided the original work is properly cited.

This paper studies the feasibility of a real-time monitoring system to provide prompt analysis support of workers' behaviour on dam construction sites. The system makes use of wireless sensor tracking technology and a set of servers for the running of software, handling collected data, real-time site state visualization, and remote interaction communications. The low-level ZigBee-based tracking technology network hardware utilizing fingerprinting software technology was employed. The system was found to be able to cover a large field whilst retaining its simple and easily deployable features. The proposed system was successfully implemented on the Xiluodu arch dam construction site and ultimately helped overcome the original shortcomings in worker safety management and has advanced the means of administration and management's awareness and culture to new levels. The field tests also show that the received signal strength indicator (RSSI)-based localization algorithm implemented on ZigBee devices is reliable and is accurate enough at 3 to 5 meters. In conclusion, the system proved to be very useful for the management of field safety worker behaviour analyses in the case of such a high arch dam and also for similar hydraulic projects.

1. Introduction

Sensory technologies have developed quickly and are being utilized in structural health monitoring in civil and hydraulic engineering [1–5]. As result, a great contribution has been made to the control of cracking in mass concrete [5] and to the optimal identification of dams' structural characteristic changes [6].

The major industries of mining and hydraulic engineering, however, still have the poorest Health and Safety (H&S) record compared with all other industries. In China [7], the probability of construction worker fatalities in these industries is higher than that of all other industries, with the economic losses being measured each year in billions. Similar situations have been recorded worldwide. Health and safety control is inadequate in terms of preventing risks which, because of their specific nature, are unpredictable. At present, the health and safety management of people on a large hydroelectric power construction project site mainly depends, on contractor supervision and owner inspections. To better assure the H&S of people in construction, such

sole dependence on patrolling officers for control purposes should be reduced and in part replaced by a more objective evaluation of worker effort. Techniques such as the tracking of the location of workers and analysis of workers' behaviour would be a helpful site control inclusion. For example, the availability of an automatic detection and intelligent tracking system, to achieve instant control feedback information such as the warning of the presence of workers in certain zones, is likely to be helpful in this regard. To date, few studies have presented such techniques.

Tracking technologies have attracted the attention of many researchers and engineers in recent years. Several reasons ranging from a basic need for increased awareness of dangers to health and safety, to the development of specific applications for project quality inspection during the execution phase, have justified their adoption on construction sites. In general, all stakeholders (e.g., owners, contractors, architects, engineers, visitors, etc.) would benefit from such systems, in that successful projects are often determined by the achievement of quality linked to the control of worker performance.

TABLE 1: Comparisons of different tracking technologies.

	RFID passive	RFID active	ZigBee	WiFi	GPS
Power usage	None	Low to medium	Medium	High	Medium
Data rate	Low	Low to medium	Medium	High	N/A
Coverage	Low	Medium	High	High	Very high (outdoor)
HW costs	Low	Medium	Medium	High	High
Advantage	Low price No battery Required in tag	Low price	Low price	Popular devices (AP)	Long range coverage
Disadvantage	Very short range	Low precision	Power consumption	High power consumption	Only outdoor workplace
Deployability	Easy	Easy	Easy	Medium	Easy
Accuracy	Bad	Good	Good	Bad	Bad
Maintainability	Good	Good	Good	Bad	Good
Stability	Good	Good	Good	Bad	Good

Location tracking has already been applied to provide better documentation, analysis, and understanding of the best safety practices and the correction of poorer practices executed in the field. The integration of information technology and sensors networking technology is, in fact, widely applied in worker management systems on construction sites. For example, by using a wireless and untethered tracking technology and a local server running a software tool to handle collected data, real-time site state visualization can be achieved and remote interaction with safety inspectors can be made possible [8]. A proactive real-time safety management system using ultra-wide band technology and implementing proactive virtual fencing logics has been developed by Carbonari et al. [9]. Modern real-time locating systems (RTLs) use various locating techniques including received signal strength indicator (RSSI), time of arrival (TOA), time difference of arrival (TDOA), and angle of arrival (AOA) [10, 11]. Location sensing for infrastructure management and construction operations, however, has been mostly limited to the outdoor environment, where satellites are in view for positioning information. radio frequency identification (RFID) technology [12–15] is a low-cost location sensing solution for indoor construction [13, 14] and underground facilities [15], where satellite navigation systems cannot be used. Wireless local area networks (WLANs, or WiFi) have evolved rapidly over the last several years and are becoming increasingly popular. A design of an outdoor WiFi localization system [16] based on a GPS utilizes [17, 18] a rotating unidirectional multielement Yagi-type unidirectional antenna to determine in real time the direction of the maximum signal strength from a WiFi access point [19]. Real time GPS-based outdoor WiFi localization systems with an associated map display have been at the frontiers of research in recent years [20].

In this paper, alongside a system of real-time workers' behaviour monitoring analysis, a methodology based on the ZigBee tracking location model is proposed in detail. A worker behavior analysis model with prewarning components was proposed. An application of this management system was used to support inspectors in charge of the Xiluodu arch dam during the construction period.

2. Methodology and Model

2.1. Position Calculation Method. RTLS is an emerging application field that uses physical, geometric, and logical location information concerning people and objects. The location estimation and the tracking of people and objects are the most important tasks among the many constituent technologies in tracking technology. There is a wide range of options for sensor technologies that are suitable for creating an RTLS sensor network. Those options include RFID passive, RFID active, ZigBee, WiFi, and GPS. Choice of the appropriate sensor technology depends upon several factors including cost, environment, infrastructure, latency, and desired accuracy. Table 1 provides a brief and general comparison of these technologies and their advantages and disadvantages relative to their applications within a large construction site. After many extensive experiments on a dam construction site, the ZigBee technology was chosen.

Two major types of localization algorithms were considered in this study. One was a triangulation algorithm, based on an electromagnetic wave propagation model, and the other was fingerprinting which is based on statistical theory and proven industry practice.

Triangulation is the most common technique used to estimate a location; its goal is to map RSSI as a function of distance [21]. However, RSSI signals obtained are very unstable in the complicated and propagation-hazard workplace such as a dam construction site. It is very difficult to achieve accurate relative positioning just by the distance function, or some variations to the function, in the complicated electromagnetic circumstances. Hence, at an early stage of the project, this method was abandoned.

The fingerprinting technique is based on the specific behaviour of radio signals in a given environment, including reflections and fading, rather than on the theoretical strength-distance relationship of the triangulation method. In fingerprinting algorithms, a target node matches points sampled on the RSSI map (fingerprinting) which records the RSSI values of reference nodes with fixed positions at different sampled points with the closest RSSI values to the

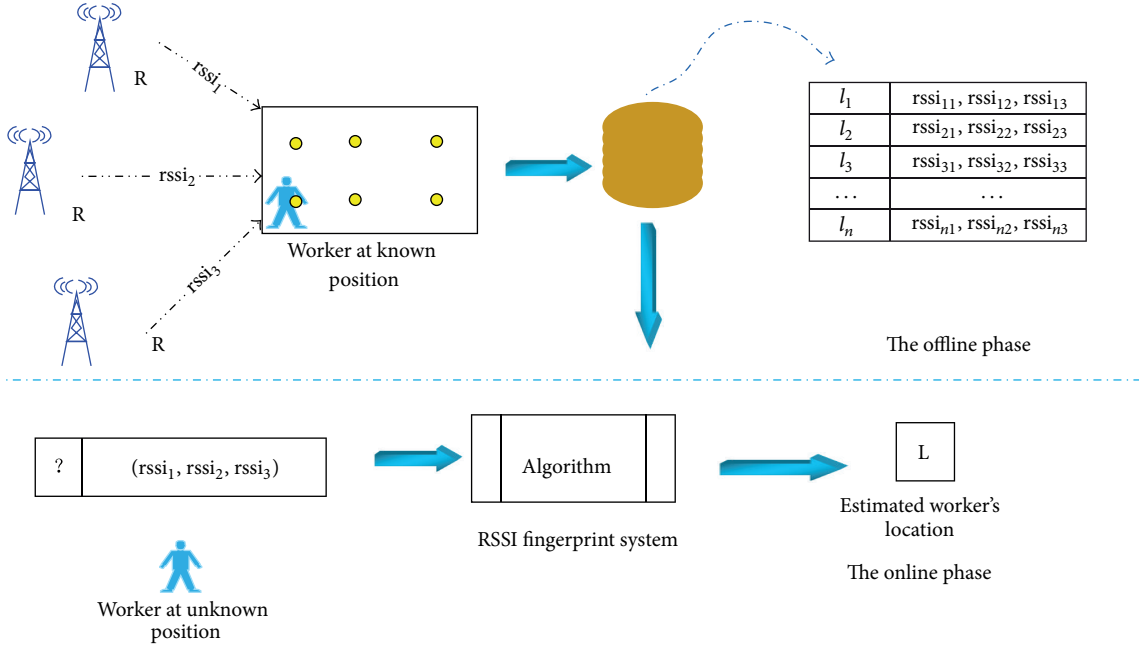


FIGURE 1: Schematic flow of RSSI fingerprint system of dam site.

target [22]. A typical method using RSSI mapping is the k-nearest neighbour (kNN) search [23]. In this algorithm, a dataset of reference node RSSI values at different sampled points is used to obtain an RSSI signature map stored in n-dimensional space. During implementation, the map is stored in computer memory to gain high performance. As moving tags obtain RSSI values from the reference nodes in real time, the system searches the database to search the k-nearest matching data records, also in real time. In order, therefore, to determine target position locations information using the k-data records, closeness (or proximity) is defined as a Euclidean distance calculated using the following equation:

$$D_t = \sqrt{\sum_{j=0}^N (RSSI_{tj} - RSSI_{\text{test point}-j})^2} \quad (1)$$

In (1), $RSSI_{tj}$ is the RSSI value read from reference node j at location t and $RSSI_{\text{test point}-j}$ is the RSSI value read from reference j at the target position. Once the RSSI value related to an unknown place is collected, the system evaluates the above formula to obtain a set of D values, the “closed” value of the anchor point, which is supposed to be near the unknown place.

For the dam site, the RSSI fingerprint system is shown in Figure 1. There are two separate phases: (1) the offline phase, wherein the RSS fingerprint database map is constructed, and (2) the online phase, wherein real-time localization is calculated and the unknown locations are determined by a matching with the existing RSSI map. In the offline phase, the distance between two nearby anchor points is approximately 1 meter. It is time consuming to construct the fingerprint database.

To gain maximized performance, the in-memory database SQLite is used. It is simple to use SQLite in memory

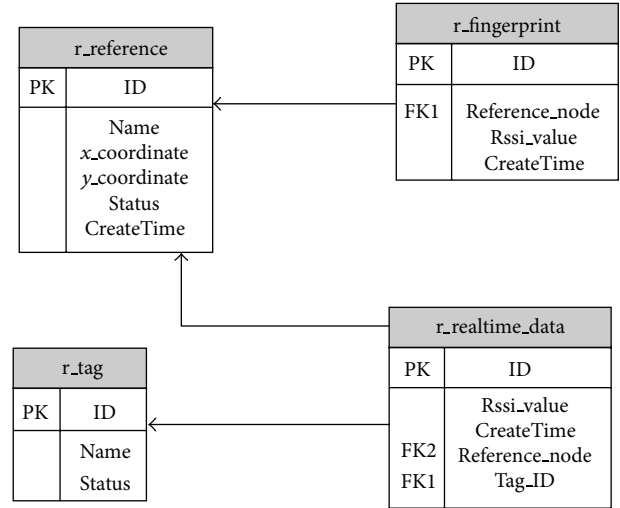


FIGURE 2: Schematic of database model.

mode and to open the database using the special filename “:memory:”. The API call is as follows:

```
rc = sqlite3_open(“:memory:”, &db).
```

The fingerprint system core engine records tag data, reference nodes, fingerprint information, and collected real-time positions. The database model (Figure 2) maps these data to individual but normalized tables. Table 2 illustrates each column of the table in detail.

2.2. Behaviour Tracking Analysis Model. Construction site management involves workers, supervisors, contractors, visitors, and owners. How to use tracking technology to effectively manage project personnel on site is an important

TABLE 2: Physical design of key data tables in RSSI fingerprint system.

	Column	Data type	Notes
Reference nodes table (r_reference)	ID	Int	Primary key
	Name	Varchar	
	x-coordinate	Double	
	y-coordinate	Double	
	Status	Int	Valid or invalid
	CreateTime	Timestamp	
Fingerprint table (r_fingerprint)	ID	Int	Primary key
	Reference_node	Int	Foreign key to id in r_reference
	Rssi_value	Double	Rssi value for the reference node
	CreateTime	Timestamp	
Real-time data table (r_realtime_data)	ID	Int	Primary key
	Tag_ID	Int	Foreign key to id in r_tag
	Reference_node	Int	Foreign key to id in r_reference
	Rssi_value	Double	Real-time RSSI value for the reference node
	CreateTime	Timestamp	
Tag table (r_tag)	ID	Int	Primary key
	Name	Varchar	
	Status	Int	Valid or invalid

question in modern management. Automatic movement detection data and subsequent analysis of that data to produce accurate and appropriate information usable by management are relied upon.

User behaviour analysis has successfully made use of different technologies in various industries [24, 25], especially during this Internet age. Internet users frequently receive personalized advertisements from Google or other companies based on very complex analysis systems. On a dam construction site, there is already much knowledge and many rules relating to project quality. In this study, modern sensor technology has been used to make use of this prior knowledge.

For example, a worker had an expected trajectory represented in Figure 3(b), but the actual result is in Figure 3(c). The worker was supposed to spend more time in pouring block 1 than that in pouring block 2. However, he spent all the time on block 2. It means the difference between actual data and expected data. To analyze this behaviour difference data and feedback, the output to other subsystems, such as the HR system, needs to get this result as input to have performance report of the involving worker's salary.

The worker's behaviour can be analyzed by following the three steps: prepare a predefined trajectory, obtain the worker's trajectory, and analyze.

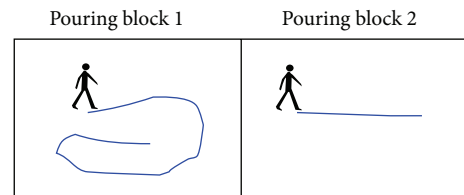
Prepare Predefined Trajectory. According to the construction work plan, every worker should follow a predefined procedure in each specific workspace so that every worker has a predefined trajectory in the form of a series of data including time values and position values, as shown in Table 3(a).

Obtain Actual Worker's Trajectory. In this step, the worker's trajectory data is gathered and prepared as a series of time values and position values as in Table 3(b).

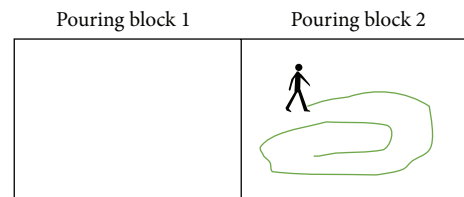
Analysis. There are various algorithms which measure the degree of similarity between two trajectories including



(a) Field workplace



(b) Expected behaviour



(c) Result behaviour

FIGURE 3: Dam site field behaviour for subsequent analysis.

Euclidean distance, dynamic time warping (DTW), and longest common subsequence (LCSS). For this step, to simplify the computing procedure, Euclidean distance was used to measure similarity.

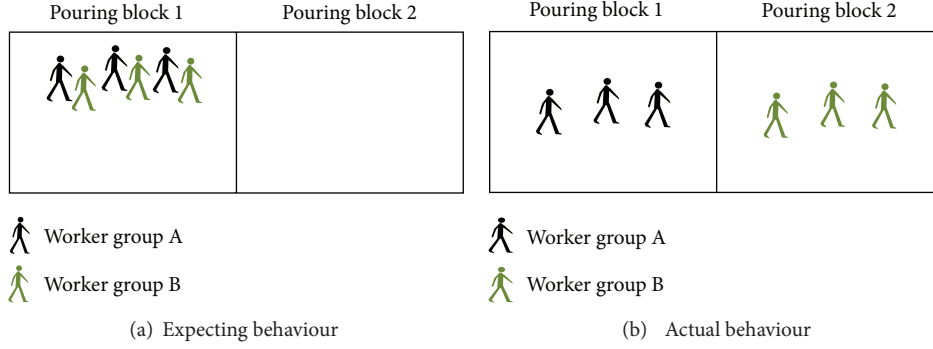


FIGURE 4: The behaviour analysis of different worker teams.

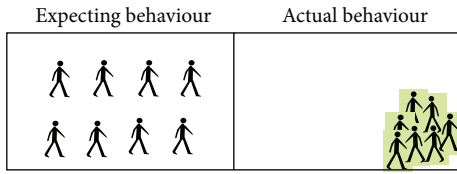


FIGURE 5: The behaviour analysis of worker positioning.

TABLE 3: (a) Worker defined time values and position values. (b) Worker actual time values and position values.

(a)		
Item	Timestamp	Position (x, y)
1	2013-4-4 11:22:23	101, 201
2	2013-4-4 11:23:26	101, 202
3	2013-4-4 11:24:28	104, 203
4	2013-4-4 11:25:28	104, 203
5	2013-4-4 11:26:28	105, 203
6	2013-4-4 11:27:28	106, 203

(b)		
Item	Timestamp	Position (x, y)
1	2013-4-4 11:22:24	100, 200
2	2013-4-4 11:23:24	101, 200
3	2013-4-4 11:24:24	102, 201
4	2013-4-4 11:25:28	104, 204
5	2013-4-4 11:26:28	105, 202
6	2013-4-4 11:27:28	106, 205

If two sequences, c, c' , are given as w_1, w_2, \dots, w_n and w'_1, w'_2, \dots, w'_n , the similarity can be defined as

$$D(c, c') = \sqrt{(w_1 - w'_1)^2 + \dots + (w_n - w'_n)^2} \quad (2)$$

The result is stored in a database and is fed back to other subsystems, such as HR via a web service interface.

If the two sequences do not have the same length, one sequence must be resampled.

This methodology can also be used in other cases, for example, to compare the performance of coworkers in the same group (similar duty and similar trajectory).

TABLE 4: The types of alarm levels.

Emergency	This level designates system as unusable
Alert	This level indicates that immediate action is needed
Critical	A critical condition, action should be undertaken soon
Warning	This level indicates that a warning condition is detected
Notice	This level designates a normal but significant condition
Information	This level designates information messages only

In the following scenario, worker group A and worker group B are supposed to be working at the same place and should work closely together, as shown in Figure 4(a). Actual scenario were that worker group A and worker group B worked at different pouring block, illustrated in Figure 4(b).

There are many dangerous places on a dam construction site. The positions of every worker who comes close to such places are filed into the system. If the records accumulate to a certain level, alarms are triggered automatically and safety officers are notified. The types of alarm levels are illustrated in Table 4.

In the other cases, to improve the quality control of concrete block pouring, the trajectory should be well distributed, as shown in Figure 5. The actual results show that workers spent most of the time pouring concrete in the block corner, probably spending time on matters other than pouring concrete. Not only the workers, of course, but also plant trajectories can be tracked and analyzed. To achieve a high quality mass concrete structure, concrete vibration plant should follow a predefined trajectory.

3. Description of the Real-Time Monitoring System

3.1. *Overview of System.* This system focusses mainly on providing automatic capture of real-time object multimovement data which can be used to analyze the action characteristics of workers on a dam site. Figure 6 is a schematic of the action information acquiring, collecting, and analyzing the system.

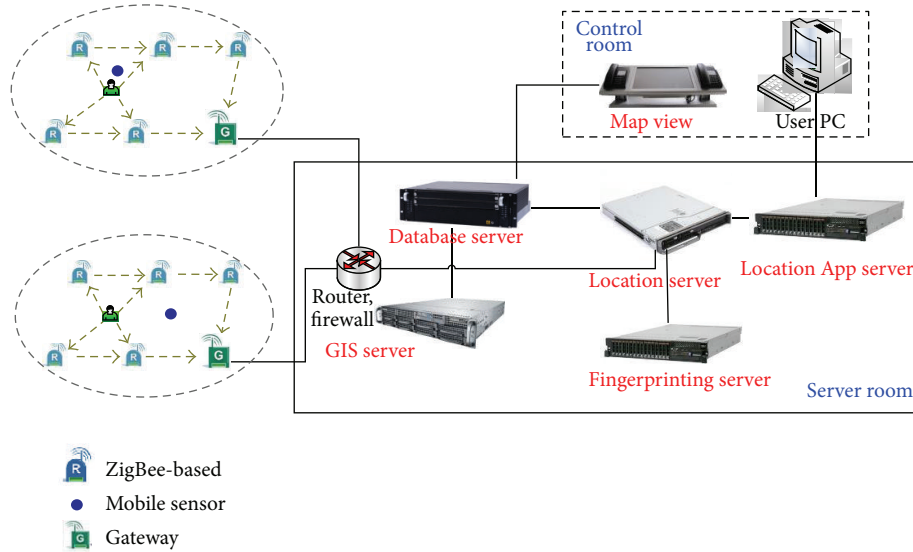


FIGURE 6: Component overview of the real-time monitoring system.

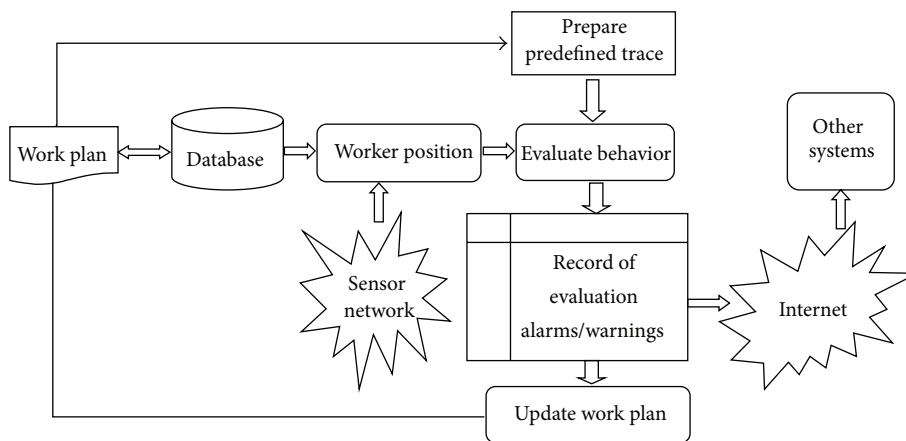


FIGURE 7: Logic approach to monitor worker behavior.

It includes (1) fixed reference nodes (ZigBee-based) installed in the pour concrete dam pavement (see Figure 9(a)); (2) the installed Gateway (ZigBee-Ethernet); (3) moving nodes carried by the workers themselves used to track personnel movements; (4) a router firewall; (5) a database server; (6) client to see the map of worker movements in real time; (7) the GUI client to management system; (8) the location server which runs the locating engine; (9) a location App Server which runs the safety management software; (10) a GIS Server which provides a vector map facility; (11) a fingerprint data server which stores the fingerprint data.

3.2. System Features and Functions. As previously stated, dam construction sites are very complex working environments, due to their dynamic nature and the concurrent involvement of numerous resources and supply components. The system described in this study has been provided with a first set of features, as illustrated above in Section 3.1. There is a potential for extension to further services, based on the same basic

concept relying on real-time control. The system includes both the control logic and hardware wireless systems for real-time resources tracking, as shown in Figure 7. In particular, it is assumed that the first edition of the work plan includes the list of tasks and work teams to be employed. Therefore, given a list of the teams present on site during each work phase, the predefined position coordinates of workers provide all the relevant data and select the areas in which each worker or team is allowed to operate or pass through. Monitoring of worker behaviour is then accomplished using the following logic. If one or more workers are found to operate in the area without being explicitly authorized, on the basis of the input provided by the work plan, a warning message is generated. In addition, the system records all worker trajectories even when they are not in dangerous zones. The collected data is then used by coordinators and inspectors to analyze the actual progress of work on site and to promptly identify possible deviations from what had been planned. The tracking system must continuously collect resources positional data on site

during work progress. It is worth emphasizing once again the ability of the system to act in a way which not only prevents interference, but also signals deviations from the planned schedule, allowing the work planners to become quickly aware of the need to update the plan. This system is one of closed-loop control with the ability to learn from experience and self-adapt.

The main functions of the system are as follows.

- (1) Worker positioning data service: worker position data can be stored consistently utilizing any modern database such as Oracle and Microsoft SQL Server. Other systems provide positioning service via the Web. The system of this study is designed to be flexible and to provide a quick response even when the demand loads are heavy.
- (2) Alarm and warning service: a worker can issue a critical alarm actively by pressing his tag emergency button; the control center can show the local concerned and the warning information. When a worker enters a dangerous or forbidden, zone, an alarm message will alert both the worker and the safety inspectors. When worker trajectories deviate from those planned, the system triggers warnings of the appropriate types.

3.3. The ZigBee RTLS Software Interface. The ZigBee RTLS software includes server software, PC client software, and Web interface. The server software consists of (1) location engine server: Real-time position calculations of tags using the fingerprint mapping algorithm; (2) management of all tag configurations and diagnosing functions; (3) system administration: user management, system level parameters, and others; (4) data import, export, backup, and restore; (5) Web mapping service (WMS) standard compliant map server, storage and spatial data display and any client can use the map service by embedding a JavaScript snippet into the standard html page; (6) the entire log and diagnosis information that can be configured into different catalogues and levels; the output destination can be selected from local disk file; TCP/IP socket is for facilitating Web services; (7) fault tolerance and load balancing; One server's fault will not lead to failure of the whole system as the faulty server can be detected and isolated from the whole system and the system load can be distributed to other servers according to resource usage (CPU, memory, disk, etc.); (8) message server, and user-defined messages including warnings and alert information to workers which are dispatched and delivered.

ZigBee RTLS Client software interface, shown in Figure 8(a), is a typical windows platform application written in C# 4.0 and NET Framework 4.0. There are five areas as follows: (1) the toolbar area contains the functions from left to right of "real-time monitor," "real-time alarm," "information collection," "historical trace" "special zones," "attendance management," "user management," "device management," "workers management," "system management," "system setting," "lock;" (2) shortcut navigation area such as the Microsoft Outlook navigation panel; (3) main show area, where a selected area on site and the workers can be shown

with zoom in and out operations; (4) alarm indication area, whereby colour changes indicate alarm levels; (5) status bar and notification area of system information which are divided into sections, each of which shows a different type of information including current operations, the current user, current linkage status to server, and current notification message.

The main functions are as follows:

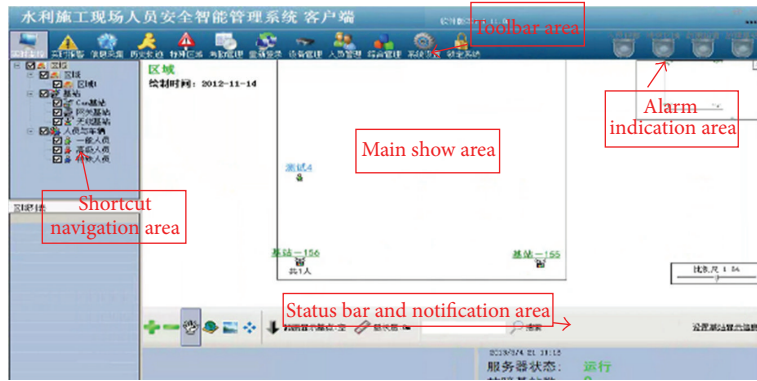
- (1) GIS map: shows tag real-time data on a GIS map allowing zooming in and out;
- (2) data query: query a tag's current and historical position data;
- (3) zone management: classification of worker locations in the different types of zones. Assignment of workers to their appropriate zones. If a worker enters the wrong zone, the system raises an alarm;
- (4) user management, authentication, security, and system usage logging functions;
- (5) worker behaviour analysis and assessment;
- (6) reporting system status and worker assessments.

The Web interface is similar to the client software interface, but it is also able to provide access for both a PC and other Internet surfing devices such as tablets and mobile phones as shown in Figure 8(b). It was developed using ASP.NET MVC 4 and the modern metro UI style. Popular Web browsers including IE 8.0+, Mozilla Firefox, and Google Chrome have been tested and verified. In addition, Ajax technology has been extensively used to achieve the best user experience.

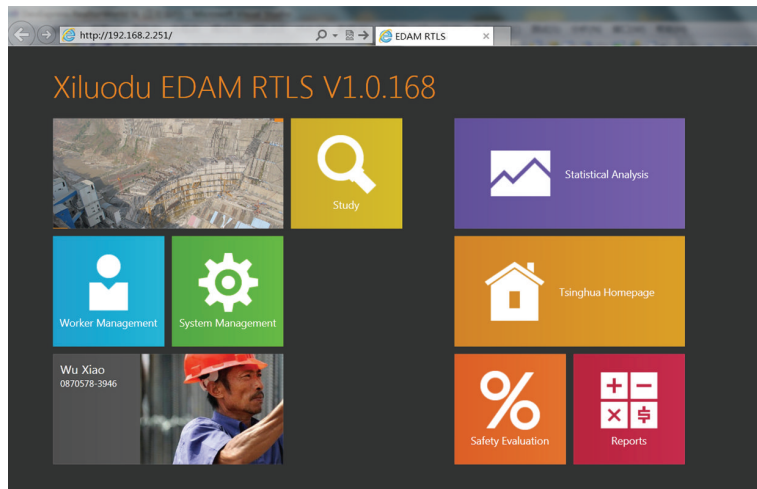
4. On-Site Test Case

4.1. The Construction Site Setup. The Xiluodu hydroelectric power station [26, 27] is the second largest in China and can produce 13.86 million kW of power. This is close to the capacity of the Three Gorges hydroelectric power station. The project is located in the Jinshajiang River, in Leibo County of Sichuan Province. The total amount of concrete poured is about 600 million cubic meters, and the total length of the tunnel is about 100,000 m. Many workers are engaged in the concreting of blocks and tunnels, and the implementation of the proposed system has an important significance, therefore for the control of the quality of the concrete and the scheduled progress.

Figure 9 shows the system installed at the Xiluodu dam site. The four numbered reference nodes, 155 #, 156 #, 157 #, and 158 #, were installed at the four corners of no. 29 monolith and no. 18 block in that monolith. The gateway platform was installed on the right bank at El.610 m. After setting up the system, on-site commissioning was carried out. Each reference node and each gateway were basically stable and the signal transmission between reference node and moving tags was in good condition. Personnel positioning displays were able to achieve a data refresh interval of 8.75 seconds. Commissioning requirements were therefore satisfied.



(a) Client interface



(b) Web interface

FIGURE 8: ZigBee RTLS Client and Web software interface.



(a) Installation scene



(b) Installation position

FIGURE 9: Install ZigBee-based devices in dam construction site.

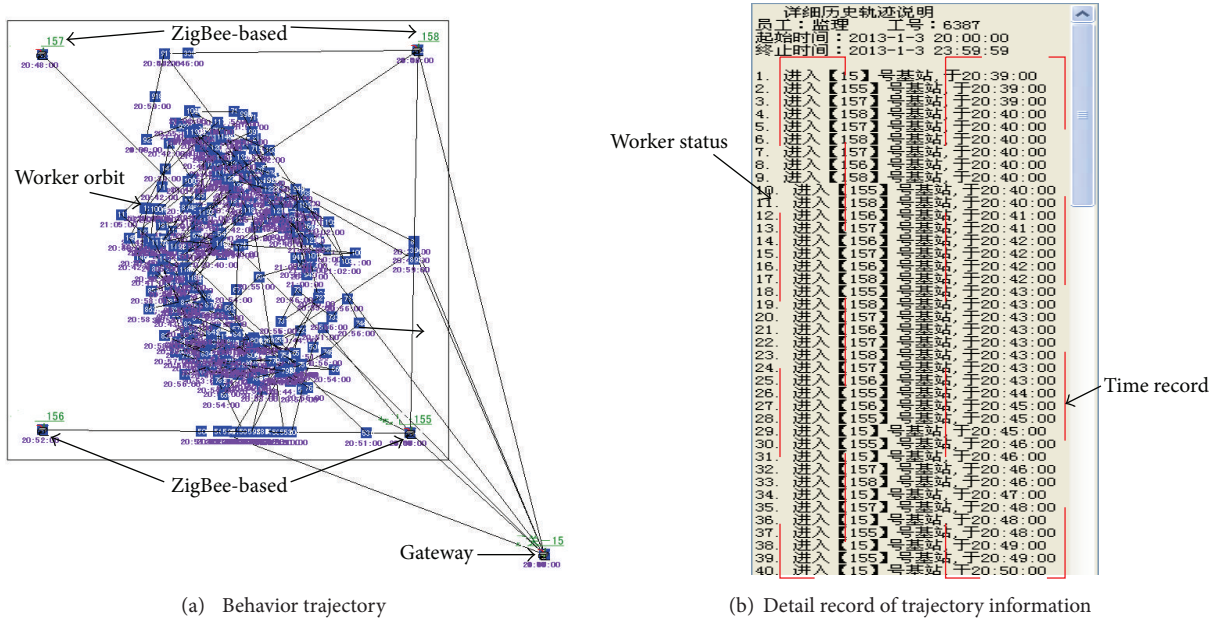


FIGURE 10: Workers history orbit.

4.2. Discussion on Behaviour Trajectory. Figure 10 shows one worker’s trajectory between entering a concrete pour block at 20:39 on Jan. 3 2013, to leaving the block at 8:26 in the next morning. The system monitored activities were within location 281. The location information can be customized once the beginning and ending time of the positioning information has been defined. The tracking lines shown in Figure 10(a) illustrate that the worker has finished his job according to predetermined plan at a predetermined place. The activities within the scope of detailed trajectory text descriptions can also verify the conclusion. A total of 281 active positioning message information, seen in Figure 10(b) (only information about the part-time segment), is the original data and can be exported and used by other analysis tools. The test application shows real-time monitoring system for worker behaviour, which functions by checking whether any worker operates within a predetermined place or a forbidden area is feasible, while following the predefined work plan. If emergency situations occur, the worker can trigger an emergency call for help. The safety officers can take emergency measures as appropriate, taking account of prearranged planning.

4.3. Localization Accuracy Analysis. Based on this field test, the real-time worker monitoring system gives relatively accurate position coordinates data. The field test also showed that the RSSI-based localization algorithm implemented by ZigBee devices is reliable and is accurate enough for the tracking purpose. The tracking accuracy is 3 to 5 meters within the coverage range of the tags carried by worker, even if obstacles are interposed between blind tags and routers. The system objective of this study, for a large dam construction site, does not require very precise tracking. In fact, it performs a kind of zone level of accuracy as opposed to tracking the exact point. In other words, it estimates those workers present within a given area. Other applications, where more

accurate localization is needed (e.g., for collision avoidance, hazards generated by objects falling from heights), were not considered in our study. For that reason, the ZigBee-based approach of this study was preferred, since it offers two important benefits: firstly, its reference nodes are battery-operated, small, and solid and are therefore easy to deploy as dam concrete pouring rises; secondly, the wireless sensor networks make up a mesh communication tree which is self-reconfigurable when routers are added, taken away, or moved about. Hence, the reality of dynamic changes to schedules as time advances presents no problem to the system.

5. Conclusions

This paper presents a real-time worker behavior monitoring system based on ZigBee-based tracking technology. The proposed idea offers an effective and efficient alternative for acquiring knowledge useful for supporting the decision-making process to evaluate worker behavior in real time.

The users were allowed to identify the factors, most influential to the system’s successful implementation. The following has been established for management use: (1) dam construction worker behavior, (2) online real-time monitoring over the whole work area, (3) an evaluation system for early warning and forecasting refinement for the owners of construction quality and worker safety management, (4) rapid response to any quality and safety problems, (5) effective control of safety and quality, and (6) the implementation of worker behaviour analysis following the acquisition of the real-time monitoring data.

To achieve the online, real-time, intelligent tracking identification feature, the monitoring system included many functions such as the worker emergency call facility, a track history of what actually happened, and the ability to query what is happening in a specific location. The field test showed

that the RSSI-based localization algorithm implemented on ZigBee devices is reliable and sufficiently accurate.

Acknowledgments

This research work was supported by the National Natural Science Foundation of China (no. 11272178), National Basic Research Program of China (973 Program) Grant nos. 2013CB035902 and 2011CB013503, Special Foundation for Public Welfare Industry of the Ministry of Water Resources (2010001035), Tsinghua University Initiative Scientific Research Program, and Foundation of State Key Laboratory of Hydrosience and Engineering (2011-KY-3). The authors are very grateful to the China Three Gorges Corporation for allowing access to one of its construction sites.

References

- [1] T.-H. Yi, H.-N. Li, and M. Gu, "Optimal sensor placement for structural health monitoring based on multiple optimization strategies," *Structural Design of Tall and Special Buildings*, vol. 20, no. 7, pp. 881–900, 2011.
- [2] T. H. Yi, H. N. Li, and X. D. Zhang, "Sensor placement on Canton tower for health monitoring using asynchronous-climb monkey algorithm," *Smart Materials and Structures*, vol. 21, no. 12, Article ID 125023, pp. 1–12, 2012.
- [3] T.-H. Yi, H.-N. Li, and M. Gu, "A new method for optimal selection of sensor location on a high-rise building using simplified finite element model," *Structural Engineering and Mechanics*, vol. 37, no. 6, pp. 671–684, 2011.
- [4] S. Hoon, R. Charles, F. M. Hemez, and et. al, "A review of structural health monitoring literature: 1996–2001," Los Alamos National Laboratory Report LA-13976-MS, Massachusetts Institute of Technology, 2004.
- [5] P. Lin, Q. B. Li, and H. Hu, "A flexible network structure for temperature monitoring of a super high arch dam," *International Journal of Distributed Sensor Networks*, vol. 2012, Article ID 917849, 2012.
- [6] Z. R. Wu, *Safety Control Theory and Its Applications on Hydraulic Structures*, Higher Education Press, Beijing, China, 2003.
- [7] Q. Qian and X. Rong, "State, issues and relevant recommendations for security risk management of china's underground engineering," *Chinese Journal of Rock Mechanics and Engineering*, vol. 27, no. 4, pp. 649–655, 2008.
- [8] N. Berardo, V. Massimo, and C. Alessandro, "A monitoring system for real-time interference control on large construction sites," *Automation in Construction*, vol. 29, pp. 148–160, 2013.
- [9] A. Carbonari, A. Giretti, and B. Naticchia, "A proactive system for real-time safety management in construction sites," *Automation in Construction*, vol. 20, no. 6, pp. 686–698, 2011.
- [10] D. Gabriel, C. Kevin, and C. Joan, "A survey of active and passive indoor localisation systems," *Computer Communications*, vol. 35, no. 16, pp. 1939–1954, 2012.
- [11] R. Alessandro, C. Marco, B. Luca, and C. Matteo, "Marco tagliasacchi an integrated system based on wireless sensor networks for patient monitoring, localization and tracking," *Ad Hoc Networks*, vol. 11, no. 1, pp. 39–53, 2013.
- [12] Y.-J. Tu, W. Zhou, and S. Piramuthu, "Identifying RFID-embedded objects in pervasive healthcare applications," *Decision Support Systems*, vol. 46, no. 2, pp. 586–593, 2009.
- [13] N. R. Saiedeh and M. Osama, "GPS-less indoor construction location sensing," *Automation in Construction*, vol. 28, pp. 128–136, 2012.
- [14] Christopher B. Roberts "The impact of information technology on the management of system design," *Technology in Society*, vol. 18, no. 3, pp. 333–355, 1996.
- [15] K. F. Zhang, M. Zhu, Y. J. Wang, E. J. Fu, and C. William, "Underground mining intelligent response and rescue systems," *Procedia Earth and Planetary Science*, vol. 1, no. 1, pp. 1044–1053, 2009.
- [16] B. P. Crow, I. Widjaja, J. G. Kim, and P. T. Sakai, "IEEE 802.11 wireless local area networks," *IEEE Communications Magazine*, vol. 35, no. 9, pp. 116–126, 1997.
- [17] T.-H. Yi, H.-N. Li, and M. Gu, "Characterization and extraction of global positioning system multipath signals using an improved particle-filtering algorithm," *Measurement Science and Technology*, vol. 22, no. 7, Article ID 075101, 2011.
- [18] T.-H. Yi, H.-N. Li, and M. Gu, "Recent research and applications of GPS-based monitoring technology for high-rise structures," *Structural Control and Health Monitoring*, 2012.
- [19] Y.-S. Chiou, C.-L. Wang, S.-C. Yeh, and M.-Y. Su, "Design of an adaptive positioning system based on WiFi radio signals," *Computer Communications*, vol. 32, no. 7–10, pp. 1245–1254, 2009.
- [20] A. Ibrahim and D. Ibrahim, "Real-time GPS based outdoor WiFi localization system with map display," *Advances in Engineering Software*, vol. 41, no. 9, pp. 1080–1086, 2010.
- [21] K. Yun and D. Kim, "Robust location tracking using a dual layer particle filter," *Pervasive and Mobile Computing*, vol. 3, no. 3, pp. 209–232, 2007.
- [22] X. Luo, W. J. O'Brien, and C. L. Julien, "Comparative evaluation of received signal-strength index (RSSI) based indoor localization techniques for construction jobsites," *Advanced Engineering Informatics*, vol. 25, no. 2, pp. 355–363, 2011.
- [23] P. Bahl and V. N. Padmanabhan, "RADAR: an In-Building RF-Based User Location and Tracking System," in *Proceedings of the 9th Annual Joint Conference of the IEEE Computer and Communications Societies (INFOCOM '00)*, pp. 1–10, Tel-Aviv, Israel, 2000.
- [24] J. T. Pittman and K. M. Ichikawa, "iPhone applications as versatile video tracking tools to analyze behavior in zebrafish (*Danio rerio*)," *Pharmacology Biochemistry and Behavior*, vol. 106, pp. 137–142, 2013.
- [25] F. Sultan, "Consumer response to the internet: an exploratory tracking study of on-line home users," *Journal of Business Research*, vol. 55, no. 8, pp. 655–663, 2002.
- [26] P. Lin, S. Z. Kang, Q. B. Li et al., "Evaluation on rock mass quality and stability of xiluodu arch dam under construction phase," *Chinese Journal of Rock Mechanics and Engineering*, vol. 10, 2012.
- [27] P. Lin, X. L. Liu, Y. Hu, W. B. Xu, and Q. B. Li, "Deformation and stability analysis on xiluodu arch dam under stress and seepage condition," *Chinese Journal of Rock Mechanics and Engineering*, vol. 32, no. 6, pp. 1137–1144, 2013.

Research Article

The Node Arrangement Methodology of Wireless Sensor Networks for Long-Span Bridge Health Monitoring

Guang-Dong Zhou¹ and Ting-Hua Yi^{2,3}

¹ College of Civil and Transportation Engineering, Hohai University, Nanjing 210098, China

² School of Civil Engineering, Dalian University of Technology, Dalian 116024, China

³ State Key Laboratory of Subtropical Building Science, South China University of Technology, Guangzhou 510641, China

Correspondence should be addressed to Guang-Dong Zhou; dagongzhougd@163.com

Received 4 July 2013; Accepted 26 August 2013

Academic Editor: Hong-Nan Li

Copyright © 2013 G.-D. Zhou and T.-H. Yi. This is an open access article distributed under the Creative Commons Attribution License, which permits unrestricted use, distribution, and reproduction in any medium, provided the original work is properly cited.

Wireless sensor networks (WSNs), which are a promising technology for the implementation of long-span bridge health monitoring, have gained increasing attention from both the research community and actual users. The limited energy of sensor emphasizes the importance of performance optimization of WSNs. In this paper, a methodology and strategy of node arrangement are developed to improve the performance of WSN for long-span bridge health monitoring, including balancing energy consumption, increasing data capacity, and reducing deployment cost. A composite WSN organized by sensor nodes and relay nodes is introduced for structural health monitoring. The energy consumption model of the composite WSN is firstly presented. And then, the data acquisition efficiency (DAE) defined as data capacity per unit deployment cost is suggested to evaluate the performance of WSN. Subsequently, the node arrangement is divided into two phases of sensor node arrangement and relay node arrangement. An improved general genetic algorithm is proposed to configure sensor nodes, and a nonuniform node arrangement method is developed to distribute relay nodes. Based on the DAE, the theoretical formulae of nonuniform node arrangement are deduced. The process of two-phase node arrangement is also provided for practical bridge engineers.

1. Introduction

Long-span bridges, which are characterized by low stiffness, low damping, and long service period, are susceptible to random vibration, such as vehicle load, strong wind, ambient vibration, and seismic motion [1, 2]. Structural health monitoring (SHM), which can assess existing or newly built bridges, has been implemented on bridges in Europe, USA, Canada, Japan, Korea, China, and other countries [3]. Because the modal parameters, for example, frequency, modal shape, and damping ratio, are the sensitive indexes of the structural properties such as stiffness and damage, vibration-based methodology has been widely developed in the past few decades to evaluate structural performance and identify structural damage or deterioration [4–7]. So vibration monitoring is an important component in SHM system of bridges. In most cases, traditional wired accelerometers are employed. However, the span of long-span bridges almost

exceeds 1000 m; miles of cables used for data communication induce the costs of sensor installation, maintenance, and repair extremely high. The Bill Emerson Memorial Bridge is instrumented with 84 accelerometer channels with an average cost per channel of over \$15 K, including installation [8]. According to the Yongjong Bridge facility manager, cable wiring accounts for 50% of the total installation cost [9]. Furthermore, changes in long cable temperatures and noises occur at connections between sensor and cable may cause the test data distortion.

The advancement in wireless technology has made the low cost, on-board computation, small size, ease of installation, and wireless communication sensors feasible. Those attractive features of wireless sensors motivate the shift of long-span bridges vibration monitoring away from traditional wired schemes towards the use of wireless sensor networks (WSNs), which provide a promising alternative to traditional wired sensor networks [10]. Many researchers

have contributed to employ WSNs to monitor long-span bridges vibration, and several types of wireless accelerometer are developed [11–13]. Recent successful implementations of such WSNs for full-scale SHM have demonstrated the potential of the technology [14–19]. The dimension of long-span bridges in the longitudinal direction is much larger than that in the other two directions, so the linear array is employed to arrange the wireless accelerometer networks in general. The wireless accelerometers (collectively referred to as sensor nodes in WSNs) are uniformly placed on the girder along the span one by one. The data collected by wireless accelerometers is transmitted to the sink by multihop. Most of the wireless accelerometers are powered by battery, which means that the energy of a sensor is limited. The sink has distinctive characteristics when compared to other nodes, such as more energy capacity, more processing power, and more memory, which makes them perfect to perform high demand processing and storing tasks. In this type of WSN, the nodes close to the sink are responsible for not only collecting data and transmitting those data to next node but also retransmitting data from other nodes. The nearer the node is away from the sink, the heavier the traffic load is. As a result, nodes near the sink would deplete their energy quickly, leading to what is called an “energy hole” near the sink. Once the “energy hole” appears, no more data can be transmitted to the sink, and the network life ends. But a great amount of energy of nodes far from the sink is unused. Existing experimental results show that if nodes are distributed uniformly in the network, up to 90% of the total initial energy of those nodes is left when the network lifetime is over [20]. So the performance of the WSN is very poor. However, the application research of WSNs in civil engineering mainly focuses on wireless accelerometer development, WSNs implement on bridges, and data processing. The optimal wireless accelerometer arrangement, which aims to eliminate “energy hole,” balance energy consumption in WSNs, and improve the performance of network, attracted little attention. But this is the prior work to carry out vibration monitoring using WSNs which cannot be neglected.

In the field of WSNs, some achievements about the “energy hole” had been made. Li and Mohapatra [21] presented an analytical model for the “energy hole” problem in WSNs with uniform node distribution. Then, Olariu and Stojmenović [22] proved that the “energy hole” problem is unavoidable in WSNs under the conditions that the nodes in the network are distributed uniformly and data are collected uniformly. At the same time, they discussed the nonuniform node distribution strategy and stated that a balanced energy depletion is possible [23]. Afterward, Lian et al. [20] proposed a nonuniform node distribution strategy to enhance the total amount of sensed data (data capacity) of WSNs. More recently, Wu et al. [24] assumed that all the nodes are deployed in a circular area and developed a nonuniform node distribution that the number of nodes in the outer annulus is geometric proportional to that in the inner annulus. Hossain et al. [25] provided an analytical method for placing a number of nodes in a linear array such that each node dissipates the same energy per data gathering cycle. All of the algorithms presented above assume that the architecture and responsibility of all

nodes in WSNs are identical and the energy consumption of data sensing can be negligible. Furthermore, the performance involving deployment cost and data acquisition capability of the WSNs is unconsidered. This is fit for general applications of WSNs, such as habitat monitoring, medical care, precision agriculture, or military surveillance. But in WSNs for long-span bridge vibration monitoring, the sampling rate is extremely high, more than 50 Hz sometimes, and the energy consumption relating to data sensing is an important component in all of the node energy dissipation. On the other hand, the wireless accelerometer usually consists of a wireless network node platform and a sensor board. The cost of sensor board almost accounts for 50% of the total sensor cost. So, in order to balance the monitoring cost and data capacity, employing some nodes without sensor board, which are named as relay nodes in this paper, in retransmitting data is an advisable choice. A rational WSN for long-span bridge vibration monitoring should contain sensor nodes and relay nodes. When integrating energy consumption, network cost, data capacity, and inhomogeneous nodes, the nonuniform node distribution strategy of WSNs has much difference. Until recently, there is some lack of knowledge about this topic. The purpose of this paper is to provide an analytical framework for arranging sensor nodes and relay nodes in WSN nonuniformly, so that the energy dissipation of each node is uniform, and the performance of the network is maximized. We preliminarily focus on the composite WSN for structural vibration monitoring of long-span bridges that is organized by sensor nodes and relay nodes.

The remainder of this paper is organized as follows. Section 2 gives a system description of the composite WSN, energy consumption model, and network performance index. In Section 3, the improved general genetic algorithm (GGA) for sensor nodes configuration, the nonuniform node arrangement method for relay nodes configuration, and the process of two-phase node arrangement are presented. Finally, some concluding remarks are given.

2. WSN Performances

2.1. System Description. As mentioned before, the WSN for long-span bridges vibration monitoring can be set as a linear array. The composite WSN including sensor nodes and relay nodes is placed on one side of the girder as a line, as shown in Figure 1. Total n sensor nodes are deployed along a straight line of length d . The hop-by-hop communication is performed from the source node (sensor node) to sink. The sensor nodes are in charge of sensing data, receiving data, and transmitting data. The transmitted data include the data sensed by local sensor node and the data from other nodes. The relay nodes, which have the same wireless network node platform as the sensor node and without sensor board, are only responsible for retransmitting data. The locations of sensor nodes can be optimized by traditional wired sensor place method to fulfill the requirements of structural model identification and condition assessment. The relay nodes are arranged to balance energy dissipation in the composite WSN and improve performance of the composite WSN.

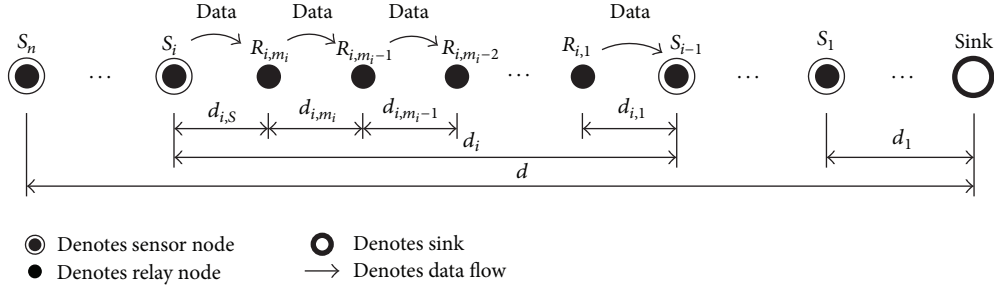


FIGURE 1: The linear composite WSN for bridge vibration monitoring.

In order to use the mathematical description expediently, the composite WSN for long-span bridge vibration monitoring is simplified. The following reasonable assumptions and stipulations are applied in the analysis.

- (1) Assume that all nodes in WSN cannot be moved and do not have energy replenishment capabilities in the process of vibration monitoring. Once energy is exhausted, the node can not work anymore. Each sensor node collects data continuously at a predetermined sampling frequency and generates l bits data per collecting cycle.
- (2) All sensor nodes are identical, and each one has an ID number. Let S_i ($i = 1 \cdots n$) denote the i th sensor node in the network, where S_1 is closest one to the sink and S_n is farthest one. All relay nodes are homogeneous, and each one has an ID number also. The total number of relay nodes in the interval of sensor nodes S_i and S_{i-1} is indicated as m_i . The ID number of relay node is assigned to $R_{i,j}$, where i denotes the relay node that belongs to the interval of sensor nodes S_i and S_{i-1} , and j denotes the j th ($j = 1 \cdots m_i$) relay sensor, as illustrated in Figure 1.
- (3) The sensor node placement is specified by $d = [d_1, \dots, d_n]$, where d_i ($2 \leq i \leq n$) denotes the distance between adjacent sensor nodes S_i and S_{i-1} . Let d_1 denote the distance between S_1 and sink. The symbol $d_{i,j}$ ($2 \leq j \leq m_i$) denotes the distance between adjacent relay nodes $R_{i,j}$ and $R_{i,j-1}$. The distance between $R_{i,1}$ and S_{i-1} is denoted as $d_{i,1}$, and the distance between S_i and R_{i,m_i} is denoted as $d_{i,s}$.
- (4) All nodes in the WSN have same initial energy of E_0 , and the sink has no energy limitation. The energy consumption of relay node relates to transmitting data and receiving data. Because of the much higher sampling frequency of wireless accelerometer than general wireless sensor, the energy consumption of data collecting cannot be neglected. So the energy of sensor node is consumed in collecting data, transmitting data, and receiving data.
- (5) Assume that the maximum radio range of each node in WSN is d_{\max} , which is much less than the distance d_i . This is rational because the distance between sensor nodes, which are located in critical sections

like 1/2 or 1/4 of main span, always exceeds 200 m, and the economical transmission range of wireless node is tens of meters in general. On this occasion, relay nodes are required in every interval of sensor nodes. The radio of the node is capable of adjusting its transmitting power to reach a node at a distance less than d_{\max} from it [23, 24]. Furthermore, it is assumed that there is a perfect data transmission route from the source node to the sink. As a result, there is no message failure due to insufficient signal to noise ratio within the radio range from a transmitting node and no data aggregation at any forwarding node.

2.2. Energy Consumption Model. A typical wireless accelerometer used for bridge vibration monitoring comprises three basic units: sensing unit, processing unit, and transceivers. The processing energy, which depends on the computation hardware architecture and the computation complexity, is another meaningful topic and not accounted for here. So the energy for sensing, energy for receiving, and energy for transmitting are considered and can be formulated as [26]

$$E_t = \alpha l + \beta l d^k, \quad \text{where } k = \begin{cases} 2 & \beta = \beta_1 \text{ if } d < d_0, \\ 4 & \beta = \beta_2 \text{ if } d \geq d_0, \end{cases} \quad (1)$$

$$E_r = \gamma l,$$

$$E_s = \eta l,$$

where E_t represents energy consumption for transmitting l bits data to distance d , α , γ , and η represent node specific energy consumption coefficients in the transmitter circuitry, receiver circuitry, and sensor circuitry, respectively, β, β_1 , and β_2 represent the energy required to transmit per bit over a per unite distance in different cases, E_r and E_s represent energy consumption for receiving and collecting l bits data, respectively, and k represents the path loss exponent. If the transmission distance is less than d_0 that is a node specific critical distance, the free space model is employed to describe the energy loss in path. k and β are set as 2 and β_1 , respectively. Otherwise, the multipath fading model is used. k and β are set as 4 and β_2 , respectively.

2.3. Data Acquisition Efficiency. Theoretically, the more sensor nodes are used, the better the dynamic response of long-span bridges is described. But the cost of monitoring is

increased correspondingly. On the other hand, there are tens of thousands of DOFs in a bridge. It is impossible that all DOFs are placed with wireless accelerometers. As a result, for a specific bridge, the investment is always limited, and the WSN scale is constrained. So it is very significant for vibration monitoring of long-span bridges that the data capacity is maximized through optimizing locations of nodes. Therefore, the metrics of WSN performance should contain two aspects, deployment cost and data capacity, which is more reasonable than the single index of lifetime or cost. In this paper, the data acquisition efficiency (DAE) defined as data capacity per unit deployment cost is proposed to evaluate the performance of WSN for long-span bridge vibration monitoring. The DAE is expressed as

$$\mu = \frac{tl(\sum_{i=1}^n f_i)}{an + bm}, \quad (2)$$

where μ represents the DAE, t represents the network lifetime defined from the network starting work to any one node that exhausts its energy, f_i represents the sampling frequency of the i th sensor node S_i , n and m represent the total number of sensor nodes and relay nodes in composite WSN, respectively, and a and b represent the cost of per sensor node and per relay node, respectively.

3. Theoretical Model

Two types of nodes are integrated in the WSN for long-span bridge health monitoring. The function of sensor nodes is dynamic response monitoring, and that of relay nodes is retransmitting data and balancing energy consumption in WSN. Because of the different functions, two-phase node arrangement is developed in this paper. The first phase is sensor node arrangement, and the second phase is relay node arrangement.

3.1. Sensor Node Arrangement. The objective of structural vibration monitoring is measuring the dynamic responses of bridge, so the sensor node arrangement is the most important work in the course of WSN deployment. Because of the existence of relay nodes, there is no need to take communication range of wireless sensor into account. Therefore, a conventional wired sensor optimization method, the GGA that is based on some modern biologic theories such as the genetic theory by Morgan, the punctuated equilibrium theory by Eldridge and Gould, and the general system theory by Bertalanffy, is employed to optimize the locations of sensor nodes [2, 27]. This algorithm is superior in biologies to the classical genetic algorithm (GA). The dual-structure coding system, in which the chromosomes of individual are composed of append code and variable code, is used to initialize the population. This coding system can assure that the total number of sensor nodes is unchanged in the crossover and mutation. The two-quarter selection, whose process is two-parent selection \rightarrow crossover \rightarrow a family of four \rightarrow two-quarter selection \rightarrow mutation \rightarrow a family of four \rightarrow two-quarter selection \rightarrow next generation, is introduced in the evolution. For improving the convergence speed and

reliability of globally optimal solution, the worst elimination policy is proposed here. In every generation, the individual with the worst fitness value is firstly selected as one parent. By this way, the worst one is eliminated inevitably, and the population always moves toward higher fitness value.

In the process of evolution, the gradual change and sudden change are combined. In general, the gradual change is adopted. When the best fitness value of the population keeps constant in several generations, it reveals that the iteration falls into local optimal solutions. The evolutionary processing turns to sudden change. Until the best fitness value changes, the evolutionary processing turns back to the gradual change. If the sudden change happens at preset times sequentially, it indicates that the global optimal solution is achieved and the iteration can be stopped. In the stage of gradual change, crossover is first, and mutation is second, while in the stage of sudden change, mutation is first and crossover is second. In this way, the drawbacks of GA that the results incline to local optimal space easily can be avoided effectively.

The partially matched crossover (PMX) is applied in the crossover. Two crossover points in append code are selected randomly. The interval between the two crossover points forms a matched segment. The two parents exchange the two matched segments. The repeated append code in one parent is replaced by the matched append code at the specified arbitrary element in the other parent and vice versa. In the stage of gradual change, the swap mutation is employed. The two append codes at the randomly selected points exchange within each parent, which makes the mutation slight. Accordingly, the solutions move a small step toward adjacent area. And in the stage of sudden change, the inversion mutation is used. The segment between two randomly selected points flips left to right, which results in a serious mutation. So the solutions jump out of local area and arrive in a new space. It can be concluded that the combing of swap mutation and inversion mutation can avoid that the results fall into local optimal space.

It is well known that the measured data with high signal-to-noise ratio, which is critical for model identification and damage detection, can be obtained on the DOFs with possible large amplitudes of vibration. The modal strain energy (MSE) provides a rough measure of the dynamic contribution of each candidate sensors to the target mode shapes and tells which DOFs capture most of the relevant dynamic features of the structure. Therefore, the objective of sensor node arrangement can be interpreted as finding a reduced configuration of sensor node placements, which maximizes the measured MSE of the bridge, so that the structural dynamic behavior can be well characterized. So in this paper, the MSE is taken as the fitness function in GGA. Suppose that the mode shape matrix of a long-span bridge is $\Phi = [\phi_1, \phi_2, \dots, \phi_q]$ (subscript q is the number of mode shape vectors) and the number of sensor nodes is n ; the fitness function can be given as

$$g = \sum_{x=1}^q \sum_{y=1}^q \sum_{z \in n} \sum_{e \in n} |\phi_{zx} k_{ze} \phi_{ey}|, \quad (3)$$

where ϕ_{zx} represents the deformation of z th component in the x th model vector, ϕ_{ey} represents the deformation of e th

component in the y th model vector, and k_{ze} represents the stiffness coefficient between the z th DOF and the e th DOF. $z \in n$ and $e \in n$ mean that z and e are restricted in the locations where wireless sensors are placed.

3.2. Relay Node Arrangement. Further analyzing the DAE indicates that if the number of sensor nodes and relay nodes in different WSNs is the same, the longer the network lifetime is, the higher the DAE is. Ideally, the WSN has the longest lifetime if all nodes exhaust their energy simultaneously. And the most excellent performance of WSN can be obtained. So pursuing high DAE can be realized by balancing energy consumption in WSN. The “energy hole” is avoided accordingly. And the effective way of balancing energy consumption of nodes is adjusting data transmission distance. In linear WSN, the data transmission distance relates to node location. Therefore, the optimization of WSN performance is selecting optimal locations of relay nodes, so that the energy consumption per second of every node in WSN is identical. The nonuniform node arrangement method is deduced for configuring the relay nodes.

According to the energy consumption model formulated by (1), the energy consumption of sensor node S_i per second is

$$E'_{s_i} = E'_t + E'_r + E'_s = \alpha l \sum_{p=i}^n f_p + \beta l d'_{i,s}{}^k \sum_{p=i}^n f_p + \gamma l \sum_{p=i+1}^n f_p + \eta l f_i, \quad i = 1 \cdots n, \quad (4)$$

where superscript $'$ represents that the value is temporary.

And the energy consumption of relay node $R_{i,j}$ per second is

$$E'_{R_{i,j}} = E'_t + E'_r = \alpha l \sum_{p=i}^n f_p + \beta l d'_{i,j}{}^k \sum_{p=i}^n f_p + \gamma l \sum_{p=i}^n f_p, \quad (5)$$

$$j = 1 \cdots m_i.$$

Then, the energy consumption of the farthest sensor node and relay node ($i = n$) from the sink can be obtained:

$$E'_{S_n} = \alpha l f_n + \beta l d'_{n,s}{}^k f_n + \eta l f_n, \quad (6)$$

$$E'_{R_{n,j}} = \alpha l f_n + \beta l d'_{n,j}{}^k f_n + \gamma l f_n. \quad (7)$$

In order to balance energy consumption and avoid “energy hole,” the energy consumption of every node in composite WSN should be balanced. The formula can be obtained as follows:

$$E'_{S_n} = E'_{R_{n,j}} = E'_{S_i} = E'_{R_{i,j}}. \quad (8)$$

Substituting (8) into (7), the $d'_{n,j}$ can be derived as

$$d'_{n,j} = \left[\frac{E'_{S_n} - \alpha l f_n - \gamma l f_n}{\beta l f_n} \right]^{1/k}. \quad (9)$$

And substituting (6) and (8) into (4) results in

$$d'_{i,s} = \left[\frac{E'_{S_n} - \alpha l \sum_{p=i}^n f_p - \gamma l \sum_{p=i+1}^n f_p - \eta l f_i}{\beta l \sum_{p=i}^n f_p} \right]^{1/k}. \quad (10)$$

Similarly, substituting (6) and (8) into (5) results in

$$d'_{i,j} = \left[\frac{E'_{S_n} - \alpha l \sum_{p=i}^n f_p - \gamma l \sum_{p=i}^n f_p}{\beta l \sum_{p=i}^n f_p} \right]^{1/k}. \quad (11)$$

Then the total number of relay node m_i in the interval of sensor nodes S_i and S_{i-1} can be calculated as

$$m_i = \left\lceil \frac{d_i - d'_{i,s}}{d'_{i,j}} \right\rceil, \quad (12)$$

where $\lceil \cdot \rceil$ represents rounding toward positive infinity, which keeps the number of relay node integral.

Because m_i is rounded toward positive infinity, the distance between two adjacent relay nodes and the distance between relay node and sensor node are shortened. So the final distances are

$$d_{i,s} = d'_{i,s} \left[1 - \frac{(d'_{i,j} \times m_i + d'_{i,s}) - d_i}{d'_{i,j} \times m_i + d'_{i,s}} \right], \quad (13)$$

$$d_{i,j} = d'_{i,j} \left[1 - \frac{(d'_{i,j} \times m_i + d'_{i,s}) - d_i}{d'_{i,j} \times m_i + d'_{i,s}} \right].$$

There is no data generated between any two adjacent sensor nodes, so the data quantity retransmitted by relay nodes between two adjacent sensor nodes is uniform. Therefore, $d_{i,j}$ should be equal to $d_{i,1}$ to balance the energy dissipation of all relay nodes that belong to two adjacent sensor nodes. Then, $d_{i,j}$ and $d_{i,1}$ can be unified into $d_{i,R}$ for simplicity.

As a result, the final energy consumption E_{S_i} of sensor node S_i per second can be acquired as follows:

$$E_{S_i} = \alpha l \sum_{p=i}^n f_p + \beta l d_{i,S}{}^k \sum_{p=i}^n f_p + \gamma l \sum_{p=i+1}^n f_p + \eta l f_i. \quad (14)$$

And the final per second energy consumption E_{R_i} of relay nodes which belong to the interval of S_i and S_{i-1} is

$$E_{R_i} = \alpha l \sum_{p=i}^n f_p + \beta l d_{i,R}{}^k \sum_{p=i}^n f_p + \gamma l \sum_{p=i}^n f_p. \quad (15)$$

So the network lifetime t can be easily calculated:

$$t = \frac{E_0}{\max[E_{S_i}, E_{R_i}]}. \quad (16)$$

Accordingly, the DAE μ is

$$\mu = \frac{t l (\sum_{i=1}^n f_i)}{(a n + b \sum_{i=1}^n m_i)}. \quad (17)$$

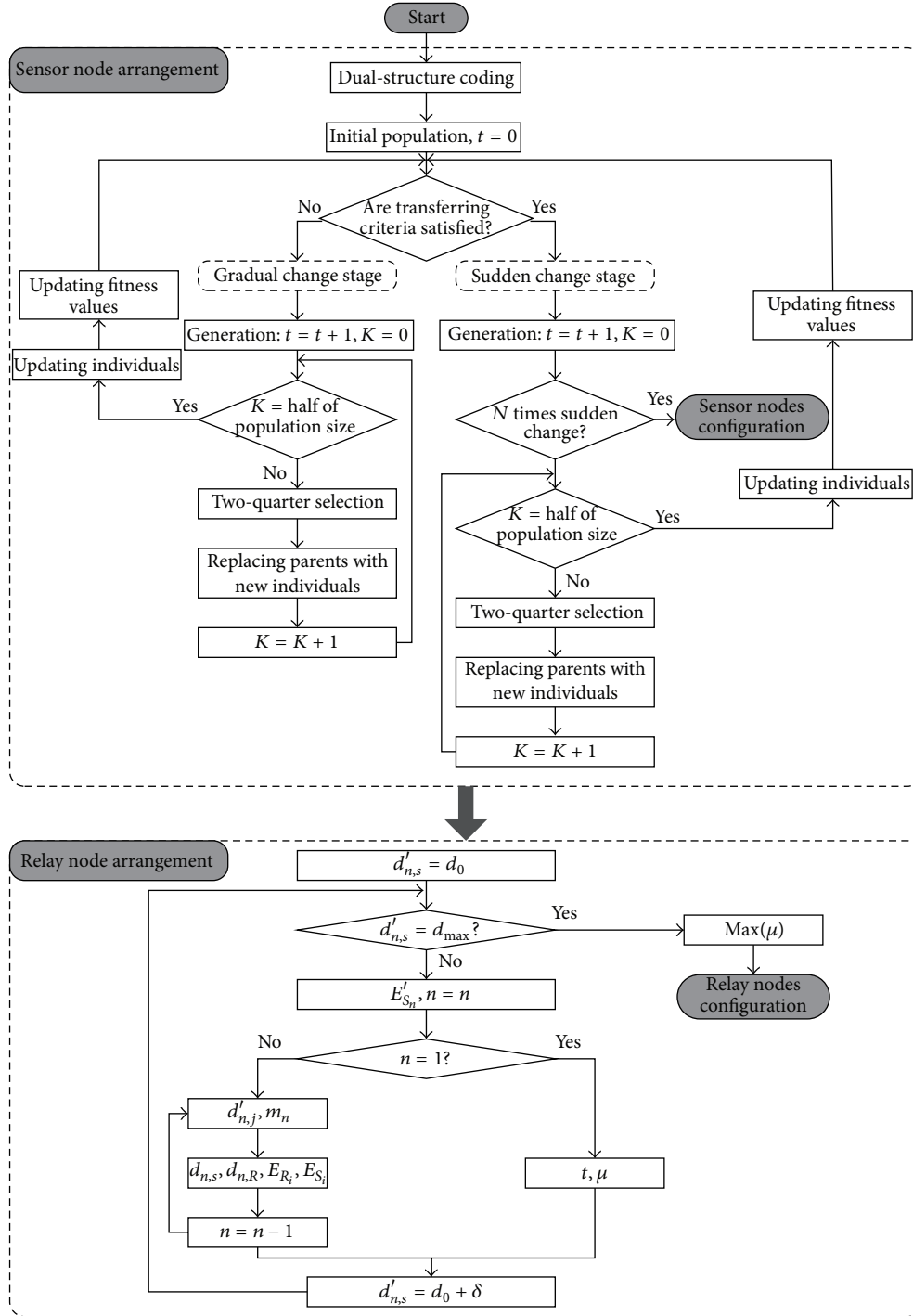


FIGURE 2: The flow chart of two-phase node arrangement.

It should be noted that the final node energy consumptions of different nodes do not satisfy (8) anymore because of rounding in (12). Moreover, the remainder in (12) is not the same in different time. So the absolutely optimal WSN is impossible. But a suboptimal WSN, in which the energy consumption of all nodes is almost synchronous, can be

achieved. The difference of energy consumptions of different nodes is little and can be accepted by civil engineering. On the other hand, the energy consumption of data sensing is taken into account in the total energy consumption, so the proposed method in this paper is more suitable for WSN with high sampling rate, such as the WSN for long-span bridge

health monitoring. In those WSNs with low sampling rate, the energy for sensing is little, and the influence of the energy for sensing on the energy balance in WSN is not significant.

3.3. Implementation Procedures. The theoretical model that is present in last two sections looks very complex on the surface. The whole flow chart to find the optimal nodes locations is shown in Figure 2, so that the proposed two-phase node arrangement method in this paper can be easily implemented. Some details are also listed as follows.

Phase I (sensor node arrangement)

Step 1. Initializing the population. In each individual, the append code is generated by shuffle method, and the variable code (0 or 1) is created randomly.

Step 2. Calculating the fitness value of every individual in the population.

Step 3. Selecting the individual with the worst fitness value as one parent and selecting an individual randomly from the left individual as another parent.

Step 4. Judging the type of change according to the best fitness value in the population.

Step 5. Executing two-quarter selection to generate two new individuals.

Step 6. Selecting two-parent randomly and repeating Steps 4 and 5 until the time of iteration is equal to half of the population size.

Step 7. Updating individuals and fitness values of the population.

Step 8. Repeating Steps 3~7 until the stopping criteria are achieved.

Phase II (relay node arrangement)

Step 1. Setting i to be equal to n and $d'_{n,s}$ to be equal to d_0 and then computing E'_{S_n} by (6).

Step 2. Calculating $d'_{n,j}$ by (9) and then calculating m_n by (12).

Step 3. Adjusting $d'_{n,s}$ and $d'_{n,j}$ by (13). The final $d_{n,s}$ and $d_{n,R}$ are obtained.

Step 4. Replacing n with i and repeating Steps 2 and 3. Calculating all parameters $d_{i,s}$, $d_{i,R}$, E_{S_i} , and E_{R_i} ($i = 1 \cdots n$).

Step 5. Calculating t and μ by (16) and (17).

Step 6. Increasing $d'_{n,s}$ by a small increment δ and repeating Steps 1~5. The iteration is ended until $d'_{n,s}$ is increased to d_{\max} .

Step 7. Selecting the arrangement with the maximum μ as the best configuration.

4. Conclusions

WSNs, which are characterized by cable independence, low cost, easy installation, and on-board processing capability, attract more and more attentions in structural vibration monitoring of long-span bridges. It is meaningful to improve the performance of WSNs through maximizing the data capacity and reducing the deployment cost. The composite WSN constituted by sensor nodes and relay nodes is a good configuration for SHM of long-span bridges. The DAE defined by data capacity per unit WSN cost is a promising index to evaluate the performance of WSNs. Two-phase node arrangement methodology and strategy are proposed to configure the composite WSN. The locations of sensor nodes are firstly optimized by GGA to satisfy the structural condition assessment. And then, the nonuniform node arrangement method is proposed to configure the relay nodes to fill the blanks between sensor nodes, which is deduced from the principle of maximizing DAE, balancing energy consumption, eliminating “energy hole,” and maximizing network performance. The step-by-step procedures make the theoretical formulates implemented easily in practice. It should be pointed out that the proposed method is a tentative work about the topic of WSN optimization for long-span bridge health monitoring, and more extensively research will be conducted in the future.

The further work is applying the method and strategy developed in this paper to arrange a composite WSN for a long-span suspension bridge, so that the efficiency of the proposed approach can be demonstrated extensively.

Acknowledgments

This research work was jointly supported by the Science Fund for Creative Research Groups of the NSFC (Grant no. 51121005), the National Natural Science Foundation of China (Grant nos. 51308186 and 51222806), the Starting Research Fund from the Hohai University (Grant no. 2013B01414), and the Research Fund of State Key Laboratory of Subtropical Building Science (Grant no. 2013KB10).

References

- [1] T. H. Yi and H. N. Li, “Methodology developments in sensor placement for health monitoring of civil infrastructures,” *International Journal of Distributed Sensor Networks*, vol. 26, pp. 1–11, 2012.
- [2] T. H. Yi, H. N. Li, and X. D. Zhang, “Sensor placement on Canton Tower for health monitoring using asynchronous-climb monkey algorithm,” *Smart Materials and Structures*, vol. 21, no. 12, Article ID 125023, 2012.
- [3] J. M. Ko and Y. Q. Ni, “Technology developments in structural health monitoring of large-scale bridges,” *Engineering Structures*, vol. 27, no. 12, pp. 1715–1725, 2005.
- [4] S. W. Doebling, C. R. Farrar, and M. B. Prime, “A summary review of vibration-based damage identification methods,” *Shock and Vibration Digest*, vol. 30, no. 2, pp. 91–105, 1998.
- [5] A. Alvandi and C. Cremona, “Assessment of vibration-based damage identification techniques,” *Journal of Sound and Vibration*, vol. 292, no. 1-2, pp. 179–202, 2006.

- [6] A. Deraemaeker, E. Reynders, G. De Roeck, and J. Kullaa, "Vibration-based structural health monitoring using output-only measurements under changing environment," *Mechanical Systems and Signal Processing*, vol. 22, no. 1, pp. 34–56, 2008.
- [7] T.-H. Yi, H.-N. Li, and M. Gu, "A new method for optimal selection of sensor location on a high-rise building using simplified finite element model," *Structural Engineering and Mechanics*, vol. 37, no. 6, pp. 671–684, 2011.
- [8] S. Jang, H. Jo, S. Cho et al., "Structural health monitoring of a cable-stayed bridge using smart sensor technology: deployment and evaluation," *Smart Structures and Systems*, vol. 6, no. 5-6, pp. 439–459, 2010.
- [9] M. J. Chae, H. S. Yoo, J. Y. Kim, and M. Y. Cho, "Development of a wireless sensor network system for suspension bridge health monitoring," *Automation in Construction*, vol. 21, no. 1, pp. 237–252, 2012.
- [10] H. Jo, S. H. Sim, T. Nagayama et al., "Development and application of high-sensitivity wireless smart sensors for decentralized stochastic modal identification," *Journal of Engineering Mechanics*, vol. 138, no. 6, pp. 683–694, 2011.
- [11] J. P. Lynch and J. L. Kenneth, "A summary review of wireless sensors and sensor networks for structural health monitoring," *The Shock and Vibration Digest*, vol. 38, no. 2, pp. 91–128, 2006.
- [12] J. A. Rice and B. F. Spencer Jr., "Structural health monitoring sensor development for the Imote2 platform," in *Sensors and Smart Structures Technologies for Civil, Mechanical, and Aerospace Systems*, vol. 6932 of *Proceedings of SPIE*, March 2008.
- [13] R. A. Swartz and J. P. Lynch, "Strategic network utilization in a wireless structural control system for seismically excited structures," *Journal of Structural Engineering*, vol. 135, no. 5, pp. 597–608, 2009.
- [14] J. P. Lynch, Y. Wang, K. J. Loh, J.-H. Yi, and C.-B. Yun, "Performance monitoring of the Geumdang Bridge using a dense network of high-resolution wireless sensors," *Smart Materials and Structures*, vol. 15, no. 6, pp. 1561–1575, 2006.
- [15] S. Kim, S. Pakzad, D. Culler et al., "Health monitoring of civil infrastructures using wireless sensor networks," in *Proceedings of the 6th International Symposium on Information Processing in Sensor Networks (IPSN '07)*, pp. 254–263, IEEE, April 2007.
- [16] S. N. Pakzad, "Development and deployment of large scale wireless sensor network on a long-span bridge," *Smart Structures and Systems*, vol. 6, no. 5-6, pp. 525–543, 2010.
- [17] M. Kurata, J. Kim, Y. Zhang et al., "Long-term assessment of an autonomous wireless structural health monitoring system at the new Carquinez Suspension Bridge," in *Nondestructive Characterization for Composite Materials, Aerospace Engineering, Civil Infrastructure, and Homeland Security*, vol. 798312 of *Proceedings of SPIE*, March 2011.
- [18] M. J. Chae, H. S. Yoo, J. Y. Kim, and M. Y. Cho, "Development of a wireless sensor network system for suspension bridge health monitoring," *Automation in Construction*, vol. 21, no. 1, pp. 237–252, 2012.
- [19] X. Hu, B. Wang, and H. Ji, "A wireless sensor network-based structural health monitoring system for highway bridges," *Computer-Aided Civil and Infrastructure Engineering*, vol. 28, no. 3, pp. 193–209, 2013.
- [20] J. Lian, K. Naik, and G. B. Agnew, "Data capacity improvement of wireless sensor networks using non-uniform sensor distribution," *International Journal of Distributed Sensor Networks*, vol. 2, no. 2, pp. 121–145, 2006.
- [21] J. Li and P. Mohapatra, "An analytical model for the energy hole problem in many-to-one sensor networks," in *Proceedings of the IEEE Vehicular Technology Conference*, vol. 62, p. 2721, IEEE, 2005.
- [22] S. Olariu and I. Stojmenović, "Design guidelines for maximizing lifetime and avoiding energy holes in sensor networks with uniform distribution and uniform reporting," in *Proceedings of the 25th IEEE International Conference on Computer Communications (INFOCOM '06)*, vol. 6, pp. 1–12, April 2006.
- [23] I. Stojmenovic and S. Olariu, "Data-centric protocols for wireless sensor networks," in *Handbook of Sensor Networks: Algorithms and Architectures*, pp. 417–456, 2005.
- [24] X. Wu, G. Chen, and S. K. Das, "Avoiding energy holes in wireless sensor networks with nonuniform node distribution," *IEEE Transactions on Parallel and Distributed Systems*, vol. 19, no. 5, pp. 710–720, 2008.
- [25] A. Hossain, T. Radhika, S. Chakrabarti, and P. K. Biswas, "An approach to increase the lifetime of a linear array of wireless sensor nodes," *International Journal of Wireless Information Networks*, vol. 15, no. 2, pp. 72–81, 2008.
- [26] J. Li and P. Mohapatra, "Analytical modeling and mitigation techniques for the energy hole problem in sensor networks," *Pervasive and Mobile Computing*, vol. 3, no. 3, pp. 233–254, 2007.
- [27] T.-H. Yi, H.-N. Li, and M. Gu, "Optimal sensor placement for structural health monitoring based on multiple optimization strategies," *Structural Design of Tall and Special Buildings*, vol. 20, no. 7, pp. 881–900, 2011.

Research Article

The Nonuniform Node Configuration of Wireless Sensor Networks for Long-Span Bridge Health Monitoring

Guang-Dong Zhou¹ and Ting-Hua Yi^{2,3}

¹ College of Civil and Transportation Engineering, Hohai University, Nanjing 210098, China

² School of Civil Engineering, Dalian University of Technology, Dalian 116024, China

³ State Key Laboratory for Disaster Reduction in Civil Engineering, Tongji University, Shanghai 200092, China

Correspondence should be addressed to Ting-Hua Yi; yth@dlut.edu.cn

Received 4 July 2013; Accepted 26 August 2013

Academic Editor: Hong-Nan Li

Copyright © 2013 G.-D. Zhou and T.-H. Yi. This is an open access article distributed under the Creative Commons Attribution License, which permits unrestricted use, distribution, and reproduction in any medium, provided the original work is properly cited.

This paper presents a nonuniform node configuration of wireless sensor networks (WSNs) for long-span bridge health monitoring. The methodology and strategy of two-phase node arrangement for nonuniform WSN configuration are firstly presented, and then numerical examples are carried out by a long-span suspension bridge. Three cases, which are four sensor nodes distributed on one side of the girder, ten sensor nodes distributed on one side of the girder, and eight sensor nodes distributed averagely on two sides of the girder, are employed. In case I and case II, three schemes that are the nonuniform node configuration arranged by the two-phase node arrangement method, the uniform nodes configuration, and the independent sensor nodes configuration are used for comparison. And in case III, two schemes that are nonuniform nodes configuration and the independent sensor nodes configuration are adopted. The results indicate that the nonuniform node configuration can balance energy consumption, eliminate “energy hole,” and maximize network performance effectively, which shows the most outstanding performance when compared with other conventional node configurations. So, the efficiency of the two-phase node arrangement method is validated.

1. Introduction

In recent years, a large number of long-span cable-supported bridges have been built throughout to fulfill the requirements of modern society for advanced transportation systems [1], for example, the Akashi Kaikyo Bridge with a main span of 1990 m in Japan, the Great Belt Bridge with a main span of 1624 m in Denmark, and the Runyang Suspension Bridge with a main span of 1490 m in China [2]. With the development of material and construction technology, bridges tend to light weight, low stiffness, and low damping, which make those bridges sensitive to dynamic loads. In order to verify new construction design assumptions, detect potential damage, and prevent catastrophic failure, structural health monitoring (SHM) is implemented on many existing or newly built bridges all over the world.

A typical SHM system includes three major components: a sensor system, a data processing system (including the data acquisition, transmission, and storage), and a health

evaluation system [3]. The sensors are used to monitor structural status and environmental parameters, which provide necessary data for structural assessment. In the past few decades, numerous vibration-based damage detection approaches have been developed [4], which promote that the structural vibration monitoring is an important issue in SHM. Ideally, if all degree of freedoms (DOFs) of a bridge are placed with accelerometers, the dynamic response can be fully characterized. However, the high costs of data acquisition systems (including development, purchase, and maintenance costs for the accelerometers, as well as resource and communication costs) and accessibility limitations constrain in many cases the scale of the network. So, the optimization of accelerometer placement, which aims to select the optimal locations of accelerometers so that the behavior of bridges can be well identified, is a key work prior to dynamic monitoring of bridges [5]. Up to now, a large number of methodologies of optimal wired accelerometer placement have been developed for long-span bridge health monitoring based on different

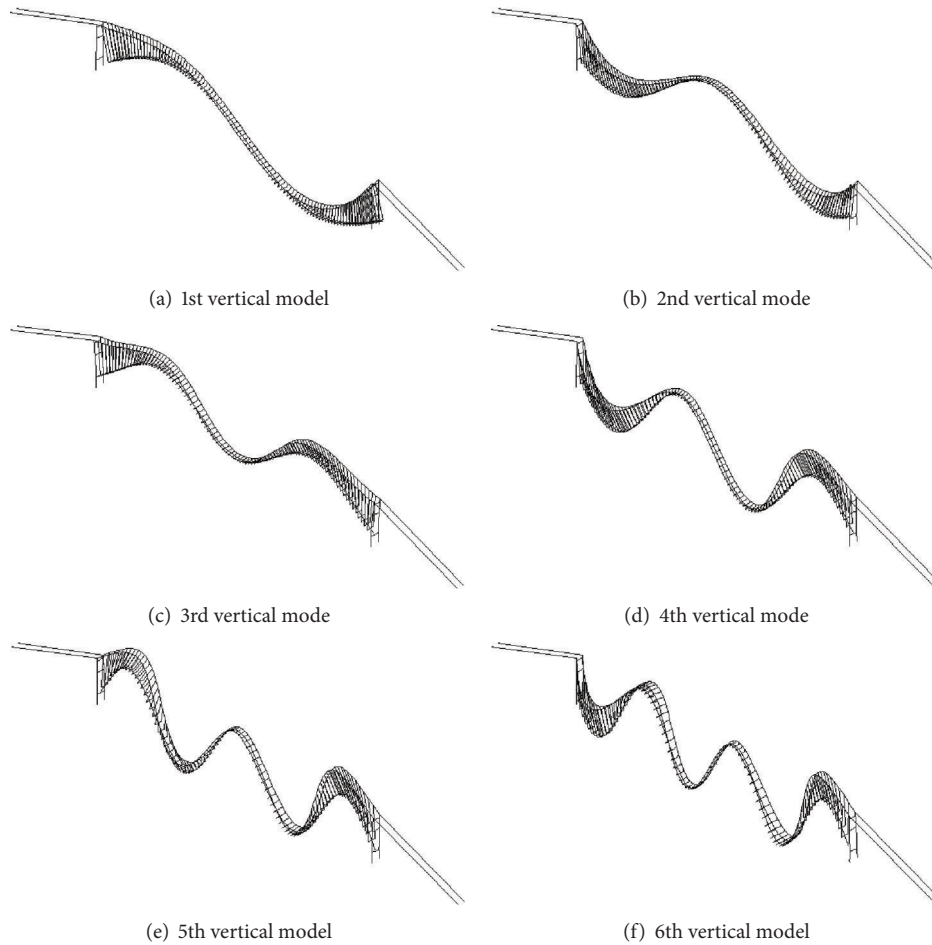


FIGURE 1: The first six vertical model shapes.

criteria, such as the effective independence (EI) method [6, 7], the QR decompose method [8, 9], the MinMAC algorithm [10], and so forth. A comprehensive survey of gradient-based local optimization methods for accelerometer placement can be found in Li et al. [11]. More recently, combinatorial optimization methods based on the biological and physical analogue have been extensively used for the optimization of optimal accelerometer placement problems due to their many advantages over the classical optimization techniques such as being a blind search method and being highly parallel. Among them, the most powerful heuristics are based on the genetic algorithms (GAs). Yao et al. [12] took GA as an alternative to the EFI method, and the determinant of the FIM is chosen as the objective function. Yi et al. [13, 14] improved some drawbacks of GAs and proposed a generalized genetic algorithm (GGA) for sensor placement of high-rise structural health monitoring. Moreover, the monkey algorithm (MA), which was firstly designed by Zhao and Tang [15] from the inspiration of mountain-climbing processes of monkeys, has been introduced in the field of optimal accelerometer placement by Yi et al. [16]. And then, the dual-structure coding method and asynchronous-climb process were incorporated in the MA, and the convergence speed is improved dramatically [17]. All of those methods

mentioned before are fit for wired accelerometer, in which the distance between any two sensors is unconstrained.

Rapid advances in sensors, wireless communication, microelectromechanical systems (MEMS), and information technologies have significant impacts on SHM. Compared to conventional wired sensor, wireless sensor has many attractive features, including ease of installation, wireless communication, onboard computation, relatively low cost, and small size [18]. Several researchers have contributed to wireless sensors technology in monitoring bridge structures from sensor development and applications [19–27], providing important insight into the potential of wireless sensor networks (WSNs) technology for long-term monitoring. In real-world SHM of long-span bridges, linear network that the wireless sensors are deployed on the girder one by one along a straight line is adopted in common since the span is much larger than the height. In this type of WSN, multihop and single-line route are employed, and the nodes near the sink bear heavy transmission load. As a result, those nodes would deplete their energy quickly, leading to what is called an “energy hole” near the sink. A lot of energy of nodes far from the sink is wasted, which induces that the performance of the WSN is poor. The practical implements indicate that the limited energy of wireless sensor which is the

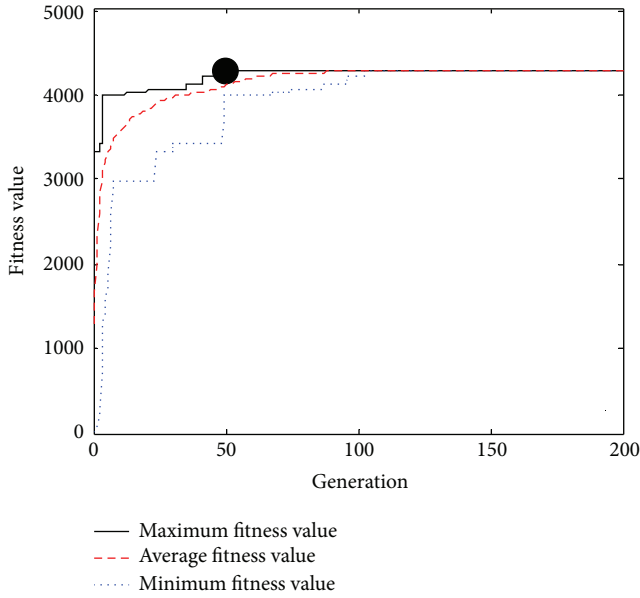


FIGURE 2: Evolution progress of the GGA with four sensor nodes.

greatest obstacle that hinders dense network is distributed for long-term monitoring. Therefore, many contributions were conducted on eliminating “energy hole,” balancing energy consumption, and optimizing performance of WSNs. An analytical model for the “energy hole” problem in uniform node distribution WSNs was presented by Li and Mohapatra [28]. And then, Stojmenovic and Olariu [29] proved that the “energy hole” problem is unavoidable in WSNs if the nodes in the network are distributed uniformly and data are collected uniformly and discussed the possibility of the nonuniform node distribution strategy to balance energy depletion. Subsequently, Lian et al. [30] and Wu et al. [31] proposed different nonuniform node distribution strategies under different assumptions, respectively. Furthermore, Hossain et al. [32] provided an analytical method for placing a number of nodes in a linear array such that each node dissipates the same energy per data gathering cycle. It can be concluded from the presented achievements that nonuniform node distribution is a good configuration with respect to eliminating “energy hole.” However for WSNs of SHM, there are many special properties like high sampling frequency, continuous data flow and long-term monitoring, which induce that the existing methods cannot be used directly.

Being different from general WSNs that are used in habitat sensing, environmental monitoring, automated health care, and so forth, the sampling rate of WSN for long-span bridge health monitoring is more than 50 Hz in most occasions. So, the energy consumption for data sensing is significant and cannot be ignored. On the other hand, the nodes are distributed as a straight line along the bridge span. The data are transmitted by multihop and single-line route. This paper develops a nonuniform node configuration of WSN for long-span bridge health monitoring. A two-phase node arrangement method used for nonuniform node configuration is presented at first. Based on the introduced

method, the WSN configurations under different test cases are carried out by a long-span suspension bridge, and the performances of those configurations are evaluated. Three cases with different sensor nodes and different monitoring requirements are executed, so that the performance of the WSN with nonuniform node configuration can be displayed extensively. For comparing the results of the two-phase node arrangement method, other WSN schemes with the same monitoring requirements are also provided.

2. Two-Phase Node Arrangement Method

Considering the cost of the WSN and the requirement of the bridge health monitoring, the reasonable strategy is that the WSN is organized by two types of nodes, sensor node and relay node, which is named as composite WSN. The sensor node and relay node have the same node platform. The relay node with low price does not instrument with sensor board. In this WSN, the sensor node is responsible for vibration monitoring and data retransmission, and the relay node is only responsible for retransmitting data. Therefore, the investment of the WSN deployment is reduced dramatically.

According to the characteristics of the composite WSN, two-phase node arrangement method can be adopted to implement the nonuniform node configuration. The first phase is sensor node arrangement to fulfill the requirement of the bridge health monitoring, and the second phase is relay node arrangement to balance the energy consumption of nodes in WSN and improve the performance of the WSN. In the phase of sensor node arrangement, there is no need to take the data transmission range into account for the existence of relay nodes. So, the improved general genetic algorithm (GGA), which is superior in biologics to the classical genetic algorithm (GA), is employed. The dual-structure coding system, in which the chromosomes of an individual are composed of append code and variable code, is used to initialize the population. The two-quarter selection, whose process is two-parent selection \rightarrow crossover \rightarrow a family of four \rightarrow two-quarter selection \rightarrow mutation \rightarrow a family of four \rightarrow two-quarter selection \rightarrow next generation is introduced in the evolution. In the process of evolution, the gradual change and sudden change are combined to avoid local optimal solution. In general, the gradual change is adopted. When the best fitness value of the population keeps constant in several continuous generations, the evolutionary processing turns to sudden change. Until the best fitness value changes, the evolutionary processing turns back to the gradual change. The partially matched crossover (PMX) is applied in the crossover, while the swap mutation and inversion mutation are used in the gradual change and the sudden change, respectively. The modal strain energy (MSE) is taken as the fitness function in GGA. In the phase of relay node arrangement, the relay nodes are configured by the nonuniform node arrangement method based on the principle that the energy of all nodes in WSN is depleted almost simultaneously. Using the data acquisition efficiency (DAE) that is defined as data capacity per unit deployment cost, the closed-form solutions for the number and

TABLE 1: The first eight vertical model frequencies.

Model	1	2	3	4	5	6	7	8
Frequency (Hz)	0.0879	0.1228	0.1662	0.1885	0.2406	0.2493	0.3450	0.4025

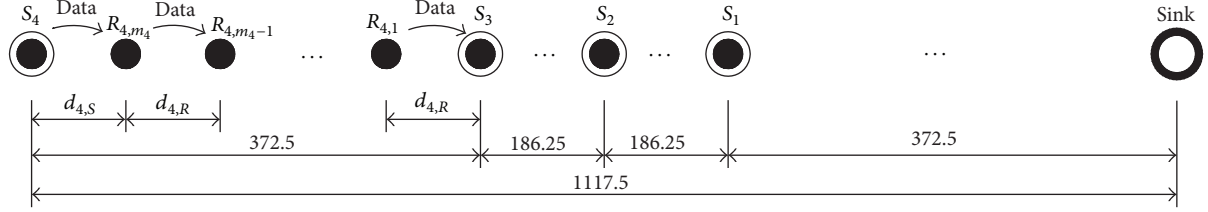


FIGURE 3: Non uniform node configuration (unit: m).

the location of relay nodes within two adjacent sensor nodes can be obtained.

3. Simulation Environment

The long-span suspension bridge, with main span of 1490 m, is used to demonstrate the effectiveness of the two-phase node arrangement method. The bridge is a single-span-double-joint steel box girder bridge. The width and height of the full-joint streamlined steel box girder are 36.3 and 3.0 m, respectively. 182 suspenders are used to transfer the load of girder to main cables, and the distance between two adjacent suspenders is 16.1 m. The two side spans are 470 m, and there is no suspender in the side span. The two towers with three-story frame structure are applied. The heights of the two towers are about 210 m. There are two tower columns with three prestressed concrete crossbeams (top, middle, and bottom crossbeams) in each tower. An updated three-dimensional finite element model is established in order to provide input data for the WSN arrangement. The main girder and main towers are simulated by spatial beam elements, and the main cables and suspenders are simulated by 3D linear elastic truss elements with three DOFs at each node. Then, the model shapes, and model frequencies can be obtained by model analysis. For simplicity, only vertical model shapes relating to main girder are accounted for here. The first six vertical model shapes are plotted in Figure 1, and the first eight vertical model frequencies are listed in Table 1. The 1st vertical model frequency is only 0.0879 Hz, no more than 0.1 Hz, which reveals the super low stiffness of this long-span suspension bridge.

The parameters of node are listed in Table 2 [33]. In the table, E_0 represents the initial energy of node, d_{\max} represents the maximum radio range of node, l represents data quantity per collecting cycle, d_0 represents a node specific critical distance, α , γ , and η represent node specific energy consumption coefficients in the transmitter circuitry, receiver circuitry, and sensor circuitry, respectively, β_1 and β_2 represent the energy required to transmit per bit over a per unit distance in different cases, and a and b represent the cost per sensor node and per relay node, respectively. The parameter about sensing data is excluded by relay node.

TABLE 2: The parameters of node.

Parameters	Value	Unit
E_0	40	J
d_{\max}	80	m
l	5	bit
d_0	30	m
α	4.5×10^{-8}	J/bit
β_1	1.0×10^{-10}	J/bit/m ²
β_2	1.0×10^{-15}	J/bit/m ⁴
γ	1.35×10^{-7}	J/bit
η	6.0×10^{-8}	J/bit
a	200	USD
b	100	USD

Three cases, which are four sensor nodes placed in the same girder side, ten sensor nodes placed in the same girder side, and eight sensor nodes placed averagely in two girder sides, are considered here.

4. Results Analysis

4.1. Case I. In this case, a total number of four sensors are used for vertical vibration monitoring. The two-phase node arrangement is carried out. In the first phase, the locations of sensor nodes are optimized by improved GGA; in the second phase, the relay nodes are configured by nonuniform node arrangement method.

It is well known that the path of searching is selected randomly in random search algorithm, so the different results are obtained by several times of calculation. The better choice is selecting the best one from those results. For the GGA, there are a number of parameters that are problem specific and need to be explored and tuned so that the best algorithm performance is achieved. The population size of 300 is selected. The GGA processes have been run for 10 times with different stochastic initial populations, and the best one is adopted. The fitness convergence curves are shown in Figure 2. It can be seen that only 54 generations are needed to reach the optimal value. The maximum fitness values tend to a constant quickly, and the average values and the minimum

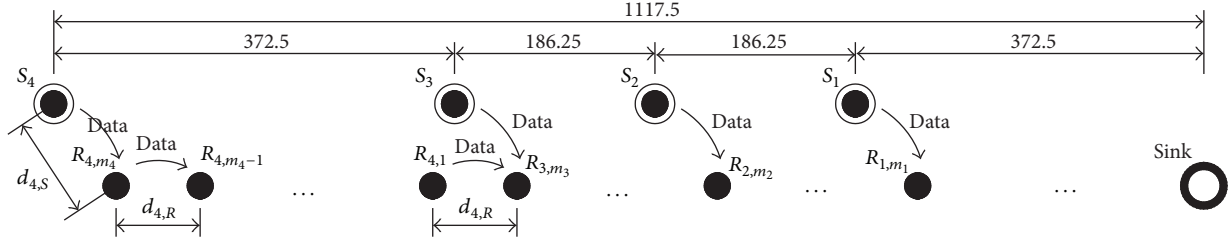


FIGURE 4: Independent sensor node configuration (unit: m).

TABLE 3: The sampling frequency of sensor nodes.

Sensor node ID	S_1	S_2	S_3	S_4
Sampling frequency (Hz)	40	50	40	50

fitness values steadily tend to the maximum fitness values along with increasing number of generation, which shows a good characteristic of convergence. After 100 iterations, both the average fitness values and the minimum fitness values converge to the best one. The best sensor node locations are plotted in Figure 3. The sink is placed on the right end of the girder. Because there are only four sensor nodes, the optimal result is in accordance with the experienced deployment. The sensor nodes are placed in 6/8 section, 4/8 section, 2/8 section, and 1/8 section of the main span, respectively. The smallest distance is 186.25 m, that is, much longer than the ultimate transmission range, which means that the relay nodes are needed in every sensor nodes interval.

Commonly, the sampling frequencies of all sensor nodes for vibration monitoring are identical so that the structural models can be identified. In this paper, to make the simulation environment more general, two types of sampling frequencies, 40 Hz and 50 Hz, are used by different sensor nodes and are listed in Table 3. The relay nodes are employed to fill the banks of sensor nodes intervals. Scheme I is named as nonuniform configuration, and the relay nodes are configured by the proposed nonuniform node arrangement method, as shown in Figure 3. In the figure, S_i ($i=1, 2, 3, 4$) denotes the i th sensor node in the network, and m_i represents the total number of relay nodes in the interval of sensor nodes S_i and S_{i-1} . $R_{i,j}$ denotes the ID number of relay node, where i denotes the relay node belong to the interval of sensor nodes S_i and S_{i-1} and j denotes the j th ($j=1, \dots, m_i$) relay sensor. The symbol $d_{i,j}$ denotes the distance between adjacent relay nodes $R_{i,j}$ and $R_{i,j-1}$. The distance between S_i and R_{i,m_i} is denoted as $d_{i,s}$. The values of m_i , $d_{i,s}$, and $d_{i,j}$ are calculated through the nonuniform node arrangement method. Besides scheme I, other two schemes with the same number of relay nodes are also employed for comparison. Scheme II is a uniform configuration, and the relay nodes are placed uniformly, which is very popular in vibration monitoring of long-span bridges, and it can be executed easily. The sketch of this scheme is not displayed for its simplicity. In this scheme, the number of relay nodes is assigned to sensor nodes interval proportional to the distance between two adjacent sensor nodes. Because the computed number of

relay nodes is integrated, the distances of adjacent relay nodes are not equal accurately. Scheme III is an independent sensor node configuration, and the sensor node is only responsible for sensing data and transmitting it, as shown in Figure 4. In this scheme, the energy of sensor nodes is saved. The number of relay nodes is assigned to sensor nodes interval proportional to the values of which the distance between two adjacent sensor nodes multiplies with quantity of transmitted data. The detailed node configurations of the three schemes are listed in Table 4. In the table, DAE represents the data acquisition efficiency. In scheme I, the nearer the relay nodes are close to the sink, the shorter the distance of two adjacent relay nodes is. However, it is not proportional to distance from the relay node to the sink. Both the sensor nodes and the relay nodes are arranged nonuniformly. In scheme II, the distances of node intervals are almost equal. In scheme III, although the distances of node intervals are nonuniform, the WSN is not optimized completely. When comparing network lifetime and DAE in Table 3, it can be seen that scheme I has the longest network lifetime and highest DAE, which indicates the highest performance of this scheme. The network lifetime of scheme II is no more than half of that of scheme I. This scheme has the lowest DAE, although it is the most common one in practice. In scheme III, the sensor nodes are protected perfectly, but their potential is not stimulated. So, the DAE of this scheme is lower than that of scheme I.

Figure 5 displays the residual energy of nodes in different schemes when the networks die. In the figure, S_i ($i=1, 2, 3, 4$) represents the sensor node ID, and R_i represents all relay nodes that belong to the interval of S_i and S_{i+1} . It can be seen from the figure that the energy consumption of nodes in scheme I is almost uniform and the “energy hole” is avoided effectively. When the network lifetime ends, the maximum residual energy is no more than 2.0 J, which is less than 5% of the initial energy. Although the energy consumption is not balanced accurately, the difference can be accepted by civil engineering. In scheme II, the energy of sensor node and relay node near the sink is consumed quickly because of heavy data traffic load. And the left energy of the node and relay node farthest from the sink is more than 30 J. The “energy hole” appears in this scheme, and a large amount of energy in WSN is wasted. In scheme III, the energy consumption of sensor node is not more than half when the first relay node exhausts its power. The energy in the WSN is used inefficiently although the “energy hole” is eliminated. Considering three factors of network lifetime, DAE, and

TABLE 4: Node arrangements of different schemes.

Scheme	Node interval (Unit: m)								Total node	Network lifetime (Unite: s)	DAE
	$d_{4,S}$	$d_{4,R}$	$d_{3,S}$	$d_{3,R}$	$d_{2,S}$	$d_{2,R}$	$d_{1,S}$	$d_{1,R}$			
Scheme I	37.56	37.22	31.25	31.00	26.86	26.56	25.06	24.21	34	3.81×10^4	3.26×10^4
Scheme II	33.86	33.86	31.04	31.04	31.04	31.04	33.86	33.86	34	1.49×10^4	1.28×10^4
Scheme III	20.69	41.39	31.04	31.04	31.04	31.04	28.65	28.65	34	2.57×10^4	2.20×10^4

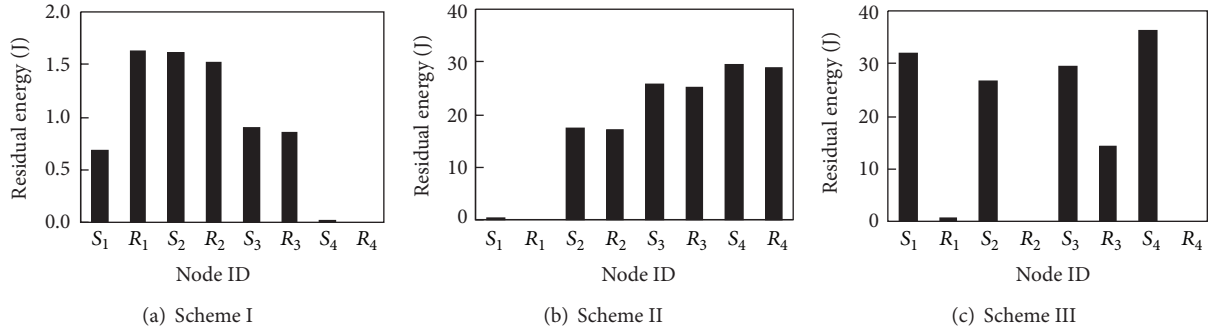


FIGURE 5: Residual energy of nodes in different schemes.

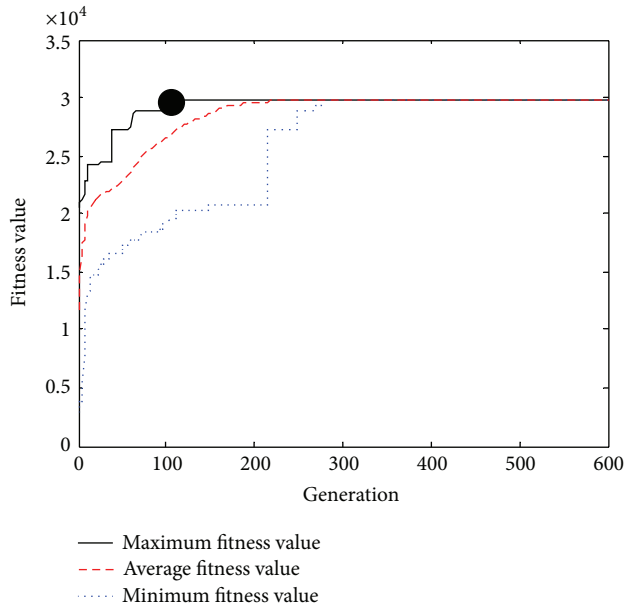


FIGURE 6: Evolution progress of the GGA with ten sensors.

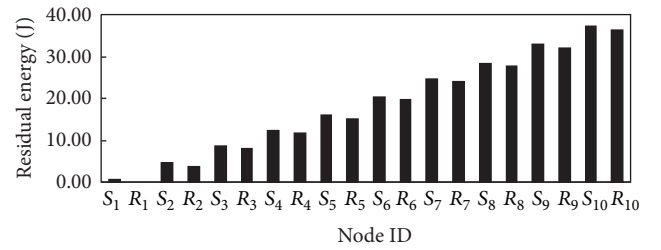


FIGURE 8: Residual energy of nodes in scheme II.

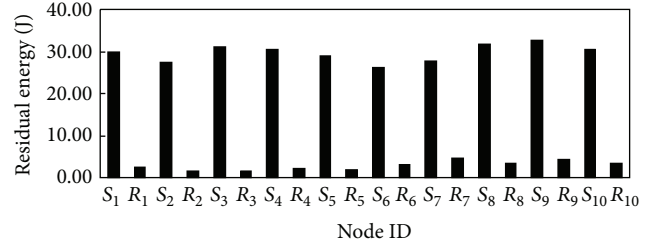


FIGURE 9: Residual energy of nodes in scheme III.

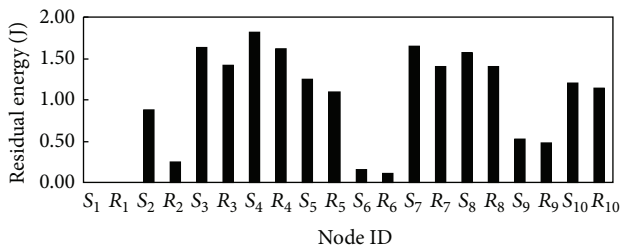


FIGURE 7: Residual energy of nodes in scheme I.

balancing energy consumption, the maximum performance can be obtained in scheme I.

4.2. Case II. In this case, 10 sensor nodes are adopted. Similarly, the sensor nodes are firstly placed by improved GGA. And then, the relay nodes are distributed by nonuniform node arrangement method. The population size of 500 is used this time. The process of convergence is shown in Figure 6. The excellent ability of global optimal solution searching of improved GGA is demonstrated also. The maximum fitness value converges to the best quickly. Three schemes like case I are employed also. The sampling frequency of different

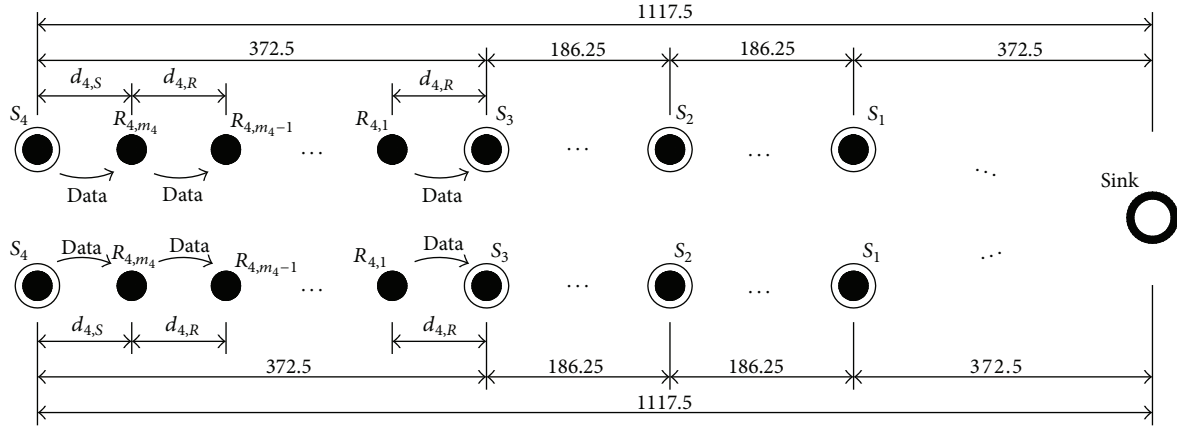


FIGURE 10: Two independent linear arrays (unit: m).

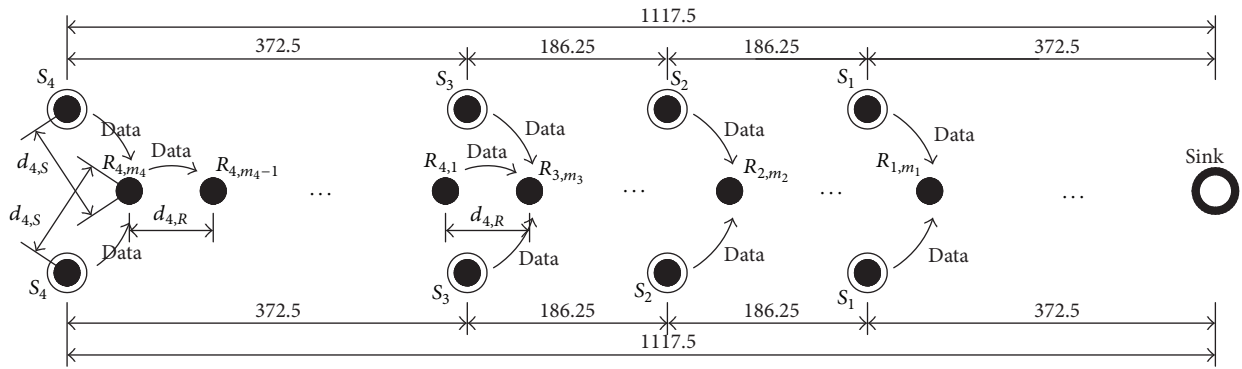


FIGURE 11: Linear array of relay node with two side sensor node (unit: m).

sensor is specified by different value. The performance of the three WSN schemes is listed in Table 5. The highest value of network lifetime and DAE is acquired in nonuniform configuration. The network lifetime and DAE of other two schemes are much less than that of scheme I. The residual energy of nodes in scheme I, II and III, is given in Figures 7, 8, and 9, respectively. Like case I, the node configuration arranged by the two-phase node arrangement method has the lowest residual energy. The maximum residual energy is only 1.81 J. Comparing with that in Figure 5(a), the value of residual energy shows a few changes. The robustness of the proposed method is validated. In scheme II, the maximum residual energy is 37.14 J, more than 90% of the initial energy of the node. Big “energy hole” is formed in this network. When compared with scheme II in case I, with the number of nodes increasing, more energy is left. It can be deduced that there may be no data transmitted to sink when the scale of this type of WSN scheme is big enough. In scheme III, the residual energy is almost 30 J, which is similar in case I. When 10 sensor nodes are used, the best performance is also shown in scheme I.

4.3. Case III. Because of the low stiffness, the torsional vibration of the long-span bridges under skew wind or other nonuniform excitation cannot be neglected on some

TABLE 5: Performance of different WSN schemes.

Scheme	Total node	Network lifetime (unit: s)	DAE
Scheme I	70	4.52×10^4	4.67×10^4
Scheme II	70	1.89×10^4	1.95×10^4
Scheme III	70	3.21×10^4	3.32×10^4

occasions. To monitor the torsional vibration, accelerometers should be placed on the two sides of the girder, assuming there are four sensor nodes on each side. Two schemes are discussed in this case. In scheme I, the data on each side are transmitted independently and gathered to sink at last, as displayed in Figure 10. So, there are two independent linear arrays in the WSN. And in scheme II, one linear array placed in the isolation strip that is only organized by relay nodes is used for retransmitting data, as shown in Figure 11. The sensor nodes are only responsible for collecting data and transmitting it to the nearest relay node.

After calculating, the network lifetime and DAE of scheme I are 3.81×10^4 and 3.26×10^4 , respectively, and those of scheme II are 1.76×10^4 and 2.50×10^4 , respectively. Although the total number of relay nodes in scheme I is much more than that in scheme II, the network lifetime is longer, and the DAE is higher. The higher performance

of nonuniform node configuration arranged by proposed method is displayed obviously.

5. Conclusions

WSNs, which are identified as one of the most important technologies of the XXI century, have been widely used in SHM of long-span bridges. The limited energy of sensor node makes the performance of WSNs sensitive to energy consumption of every node in network. For WSN of long-span bridge health monitoring, the performance is critical since the test with long period and high sampling rate is required. Through balancing energy consumption, avoiding “energy hole,” and increasing data capacity, the performance of WSNs can be improved. The performance of nonuniform node configuration that is deployed by two-phase node arrangement method is demonstrated by three different cases. In every case, the scheme configured by the proposed method is compared with other scheme. In the uniform configuration, the “energy hole” cannot be avoided. The bigger the network is, the more energy is wasted. The performance of the uniform WSN is so poor that it is not fit for linear network. In the independent sensor node configuration, the sensor nodes are removed from the route of data retransmission. So, the potential of sensor nodes is not utilized adequately. The performance of this type of configuration is a little worse than that of the nonuniform node configuration. In the nonuniform node configuration deployed by the two-phase node arrangement method, the energy of nodes is consumed almost synchronously. The longest network lifetime and the highest DAE are obtained in this configuration, and the most outstanding performance is shown. At the same time, the performance is stable on different test occasions. In the simulation, there are no special requirements presented; so the proposed two-phase node arrangement method can be used for WSN configuration of real-word long-span bridge health monitoring with the main properties of high sampling frequency, continuous data flow, and long-term monitoring extensively.

It should be noted that the results in this paper are deduced based on the assumed theoretical models. The real environments of WSN are more complex, and many others factors affect the performance of WSNs. More factors influencing the performance of WSNs such as quality of service, energy efficiency route, and network topology should be further performed in the future to the generalization of the model developed in this paper.

Acknowledgments

This research work was jointly supported by the Science Fund for Creative Research Groups of the NSFC (Grant no. 51121005), the National Natural Science Foundation of China (Grant no. 51308186, 51222806), the Starting Research Fund from the Hohai University (Grant nos. 2013B01414), and the Research Fund of State Key Laboratory for Disaster Reduction in Civil Engineering (Grant no. SLDRCE12-MB-03).

References

- [1] Y. L. Xu, W. W. Guo, J. Chen, K. M. Shum, and H. Xia, “Dynamic response of suspension bridge to typhoon and trains. I: field measurement results,” *Journal of Structural Engineering*, vol. 133, no. 1, pp. 3–11, 2007.
- [2] A. Q. Li and C. Q. Miao, *Health Monitoring of Bridge Structures*, China Communications Press, Beijing, China, 2009.
- [3] G. W. Housner, L. A. Bergman, T. K. Caughey et al., “Structural control: past, present, and future,” *Journal of Engineering Mechanics*, vol. 123, no. 9, pp. 897–971, 1997.
- [4] S. W. Doebling, C. R. Farrar, and M. B. Prime, “A summary review of vibration-based damage identification methods,” *Shock and Vibration Digest*, vol. 30, no. 2, pp. 91–105, 1998.
- [5] D. S. Li, H. N. Li, and C. P. Fritzen, “The connection between effective independence and modal kinetic energy methods for sensor placement,” *Journal of Sound and Vibration*, vol. 305, no. 4-5, pp. 945–955, 2007.
- [6] D. C. Kammer, “Sensor placement for on-orbit modal identification and correlation of large space structures,” *Journal of Guidance, Control, and Dynamics*, vol. 14, no. 2, pp. 251–259, 1991.
- [7] D. C. Kammer and M. L. Tinker, “Optimal placement of triaxial accelerometers for modal vibration tests,” *Mechanical Systems and Signal Processing*, vol. 18, no. 1, pp. 29–41, 2004.
- [8] C. Schedlinski and M. Link, “An approach to optimal pick-up and exciter placement,” in *Proceedings of the 14th International Modal Analysis Conference (IMAC '96)*, pp. 376–382, SPIE the International Society for Optical Engineering, Dearborn, Mich, USA, February 1996.
- [9] D. S. Li, H. N. Li, and C. P. Fritzen, “Load dependent sensor placement method: theory and experimental validation,” *Mechanical Systems and Signal Processing*, vol. 31, pp. 217–227, 2012.
- [10] T. G. Carne and C. R. Dohrmann, “A modal test design strategy for model correlation,” in *13th International Modal Analysis Conference*, vol. 2460 of *Proceedings of SPIE*, p. 927, SPIE the International Society for Optical Engineering, 1995.
- [11] D. S. Li, Y. Zhang, L. Ren, and H. N. Li, “Sensor deployment for structural health monitoring and their evaluation,” *Advances in Mechanics*, vol. 41, no. 1, pp. 39–50, 2011.
- [12] L. Yao, W. A. Sethares, and D. C. Kammer, “Sensor placement for on-orbit modal identification via a genetic algorithm,” *AIAA Journal*, vol. 31, no. 10, pp. 1922–1928, 1993.
- [13] T. H. Yi, H. N. Li, and M. Gu, “Optimal sensor placement for health monitoring of high-rise structure based on genetic algorithm,” *Mathematical Problems in Engineering*, vol. 2011, Article ID 395101, 12 pages, 2011.
- [14] T. H. Yi, H. N. Li, and M. Gu, “Optimal sensor placement for structural health monitoring based on multiple optimization strategies,” *The Structural Design of Tall and Special Buildings*, vol. 20, no. 7, pp. 881–900, 2011.
- [15] R. Zhao and W. Tang, “Monkey algorithm for global numerical optimization,” *Journal of Uncertain Systems*, vol. 2, no. 3, pp. 165–176, 2008.
- [16] T. H. Yi, H. N. Li, and X. D. Zhang, “A modified monkey algorithm for optimal sensor placement in structural health monitoring,” *Smart Materials and Structures*, vol. 21, no. 10, Article ID 105033, 2012.
- [17] T. H. Yi, H. N. Li, and X. D. Zhang, “Sensor placement on canton tower for health monitoring using asynchronous-climb

- monkey algorithm,” *Smart Materials and Structures*, vol. 21, no. 12, Article ID 125023, 2012.
- [18] H. Jo, S. H. Sim, T. Nagayama et al., “Development and application of high-sensitivity wireless smart sensors for decentralized stochastic modal identification,” *Journal of Engineering Mechanics*, vol. 138, no. 6, pp. 683–694, 2011.
- [19] J. P. Lynch, Y. Wang, K. J. Loh, J.-H. Yi, and C.-B. Yun, “Performance monitoring of the Geumdang Bridge using a dense network of high-resolution wireless sensors,” *Smart Materials and Structures*, vol. 15, no. 6, pp. 1561–1575, 2006.
- [20] J. P. Lynch and K. J. Loh, “A summary review of wireless sensors and sensor networks for structural health monitoring,” *Shock and Vibration Digest*, vol. 38, no. 2, pp. 91–130, 2006.
- [21] S. Kim, S. Pakzad, D. Culler et al., “Health monitoring of civil infrastructures using wireless sensor networks,” in *Proceedings of the 6th IEEE International Symposium on Information Processing in Sensor Networks (IPSN '07)*, pp. 254–263, IEEE, Massachusetts, Mass, USA, April 2007.
- [22] S. N. Pakzad, “Development and deployment of large scale wireless sensor network on a long-span bridge,” *Smart Structures and Systems*, vol. 6, no. 5-6, pp. 525–543, 2010.
- [23] S. Jang, H. Jo, S. Cho et al., “Structural health monitoring of a cable-stayed bridge using smart sensor technology: deployment and evaluation,” *Smart Structures and Systems*, vol. 6, no. 5-6, pp. 439–459, 2010.
- [24] S. Cho, H. Jo, S. Jang et al., “Structural health monitoring of a cable-stayed bridge using wireless smart sensor technology: data analyses,” *Smart Structures and Systems*, vol. 6, no. 5-6, pp. 461–480, 2010.
- [25] M. Kurata, J. Kim, Y. Zhang et al., “Long-term assessment of an autonomous wireless structural health monitoring system at the New Carquinez Suspension Bridge,” in *Nondestructive Characterization for Composite Materials, Aerospace Engineering, Civil Infrastructure, and Homeland Security*, vol. 7983 of *Proceedings of SPIE*, p. 798312, International Society for Optics and Photonics, California, Calif, USA, March 2011.
- [26] M. J. Chae, H. S. Yoo, J. Y. Kim, and M. Y. Cho, “Development of a wireless sensor network system for suspension bridge health monitoring,” *Automation in Construction*, vol. 21, no. 1, pp. 237–252, 2012.
- [27] X. Hu, B. Wang, and H. Ji, “A wireless sensor network-based structural health monitoring system for highway bridges,” *Computer-Aided Civil and Infrastructure Engineering*, vol. 28, no. 3, pp. 193–209, 2013.
- [28] J. Li and P. Mohapatra, “An analytical model for the energy hole problem in many-to-one sensor networks,” in *Proceedings of the 62nd IEEE Vehicular Technology Conference (VTC '05)*, vol. 4, pp. 2721–2725, IEEE, September 2005.
- [29] I. Stojmenovic and S. Olariu, “Data-centric protocols for wireless sensor networks,” in *Handbook of Sensor Networks: Algorithms and Architectures*, pp. 417–456, 2005.
- [30] J. Lian, K. Naik, and G. B. Agnew, “Data capacity improvement of wireless sensor networks using non-uniform sensor distribution,” *International Journal of Distributed Sensor Networks*, vol. 2, no. 2, pp. 121–145, 2006.
- [31] X. Wu, G. Chen, and S. K. Das, “Avoiding energy holes in wireless sensor networks with nonuniform node distribution,” *IEEE Transactions on Parallel and Distributed Systems*, vol. 19, no. 5, pp. 710–720, 2008.
- [32] A. Hossain, T. Radhika, S. Chakrabarti, and P. K. Biswas, “An approach to increase the lifetime of a linear array of wireless sensor nodes,” *International Journal of Wireless Information Networks*, vol. 15, no. 2, pp. 72–81, 2008.
- [33] J. Li and P. Mohapatra, “Analytical modeling and mitigation techniques for the energy hole problem in sensor networks,” *Pervasive and Mobile Computing*, vol. 3, no. 3, pp. 233–254, 2007.

Research Article

An Intelligent Energy Management System for Educational Buildings

Ahmad Al-Daraiseh,¹ Nazaraf Shah,² and Eyas El-Qawasmeh¹

¹ King Saud University, Riyadh, Saudi Arabia

² Coventry University, Priory Street, Coventry, UK

Correspondence should be addressed to Nazaraf Shah; nazaraf.shah@coventry.ac.uk

Received 13 April 2013; Revised 6 August 2013; Accepted 21 August 2013

Academic Editor: Ting-Hua Yi

Copyright © 2013 Ahmad Al-Daraiseh et al. This is an open access article distributed under the Creative Commons Attribution License, which permits unrestricted use, distribution, and reproduction in any medium, provided the original work is properly cited.

There is a wide variation in the energy consumption between different educational institutions due to the adoption of different management strategies and different levels of occupants' environmental understanding. The presence of large amounts of information and communication technology (ICT) equipment and heating, ventilation, and air conditioning (HVAC) system causes a major consumption of energy in higher education institution (HEI) buildings. The main objective of this research is to investigate the use of ICT to optimize the energy consumption in HEI buildings and reduce carbon dioxide (CO₂) emission. The first phase of the system has been implemented at King Saud University to measure energy consumption through sensors that read energy consumption of electrical appliances and devices every 10 seconds. The analysis of collected data allows us to develop and employ energy saving strategies that lead to a reduction in total energy consumption. Our preliminary results show that up to 17% of energy consumption can be reduced by simply dealing with standby energy loss of labs' computers. The novelty of this research comes from the use of a functional database approach to deal with high volume of data and query performance and the incorporation of a timetabling system in energy management system.

1. Introduction

Today's world is facing an unprecedented challenge in controlling increasing greenhouse gases emission, which is the main cause of global warming. CO₂ makes 72% of the total emissions of the greenhouse gases [1]. The burning of fossil fuel in order to generate energy for domestic, public, commercial, and industrial use is a major source of CO₂ emission. Any attempt to deal with the issue of global warming requires the reduction of CO₂ emission, which in return requires a reduction in the use of energy generated by fossil fuel.

Climate change and the increase in energy bills are the main driving forces behind a new wave of energy management systems for residential, public, industrial, and commercial buildings. Most of the currently available energy management systems are concerned with real-time energy consumption monitoring and the displaying of energy consumption statistical and real-time data [2–5]. These systems play a crucial role in providing a detailed picture of

energy consumption to occupants and building managers of residential, commercial, and educational buildings. These systems contribute towards influencing the energy consumption behavior of residential building occupants and building managers of commercial and industrial buildings. However, the majority of these systems does not automatically adjust energy usage and leave it to the occupants to respond appropriately to reduce their energy consumption [2–5]. Furthermore, these systems have serious limitations in their integration with HVAC.

The proposed project integrates all energy consumption appliances, machines, and devices into a uniform system using a service oriented architecture (SOA) [6]. This integrated system provides a comprehensive picture of energy consumption and enable the employment of effective energy consumption strategies in a uniform and consistent manner. These energy management strategies range from automatic adjustment of various electrical systems and advice generation for human operator for the use of a human as an actuator.

The system fine-tunes these strategies by learning from past events and their associated actions.

Currently, some energy management systems provide general energy saving tips but do not consider the occupants' energy consumption profiles and the external physical environmental conditions (e.g., external temperature and sunlight, etc.). The proposed project attempts to influence HEI staff, students, and building manager' behavior towards saving energy and taking automatic energy-aware actions to optimize energy consumption while maintaining the quality of work and level of comfort of students and staff.

The process of creating greener higher educational institutions involves efficient use of energy in educational buildings and promoting environmental awareness within students and institutional staff [7]. The proposed project is an effort to make a greener HEI by using ICT based solution to optimize energy consumption and create awareness of green issues and sustainability. The proposed system attempts to address the issue of sustainability and CO₂ emission reduction in HEIs by taking into account occupants' energy consumption profiles and internal as well as external physical conditions. The motivation behind this approach is to provide the staff, students, and building managers with effective advice on their energy consumption, so they can take appropriate actions towards achieving efficient energy consumption in addition to considering automatic energy-aware actions for saving energy, such as the switching off lights or network printers in a laboratory when all computers are already switched off. The fact that the system has to deal with a large volume of sensor data and respond to various queries in an acceptable time is a great challenge. We attempt to deal with this issue using functional database approaches, which allows us to split a higher-level query into low-level queries and then combine their results by applying a service composition approach. Our proposed approach brings together functional database features and a web services composition to deal with the challenge posed by huge volumes of sensor data coming from various sources. The distinguishing feature of the system is that it takes into account the occupancy time of various rooms in the building from a timetabling system. It is believed that this feature will greatly improve the energy consumption of HVAC.

The organization of this paper will be as follows. Section 2 describes the current related work. Section 3 presents the system architecture. Section 4 describes the SOA approach for designing and development of the system. Section 5 provides a description of various components related to management of huge volumes of data and reasoning over that data. Section 6 discusses the implementation of the system. In Section 7 we present the results. Section 8 provides a brief discussion and conclusion of the paper.

2. Current Related Work

Currently, there are a variety of commercial and domestic energy management systems available. Most of them are implemented within what are called building management systems, and the majority of these systems does not include

occupants in the energy management loop. Current energy management systems can be broadly divided into three categories as follows.

- (1) The first category consists of energy monitoring sensors and energy consumption data displays. These are basic systems that read energy consumption and show the consumption on a display. These are more suitable for domestic environment as they depend on human for judgement and actions.
- (2) The second category of these systems is those systems that extend the capability of the first group by allowing alert generation on excessive usage of energy or on some conditions set by the user.
- (3) The third category of energy management systems employs advanced networking and energy monitoring technologies. These systems allow the users to view energy consumption at appliances level and control the appliance usage from anywhere via a web interface.

In the following, we discuss some well-known energy management systems that belong to the third category, as these are the most promising technology for effective energy management.

- (1) AIM (<http://www.ict-aim.eu/home.html>) is a 7th Framework Programme funded project for the design and implementation of a system that aims to minimize energy waste in a domestic environment. In contrast, Digital environmental home energy management system (DEHEMS) uses wireless sensor monitoring network to control home appliances according to user profiles [8].
- (2) Sarnadas et al. proposed an architecture for home energy appliances management and control [9] that focuses on the use of hardware components such as sensors, actuators, and communication network to manage energy consumption in home environment. Another strand of research focuses on providing intelligent interfaces to increase awareness of energy usage and hence influence the householder's behaviour [10, 11].
- (3) There are a number of freely available web based tools for providing householders with common sense advice on their energy consumption (<http://www.google.com/powermeter/about/>, <http://www.microsoft-hohm.com/>, <http://www.imeasure.org.uk/>); however, these tools heavily rely on users' manual input. There are also a number of commercial ICT based energy management systems available (<http://www.plugwise.com/idplugtype-g/home-efficiency>, <https://www.ewgeco.com/>). These tools and systems broadly focus on issues of energy consumption monitoring, displaying, and basic statistical analysis of energy consumption data.
- (4) The goal of the DEHEMS [8] is to empower householders in using their energy consuming appliances

by increasing visibility of energy consumption data and providing intelligent advice on their energy use based on their profiles, and the appliances' profiles.

- (5) Energy surveillance system (ESS). "This system is a web-based energy monitoring system that allows the user to compare energy usage by equipment type, store location, fuel type, or time of day. The web based energy monitoring software allows remote access to the crucial data for energy savings in different locations. The system is built to monitor up to 17 subloads per module within a facility to better detect energy leaks, provide benchmark reports and bill verification, and be alerted when abnormal energy usage occurs" (<http://www.egenergy.com/energy-monitoring#>).

Although some of these systems can be used for energy management in HEIs, they do not provide an effective energy management solution in educational institutions' environment by disregarding timetabling and event-management systems.

There is also an expanding strand of research on HVAC control and occupant behaviour modelling for reducing energy consumption in residential, commercial, and educational buildings. However, their main focus has been on reducing energy consumption while maintaining occupant comfort in terms of maintaining indoor temperature and air quality. The majority of this literature disregards appliances/machine level energy consumption optimization and inclusion, of timetabling and event management systems.

Mamidi et al. proposed an adoptive multiagent system that learns about occupants' behaviour in order to optimize HVAC operation [12]. They use machine learning technique to predict occupancy of the rooms up to an hour in advance to allow HVAC to minimize energy consumption while maintaining occupants' comfort. Their system only deals with temperature control, and they do not give any consideration to energy consumed by PCs and laptops in labs. They also do not include humans in the energy conservation loop.

Hagras et al. proposed an integrated approach using fuzzy logic, neural networks, and genetic algorithm to learn building thermal responses to external weather conditions, internal occupants requirements, and building plants response [13]. Their proposed system works with an existing building management system to reduce the energy demand, but it does not deal with appliance and device level energy consumption and monitoring.

Rogers et al. demonstrate in a simulated environment where a heating agent can optimize heating use to minimize cost and carbon emissions whilst satisfying the home owners comfort requirements [14]. Their simulation shows promising results, but it only considers energy consumption of maintaining home's environmental comfort.

Wang et al. proposed an hierarchical agent based approach to minimize the conflict between occupants' comfort and energy consumption [15]. Their proposed system takes into account management of lighting systems and the built environment temperature without any regard to

appliance level and device level energy monitoring and optimization.

Mo and Mahdavi present an agent based framework for building operators and individual occupants' to negotiate their control activities [16]. Their simulation results suggest that agent-based bilateral control strategy improve occupancy requirements while maintaining optimal energy consumption. Their focus is on temperature and lighting in the built environment.

Yu applied a genetic programming (GP) approach to model occupant behaviour by taking into account variation in occupancy timing [17]. This approach applies GP to learn occupants' behavioural rules and predict the presence of an occupant in a single-person office. It is not suitable for multiple occupancy settings.

Kolokotsa et al. proposed a system that integrates an open architecture and a fuzzy controller, which incorporates thermal comfort, visual comfort, and indoor air quality [18]. The fuzzy controller's structure is adjusted to the users' requirements, which are monitored via a smart card system, and then attempts to optimize energy consumption while maintaining occupants comfort. This system does not address energy consumption at the appliance level.

Figureiredo and Costa have implemented a predictive controller above a data acquisition platform for energy management in buildings [19]. The predictive controller optimises the preferences of the user, which come from several distributed user interfaces while meeting constraints of minimising energy waste.

Timetabling and event-management systems provide rich information for energy management systems. The use of this information can optimize the operation of HVAC in HEIs and appliances level energy consumption. Using this information, the energy management system is able to switch on and off air conditioning and other appliances at a critical time without affecting the comfort of the occupants. It is believed that the proposed system incorporating this information will result in considerable energy saving, as the Kingdom of Saudi Arabia's weather conditions require substantial use of air conditioning. Devices in standby mode waste a considerable amount of energy. Our preliminary results have shown that this hidden energy waste of PC/laptop in computer labs is up to 18% of total energy consumption.

3. System Architecture

In this section, we briefly describe the energy management system's high level architecture as shown in Figure 1. The system is based on a sensor network of energy consumption measuring sensors, occupancy sensors, and temperature and humidity sensors. The Zigbee protocol is used for networking and data exchange. The choice of the Zigbee communication and networking protocol was made so that various Zigbee compliant sensors can be easily incorporated into the network as required. The monitoring system collects data from sensors and sends the data to a data sever via Internet connection.

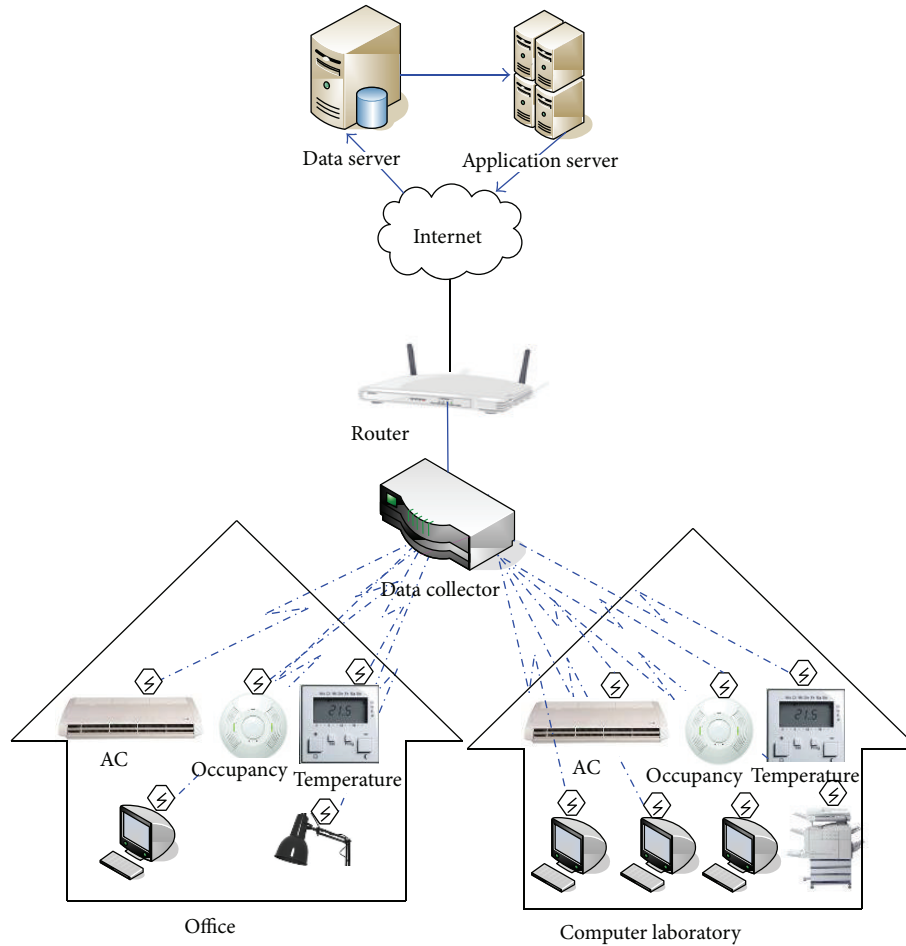


FIGURE 1: System architecture.

3.1. Monitoring Subsystem. Energy consumption and physical environment parameters monitoring functionality is the backbone of our energy management System. It provides essential energy consumption information and parameters to be used by the reasoning subsystems.

The sensors collect energy consumption data of electrical appliances every 10 seconds and send the data to the local data collector, which in turn forwards the data to the central server. Occupancy and temperature sensors are also incorporated into the system in order to detect the presence of people in labs and offices and also room temperature and humidity levels. The real-time collection of data makes it possible to understand the correlation between appliances, statistical analysis, and intelligent advice generation. It also allows building managers to have real-time energy consumption levels for all the equipments and devices.

3.2. Data Storage. The sensor network enables us to monitor the equipments and machines and to create their profiles. The formation of profiles requires initial input from building managers as well, for example, information about various settings of air conditioning. The incoming data from the data collector is stored in a data server. The collected data grows

rapidly. It is resource consuming to extract meaningful information from a database containing raw energy consumption data. In order to reduce response time of queries, the raw data needs to be preprocessed and analyzed to convert it into meaningful information and store it in a collection of analytic databases. The analytic data can be aggregated into a high or abstract level of information about energy usage based on categories such as type of equipment, labs, floor, and period of time.

The long-term storage of data enables the system to use historical data patterns of energy consumption to detect abnormality in energy consumption while incorporating factors such as cold day and hot day. Occupancy data is a main source to identify energy waste due to equipment ON, standby, or idle states.

Having millions of records of energy consumption data coming directly in real time from hundreds of appliances poses a performance problem for data storage, retrieval and reasoning. One of the solutions to data storage and retrieval is TimeSeries DataBlade [20] TimeSeries DataBlade, which has an advantage over traditional relational database management systems “RDBMSs” in its organization and manipulation of time-stamped data. The application of TimeSeries

DataBlade provides a potential solution to the performance degradation of the reasoning process which results from reasoning over a huge volume of data. Another solution could be the use of Hypertable DBMS [21].

3.3. Application Server. Our proposed system makes intelligent use of monitored energy consumption data collected by the monitoring subsystems. On detection of any abnormality in energy consumption, the system tries to figure out the underlying cause by using available data on energy consumption and device profiles or interacting with building managers to get the required information. The application server hosts the proposed intelligent energy management system. We use Glassfish (<http://glassfish.java.net/>) open source application server, which uses Jess Expert Shell [22] as a library to support the reasoning capabilities of the system.

3.4. Rule Base. The intelligent energy management system will be populated with rules prepared with the help of the building manager's knowledge and energy consumption optimization knowledge available in the literature. These rules contain experiential knowledge about energy saving in educational institutions and commercial buildings.

In order to be able to incorporate a new rule, a user interface is provided for the building manager to set values of various parameters and the consequences of such values. This information will then be translated by the system into rules and templates and will be added to the rule base. On the addition of a new rule, the system checks if any inconsistency occurs. If so, the system will try to reconcile amongst rules by interacting with the building manager and making suggestions. The rule base system is modelled using a well-known heuristic classification approach [23]. A typical rule for diagnosing abnormal consumption of energy by air conditioning of a room is shown in Figure 2. The intelligent system discovers the abnormal consumption based on historical data and tries to establish the underlying cause of this abnormality.

3.5. Knowledge Base. The knowledge base encodes knowledge about pieces of advices and their semantics. This knowledge is used as facts by the Jess expert shell. We classify energy consumption activities related to various electrical appliances in home environment [24] into a hierarchy, which will be extended to incorporate new concepts and relations that exist in the HEI domain. The ontological representation as a hierarchy provides the semantics to these activities and provides a rich structure for reasoning rules. This classification also links the pieces of advice with their associated activities. These energy consumption activities are distinct in a way that they are uniquely associated with various appliances.

4. Service Oriented Architecture (SOA)

The development of the system is driven by SOA. SOA is a paradigm that allows software developers to focus on the fulfillment of required enterprise functionalities at a conceptual level by providing standardized communication

protocols, interfaces, workflows, and service management. SOA enables developers to compose the existing service without being concerned with any barriers caused by heterogeneous operating and hardware systems.

The key property of SOA is that it allows services to publish their interfaces and related information, so they become searchable and can be discovered over the Internet. Those services having been discovered and selected can be composed in a certain way to provide certain functions that meet specific application requirements [25]. The rationale for using the SOA approach in design, development, and deployment of the system is to provide standard interfaces for services to be used by other systems.

5. Handling Large Volumes of Sensor Data

We attempt to address the challenge of storing and querying huge volumes of data through functional data services that could compose answers to various energy consumption queries while satisfying the real-time requirement. The proposed architecture of functional data service is shown in Figure 3. Our proposed approach uses a large number of web services with different functionalities to access, handle, and retrieve information over a semantic functional database. The functional characteristic is provided by the fact that the query language is a functional language and the semantic characteristic is offered by the semantic dictionary that describes the structure of the data in terms of types and properties.

The collection of web services (WS) facilitates access to the information as well as the description of the information. This approach enables various high level functionalities. This component offers access to the information for individual users and for other applications as well as providing the connection between an existing relational database (RDB) and a functional database that is built based on the RDB's data. Subsets from the RDB data are transferred into functional data sets. The data subsets represent the most frequently used data and provide the basis for the structure of the functional database. The relational database is accessed only if the necessary information cannot be found in the functional database. The data retrieved from the relational database is then stored in the functional database.

Our proposed approach is to limit the use of relational databases by offering a functional database. Functional datasets contain data from the relational database with semantic annotations. Initially, the functional database contains only a few semantically described datasets, which may not answer all the necessary queries. In this case, a query to the system tries to gather the data from the functional database and takes from there all the information that has been found; the rest of the data that could not be found in the functional database would be searched for in the relational database. The new gathered data is tested to see if it will fit a specific dataset or, in the contrary case, will be used to describe a new dataset. The new datasets will be used later on in other queries. All the datasets in this model have a semantic description of the data that they contain. This means that

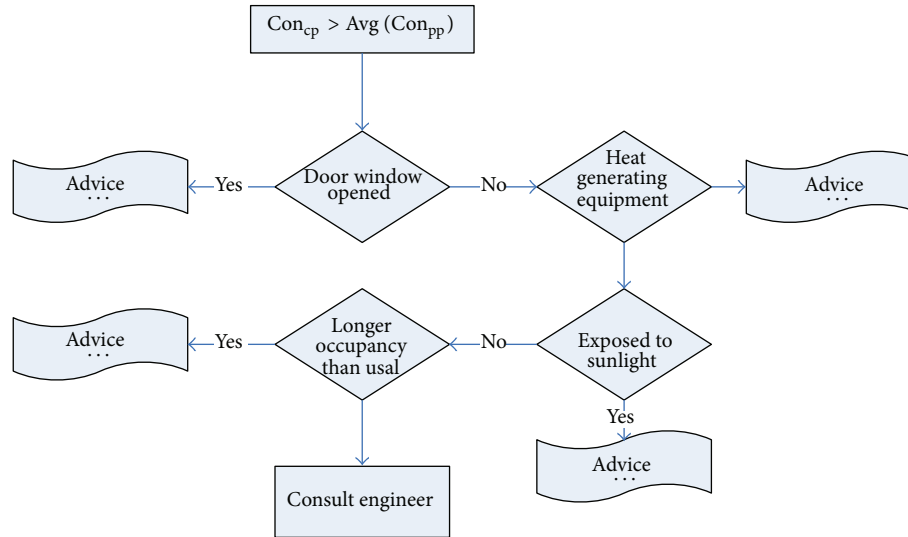


FIGURE 2: Rule for diagnosing air conditioning abnormal consumption.

the functional database is initially smaller and will expand as necessary. Each WS has a specific functionality and can be triggered by different user requests.

5.1. Management System. The management system component is a collection of web services (WS), which facilitate the access to the information as well as the description of the information. This component provides various high level functionalities and offers access to the information for individual users and for other applications. It also provides connection between an existing relational database (RDB)/Hypertable and a functional database that is built based on the RDB's/Hypertable data. From the RDB, data subsets are transferred into functional datasets. The data subsets represent the most frequently used data and provide a base for the structure of the functional database. The relational database is accessed only if the necessary information cannot be found in the functional database. The data that was retrieved from the relational database is then stored in the functional database. This component handles the external requests, forwards specific tasks to the reasoning component, connects the system to an adjacent RDB and provides the responses to the external requests, such as requests for energy consumption data of last summer or last one year.

5.2. Reasoning Component. The reasoning component operates over the datasets that form the functional database. This component represents the part of the system concerned with the logic and reasoning. Furthermore, this component queries the functional database, checks conditions, and transforms data. The reasoning component consists of multiple functions with different functionalities over the datasets. These functionalities form a set of functions. The reasoning component has a functional engine, a resource description framework (RDF) reasoning component which also provides access to a RDF query language.

These functions offer access to and manipulation of data from the database. This component provides the functional layer of the database and the logic of the system. It acts as a bridge between the user's access provider component and the functional database.

Operations over the functional database such as find, update and delete are performed by this component. The functions from this set are passed to the functional engine, and the engine makes the connection to the semantic dictionary, from where it retrieves the semantic description of data that need to be queried. The data gathered from the Semantic Dictionary is passed from the functional engine to the RDF reasoning engine. The RDF reasoning engine contains an RDF query language, which is able to query the RDFS and the RDF files of the database for retrieving the necessary information. There are different tools available that can offer the above mentioned functionalities. For example, the functional engine provided by Clojure (<http://clojure.org/>). Furthermore, the RDF reasoning engine can be described by Jena (<http://jena.sourceforge.net/index.html>), which already offers an API for RDF querying.

5.3. Functional Database. The functional database itself is structured semantically into datasets, with each dataset being represented by RDF. Each set contains summarized data, and the description of each set will be represented in the resource description framework schema (RDFS). For example, a table in a relational database which contains all persons that belong to the university with different columns such as name, age, occupations, and address can be divided based on the semantics of the data in different datasets for the functional database as a "Persons" set. A "Persons" set will be defined by an RDF file as a dataset, which will hold all the data structured into objects with the characteristic that all the objects in this data set are a "Person" type. The RDF schema describes that a "Person" type has mandatory characteristics such as "name", "age" and other optional characteristics too. Furthermore we

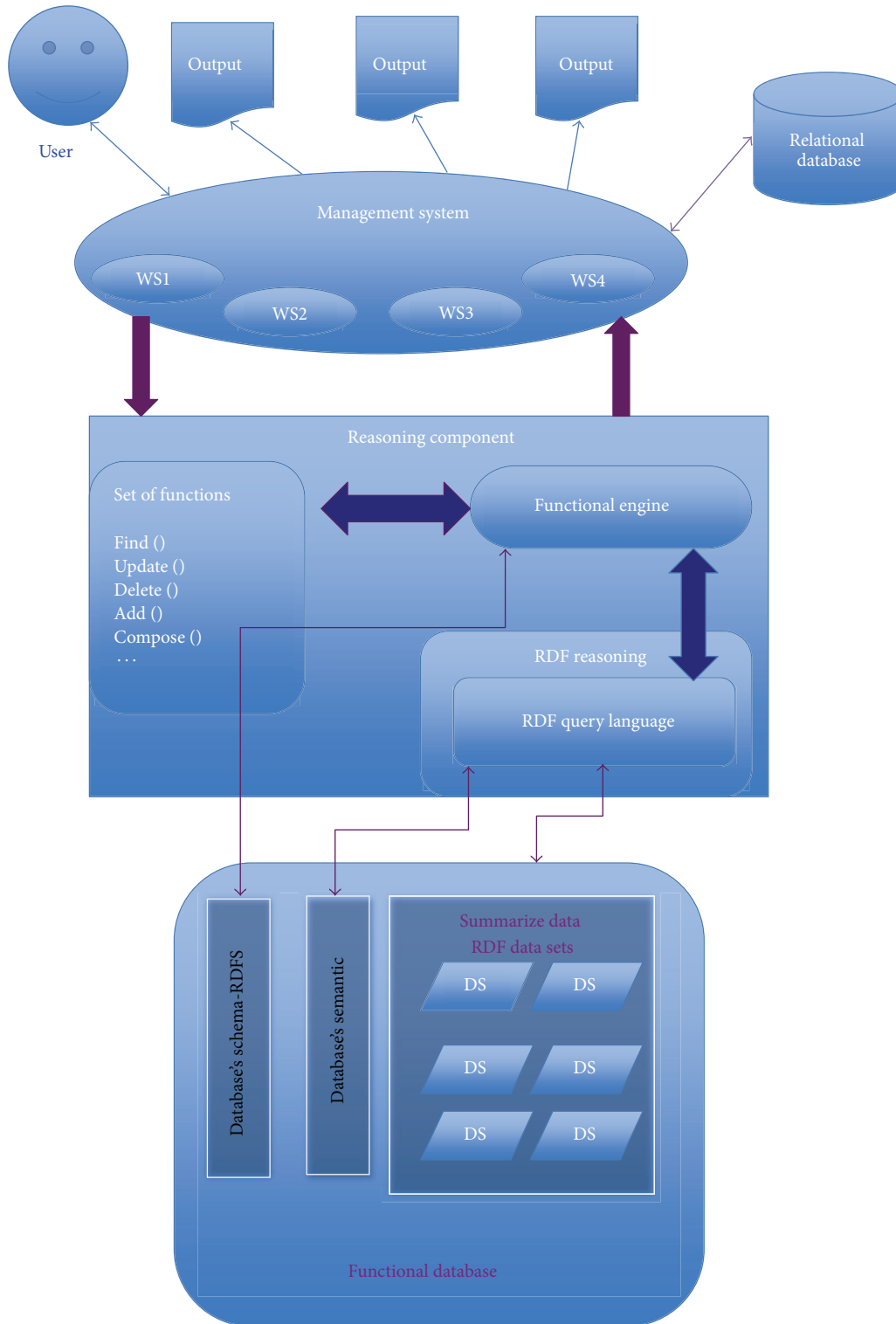


FIGURE 3: Functional data architecture.

can have another dataset, for example, “Staff” which will hold extra information over the “Person” dataset, for those persons from the university database that are employed at the university; each object would add proprieties which are specific to a “Staff” type (as well described previously in an

RDFS). So, in the “Staff” dataset, we could refer to a specific object from the “Person” dataset adding to it some other staff-specific proprieties such as employee number and office number. It is a useful approach because many other datasets can be built on the composition of other existing datasets

by adding extra information to it based on the semantic description of that dataset.

The RDFS describes the datasets and their content, from the point of view of what data can be stored inside and the definition of it; and the Semantic Dictionary of the database holds the semantic description of different properties and how they link to each other. As mentioned in previous example, the characteristic “Name” found in a dataset holding the “Person” data type can be semantically described in the dictionary of the database as a composer of “First Name”, “Middle Name” and “Last Name” and then even if other datasets have the “Name” characteristic in a different format, it will be known how to semantically search for the needed data.

The advantage of having functional database encompassing semantic data sets is to provide a smaller search time for reasoning. Multiple functions of the reasoning component can be called by a single WS. The reasoning component handles different functions over the datasets. Each function retrieves the necessary data for reasoning from one or more datasets in order to send back to the web services a proper response. Each function looks for the needed dataset/s in the functional database and composes the information received from them, for example, the composition of the monthly energy consumption data.

6. Implementation

The system adopts web technologies to provide the interfaces for the users to view energy consumption of various appliances/devices and also acts as an actuator in order to take optimal energy consumption actions. We used Protégé (<http://protege.stanford.edu/>) as a tool to create devices/appliances ontology. Currently, we have around 80 concepts relating to electricity appliances/devices defined and around 50 tips regarding energy saving having been encoded. The inference engine, which supports reasoning over knowledge base is Jess expert shell [22]. JessTab (<http://www.ida.liu.se/~her/JessTab/>) was used to integrate Jess and ontology, so the relations between the concepts defined in ontology can be exploited and reasoned.

6.1. Monitoring System. The energy consumption monitoring system has been installed in 10 computer laboratories and 10 offices to collect energy consumption data. A total number of 500 sensors were installed.

The sensors used to monitor and collect the energy usage are Plugwise (<http://www.plugwise.com/idplugtype-g/>) sensors and an electricity clamp meter (<http://www.currentcost.com/products.html>). The Plugwise sensor monitors individual electricity appliance or a collection of appliances, which share the same plug. The clamp meter is attached to the wire of main electricity switch that gathers the total electricity consumption. Both of them make use of radio transmissions to transfer the data to an Internet gateway, which process and send data to a centralized server for other applications to consume. In the following section we describe

the characteristics and component of Plugwise network for energy consumption monitoring.

6.1.1. Plugwise Network. Plugwise is a commercial product that enables measurement of energy consumption of electrical appliances and devices. The energy consumption measuring sensors are called Circles. Plugwise devices that are connected to the ZigBee network are called modules; examples are Circles, Circle+, and Stick. Plugwise is based on the Zigbee 2.4 GHz wireless mesh network. According to Plugwise configuration, each module can communicate to at least three other modules, and the distance between two modules is limited to 5–10 meters. A configuration file allows the setting of time intervals for energy consumption reading. All Circles within the network are synchronized with a built-in clock of Circle+, which in turn gets synchronized with computer. Plugwise consists of following components.

Circle. The Circle is a plug, which is placed between the wall socket and the plug of an appliance. It measures the energy consumption of the connected appliance and stores the data in its own memory. Energy consumption data is transmitted to the Plugwise software, installed on PC via a wireless Zigbee mesh network. In fact the circle is an energy consumption measuring sensor with an additional functionality of switching off and switching on the appliance attached to it. The Circle gets power from the socket it is plugged into, and the power dissipation of a Circle (node) ranges from 0.55 to 1.1 Watt.

Circle+. It is a Zigbee coordinator. The Circle+ contains additional characteristics within the network, apart from the basic functions of the Circle. It functions as a coordinator in a Plugwise network. It keeps track of the Circles, which are part of the network, and communicates this information to the Stick attached to a computer/data collector. The Circle+ includes a real-time clock and a battery, which synchronizes the time periodically with the other Circles.

Stick. It is also called a main controller. The Stick communicates directly with the Zigbee coordinator also known as the Circle+. The Circle+ communicates with other nodes (Circles) in the mesh network topology.

Source. The Source is the Plugwise software program, which is installed on the PC. The program gives insight into the energy consumption of the connected appliances by means of clear overviews and graphs. The Source also comes with a web server and its own scripting language.

Stretch Lite Pro. Stretch Lite Pro is used to manage multiple Plugwise networks. A single Plugwise network contains at maximum 50 Circles and one Circle+. We have installed multiple Plugwise networks to monitor energy consumption in various labs and offices. Communication with a Plugwise network is done through the Plugwise USB stick, called “Stick”. Each Stick is plugged into a Stretch Lite Pro, which is connected by a UTP cable to the physical network, and


```
(subclass EnergyMeasure ConstantQuantity)
(=>
  (and
    (equal (MeasureFn ?NUMBER ?UNIT) ?QUANT)
    (instance ?UNIT UnitOfEnergy))
    (instance ?QUANT EnergyMeasure))
```

Box 1

```
(subclass EnergyStarAttribute RelationalAttribute)
(instance EnergyStar5Rating EnergyStarAttribute)
(instance EnergyStar4Rating EnergyStarAttribute)
```

Box 2

on students and staff. The baseline case is also to be used to assess the impact of energy saving strategies employed by the system. Table 1 shows power consumption and waste due to standby mode during the first month of monitoring. In the second month, students and staff were made aware of the fact that a power consumption monitoring system was installed and how their energy consumption actions can contribute to reduction in energy waste. Table 2 shows the consumption in the second month. The results in Table 2 show a reduction of 8.53% in energy consumption due to the awareness activities that targeted students and staff. They also show that the energy waste is 11.36% down from 20.47% in the first month. Figures 6 and 7 show comparison of energy waste reduction during two months for both labs and offices. These figures indicate a reduction in energy waste as a result of energy consumption awareness and our implemented system.

In the third month, we have enabled the system to take automatic actions to deal with standby losses by detecting and switching off the devices, which are not being used. Simple rules were used to make sure that there is no lab session (according to lab schedule) and that the device consumption is comparable to the baseline waste value for the same device, if so the device is switched off. The trend in one week of monitoring data shows an additional 8.46% reduction in energy consumption due to reducing waste to only 1.45% of the total consumption which was achieved by creating energy consumption awareness and with the help of the energy monitoring system.

The following observations were made based on Tables 1 and 2.

- (1) Employing an awareness program reduced waste energy by almost 50%.
- (2) Using the system to reduce waste brought the waste percentage down to 1.49%.
- (3) The waste in general is very high due to cultural factors in addition to low energy cost in KSA.
- (4) Waste in offices is much higher than that in labs. We believe that the reason is that only one faculty controls the office.

- (5) In offices, the results of the awareness program varied greatly. We believe that the reason is it is hard sometimes to change the use habits of some people.

Currently, we are employing two strategies to lower energy waste: first creating energy consumption awareness among students and staff and secondly incorporating rules in an intelligent system to act as an actuator and automatically to switch off computers and other devices when they go into standby mode.

When the system detects abnormality in energy consumption (e.g., standby), it activates the JESS rule base. The JESS fires an applicable rule which in turn switch off standby appliances. The Plugwise sensors attached to appliance allow switching off and switching on of appliances remotely by receiving message from the software. The reasoning process consults timetabling system event management systems to ensure that the machine/appliance is not scheduled to stay in standby mode.

We display a peripheral message on each login to show the standby power waste to computer users for the last 30 days in order to make all users aware of standby effect on the overall energy consumption. In the next phase, we plan to incorporate more graphics such as a footprint showing the amount of CO₂ generated by the standby energy waste.

Awareness scheme has been used for educational purpose and as an attempt to influence staff and students behaviours towards efficient energy usage. There are lines of research evidence that energy consumption awareness resulted in efficient energy usage [8, 27–29].

Even in absence of occupant awareness the system is able to take automatic actions to reduce energy consumption.

8. Discussion and Conclusion

There are a number of energy management systems available for domestic commercial and industrial environment. Deploying these systems in HEI will not bring the same benefits due to different energy consumption requirements. HEI buildings consist of a large number of classrooms and laboratories, and their allocation is done via timetabling

TABLE 1: Energy consumption of labs and offices during the first month.

Lab/office no.	No. of appliances	Total consumption (KWh)	Waste (KWh)	Waste %
LAB_1	25	859.03	236.93	27.58
LAB_2	25	921.28	252.02	27.36
LAB_3	25	771.13	143.45	18.60
LAB_4	25	637.66	163.79	25.69
LAB_5	25	1078.3	91.29	8.47
LAB_6	30	785.89	118.49	15.08
LAB_7	30	875.71	273.1	31.19
LAB_8	35	1820.34	227.64	12.51
LAB_9	35	1332.99	112.87	8.47
LAB_10	35	1358.85	328.27	24.16
LAB's total	290	10441.18	1947.87	18.66
Office_1	3	93.72	37.44	39.95
Office_2	3	100.78	31.75	31.5
Office_3	3	59.07	32.89	55.68
Office_4	4	74.03	45.63	61.64
Office_5	4	172.37	36.66	21.27
Office_6	4	84.99	43.06	50.66
Office_7	3	99.77	30.03	30.1
Office_8	4	104.98	39.94	38.04
Office_9	3	43.69	34.48	78.91
Office_10	3	49.26	38.19	77.54
Offices' total	34	882.66	370.06	41.93
Total	224	11323.84	2317.92	20.47

TABLE 2: Energy consumption of labs and offices during the second month.

Lab/office no.	No. of appliances	Total consumption (KWh)	Waste (KWh)	Waste %
LAB_1	25	775.14	137.8	17.78
LAB_2	25	819.63	131.89	16.09
LAB_3	25	716.31	78.66	10.98
LAB_4	25	561.1	73.31	13.06
LAB_5	25	1038	43.67	4.21
LAB_6	30	731.99	54.79	7.49
LAB_7	30	767.85	145.63	18.97
LAB_8	35	1720.52	109.67	6.37
LAB_9	35	1288.34	60.1	4.67
LAB_10	35	1228.61	174.36	14.19
LAB's total	290	9647.50	1009.88	10.47
Office_1	3	72.6	12.48	17.19
Office_2	3	88.57	17.32	19.55
Office_3	3	43.89	14.95	34.06
Office_4	4	56.21	24.57	43.71
Office_5	4	147.55	7.33	4.97
Office_6	4	60.7	14.35	23.64
Office_7	3	88.22	16.38	18.57
Office_8	4	76.82	6.66	8.66
Office_9	3	36.96	26.52	71.75
Office_10	3	39.31	26.44	67.26
Offices' total	34	710.84	167	23.5
Total	224	10358.34	1176.88	11.36

```
(=>
  (and
    (instance ?X Dishwasher)
    (not (attribute ?X Compact))
    (attribute ?X EnergyStar5Rating)
    (annualEnergyConsumption ?X (MeasureFn ?ENERGY KilowattHour)))
  (lessThanOrEqualTo ?ENERGY 295))
```

Box 3

```
(=>
  (and
    (instance ?X Dishwasher)
    (not (attribute ?X Compact))
    (attribute ?X EnergyStar4Rating)
    (annualEnergyConsumption ?X (MeasureFn ?ENERGY KilowattHour)))
  (lessThanOrEqualTo ?ENERGY 324))
```

Box 4

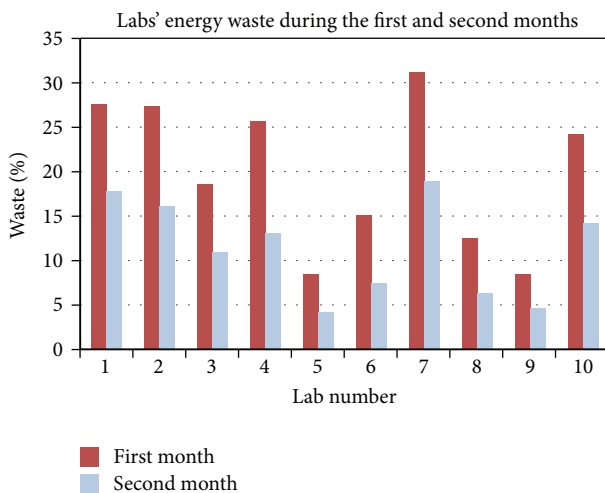


FIGURE 6: Labs' energy waste comparison.

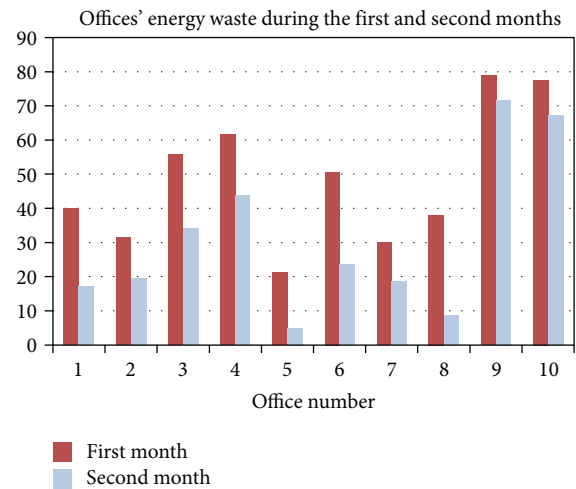


FIGURE 7: Offices' energy waste comparison.

systems. Such occupancy requires an adoptive energy management system that is sensitive to timetabling systems. Event management systems also provide a valuable input for energy management systems to optimise energy consumption. The nature of the building that the system will be employed in has its uniqueness. This is due to the fact that most of the rooms do not have windows. In the absence of windows, people tend to leave lights on when they leave the room. Our preliminary study confirms that energy consumption can be greatly reduced if the deployed energy management system is able to deal with this situation. The proposed system employs state-of-the-art technologies to harvest data from various sources in a seamless way to provide optimal energy consumption in the HEI environment. The next phase of the project will include deployment of energy consumption sensors in more labs and offices. Occupancy sensor and

temperature sensor will also be deployed in order to reduce energy waste of HVAC.

In this paper, we have presented a high level architecture and framework for the development of intelligent energy management system for HEI buildings and also results of the first phase of the project. The proposed system employs a functional data web services approach to provide semantic to data and enable optimal query services by composing services in various ways. One of the distinguishing features of the system is the use of information from timetabling and event management systems. Timetabling and event management systems provide a more accurate picture of occupancy timings, which help the energy management system to schedule HVAC activities in an energy efficient manner. The system also keeps students and staff in the loop and provides them with information on their energy consumption activities in

an attempt to influence their future energy consumption behaviour. Our preliminary study onto energy consumption reveals that the vast majority of equipment stays in the standby mode unnecessarily. In the first phase of the project, the system identifies the hidden energy waste in laboratories and offices and takes appropriate measures to optimise energy consumption.

Using both an awareness program and the developed system, we were able to reduce energy waste down to 14.9% of the total energy used.

Conflict of Interests

All authors are academic, and they do not have financial interest or any other interest in commercial products mentioned in this paper. The commercial products are purely mentioned as a potential candidate for a solution, but the project uses all open sources technologies. The authors do not recommend the use of any commercial products in this paper.

Acknowledgment

The authors would like to thank the National Plan for Sciences and Technology (NPST) at the King Saud University for their support for this Project (no. 11-ENE-1605-02).

References

- [1] IEO International Energy Outlook, 2009, [http://www.eia.doe.gov/oiaf/ieo/pdf/0484\(2009\).pdf](http://www.eia.doe.gov/oiaf/ieo/pdf/0484(2009).pdf).
- [2] Google PowerMeter, <http://www.google.com/powermeter/about/partners.html>.
- [3] Hohm, Microsoft, <http://www.microsoft-hohm.com/>.
- [4] i-Measure, Oxford University, <http://www.imeasure.org.uk/>.
- [5] ewgeco, <https://www.ewgeco.com/>.
- [6] *Service-Oriented Architecture: Concepts, Technology, and Design*, Prentice Hall, Upper Saddle River, NJ, USA, 2005.
- [7] M. Dahle and E. Neumayer, "Overcoming barriers to campus greening: a survey among higher educational institutions in London, UK," *International Journal of Sustainability in Higher Education*, vol. 2, no. 2, 2001.
- [8] 2013, <http://www.dehems.eu/>.
- [9] R. Sarnadas, P. Fonseca, and J. Paulo Teixeira, "Intelligent architecture for home appliances and energy management control," in *Proceedings of the Conference on Design of Integrated Circuits and Systems*, Lisbon, Portugal, 2005.
- [10] J. Karlgren, L. E. Fahlén, A. Wallberg et al., *Socially Intelligent Interfaces for Increased Energy Awareness in the Home, Internet of Things*, Springer, Berlin, Germany, 2008.
- [11] G. Wood and M. Newborough, "Energy-use information transfer for intelligent homes: enabling energy conservation with central and local displays," *Energy and Buildings*, vol. 39, no. 4, pp. 495–503, 2007.
- [12] S. Mamidi, Y.-H. Chang, and R. Maheswaran, "Improving building energy efficiency with network of sensing learning and prediction agents," in *Proceeding of the 11th International Conference on Autonomous Agents and Multiagent Systems*, 2012.
- [13] H. Hagras, I. Packham, Y. Vanderstockt, N. McNulty, A. Vadher, and F. Doctor, "An intelligent approach for energy management in commercial building," in *Proceedings of the Systems Man and Cybernetics*, 2008.
- [14] A. Rogers, S. Maleki, S. Ghosh, and N. Jennings, "An intelligent agent for home heating management," in *Proceedings of the 11th International Conference on Autonomous Agents and Multiagent Systems*, 2012.
- [15] Z. Wang, R. Yang, and L. Wang, "Multi-agent control system with intelligent optimization for smart and energy-efficient buildings," in *Proceedings of the 36th Annual Conference of the IEEE Industrial Electronics Society (IECON '10)*, pp. 1144–1149, November 2010.
- [16] Z. Mo and A. Mahdavi, "An agent-based simulation-assisted approach to bi-lateral building systems control," in *Proceedings of the 8th International IBPSA Conference*, Eindhoven, The Netherlands, 2003.
- [17] T. Yu, "Modeling occupancy behavior for energy efficiency and occupants comfort management in intelligent buildings," in *Proceedings of the 9th International Conference on Machine Learning and Applications (ICMLA '10)*, pp. 726–731, December 2010.
- [18] D. Kolokotsa, K. Niachou, V. Geros, K. Kalaitzakis, G. S. Stavrakakis, and M. Santamouris, "Implementation of an integrated indoor environment and energy management system," *Energy and Buildings*, vol. 37, no. 1, pp. 93–99, 2005.
- [19] J. Figureiredo and J. Costa, "A SCADA system for energy management in intelligent buildings," *Journal of Energy and Buildings*, vol. 49, pp. 85–98, 2012.
- [20] TimeSeries DataBlade, <http://www.ibm.com/developerworks/data/library/techarticle/dm-0510durity2/>.
- [21] Hypertable: An Open Source, High Performance, Scalable Database, <http://hypertable.org/>.
- [22] Jess Expert Shell, <http://herzberg.ca.sandia.gov/>.
- [23] E. H. Shortliffe, *Computer Based Medical Consultations: MYCIN*, Elsevier, New York, NY, USA, 1976.
- [24] N. Shah and C.-F. Tsai, "Intelligent household energy management recomender system," in *Proceedings of the International Conference on Green Computing*, Athens, Greece, 2010.
- [25] M. P. Papazoglou, P. Traverso, S. Dustdar, and F. Leymann, "Service-oriented computing: state of the art and research challenges," *Computer*, vol. 40, no. 11, pp. 38–45, 2007.
- [26] Plugwise in Business Environment, 2013, http://www.plugwise.com/sites/default/files/plugwise_in_a_business_environment_20110929.pdf.
- [27] T. Hargreaves, M. Nye, and J. Burgess, "Making energy visible: a qualitative field study of how householders interact with feedback from smart energy monitors," *Energy Policy*, vol. 38, no. 10, pp. 6111–6119, 2010.
- [28] A. Faruqi, S. Sergici, and A. Sharif, "The impact of informational feedback on energy consumption—a survey of the experimental evidence," *Energy*, vol. 35, no. 4, pp. 1598–1608, 2010.
- [29] F. W. Siero, A. B. Bakker, G. B. Dekker, and M. T. C. Van Den Burg, "Changing organizational energy consumption behaviour through comparative feedback," *Journal of Environmental Psychology*, vol. 16, no. 3, pp. 235–246, 1996.

Research Article

Field Measurement of Wind Effects of Roof Accessory Structures on Gable-Roofed Low-Rise Building

Peng Huang, Ming Gu, Chun-guang Jia, and Da-long Quan

State Key Laboratory of Disaster Reduction in Civil Engineering, Tongji University, Shanghai 200092, China

Correspondence should be addressed to Ming Gu; minggu@tongji.edu.cn

Received 4 July 2013; Accepted 13 August 2013

Academic Editor: Ting-Hua Yi

Copyright © 2013 Peng Huang et al. This is an open access article distributed under the Creative Commons Attribution License, which permits unrestricted use, distribution, and reproduction in any medium, provided the original work is properly cited.

The components and claddings of low-rise buildings are usually destroyed first during typhoon disasters in coastal areas. Roof accessory structures can change the flow pattern on the roof, thus effectively reducing the wind load on the roof surface and the damage to the low-rise buildings. Three types of aerodynamic mitigation plates, that is, (1) 0.3 m high full-length roof-edge plate, (2) 0.3 m high and 0.5 m + 0.5 m long roof-corner plate, and (3) discrete roof-edge plates with different spaces (which can be used as advertisement boards), are studied on the basis of the field measurement results under roof pitches of 10° and 18.4°. By comparing the results of the roof with and without constructed plates, it is implied that the three types of plates can affect the formation of conical vortexes and can significantly reduce the mean and fluctuating pressure coefficients in the windward corner. Compared with the constructed plate, the roof ridge has a larger influence on the wind loads on leeward roof.

1. Introduction

Recent natural calamity investigations show that wind-induced disasters cause large economic losses and many casualties worldwide annually. Most of these losses are related to damages in residential, industrial, and other low-rise buildings. Many notable full-scale studies of wind loads on low-rise buildings have been conducted, which helps to compare their results with wind-tunnel test and numerical simulations. In 1974, the Building Research Establishment in the United Kingdom initiated a program of full-scale measurements on a special constructed experimental building in Aylesbury, England [1]. The building has two stories, 13.3 m in length and 7 m in span. The roof of the building can be adjusted between 5° and 45°. In the late 1980s, the TTU experiment, a famous full-scale experiment on a low-rise building, was conducted in Lubbock, TX, USA [2]. The building was 13.7 m in length, 9.1 m in span, and 4 m in height. Almost at the same time, the United Kingdom established a full-scale model in Silsoe comprising a steel frame building, which is 24 m in length, 12.9 m in span, and 3 m in height. The above experiment is called the Silsoe experiment [3]. Then, a 6 m cube was constructed at the Silsoe Research Institute at the beginning of the 21st century [4]. In China, Hunan University developed

a set of field measurements for wind effect on a low-rise building [5]. This low-rise building can be moved to the landing position of typhoons to enable field measurement during typhoons.

Many factors can affect the distribution of wind pressure on buildings, such as geometric shape, size of the building, roof covering, and openings on the wall [6]. Stathopoulos [7] found that the maximum negative pressures (suction) occur at the edges and corners of the roof because of the flow separation. Stathopoulos and Baskaran [8] learned that isolated parapet has little effect on reducing the mean pressure coefficient and the pressure peak in the roof corner. In another study, Kopp et al. [9] elaborately examined the wind effects on the flat roof parapets of low-rise buildings and the wind loads on the parapets. They found that the magnitude of wind loads and their distribution largely depend on the architectural detail. Recently, Blessing et al. [10] assessed the effectiveness of aerodynamic edge devices in reducing wind effects over the roof corners and edge regions of the Wall of Wind (WoW), a large-scale six-fan testing facility. Suaris and Irwin [11] investigated the effectiveness of parapets mounted at the roof edge on mitigating peak suction near the roof corners of the low-rise buildings. Bitsuamlak et al. [12]



FIGURE 1: Full-scale low-rise test building.

studied some simple architectural elements for reducing high-wind-induced suction occurring at the roofs and wall corners of low-rise buildings in a boundary-layer wind tunnel and in the WoW.

A field laboratory has been set up near Shanghai Pudong International Airport by the State Key Laboratory of Disaster Reduction in Civil Engineering of Tongji University to study the turbulence characteristics of near-ground wind and wind loads on full-scale low-rise buildings. The plane size of the building is $10\text{ m} \times 6\text{ m}$, and the eave height is 8 m. The main feature of this building is that the roof pitch can be adjusted from 0° to 30° by using a lifting device. The architectural appearance of the pitch-adjustable building was designed according to the typical characteristics of the low-rise buildings in villages of South China. The pitch-adjustable building has roof accessory structures (aerodynamic wind-resistance devices) installed in the roof to measure the wind loads on the roof and the wind-resistance effect. Some of the results are valuable for the wind-resistance design of low-rise buildings in the coastal regions.

2. Experimental Apparatus Equipment and Data Processing Method

Pudong New District in Shanghai is an area where strong winds, particularly strong typhoons, frequently occur each year. The field laboratory is located in a flat area close to the estuary of the Yangtze River and near the Shanghai Pudong International Airport. The field laboratory consists of a test building and two meteorological towers. The steel-structure test building is 10 m in length, 6 m in width, and 8 m in eave height. The test building features an adjustable roof pitch ranging from 0° to 30° . Figure 1 shows an image of the full-scale building.

A mechanical anemometer (R. M. Young 05305) and an ultrasonic anemometer (R. M. Young 81000) were installed in a 10 m high meteorological tower, which is located about 25 m to the east of the pitch-adjustable building. The ultrasonic anemometer can be used to measure the wind velocity of the standard point. These two anemometers were employed for

mutual correction to provide real and effective wind velocity data [13].

There are two types of pressure transducers that were used to measure the surface pressures on the roof of the test building. These transducers are all developed by Kunshan Shuangqiao Sensor Measurement Controlling Co., Ltd. A total of 94 microdifferential pressure sensors with the range of $\pm 1\text{ kPa}$ (CYG1220) were mounted to measure the wind pressure without rain. A total of 20 diaphragm pressure sensors with the range of $\pm 2.5\text{ kPa}$ (CYG1516) were installed under the roof to study the wind-rain-induced effects on pressure [14]. The photos of the two types of transducers are shown in Figure 2.

The southeastern wind is the prevailing wind direction in Shanghai, based on the wind rose of this city. Therefore, more transducers are placed at the southeastern corner [15]. The locations of the pressure taps are shown in Figure 3. The detailed information of the field measurement laboratory, the installed equipment, and the low-rise building model can be found in the paper of Huang et al. [16].

The sample frequency of the anemometer and wind-pressure data acquisition is 20 Hz, and the sampling duration adopted for each data record is 10 min. The wind-pressure coefficient on the roof surface is defined as

$$C_{p_i} = \frac{p_i - p_\infty}{0.5\rho v^2}, \quad (1)$$

where p_i is the pressure of tap i , p_∞ is a static reference pressure and is obtained by the static system that extends to a box below the outdoor ground through a long tube, and v denotes the reference wind velocity measured by the anemometer at the top of the 10 m high meteorological tower near the building. The mean and fluctuating pressure coefficients are then defined by the average value and standard deviation of the pressure coefficient time series; that is,

$$\begin{aligned} C_{p_i, \text{mean}} &= \text{mean} \left(\frac{p_i - p_\infty}{0.5\rho v^2} \right), \\ C_{p_i, \text{rms}} &= \text{std} \left(\frac{p_i - p_\infty}{0.5\rho v^2} \right). \end{aligned} \quad (2)$$



(a) CYG1220 (b) CYG1516

FIGURE 2: Photos of two types of pressure sensors.

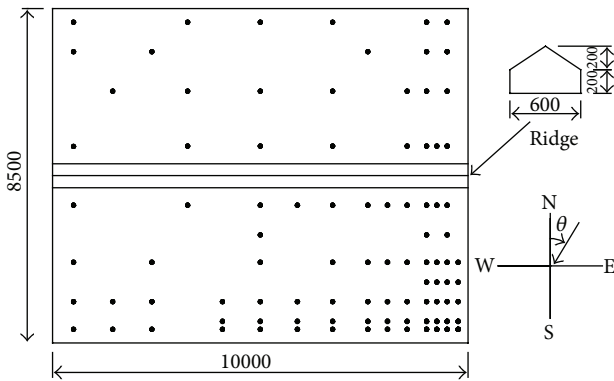


FIGURE 3: Layout of measuring points on the roof.

3. Test Results and Discussion

3.1. Introduction of Aerodynamic Mitigation Plates and Working Conditions. Because of the short time of field measurement and natural wind direction, only three types of aerodynamic mitigation plates, that is, (1) 0.3 m high full-length roof-edge plate, (2) 0.3 m high and 0.5 m + 0.5 m long roof-corner plate, and (3) discrete roof-edge plates with different spaces (which can be used as advertisement boards), are studied based on the field measurement results under roof pitches of 10° and 18.4°.

In the test, the 0.3 m high full-length roof-edge plate is erected at the northern edge of the roof under a roof pitch of 18.4° (see Figure 4).

The second type of the aerodynamic mitigation plates is used to increase the height of the roof corner, which is 0.3 m high and 0.5 m long in both sides along the roof-edge corner. Considering the wind direction in the field measurement building, the roof-corner plates are erected only in the southeastern corner of the building under a roof pitch of 10° (see Figure 5).

The discrete roof-edge plates include two, three, and four pieces with clear spaces of 2.6, 1.5, and 1.0 m, respectively. These plates are 0.7 m in height and 0.5 m in width and can

be used as advertisement boards, which are erected at the southern edge of the roof under a roof pitch of 10° (see Figure 6).

After a period of field measurement, the mean and fluctuating wind-pressure coefficients of each measuring point under natural wind condition are obtained. The effect of these three types of constructed measurement will be discussed below on the basis of the variation of the mean wind-pressure coefficient and fluctuating wind-pressure coefficient before and after the erection of the constructed plate.

3.2. Results of Full-Length Roof-Edge Plate under a Roof Pitch of 18.4°

(a) Mean Wind-Pressure Coefficient. The field measurement results of the building under a roof pitch of 18.4° are obtained. The mean wind-pressure coefficient of the roof without the constructed plate in the 40° wind direction and the roof with the constructed plate in the 35° wind direction are shown in Figure 7.

Figure 7(a) shows the distribution of the mean wind-pressure coefficients on the roof without a constructed plate in the 40° wind direction at a mean wind speed of 10.0 m/s. Because of the effect of the conical vortex in the 40° wind direction, two large negative pressure centers occur on the corner of the windward roof, whose minimum mean wind-pressure coefficients are -2.6 and -1.6, respectively. For the positive wind pressure, the maximum positive pressure coefficient on the windward side is only 0.2. Two negative pressure centers behind the roof ridge emerged on the leeward side; the minimum negative pressure coefficients of these centers are -1.8 and -1.2.

Figure 7(b) shows the distribution of the mean wind-pressure coefficients on the roof with a constructed plate in the 35° wind direction at a mean wind speed of 8.0 m/s. The conical vortex is completely destroyed under the effect of the full-length roof-edge plate, which is located in the windward corner. In addition, the two negative pressure centers in the corner are no longer existing, whereas the



FIGURE 4: 0.3 m high full-length roof-edge plate.



FIGURE 5: 0.3 m high and 0.5 m + 0.5 m long roof-corner plate.

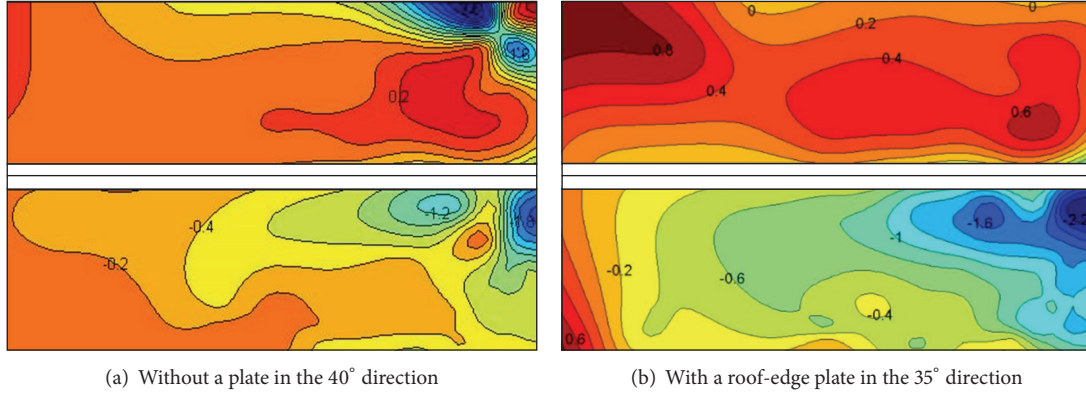
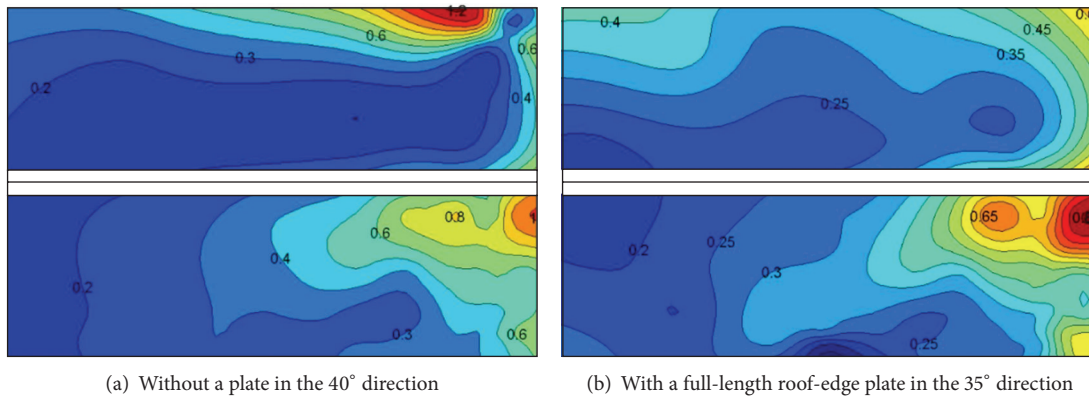


FIGURE 6: Discrete roof-edge plates.

maximum positive pressure coefficient on the windward roof is about 0.6. The leeward roof is mainly influenced by the roof ridge. Therefore, the negative pressure centers behind the roof ridge still exist. The maximum absolute values of the negative pressure centers have increased to some extent because of the air-flow lifting effect of the constructed plate. The differences could also be caused by the 5° difference between the wind

direction angle of the field measurement of the roof with a constructed plate and that without a constructed plate.

(b) *Fluctuating Wind-Pressure Coefficient.* Figures 8(a) and 8(b) show the distribution of the fluctuating wind-pressure coefficients on the roof without and with a constructed plate in the 40° and 35° wind directions, respectively. Similar

FIGURE 7: Mean pressure coefficients under a roof pitch of 18.4° .FIGURE 8: Fluctuating pressure coefficients under a roof pitch of 18.4° .

to the distribution of the mean pressure coefficients, two large fluctuating pressure centers occur on the corner of the windward roof without a constructed plate (Figure 8(a)); the maximum pressure coefficients are 1.2 and 0.6. The two pressure centers in the corner no longer exist on the roof with a constructed plate (see Figure 8(b)). The constructed plate can also significantly reduce the fluctuating pressure coefficients in the windward corner.

The maximum fluctuating pressure centers of the leeward roof with a constructed plate decreased to some extent compared with those without a constructed plate.

3.3. Results of the 0.3 m High and 0.5 m + 0.5 m Long Roof-Corner Plate under a Roof Pitch of 10° . The mean pressure results obtained by field measurement for this type of structure are not satisfactory; therefore, only the fluctuating wind pressures on the roof are discussed in this section. As the effect of the roof accessory structures on wind pressure under a small roof pitch is more evident than that of those under a large roof pitch, only the fluctuating pressures on the roof under a roof pitch of 10° are discussed here.

Figure 9(a) shows the field measurement result of the fluctuating pressure coefficient distribution on the roof without a roof-corner plate in the 145° wind direction at a mean wind speed of 10.0 m/s. By comparing the results under a roof pitch of 18.4° , we can observe that the conical vortex

becomes more evident in the corner of the windward roof because of the lessened roof pitch. The fluctuating wind-pressure coefficient becomes larger, and two pressure centers occur on the corner of the windward roof, whose maximum fluctuating pressure coefficients are 1.6 and 0.9.

After the erection of the roof-corner plate, when the air flow blows on the structure directly in the 145° wind direction at a mean wind speed of 7.5 m/s, the fluctuating pressure coefficients on both sides of the windward corner become smaller because the corner plate destroys the conical vortex located in the corner (see Figure 9(b)). The maximum fluctuating pressure coefficient is only 1.20, and the position of that coefficient is changed correspondingly.

For the leeward roof, the maximum fluctuating pressure coefficient decreases from 0.6 to 0.4, and the whole fluctuating pressures also decrease at a certain degree before and after the erection of the roof-corner plate.

3.4. Results of the Discrete Roof-Edge Plates under a Roof Pitch of 10° . By considering the effects of roof pitch and the space limitation, we decided to present only the fluctuating pressures of the four pieces of the roof-edge plates with a clear space of 1.0 m under a roof pitch of 10° .

Figure 10 shows the distribution of the fluctuating wind-pressure coefficient on the roof without and with roof-edge plates in 180° , 170° , and 160° wind directions. Figures 10(a),

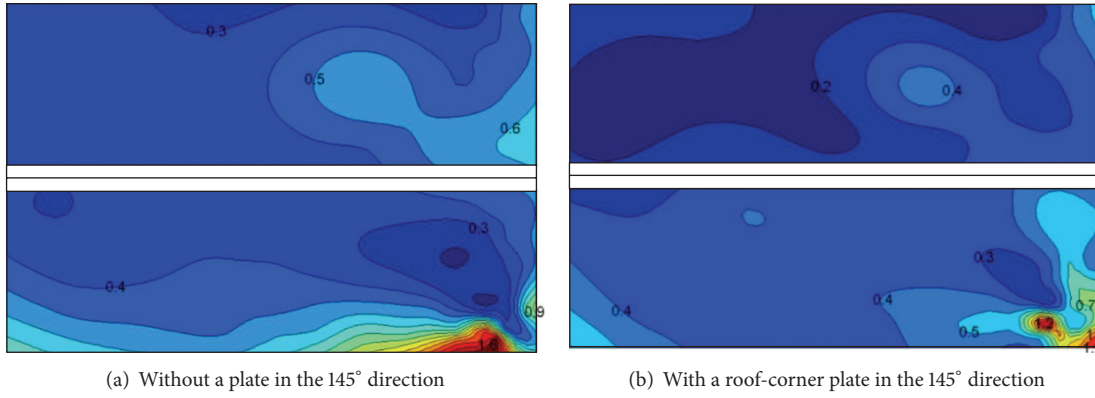


FIGURE 9: Fluctuating pressure coefficients under a roof pitch of 10°.

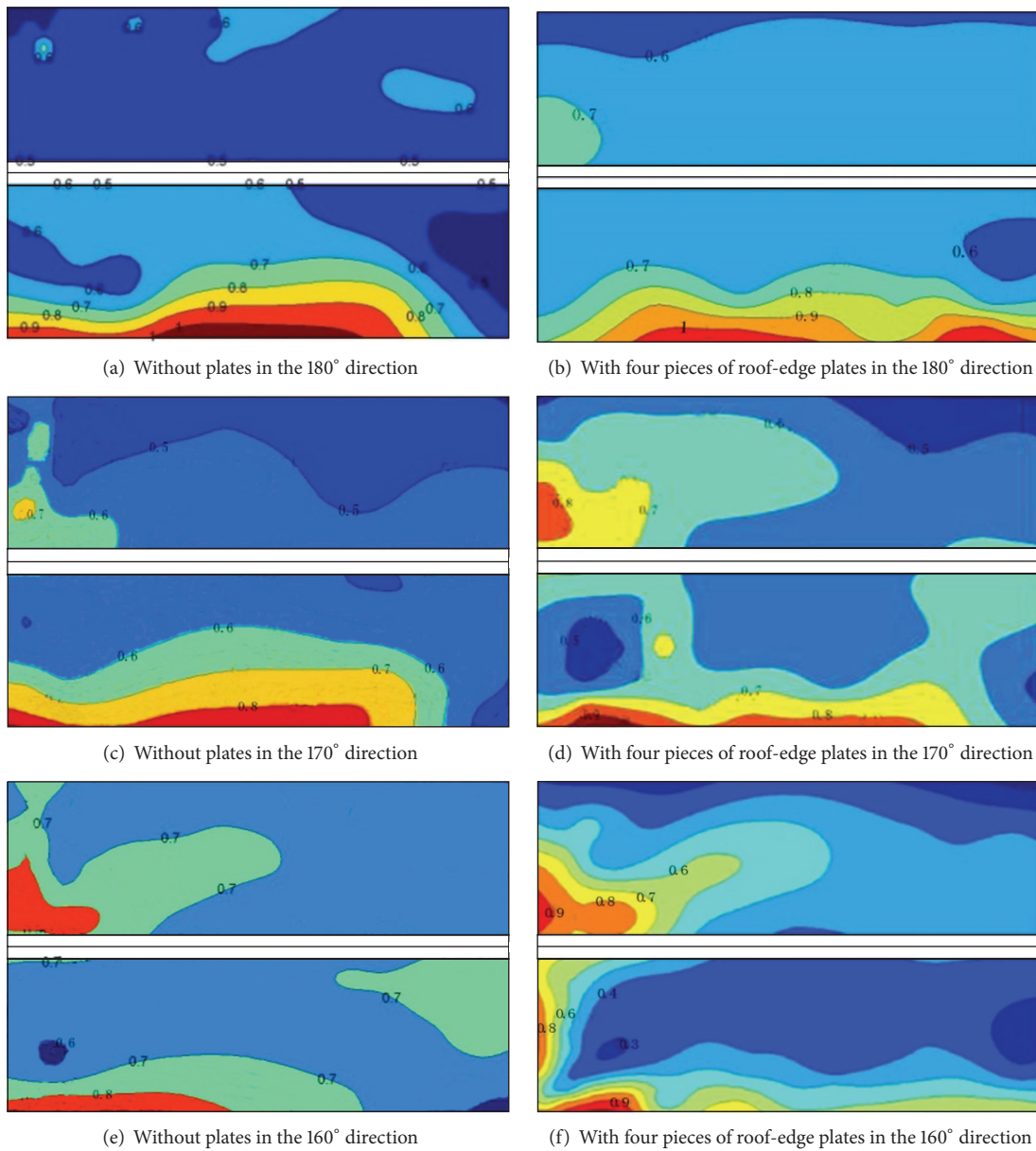


FIGURE 10: Fluctuating pressure coefficients under a roof pitch of 10°.

10(c), and 10(e) show the cases of the original roof wherein the wind directions are almost normal. The variations of the fluctuating pressure coefficients are mild, and the maximum value is about 1.1. After the erection of the four pieces of roof-edge plates at a mean wind speed of 8.0 m/s, the fluctuating pressure coefficients on the windward roof decrease to some extent (see Figures 10(b), 10(d), and 10(f)). The maximum fluctuating pressure coefficient is about 1.0, and the position of that coefficient is changed correspondingly.

The local fluctuating wind pressures behind the roof-edge plates have increased because of the wake flows by the roof-edge plates.

4. Conclusions

The wind effect of three types of roof accessory structures (aerodynamic mitigation plates) are studied in the paper on the basis of the field measurement of a full-scale low-rise building under roof pitches of 10° and 18.4°. The following conclusions are obtained.

(1) The full-length roof-edge plate has an obvious effect on air-flow lifting, which affects the formation of the conical vortex. Air-flow lifting also results in the effective reduction of the mean and fluctuating wind-pressure coefficients in the windward roof. Compared with the constructed plate, the roof ridge has a larger influence on the wind loads on the leeward roof.

(2) The roof-corner plate can also affect the formation of the conical vortex, which makes the maximum fluctuating pressure coefficient in the corner decrease significantly and the position of that coefficient change correspondingly.

(3) The discrete roof-edge plates can reduce the fluctuating pressure coefficients on the windward roof to some extent. The local fluctuating wind pressures behind the roof-edge plates are increased because of the wake flows caused by the windshield plates.

Conflict of Interests

The authors (Peng Huang, Ming Gu, Chun-guang Jia, and Da-long Quan) declare that there is no conflict of interests regarding the publication of this paper.

Acknowledgment

This paper is supported by the Chinese National Natural Science Foundation (Grants nos. 51178352, 90715040, and 91215302), which is gratefully appreciated.

References

- [1] K. J. Eaton and J. R. Mayne, "The measurement of wind pressures on two-storey houses at Aylesbury," *Journal of Industrial Aerodynamics*, vol. 1, pp. 67–109, 1975.
- [2] M. L. Levitan and K. C. Mehta, "Texas Tech field experiments for wind loads part I: building and pressure measuring system," *Journal of Wind Engineering and Industrial Aerodynamics*, vol. 43, no. 1–3, pp. 1565–1576, 1992.
- [3] R. P. Hoxey and P. J. Richards, "Full-scale wind load measurements point the way forward," *Journal of Wind Engineering and Industrial Aerodynamics*, vol. 57, no. 2–3, pp. 215–224, 1995.
- [4] M. Sterling, C. J. Baker, and R. P. Hoxey, "Short term unsteady wind loading on a low-rise building," *Wind and Structures*, vol. 6, no. 5, pp. 403–418, 2003.
- [5] Y. M. Dai, X. G. Yan, X. J. Wang et al., "Statistics and Analysis of typhoons landing and failure mechanism of coastal low-rise buildings in China," *Applied Mechanics and Materials*, vol. 226–228, pp. 1072–1075, 2012.
- [6] J. D. Holms, *Wind Loading of Structures*, Spon Press, 2001.
- [7] T. Stathopoulos, "Wind pressures on flat roof edges and corners," in *Proceedings of the 7th International Conference on Wind Engineering*, Aachen, Germany, July 1987.
- [8] T. Stathopoulos and A. Baskaran, "Turbulent wind loading of roofs with parapet configurations," *Canadian Journal of Civil Engineering*, vol. 15, no. 4, pp. 570–578, 1988.
- [9] G. A. Kopp, C. Mans, and D. Surry, "Wind effects of parapets on low buildings: part 4. Mitigation of corner loads with alternative geometries," *Journal of Wind Engineering and Industrial Aerodynamics*, vol. 93, no. 11, pp. 873–888, 2005.
- [10] C. Blessing, A. G. Chowdhury, J. Lin, and P. Huang, "Full-scale validation of vortex suppression techniques for mitigation of roof uplift," *Engineering Structures*, vol. 31, no. 12, pp. 2936–2946, 2009.
- [11] W. Suaris and P. Irwin, "Effect of roof-edge parapets on mitigating extreme roof suction," *Journal of Wind Engineering and Industrial Aerodynamics*, vol. 98, no. 10–11, pp. 483–491, 2010.
- [12] G. T. Bitsuamlak, W. Warsido, E. Ledesma, and A. G. Chowdhury, "Aerodynamic mitigation of roof and wall corner suction using simple architectural elements," *Journal of Engineering Mechanics-ASCE*, vol. 139, no. 3, pp. 396–408, 2013.
- [13] H. F. Bai, T. H. Yi, H. N. Li, and L. Ren, "Multisensors on-site monitoring and characteristic analysis of UHV transmission tower," *International Journal of Distributed Sensor Networks*, vol. 2012, Article ID 545148, 10 pages, 2012.
- [14] T. H. Yi, H. N. Li, and X. Y. Zhao, "Noise smoothing for structural vibration test signals using an improved wavelet thresholding technique," *Sensors*, vol. 12, no. 8, pp. 11205–11220, 2012.
- [15] T. H. Yi and H. N. Li, "Methodology developments in sensor placement for health monitoring of civil infrastructures," *International Journal of Distributed Sensor Networks*, vol. 2012, Article ID 612726, 11 pages, 2012.
- [16] P. Huang, X. Wang, and M. Gu, "Field experiments for wind loads on a low-rise building with adjustable pitch," *International Journal of Distributed Sensor Network*, vol. 2012, Article ID 451879, 10 pages, 2012.

Research Article

Probabilistic Fatigue Assessment Based on Bayesian Learning for Wind-Excited Long-Span Bridges Installed with WASHMS

Zhi-Wei Chen¹ and Xiao-Ming Wang²

¹ Department of Civil Engineering, Xiamen University, Fujian 361005, China

² Urban System Program, Sustainable Ecosystems, Commonwealth Scientific and Industrial Research Organization (CSIRO), Melbourne, VIC, Australia

Correspondence should be addressed to Zhi-Wei Chen; cezhiwei@xmu.edu.cn

Received 3 July 2013; Accepted 14 August 2013

Academic Editor: Ting-Hua Yi

Copyright © 2013 Z.-W. Chen and X.-M. Wang. This is an open access article distributed under the Creative Commons Attribution License, which permits unrestricted use, distribution, and reproduction in any medium, provided the original work is properly cited.

For long-span bridges located in wind-prone regions, it is a trend to install in situ Wind and Structural Health Monitoring System (WASHMS) for long-term real-time performance assessment. One of the functions of the WASHMS is to provide information for the assessment of wind-induced fatigue damage. Considering the randomness of wind, it is more reasonable to describe wind-induced fatigue damage of bridge in a probabilistic way. This paper aims to establish a probabilistic fatigue model of fatigue damage based on Bayesian learning, and it is applied to a wind-excited long-span bridge installed with a WASHMS. Wind information recorded by the WASHMS is utilized to come up with the joint probability density function of wind speed and direction. A stochastic wind field and subsequently wind-induced forces are introduced into the health monitoring oriented finite element model (FEM) of the bridge to predict the statistics of stress responses in local bridge components. Bayesian learning approach is then applied to determine the probabilistic fatigue damage model. The Tsing Ma suspension bridge in Hong Kong and its WASHMS are finally utilized as a case study. It shows that the proposed approach is applicable for the probabilistic fatigue assessment of long-span bridges under random wind loadings.

1. Introduction

To meet social and economic needs of the community for efficient and convenient transportation systems, many long-span bridges have been built throughout the world, and the super long suspension bridges with main span length beyond 3000 meters are also under consideration. They become more flexible and susceptible to strong winds as their span length increases. Long-span bridges in wind-prone regions suffer considerable buffeting-induced vibration, which appears within a wide range of wind speeds and lasts for almost the whole design life of the bridge. Frequent occurrence of the buffeting may cause fatigue damage of steel girders or other structural members of the long-span bridge.

To protect such immense capital investments and ensure user comfort and bridge safety during the serviceability stage, structural health monitoring systems (SHMSs) have been installed on bridges to monitor their integrity, durability, and reliability. According to Ko and Ni [1], the main objectives of

long-term SHMSs are (i) the validation of design assumptions and parameters and the potential improvement of design specifications and guidelines for future similar structures; (ii) the detection of anomalies in loading and responses and possible damage or deterioration at an early stage to ensure structural and operational safety; (iii) the provision of real-time information for safety assessments immediately after disasters and extreme events; (iv) the provision of evidence and instructions for planning and prioritizing bridge inspection, rehabilitation, maintenance, and repair; (v) the monitoring of repairs and reconstruction with the view of evaluating the effectiveness of maintenance, retrofit, and repair works; and (vi) the generation of large amounts of in situ data for cutting-edge bridge engineering research, such as wind- and earthquake-resistant designs, new types of structures, and smart material applications.

Nowadays, many countries around the world have recognized the significance of implementing long-term SHMSs for long-span bridges. Many long-span bridges with spans

of 100 m or longer in Europe [2, 3], the United States [4, 5], Canada [6, 7], Japan [8], South Korea [9, 10], China [11–15], and other countries have been instrumented with long-term monitoring systems. In the past decade, significant progress has been made in sensing technology, and kinds of innovative sensing systems such as fiber optic sensors, wireless sensors, and global positioning system (GPS) are now becoming commercially available [16–20]. A sensing system is essential for realizing structural health monitoring of bridges. Given that there are tens of thousands of components in a large-scale civil structure, determination of critical locations to damage [21, 22] and optimal sensor placement [23–25] are vital for an effective structural health monitoring system.

Currently, many works have been carried out in regard to traffic-induced fatigue damage of steel bridges [26], but there has been very limited research on buffeting-induced fatigue damage of long-span bridges [21, 27, 28]. Li et al. [29] used the strain data recorded by the wind and structural health monitoring system (WASHMS) installed on the Tsing Ma Bridge to assess fatigue damage of the structural members at the strain gauge points for a single typhoon. Liu et al. [30] analyzed the buffeting-induced stresses in a long suspension bridge based on a structural health monitoring oriented FEM of the Tsing Ma Bridge. Subsequently, Xu et al. [21] assessed the long-term buffeting-induced fatigue damage in a long suspension bridge. However, most of them use the deterministic methods without considering the effects of uncertainties in both external loadings and structural parameters. In reality, uncertainties exist in external loadings, structural modeling, and structural parameter in fatigue assessment. Furthermore, few literatures use probabilistic approaches to assess fatigue damage of long-span bridges under stochastic wind loading. To investigate the failure probability of wind-induced fatigue damage for a given time epoch at a typical location, it is necessary to develop probabilistic approach for fatigue assessment of wind-excited long-span bridges.

This paper aims to establish a probabilistic fatigue model of fatigue damage based on Bayesian learning, and it is applied to a wind-excited long-span bridge with multiple types of sensors installed on it. Wind information recorded by the WASHMS is utilized to come up with the joint probability density function of wind speed and direction. A stochastic wind field and subsequently wind-induced forces are introduced into the health monitoring oriented-FEM of the bridge to predict the statistics of stress responses in bridge structural members. Bayesian learning approach is then applied to determine the probabilistic fatigue model. The Tsing Ma suspension Bridge in Hong Kong and the data recorded by the WASHMS installed in the bridge are finally utilized as a case study.

2. Wind-Induced Critical Stress Analysis

2.1. Long-Span Bridges and WASHMS. For long-span bridges located in wind-prone regions, it is a trend to install WASHMS on the bridge for long-term real-time bridge performance assessment. The Tsing Ma suspension Bridge in Hong Kong is an example among these bridges. It is a suspension bridge with an overall length of 2,160 m and a

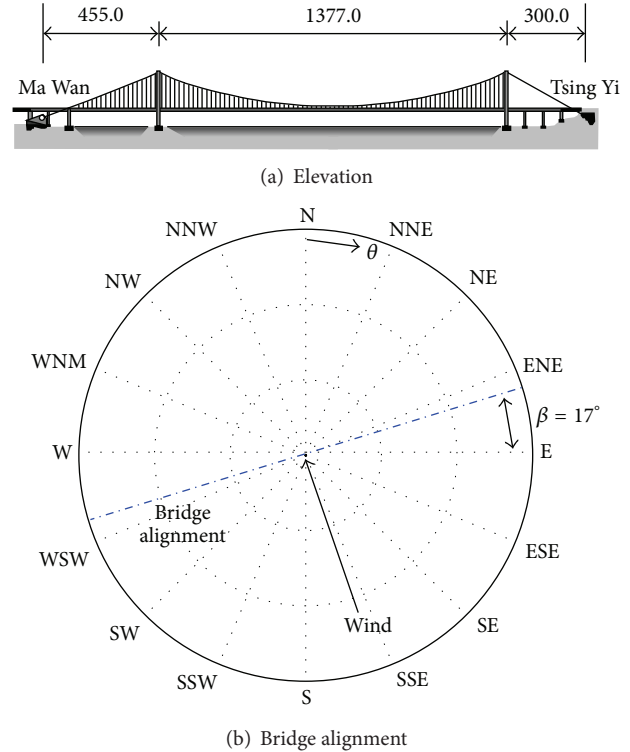


FIGURE 1: Tsing Ma Bridge in Hong Kong.

main span of 1,377 m between the Tsing Yi Tower in the east and the Ma Wan tower in the west (see Figure 1(a)). The bridge deck carries a dual three-lane highway on the top deck and two railway tracks and two carriageways on a lower level within the bridge deck. The alignment of bridge deck deviates for 17° counterclockwise from the east-west axis (see Figure 1(b)).

To monitor the functionality, safety, and integrity of the bridge, the WASHMS was installed in 1997 and is operated by the Highways Department of the Government of the Hong Kong Special Administrative Region [31]. Its integrated architecture is composed of five systems: (1) sensory, (2) data acquisition and transmission, (3) data processing and control, (4) bridge health evaluation, and (5) inspection and maintenance systems [31]. The sensory system comprises 300 sensors installed in the bridge, which include anemometers, temperature sensors, corrosion cells, hygrometers, barometers, rain-fall gauges, weigh-in-motion stations, digital video cameras, weldable foil-type strain gauges, servo-type accelerometers, level sensing stations, displacement transducers, tiltmeters, buffer sensors, bearing sensors, and tension magnetic gauges. The layout of the sensory and data acquisition systems on the Tsing Ma Bridge is illustrated in Figure 2. The sensors are grouped into four categories to monitor the environmental, traffic, global, and local conditions of the bridge.

2.2. Joint Probability Density Function of Wind Speed and Direction. Compared with the approach which considers the mean wind speed only, it is better to establish a joint probability distribution function of wind speed and wind direction in

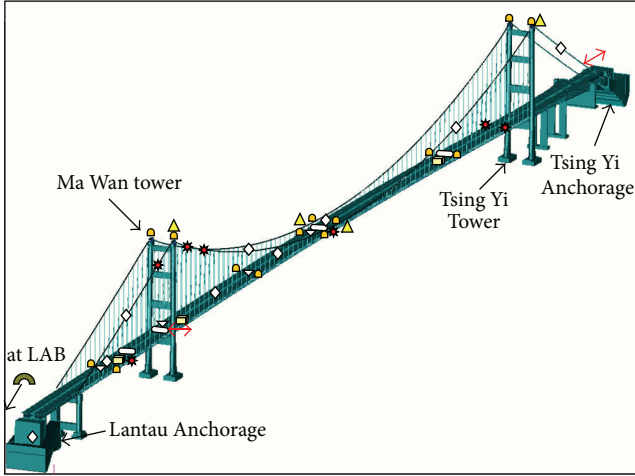


FIGURE 2: Layout of the sensory and data acquisition systems [32].

the assessment of wind-induced fatigue damage. Wind speed and wind direction are chosen as two coefficients considered in the probabilistic model of wind loading. To build the model, it requires a great amount of field measurement wind data collected at the bridge site. In this study, 19,775 hourly monsoon wind records of hourly mean wind speed and direction within the period between January, 1, 2000 and December, 31, 2005 from the anemometer installed on the top of the Ma Wan tower are used to find the joint probability density function of hourly mean wind speed and direction [21]. It was assumed that (1) the distribution of the component of wind speed for any given wind direction follows the Weibull distribution and (2) the interdependence of wind distribution in different wind directions can be reflected by the relative frequency of occurrence of wind. Consider

$$P(U, \Phi) = \int_0^U f(u | \phi) \left[\int_0^\Phi f(\phi) d\phi \right] du, \quad (1)$$

$$f(u | \phi) = \frac{k(\phi)}{\lambda(\phi)} \left(\frac{u}{\lambda(\phi)} \right)^{k(\phi)-1} \exp \left[- \left(\frac{u}{\lambda(\phi)} \right)^{k(\phi)} \right]$$

in which ϕ is the wind direction ($0 \leq \phi \leq 2\pi$), u is the wind speed, $f(\phi)$ is the probability density function of wind direction ϕ , $f(u | \phi)$ is the conditional density function of u at any given ϕ , $k(\phi)$ and $\lambda(\phi)$ are the shape and scale parameters of Weibull distribution and were estimated using wind data recorded at the bridge site.

The 19,775 hourly monsoon records were classified into 16 sectors of the compass with an interval of $\Delta\phi = 22.5^\circ$ according to the hourly mean wind direction (see Figure 1(b)). In each sector, mean wind speed was further divided into 16 ranges from zero to 32 m/s with an interval of $\Delta u = 2$ m/s, leading to a total of 256 cells. The detail information on the joint probability density function can be found in [21].



FIGURE 3: 3D finite element model of Tsing Ma Bridge.

2.3. Wind-Induced Critical Stress Analysis. Strain gauges for strain measurements in the WASHMS installed on a long span bridge are always limited. Not all stress responses of local structural components can be directly monitored. To facilitate the complete assessment of bridge safety, a structural health monitoring oriented FEM is required for a long span bridge so that stresses/strains in all important bridge components can be directly estimated. In this regard, Liu et al. [30] established a complex structural health monitoring (SHM) oriented-FEM for the Tsing Ma Bridge with significant modeling features of the bridge deck included for the good replication of geometric details of the as-built decks (see Figure 3). The proposed SHM oriented-FEM was also updated using the measured first 18 natural frequencies and mode shapes of the bridge. It turned out that the updated FEM could provide comparable and reliable structural dynamic modal characteristics.

Based on the established structural health monitoring oriented FEM, Liu et al. [30] further proposed a numerical simulation for wind-induced stress analysis of long-span bridges. Significant improvements were demonstrated with the fact that the effects of the spatial distribution of both buffeting forces and self-excited forces on a bridge deck structure were taken into account, and the local strain/stress, which is prone to cause local damage, was able to be directly estimated. The field measurement data including wind, acceleration, and stress recorded by the WASHMS installed on the Tsing Ma Bridge during Typhoon York were analyzed and compared with the numerical results to verify, to some extent, the proposed procedure. This procedure will be used to find out wind-induced critical stress responses as the first step in the probabilistic wind-induced fatigue damage model proposed in this study.

There are a total of 15,904 beam elements used to model the Tsing Ma Bridge deck. Wind-induced critical stress analysis is carried out by considering a 15 m/s mean wind speed perpendicular to the bridge axis from the south for one hour. By comparing the maximum values and the standard deviations of all stress time histories, the cross sections of the bridge deck at the Tsing Yi Tower and Ma Wan tower are identified as the most critical sections. The six elements of no. 34417 and 38417, 40903 and 48917, 58417, and 59417 in the cross section of the bridge deck at the Tsing Yi Tower (CH25000 in Figure 1(a)) are critical members (see Figure 4). Figure 5 shows one-hour stress time history of the element 40903 under a 15 m/s mean wind speed perpendicular to the bridge axis from the south.

3. Probabilistic Cumulative Fatigue Damage Model

Considering the randomness of wind speed and direction, it is more reasonable to describe wind-induced fatigue

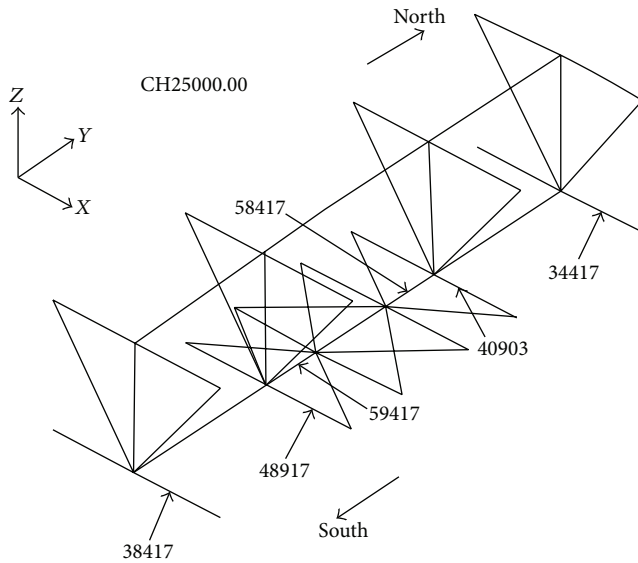


FIGURE 4: Critical deck section and critical elements identified.

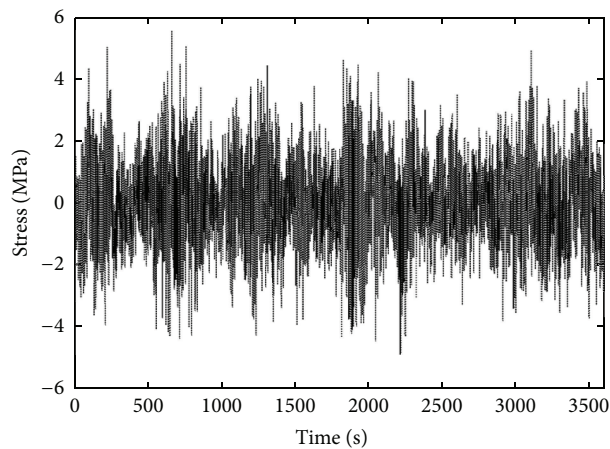


FIGURE 5: Hourly stress time history of element 40903.

damage of a large-scale bridge in a probabilistic way. To establish a probabilistic cumulative fatigue damage model, several steps of work should be carried out. In the first step, the hourly mean wind in a given returned period is drawn out to compose a stochastic process using the Monte Carlo simulation method based on the joint probabilistic distribution of mean wind speed and direction. Then, the stochastic process of hourly wind-induced fatigue damage is developed based on the stochastic process of hourly mean wind and the hourly fatigue damage database. Finally, the probabilistic cumulative fatigue damage model is established using the Bayesian learning method.

3.1. Stochastic Process of Hourly Normal Mean Wind Speed. The wind return period is selected as 120 years in this study. The hourly mean wind speed and direction in 120 years are considered to be stochastic processes, which are composed of $120 \times 365 \times 24$ sets of hourly mean wind speed and direction. Two-step Monte Carlo simulation method is utilized to draw

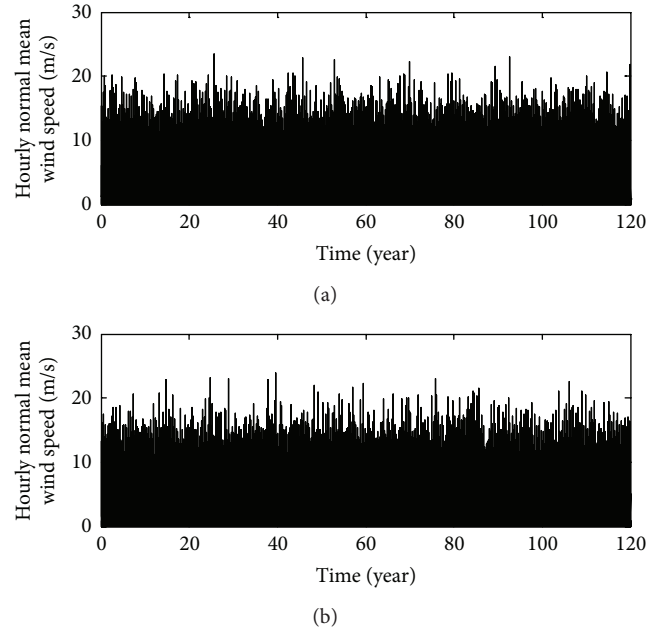


FIGURE 6: Two samples of hourly normal mean wind speed in 120 years.

out the hourly mean wind speed and direction based on the joint probability density function of wind speed and direction. To avoid the appearance of the abnormal mean wind speed, the maximum wind speed for a given wind direction should be given for a designated wind return period in the Monte Carlo simulation [21].

After the hourly mean wind speed and direction are generated at the average bridge deck level in 120 years, the hourly normal mean wind speed (mean wind component perpendicular to bridge axis) could be calculated based on the fact that the alignment of bridge deck deviates for 17° in counterclockwise from the east-west axis (see Figure 1(b)). As a result, the stochastic processes of hourly normal mean wind speed can be determined. A total of 200 samples of hourly normal mean wind speeds are general for a return period of 120 years, and two of them are plotted in Figure 6.

3.2. Stochastic Process of Hourly Wind-Induced Fatigue Damage. Based on the simulated hourly wind-induced stress responses of critical members, wind-induced hourly fatigue damages could be estimated according to the recommended methods in the British Standard BS5400 [33]. The type of welded connection for the elements 34417, 38417, 40903, and 48917 are classified as F2, and the type of welded connection for the elements 58417 and 59417 is classified as F. In the following, the wind-induced hourly fatigue damage and cumulative fatigue damage are presented for the element 40903 only.

The hourly wind-induced fatigue damage mentioned above is estimated for different normal mean wind speeds ranging from 5 m/s to 30 m/s with an interval of 5 m/s in this study. The linear interpolation is used for other wind speeds to form an hourly fatigue damage database. To consider the effect of wind terrain, wind over the overland fetch and the

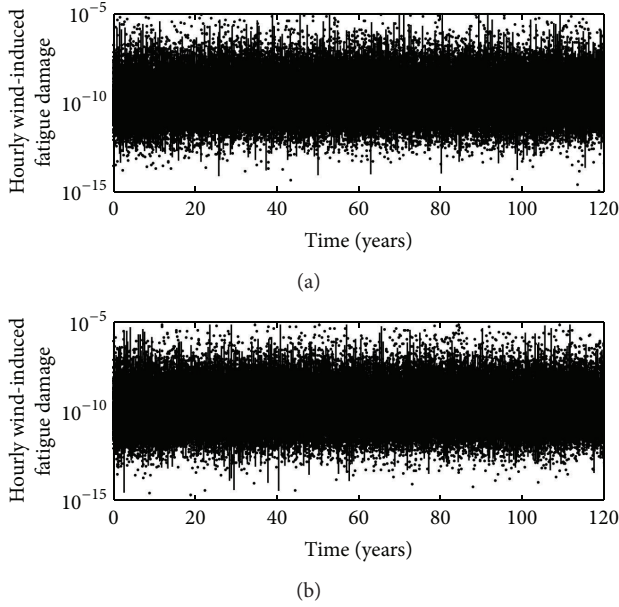


FIGURE 7: Two samples of hourly wind-induced fatigue damage in 120 years.

open-sea fetch on the bridge site are respectively assessed to have two hourly fatigue damage databases. To obtain the stochastic process of hourly wind-induced fatigue damage, the hourly fatigue damage databases are applied to each sample of hourly normal mean wind speed (see Figure 6) to have the corresponding sample of hourly wind-induced fatigue damage as depicted in Figure 7. Fatigue damage induced in the each hourly stress time history is calculated using Miner's rule and British *S-N* curves in BS [33]. Fatigue damage is a nondimensional parameter, which begins with zero and accumulates along with each load cycle applied to bridge structures, and fatigue failure occurs when cumulative fatigue damage is equal to one. It can be seen that the samples of hourly wind-induced fatigue damage are different from each other owing to the random nature of wind speed and direction. A probabilistic model of cumulative fatigue damage is therefore required for structural reliability analysis.

3.3. Probabilistic Cumulative Fatigue Damage Model. Based on the linear fatigue damage cumulative rule, each sample of hourly wind-induced fatigue damage yields a damage index for a given time period such as 120 years. Such a damage index is a random variable. To determine its probabilistic distribution or probabilistic model of cumulative fatigue damage, the model parameters should be estimated from samples. The traditional model parameter estimation methods assume model parameters to be deterministic and all samples come from the same probabilistic model. This is not definitely suitable for the current study because the WASHMS provides new measurement data year after year. The probabilistic cumulative fatigue damage model should be updatable. In this regard, Bayesian parameter learning approach is adopted for the parameter estimation in this study. Bayesian parameter learning has its advantages over traditional methods, allowing the model parameters considered to be random

variables following probability distributions, facilitating the updating process as new samples introduced to modify the prior model, and offering the estimation of the sample size in a statistical view for reliable parameters estimation.

Neapolitan [34] presented the Bayesian parameter learning method for one random variable with a normal distribution. The initial parameters of the distribution include the mean value μ and the absolute variance $\beta = \sum_{i=1}^{\alpha} (\hat{x}^i - \mu)^2$, estimated from the initial sample set $\{\hat{x}^1, \hat{x}^2, \dots, \hat{x}^{\alpha}\}$. α is the size of initial sample. For a new sample set $d = \{x^{(1)}, x^{(2)}, \dots, x^{(M)}\}$, the parameters can be updated in the following way:

$$\begin{aligned} \bar{x} &= \frac{\sum_{h=1}^M x^{(h)}}{M}; & s &= \sum_{h=1}^M (x^{(h)} - \bar{x})^2, \\ \mu^* &= \frac{\alpha\mu + M\bar{x}}{\alpha + M}; & \beta^* &= \beta + s + \frac{\alpha M(\bar{x} - \mu)^2}{\alpha + M}, \\ \alpha^* &= \alpha + M, \end{aligned} \quad (2)$$

where μ^* and β^* are the updated model parameters, and α^* is the size of all samples. The mean and standard deviation of the normal distribution after one step updating become

$$\hat{\mu} = \mu^*; \quad \hat{\sigma}^2 = \frac{\beta^*}{\alpha^*}. \quad (3)$$

It is important to know how many samples are required to have reasonably accurate parameter estimation. Another parameter r , ($r = 1/\sigma^2$, where σ is a standard deviation), following a gamma distribution, is introduced for determination of sample size. The ratio S of the standard deviation to the mean of the parameter r can be derived as

$$S = \frac{\text{Std}(r)}{E(r)} = \sqrt{\frac{2}{\alpha^*}}. \quad (4)$$

It can be seen that the ratio S depends on the size of sample α^* only. With the increase of sample size, the ratio S decreases and the parameter r tends to be constant. By assuming the ratio S being 0.1, the corresponding sample number required is 200.

The 200 samples are used in this study for estimating the parameters in the probabilistic cumulative fatigue damage model. In consideration of the nonnegative character of cumulative fatigue damage, the cumulative fatigue damage index $\{X_1, X_2 \dots X_N\}$ is assumed to follow the log-normal distribution. Thus, the logarithmic damage index $\{\log(X_1), \log(X_2) \dots \log(X_N)\}$ follows the normal distribution. The parameters of the logarithmic damage index $\{\log(X_1), \log(X_2) \dots \log(X_N)\}$ of the normal distribution could be estimated by the Bayesian parameter learning approach. With the parameters of logarithmic damage index λ_X and ζ_X , the mean value μ_X and standard deviation σ_X of the damage index are obtained [35] as follows:

$$\begin{aligned} \mu_X &= \exp\left(\lambda_X + \frac{1}{2}\zeta_X^2\right), \\ \sigma_X^2 &= \mu_X^2 \left[\exp(\zeta_X^2) - 1\right]. \end{aligned} \quad (5)$$

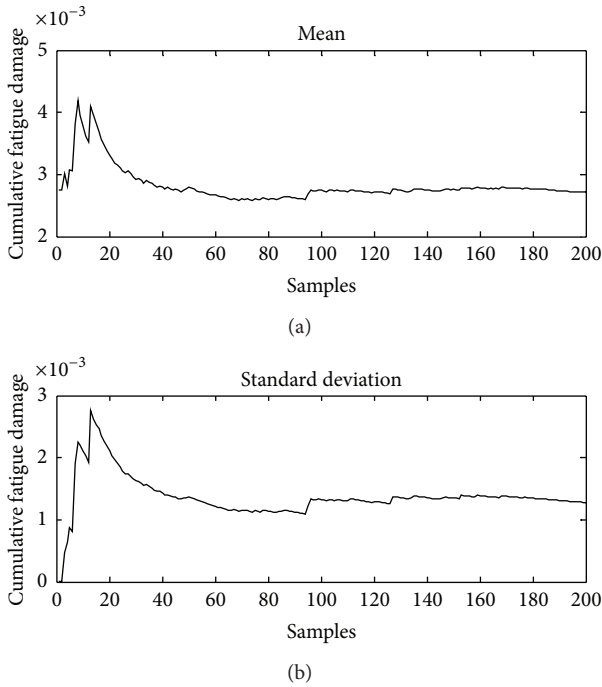


FIGURE 8: Mean and standard deviation of cumulative fatigue damage index.

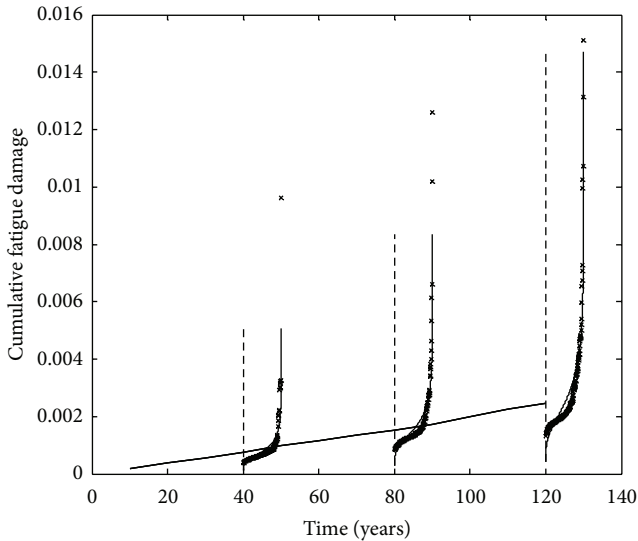


FIGURE 9: Probability distribution function of cumulative fatigue damage.

The resulting mean and standard deviation of the cumulative fatigue damage index for 120 years are displayed in Figure 8 against the size of the samples. It can be seen that when the size of samples is increased to 150, the two parameters become stable already.

To check if the assumption of lognormal distribution is reasonable for cumulative fatigue damage index, the probability distribution function of cumulative fatigue damage index for different time periods, such as 40 years, 80 years, and 120 years, is calculated using the proposed model with

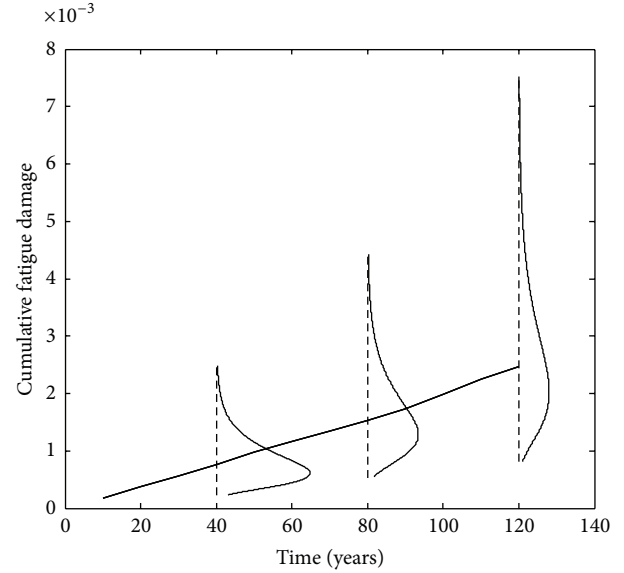


FIGURE 10: Probability density function of cumulative fatigue damage.

updated parameters, and the results are plotted in Figure 9. Meanwhile, the 200 samples are sorted in ascending order, and the probability distribution function is then directly obtained from these samples using the following equation:

$$F_n = \frac{n}{N + 0.5}, \quad (6)$$

where n is the sequence number of samples in ascending order and N is the size of samples. It can be seen from Figure 9 that the samples follow the proposal model well. The probability density function of cumulative fatigue damage index is also calculated using the proposed model with the updated parameters. The resulting density functions are plotted in Figure 10 for different time periods. The updated mean parameters are also plotted in Figure 10 to provide some indication of the fatigue damage index distribution. Both probability distribution functions and the probability density functions indicate that monsoon wind-induced bridge fatigue damage indices are far less than one. The monsoon wind-induced fatigue damage to the bridge is not significant. However, it should be pointed out that the fatigue damage to the bridge caused by typhoon and traffic loading is not considered in this study. It is being proposed to apply the similar procedure to consider typhoon and traffic loading-induced fatigue damage.

4. Conclusions

A probabilistic cumulative fatigue damage model has been established based on the Bayesian learning approach for wind-excited long-span bridges installed with multiple types of sensors for long-term health monitoring. The Tsing Ma Bridge in Hong Kong and the measurement data from its WASHMS have been used as a case study. The results from the case study show that the proposed approach is applicable for

the probabilistic fatigue life assessment of large-scale bridges under random wind loadings. The results also show that monsoon wind-induced fatigue damage to the bridge is not significant because the fatigue damage to the bridge caused by typhoon and traffic loading is not considered in this study. It is being proposed to apply the similar procedure to consider the total fatigue damage caused by a combination of monsoon wind, typhoon wind, and traffic loading.

Acknowledgments

The authors wish to acknowledge the financial supports from the National Natural Science Foundation of China (NSFC-51108395) and the Fundamental Research Funds for the Central Universities (2012121032). Sincere thanks should go to the Highways Department of Hong Kong for providing the authors with the field measurement data. Any opinions and concluding remarks presented in this paper are entirely those of the authors.

References

- [1] J. M. Ko and Y. Q. Ni, "Technology developments in structural health monitoring of large-scale bridges," *Engineering Structures*, vol. 27, no. 12, pp. 1715–1725, 2005.
- [2] F. Casciati, "An overview of structural health monitoring expertise within the European Union," in *Proceedings of the 1st International Conference on Structural Health Monitoring and Intelligent Infrastructure (SHMII-1 '03)*, pp. 31–37, Balkema, Lisse, The Netherlands, November 2003.
- [3] J. M. W. Brownjohn, P. Moyo, P. Omenzetter, and S. Chakraborty, "Lessons from monitoring the performance of highway bridges," *Structural Control and Health Monitoring*, vol. 12, no. 3-4, pp. 227–244, 2005.
- [4] D. J. Pines and A. E. Aktan, "Status of structural health monitoring of long-span bridges in the United States," *Progress in Structural Engineering and Materials*, vol. 4, no. 4, pp. 372–380, 2002.
- [5] M. L. Wang, "State-of-the-art applications in health monitoring," in *Proceedings of the Workshop on Basics of Structural Health Monitoring and Optical Sensing Technologies in Civil Engineering*, pp. 113–142, National Central University, 2004.
- [6] M. S. Cheung, G. S. Tadros, T. Brown, W. H. Dilger, A. Ghali, and D. T. Lau, "Field monitoring and research on performance of the confederation bridge," *Canadian Journal of Civil Engineering*, vol. 24, no. 6, pp. 951–962, 1997.
- [7] A. A. Mufti, "Structural health monitoring of innovative Canadian civil engineering structures," *Structural Health Monitoring*, vol. 1, no. 1, pp. 89–103, 2002.
- [8] S. Sumitro, Y. Matsui, M. Kono, T. Okamoto, and K. Fujii, "Long span bridges health monitoring system in Japan," in *Health Monitoring and Management of Civil Infrastructure Systems*, Proceedings of SPIE, pp. 517–524, Bellingham, Wash, USA, 2001.
- [9] H. M. Koh, J. F. Choo, S. K. Kim, and C. Y. Kim, "Recent application and development of structural health monitoring systems and intelligent structures in Korea," in *Proceedings of the 1st International Conference on Structural Health Monitoring and Intelligent Infrastructure (SHMII-1 '03)*, pp. 99–111, Lisse, The Netherlands, November 2003.
- [10] C. B. Yun, J. J. Lee, S. K. Kim, and J. W. Kim, "Recent R&D activities on structural health monitoring for civil infrastructures in Korea," *KSCE Journal of Civil Engineering*, vol. 7, no. 6, pp. 637–651, 2003.
- [11] H. F. Xiang, "Health monitoring status of long-span bridges in China," in *Proceedings of the Workshop on Research and Monitoring of Span Bridges*, pp. 24–31, 2000.
- [12] J. P. Ou, "The state-of-the-art and application of intelligent health monitoring systems for civil infrastructures in mainland of China," in *Progress in Structural Engineering, Mechanics and Computation*, pp. 599–608, London, UK, 2004.
- [13] K.-Y. Wong, "Instrumentation and health monitoring of cable-supported bridges," *Structural Control and Health Monitoring*, vol. 11, no. 2, pp. 91–124, 2004.
- [14] T. H. Yi, H. N. Li, and M. Gu, "Experimental assessment of high-rate GPS receivers for deformation monitoring of bridge," *Journal of the International Measurement Confederation*, vol. 46, no. 1, pp. 420–432, 2013.
- [15] T. H. Yi, H. N. Li, and M. Gu, "Wavelet based multi-step filtering method for bridge health monitoring using GPS and accelerometer," *Smart Structures and Systems*, vol. 11, no. 4, pp. 331–348, 2013.
- [16] D. A. Grivas and M. Garlock, "Sensing systems for bridges: an assessment of the state-of-the-art," in *Recent Developments in Bridge Engineering*, K. M. Mahmoud, Ed., pp. 269–284, Balkema, Lisse, The Netherlands, 2003.
- [17] S. Sumitro and M. L. Wang, "Sustainable structural health monitoring system," in *Proceedings of the International Workshop on Advanced Sensors, Structural Health Monitoring and Smart Structures*, 2003.
- [18] J. P. Lynch, K. H. Law, A. S. Kiremidjian et al., "Design and performance validation of a wireless sensing unit for structural monitoring applications," *Structural Engineering and Mechanics*, vol. 17, no. 3-4, pp. 393–408, 2004.
- [19] B. F. Spencer Jr., M. E. Ruiz-Sandoval, and N. Kurata, "Smart sensing technology: opportunities and challenges," *Structural Control and Health Monitoring*, vol. 11, no. 4, pp. 349–368, 2004.
- [20] T.-H. Yi, H.-N. Li, and M. Gu, "Characterization and extraction of global positioning system multipath signals using an improved particle-filtering algorithm," *Measurement Science and Technology*, vol. 22, no. 7, Article ID 075101, pp. 1–11, 2011.
- [21] Y. L. Xu, T. T. Liu, and W. S. Zhang, "Buffeting-induced fatigue damage assessment of a long suspension bridge," *International Journal of Fatigue*, vol. 31, no. 3, pp. 575–586, 2009.
- [22] Z. W. Chen, Y. L. Xu, Y. Xia, Q. Li, and K. Y. Wong, "Fatigue analysis of long-span suspension bridges under multiple loading: case study," *Engineering Structures*, vol. 33, no. 12, pp. 3246–3256, 2011.
- [23] M. Meo and G. Zumpano, "On the optimal sensor placement techniques for a bridge structure," *Engineering Structures*, vol. 27, no. 10, pp. 1488–1497, 2005.
- [24] T.-H. Yi, H.-N. Li, and M. Gu, "Optimal sensor placement for structural health monitoring based on multiple optimization strategies," *Structural Design of Tall and Special Buildings*, vol. 20, no. 7, pp. 881–900, 2011.
- [25] T. H. Yi, H. N. Li, and X. D. Zhang, "Sensor placement on Canton Tower for health monitoring using asynchronous-climb monkey algorithm," *Smart Materials and Structures*, vol. 21, no. 12, pp. 1–12, 2012.
- [26] J. W. Fisher, *Fatigue and Fracture in Steel Bridges: Case Studies*, John Wiley and Sons, 1984.

- [27] M. Virlogeux, "Wind design and analysis for the Normandy Bridge," in *Aerodynamics of Large Bridges*, A. Larsen, Ed., vol. 31, pp. 183–216, Balkema, Rotterdam, the Netherlands, 1992.
- [28] M. Gu, Y. L. Xu, L. Z. Chen, and H. F. Xiang, "Fatigue life estimation of steel girder of Yangpu cable-stayed bridge due to buffeting," *Journal of Wind Engineering and Industrial Aerodynamics*, vol. 80, no. 3, pp. 383–400, 1999.
- [29] Z. X. Li, T. H. T. Chan, and J. M. Ko, "Evaluation of typhoon induced fatigue damage for Tsing Ma Bridge," *Engineering Structures*, vol. 24, no. 8, pp. 1035–1047, 2002.
- [30] T. T. Liu, Y. L. Xu, W. S. Zhang, K. Y. Wong, H. J. Zhou, and K. W. Y. Chan, "Buffeting-induced stresses in a long suspension bridge: structural health monitoring oriented stress analysis," *Wind and Structures*, vol. 12, no. 6, pp. 479–504, 2009.
- [31] K. Y. Wong, C. K. Lau, and A. R. Flint, "Planning and implementation of the structural health monitoring system for cable-supported bridges in Hong Kong," in *Nondestructive Evaluation of Highways, Utilities, and Pipelines IV*, Proceedings of SPIE, pp. 266–275, Newport Beach, Calif, USA, March 2000.
- [32] K. Y. Wong, "Stress and traffic loads monitoring of tsing Ma bridge," in *Proceedings of the China Bridge Congress*, Chongqing, China, 2007.
- [33] BS, *BS5400: Part 10, Code of Practice For Fatigue*, British Standards Institution, London, UK, 1980.
- [34] R. E. Neapolitan, *Learning Bayesian Network*, Northeastern Illinois University, Chicago, Ill, USA, 2004.
- [35] H.-S. Ang Alferdo and W. H. Tang, *Probability Concepts in Engineering Planning and Design*, John Wiley and Sons, New York, NY, USA, 1975.

Research Article

Calibration of the Performance of Bidirectional Shaker Table in Centrifuge Model Tests Using Sensor Networks

Hongjun Li,¹ Hong Zhong,² Xuedong Zhang,¹ Yanyi Zhang,¹ and Yujing Hou¹

¹ State Key Laboratory of Simulation and Regulation of Water Cycle in River Basin, China Institute of Water Resources and Hydropower Research, Beijing 100048, China

² Faculty of Infrastructure Engineering, Dalian University of Technology, Dalian 116024, China

Correspondence should be addressed to Hongjun Li; lijunli1995@163.com

Received 20 May 2013; Accepted 18 June 2013

Academic Editor: Hong-Nan Li

Copyright © 2013 Hongjun Li et al. This is an open access article distributed under the Creative Commons Attribution License, which permits unrestricted use, distribution, and reproduction in any medium, provided the original work is properly cited.

Great concern for the safety of high rock-fill dams which are being or to be built in the southwestern area of China with high seismicity is attracted. In order to obtain an in-depth knowledge of the mechanism of seismic-induced damage and reasonable assessment of the seismic design for rock-fill dams, comprehensive dynamic centrifuge tests which can simulate and reproduce strictly the action process of strong earthquake should be conducted. Thus, the performance and accuracy of test device have become a key problem. In the present research, refined calibration of bidirectional shaker table, which can be actuated in both horizontal and vertical directions simultaneously and placed on the swing bucket, was achieved via the distributed sensor network used in a centrifuge model test. The seismic input at the dam site and transmission along the dam axis were obtained by the five pairs of accelerometers. The extensive usage of the sensor networks technology in physical model test in centrifuge has significantly promoted the calibration of performance of bidirectional shaker table and would thus enable further insight into the dynamic response of rock-fill dam.

1. Introduction

Numerous high rock-fill dams with the height of more than 200 m are being or will be built in the southwestern area of China with high seismic risk. Hence, the issue of dam safety against strong earthquake shocks is of great concern [1, 2]. Moreover, during the 1994 Northridge earthquake, the 1995 Kobe earthquake, the 1999 Chi-Chi earthquake, and the 2008 Wenchuan earthquake, field observations on vertical ground motions showed different features from those of the horizontal motions. For example, the records at the reclaimed Port Island in Kobe showed that the ratio of peak vertical to peak horizontal acceleration was as large as 1.5 to 2. This value substantially exceeded 1/2 or 2/3, a value commonly used in engineering practice. On the other hand, the field observations also showed that vertical input motion was significantly magnified at the dam crest. Thus, vertical acceleration has been an issue of debate following recent major earthquakes, but its potential effects are yet to be investigated [3]. Additionally, given that the devastating

damage induced by large earthquakes is infrequent and unrepeatable, it is difficult to obtain the required data to study their effects by postearthquake field investigations [4]. Meanwhile, instrumentation of high rock-fill dam is expensive to maintain over a long period of time that may elapse after major shocks, and the instrumentation may not be placed in the most scientifically available locations [5]. Thus, considering the aforementioned necessity and limitations, the centrifuge model test coupled with bidirectional shaker table is a valuable tool to study the effects of ground shaking on high rock-fill dams without risking the safety of the public [6, 7].

This approach has a potential value in the ongoing monitoring of dynamic response of rock-fill dams subjected to strong earthquakes. However, how to efficiently and accurately obtain the real-time data from dynamic centrifuge model test becomes a key problem [8–10]. Historically, sensor networks have usually been used to obtain real-time data and its duration in the physical events. This knowledge used to improve the performance of the process and its

control brings about several benefits [11–13]. As we know, the automation and control systems for the real-time data via networks including the data acquisition system (DAQ) and the personal computer (PC) can be realized during the complex test processes. Nowadays, the most well-known models in the networks include Foundation Fieldbus, World-FIP, ControlNet, and DeviceNet. They provide efficient networks for the maximization of data changes and increasing flexibility [14, 15]. Moreover, with the development of the computation software, the knowledge of microprocessors and microcontrollers leads to several intelligent instrumentations to enhance the efficiency and stability of networks. Thus, the mode of sensors adopted in the networks can play an important role in conducting the model test [16]. Cheekiralla [17] pointed out that the results which were obtained from the centrifuge model tests via the wireless sensor networks installed in the sealed and high-speed vessel were sometimes difficult to interpret or understand. Thus, considering the high rotating speed and leakproofness of dynamic centrifuge test coupled with bidirectional shaker table, a sensor network constructed by the optical-fiber sensors is suggested. The instrumentation communication can be obtained efficiently and accurately by the connections with optical-fiber cable between the sensor element and data acquisition system (DAQ) [18]. The progress is more significant when the access to the measurement networks takes place by optical-fiber technology, enabling a fast reading of the processes variables or the monitoring of the test conditions.

In the present study, the dynamic model test for a typical rock-fill dam in bidirectional shaker table coupled with a geotechnical centrifuge, which uses practical instrumentation technology and optical cables for data transfer, is carried out. The acquired experience with optical-fiber technology could be used to calibrate the accuracy and performance of the bidirectional shaker table placed on the large centrifuge installed in China Institute of Water Resource and Hydropower Research [19].

2. Dynamic Model Tests in Centrifuge

As we know, the dynamic properties of rock-fill materials exhibit a close correlation with the effective confining stress and stress history. The centrifuge can simulate and reproduce the identical self-weight stresses in the prototype by applying an increasing gravitational acceleration to the physical model. Through refined control of the effective confining stress, accurate data can be obtained, which facilitates accurate solution to complex problems such as earthquake-induced response, liquefaction, and permanent deformation. It is proved that dynamic model tests in centrifuge not only provide data to improve our understanding of mechanisms of dynamic-induced damage but also provide useful proof for verification of numerical models. Additionally, with the development of sensor network for the precise measurement of stress and strains, the quantity and quality of information obtained from dynamic centrifuge tests on models can be substantially increased as a result of the improvement of instrumentation and systems for processing data.

TABLE 1: Physical parameters and scale factors.

Quantity	Unit	Symbol	Scale factor
Length	L	l	N^{-1}
Force	F	f	N^{-3}
Time (consolidation)	T	t	N^{-2}
Time (dissipation)	T	t	N^{-1}
Mass	$FL^{-1}T^2$	m	N^{-3}
Stress	FL^{-2}	σ	1
Strain	—	ϵ	1
Acceleration	LT^{-2}	a	N
Displacement	L	s	N^{-1}
Elastic modulus	FL^{-2}	E	1

For in-depth research into geotechnical problems, the physical model test is regarded as an important tool for its convenience and practical applicability. Sophisticated characteristics of the prototype can be well represented by the model. In practice, the smaller the model is, the more difficulty is involved in the manufacture and instrumentation process. The accuracy of the test results can be affected by many other factors, such as properties of materials, model design, loading techniques, measurement methods, and recording of results. More importantly, the models must be designed and examined in accordance with the laws of similarity between them and the prototypes. The laws of similarity are based on the modelling theory and dimensional analysis of the physical phenomenon involved. Scale factors for independent parameters are chosen based on the uniform factor. Given that the phenomena observed in the models reflect those of the prototype, it is necessary to meet the similarity requirements. Geometric similarity is easy to be achieved, but full similarity concerning all physical quantities involved is difficult to attain so far. In such cases, it is necessary to justify the differences, checking their influences on parameters and on the results.

The choice of materials in a model test must consider stress limits, stiffness, rupture mechanisms, the influence of temperature and humidity, and loading speed as well as size and form. However, it is a benefit that, in the centrifuge model test, unit scale of stress can be achieved by using the same materials as in the prototype. The success of experimental program mainly depends on the precision and reliability of measurements. In order to reach the same precision for tests as in the prototype, uniform scale factor must be applied to instruments in model simulations. The accuracy of model tests can be improved with the use of statistical analyses in data interpretation and appropriate instrumentation. Model instrumentation includes identifying the quantities to be measured and selecting measurement sensors and their installation and calibration processes. Table 1 presents a list of the main physical parameters and scale factors between model and prototype involved in the dynamic centrifuge model.

In general, the study of high rock-fill dam subjected to strong earthquake in actual scale is impractical. Thus, dynamic centrifuge test is an important tool to reveal



FIGURE 1: Bidirectional shaker table in the centrifuge.

the response of high rock-fill dams when subjected to real-time input motion, which can be reproduced by a small-scale model dam with near homogeneous condition in terms of dynamic parameters. Dynamic tests in centrifuge, especially those that deal with the effect of vertical accelerations on the geotechnical model, have never been developed so far for the difficulties and huge costs. In the study of rock-fill dam subjected to horizontal and vertical acceleration using reduced physical models in centrifuge, the stress level, dimensions, and geometry of model require special attention. Considering the seepage characteristic of rock-fill materials, the pore-pressure dissipation is not considered. Additionally, in order to reproduce the stress level and stress history existing in a rock-fill dam using a centrifuge, a special apparatus enabling the simulation of construction process and normal operation for the dam under increased gravity accelerations appears as an alternative. The centrifuge in IWHR (China Institute of Water Resource and Hydropower Research 2012), which has been established in combination of a bidirectional shaker table (with both horizontal and vertical actuators), has been used mainly for academic research purpose. It is certainly a promising tool for technological innovations in the geotechnical earthquake engineering.

3. Description of Bidirectional Shaker Table in Centrifuge

An R-500B bidirectional shaker table to use with a large geocentrifuge, which can further the research for dynamic response analysis of large geotechnical structures such as rock-fill dams, was established in IWHR in 2012, as shown in Figure 1. It is noted that the coupled horizontal and vertical actuators are adopted in the bidirectional shaker table. The R-500B shaker table consists of a swing basket for the centrifuge that is isolated from the centrifuge arm via 8 elastomeric pads on 8 high-strength 100 mm diameter steel studs. This isolation limits the dynamic forces transmitted from the table operation to the centrifuge arm.

The bidirectional shaker table is located inside an outer frame included in the swing basket. The table is designed to move in both the horizontal and vertical directions simultaneously using laminated rubber bearings. The vertical

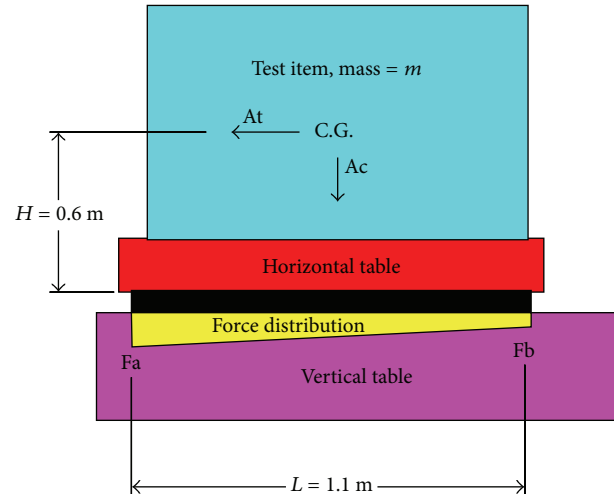


FIGURE 2: The operational system of bidirectional shaker table.

table is an aluminum plate weldment. It is driven by the vertical actuator (A_c) reacting against the base of the outer steel frame. The horizontal table is a single aluminum plate supported by laminar bearings on top of the vertical table. It is driven by the horizontal actuator (A_t) acting against the outer steel frame. The horizontal actuator is connected to the horizontal table using a combined laminated and precompressed flexure bearing that allows the horizontal table to move in the desired biaxial manner. The test item is mounted on the top of the horizontal table. Figure 2 shows the operation of the bidirectional shaker table in the centrifuge room. The system has been designed for a safety factor of 2.5 when operating at a maximum acceleration of 80 g.

Besides, the highly configurable and powerful LabVIEW-National Instruments technology which consists of a data acquisition system and ANCO-Dance system is adopted in the centrifuge model test via the sensor network. Numerous data such as displacement, strain, stress, and acceleration can be obtained by the combined system, as shown in Figure 3.

4. Dynamic Centrifuge Model Tests with Sensor Networks

The centrifuge has been employed for experiments on rock-fill dams. In the current research, the performance of the bidirectional shaker table in centrifuge model tests is calibrated using sensor networks. It is a special and innovative dynamic test apparatus, which can be actuated in both the horizontal and vertical directions simultaneously. The calibrations of the apparatus were conducted for accelerations below 40 g. The test model and distribution of optic-fiber accelerometers are shown in Figure 4. Table 2 presents the calibration coefficient of accelerometers. The soil particle composition of rock-fill material used in the test is listed in Table 3.

The soil used for the model of rock-fill dam was acquired from the Zipingpu concrete face rock-fill dam in Sichuan, China. The soil has a specific gravity of 2.19. Figure 5 shows

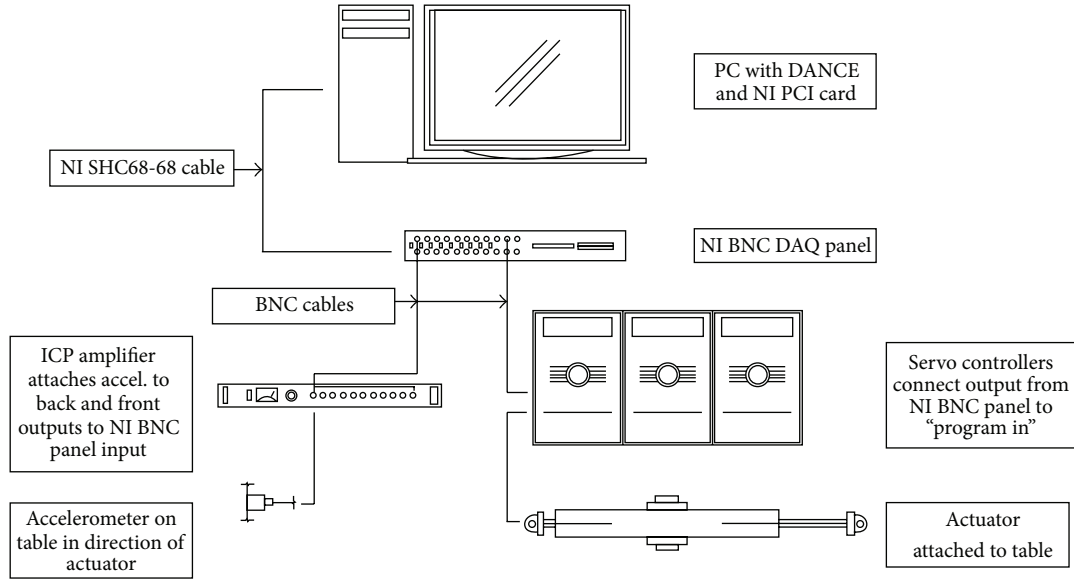


FIGURE 3: The data acquisition system in IWHR centrifuge (ANCO-Dance user manual [20]).

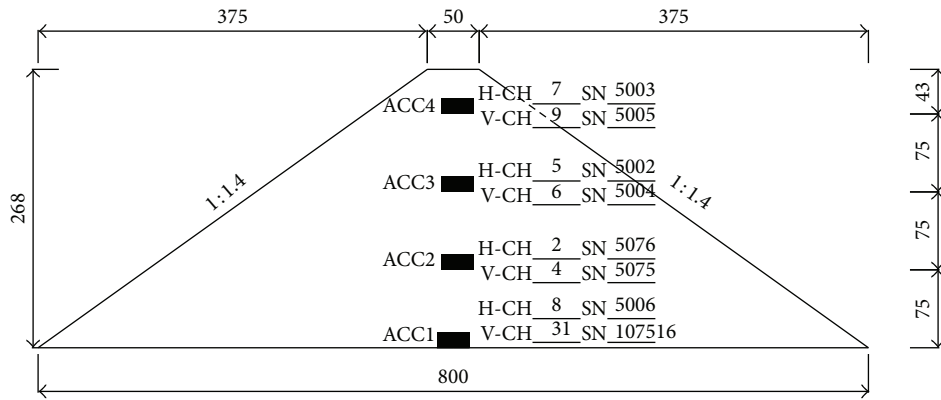


FIGURE 4: Model layout and instrumentation (unit: mm).

TABLE 2: The description of accelerometers.

Name	Channel	Serial number	Measure direction	Calibration coefficient (m/s ²)
ACC0	1	5016	Vertical	922.51
	3	5015	Horizontal	960.3
ACC1	31	107516	Vertical	96.81
	8	5006	Horizontal	942.31
ACC2	4	5075	Vertical	1000
	2	5076	Horizontal	915.89
ACC3	6	5004	Vertical	970.30
	5	5002	Horizontal	1010.31
ACC4	9	5005	Vertical	1010.31
	7	5003	Horizontal	980



FIGURE 5: Photo of preearthquake test model.

the photo of the dam model on the bidirectional shaker table. The models were symmetric with an initial height of 268 mm.

They were constructed by sequentially placing the five horizontal layers of soil on the table. The soil was compacted to reach the designated dry density. Five pairs of miniature accelerometers were buried in the model to monitor and

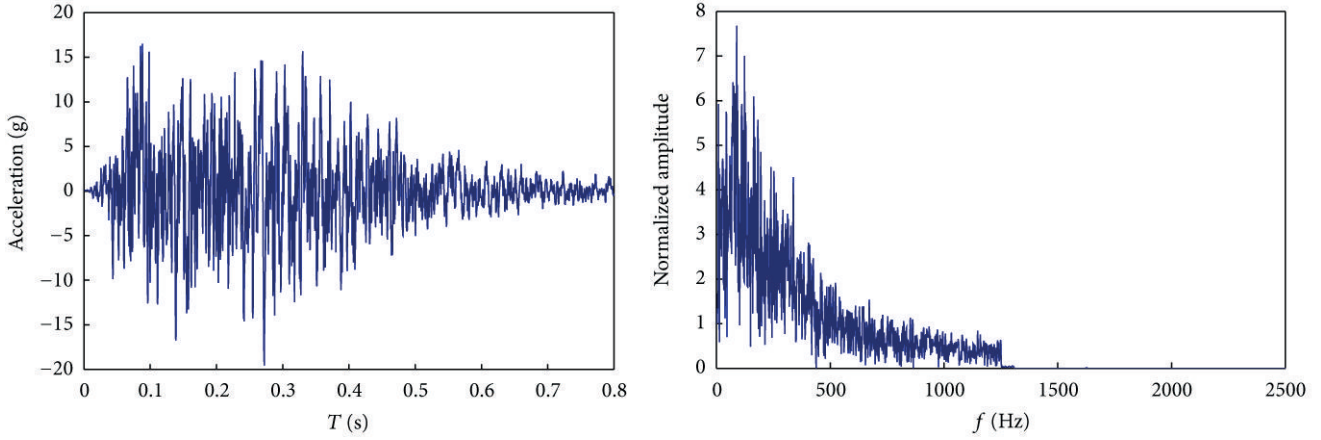


FIGURE 6: Input motion and Fourier amplitude spectrum.

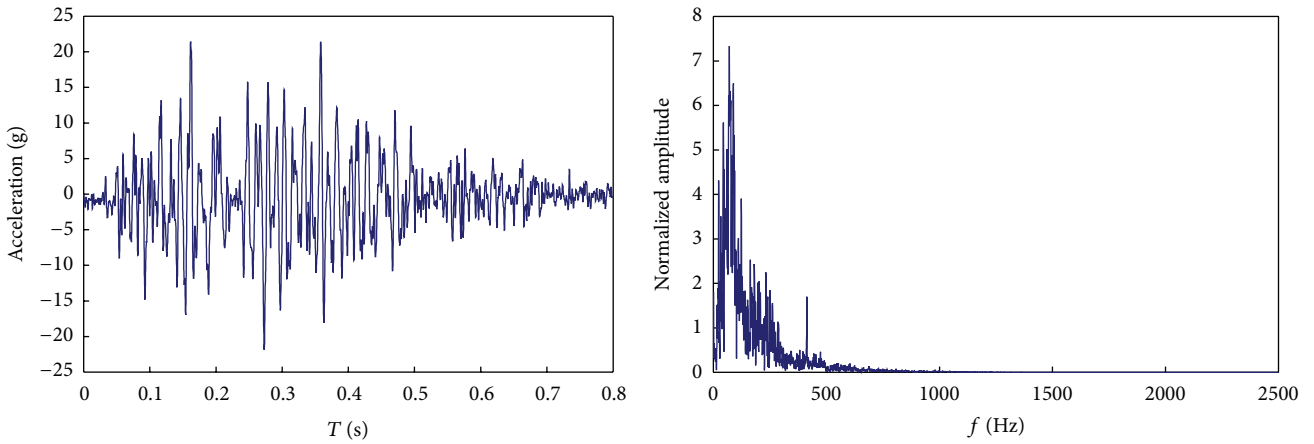


FIGURE 7: Time history of horizontal acceleration recorded by ACC0 and Fourier amplitude spectrum.

TABLE 3: The grading of rock-fill materials.

Number	Particle diameter/mm	Mass/kg
1	5~10	26.7
2	2~5	17
3	1~2	8.5
4	<1	17.8
Total mass		70

TABLE 4: Cases of dynamic model test.

Cases	Centripetal acceleration/g	Horizontal acceleration/g	Vertical acceleration/g
1	40	20	0
2	40	20	20

record the dynamic response in the dam (Figure 4), and the optic-fiber sensors were numbered as ACC0 (located on the shaker table), ACC1, ACC2, ACC3, and ACC4, respectively. Each pair of sensors can measure the horizontal and vertical dynamic responses of the dam simultaneously. After the installation of the model on the centrifuge machine, the speed of the centrifuge was slowly increased to reach a desirable centripetal acceleration of about 40 g in 15 min. At this moment, an acceleration time history recorded in a real earthquake scaled to the amplitude of 20 g (corresponding to 0.5 g for the prototype) was triggered. The duration of

the input motion is 0.8 second and the time increment is 0.0002 second. The time history of input motion and Fourier amplitude spectrum are shown in Figure 6. In this study, the same input motion is used in the horizontal and vertical directions. Considering the high permeability of rock-fill materials, the accumulation and dissipation of excess pore pressure were neglected. For in-depth comparison, two model tests which were actuated in two different modes were performed for this rock-fill dam to reveal the performance of the bidirectional shaker table in centrifuge, as listed in Table 4. Additionally, one refined software application, which is formulated based on LabVIEW package, was developed to record the test data.

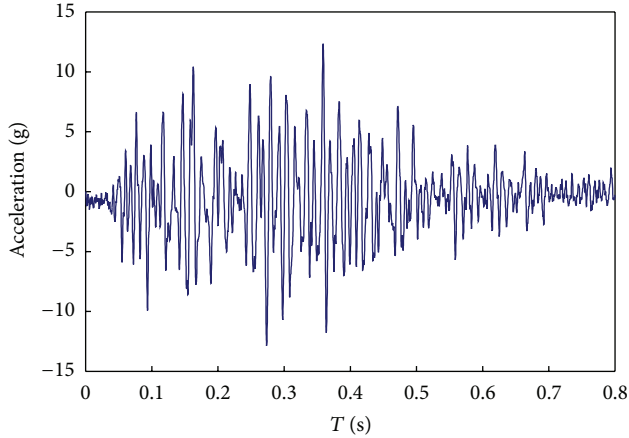


FIGURE 8: Time history of horizontal response acceleration recorded by ACC1.

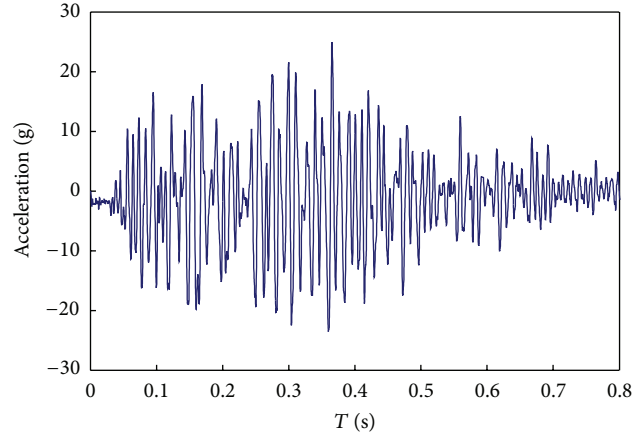


FIGURE 10: Time history of horizontal response acceleration recorded by ACC3.

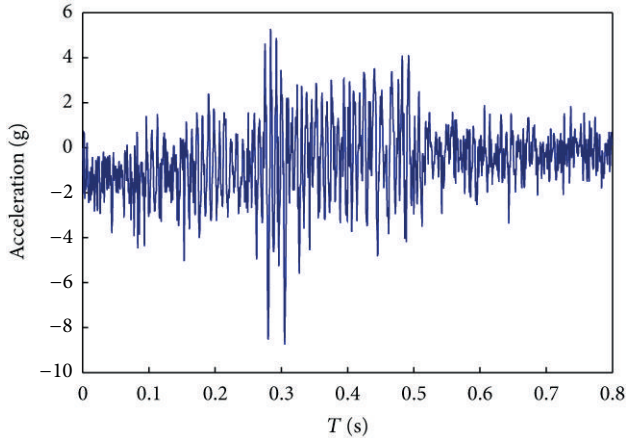


FIGURE 9: Time history of horizontal response acceleration recorded by ACC2.

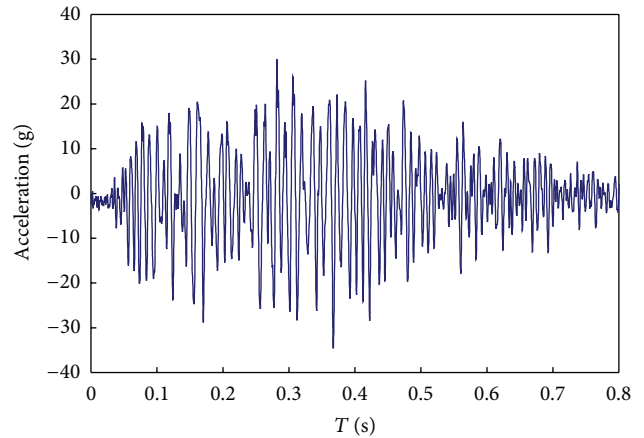


FIGURE 11: Time history of horizontal response acceleration recorded by ACC4.

4.1. Model Dam Subjected to Unidirectional Earthquake (Case 1). Figures 7, 8, 9, 10, and 11 show the time histories of the response acceleration (model scale) and their Fourier amplitude spectra during the simulated earthquake along the height of the rock-fill dam. The maximum input seismic acceleration on the bottom of the container was 20 g, with some high-frequency contents as illustrated by its corresponding Fourier amplitude spectrum. Good consistency of amplitude and Fourier spectrum between the input motion and the record on the accelerometer ACC0-H located on the shaker table can be obtained, with only minor difference observed. Besides that, the accelerometer ACC4-H in the upper portion, located at 43 mm below the top of the embankment, recorded a peak acceleration of 35 g. The amplification factor on the dam crest in the horizontal direction is about 1.6 times. From the recordings by the accelerometers ACC2-H and ACC3-H, it is noted that the corresponding amplitude of response acceleration decreased at the middle of the dam. This phenomenon has also been found from the in situ field

monitoring and the results from the numerical analysis of rock-fill dams.

4.2. Model Dam Subjected to Bidirectional Earthquake (Case 2). Figures 12, 13, 14, 15, 16, and 17 provide the time histories of response acceleration in the horizontal and vertical directions as well as the corresponding Fourier spectra. The response acceleration was measured by the distributed accelerometers along the dam axis. The measured maximum input acceleration from the pairs of accelerometer ACC0 was 20.5 g in the horizontal direction and 20.7 g in the vertical direction, which is very close to the design that the model be shaken in the horizontal and vertical directions with the same magnitude of acceleration (20 g). From the recordings by the accelerometers along the dam axis, the peak acceleration in the horizontal direction decreased by 20% at ACC1-H but increased 45% at ACC4-H, lower than that measured in the case 1 test. The similar trend of variations in the acceleration was also found in the vertical direction. Figure 18 shows the distribution of amplitude of measured accelerations in

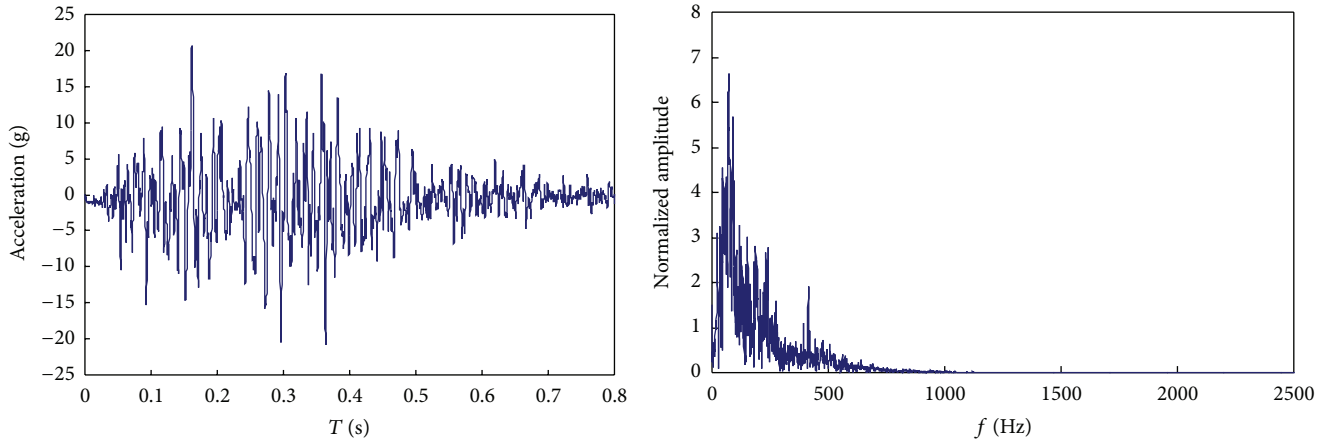


FIGURE 12: Time history of horizontal acceleration recorded by ACC0 and Fourier amplitude spectrum.

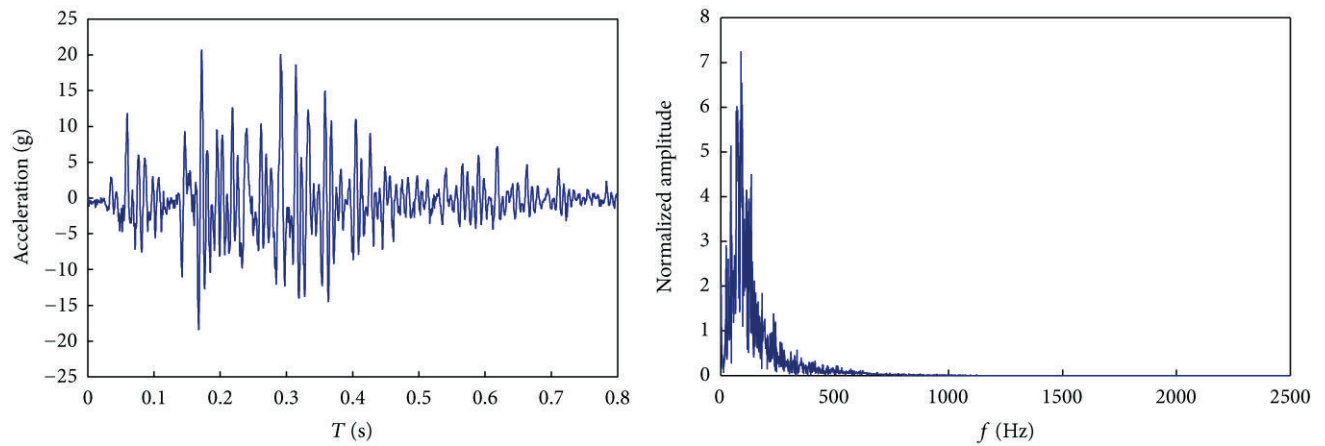


FIGURE 13: Time history of vertical acceleration recorded by ACC0 and Fourier amplitude spectrum.

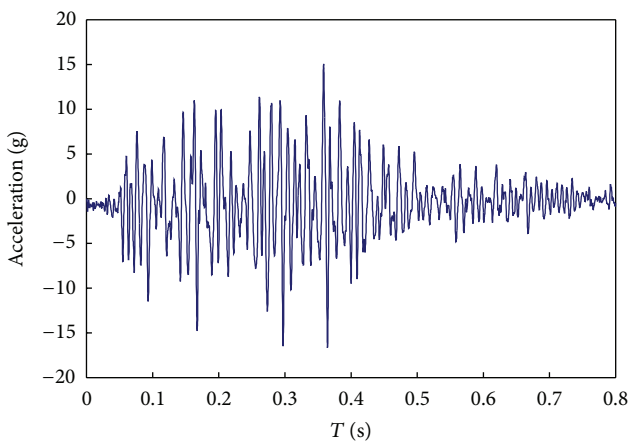


FIGURE 14: Time history of horizontal acceleration recorded by ACC1.

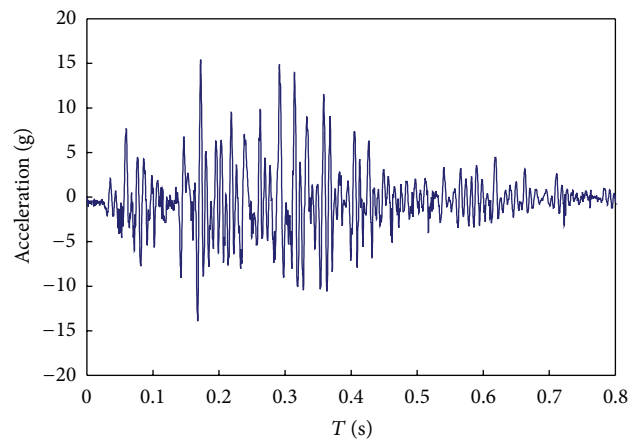


FIGURE 15: Time history of vertical acceleration recorded by ACC1.

the middle section with the height of the model dam. It is shown that the maximum amplitude of acceleration in the horizontal direction and the corresponding acceleration in

the vertical direction tended to decrease slightly in the middle of the dam but increased more rapidly in the upper portion, during the bidirectional shaking (refer to Figure 18). This may

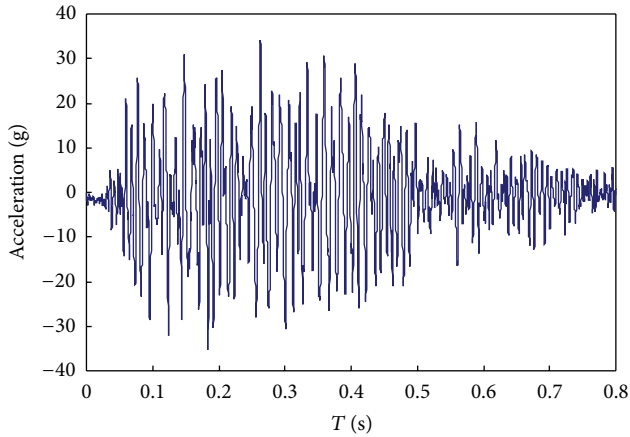


FIGURE 16: Time history of horizontal acceleration recorded by ACC4.

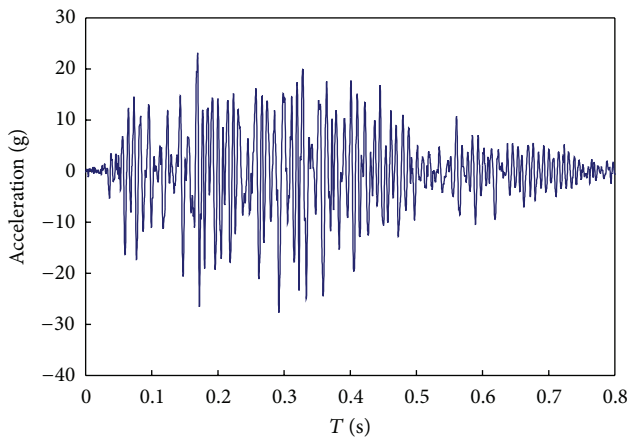


FIGURE 17: Time history of vertical acceleration recorded by ACC4.

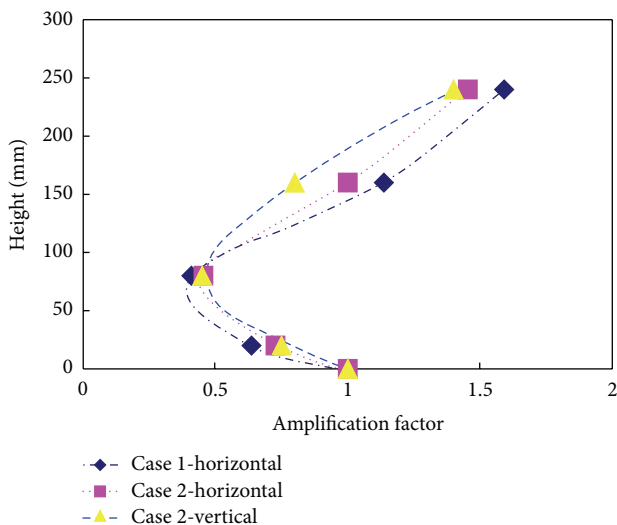


FIGURE 18: Amplitude of response acceleration along the dam height.

result in a higher peak acceleration observed near the dam crest.

5. Conclusion

In summary, two typical centrifuge model tests coupled with the distributed sensor network on a rock-fill dam were carried out to investigate its dynamic response when subjected to uniaxial and biaxial shaking. Good agreement between input motion and the record of shaker table has been observed based on the optimized sensor network. Besides, the distribution of response acceleration along the dam axis is consistent with that obtained from in situ tests and numerical analysis. The sensor network adopted in the dynamic centrifuge model test can provide reliable data to track the dynamic response of rock-fill dam when subjected to an earthquake excited in both the horizontal and vertical directions. It is concluded that the performance of the bidirectional shaker table in centrifuge can be guaranteed based on the test results recorded by the sensor network. The bidirectional shaker table in conjunction with the large centrifuge is proved to be an effective and powerful tool for the design and analysis of high rock-fill dams with high seismic risk.

Acknowledgments

The financial support by the National Nature Science Foundation of China (51009021), Special Scientific Research Foundation of China Institute of Water Resources and Hydropower Research (Yanjil307), and the National Key Basic Research Program of China (no. 2013CB036404) and experimental data and technological support from the Centrifuge Laboratory are gratefully acknowledged.

References

- [1] H. B. Seed, "Considerations in the earthquake-resistant design of earth and rockfill dams," *Geotechnique*, vol. 29, no. 3, pp. 215–263, 1979.
- [2] H. Li, S. Chi, G. Lin, and H. Zhong, "A modified approach for determination of nonlinear properties in seismic response analyses for 200 m high core rock-fill dams," *Canadian Geotechnical Journal*, vol. 45, no. 8, pp. 1064–1072, 2008.
- [3] H. B. Seed, R. Pyke, and G. R. Martin, "Effect of multidirectional shaking on liquefaction of sands," Tech. Rep. PB-258 781, California University, Berkeley, Calif, USA, 1975.
- [4] H.-N. Li, T.-H. Yi, M. Gu, and L.-S. Huo, "Evaluation of earthquake-induced structural damages by wavelet transform," *Progress in Natural Science*, vol. 19, no. 4, pp. 461–470, 2009.
- [5] J. A. Portugal, *Physical modelling with centrifuge [Ph.D. thesis]*, Lisboa College Technician Institute, Portugal, 1999.
- [6] P. Hu, Q. P. Cai, G. Y. Luo et al., "Centrifuge modeling of failure patterns in mixed soil layers induced by normal faults," in *Proceedings of the 17th International Conference on Soil Mechanics and Geotechnical Engineering*, pp. 594–597, 2009.
- [7] C. W. W. Ng, X. S. Li, P. A. van Laak, and D. Y. J. Hou, "Centrifuge modeling of loose fill embankment subjected to uniaxial and bi-axial earthquakes," *Soil Dynamics and Earthquake Engineering*, vol. 24, no. 4, pp. 305–318, 2004.

- [8] T.-H. Yi, H.-N. Li, and M. Gu, "A new method for optimal selection of sensor location on a high-rise building using simplified finite element model," *Structural Engineering and Mechanics*, vol. 37, no. 6, pp. 671–684, 2011.
- [9] T.-H. Yi, H.-N. Li, and M. Gu, "Optimal sensor placement for structural health monitoring based on multiple optimization strategies," *The Structural Design of Tall and Special Buildings*, vol. 20, no. 7, pp. 881–900, 2011.
- [10] T.-H. Yi, H.-N. Li, and X.-D. Zhang, "Sensor placement on Canton Tower for health monitoring using asynchronous-climbing monkey algorithm," *Smart Materials and Structures*, vol. 21, no. 12, Article ID 125023, 12 pages, 2012.
- [11] S. Yin, J. Cui, L. Liu, and S. Wei, "Calibration techniques for low-power wireless multiband transceiver," *International Journal of Distributed Sensor Networks*, vol. 2013, Article ID 754206, 8 pages, 2013.
- [12] D. Wu, D. Zhang, G. Tan, L. Sun, J. Li, and J. Liu, "Improvement and performance evaluation for multimedia files transmission in vehicle-based DTNs," *International Journal of Distributed Sensor Networks*, vol. 2013, Article ID 358267, 10 pages, 2013.
- [13] D. Ho, K. Nguyen, H. Yoon, and J. Kim, "Multiscale acceleration-dynamic strain-impedance sensor system for structural health monitoring," *International Journal of Distributed Sensor Network*, vol. 2012, Article ID 709208, 17 pages, 2012.
- [14] T.-H. Yi, H.-N. Li, and M. Gu, "Characterization and extraction of global positioning system multipath signals using an improved particle-filtering algorithm," *Measurement Science and Technology*, vol. 22, no. 7, Article ID 075101, 11 pages, 2011.
- [15] T.-H. Yi, H.-N. Li, and M. Gu, "Recent research and applications of GPS-based monitoring technology for high-rise structures," *Structural Control and Health Monitoring*, vol. 20, no. 5, pp. 649–670, 2013.
- [16] R. S. Ramires, *Method for data protection against communication failures in wireless smart sensors networks [Ph.D. thesis]*, Polytechnic School, University of São Paulo, São Paulo, Brazil, 2007.
- [17] S. M. S. L. Cheekiralla, *Development of a wireless sensor unit for tunnel monitoring [M.S. thesis]*, Civil Engineering Department and Ambient of the MIT-Massachusetts Institute of Technology, Boston, Mass, USA, 2004.
- [18] D. W. Wilson, G. H. Weber, T. Slankard et al., "Visualization in experimental earthquake engineering," in *Proceedings of the CITRIS Workshop on Sensor, Sensor Networks and Sensor Applications*, University California, Davis, Calif, USA, 2004.
- [19] Y. J. Hou, X. G. Wang, Z. P. Xu, Y. F. Wen, and P. Ibanez, "Development of horizontal and vertical 2D shaker in IWHR 450g-ton centrifuge," in *Physical Modelling in Geotechnics*, S. Springman, J. Laue, and L. Seward, Eds., pp. 245–250, 2010.
- [20] ANCO Engineerings Inc. DANCE USER'S GUIDE, 12, 2010.